Pulse Metal Inert Gas based Wire Arc Additive Manufacturing of an Austenitic Stainless Steel

Cunningham, Chloe

Award date:
2020

Awarding institution:
University of Bath

Pulse Metal Inert Gas based Wire Arc Additive Manufacturing of an Austenitic Stainless Steel

Chloe Rose Cunningham

A thesis submitted for the degree of Doctor of Philosophy

University of Bath

Department of Mechanical Engineering

April 2020

Abstract

Metal additive manufacturing (AM) is having a major impact on the future of production processes providing new alternatives to conventional forging, casting, and machining processing routes. To aid in industrial adoption, qualification and certification processes, an understanding of the effects of the process parameters on the material properties of AM material to obtain a balance between repeatable satisfactory material properties and productivity is required. This thesis reports on Wire Arc Additive Manufacturing, a Directed Energy Deposition process for austenitic Type 316L stainless steel, one of the most commonly used stainless steels due to its combination of strength and corrosion resistance.

This research investigates the effects of deposition rate (0.75 kg/hr and 3.00 kg/hr), heat input (and cooling strategy (60°C and 150°C interpass temperature control, and in-process LN_2 cryogenic cooling localised to the melt-pool) on the materials characterisation and mechanical performance of Type 316L stainless steel produced via WAAM. The addition of silicon to the wire composition is also explored. WAAM machine is developed by the author to study these effects encompassing a Pulse Metal Inert Gas based setup, advantageously feeding the wire coaxial to the welding torch.

The results showed that the process parameters influenced the solidification mode, morphology, δ-ferrite content, texture, grain size, oxide inclusion size and distribution, relative density, and substrate distortion. The results from the mechanical analysis showed that whilst the yield strength and ultimate tensile strength readily exceed the ASTM A240/A240M (2004) specification the process parameters that induce higher cooling rates result in a statistically significant increase in tensile strength. Higher deposition rates however, reduced ductility, which was below that required by ASTM A240/A240M (2004). Relations between oxide inclusion frequency and Feritscope™ measurements prior to deformation with uniform elongation are established, whereas the relative density was found to have a negligible effect on uniform elongation. The wire with additional silicon composition reduced the oxide number frequency and provided higher tensile strength and Young's Modulus than the Type 316L wire composition at 0.75 kg/hr.

In-process cryogenic cooling localised to the melt-pool was demonstrated to improve the overall performance of the WAAM material whilst eliminating interpass dwells periods. The grain size and texture of the low linear heat input, 0.75 kg/hr 316L samples were significantly changed in comparison to the large directional columnar grain growth observed for other processing conditions. This provided major benefits to Young's Modulus for which for the majority of the experiments was significantly lower than the specification for wrought material.

Acknowledgements

It has been a fantastic experience and privilege to study wire arc additive manufacturing and the related physical metallurgy in the past years and I would like to thank Renishaw PLC and EPSRC for funding this research.

I would like to acknowledge my supervisor Professor Stephen Newman for his encouragement towards taking the PhD route. His academic guidance and kindness have been instrumental throughout the process.

From Renishaw, I would like to thank my industrial supervisor, Andy Wescott, and Andrew Davis and Dr Jenna Tong for their willingness to support my research, for sharing their expertise and for the interesting discussions. Thanks to Steve Chandler and Steve Munday for their assistance with wire EDM.

Thanks to my second and third supervisor's Dr Vimal Dhokia and Dr Alborz Shokrani, and Brian Rutter particularly for review of my thesis manuscript. I am grateful to Dr Jie Wang for her interest in my research and the help with the initial tensile tests in the Department of Civil Engineering. I would like to thank Craig Bayliss for teaching me how to weld, and Mathew Ball for his generous help with metallurgical preparation and optical microscopy. Will Bazeley for his assistance with tensile testing, expertise, and wit. I would like to thank the manufacturing lab 'residents': Andy Green, Luke Brodhurst and Paul Yates for their help and general know-how. Thanks too, to Guy Brace and the machine workshop technicians for their help with substrate preparation, and at the time seemingly endless tensile specimen machining. Without the support of these individuals, the past few years would have been difficult, and a lot less enjoyable. Thanks too, to Dr Riccardo Tosi at the MTC Ltd. for helping with the wire chemical analysis.

I would like to thank my parents Bernadette Burke and Mark Cunningham for their relentless support, inspiration, and lessons in hard-work. They have got me to where I am today and continue to steer me in the right direction.

Thanks to Mark and Sarah, and my sister Becky for checking in on me. Also, for my friends for their understanding and escapism when required, with particular note to Megan Henson on the latter.

To Dr Nneji Kemakolam, thank you for the support, laughs, and belief. It is hard to imagine the last few years without you.

Declaration

A large part of the work described in this thesis is based on articles that have been or are intended to be, published elsewhere. For each of them, the candidate C R Cunningham contributed principally to all aspects of the work described therein:

BS PAS 6012. 2019. Wire arc additive manufacturing. Guide. (ASTM WK 69732 under development)

CUNNINGHAM, C. R., WANG, J., DHOKIA, V., SHOKRANI, A. & NEWMAN, S. T. 2019. Characterisation of austenitic 316LSi stainless steel produced by wire arc additive manufacturing with interlayer cooling. *Solid Freeform Fabrication 2016: Proceedings of the 30th Annual International Solid Freeform Fabrication Symposium – An Additive Manufacturing Conference,* 2019.

CUNNINGHAM, C. R., FLYNN, J. M., SHOKRANI, A., DHOKIA, V. & NEWMAN, S. T. 2018. Invited review article: Strategies and processes for high quality wire arc additive manufacturing. *Additive Manufacturing,* 22**,** 672-686.

CUNNINGHAM, C. R., WIKSHÅLAND, S., XU, F., KEMAKOLAM, N., SHOKRANI, A., DHOKIA, V. & NEWMAN, S. T. 2017. Cost modelling and sensitivity analysis of wire and arc additive manufacturing. *Procedia Manufacturing,* 11**,** 650-657.

Table of contents

List of figures

List of tables

Table of Abbreviations

AM	Additive Manufacturing
ANOVA	ANalysis Of VAriance
ASTM	American Society for Testing and Materials
AWS	American Welding Society
BCC	Body Centred Cubic
CMT	Cold Metal Transfer
CRYO	In-process CRYOgenic cooling localised to the melt-pool
DED	Directed Energy Deposition
DI/DO	Digital Input/ Digital Output
E	Young's Modulus
EBSD	Electron Back-Scatter Diffraction
E-DED	Electron beam Directed Energy Deposition
EDS	Energy Dispersive Spectroscopy
EMI	Electromagnetic Interference
E-PBF	Electron beam-based Powder Bed Fusion
FCC	Face Centred Cubic
GND	Geometrically Necessary Dislocations
HHI	High Heat Input
HIT	High Interpass Temperature
IPF	Inverse Pole Figure
L-DED	Laser beam Directed Energy Deposition
LEV	Local Exhaust Ventilation
LHI	Low Heat Input
LIT	Low Interpass Temperature
L-PBF	Laser-based Powder Bed Fusion
MIG	Metal Inert Gas
ODS	Oxide Dispersion Strengthening
OES	Optical Emission Spectroscopy
PA	Plasma Arc
PBF	Powder Bed Fusion
PPE	Personal Protective Equipment
SEM	Scanning Electron Microscopy
TIG	Tungsten Inert Gas
TRIP	TRansformation Induced Plasticity
TS	Travel Speed
TWIP	TWinning Induced Plasticity
UTS	Ultimate Tensile Strength
WAAM	Wire Arc Additive Manufacturing
WFS	Wire Feed Speed
σ_{ys}	Yield strength

Introduction

Chapter 1

1.1 Introduction

This research investigates wire arc additive manufacturing (WAAM) for producing austenitic Type 316L stainless steel to establish the material properties relative to conventional material standards. In this chapter, WAAM is introduced within the field of additive manufacturing (AM) together with a description of its advantages compared to other directed energy deposition (DED) processes. The effects of the comparatively high levels of heat input in WAAM are discussed, highlighting the need for heat management strategies. Furthermore, austenitic stainless steel is introduced as a materials category and its industrial applications and use in AM are discussed.

The field of AM is has been subject to many developments and innovations in recent years. Early forms of AM for polymers date back as far as the 1960s (Gibson et al., 2010). The development of modern commercial metal AM processes for functional parts began in the 1990s, although the initial application of fabricating whole metallic components additively was first patented by Baker (1925). This utilised welding technology to develop example parts as shown in Fig. 1.1. Introductory literature on the various additive manufacturing technologies is provided by Gibson et al. (2010) and Frazier (2014) provides a more recent overview of AM technology challenges, qualification, business aspects.

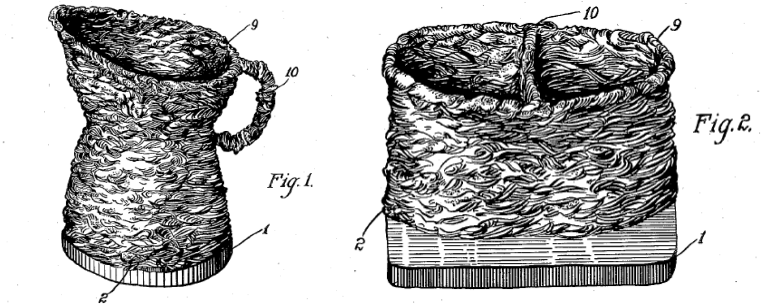

Figure 1.1 Example parts as demonstrated in a patent assigned to Baker (1925)

AM at a fundamental level involves the combination of relative motion between a fusion source and feedstock. In contrast to polymer AM, the molten pool is typically small in metallic AM and subject to much higher temperatures (Milewski, 2017). Combined with relatively rapid travel speeds, this produces high cooling rates and large thermal gradients (Guan et al., 2014). Depending upon the material or alloy being deposited, these high cooling rates can produce unique solidification grain structures and non-equilibrium grain structures that are not possible to produce using traditional processing methods (Gibson et al., 2010, Frazier, 2014). For further reading, Sames et al. (2016) review the critical aspects of the metallurgy and processing science of metallic AM and Bourell et al. (2017) discuss the material selection in AM and the implications for process selection.

In recent years, AM has become an established manufacturing route alongside casting, forming, machining, joining and surfacing processes. Defined by BS ISO/ASTM 52900:2015

as “a process of joining materials to make objects from 3D model data, usually layer upon layer”, AM is often cited as offering direct and decentralized production, with reduced dependency on expensive and dedicated tooling. Often greater levels of complexity compared to traditional manufacturing is offered.

Whilst the field of AM has been subject to many technological advancements in the past three decades, the high cost (purchase, operation, maintenance, and depreciation) of AM machines and materials present major challenges to AM progression (Wu et al., 2017b). There has been limited ability to replace conventionally made parts economically, particularly large parts. The application of AM has therefore been primarily focused on niche, high-value, and technically-demanding parts of small-build volumes, where the benefit of greater design freedom can offset the high cost.

1.1.1 Directed Energy Deposition

Defined by BS ISO/ASTM 52900 (2015) as an “additive manufacturing process in which focused thermal energy is used to fuse materials by melting as they are being deposited”, DED may use laser beam (L-DED), electron beam (E-DED) or an electric arc as a thermal energy source as outlined in Fig. 1.2 (ASTM F3187-16, 2016). Although not stated in the standard, there are examples of where thermal energy sources are also combined (Acherjee, 2018). Powder or wire is used as feedstock, or both may be used concurrently (Abioye et al., 2013), and multiple wires may also be used (Martina et al., 2019). The electric arc technology can be Metal Inert Gas (MIG), Tungsten Inert Gas (TIG) or Plasma Arc (PA) which are discussed further in §1.1.3.

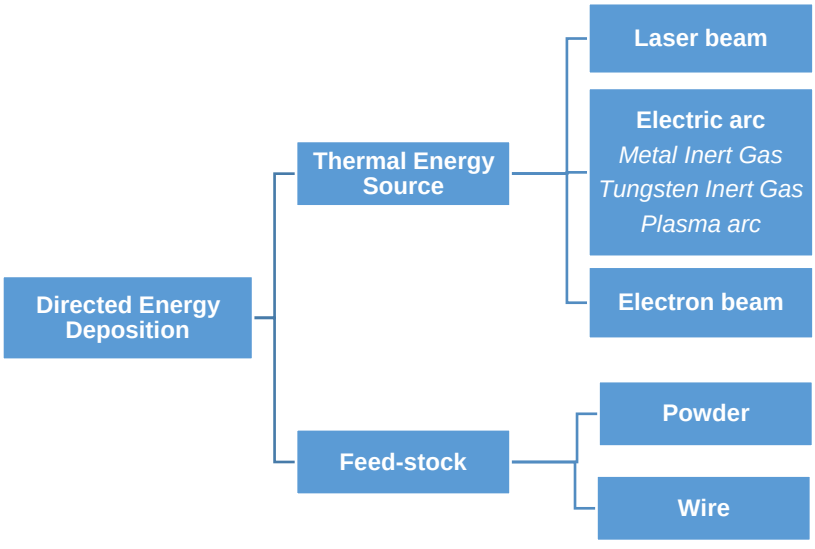

Figure 1.2 DED classified by power source and feedstock

Unconstrained build volumes mean that DED processes are more suited to the manufacture of larger part types than alternative AM approaches such as metal Powder Bed Fusion (PBF) which operate within enclosed inert build chambers (Bhavar et al., 2014) with substantially lower deposition rates as shown in Table 1.1. PBF has been investigated

extensively within the literature with a continuously expanding comprehensive understanding of defect generation (Khairallah et al., 2016), predictive simulation and process monitoring requirements (Grasso and Colosimo, 2017), effects of process parameters and material capability and can be considered a more mature AM technology. However, in recent years, DED technologies have broadened the applicability of AM beyond the scope of PBF by enabling the cost-effective AM of medium to large complexity metallic components. As shown in Table 1.1, Binder Jetting processes, also provides a high deposition rate for AM, however, limits are placed upon part size due to the need for high-temperature burn-out of the binder element, whilst part performance is often limited by porosity.

Table 1.1 Typical process characteristics of powder bed fusion, DED and binder jetting.

Process Characteristics	**Powder bed fusion**	**DED**		**Binder Jetting**
Feedstock	Powder	Powder	Wire	Powder
Deposition Rate (cm^3/h)	5-20	Up to 300	500 - 1300	16-8200
Roughness	Ra 4- Ra 6	Ra 10- Ra 200	Ra 500	-
Layer thickness	0.02-0.1mm	0.3-1.5mm	1-2mm	0.05
Build volume	Limited	Unlimited	Unlimited	Limited
Reference	(Renishaw, 2017, Renishaw, 2016)	(Candel-Ruiz et al., 2015)	(Williams et al., 2016)	(Desktop Metal, 2017)

A compromise of the high deposition rate in DED is that the as-built surfaces can be uneven and of a wider manufacturing tolerance than PBF and conventionally manufactured parts. This means that DED processes can often be reliant on post-process finishing to meet dimensional and geometric requirements. However, even with post-processing accounted for, the substantial raw material (Yilmaz and Ugla, 2016) and cost savings have been demonstrated in comparison to CNC machining and forging processes (Martina and Williams, 2015). Besides new part manufacture, as a DED process, WAAM can also be readily applied to feature addition and repair applications. DED processes usually do not require specific tooling, as in casting and forging, therefore, manufacturing costs can be significantly lower specifically for low production volumes of conventionally forged parts and a significant reduction in cycle time can be expected (Dutta and Froes, 2014).

The ability to use wire as feedstock in DED offers high-efficiency material deposition, eliminates the need for peripheral powder recycling processes (Tang et al., 2015), and reduces health and safety concerns. A significant reduction in the price of wire per kilogram is often found compared to powder in a range of engineering materials including aerospace alloy Ti-6Al-4V (Martina and Williams, 2015), stainless steel and nickel-based superalloys as shown in Table 1.2.

Table 1.2 Cost per kilogram in wire and powder compiled from supplier quotes (2016).

Feedstock	Cost per kilogram (£/KG)			
	Ti-6Al-4V	*Inconel 718*	*Inconel 625*	*Stainless Steel 316L*
Wire	120	58	49	12
Powder	280	80	80	40

1.1.2 WAAM

WAAM is a DED technology that uses an electric arc as a fusion source to melt wire feedstock. In principle, any arc welding fusion welding process covered in ISO/TR 25901-3:2016 can be integrated into a WAAM machine. However, due to the need for automated, high-quality deposition (i.e. low contamination and high levels of cleanliness), the following arc technologies are commonly applied:

a) MIG;
b) TIG; and
c) PA

In MIG, the wire is fed co-axially through the torch as a consumable electrode as shown in Fig 1.3a. Whereas the wire is separately fed into the melt pool in the non-consumable electrode PA and TIG processes as shown in Fig 1.3b and may require re-orientation for consistent deposition allowing for changing tool path directions in WAAM.

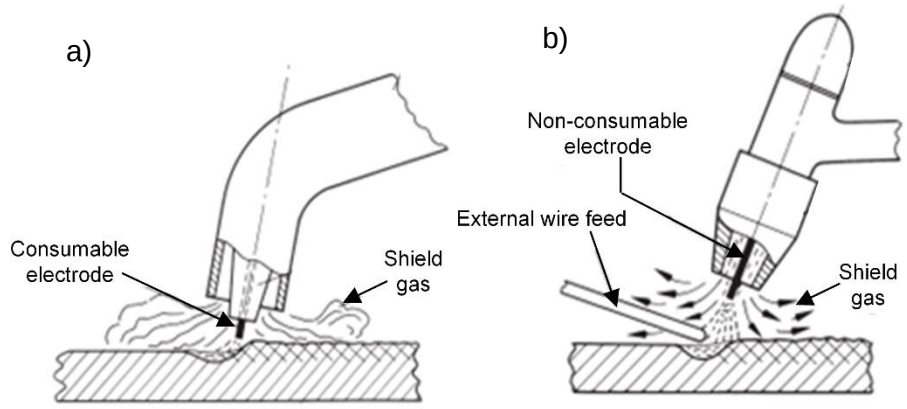

Figure 1.3 Schematic of a) consumable (MIG/MAG) b) non-consumable (TIG/TAG, PA) arc technologies

The weldability of materials for each arc technology can differ and guides the selection of arc technology for WAAM. The weldability may vary depending on the polarity applied. Typically, non-consumable electrode processes (i.e. PA and TIG) use direct current electrode negative polarity to avoid overheating and deterioration of torch elements. However, for materials that require cathodic cleaning action due to oxides on the surface, alternating current and variable polarity might be used for non-consumable electrode arc technologies.

Table 1.3 presents a non-exhaustive list of several commercial WAAM machine manufacturers and/or service providers able to produce WAAM components and the

advertised range of materials available. The aerospace industry, as an early adopter of WAAM, has seen the process mature significantly for the production of large titanium alloy aerospace components previously conventionally forged and machined. For example, WAAM parts produced by Norsk Titanium achieved US Federal Aviation Authority certification for the production of WAAM parts for the Boeing 787 Dreamliner in 2015 (Metal Powder Report, 2017). Other applications of WAAM have been demonstrated in space (Relativity Space, 2019), nuclear (Kussmaul et al., 1983) and marine industries (Huisman, 2020), as well as in design, architecture (MX3D, 2019) and art (Print Pioneers, 2020). Many of the companies referenced have become involved in WAAM within the last decade indicating that WAAM is becoming increasingly industrialized, with rapid growth in both numbers of end-users and equipment suppliers.

Table 1.3 Commercial WAAM machine manufacturers and/or service providers categorised by material

Commercial WAAM machine manufacturers and/or service providers	Materials advertised
Norsk Titanium AS (2017)	Ti6Al4V
Gefertec (2020)	Inconel 718, 625, Ti6Al4V, INVAR and range of mild steels, stainless steel & aluminium alloys.
Prodways (2017)	Ti6Al4V
Mazak (2020)	Not specified
Glenalmond Group (2020)	Ti6Al4V, Inconel
WAAM3D (2020)	Ti6Al4V, Inconel, Aluminium 6213 + more
AML3D (2020)	Aluminium 2319, 4043, 5183, 5356, 5087 Ti-6Al-4V, Grade 5, Grade 23, INVAR, Inconel 625, Inconel 718, Nickel Aluminium Bronze, ER70, ER80, ER90, ER120, Maraging grade 250, Stainless (316L, 2205)
Big Metal Additive (2020)	Not specified

1.1.3 Advantages of WAAM

Compared to electron beam and laser, the use of an electrical arc as a fusion source provides several advantages. A major benefit of the WAAM process relates to the low capital investment as the components of a WAAM machine may be derived of open architecture equipment, sourced from an array of suppliers in the mature welding industry (Anzalone et al., 2013). This allows the production of parts with a high level of cost-effectiveness compared to Laser-based Powder Bed Fusion (L-PBF) and conventional forging and CNC machining (Cunningham et al., 2017, Martina and Williams, 2015). Meanwhile, with typical layer heights of 1-2mm, surface waviness of 500 μm (Williams et al., 2016) and deposition rates up to 10 kg/hr (Martina et al., 2019), WAAM productivity and material removal if required is similar to L-DED and E-DED approaches.

WAAM does not need a vacuum environment to operate as required in E-DED (Milewski, 2017). As such, prolonged setup and ramp-down times can be avoided which is also advantageous in materials that degrade with long-term exposure to high temperatures, for

example, over-ageing of precipitate hardened materials (Sames et al., 2017). E-DED processes also have increased susceptibility to element depletion and evaporation during processing Taminger and Hafley (2003), which can affect final part performance and require custom feedstock or additional processing to mitigate the losses.

In comparison to laser-based methods, the use of the electrical arc offers a higher efficiency fusion source (Jackson et al., 2016). This is of benefit from an energy consumption perspective, in particular, for reflective metal alloys of poor laser coupling efficiency such as aluminium, copper (Gu et al., 2012) and magnesium (Guo et al., 2016).

1.1.4 The influence of WAAM heat input on part quality

WAAM has a lower heat source intensity than L-DED and E-DED as shown in Table 1.4 providing a unique processing characteristic, which influences the residual stresses, microstructure, and material properties.

Table 1.4 Adapted from welding data provided by Lancaster (1987).

DED fusion source		Heat source intensity (W/cm^3)
Laser		10^{10} -10^{12}
Electron beam		10^{10} -10^{12}
Electric arc	Plasma arc	5 x 10^6 - 5 x 10^{10}
	Gas metal arc	5 x 10^6 - 5 x 10^8

WAAM develops lower cooling rates and larger melt pools than L-DED, as the fusion source moves more slowly to provide the heat for melting. This cooling rate decreases further, for example, with the use of a weaving tool path. Additionally, high current setting and continuous deposition without cooling may lead to further reduced cooling rates relative to L-DED. In contrast, WAAM typically offers higher cooling rates and lower build temperatures than E-DED, due to the limited heat dissipation within the high vacuum environment which can lead to substantial heat accumulation during a build.

Williams et al. (2016) and Ding et al. (2015a) regarded the high levels of residual stress and part distortion caused by the high heat input in WAAM a major obstacle to industrial uptake of the process. In-process distortion can lead to failure in meeting geometrical properties and can affect the stability and accuracy of the weld bead if contact tip distance error occurs. Whilst part distortion may be constrained by fixtures during the build, these are often required to be robust and the cost can erode the often-cited benefit of tool-less manufacture in AM, large distortions can occur upon release from a fixture as shown in Fig. 1.4 (Xu et al., 2018a). Heat treatments can be used to eliminate severe distortion, although this method cannot be relied upon to remove the distortion completely, particularly for large builds. The significant residual stress can also affect the fatigue life (Barsoum and Barsoum, 2009), and stress corrosion resistance (Toribio, 1998) and introduce microstructural

features such as dense dislocation network structures and twin grain boundaries (Pham et al., 2017) that differ from conventionally manufactured parts.

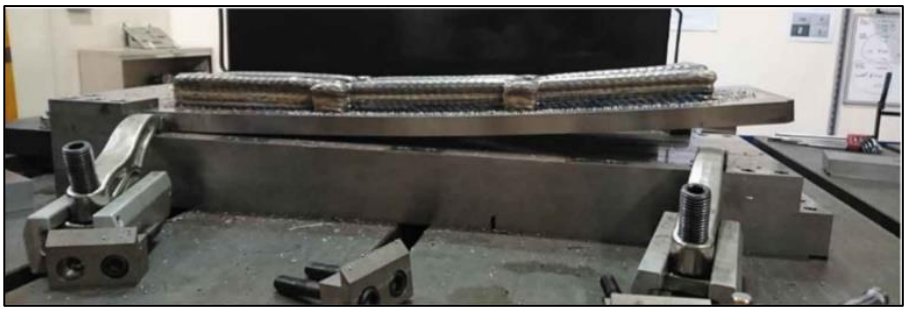

Figure 1.4 Structural distortion of a WAAM part due to residual stress (Xu et al., 2018a)

The thermal conditions of the AM process also strongly affect the process-structure-property relationship for a given material. The fusion source heat input determines the thermal gradient (G) and growth rate (R) in solidification, affecting the solute segregation, morphology and scale of microstructural features as shown in Fig. 1.5.

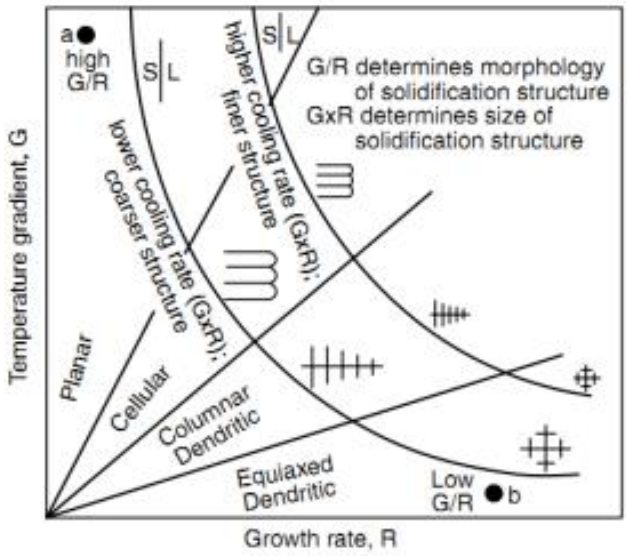

Figure 1.5 Solidification map showing the variation of melt pool microstructures as a function of the temperature gradient (G), growth rate (R) (Kou, 2002)

The thermal conditions in WAAM mean that a fine equiaxed microstructure tends to be uncommon, as, beyond an epitaxial growth zone close to the substrate, the high levels of heat input promotes a competitive grain growth process in which the total number of grains reduces leading to grain enlargement (Kou, 2002) and anisotropic material properties. The macroscale textured columnar grain structures that are typical in the microstructure of Ti-6Al-4V produced by WAAM without any process enhancements to interrupt the competitive grain growth, can be seen in Fig 1.6 (Baufeld and van der Biest, 2009).

The coarse, columnar type of microstructure directly impacts material properties. For example, refinement of the grain size improves tensile strength according to the well-known Hall-Petch equation (Hall, 1951). Although a strongly textured microstructure can be

beneficial for applications requiring high temperature creep resistance (Murr, 2015), at regular operating temperatures it can often provide lower mechanical strength, toughness and corrosion resistance compared to a fine equiaxed microstructure (Reed, 2006). Heat treatment cannot always be a solution for refining the microstructure as there is a lack of driving force in the solidified WAAM deposit for the recrystallisation to occur and generate newly refined grains (Collins et al., 2016). The initial morphology can even persist through phase transformations, as demonstrated in WAAM of Ti-6Al-4V, where the strong fibre texture of the large prior β grains decompose to an undesirable α texture (Donoghue et al., 2016).

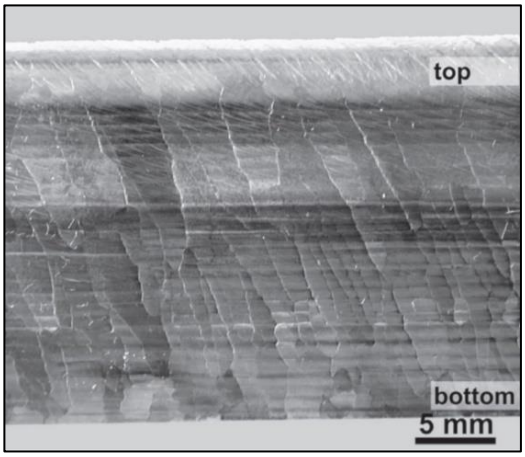

Figure 1.6 Large columnar WAAM grain growth shown in Ti-6Al-4V (Baufeld and van der Biest, 2009).

Furthermore, whilst precipitation hardened materials may be solutionised and aged in a post-build heat treatment to develop the desired microstructure, processing issues may arise during the WAAM process as a result of grain growth and solute segregation during deposition leading to defective parts. Solidification cracking is promoted by excessive solute segregation, in the presence of high levels of residual stresses and enlarged grain size (David et al., 2003, Withers, 2007), both of which are common in WAAM. The crack resistance is particularly poor in materials with a high coefficient of thermal expansion and extensive solute segregation, such as heat treatable aluminium alloys and materials where crystal structure is easily degraded due to the heat-induced grain coarsening, such as in ferritic stainless steels (Amuda and Mridha, 2013).

Instances where the high levels of heat input and build temperatures can be undesirable include for Inconel 718 (Baufeld, 2011) and Inconel 625 (Liu et al., 2013), where the deleterious Laves phase to develop. Other examples include the sensitization of carbides in stainless steels, and prevention of the development of finely dispersed of solid-state strengthening precipitates in the WAAM production of the aluminium alloy 2219 (Bai et al., 2015a). Lower heat input processes may also act to reduce porosity content due to the reduction in droplet temperature as well as gas solubility in the weld pool (Pal and Pal, 2010). As AM processes have multiple complex thermal cycles, the accumulative effects

of the heat input can influence the boundary conditions of solidification characteristic. As the heat input is high in WAAM, the cooling rate can vary widely from a relatively high cooling rate by conduction at the substrate to low cooling rates later on in the build as heat accumulates between layers as heat dissipation becomes less effective and pre-heat is usually present from previously deposited material (Wang et al., 2016a). The accumulation of heat can also affect the geometry of the weld bead in the build direction, which can lower the material efficiency and increase the amount of post-process machining. In the worst cases, heat accumulation can cause complete loss of weld bead dimensional control (Lu et al., 2017).

Heat accumulation is also affected by the part design where heat is rapidly dissipated by conduction through the build platform for the first layer as shown in Figure 1.7a. Depending on a thin wall, or bulk deposition types as shown in Fig 1.7b and Fig 1.7c respectively, the path planning strategies and the boundary conditions for solidification can vary locally throughout the build. The varied thermal gradient and growth rate can translate to transitions in the microstructure. Local variations in material properties have been attributed to different microstructures in the top layers in contrast to the middle layers for WAAM deposits in Ti-6Al-4V (Wang et al., 2012), maraging steel (Xu et al., 2018b) and Al-6.3%Cu (Cong et al., 2017).

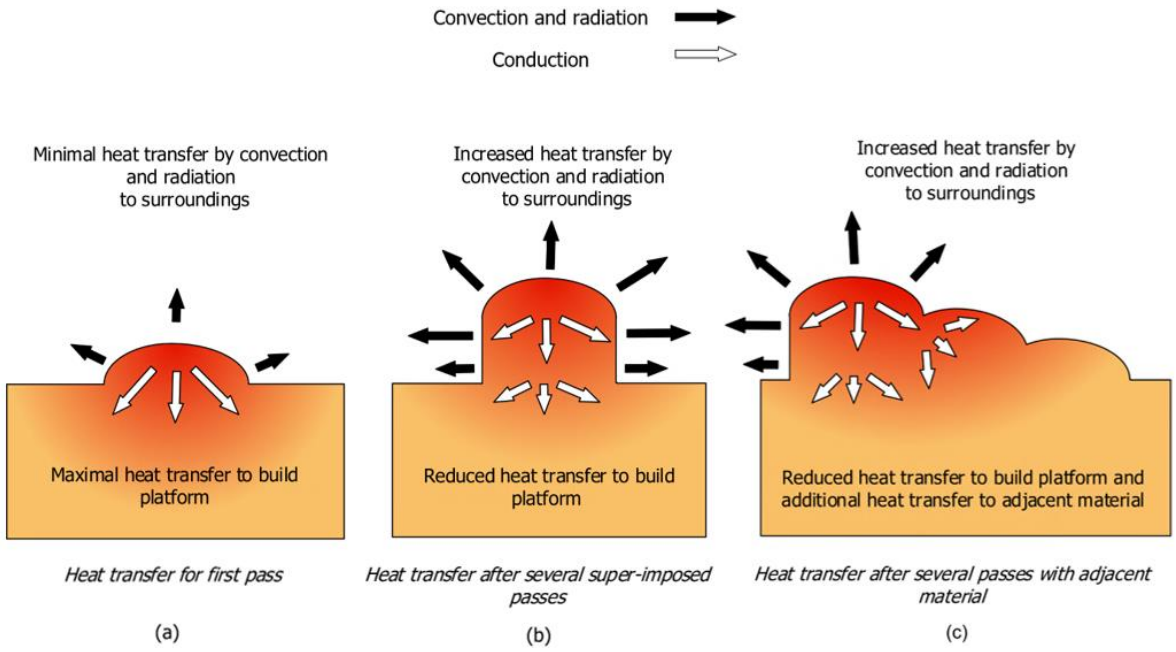

Figure 1.7 Schematic diagram of the heat dissipation modes a) at the beginning of WAAM b) during the build of a thin wall part and c) for a part with overlapping weld beads

Research and developments have allowed the WAAM process to develop production capability number of materials where static mechanical properties are close to those found in wrought and cast can be produced (Pan et al., 2018). The yield strength (σ_{ys}), ultimate tensile strength (UTS) and elongation of several WAAM materials are shown in Table 1.5, and it can be seen that although satisfactory performance is achieved in Ti-6Al-4V with

additional inter-layer rolling. In Aluminium 2219 and Inconel 718, the mechanical properties are inferior to that of wrought with substantial anisotropy, indicating that further research is required to elevate the material properties of WAAM components.

Table 1.5 WAAM mechanical properties reported in the literature compared to industrial standards

Material/ Orientation	Process	σ_{ys} (MPa)	UTS (MPa)	Elongation (%)	Ref.
Ti-6Al-4V	**Wrought**	**≥830**	**≥900**	**≥10**	**(BS EN 3312, 2012)**
(X-Y)	As-built	870±30	920±20	12±5	(Martina et al., 2013)
(X-Y)	Rolled	1030±5	1080±15	13±1.5	
(Z)	Rolled	990±30	1080±5	13±1	
(X-Y)	As-built	868	971	8.6	(Antonysamy, 2012)
(Z)	As-built	803	918	14.5	
Inconel 718	**Wrought**	**≥1034**	**≥1276**	**≥12**	**(SAE International, 1965)**
(X-Y)	As deposited	473 ± 6	828 ± 8	28±2	(Baufeld, 2011)
Aluminium 2219	**(T851)**	**≥317**	**≥427**	**≥8**	**(SAE International, 2017)**
(X-Y)	As-built	114±4.8	263±0.5	18±0.5	(Gu et al., 2014)
(Z)	As-built	106±0.8	258±2.2	15.5±1	
(X-Y)	Special HT	269±28,	418±22	10.24	(Bai et al., 2017)
(Z)	Special HT	254±28	365±28	7.44	

To be able to leverage the advantages of WAAM for production of engineering components, the effects of the high levels of heat input in WAAM require management tailored to the material and its physical metallurgy. The heat input can be influenced through the primary process selections and path planning strategy. Additional processes may also be used to enhance the WAAM process to minimise or mitigate the heat-related processing challenges and reduce the post-processing required. This is detailed in Chapter 3, which reviews the primary process selections, additional processes and build strategies that may be used for heat management in WAAM.

1.1.5 Austenitic stainless steels

Since their invention at the beginning of the 19th century, stainless steels have evolved into an important class of engineering materials that are widely used in a variety of industries and environments. Stainless steels are classified based on the predominant metallurgical phase present or ability to form hardening precipitates with ageing heat treatment and include martensitic, ferritic, austenitic, duplex or precipitation hardening stainless steels. The global stainless steel market size is projected to reach USD 133.84 billion by 2025 with the austenitic 300 series worth USD 71.9 billion by 2025 at an estimated compound annual growth rate of 5.1% (Grand View Research Inc, 2019).

Austenitic stainless steels are widely used due to their excellent corrosion resistance and because they are readily formed and durable. Out of the austenitic stainless steels, Type 304 and Type 316 grade stainless steels comprise the first and second most used stainless steel alloys globally. The popularity of the Type 316 grade of stainless steel can be attributed to the combination of excellent thermodynamic performance by retaining a predominantly

face-centred cubic (FCC) crystal structure at all temperatures and the high levels of corrosion resistance. Typical applications of Type 316 stainless steel take advantage of its combination of relatively high-temperature strength performance and corrosion resistance.

It is a widely used material within the nuclear industry (Cattant et al., 2008, Yu et al., 1992). The first wall panel, an important assembly within nuclear power plants, is a complex assembly of type 316 parts (Baldev et al., 2013) manufactured in multiple steps including machining, assembling, pre-welding, HIP, post-machining and final heat treatments. Such assemblies with multiple manufacturing stages are strong candidates for applications of AM where the benefit of part consolidation may prove advantageous (Zhong et al., 2017) and WAAM in particular due to the scale of the parts. For an AM material to replace conventionally manufactured products in this industry, minimum standards regarding the stress corrosion cracking, corrosion fatigue, and irradiation resistance must be achieved. Other applications of Type 316L stainless steel include as a biomaterial for small fixation devices such as pins, screws, and plates (Breme et al., 2016), chemical processing equipment including pulp and paper and textile processing (Garner, 2017) and parts that are exposed to marine environments such as sea-water pump impellers, flash chamber wall linings, screens and demisters in multi-stage flash distillation desalination plants, and structures (Glover, 1982). The stability of the FCC structure at low temperatures means that austenitic grades such as Type 316 stainless steel are also uniquely suited to cryogenic applications.

Whilst Type 316L stainless steel has been broadly investigated in the field of PBF, investigations into the capability of WAAM for manufacturing parts of Type 316L stainless steel has been comparatively limited. In particular, the interaction of the heat input, interpass temperature and cooling strategy on the material properties is not well understood despite being able to erode the cost-effectiveness of WAAM, a key driver in its application. This is reviewed in Chapter 4, which describes the welding metallurgy and highlights the current state-of-the-art and limitations in WAAM of Type 316L stainless steel.

1.2 Aims and objectives

This research aims to establish the effects of processing parameters on the materials characterisation and mechanical performance of Type 316L stainless steel produced by WAAM. The processing parameters investigated include the deposition rate, linear heat input cooling strategy by interpass cooling and in-process cryogenic cooling behind the melt pool and addition of silicon to the wire chemical composition.

The main objectives of this research are presented as follows:

i. To critically study the process selections, state-of-the-art build strategies and additional processes in WAAM, and evaluate their capability with respect to addressing WAAM heat-related materials processing challenges. (Chapter 3)
ii. Review the literature on the welding metallurgy and materials characterisation for WAAM of Type 316L stainless steel. (Chapter 4)
iii. To design, specify and assemble a WAAM research machine capable of implementing interpass temperature control build strategies and cryogenic in-process cooling near the melt-pool. (Chapter 5)
iv. Investigate the effects of heat input and interpass temperature control build strategy with varying silicon wire composition across a range of allowable heat input parameters and deposition rates (Chapter 6)
v. Compare the effects of WAAM implemented with an interpass temperature control build strategy and in-process additional cooling with cryogenic LN_2 behind the melt-pool for a range of deposition rates and allowable linear heat inputs. (Chapter 6)

Based on background and context outlined in Chapter 1, this aim, and the objectives are believed to represent a valid research theme that is relevant to the high-value manufacturing sector. It is also believed that areas have not been previously investigated, creating an opportunity for the creation of new knowledge in the field of AM.

1.3 Research boundaries

The research to be undertaken can be considered to be constrained by four major research boundaries presented in Fig. 1.8, namely material, welding technology, additional processes & build strategies, and part type.

The welding technology is restricted to high energy density power beam approaches that are suited to DED. As described in §1.1.4 WAAM has several benefits compared to L-DED and E-DED and is identified as the high energy density welding technology to be investigated. Within this category, the pulse-MIG based WAAM approach is investigated due to the high deposition rate achievable, and the benefits in terms system and path planning complexity that occur with the co-axial wire feed relative to the welding torch.

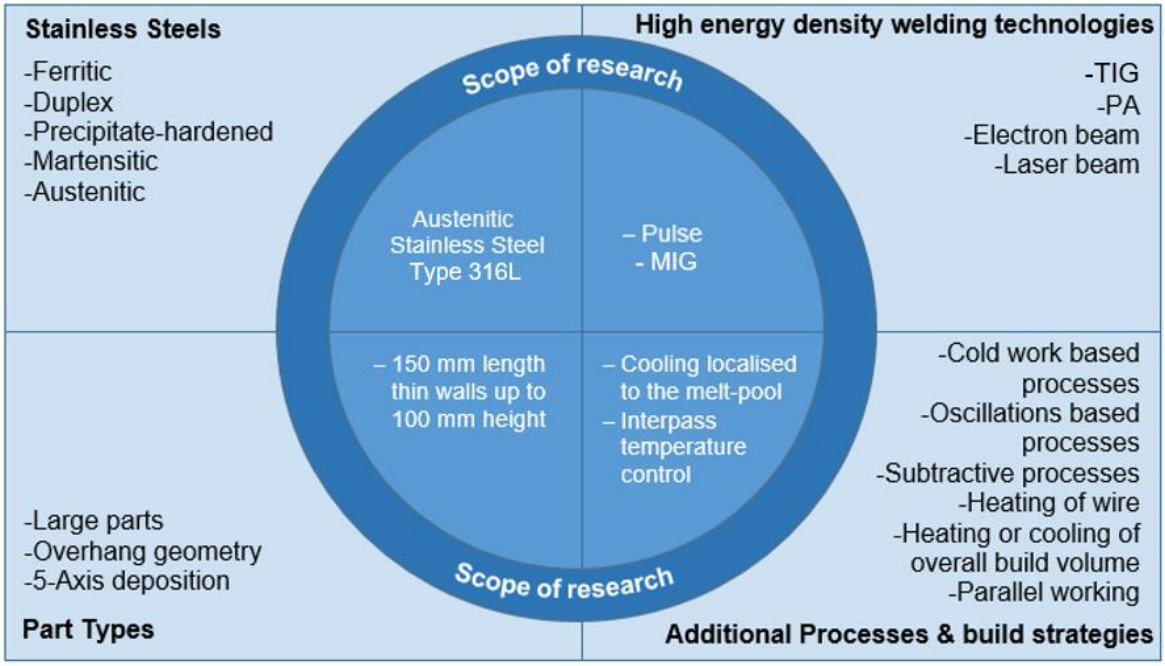

Figure 1.8 Scope of the research defined by the research boundaries

The material to be investigated is the Type 316L austenitic stainless steel. This is a commonly used alloy both conventionally and within AM with major commercial importance due to the combination of corrosion resistance, strength and ductility offered as outlined in §1.1.6. The part types to be developed with the WAAM system in this research are arbitrarily defined as less than 150 mm in any direction, prismatic and comprise of thin wall sections only. This size is considered adequate for extracting samples for materials characterisation as outlined in §4.5, whilst large enough to be representative of larger parts typically produced by WAAM.

Besides the research boundaries presented in Fig. 1.8, the research is limited by the evaluation criteria that are used to characterise the material performance. While the dynamic performance and corrosion resistance are also important in the application of AM for type 316L stainless steel parts this research focuses primarily on the correlation of the microstructural features, texture, phase content & ferrite morphology, oxide inclusion diameter and frequency, fracture surface dimple size and frequency, and chemical composition analysis to the monotonic mechanical properties (tensile strength, Young's modulus, uniform elongation, micro-hardness) and physical properties (relative density and distortion). While the geometry of the WAAM deposit is important to the so-called Buy-to-Fly ratio in the aerospace industry. This research focuses on the intrinsic physical and mechanical properties to understand the process-property relationship with several authors showing methods for improving wall waviness (Geng et al., 2018, Yehorov et al., 2019), which might be deployed once the region of the process map for desirable performance characteristics is identified.

1.4 Thesis structure

This thesis investigates the WAAM process for additively manufacturing (AM) austenitic Type 316L stainless steel. The overall thesis structure is presented in Fig. 1.9 and has been organised into 7 chapters. Chapter 2 and Chapter 3 reviews the strategies and processes for heat management in WAAM and the welding metallurgy and current state-of-the-art in WAAM of Type 316L stainless steel, respectively. Chapter 4 outlines the research methodology. Chapter 5 presents the experimental testing carried out to further investigate the capability of the process, and the impact of the process variables. Chapter 6 discusses the experimental results and Chapter 7 draws conclusions from the research and identifies areas for potential future work.

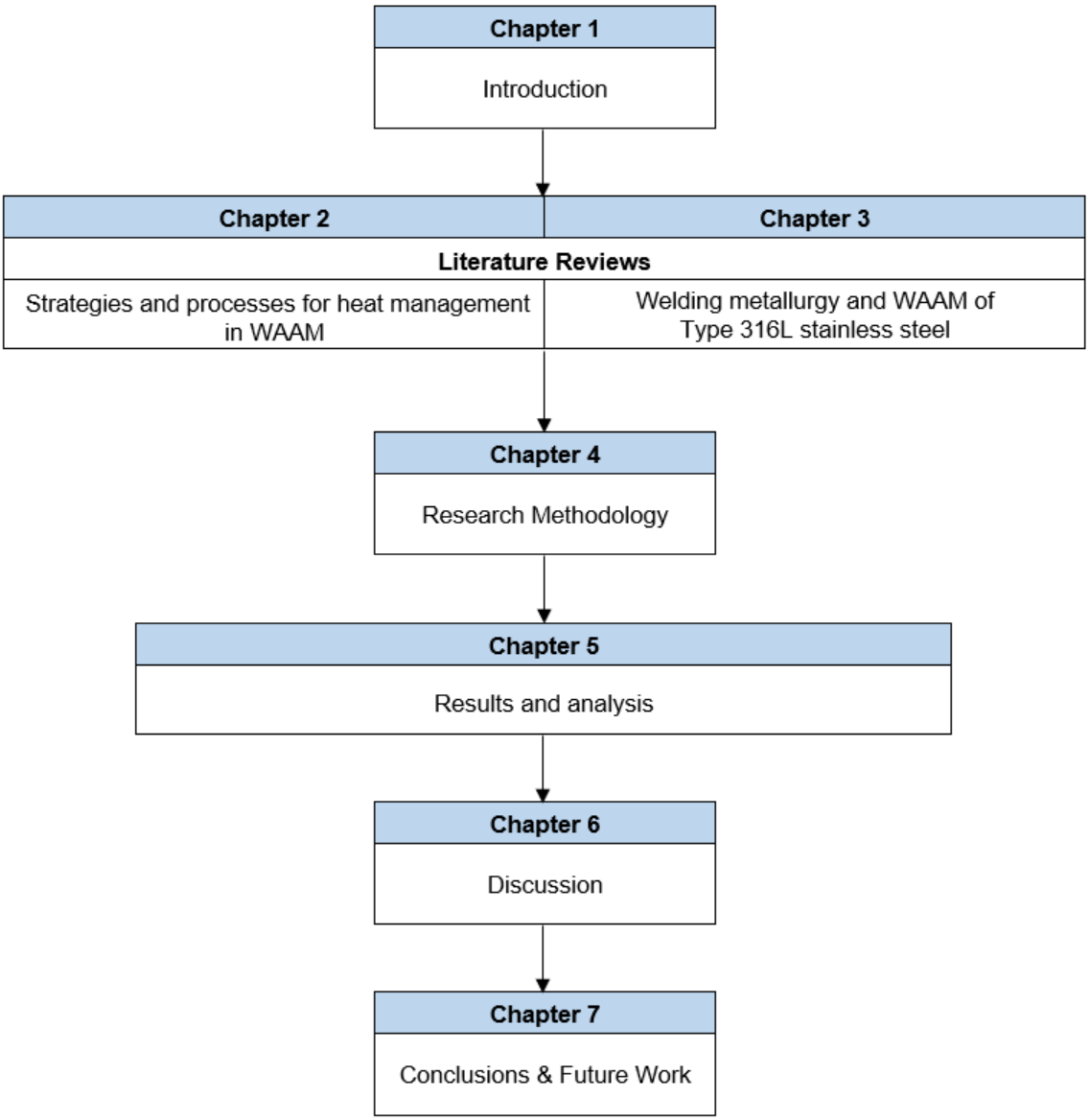

Figure 1.9 Organisation of thesis chapters

Strategies and processes for heat management in WAAM

Chapter 2

2.1 Introduction

With the growing acceptance in the market for additively manufactured end-use products, the development of strategies and processes to overcome the heat-related materials processing challenges in WAAM are of prime importance. This review outlines how the heat-related materials processing challenges can be mitigated through considered primary process selections and build strategy, and enhancement of the as-built quality through additional processes. An overview of the primary process selections, additional processes and build strategies that may be used are presented, concluding with a capability framework for the heat-related materials processing challenges that may be addressed by the current state-of-the-art approaches in WAAM.

2.2 Primary process selections in WAAM

The primary process selections include the welding technology, welding process parameters, shield gas, wire, motion system and substrate as shown in Fig 2.1.

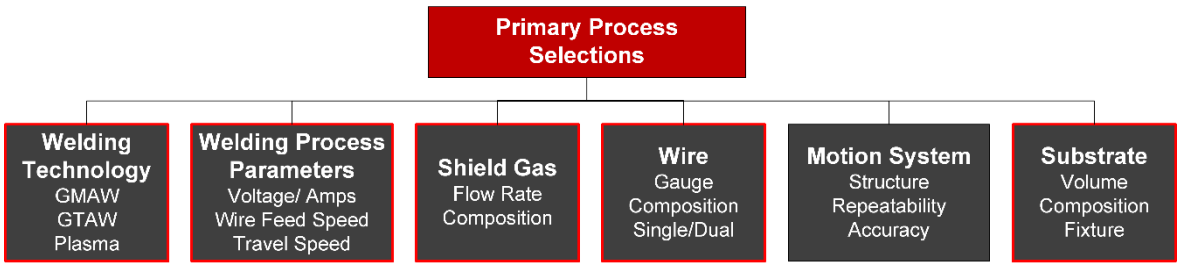

Figure 2.1 Primary process selections to perform materials characterisation in WAAM

All primary process selections have the potential to change the heat input and subsequently the material processing challenges faced in WAAM. The motion system is also important in terms of maintenance of arc length and the relative position of the wire on heat input and weld bead dynamics (Wu et al., 2017a). However, a discussion will be omitted in this chapter as modern motion systems provide high levels of repeatability and accuracy, leading to a minimal influence on the heat-related processing challenges. Furthermore, the welding technology that may be used has been covered in §1.1.2, with each electric arc category and variants within also covered in detail by Pan et al. (2018). The following sections explore how the remaining primary process selections can influence the heat input of the WAAM process.

2.2.1 Welding process parameters

The welding parameters, including current (I), voltage (V), wire feed speed (WFS) and travel speed (TS) are instrumental to the thermal profile in WAAM and thus the material properties, dimensional stability and wettability of substrate (Wu et al., 2017a). The heat input is determined by the following equation:

$$Heat\ input = \frac{VI}{TS}$$

Constant specific heat input is represented by the WFS/TS ratio and is one way to ensure adjustments of the process parameters will also result in stable deposition. Williams et al. (2016) found that a WFS/TS ratio of 30 effectively resulted in stable deposition for PA-based WAAM of Ti-6Al-4V. Many welding power supplies include synergic welding programs to ensure welding processes are stable for a given material. However, these have been designed for single-pass welding processes i.e. cool substrate, synergic programs may not remain suitable if heat accumulates during a WAAM build. Due to the narrow processing window in WAAM, there is subsequently limited ability to control the heat dissipation characteristic to transfer across solidification modes and to modify the microstructure as seen in electron beam based powder bed fusion (E-PBF) (Dehoff et al., 2014).

2.2.2 Shielding gas

An adequate flow rate of shielding gas is required to flood the area surrounding hot weld metal in WAAM to exclude atmospheric gases and prevents the formation of detrimental oxides, nitrides and porosity (Lancaster, 1987). The flow rate affects the heat transfer; however, this parameter has a small processing window where high flow rates can introduce porosity to the material as turbulence draws in atmospheric gases to the gas column. The composition of the shield gas influences the heat transfer in the welding zone (Costanza et al., 2016). Argon is commonly used and additions of elements of higher dissociation and ionization potential than argon, such as active gases such as carbon dioxide, or helium, nitrogen and hydrogen (Murphy et al., 2009) offer the ability to able to raise the temperature of the arc (Ebrahimnia et al., 2009). Sequeira Almeida and Williams (2010) were able to produce Ti-6Al-4V samples with refined prior β grains due to enhanced cooling rate provided by using an argon shielding gas mixture with higher helium content.

2.2.3 Wire

The wire gauge and the number of wires fed into the arc for given welding process parameters affect the deposition rate, the heat transfer within the melt pool, imparting a chilling effect as mass is increased (Wu et al., 2017c). This can lead to lack of fusion defects without careful optimisation of the welding processing parameters. It has been shown

possible to use multiple wires for in-situ alloying. This is useful for materials of compositions that are difficult to obtain in singular wire form such as γ- titanium aluminide (Ma, 2015) and iron aluminide (Shen et al., 2015). The wire composition can also affect solidification characteristic by addition of inoculants. These can act as heterogeneous nuclei, increasing the number of locations from which grains can develop, or increase the level of constitutional supercooling. This acts to increase the nucleation of new grains refining weld grain size. Inoculation of metals to achieve grain refinement has been effectively demonstrated by Bermingham et al. (2015) in Ti-6Al-4V with trace boron additives, Mereddy et al. (2017) investigated the addition of silicon to commercially pure titanium, and Haselhuhn (2016) in 4047 and 4943-based aluminium alloys with additions of magnesium, strontium and titanium boride.

2.2.4 Substrate and fixtures

The stiffness of the substrate provides resistance to distortion. Mechanical tensioning of the workpiece through heavy jigs, fixings, clamps and other technologies, can also restrict the possible distortion, however, may increase the formation of residual stresses. (Nitschke-Pagel and Wohlfahrt, 2002). While these mechanical adjustments might prove effective, they require extra financial resources and can restrict the flexibility of changes regarding product geometry. The thickness and composition of the substrate are important because it determines the efficacy of the heat sink effect from the weld through the substrate by conduction.

2.3 Additional processes

Additional processes are increasingly implemented in WAAM to improve the performance of the WAAM process beyond that provided by the primary process selections and can mitigate the detrimental effects of excessive heat input in WAAM. The additional processes that may be used in WAAM are shown in Fig 2.2 and are classified by the timing of application relative to deposition: in-process, inter- or intra-layer, or post-process, and by the overarching process mechanism.

Besides enabling a part to be built to specification, it is possible that the additional processes can augment the capability of WAAM to generate material properties superior to that of forged and provide localised ability to manipulate grain size and solidification mode throughout the part, providing a route to functionally graded materials. In addition, by providing enhanced as-built material properties there is also an opportunity for reducing the overall post-processing time and cost for WAAM parts by eliminating post-processing steps, as well as benefiting parts where heat treatment is unfeasible such as repair or feature addition applications.

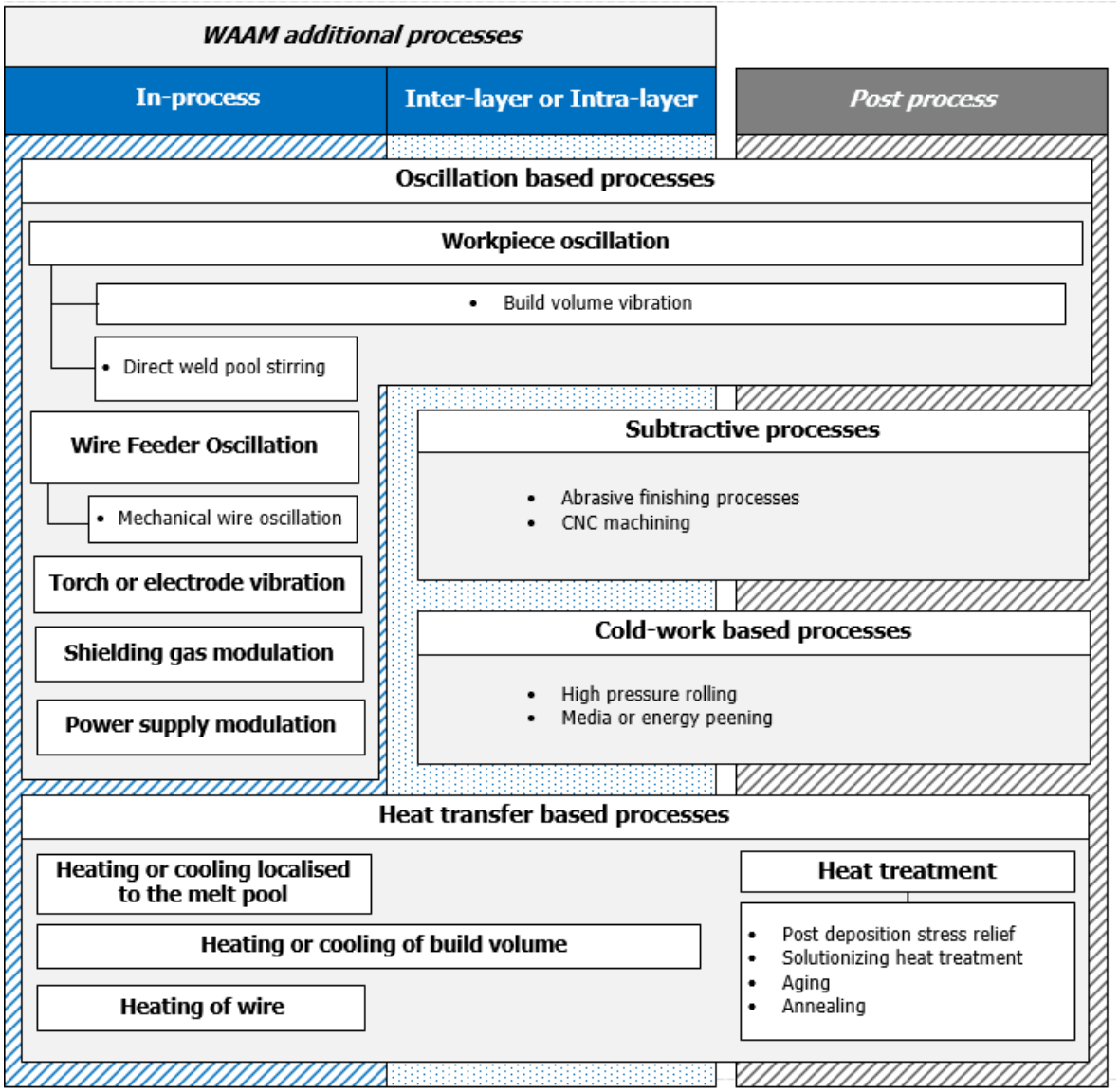

Figure 2.2 Classification of additional processes in WAAM (adapted from (Cunningham et al., 2018)).

Although WAAM post-processes are commonly used, these form costly and often time-consuming aspects of the process chain. Furthermore, as outlined in §1.6, these approaches are often unsuccessful in addressing the heat-based materials processing challenges in WAAM. The following sections consequently review the capability of the in-process and inter/intra-layer additional processes.

2.3.1 Oscillation-based additional processes

The oscillation based additional processes that can be applied in WAAM are classified by the target of the oscillation or modulation involving the workpiece, wire, torch or electrode oscillation and shielding gas or power supply. These processes have been applied in the welding industry to improve the quality of welds for a wide range of applications. Oscillation based processes can promote melt pool stirring which can lead to fragmentation of dendrites from the mushy zone at the rear of the melt pool and grain detachment from the partially melted grains at the melt pool sides (Kou, 2002). As these particles are swept into

the melt pool, they provide starting points for nucleation events, significantly decreasing the Gibbs free energy required resulting in greater nuclei generation. Constitutional supercooling and a refined microstructure may also be encouraged due to increased mixing experienced within the melt pool (Kou and Wang, 1986). A reduction in the level of solute segregation may also occur due to the greater grain boundary area, with associated benefits to the material properties and crack resistance during processing, although residual stress levels remain unchanged.

2.3.1.1 Power supply modulation

Pulsing of the welding power supply current is a widely used technique and is a commonly available feature of modern welding power supplies to improve material properties, and process stability. This process can decouple the metal transfer process from the baseplate heating process, as shown in Fig 2.3 (Pal and Pal, 2010). The low current phase manages the arc stability and the high current phase, the droplet detachment. The frequency of pulse can excite the melt pool, changing the melt pool oscillations and subsequently the cooling rate.

Examples of pulse current being used to improve material properties include WAAM of AZ31 magnesium alloy, where it was found to produce samples with refined equiaxed grains of higher UTS and yield strength than the non-pulsed current approach. Maximum grain refinement was found at the resonant frequency of the melt-pool, although this reduced geometrical accuracy. In pulsed current welding of aluminium 7050, the grain size was reduced and precipitates in a uniformly distributed enough to enable direct ageing of the material bypassing usually required solution heat treatment to correct the grain growth, which is a cost and time-intensive process (Balasubramanian et al., 2007).

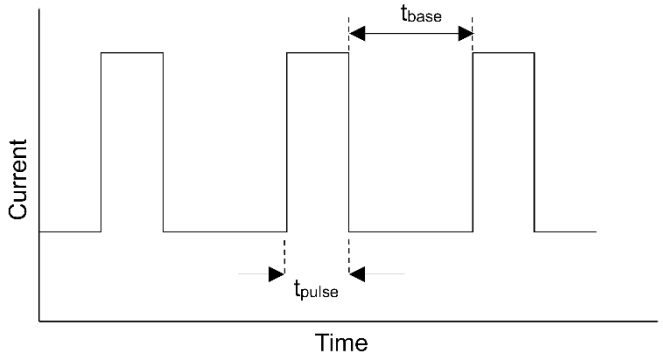

Figure 2.3 Schematic current waveform of single pulsed MIG adapted from (Pal and Pal, 2010)

Double pulse waveforms may also be used where the pulse magnitude and frequency are time-dependent as shown in Fig 2.4 (Wang and Xue, 2017). This is reported to reduce porosity and refinement compared to standard pulse methods (Wang and Xue, 2017). An alternating arc force can also be provided by alternating current or variable polarity methods, which are often preferred for removal of oxide layers in light metals. Variable

polarity differs from alternating current in that the balance of the two polarities can be changed independently (Kishore Babu and Cross, 2012).

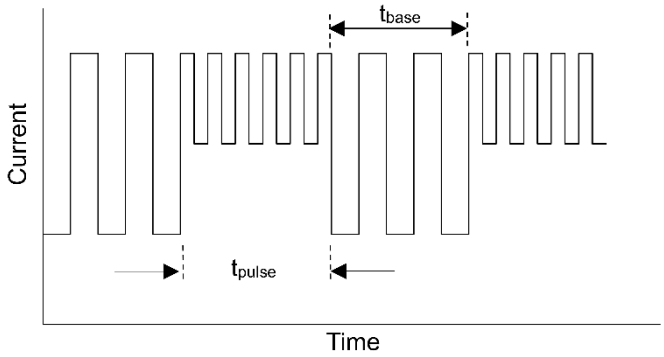

Figure 2.4 Schematic current waveform of double pulsed MIG adapted from (Wang and Xue, 2017)

Wang et al. (2017) combined both variable polarity and double pulse methods in autogenous TIG welding of aluminium alloy 2124. The amount of fine equiaxed grains increased significantly with a clear reduction of the coarse dendrite grains found with the conventional double-pulsed approach as shown in Fig 2.5.

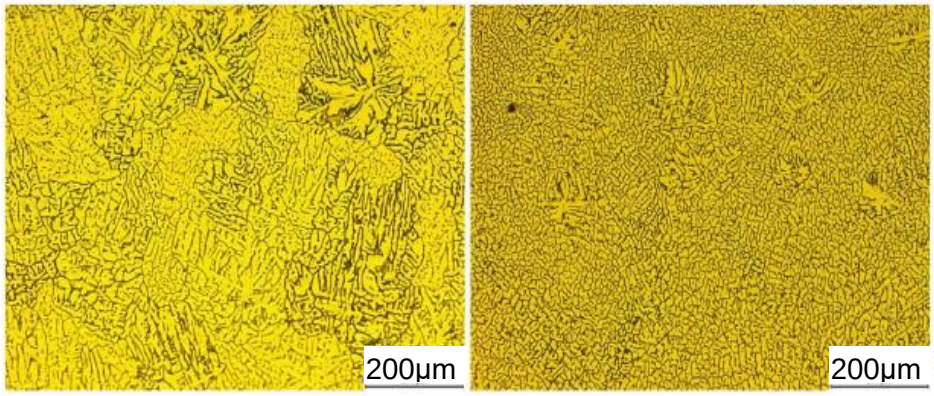

Figure 2.5 Microstructure of the weld zone a) conventional double pulse b) double pulse and variable polarity (Wang et al., 2017)

The electrical arc may also be excited via ultrasonic arc modulation. Hua et al. (2017) demonstrated this by superimposing an ultrasonic sinusoidal current of frequency 20 kHz to a DC TIG welding power supply current waveform. Grain refinement through violent melt pool stirring in nickel filler metal FM-52M. This reduced the detrimental grain boundary length with more extensive branching of dendrites, which subsequently reduced the susceptibility to ductility dip cracking. In the same study, this technique was also found to be advantageous in the reduction of the brittle Laves phase formation through the dispersion of local niobium concentration to levels lower than the phase precipitation threshold.

2.3.1.2 Shielding gas modulation

Discrete periodic supply of two different shielding gases to the welding region leverages the beneficial properties of each shielding gas (Ley et al., 2015). Wood (2006) found that with this process metal transfer modes could be transitioned from spray transfer, buried arc globular transfer, and short-circuiting for a given arc heat input. The arc diameter reduced significantly the switching from argon to carbon dioxide indicating a vigorous stirring melt pool effect. Ley et al. (2015) found for the same level of heat input to the workpiece, the periodic shield gas modulation was able to reduce helium flow, which reduced distortion of the workpiece. Chinakhov (2017) found that weld bead droplet detachment could be regulated, and frequency increased to reduce workpiece heating time, penetration depth, and mean droplet size.

2.3.1.3 Weld torch or electrode vibration

Weld torch or electrode vibration causes melt pool stirring by imparting oscillations to the melt pool. Fan et al. (2018) demonstrated that the vibration of the welding torch in MIG improved the stability of metal transfer. Biradar and Raman (2012) applied mechanical oscillations to the welding torch in the weld travel direction in TIG welding of 6061 plates with 4043-filler material and found increased levels of grain refinement and improved ductility. In the vibration of the electrode in TIG, higher arc pressure improved the penetration compared to conventional TIG (Chen et al., 2017a).

2.3.1.4 Wire oscillation

Watanabe et al. (2010) reported improved mechanical properties for ultrasonic wire oscillation in TIG of ferritic stainless steel for the same level of heat input, with a columnar-to-equiaxed transition promoted at the weld centre-line and ductility improved significantly as shown in Fig 2.6. Wu and Kovacevic (2002) found wire oscillation initiated more rapid and stable droplet transfer, improving the surface finish, and increasing deposition rate. With this approach, the minimum current could be reduced by 10-20% compared with pulsed-current welding, showing that ultrasonic wire oscillation can allow a reduction in heat input whilst maintaining stable metal transfer, as well as directly impact the melt pool dynamics for grain refinement.

Cold Metal Transfer (CMT), an advanced MIG process developed by Fronius GmbH (Fronius, 2020) in the 1990s, combines wire and pulse oscillations to synchronise short circuit-controlled bead transfer. This process is effective in joining of dissimilar materials. CMT pulse showed improved hardness in a Cu-Al alloy compared to standard pulse MIG (Queguineur et al., 2017). Sequeira Almeida and Williams (2010) found the large columnar prior β grain were refined in Ti-6Al-4V. Further improvements were found for variable polarity CMT using Al-6Mg filler wire, where a columnar to equiaxed transition was made and UTS was maximised compared to pulse CMT (Zhang et al., 2018a). Cong et al. (2017)

found that the porosity was reduced in the aluminium alloy (6.3%Cu) using CMT variable polarity pulse. Ola and Doern (2014) by measuring the secondary dendrite arm spacing of CMT welds of Inconel 718 inferred that the cooling rate could be increased to levels expected of laser-based welding.

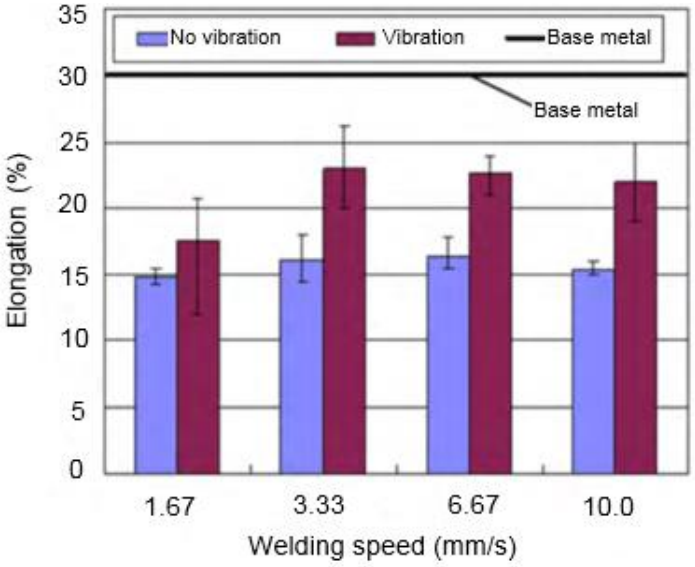

Figure 2.6 Fracture elongation of samples vs. travel speed, with and without ultrasonic wire oscillation adapted from Watanabe et al. (2010)

2.3.1.5 Workpiece oscillation

The workpiece oscillations can be imparted by a periodic external force on the build volume or melt-pool directly. A typical approach is shown in Fig 2.7 by Wen et al. (2015) in which a 2 kW transducer drives a tapered horn resonator and frame, although oscillation may also be generated by piezoelectric effect or by electromagnetic vibration. Thavamani et al. (2018) were able to refine the microstructure and hence reduce the hot cracking susceptibility of Inconel 718 and improve solute distribution through the ultrasonic oscillation of the build plate for TIG. Multiple researchers have investigated this for welding applications; however, investigation for WAAM has been limited perhaps due to the extensive energy requirement for oscillation of large parts.

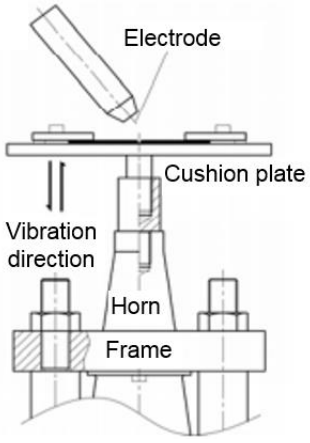

Figure 2.7 Schematic of build plate oscillation (Wen et al., 2015)

Kou and Le (1985) directly modified the grain structure and solidification cracking tendency of welds using the electromagnetic approach where a magnetic field is produced parallel to the welding electrode by single or multiple magnetic oscillators (Yuan et al., 2016b). The electromagnetic stirring produces a Lorentz force, which leads to rotation of the molten metal in the melt pool (Bai et al., 2013, Kou and Wang, 1986). This process is most effective applied in the circular or transverse direction relative to the weld. Improvements to cracking resistance were found with this approach for nickel-based filler metal FM-52 (Yu et al., 2013b). The effectiveness of the mechanism is attributed to the ability to force columnar grains to reverse their orientation at regular intervals obstructing the progression of a crack propagation site as shown in Fig 2.8.

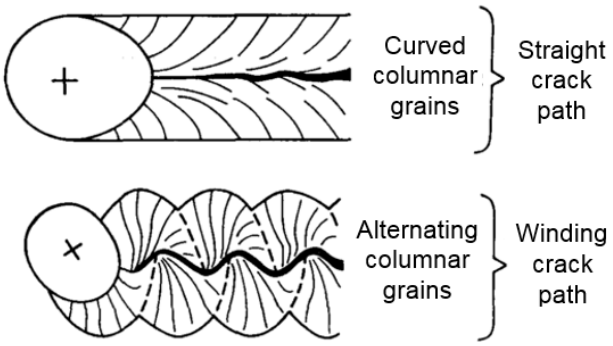

Figure 2.8 Schematic of crack path obstruction due to the circular electromagnetic oscillation of the arc (Kou and Le, 1985)

Yuan et al. (2016b) reported that lower frequency operation was more effective for grain refinement as this allows enough time for the solidifying portion of the melt pool to be reheated and providing more dendrite fragments. Mousavi et al. (2003) reported an intermediate frequency was most appropriate for grain refinement as at lower frequencies, columnar grain growth become more established and at higher frequencies, the ripples overlap and counteract each other. Matsuda et al. (1986) noted that the stronger the magnetic field correlated with improved grain refinement; however, this was counterbalanced by increased surface roughness and burn-through.

Placement of a high-temperature ultrasonic probe into the mushy zone of the melt pool also oscillates the melt pool directly. This has been found to induce significant levels of grain refinement for difficult-to-weld magnesium alloys AZ31 and AZ91 (Yuan et al., 2016a). The improvement was attributed to the dendrite fragmentation within the mushy zone. This approach has the advantage of reducing the power requirement compared to build volume oscillation; however, due to the probe offset from the arc, it leaves an unrefined zone at the end of deposits as shown in Fig 2.9, which would have to be considered in WAAM path planning and potentially introducing zones of runoff waste.

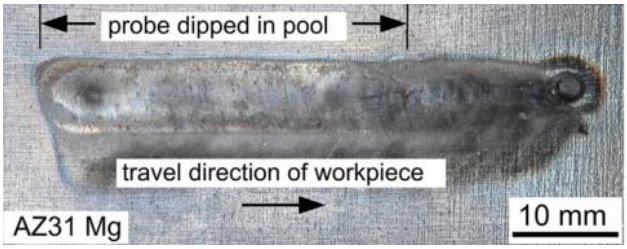

Figure 2.9 Weld bead of AZ31 Mg, showing where the ultrasonic probe is dipped into the melt pool and unrefined zone due to probe-torch offset (Yuan et al., 2016a)

2.3.2 Heat transfer-based additional processes

The following sections introduce the heat transfer-based additional processes that may be applied in-process (interacts with melt-pool directly) or inter-layer or intra-layer (interacts with melt-pool indirectly) to change the total heat flux to the part during the AM build.

2.3.2.1 Cooling localised to the melt pool

Li et al. (2018a) demonstrated the effects of cooling relative to the melt pool in WAAM of aluminium alloy 2325 with a thermo-electric cooling device. It was shown that this was an effective way of maintaining stable heat dissipation characteristics without reducing the heat input and WFS. For equivalent welding processing parameters, this changed the weld bead geometry, increasing weld bead height meant that fewer deposition passes were required. It was shown that microstructure could be refined, and although an interpass dwell was still required, this was reduced by 60.9% compared to without in-process cooling. This was used to establish a similar thermal boundary condition at the substrate and multilayer position, compensating for the poorer heat dissipation at the multilayer level.

There have also been multiple publications investigating continuous cooling for welding. Wells and Lukens (1986) investigated the effects of forced convective cooling behind the welding torch in autogenous TIG welding of Ti-6Al-4V. They developed a cooling device in which helium gas, cooled by a surrounding water-cooled manifold is discharged through multiple holes in an impingement plate. The method was found to be effective in refining the microstructure of Ti-6Al-4V welds, by reducing time at transformation temperature and changing the shape of the melt pool.

Van der Aa (2007) using a similar device applying solid CO_2 behind the melt pool found that this approach could significantly reduce residual stress in single pass butt-welding Ti-6Al-4V and Type 316L stainless steel. The distance from the cooling source to the melt pool was found to be critical to the efficacy of this process as the mechanism of stress reduction was dependent on influencing the melt pool shape and thermal field. To position the device close enough to the arc, whilst preventing turbulence, a physical shield was required, which offset the point of cooling to a minimum distance of 25mm. For this reason, microstructural refinement was only found in materials of high thermal conductivity, as the critical portion of

cooling is otherwise passed by the time that the cooling jet impinges. The buckling of thin sheets could be eliminated with this approach as shown in Fig 2.10 indicating a significant reduction in residual stress.

Kala et al. (2014) found with cooling localised to the melt pool with liquid nitrogen that the process was also limited by severe arc disturbance. In this instance, an argon curtain was used to protect the arc, however, the extended distance from cooling jet to arc limited the efficacy of the process with regards to residual stress. Elimination of hot cracking and reduction in mechanical strain was possible in aluminium alloy 2024 with the use of a trailing heat sink of liquid nitrogen (LN_2) (localised to the melt-pool) discharged from a spray nozzle, indicative of a reduction in residual stress (Yang et al., 2000).

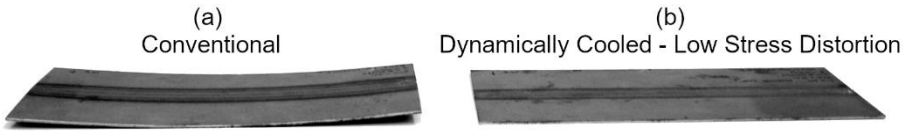

Figure 2.10 Distortion found in a) conventional butt welding and b) Dynamically Cooled – Low-Stress Low Distortion of 1.5mm thick Type 316L sheet (2007)

2.3.2.2 Heating relative to the melt pool

Heating processes can occur in the front or behind the melt pool at the centreline and with a parallel offset from the travel path. Bai et al. (2015b) investigated the effects WAAM set up with symmetric induction coils mounted positioned ahead of and behind the welding torch as shown in Fig 2.11. Both positions were shown to reduce residual stresses by causing the distribution of heat to be more evenly distributed throughout the build. Norsk Titanium, a WAAM machine manufacturer and supplier to the aerospace industry produces parts by pulsed plasma arc-based WAAM with preheat applied by another plasma torch ahead of the deposition weld torch (Norsk Titanium AS, 2017). Qian et al. (2008) investigated the effect of using a laser as an assisting heat source in plasma arc deposition. The shielding gas used in plasma arc deposition absorbed the laser energy and ionized gas molecules to improve the energy density of the plasma arc and arc diameter. This corresponded to improvements to a minimum resolution of the process and part accuracy.

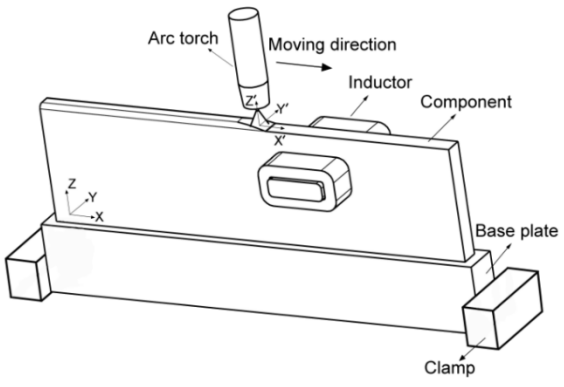

Figure 2.11 Induction pre-heating ahead of the melt pool (Bai et al., 2015b).

2.3.2.3 Heating of the wire

Systems that provide pre-heating of the wire are widely available in the welding industry for TIG. The primary benefit from a welding perspective is that the energy from the arc can melt a greater volume of wire compared to cold wire, which subsequently increases deposition rates and productivity. Typically the wire feeder resistively heats the incoming wire feed (Hori et al., 2003). Silwal and Santangelo (2018) investigated hot-wire TIG dynamics and found that for the same welding parameters the droplet detachment occurred at a higher velocity and frequency, and smaller bead width compared to the cold wire approach. This resulted in a greater cooling rate and with greater melt pool mixing. This approach thus demonstrates the potential for grain refinement for WAAM as evidenced by Li et al. (2019) for titanium alloy.

2.3.2.4 Cooling of the build volume

Substrate cooling is a commonly applied approach in WAAM to achieve in-process cooling of the build volume. Approaches have included the use of conformal cooling channels and thermally conductive backing plates. Lu et al. (2017) embedded a pipe through a copper backing plate in MIG based WAAM combining both approaches and was able to prevent the loss of geometrical control with heat accumulation Fig 2.12.

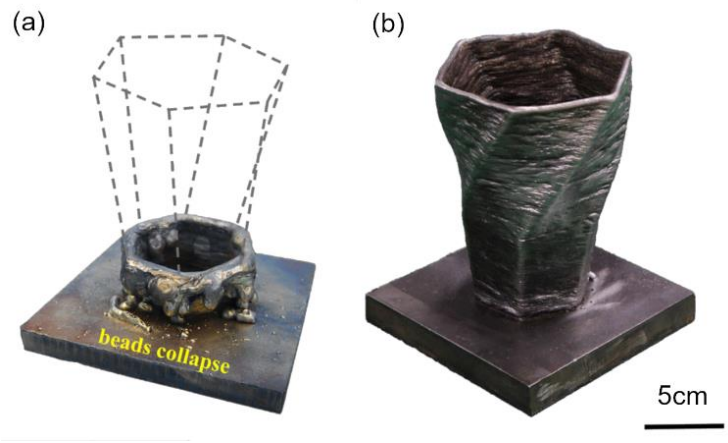

Figure 2.12 WAAM deposition (a) without (b) with water cooling of the base of the substrate (Lu et al., 2017)

In contrast, Haselhuhn (2016) found that WAAM implemented with water-based conformal substrate cooling negatively affected print quality by causing an increase in weld arc to wander, more weld spatter, increased deposit minimum resolution and diminished surface finish, indicating that process parameters require updating to the new thermal boundary condition. Whilst shown to be effective in the example provided by Lu et al. (2017) cooling of the build volume via the substrate is highly dependent on conduction. The effectiveness of this approach in terms of heat management may be limited for components of larger size and lower thermal conductivities.

Several types of cooling gases have been investigated for intra-layer convective cooling of the build volume for WAAM of mild steel cylindrical pipe structures (Henckell et al., 2017).

It was found that this process was effective in improving the stability of the layer geometry and mechanical properties through grain refinement. Application of the cooling gases was found to be more effective when positioned closer to the welding torch with a cooling gas mixture of nitrogen with 5% H_2. However, a possible disadvantage of gas mixtures is the possibility of adsorption of the additional gas, which in some cases can be detrimental e.g. nitrides and hydrogen cracking. Whilst use of argon would overcome this issue, according to the flow rates reported by Henckell et al. (2017) use of this gas would increase consumption from 15 L/min to 45 L/min compared to WAAM without additional convective cooling. Argon gas consumption is a key cost driver in WAAM (Cunningham et al., 2017), therefore this increase in flow rate may reduce cost-effectiveness.

Wu et al. (2018a) investigated inter-layer cooling using compressed CO_2 gas in WAAM production of Ti-6Al-4V using the set up presented in Fig 2.13. This process was able to reduce the oxidation of the specimens produced as well as refined microstructure, improved hardness, and enhanced strength. The improvements to geometric repeatability and accuracy were attributed to the careful regulation of the interpass-temperature, which was made possible by this additional process.

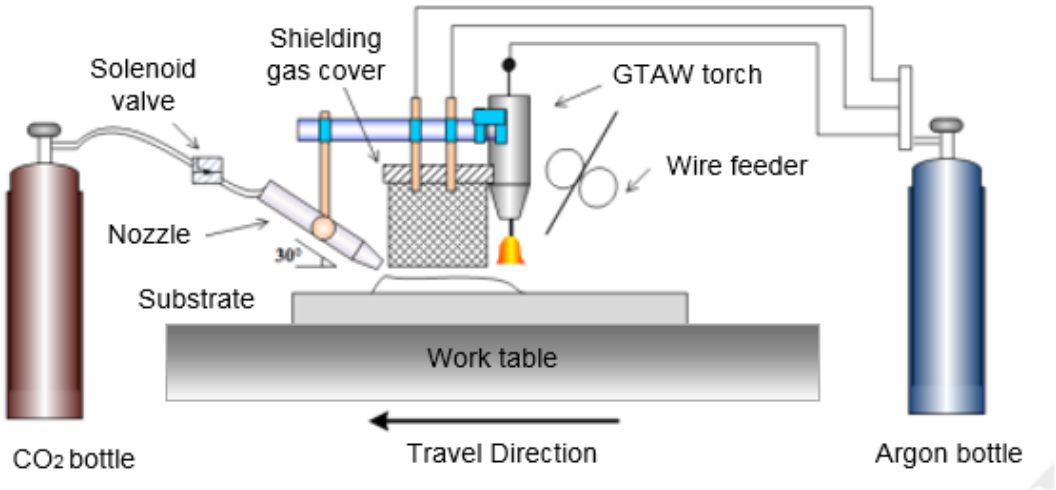

Figure 2.13 Active interpass cooling configuration of equipment adapted from (Wu et al., 2018a)

2.3.3 Cold-work based additional processes

High-pressure rolling has been developed as a process for WAAM at Cranfield University in recent years. Applied vertically, this has been shown to effectively induce recrystallisation for grain refinement, and reduce anisotropy and residual stresses in an aluminium alloy (Colegrove et al., 2017), steel (Fu et al., 2017), and titanium alloy (Donoghue et al., 2016) and Inconel 718 as shown in Fig 2.14 WAAM parts (Xu et al., 2018c). By deforming the material the geometrical properties of the weld bead can be made more repeatable (Martina et al., 2016).

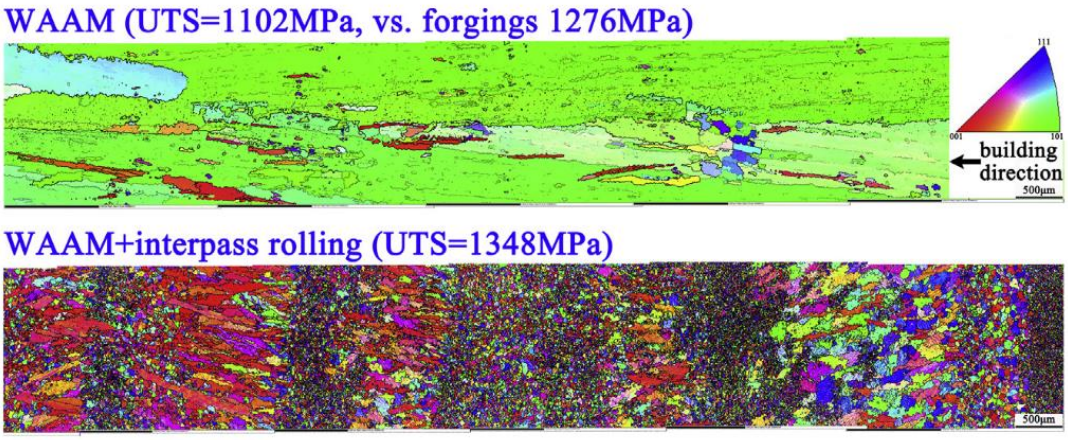

Figure 2.14 Grain refinement and reduction in anisotropy for WAAM of Inconel 718 with interpass rolling (Xu et al., 2018c)

Using equipment shown schematically in Fig 2.15, the process may be carried out immediately behind the welding torch, although the efficacy of the process is affected by the temperature at rolling. The greater thermal conductivity in aluminium alloy 2024 allowed rolling immediately behind the welding torch for grain refinement (Colegrove et al., 2017). However, the optimum interpass rolling temperature for Ti-6Al-4V was found to be 40°C necessitating an interpass dwell period (Donoghue et al., 2016). Whilst side rolling (Hönnige et al., 2017) was found to be significantly more effective than rolling vertically in terms of residual stress and distortion, there is a requirement for re-fixturing or additional tooling to support the opposing side in thin-wall deposits which may otherwise deflect. In addition, further research is required into effective depth, as woven tool paths may be too wide to allow full recrystallisation within the microstructure.

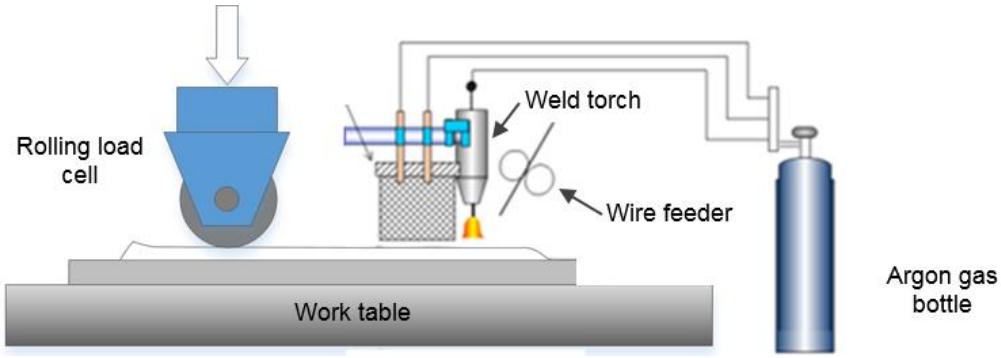

Figure 2.15 Schematic of trailing high pressure rolling in a TIG based WAAM process adapted from Donoghue et al. (2016)

Mechanical and energy-based peening methods are also possible and may include the use of electron, laser, ion, and fluid jet (Tian et al., 2018). Well adopted methods in the welding industry include shot and hammer peening and according to Coules (2013), needle ultrasonic, and laser shock peening have become more widespread in recent years. In the past, such peening processes were primarily related to surface treatments to improve fatigue life. However, as emphasised in the review paper by Sealy et al. (2018), peening

processes are now an integral method for influencing properties throughout the part in hybrid AM.

Significant improvements in material properties were achieved with laser shock peening in WAAM (Sun et al., 2018a). Side rolling and machine hammer peening reduced porosity in aluminium alloys and an increase of surface hardness by 50-70% was achieved by peening and 20% increase was achieved by side rolling with 150 kN load, as compared to as-deposited condition (Machado Santos Carvalho Neto, 2017). The use of peening, as an additional process, is particularly promising because of the lower forces applied compared to rolling were costly and robust motion system axes are required to impart the rolling forces which tends to limit applicability of the solution to 2.5D designs and high value parts.

2.4 Build strategies for heat management in WAAM

To minimise the effects of heat accumulation in WAAM the following heat-management build strategies can be used:

- A time-based interlayer dwell period;
- A temperature-based interlayer dwell period;
- Progressive reduction of the heat input from the welding torch;
- Tool path planning strategies

These build strategies are covered in the following sections.

i. A time-based interlayer dwell period

A time-based interlayer dwell period is widely used to limit build temperatures and has the benefit of being readily implementable. However, with increased distance in build height from the substrate or changes in tool path length, a time-based dwell interlayer dwell period leads to inconsistent thermal boundary conditions as the heat dissipation rate varies as discussed in §1.1.5.

ii. A temperature-based interlayer dwell period

A temperature-based interlayer dwell period overcomes this issue (Montevecchi et al., 2018), however, implementation requires temperature monitoring, which according to Ríos et al. (2018) can be difficult to accurately control with reported temperature variations up to 100 °C. Depending on the material requirements, a shorter or longer dwell period may be specified. Considerations that influence the dwell period temperature or duration include the phase transformations, the relationship between residual stresses and temperature, benefits of pre-heat and severity of grain coarsening.

A major goal of specifying a dwell period is to limit heat accumulation to allow the development of a consistent bead geometry to build the part geometry according to the path

plan. Experimentally, this steady-state deposition is identifiable by a constant melt pool size. However, appropriate dwell periods can often be based on resource-intensive trial and error to determine the time interval or interpass temperature with few systematic approaches proposed to date (Geng et al., 2017) to ensure that the dwell period is optimised for manufacturing efficiency as well as quality.

Implementing an interlayer dwell can provide consistent thermal conditions and limit anisotropy. However, the effectiveness of a dwell period approach in ensuring homogeneity throughout materials sensitive to time at temperature is also limited to sections of consistent heat dissipation rates i.e. simple geometries. Thicker sections dissipate heat more slowly increasing total “time at temperature” and varying the microstructural development compared to thinner sections. Meanwhile, time-based or temperature based dwell periods inherently reduce the productivity of WAAM machines, especially where time cooling is high compared to time depositing (Wu et al., 2017a, Ding et al., 2011, Guo et al., 2016) which disproportionately affect parts of smaller size and low thermal conductivity.

iii. Progressive reduction of the heat input from the welding torch

An alternative to introducing a dwell period is the introduction of varying heat input process parameters as the build proceeds (Cooper, 2016). This is commonly applied within layer sections generated by segmentation, to minimise heat-related geometry variations along the layer as shown in Fig 2.16 (Michel et al., 2019), where the sections process parameters have been determined to mitigate the humping and sloping of the weld bead at the start and stop of the deposition, respectively. However, all sectional process parameters may also shift to lower power levels in the build direction to limit heat accumulation, with stable deposition with the lower heat input process parameters made possible by the higher interpass temperatures compared to the start of the build.

Figure 2.16 Variation of process parameters within a layer (Michel et al., 2019)

A limitation of this approach is that for co-axially fed consumable electrode welding processes, heat input is proportional to the WFS which reduces productivity (Li et al., 2018a). Furthermore, the adjustment of the heat input process parameters is highly constrained by the weld bead geometry, providing a limited processing window in which required improvements to the microstructure and residual stresses may be accomplished, without compromising the geometrical performance measures.

iv. Tool path planning strategies

Tool path planning strategies have shown to be highly effective at maintaining layer height and in-fill accuracy to produce WAAM parts to specification with minimal post-process machining (Ding et al., 2015c, Michel et al., 2019). Tool path planning also has the potential to limit heat accumulation without reducing the productivity through the application of certain in-fill strategies and parallel working between parts and sections within parts to achieve a desired thermal profile (Michel et al., 2019). This is evidenced by various properties of welds with weaving and parallel path deposition strategy and those performed at various interlayer temperatures. However, the use of lower heat input in-fill strategies to limit heat accumulation, such as the parallel path deposition instead of weaving, may not suit the deposition path profile, where discontinuities, sharp turns, and overlaps can contribute to an unstable deposition that, layer after layer, can lead to catastrophic failure (Ding et al., 2015b, Ding et al., 2016). The lengths of the tool path within each section as shown in Fig 2.17 may be too long to achieve the desired cooling rate necessitating the need for additional heating. Parallel working between sections or parts to limit heat accumulation, on the other hand, introduces start and stop discontinuities which may not be compatible with the overall aim to avoid build error accumulation (Wang et al., 2019c). In addition, the parallel working activities between sections if not fully balanced may also result in non-value added time waiting for sections to cool before recommencing deposition.

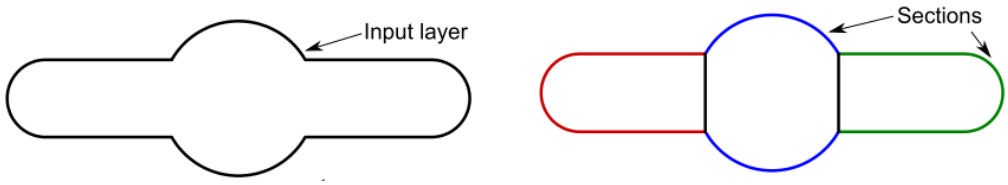

Figure 2.17 Segmentation of input layer into sections of different tool path and process parameter strategies.

2.5 Critique and research gaps

From this review, it has been established that excessive heat input and the variation in the thermal profile during WAAM comprises significant materials processing challenges in WAAM. The heat can detrimentally affect the microstructure refinement, obstruct the desired phase transformations, and precipitate distributions. Residual stresses are high due to the extreme thermal gradients and repeated thermal cycles, which distorts the part geometry. Local variations in the thermal profile cause location-dependent variations in phases and microstructures, scatter in material property measurements and ultimately inhomogeneous material performance. In this chapter, primary process selections, additional processes and build strategies that may be used in WAAM to manage the effects of heat in WAAM have been reviewed. This has revealed the enormous capabilities of additional processes for enhancing the quality of WAAM parts depending on their heat management requirements. It has been demonstrated that it is possible to overcome, or at

least mitigate the heat-based effects to satisfactory levels to produce high-performance engineering components.

However, the appropriate selection of primary processes, additional processes and build strategies depends entirely on the processing requirements and priorities of the given material. For example, higher heat input process parameters, additional heating processes, or shortened dwell periods promote high bulk build temperatures temperature and can limit the impact of the thermal cycles and development of local inhomogeneities if that is important. For example, in materials in which the cooling rate is considered too high, such as with the difficulty in developing precipitates e.g. in PH stainless (Abd-Elghany and Bourell, 2012) or for mild steel in which the temperature between 800-500°C must be greater than 30 seconds to avoid martensitic transformation (Sridharan et al., 2018). However, in some materials, the heat input from WAAM can result in over-ageing of precipitates (Sakhawat et al., 2014), excessive grain growth (Amuda and Mridha, 2013), and undesirable phase transformations (Asala et al., 2017).

It is possible to classify the additional processes by the WAAM heat-related processing challenges that they address, as shown in Table 2.1, which has been generated by the author based on the references reviewed within this chapter. Additional processes applied in-process, can directly influence the nucleation rate of new grains within the melt pool which can significantly reduce average grain size and interrupt the competitive columnar grain growth that leads to anisotropic properties. Processes such as cooling localised to melt-pool, power supply and shield gas modulation, are particularly beneficial due to the ability to affect the dynamics of the melt-pool, as well as reduce the heat input.

Power supply modulations of the heat input from the welding torch are the most commonplace additional process implemented in WAAM as a common feature of most welding power supplies. In recent years, power supply modulation additional processes have become more advanced and able to meet the requirements of WAAM. For example, with the use of advanced pulse and wire oscillation based methods such as CMT (Cong et al., 2017, Selvi et al., 2018, Zhang et al., 2018a) and variable polarity approaches (Zhang et al., 2018a, Wang et al., 2017), which are becoming increasingly popular compared to the standard pulse welding processes. The efficacy of CMT, a combination of power supply modulation and wire oscillation is indicative of the power of synergistically combining additional processes in WAAM.

Table 2.1 Effect of additional processes on the WAAM heat-related material issues (✓✓ = highly effective, ✓=can be effective, ✗=not effective).

		WAAM HEAT-RELATED MATERIALS CHALLENGES									
		Phase changes		*Grain size and morphology*			*Residual stress*			*Anisotropic properties*	
MECHANISM		*Modify time at temperature*	*Modify solute segregation*	*Increase the nucleation of new grains*	*Modify melt pool thermal gradient*	*Modify re-heat effects*	*Thermal profile around melt pool*	*High-temperature relaxation*	*Plastic strain*	*Interrupt epitaxial grain growth*	*Reduction in local differences in thermal BCs*
ADDITIONAL PROCESSES											
IN-PROCESS	Torch/electrode vibration	✗	✓✓	✓	✗	✗	✗	✗	✗	✓✓	✗
	Build volume vibration	✗	✓✓	✓	✗	✗	✗	✗	✗	✓✓	✗
	Direct melt pool stirring	✗	✓✓	✓	✗	✗	✗	✗	✗	✓✓	✗
	Wire oscillation	✗	✓✓	✓	✗	✗	✗	✗	✗	✓✓	✗
	Cooling localised to the melt pool	✓✓	✓✓	✓	✓✓	✓	✓	✗	✗	✓✓	✓✓
	Cooling of build volume	✓✓	✓	✓	✓	✓	✗	✗	✗	✗	✓
	Power supply modulation	✓	✓✓	✓	✓✓	✓	✓	✗	✗	✓	✓
	Shield gas modulation	✓	✓	✓	✓	✓	✓	✗	✗	✓	✓
	Heating localised to melt pool	✓✓	✓✓	✗	✓✓	✓	✓	✗	✗	✗	✓
	Heating of build volume	✓✓	✓	✗	✓	✓	✗	✓	✓	✓	✓
	Heating of wire	✓	✓	✗	✓✓	✓	✗	✗	✗	✗	✓
INTER/INTRA LAYER	Heating	✓	✗	✗	✓	✓	✓	✓	✗	✗	✓
	Cooling	✓	✗	✗	✓	✓	✓	✗	✗	✗	✓
	Material removal	✗	✗	✗	✗	✗	✗	✗	✗	✗	✗
	Cold work	✗	✓	✓	✗	✓	✗	✗	✓	✓✓	✗
BUILD STRATEGY											
Interlayer dwell		✓	✗	✗	✓	✓	✓	✓	✓	✗	✓

However, it is not clear if these methods can match the grain refinement achieved by oscillation based techniques such as of torch/electrode vibration, build volume vibration direct melt pool stirring, wire oscillation, which directly affect the nucleation rate through melt pool stirring and can be more useful in processing materials of high crack susceptibility. Moreover, power supply modulation is unable to affect the heat accumulation as drastically as additional cooling processes, which may also be required for where low build temperatures and efficient WAAM production is required.

As shown in Table 2.1, with the implementation of cold-working based processes it is possible to address many of heat-related materials issues in WAAM. However, due to the need for cooling of the build before rolling for effective residual stress relief and grain refinement, this is incompatible with a high interpass temperature build strategy that is sometimes preferred to minimise dwell periods and extend the ‘time at temperature’. A significant amount of non-value adding time may be added, especially as the interpass

rolling temperature may be well below the interpass temperature necessary for build stability. This compounded by the need for rolling to be carried out typically on a layer-by-layer basis. Further considerations include the cost of the robust rolling motion axes, effective deployment of the roller for complex or bulk deposits and, roller slipping and wear.

By implementing a cooling process localised to the melt pool, all of the mechanisms that can address the heat-related materials challenges covered in Table 2.1 are active, while improving productivity by eliminating the need for an interlayer dwell period or parallel working and complex path planning strategies to enhance productivity. The “time at temperature” can be limited and grain growth hindered leading to improved material properties (Queguineur et al., 2017). Furthermore, continuous cooling processes can be tailored to the material requirements by cooling capacity, flow rate etc., to provide more extensive control over microstructure and phase transformations. Application localised to the melt pool not only can limit heat accumulation and reduce local differences in the thermal boundary conditions as for cooling applied inter/intralayer but also actively influences the melt-pool dynamics. As well as the possibility of grain refinement by constitutional supercooling and additional generation of nuclei, the steady-state shape of the melt pool thermal profile may be modified with a significant reduction to peak and amplitude values of residual stresses as demonstrated in conventional welding (van der Aa, 2007).

There may be several effective routes for managing the effects of the WAAM heat input, as shown by the separate approaches taken by Norsk Titanium with high-temperature processing (Norsk Titanium AS, 2017), Cranfield University with inter-layer rolling for producing high-quality Ti-6Al-4V components. In these cases, the cost, ease of implementation, and flexibility of the additional process will determine its selection. In-process cooling near to the melt pool shows potential for addressing the heat-related materials challenges in WAAM, all the while sustaining high volumes of deposition per hour. In comparison to inter-layer cooling and in-process substrate cooling, greater control over the thermal profile during WAAM builds is provided. However, research of cooling localised to the melt-pool has primarily focused on improvements to build geometry stability and single-pass welding. The comparative capability in terms of material properties and cost compared to the more commonly implemented interpass-temperature control build strategy is not well established, forming a major research gap that will be addressed in this research

A review of the welding metallurgy and WAAM of Type 316L stainless steel

Chapter 3

3.1 Introduction

This chapter reviews the welding metallurgy of austenitic Type 316L stainless steel. This provides the underpinning knowledge of the factors that influence the material and physical properties of engineering components made by WAAM. The research relating to the AM, and in particular WAAM of Type 316L austenitic stainless steel is reviewed, with the current state-of-the-art and limitations highlighted.

3.2 Chemical composition

Stainless steel categories can be considered relative to the base 18Cr–8Ni system type 304 austenitic alloy by addition or subtraction of alloying elements as shown in Fig 3.1. The Type 316L stainless steel investigated in this research substitutes approximately 2% Mo for a nearly equal amount of Cr to improve pitting corrosion resistance (Lippold, 2005).

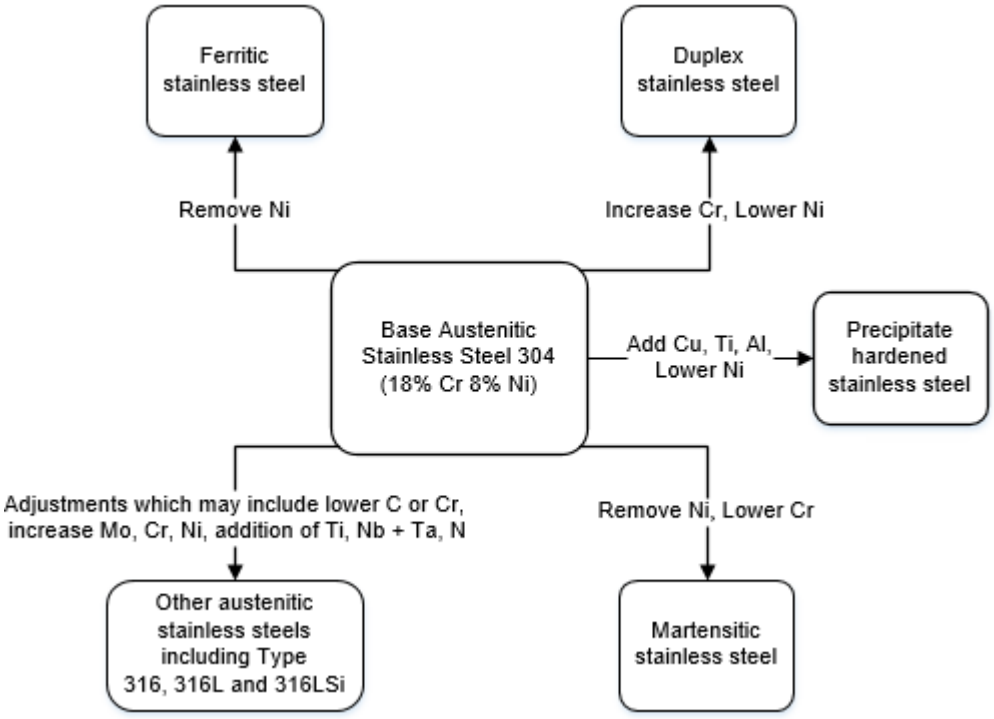

Figure 3.1 Composition of the ferritic, duplex, precipitation hardened, martensitic and other austenitic stainless steels relative to the base 304 austenitic grade adapted from (Davis, 2001)

The high corrosion resistance of type 316 stainless steel alloy can diminish upon exposure to temperatures in the range of 700-900°C. This is because the inter-granular interfaces become reactive to a chemical attack in a process termed sensitisation, where chromium and carbon combine to form carbides (Weiss and Stickler, 1972). The carbides precipitate at grain boundaries as shown in Fig 3.2 due to the limited solubility of carbon within austenite at room temperature. Sensitisation is considered a detrimental phenomenon as it depletes the available chromium, which provides the high levels of corrosion resistance in stainless steel and results in the congregation of carbides at grain boundaries and elevated susceptibility to inter-granular corrosion. The carbides (C) often take the form of $M_{23}C_6$

where Chromium (Cr), Iron (Fe), Manganese (Mn), or Nickel (Ni) represent M. The presence of molybdenum can cause the precipitation of η, an M_6C carbide, where M represents Fe, Mo, and Cr (Padilha and Rios, 2002).

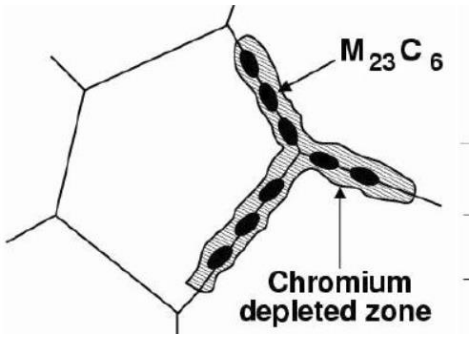

Figure 3.2 Schematic showing the precipitation of $M_{23}C_6$ carbides (ASM International, 2008).

For high-temperature applications and processes such as welding, to avoid the effects of sensitisation, lower carbon composition alloys have been developed such as Type 316L as shown in Table 3.1, where there is insufficient content to cause sensitization. This can also be achieved with the addition of strong carbide formers or stabilising elements such as niobium or titanium, which competitively react with the carbon to prevent chromium carbide formations at the grain boundaries, however, this increases the alloy cost. To improve the wettability or flow of material during welding, a high silicon (Si) and low-carbon type alloy, Type 316LSi stainless steel was also developed of chemical composition as shown in Table 3.1. Si additions are also well known for enhancing the oxidation resistance of stainless steel. As an interstitial element, proof strength also increases as a result of solid solution strengthening by 23 MPa/wt.% (Eliasson and Sandstrom, 2000).

Table 3.1 Chemical composition (wt %) of austenitic stainless steel bare electrodes, bare rods, tubular metal-cored electrodes, and strips from AWS A5.9 and (BS EN ISO 14343, 2017).

Chemical Composition		Cr	Ni	C	S	Mn	P	Si	Mo	N
Type 316	**Min**	16	11.0	0.0	0.0	1.0	0.0	0.3	2.0	-
	Max	18	14.0	0.08	0.03	2.5	0.03	0.65	3.0	-
Type 316L	**Min**	18.0	11.0	0.0	0.0	1.0	0.0	0.3	2.0	-
	Max	20.0	14.0	0.03	0.03	2.5	0.03	0.65	3.0	-
Type 316LSi	**Min**	18.0	11.0	0.0	0	1.0	0.0	0.65	2.0	-
	Max	20.0	14.0	0.03	0.03	2.5	0.03	1.0	3.0	-

The following sections outline the modifications to the chemical compositions as presented in Table 3.1 by adsorption of atmospheric gases. Adsorption of atmospheric elements to the melt pool can be caused by incomplete shielding, typically, by welding torch shielding with inert argon gas or mixes. Losses due to vaporisation may also occur with Mn shown to be the most volatile element in Type 316L stainless steel (Mukherjee et al., 2016). For laser-powder AM it was calculated vaporisation would result in 0.22 wt.% loss. As an austenite promoter any Mn vaporisation acts to increase the δ-ferrite content (see §3.3.1).

The austenitic crystal lattice contains approximately 35 wt.% of alloying elements. Incorporating foreign atoms with radii different than that of iron into the iron lattice modifies the interatomic distances within the lattice and the elastic modulus changes (Münstermann et al., 2014).

For austenitic stainless steel, Cr, Ni, Mn, Si result in substitutional solid solution strengthening, whereas N can result in interstitial solid-solution strengthening. The solubility of O in austenitic stainless steels is limited due to the large atomic radius relative to the austenite lattice and strong affinity to alloying elements such as chromium, manganese, and silicon which preferentially results in the formation of secondary phases (Kitchener et al., 1953). The presence of δ-ferrite or σ-phase within the γ-austenite matrix also results in solid-solution strengthening.

The amount of solid-solution strengthening in a metal alloy can be determined by applying the classic equations developed by Labusch (1972) and Nabarro (1977) using an expression that encompasses a lattice strain parameter term due to the particular solute atom and the solute content. However, due to high numbers of alloying elements and complex interactions, several effective empirical terms have been developed to account for solid solution strengthening. An empirical equation relating the composition of alloying elements, grain size and δ-ferrite developed by Pickering et al. (1969) is as follows:

$$\Delta\sigma_{ys} = 354C + 493N + 3.7Cr + 20Si + 2.9Ni + 0.25d_{grain}^{-0.5} + 2.5\delta \quad (4.1)$$

The elemental contents are computed in wt (%), d represents the average grain size in m, and δ is in area fraction (%).

3.2.1 Adsorption of nitrogen

Additions of nitrogen can strengthen stainless steel by interstitial solid solution strengthening. Besides entering solid solution, nitrogen introduced may also combine to form nitrides in the form of MN, where M represents Zirconium, Titanium, Niobium, or Vanadium, or M_2N where M represents Cr or Fe respectively (Padilha and Rios, 2002). Rayaprolu and Hendry (1988) noted that precipitation of chromium nitride during heat treatment caused embrittlement, but ductility was not affected when nitrogen is retained in solid solution. As an interstitial solid solution element, nitrogen provides greater strengthening than other interstitial elements such as carbon and boron, whilst retaining high levels of fracture toughness and ductility. The reduction in δ-ferrite can improve the pitting corrosion resistance (Huang 2009) and also the galling resistance (Lippold, 2005).

For these reasons, 316LN and 316N alloys have been developed with the intentional addition of nitrogen up to 0.20 wt. %. The addition of nitrogen increases the σ_{ys} of the low-carbon (316L) grades to match that of the standard grades, improve hardness and minimise the δ-ferrite formation in its role as an austenite promoter. According to Harish et al. (2012),

Type 316LN stainless steel often is welded autogenously, with Type 316L the more commonplace welding filler. Cui et al. (2019) recently developed 316L powders of increased nitrogen content for L-PBF to improve the corrosion resistance and mechanical properties of Type 316L stainless steel further. Nickel is primary cost component of type 316 stainless steel, therefore developing low nickel or nickel-free austenitic stainless steels by nitrogen addition is of commercial interest, as well as addressing the drawbacks related to human allergenic reactions (Yang and Ren, 2010).

Nitrogen can be introduced to the weld metal in several ways: diatomic N_2 molecules can dissociate at the melt-pool gas-melt interface and adsorb into the melt as atomic nitrogen. Alternatively, nitrogen can be introduced from the raw material production process or inserted directly into the liquid slag or metal via alloying additions (Simmons, 1996). Although the solubility of nitrogen in iron is only 0.04% wt.% at 1600°C and atmospheric pressure, additional elements such as Cr, Mn with an electron deficit strongly increase the nitrogen solubility (Stein and Hucklenbroich, 2004). The solubility of nitrogen in Fe-Cr-Ni-Mn-Mo base alloy at atmospheric pressure in traditional steel making follows Siewert's Law where solubility is proportional to the square root of the pressure (Wada and Pehlke, 1977).

However, as stated by several authors (Galloway et al., 2011, Zhao et al., 2013, Sato et al., 2000, Palmer and Debroy, 2000), arc welding is a complex dynamic process for which Siewert's Law fails to predict weld nitrogen content with accuracy. Nitrogen solubility in the austenitic stainless steels decreases with increasing melt temperature as shown in Fig 3.3.

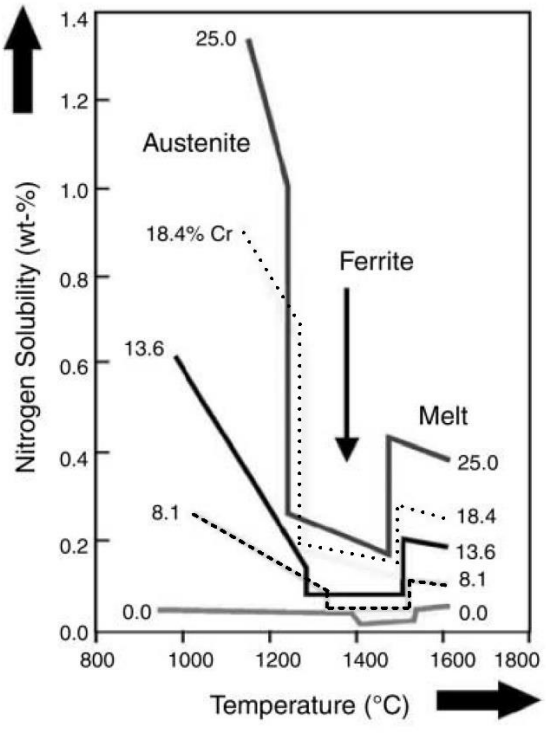

Figure 3.3 Nitrogen solubility in FeCr-alloys at 1 bar pressure (Stein and Hucklenbroich, 2004)

The solubility of nitrogen is low within the δ-ferrite region materials due to the irregular shape and limited size of the octahedral interstitial sites which results in local, tetragonal lattice distortion upon interstitially dissolving of nitrogen (Aufrecht et al., 2008). Shankar et al. (2003) showed that it was possible to introduce nitrogen to Type 316L by the addition of nitrogen to the shielding gas as shown in Fig 3.4, although nitrogen is not typically included in welding shielding gas compositions for Type 316L stainless steel. Reed (1989) compiled a summary of the contribution to yield strength by nitrogen addition and the base alloys that are most similar to Type 316L are presented in Table 3.2.

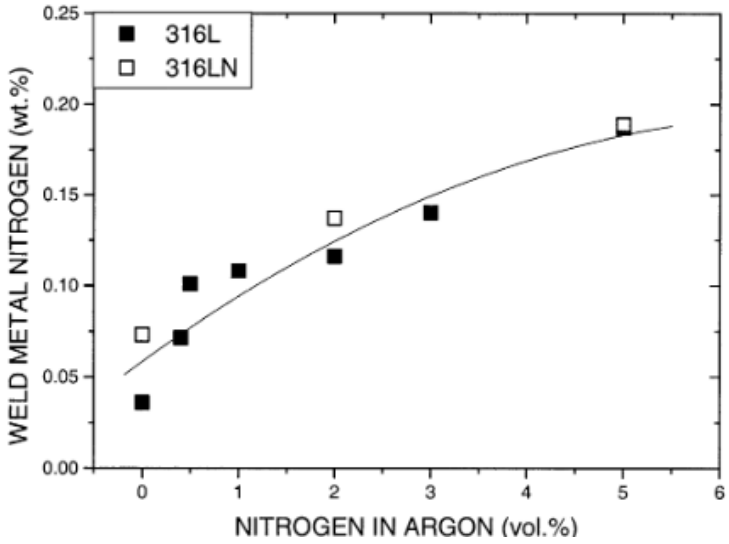

Figure 3.4 Weld metal nitrogen (wt.%) as a function of nitrogen in argon (vol%) (Shankar et al., 2003)

Table 3.2 Nitrogen solid solution strengthening contribution to yield strength for base alloys similar to Type 316L adapted and updated from (Reed, 1989).

	Contribution to Yield Strength (MPa/wt.%)	
Base alloy	**Test temperature 295K**	**Reference**
Fe-19Cr-10Ni	500	(Reed and Simon, 1988)
Fe-18Cr-10Ni	710	(Irvine et al., 1961)
Fe-Cr-Ni	440	(Pickering et al., 1969)
Fe-18Cr-14Ni-3Mo	310	(Norström, 1977)
316L	693	(Ganesan et al., 2013)

The values for contribution to strength reported indicate that for the levels of nitrogen adsorption reported by Shankar et al. (2003) of up to 0.125wt.%, 40-88MPa contribution to yield strength may be provided, which corresponds to 20%-43% of the wrought yield specification (ASTM A240/A240M, 2004). Smith et al. (2019) identified 0.08 wt.% nitrogen composition in L-DED material and its presence was cited for the increase in strength of ~40 MPa (based on 630 MPa/wt%) compared to wrought material. Moreover, it was found that the nitrogen content introduced during laser-welding was significantly lower than arc welding (Sato et al., 2000). For high nitrogen steel the effects of shielding gas content and welding heat input was also investigated (Zhao et al., 2013) showing that at higher heat inputs and higher nitrogen shielding gas contents that the nitrogen increased, although if

the shielding gas did not contain additional nitrogen the higher heat input resulted in greater de-adsorption losses. The multi-layer nature of WAAM results in slower cooling rates than welding, which means that greater nitrogen adsorption and solid solution strengthening may be possible. This is expected to be higher than that found for L-DED by referring to the results of Sato et al. (2000) for laser and arc welding, however, the contribution to strength and the effect of heat input and interpass temperature have not yet been determined.

3.2.2 Adsorption of oxygen

The dispersion of ultra-fine and stable oxide particles throughout a metal matrix to reduce grain coarsening and grain boundary sliding is known as oxide dispersion strengthening (ODS) (Klueh et al., 2005). In the past, ODS has been used to improve the creep resistance and void swelling resistance of austenitic stainless steels (Raman et al., 2016). Higher levels of hardness and tensile strength can also be achieved with ODS stainless steels as the oxide inclusions can act as effective barriers against dislocation motion during tensile deformation. Austenitic ODS steels are typically produced through the powder metallurgy (PM) route, with multiple extrusion and annealing steps (Maier et al., 2019). Oxide powders such as Y_2O_3 are often used in the mechanical alloying process to combine with the stainless steel powder using ball milling (Miao et al., 2015). The size of the inclusions are typically on the nanometre scale with diameters of ~50 nm (Wang et al., 2013) and ~5 nm (Miao et al., 2015) reported. These inclusions act to significantly increase the tensile strength of stainless steel, however at the expense of ductility, which was only restored with additional forging and hot rolling processes after solidification as shown in Fig 3.5 (Wang et al., 2013).

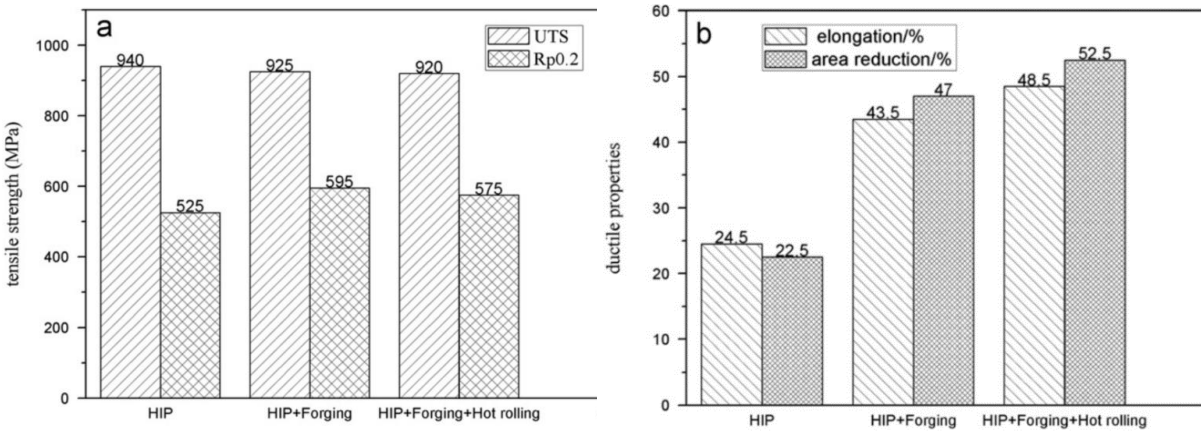

Figure 3.5 a) Ultimate tensile strength and b) elongation of ODS 304 at the various stages of the production process (Wang et al., 2013)

AM could provide a potentially cost-effective route to ODS by producing the oxides in the process without additional processing and expensive alloying additions. Atmospheric oxygen can be introduced to the melt-pool by insufficient inert-gas coverage due to the high temperatures experienced during welding and AM (Saeidi et al., 2015). Besides oxygen in the atmosphere, oxygen might also be introduced by the shielding gas. Ar-2.5%CO_2

shielding gas is recommended for use in welding of Type 316L, however, as identified by Baune et al. (2000) the CO_2 can decompose under the high temperature of the welding arc, providing another source of oxygen to the melt-pool. The exposure of the melt-pool to oxygen can lead to the development of Si, Mn, and Cr oxide inclusions throughout the austenitic metal matrix, with SiO_2 inclusions commonly found in additively manufactured 316L stainless steel as shown in Fig 3.6 due to the high levels of oxygen affinity.

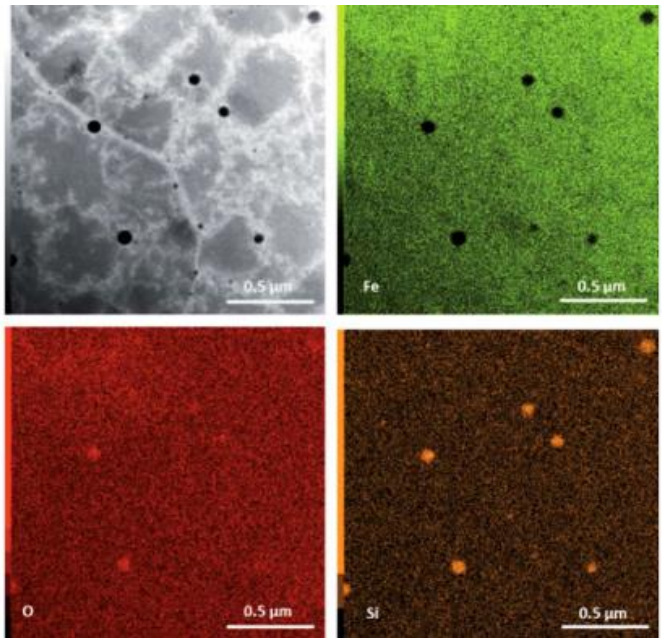

Figure 3.6 TEM elemental mapping of 316L stainless steel manufactured by L-PBF (Saeidi et al., 2015)

Eo et al. (2018) identified oxide inclusions in the microstructure of L-DED processed 316L and found the mean diameter varied within the range of 0.31-0.49 µm. The frequency of the inclusions correlated to the σ_{ys} as shown in Fig 3.7.

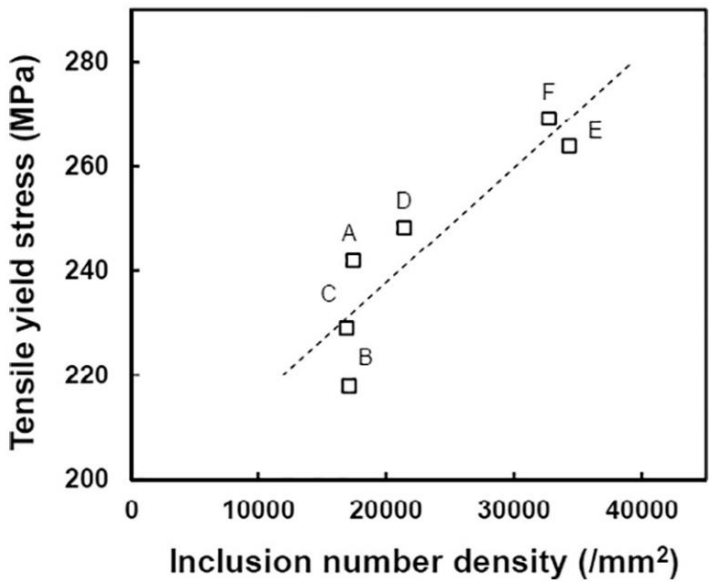

Figure 3.7 Relationship between inclusion number density and tensile yield stress for L-DED of 316L (Eo et al., 2018).

The frequency of oxide inclusions was found to depend greatly on the intensity of the laser beam rather than the travel speed, although the travel speed was shown to influence oxide size. Ziętala et al. (2016) investigated the mechanical properties and corrosion resistance of 316L produced also produced by L-DED; however, no oxides were identified in the microstructure. In contrast to strengthening found by Eo et al. (2018) several authors have found the strengthening effects to be negligibly small (<10MPa) for L-PBF (Wang et al., 2018c) despite the smaller scale of the inclusions of less than 50 nm. Lou et al. (2018) found oxide inclusions in L-PBF promoted early initiation of micro-void formation and reduced the impact toughness. Examination of a large area of the fracture surface showed that in most cases, oxide inclusions were found in the dimples, which suggested that the presence of oxides served as initiation sites for micro-void formation leading to reduced toughness. Yu et al. (2013a) also identified oxide inclusions within the dimples of the fracture surface. The size of the inclusions was also found to be dependent on the part build orientation relative to the substrate.

Eo et al. (2018) studied the effect of oxidiser additions finding that additional Si and Mn content reduced the oxygen content overall within the part. This effect was attributed to the formation of a protective oxide slag layer, which affected the kinetics of oxide development within the molten metal resulting in a higher frequency distribution of smaller inclusions. The effects of Si content and its effect on ODS, however, have not been studied for WAAM where investigation of ODS in Type 316L stainless steel has been limited. While several researchers have identified the presence of oxide inclusions in WAAM processed material, in some cases, these may have been misidentified as pores (Haden et al., 2017). Elmer and Gibbs (2019) found an increase in oxygen content in type 309 from 0.007 wt.% to 0.041wt% in the as-deposited material indicating that the increase in oxygen can be substantial in WAAM. However, the oxide inclusion size, distribution and possible contribution to strength have not been systematically investigated.

3.3 Phase composition

In this section, the δ-ferrite to γ-austenite phase transformation, δ-ferrite to intermetallic sigma phase which may be present in the as-built WAAM material are discussed. Twinning induced plasticity (TWIP), which can introduce α'-martensite phase upon plastic deformation is reviewed in § 3.5.2.

3.3.1 Ferrite to austenite phase transformations

Stainless steel Type 316L alloy is an austenitic stainless steel and upon cooling consists primarily of the FCC γ-austenite phase as shown in Fig 3.8. Depending on the exact chemical composition and manufacturing cooling rate, some additional body centred cubic (BCC) δ-ferrite may be present as shown in Fig 3.9.

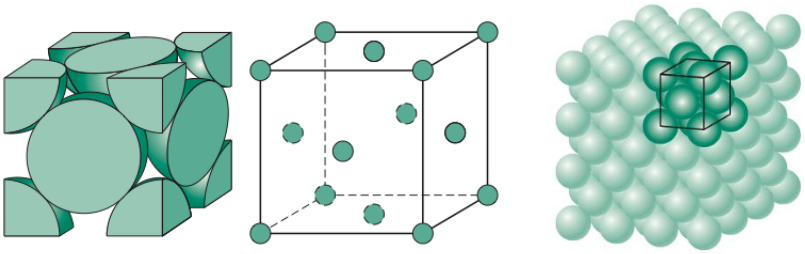

Figure 3.8 Face centred cubic (FCC) γ-austenite structure (Callister, 2003).

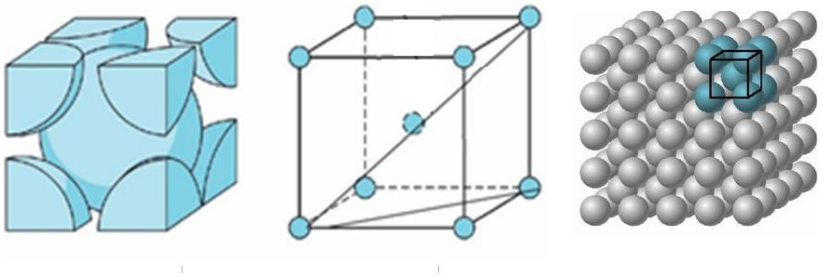

Figure 3.9 Body centred cubic (BCC) δ-ferrite structure (Callister, 2003).

The ratio of γ-austenite to the δ-ferrite phase is important for several reasons: δ-ferrite in large volumes can be detrimental to the corrosion resistance of the weld metal, due to the formation of Cr-depleted zones of reduced corrosion resistance and passivity. The presence of δ-ferrite may also have to be minimised for applications requiring low magnetic permeability, high toughness at cryogenic temperatures, and resistance to media that selectively attack δ-ferrite. However, small amounts of δ-ferrite are usually planned in welding to prevent hot cracking. Small volumes of δ -ferrite can also be strengthening due to associated reduction in austenite grain size as the ferrite progressively sub-divide the austenite grains and act as dislocation barriers. The decrease of δ-ferrite, however, can lead to higher angular distortion due to welding (Lin and Chen 2001) and also increase the risk of solidification cracking (Kou, 2002). Yılmaz and Tümer (2012), found that toughness is directly related to the amount of ferrite with Read et al. (1980) also reporting a drop in impact toughness from 203 to 143 MPa$\sqrt{m}$ with an increase in Fe(%) at 76K from 0.1 to 8.5. Padilha and Rios (2002) showed that the increase in the volumetric fraction of δ-ferrite leads to a higher value of hardness. Attainment of satisfactory material properties in additively manufactured materials requires understanding and control of the phase transformations.

The solidification process of Type 316L stainless steel can be understood in relation to the alloying elements as shown in Fe-Ni-Cr ternary diagram shown in Fig 3.10, which shows the liquidus and solidus isotherms dependent on alloying content.

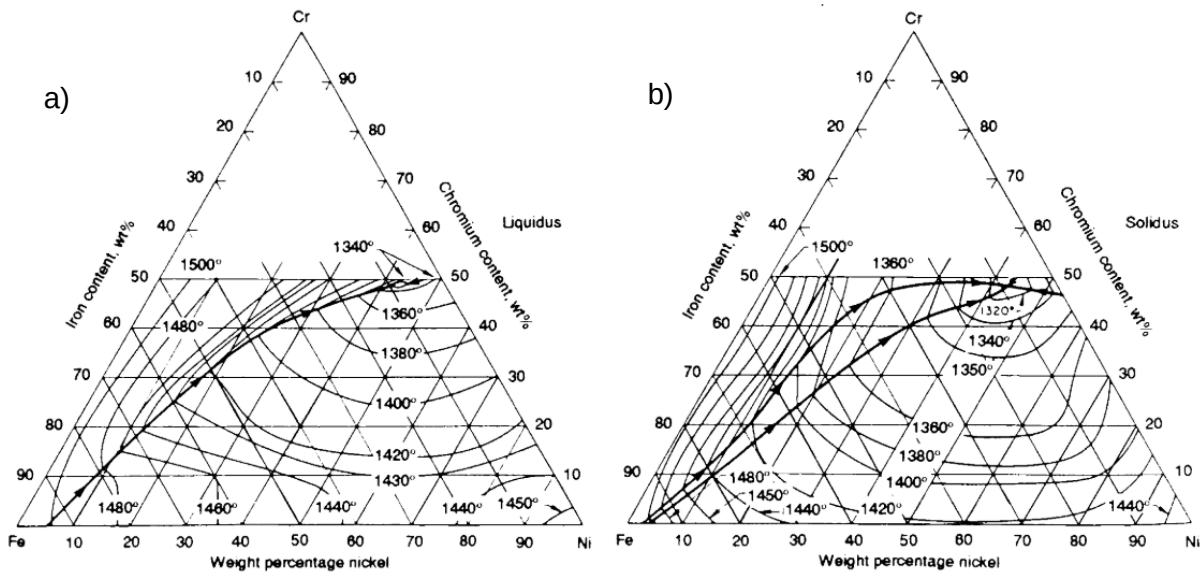

Figure 3.10 Iron-chromium-nickel ternary diagram with a projection of a) liquidus b) solidus surface as isothermal contours (Davis, 1998)

For constant Fe content, Fe–Cr–Ni pseudo-binary phase diagram can also be developed as displayed in Fig 3.11. As shown, solidification may complete entirely as δ-ferrite (F) for high Cr_{eq}/Ni_{eq} alloys, or secondary γ-austenite may be introduced as the alloy cools (FA) and may be completely transformed to γ-austenite during cooling. For Cr_{eq}/Ni_{eq} ratios lower than 18Cr–12Ni, solidification commences with primary γ-austenite (A). Although secondary δ-ferrite (AF) can exist at high temperatures under equilibrium conditions, this is entirely transformed into γ-austenite as δ-ferrite becomes unstable during cooling.

The phase transformations that occur depend on the alloying elements, which can be classified as austenite or ferrite stabilisers depending on whether they act to promote the development of austenite or ferrite, respectively. Austenite is promoted by greater volumes of C, Mn, and Ni, whereas ferritic phase transformations are promoted by greater volumes of Al, Cr, and Si. An established way of summarising the ratio of ferrite to austenite promoting alloying elements within stainless steel comprises of the equivalent chromium (Cr_{eq}) to nickel equivalent (Ni_{eq}) ratio. For Type 316L stainless steel the Cr_{eq}/Ni_{eq} is such that the triple-phase triangular region which contains liquid, δ-ferrite and the γ-austenite region is entered upon solidification.

The Fe–Cr–Ni pseudo-binary phase diagram presented in Fig 3.11 is valid for equilibrium cooling conditions; however, during welding and AM, the deposited metal can experience rapid cooling resulting in substantially different phase contents than that predicted by the pseudo-binary Fe-Cr-Ni phase diagram for equilibrium cooling. The difference is caused by the prevention of the solid-state diffusion-controlled reaction that transforms δ-ferrite to γ-austenite by rapid cooling. As a consequence, for compositions of AF solidification mode as highlighted by the annotated region in Fig 3.11 some metastable δ-ferrite can be retained within the deposited metal in cooling to room temperature (Lippold and Savage, 1979).

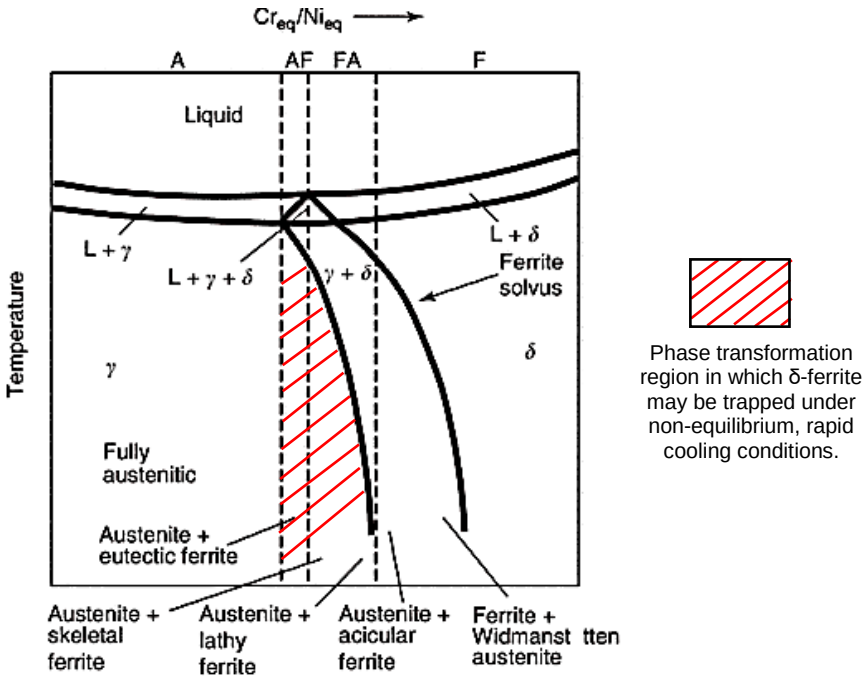

Figure 3.11 Fe–Cr–Ni pseudo-binary diagram at 70% constant iron showing possible phase compositions for equilibrium cooling conditions (Lippold, 2005) highlighting the compositions where δ-ferrite may be trapped under non-equilibrium rapid cooling conditions.

The dynamics of the welding process also result in high levels of elemental segregation within the solidified material which can also cause deviation from phase contents predicted by the pseudo-binary Fe-Cr-Ni phase diagram (Lippold, 2005). Localised regions of non-nominal composition are present which results in an inhomogeneous phase transformation decomposition throughout the material. Regions of comparatively high Cr_{eq}/Ni_{eq} ratio may be present, for example within grain cores of 316L produced by powder L-DED (Zumelzu et al., 1999). Due to their high ferrite stabiliser content, greater retained δ-ferrite is present in these regions compared to those nearer to nominal composition.

There have been efforts over the years to predict the phase content of weld metal using empirically derived constitution diagrams. An early example, the Schaeffler diagram, was published in 1949, has been extensively used for estimating the ferrite content of stainless steel weld metals based on the Cr_{eq} to Ni_{eq} ratio. Incremental improvements have been implemented over the years, the DeLong diagram, published in 1956, included the effects of nitrogen as an austenite stabiliser and improved accuracy of the reading, albeit for a more limited range of Ni_{eq} and Cr_{eq} ratios, the 300 series austenitic stainless steel. The development of the WRC 1988 diagram combined the aspects of the Schaeffler and DeLong diagrams to improve the accuracy of predictions and for a wider ferrite range. Later, the WRC-1992 constitution diagram shown in Fig 3.12 was issued which also accounted for the effects of copper as an austenite stabiliser (Kotecki and Siewer, 1992).

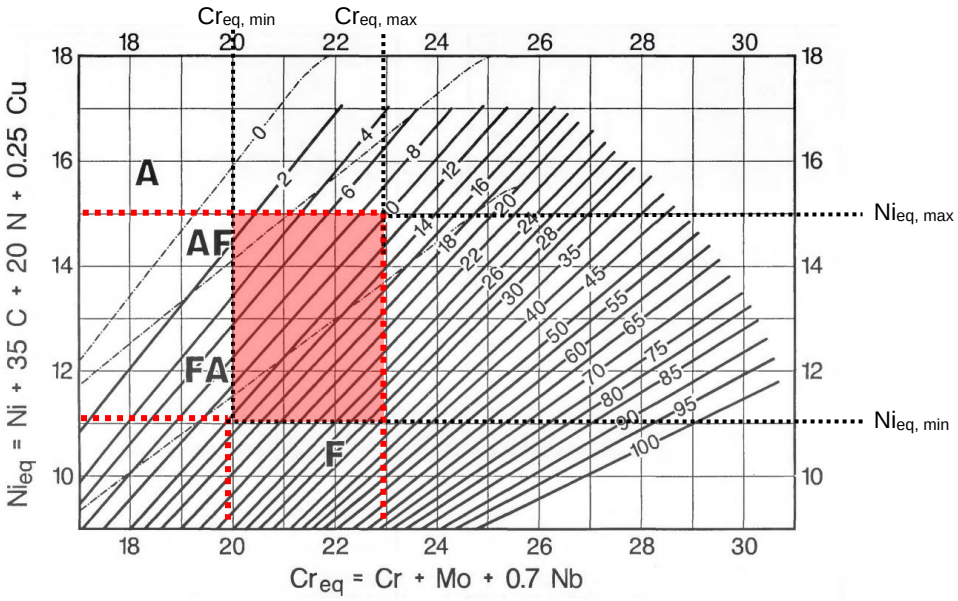

Figure 3.12 WRC-1992 constitution diagram for ferrite number prediction in stainless steel weld metals overlaid with the Cr/Ni_{eq} range of Type 316L (Kotecki and Siewer, 1992).

Whilst constitution diagrams are useful for obtaining estimates of the δ-ferrite content of the weld metal, the mode of solidification also depends on the thermal gradient and the grain nucleation rate (Inoue et al., 2013). The use of high energy density welding approaches such as electron beam and laser beam approaches are known to cause a shift in primary solidification mode in materials of equivalent composition (Fu et al., 2013, Elmer et al., 1989a). The ferrite content and the morphology of DED additively manufactured austenitic stainless components may deviate strongly from that predicted by weld constitution diagrams for advanced pulse arc welding technologies that have resulted in cooling rates similar to power beam welding.

The cyclic re-heating in multi-pass welding and AM re-heating can result in a significantly reduced ferrite number in the reheated areas. Repeat welding has been shown to reduce the percentage of δ-ferrite in the heat-affected zone (AghaAli et al., 2014). In the same way, heat accumulation during the build could additionally cause deviation of phase transformations and precipitates development in AM. The kinetics of δ-ferrite in austenitic stainless steel relates to the fraction of δ-ferrite transformed to austenite, x to the time, t, and temperature, T, as follows:

$$ln[-ln(1-x)] = 19.32 + \frac{ln\,t}{2} - \frac{19{,}860}{T} \qquad (4.2)$$

This relationship is shown graphically in Fig 3.13 showing that at high temperatures decomposition of δ-ferrite can occur rapidly and within AM timescales. Passes of higher heat input resulted in greater δ-ferrite decomposition in multi-pass welding (Gowrisankar et al., 1987) as a result of the greater re-heat distance and peak temperatures initiated. This contrasts with δ-ferrite decomposition in single-pass welding where secondary dendrite arm

spacing and diffusion time effects compensate to result in similar δ-ferrite decomposition for low and high heat input welds (Elmer, 1988).

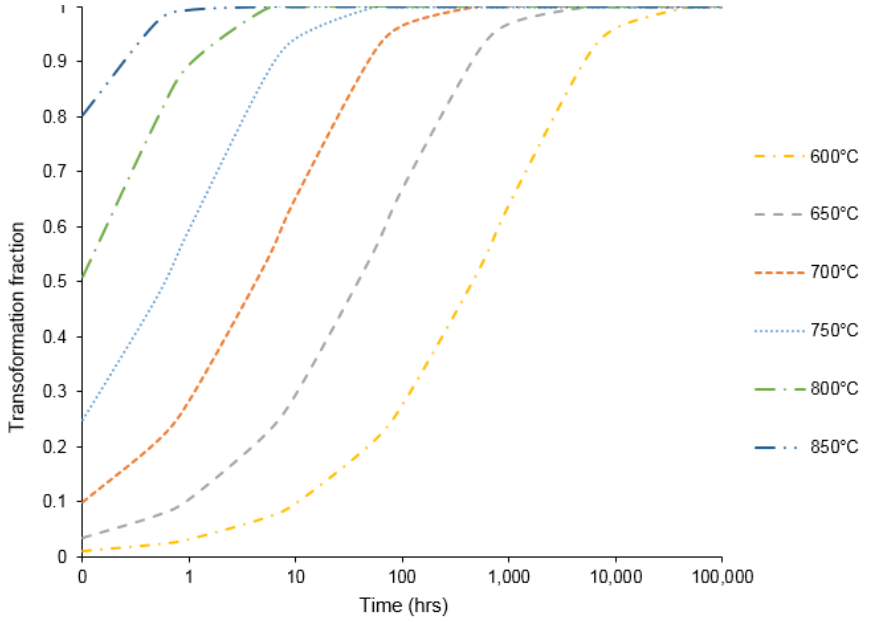

Figure 3.13 Transformation fraction of δ-ferrite with time for holding temperatures 600-850°C.

3.3.2 Intermetallic sigma (σ) and other phases

Due to the high temperatures and extended timescales required, precipitation of Fe-Cr intermetallic σ-phase as shown in Fig 3.14 is relatively uncommon in single pass welding. However, σ-phase can appear if subject to prolonged elevated temperatures and is occasionally observed in multi-pass welding (Moslemi et al., 2015) and after annealing (Kozuh et al., 2009). Chemical analysis of bulk-extracted precipitates was 44 wt.% Fe, 29.2 wt.% Cr, 8.3 wt.% Mo composition in 316L stainless steel (Lai, 1983). The σ-phase precipitates sequentially beginning at grain boundary triple points as shown in Fig 3.15, then after longer times at higher temperatures also at incoherent twin boundaries, and finally nucleating on oxide inclusions (Weiss and Stickler, 1972). The volume fraction of σ-phase increasing with heat-treatment duration (Kozuh et al., 2009).

Intermetallic sigma (σ) phase formation occurs much more rapidly in δ-ferrite than austenite, and slow cooling and post-weld heat treatment are recommended to be avoided for austenitic welds containing some ferrite to prevent σ-phase formation (TWI, 2020). The volume of σ-phase is typically sought to be minimised due be an adverse effect on impact energy, corrosion resistance and ductility (Kozuh et al., 2009). The σ-phase can lower the strength of austenite by consuming the solute elements like Cr and Mo and enhances the strength of the weld by distributing non-deformable particles in a ductile matrix. Gill et al. (1989) reported that σ-phase affects ductility and toughness more than it does any other mechanical properties. Other phases that may be developed during prolonged exposure to high temperatures, include Chi (χ), and Laves (η), Fe_2Mo, although these have not been reported in the literature for welding or WAAM.

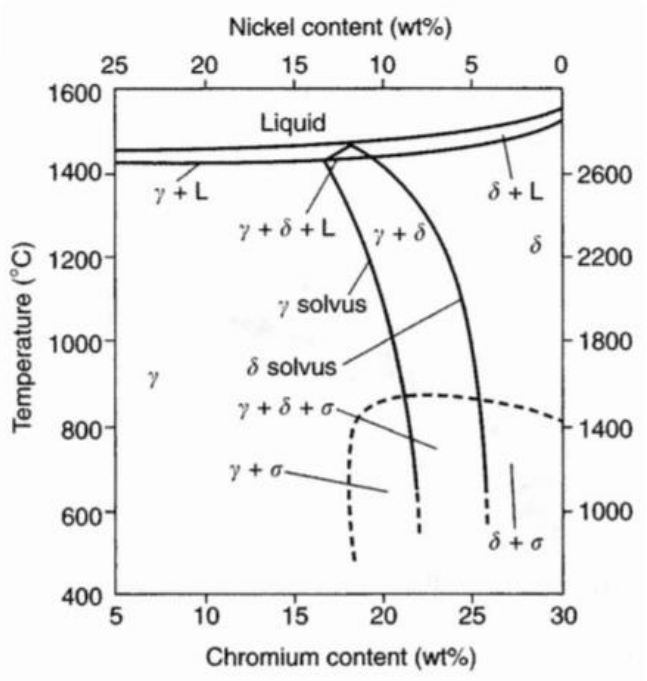

Figure 3.14 Fe–Cr–Ni pseudo-binary diagram at 70% constant iron (Lippold, 2005)

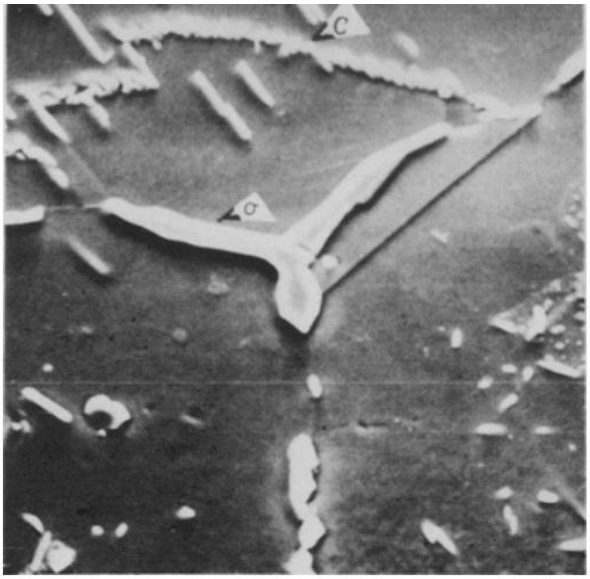

Figure 3.15 Formation of σ-phase from δ-ferrite located at grain boundary triple points (Weiss and Stickler, 1972).

For WAAM of Type 316L stainless steel, Chen et al. (2017b) identified sites of σ-phase precipitation as shown in Fig 3.16. Although the samples were annealed at 300 °C for one hour to relieve the residual stresses, σ-phase precipitation requires lengthy iso-thermal holding cycles of hundreds and sometimes thousands of hours at 550–900 °C (Padilha and Rios, 2002). It can be assumed even with WAAM reheating cycles that this time limit was not approached, and its presence cannot be explained by the existing kinetics theory for conventionally produced stainless steel.

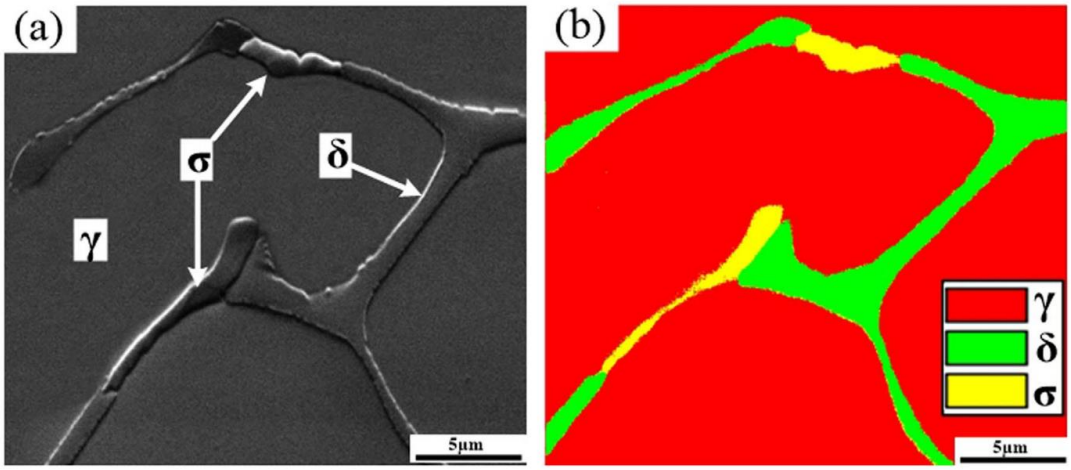

Figure 3.16 σ-phase identified in an ESBD micrograph of WAAM produced 316L. (Chen et al., 2017b)

3.4 The microstructure

The microstructure of Type 316L stainless steel produced by L-PBF has been extensively studied, revealing a hierarchical microstructure presented in Fig 3.17 for L-PBF. The hierarchal structure comprised of melt-pool boundaries, grain boundaries, sub-grains, and cellular structures. At the cell boundaries, dislocations accumulated which are discussed further in §3.6. For E-PBF, Zhong et al. (2017) also identified cellular sub-grains noting that they appeared to strengthen Type 316L whilst maintaining ductility and toughness. The long colonies of cells that crossed melt-pool boundaries smaller were believed to act as a "rope" requiring larger stress to shear the strengthened boundaries with long colonies. The fine grains and the associated Hall-Petch strengthening (Hall, 1951) has often been cited as the reason for the improvements in UTS and σ_{ys} in AM Type 316L stainless steel compared to wrought material (Bartolomeu et al., 2017).

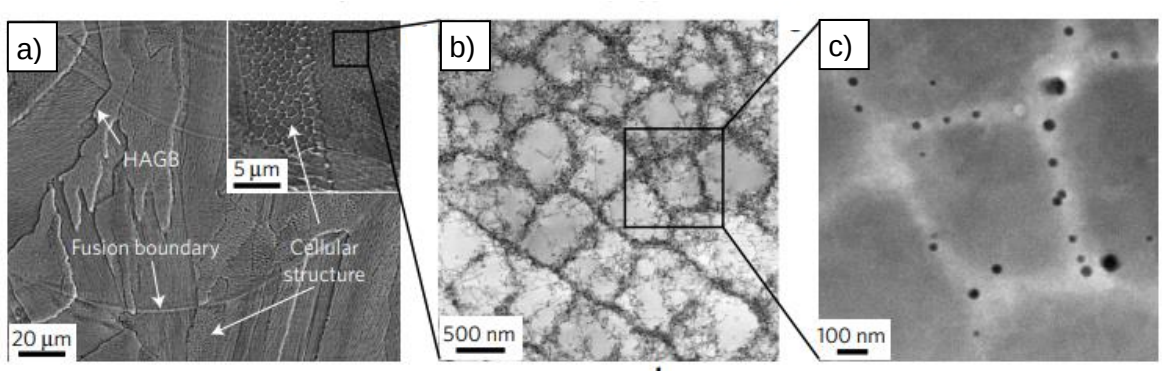

Figure 3.17 a) A SEM image, revealing fusion boundaries, high-angle grain boundaries (HAGBs), and solidification cellular structures. The inset shows the cellular structure at a higher magnification b) a TEM image of solidification cells c) high-angle annular dark-field scanning TEM image of the solidification cells shown in b) (Wang et al., 2018c).

Previous attempts to link the grain size to tensile strength, however, have not always followed the typical Hall-Petch equation: Larger grain size was linked to higher σ_{ys} (Wang et al., 2018c) and several researchers concluded that strength of L-PBF Type 316L stainless steel is mainly determined by its sub-grain cellular structures rather than the usual

number of high-angle grain boundaries. The inverse of the solidification cell diameter has been found to scale to the tensile strength in L-PBF (Trelewicz et al., 2016, Zhong et al., 2016). The contribution to σ_{ys} via this strengthening mechanism was shown to be substantial, contributing 516 MPa and 446 MPa to 590 ± 5 MPa and 450 ± 10 MPa, respectively. In contrast to the cellular microstructure reported for PBF technologies, Type 316L weld-metal often contains dendritic δ-ferrite of lacy and/or vermicular morphology (Xu et al., 2017) as depicted in Fig 3.18 (Koseki and Flemings, 1996).

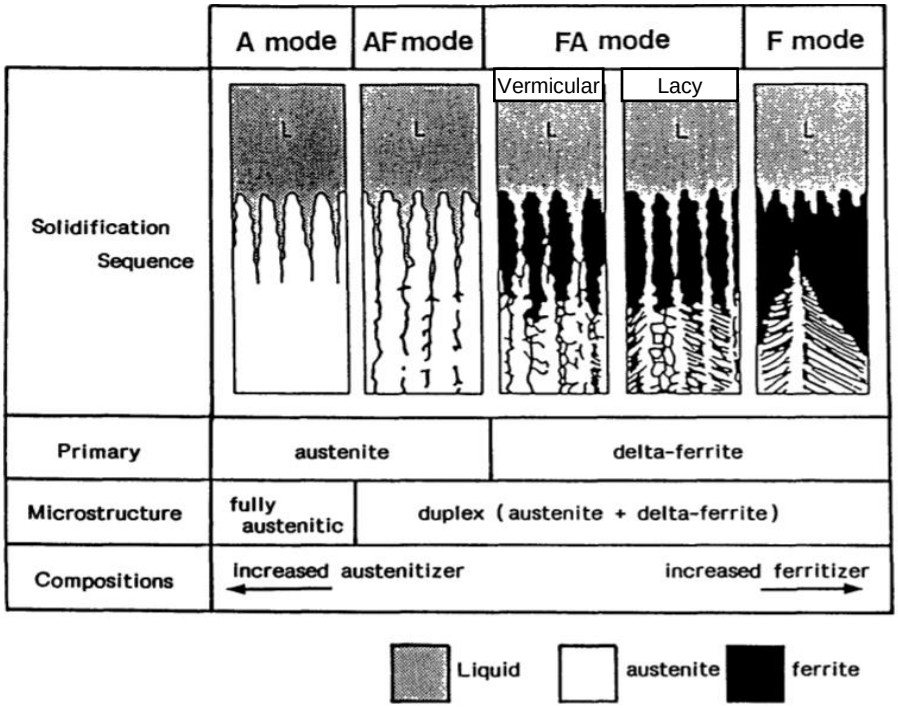

Figure 3.18 Schematic representation of solidification modes in austenitic stainless steel (Koseki and Flemings, 1996).

The heat input of DED processes is higher than that of L-PBF processes and subsequently, a different process-structure-property relationship is developed. A typical WAAM 316L microstructure is shown in Fig 3.19a, highlighting the lacy and vermicular δ-ferrite developed within the austenite matrix. A typical cold-rolled wrought 316L microstructure is shown in Fig 3.19b, in contrast to the WAAM sample, an equiaxed microstructure is present accompanied by horizontal δ-ferrite stringers with identifiable grain boundaries present.

Furthermore, compositional partitioning has also been reported within the cellular solidification structure with Cr enrichment at the solidification boundaries within the dendritic weld metal microstructure (Wenkai et al., 2015) and for WAAM as shown in Fig 3.20 (Wen et al., 2020). Compositional segregation was associated with a higher heat input processing condition. Birnbaum et al. (2019) noted, however, that compositional segregation has been reported inconsistently within the L-PBF literature, from which it was reasoned that it cannot be entirely responsible for the high-levels of strength and ductility reported.

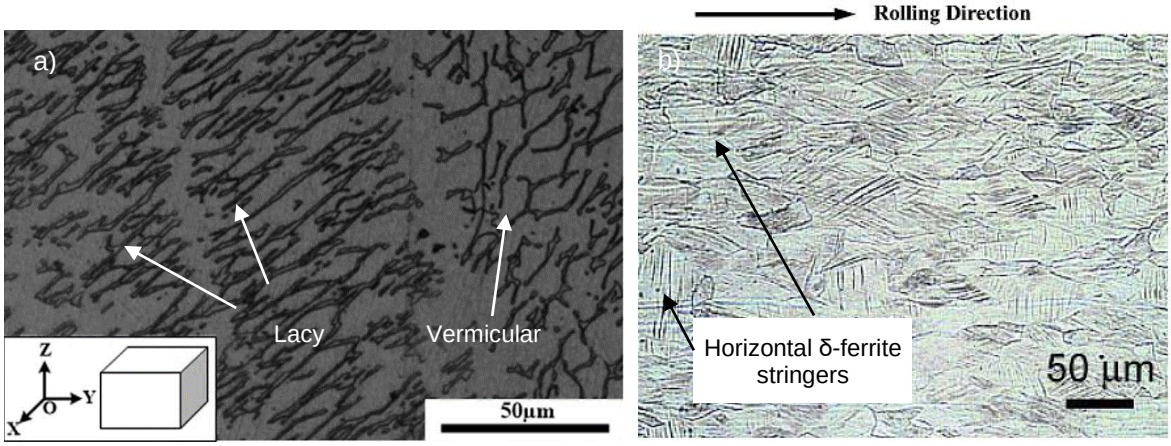

Figure 3.19 a) Lacy morphology of δ-ferrite in MIG based WAAM of 316L (Chen et al., 2017b) b) Microstructure of the cold-rolled wrought 316L stainless steel (Xue et al., 2007).

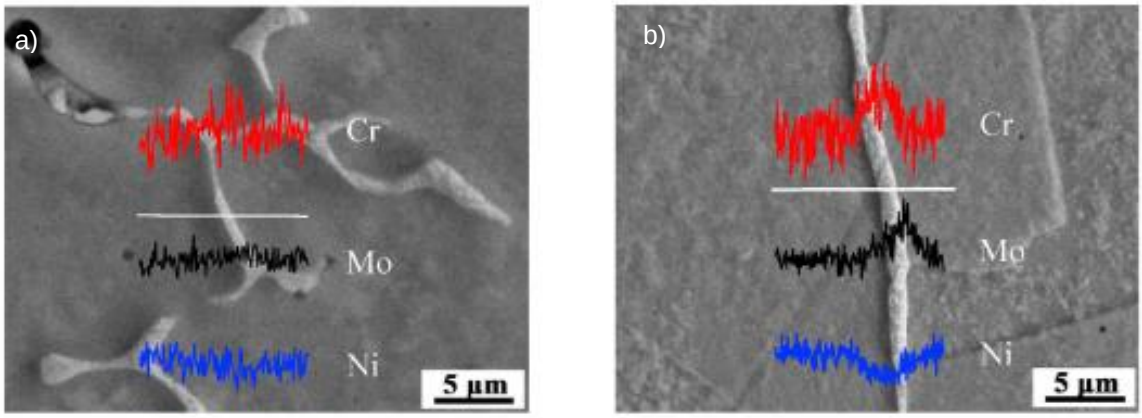

Figure 3.20 SEM-EDS line analysis results of the studied steel for low heat input and high heat input processing condition (Wen et al., 2020).

Chakkravarthy and Jerome (2020) identified large columnar grains 150-200 µm several millimetres in length aligned with the build direction in CMT based WAAM of Type 316L stainless steel. Ma et al. (2017) also found that the reduced cooling rate in L-DED produced coarser columnar grains, reducing the tensile strength, and increasing the ductility. This was supported by results by Zhang et al. (2014) where the σ_{ys} and UTS decreased with increasing laser power and decreasing scanning speed also for L-DED. However, an increase in elongation was not found as may be expected according to the Hall-Petch relationship.

Limited attempts have been made to link the scale of the microstructural features to tensile strength or elongation. Qin et al. (2019), however, found that the grain size was proportional to the mean diameter of the tensile fracture surface dimples, indicating that the scale of the microstructural features can be related to the material ductility as shown in Fig 3.21. Sanchez-Tovar et al. (2011) showed in micro-plasma arc welding of stainless steel 316L that the corrosion current density was higher in the heat-affected zone compared to the base metal, indicating that the solidification structure can worsen corrosion properties. In terms of pitting corrosion resistance, the weld zone presented the worst resistance followed by the heat-affected zone and the base metal. Queguineur et al. (2017) also investigated

the corrosion properties of Type 316L for naval applications produced by CMT based WAAM with an interpass temperature of 100°C. The WAAM material performed worse than the control sample, with corrosion potentials of − 280 mV/ECS and − 393 mV/ECS reported, respectively. Pitting corrosion resistance was also shown to be reduced relative conventionally produced samples for L-DED of Type 316L, which was attributed to the presence of chromium-rich ferrite areas (Ziętala et al., 2016).

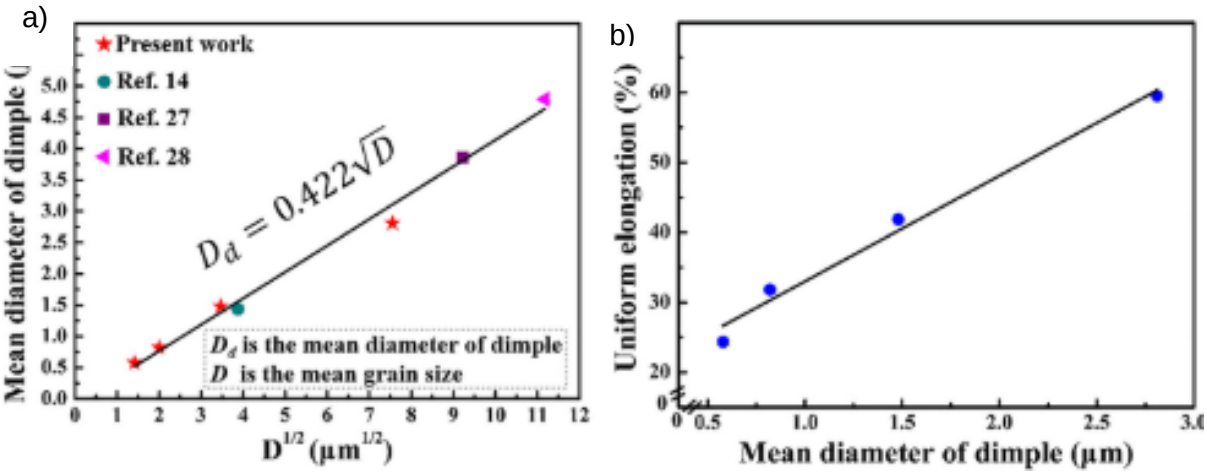

Figure 3.21 Correlation of fracture surface dimple mean diameter and a) grain size b) uniform elongation (Qin et al., 2019)

3.5 Texture & competitive grain growth

The directional thermal gradients and rapid cooling rates in AM can result in a strongly textured microstructure (Bahl et al., 2019) and anisotropic material properties. Nucleation of new grains is energetically favourable at the melt-pool outer boundary because of the low temperature and pre-existing solid-liquid interfaces. The heterogeneous nucleation of new grains in this location represents epitaxial growth, shown schematically in Fig 3.22 where the new grain grows in the same crystallographic direction as the previous grain. Grain boundaries can be difficult to identify from the fine cellular/dendritic microstructure of etched Type 316L stainless steel. Therefore, X-Ray Diffraction or Electron Back-Scatter Diffraction (EBSD) is often used rather than micrographs (Kestens and Pirgazi, 2016)

The <100> direction as shown in Fig 3.22 is an “easy growth” direction in both BCC and FCC metals as solidification proceeds most efficiently along with these directions (Kou, 2002). Depending on the thermal conditions, the easy-grain growth direction can dominate in a process called competitive grain growth. The crystallographic texture of grains strongly influence the material properties including Young’s Modulus (E) (Bohlke and Bertram, 2001), σ_{ys}, (Wang et al., 2019b) and fatigue and creep resistance.

The cubic geometry of both the fcc crystal structure, the number of independent components can be reduced to three directions <111>, <110> and <100> directions. For L-PBF, the tensile strength and ductility of 316L samples could be enhanced by ~16% and

~40% respectively, for the <110> textured microstructure compared to the more common <100> textured microstructure aligned to the build direction. This was attributed to a nano-twinning mechanism that was significantly more activated in the <110> textured stainless steel 316L samples during plastic deformation (Sun et al., 2018b). Wang et al. (2019b) found greater strength and ductility for <110> and <111> compared to <100> due to greater twinning frequency.

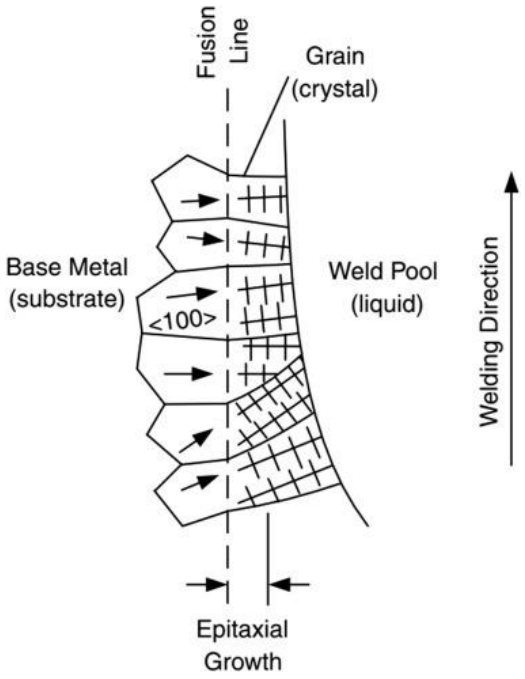

Figure 3.22 Epitaxial and competitive grain growth relative to the melt-pool (Kou, 2002)

Modification of the thermal conditions in AM can adjust the texture with several examples of tailoring of the texture in L-PBF (Andreau et al., 2019, Niendorf et al., 2013). Chakkravarthy and Jerome (2020) found that higher heat input process parameters favoured the growth of austenite towards <111> direction as shown in Fig 3.23. This has also been confirmed by Silva et al. (2009) for application of higher heat in welding of Type 309MoL-16. For the FCC unit cell structure, this direction has the least surface energy and it was suggested the higher heat input parameter could be used to engineer a pronounced increase in corrosion resistance (Murray and Clare, 2012). In contrast, Bouche et al. (2000) found that most of the grains were strongly orientated towards <001> direction in welded joints of 316L because of the higher cooling rates. The as-built texture may also be modified by heat treatment. Yadollahi et al. (2015) longer local found powder L-DED, recrystallized grains were less textured and increased in size from 45 µm to 80 µm.

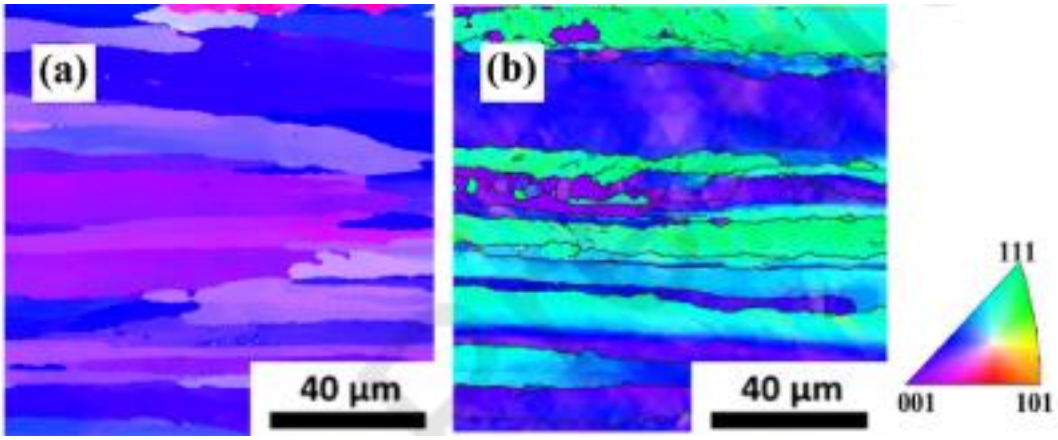

Figure 3.23 a) Orientation map of WAAM 316L material with a) lower heat input process parameters b) higher heat input process parameters

3.6 Deformation behaviour

The motion of dislocations determines the plastic deformation behaviour of materials (Callister, 2003) and the strength of the metals can be improved by hindering dislocation motion. The dense network of dislocations in L-DED austenitic stainless steel has been shown to comprise of mainly geometrically necessary dislocations (GND's), which are introduced to accommodate the strain gradient in the AM process (Sun et al., 2018b). Dislocation strengthening has been shown to comprise a major strengthening component of 316L L-DED stainless steel with mechanical properties such as hardness shown to be directly proportional to the GND density. The GND's are found to be representative of the overall dislocation density in additively manufactured material (Smith et al., 2019) with σ_{ys} proportional to $\sqrt{GND}$ (Bailey and Hirsch, 1960) as shown in Fig 3.24. However, zones of high dislocation density can detrimentally affect corrosion resistance (Solomon and Solomon, 2010). Most hardening mechanisms that hinder dislocation movement such as those enabled by solutes by solid dislocations, and precipitates, albeit leading to high strength, often reduce ductility (Raabe et al., 2013).

In L-PBF of Type 316L, a dense dislocation location network has been observed at the cellular walls (Birnbaum et al., 2019, Wang et al., 2018c) as shown in Fig 3.17. This type of dislocation network is not present in conventionally produced type 316L stainless steel. The gathering of dislocations at the cellular walls indicates a strong dislocation trapping and retention mechanism, which usually are only present at the high-angle grain boundaries in conventionally produced material. According to Liu et al. (2018), the dislocation network in AM 316L stainless steel material slows down but does not entirely block the dislocation motion, resulting in superior strength and ductility. This outlines the importance of the cellular solidification structure concerning the as-built properties of AM produced Type 316L. The dislocation network present in L-DED of type 304L has been also shown to require additional energy to initiate recrystallization compared to forged 304L (Smith et al., 2018) indicating that strength can be retained at higher temperatures than conventionally

produced material. The additional hardness provided non-recrystallised samples also outlines the importance of the microstructure in the hardness for L-DED.

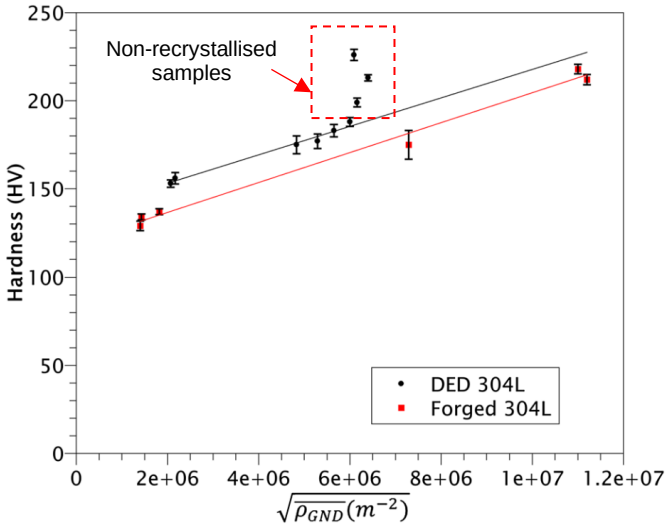

Figure 3.24 Relationship between hardness and GND (Smith et al., 2018)

Twinning induced plasticity (TWIP) and Transformation induced Plasticity (TRIP) behaviour can also improve strength and ductility as discussed in §3.6.1 and §3.6.2. These are notable mechanisms, as other strengthening mechanisms of work hardening, solid solution strengthening, precipitation hardening, grain boundary strengthening act to reduce ductility with an increase in strength (Lu et al., 2009).

3.6.1 Twinning induced plasticity (TWIP)

Twinning induced plasticity (TWIP) steels are a class of austenitic steels that can deform by both glide of individual dislocations and by mechanical twinning (De Cooman et al., 2018). This results in a dynamic grain refinement process and the introduction of new crystal orientations. The twins increasingly decrease the mean free path for dislocation glide, thus increasing the flow stress leading to an increasing work hardening capacity and superior ductility (Rahman, 2013). This can lead to combinations of high strength (ultimate tensile strength up to 800 MPa) and ductility (elongation to failure up to 100%) based on a high work-hardening capacity (Gutierrez-Urrutia and Raabe, 2012).

Mechanical twinning is promoted by higher stacking fault energy between 15 and 30 mJ/m^2 (Lu et al., 2016). TWIP steels generally achieve this stacking energy by having high contents of Mn above 20% in wt.% and C, N, Cr, Ni, Si, Mn, and Mo act to increase the stacking fault energy of the austenite (Angel, 1954). The Type 316L stainless steel, however, contains low wt%. of Mn and C, and twinning is rarely observed in material processed through conventional manufacturing routes (Mishra et al., 2013). Despite this, strong deformation twinning has been observed in the AM of 316L (Pham et al., 2017, Liu et al., 2018). Nitrogen can lead to the disassociation of dislocations deformation twinning and the nitrogen addition in AM material, especially where an inert atmosphere of nitrogen gas used during manufacture has been cited as a cause of the TWIP behaviour (Pham et al., 2017).

Pan and Chen (1995) found that deformation twinning was rarely observed in a non-restrained plate butt joint welding in contrast to the restrained experiment. The crystallographic texture has also been found to promote a higher degree of twinning activity (Shamsujjoha et al., 2018, Sun et al., 2018b, Wang et al., 2019b). It can be seen in Fig 3.25 that twinning activity is much more common in the <111> crystallographic directions. Whilst TWIP behaviour has been commonly identified in materials produced by PBF(Pham et al., 2017, Shamsujjoha et al., 2018, Wang et al., 2019b), it has only been observed in for L-DED material and it is yet to be identified as an active deformation mechanism for WAAM produced Type 316L.

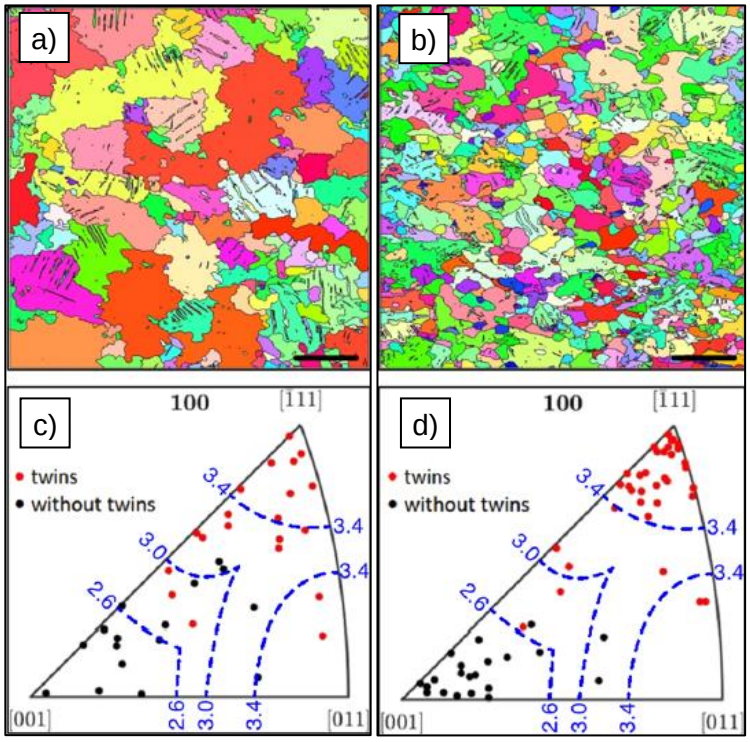

Figure 3.25 EBSD micrographs showing twinning locations (a,b) and frequency with orientation (c,d) in Type 316L produced by LB-PBF (Sun et al., 2018b).

3.6.2 Transformation induced plasticity (TRIP)

At sufficiently low deformation temperatures, the dissociation tendency of the dislocations in Type 316L stainless steel enables the formation of the ferromagnetic α'-martensite phase to which the transformation-induced plasticity (TRIP) effect is attributed. This has been observed by several authors in cold deformed Type 316L (Nakada et al., 2010). In contrast to TWIP, the lower the stacking fault energy and the less stable the γ-austenite, the higher the susceptibility to martensite formation. The transformation of austenite-to-martensite involves a volumetric expansion. This increases the dislocation density and generates the hard martensite phase in the soft austenite matrix. This can increase the strain hardening rate and delay the onset of localized necking (Grassel et al., 2000).

The volume fraction of martensite can be controlled through the steel chemical composition, of plastic strain quantity and temperature. The rate of α'martensite formation increases for

lower deformation temperatures and greater strain as shown in Fig 3.26, which shows that this can occur in strained commercial bar stock of Type 316L. Strain-induced martensite formation is also dependent on grain size. For coarse-grained Type 316L structure, at a similar level of tensile elongations (Misra et al., 2018, Gutierrez-Urrutia and Raabe, 2012) deformation proceeded only by TRIP compared to fine-grain material, which favoured TWIP and thus can be expected to be more likely to form in WAAM Type 316L of large grain sizes. The α'-martensite transformation has been shown to become pronounced below 100°C, whereas for temperatures above 250 °C the steel glide deformatio0n dominates and below 250 °C strain-induced twinning replaces the glide deformation at temperatures with the increasing strain (Kovalev et al., 2011).Greater strengthening is provided for greater levels of pre-strain and untransformed α'martensite as illustrated in Fig 3.27. Hong et al. (2019) found very low levels of α′ martensite in the L-PBF of Type 316L sample at 300K, however, this increased with reducing temperature. The lower volume of α′ martensite relative to conventional annealed material found for L-PBF of Type 316L was attributed to suppressed dislocation slip and deformation twinning during deformation, decreasing α' martensite nucleation sites, however, this can also be attributed to the refined grain size.

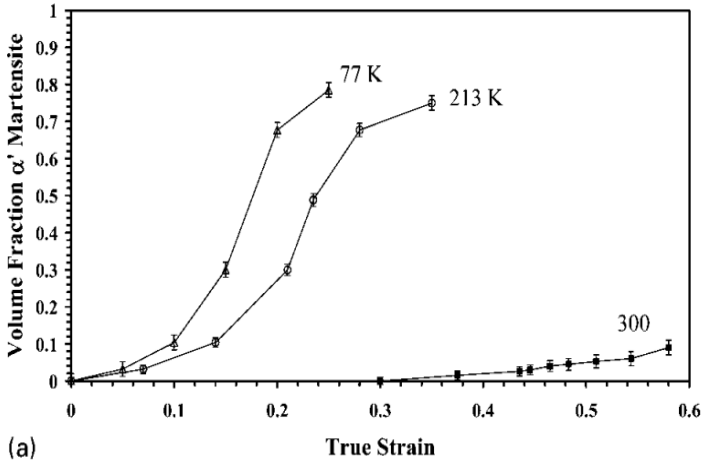

Figure 3.26 Evolution of α' martensite volume fraction at three different deformation temperatures for Type 316L fabricated from commercial bar stock with the tensile axis in the extrusion direction (Spencer et al., 2013b)

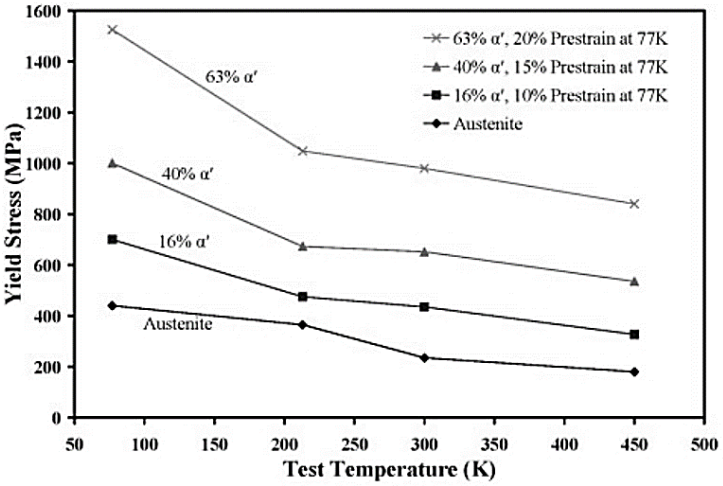

Figure 3.27 Temperature dependence of untransformed austenite in 316L stainless steel and un-tempered martensite in Fe– 21Ni–C alloy (Spencer et al., 2013a).

The introduction of α'-martensite by cold deformation and subsequent reversion by annealing produces soft recrystallized domains of lamellar coarse grains that are surrounded by hard nanograins/nano-twins (Li et al., 2018b). This microstructure was produced by 85% cold rolling and annealing at 750°C for 5–25 min. This unique microstructure has been shown to generate desirable combinations of strength and ductility in Type 316L alongside the TRIP mechanism (Kheiri et al., 2019).

3.7 Physical defects

Physical defects that occur in DED include lack of fusion, cracks, pores, stop/start flaws, and surface flaws (Seifi et al., 2017). Residual stress and inclusions may also be considered a defect if the effects on material properties or geometry are detrimental. For DED, a relatively new manufacturing technology, the effects of these defects are still being understood. For qualification purposes, efforts are being made to establish defect tolerance limits, where the acceptability of the defect depends on part design and application criticality.

For Type 316L stainless steel welding, the presence of lack of fusion voids and cracks depends on the heat input selected, as shown in Fig 3.28. These regions can serve as crack initiation sites under mechanical stress due to the less integral metallurgical bonds formed (Wenkai et al., 2015). Pores may also be introduced during the additive process or originate from the feedstock (Ryan et al., 2018).

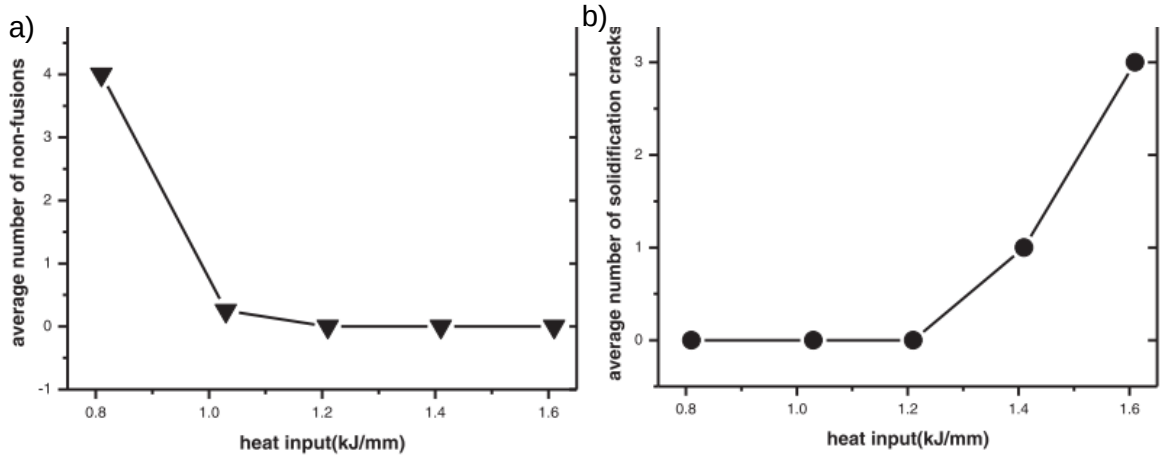

Figure 3.28 a) Average number of non-fusions detected (b) Average number of solidification cracks detected in ten entire cross-sections of each welded samples (Wenkai et al., 2015).

Porosity has been cited as a cause of reduced ductility in L-PBF samples. Studying the effect of heat input on pore distribution and mechanical properties, Jost et al. (2019) found that lower levels of heat input or energy density resulted in the lowest average pore area and highest levels of ductility and σ_{ys} as presented in Fig 3.29, although UTS was unaffected.

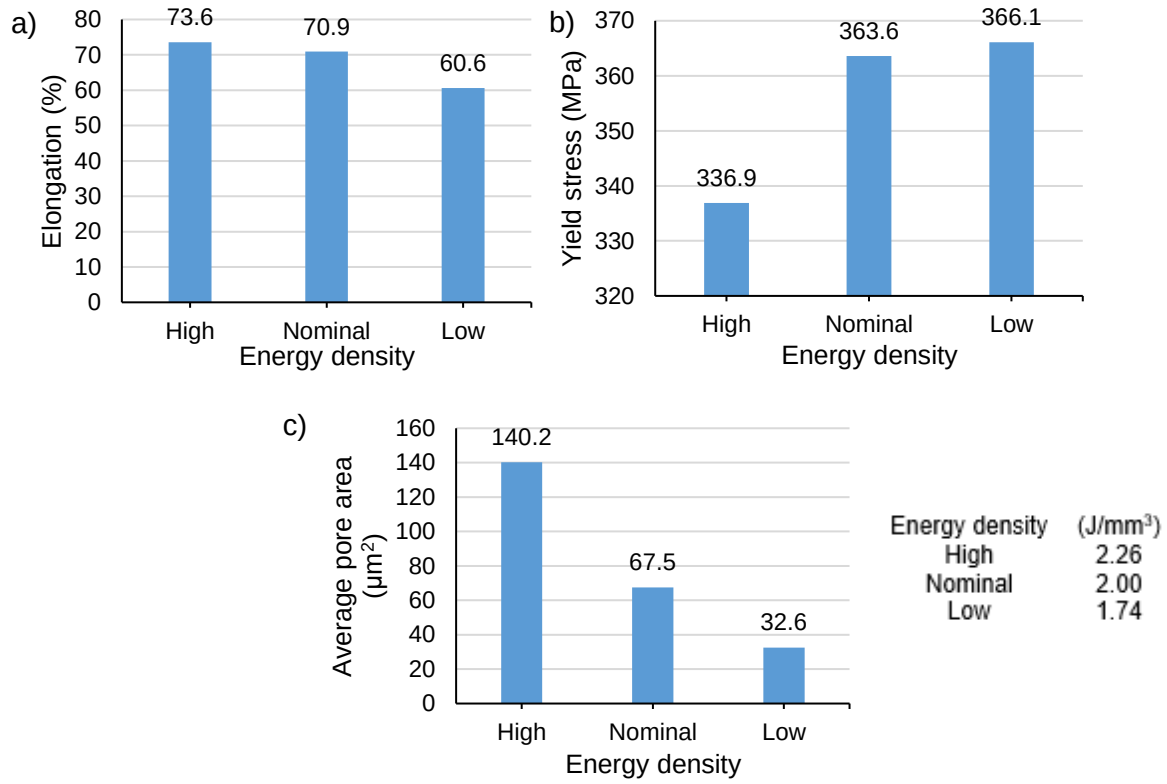

Figure 3.29 Correlation of a) Elongation, b) yield stress and c) average pore area with energy density (Jost et al., 2019).

Yadollahi et al. (2015) found that porosity was more prevalent in locations further upward from the build plate due to reduced laser penetration depths. The porosity and, lack of fusion between layers particularly longer inter-layer time intervals because the presence of intra-layer oxides was considered to have contributed to the observed ductility of 12-20% elongation.

For WAAM, there has been limited investigation regarding porosity and lack of fusion processing defects and their effect on mechanical properties. However, it has been noted that because of the high toughness of austenitic stainless steel, lack of fusion or porosity defects do not result in as severe early life failure cracks compared to other metal alloys such as Ti-6Al-4V (Leuders et al., 2014, Gordon et al., 2018). The monotonic material properties are reported to be maintained even with relatively high porosity for Type 316L L-PBF (Zhang et al., 2017). The low levels of porosity and lack of fusion defects reported for WAAM of stainless steel (Wu et al., 2018b), indicate that the material performance may not be as greatly affected by relative density as it is for example compared to microstructural features, which have been subject to a greater research effort.

3.8 Residual stresses and distortion

During solidification in the FA mode, which is typical for welding, primary δ-ferrite transforms to γ-austenite in a very short time. The γ-austenite phase has low levels of thermal conductivity and high thermal expansion of austenitic stainless steel which results in higher

levels of distortion when welding compared to other stainless steel grades, as a result of the phase transformation and thermally induced contraction welding. This can impart significant work hardening and residual stresses (Jiang et al., 2015). The residual stress-induced distortion, whilst not reported by the authors, was evident for WAAM of 316LSi as shown in Fig.4.30.

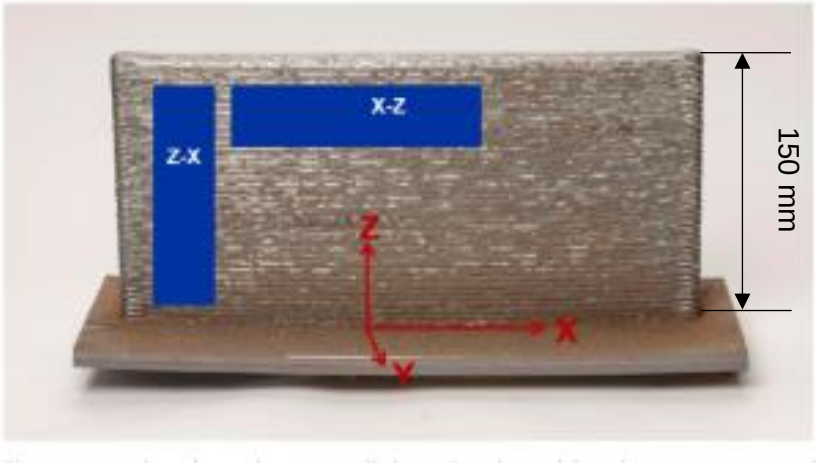

Figure 3.30 Scale of substrate distortion in MIG-based WAAM of Type 316L (also showing notch orientations parallel to the deposition layers (Z–X) and perpendicular to the layers (X–Z) for fatigue testing) adapted from (Moore et al., 2019)

Investigations into the effect of laser power and speed reveal that as the energy per unit length increased, residual stress-induced deflection upon sectioning is decreased (Wu et al., 2014). Experimental observations made for Inconel 625 L-DED builds show that the accumulation of distortion occurs with a consistent trend throughout the builds and both distortion and residual stress levels decrease with increasing dwell times from 0 to 40 s. On the other hand, changes in dwell time for the Ti6Al4V laser deposited builds have a significant impact on the accumulation of distortion, with shorter or no dwell times minimizing the distortion accumulation and even reducing it over a range of build heights (Denlinger et al., 2015). Greater levels of plastic deformation can increase dislocation density and mechanisms that affect deformation behaviour such as TRIP and TWIP as discussed in §3.6.

3.9 Mechanical properties of Type 316L stainless steel produced by AM

The mechanical properties of Type 316L stainless steel have been widely explored for L-PBF (Casati et al., 2016, Zhong et al., 2016, Khairallah et al., 2016, Wang et al., 2018a, Rännar et al., 2017, Pace et al., 2017, Pham et al., 2017). These studies report mechanical tensile strengths significantly higher than those provided by as-cast and wrought material. However, the high strength has been achieved with a large variation in ductility. Elongation values of below 15% (Saeidi et al., 2017) and above 70% have also been reported for L-PBF (Bartolomeu et al., 2017, Saeidi and Akhtar, 2018, Liverani et al., 2017). The high ductility reported is very unusual as according to the Hall-Petch relationship, the fine

microstructures that provide higher tensile strength are usually associated with a trade-off in ductility. Attempts to explain this relationship have been made by several authors (Nguyen et al., 2019, Shamsujjoha et al., 2018, Wang et al., 2018c, Sun et al., 2018b) with major contributors to this result including the dislocation structure and TWIP as introduced in §3.4 and §3.6.1, respectively.

To date, several studies have demonstrated that WAAM can achieve a UTS, $\sigma_{ys,}$ and elongation higher than that of cast material, and in the region of that provided wrought and annealed material. The mechanical properties reported within the literature for Type 316L produced by a range of WAAM process types are highlighted in Table 3.3. The horizontal specimen orientations refer to those extracted aligned to the torch travel direction and the vertical represents those extracted in an orientation aligned to the build direction.

Table 3.3 Mechanical properties of WAAM 316L stainless steel, compiled from a review of the literature.

WAAM process type	**Specimen orientation**	**Interpass build strategy – dwell duration**	**UTS (MPa)**	**σ_{ys} (MPa)**	**Elongation (%)**	**Ref**
MIG	Vertical	Fixed dwell – 2 min	533±23	235±6	48±2	(Chen et al., 2017b)
MIG-CMT continuous	Vertical	Fixed dwell - unspecified	547.0± 7.9	336.9 ± 1.7	42.0±3.7	(Rodriguez et al., 2018)
	Horizontal		577.3± 4.0	364.3± 13.9	43.4±4.7	
MIG-CMT pulsed	Vertical		536.0± 15.3	331.7± 5.4	45.6±16.7	
	Horizontal		588.0± 5.7	374.0± 11.2	45.1±3.5	
TIG^3-TopTIG	Vertical		539.9± 14.7	322.2± 2.7	43.1± 6.9	
	Horizontal		590.3± 3.6	365.5± 8.7	42.3± 2.7	
MIG-CMT	Vertical	100°C interpass temperature	537.0	313.0	41%	(Queguineur et al., 2017)
	Horizontal		551.0	369.0		
MIG – Speed Pulse	Horizontal	Fixed dwell – 20 s	550.0 ± 6	418.0	-	(Wang et al., 2019a)
MIG – Speed Arc	Horizontal	Fixed dwell – 20 s	553.0 ± 2	417.9	-	
MIG	Vertical	Fixed dwell – 10 s	619.5±13.1	344.3±10.8	-	(Wu et al., 2019a)
	Horizontal	Fixed dwell – 10 s	547.9±32.3	340.7±8.7	-	
	Vertical	Fixed dwell – 15 s	614.4±17.6	361.4±11.5	-	
	Horizontal	Fixed dwell – 15 s	580.9±27.2	340.7±8.7	-	
MIG-CMT Parallel weld bead	Vertical	Max. 400°C interpass temperature	-	283-289	-	(Moore et al., 2019)
	Horizontal		-	303-312	-	
MIG-CMT Oscillating weld bead	Vertical	Max. 400°C interpass temperature	-	324-331	-	
	Horizontal		-	372-422	-	
Double wire MIG-CMT+P 3.5 m/min	Horizontal	Not specified	480.19 ± 6.5	237.09 ± 3.3	49.89 ± 4.5	(Wu et al., 2019b)
Double wire MIG-CMT+P 5 m/min			458.52 ± 7.6	238.13 ± 7.5	48.63 ± 5.7	
Wrought (annealed)	-	-	485	170	40	(ASTM A240/A240M, 2004)
Wrought Cold/Hot-rolled strip	-	-	550-700	200-220	40	(BS EN 10088-2, 2014)

It can be seen from the results reported that mean UTS and σ_{ys} achieve the minimum standards for the wrought material. The ductility, however, is often below the uniform elongation specified for wrought material, containing high levels of scatter. High levels of variation in elongation were also found for plasma-based WAAM of 309L (Feng et al., 2018). In many instances the tensile samples have been significantly below the ASTM E8 sub-size sample recommendation, for example, a gauge length of 12 mm × 3 mm × 1.5 mm for Wu et al. (2019b) with strain rates up to 2mm/min which is significantly above that recommended by BS EN ISO 6892 (2016). This makes extracting meaningful relations between process parameters and mechanical properties from the published literature difficult.

The Young's Modulus is less commonly reported in the literature. Pham et al. (2017), however, found the E to be 183 GPa±12 GPa for L-PBF, slightly less than the E for conventional Type 316L, which was attributed to the presence of porosity in the AM sample. Joosten (2015) also identified below specification E values for unmachined WAAM samples ranging between 100-200GPa. Below specification values of E were also identified in powder L-DED, however, these were significantly lower than previously reported, averaging 3.5 GPa (de Lima and Sankaré, 2014). It was noted that many defects such as pores and cracks were present in the tested specimens, which may have influenced the result. The spread in E is an important aspect to consider when designing a structure. Lower means appreciable deformation in the beginning without significant values of stress (Riza et al., 2014). This can lead to alternative load paths being engaged and overloading of stiffer structures. In addition, light-weighting often requires stiffer, denser materials as wall thickness is reduced (Münstermann et al., 2014), meaning that it is important that additively manufactured materials can provide at least the minimum specification of E in the chosen material for these applications.

Limited data is available for additively manufactured 316LSi stainless steel, however, Akbari and Kovacevic (2018) investigated wire L-DED of this material for block specimens and thin-walls as shown in Table 3.4. The thin-wall horizontal specimens showed higher mean uniform elongation and reduced scatter compared to the vertical specimens.

Table 3.4 Mechanical properties of wire L-DED 316LSi stainless steel (Akbari and Kovacevic, 2018).

Part type	Specimen orientation	Interpass build strategy (dwell duration)	UTS (MPa)	σ_{ys} (MPa)	Elongation (%)
Flat block (see Fig 3.31a)	Horizontal -Across tool path	420s	629-635	430-440	36-40
	Horizontal-Along tool path		593-600	415-425	30-37
Thin wall (See Fig 3.31b)	Vertical	25s	484-522	220-270	32-40
	Horizontal		516-546	260-300	39-42

Overall, fatigue performance for the as-built specimens was comparable to or exceeded conventional wrought 304L and powder L-DED in the as-built condition (Gordon et al.,

2018). This contrasts strongly to L-PBF where fatigue strength has been reported to be significantly lower than conventionally produced material due to physical defects. As discussed in §3.5, an increase in the WAAM heat input improved the corrosion resistance by modifying the texture of the microstructure (Silva et al., 2009). The water-cooled cladding of stainless steel 316L with Inconel 52M the corrosion resistance of the water-cooled specimen is lower than that of the non-cooled specimen since the higher cooling rate induced in the TIG process prompts a larger volume fraction of grain boundaries and greater residual stress (Lin et al., 2017). Repeated weld repair process prompted a greater transformation of the lathy ferrite phase to short ferrite precipitates, decreasing pitting corrosion resistance (AghaAli et al., 2014). The greater sensitivity of the repaired material is the result of the higher grain boundary energy induced by the repeated welding repair process. However, the uniform corrosion resistance increased due to the overall reduction in the δ-ferrite phase.

3.9.1 Anisotropy and location-dependent properties

Rodriguez et al. (2018) and Akbari and Kovacevic (2018) showed that horizontal wire DED specimens can provide slightly greater levels of ductility than vertical specimens. Alsalla et al. (2018) also identified greater levels of ductility in horizontal specimens for L-PBF, with 41%±1.9 reported in contrast to 35%±0.6 in the vertical direction. Guo et al. (2017) attributed the lower levels of elongation and σ_{ys} in the vertical direction to weak metallurgical bonding between layers for L-PBF. Some indication anisotropy in the mechanical strength (Rodriguez et al., 2018, Queguineur et al., 2017), with samples stronger in the horizontal direction, is shown, although this was not supported by Wu et al. (2019a). Overall, there is limited data is available in terms of the anisotropy for WAAM specimens, with many studies, presenting an average of the tensile properties so that anisotropy or degradation in properties with build height cannot be identified. For powder L-DED, conversely, greater levels of ductility in the vertical build orientation have been found as shown in Table 3.5. Shamsujjoha et al. (2018) found a similar trend for L-PBF, vertical samples showed higher levels of uniform elongation (77%) compared to the horizontal direction (49%). The overall high levels of ductility and anisotropy of the L-PBF samples was attributed to higher twinning activity in the vertical samples because of the prevalent texture. Chemical analysis revealed N content to be 0.049%wt and below the ASTM A240M specification of 0.1%wt maximum, suggesting that the nitrogen atmosphere was not a factor in promoting twinning activity.

Table 3.5 Difference in yield strength and elongation in powder L-DED for 316L

Horizontal		**Vertical**		**Reference**
σ_{ys}	***e***	σ_{ys}	***e***	
495	51	275	62	(Yu et al., 2013a)
558	21	352	46	(Zhang et al., 2014)
593	30	448	66	(Griffith et al., 2000)
580	6.5	415	4	(Guo et al., 2017)

Several authors have also observed location-dependency within the material properties concerning the build-height. Yu et al. (2013a) found variation in σ_{ys} and hardness from bottom to top of the build, with micro-hardness varying from 205 ± 10 HV and 174 ± 10 HV respectively, which was also reflected in the dendrite arm spacing. Skiba et al. (2009) found that for TIG based WAAM of 308L that the micro-hardness and elongation reduced with build-height. Zhang et al. (2018b) also found lower values of micro-hardness. The lower micro-hardness at the top of the build was attributed to the lower cooling rate due to heat accumulation. Akbari and Kovacevic (2018) found that samples extracted closer to the substrate for parts as shown in Fig 3.31a as opposed to thin-wall specimens as shown in Fig 3.31b resulted in improved material properties detailed previously in Table 3.4. This result was also confirmed for powder L-DED 304L (Smith et al., 2019).

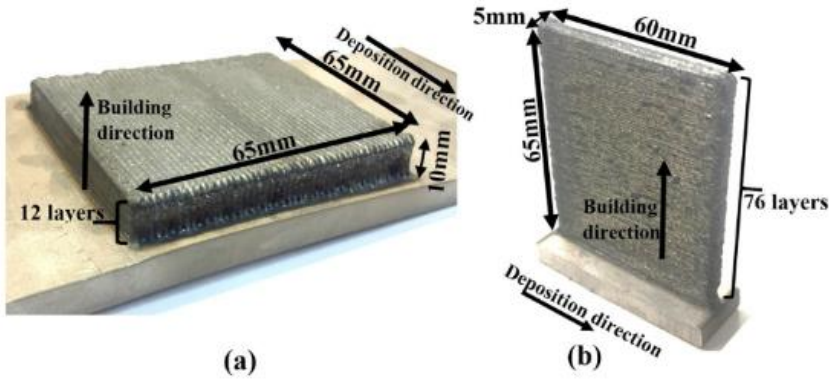

Figure 3.31 Deposition strategy where specimens were extracted a) close to the substrate in a flat block sample b) further away from the substrate in a thin-wall sample for wire L-DED (Akbari and Kovacevic, 2018).

In contrast, however, higher levels of hardness were observed close to the surface at maximum build-height for L-DED, and micro-hardness varied periodically with dendrite refinement as shown in Fig 3.32 (Li et al., 2016, Xu et al., 2017). This periodic variation is similar to that found in welding, heat-affected zone (HAZ), and base metal as shown in Fig 3.33. However, whether the periodicity in micro-hardness and fine grain zone is distinguishable depends on the final microstructure after the re-heat cycles. AghaAli et al. (2014) noted that micro-hardness increases after the first cycle of repair welding due to recrystallisation, however, decreases in the second and third repairs due to grain growth.

As a consequence of the location-dependency of the micro-hardness, the machinability and ease of post-processing of the material can be affected. Guo et al. (2017) found that the CNC cutting force in building direction was much higher because of the higher hardness compared to samples machined in the welding torch travel direction. This resulted in greater levels of tool wear and machined surface roughness.

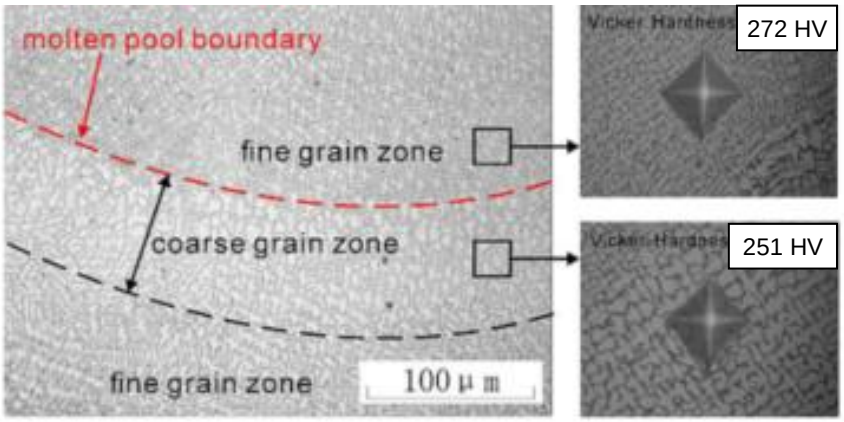

Figure 3.32 Periodic variation in hardness for the fine and coarse grain zone for L-DED 316L (Li et al., 2016)

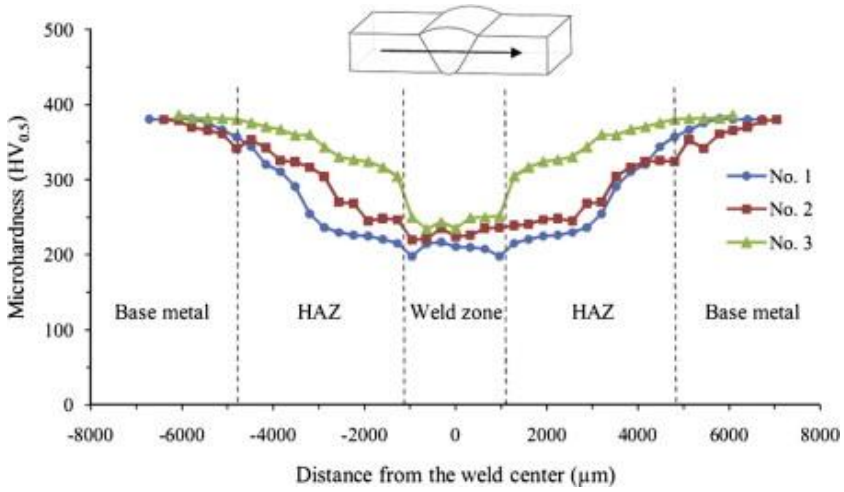

Figure 3.33 Typical Vickers microhardness values vs. distance from the welding axis (Mirshekari et al., 2014)

3.10 WAAM primary process selections, process parameters, and additional processes

The overall heat flux and thermal history of a WAAM build is determined by the primary process selections, the process parameters, and additional processes outlined in chapter 2. Principles of design for AM can also be applied to influence the heat flux and thermal history (Lockett et al., 2017) and residual stress profile (Denlinger and Michaleris, 2015); rotation of build orientation or part re-design can influence factors such as layer length, surrounding geometry and overall build time.

The process parameters directly affect the heat flux during the build and thermal history. Heat input may be changed by modifying the arc power supply or adjusting travel speeds. For WAAM, Wang et al. (2019a) investigated two different welding power supply pulse technologies. The lower heat input pulse technology resulted in higher tensile strengths, which was attributed to the finer solidification structure. Shorter interpass dwell times resulted in a coarser microstructure, lower strength, and higher elongation to failure. This was attributed to the lower cooling rates because of the increased bulk temperature in the part (Yadollahi et al., 2015). However, an interpass temperature was not specified.

Furthermore, Wu et al. (2019a) only varied the interpass dwell period between 0-15s for which signification differences in microstructural development might not be expected. The lack of phase transformations in welding after solidification mean that an interpass temperature is not often specified, although some authors have limited interpass temperature to around 100°C-150°C (Costanza et al., 2016, Mirshekari et al., 2014).

Feng et al. (2018) also explored the effect of heat input on the properties of stainless steel 308L with plasma-based, single, and dual wire-feed WAAM with an interlayer dwell period of two minutes. While the UTS remained relatively constant across the heat inputs investigated, a significant change in grain size, associated with a 10.2% increase in UTS was found as shown in Fig 3.34 for the dual-wire feed approach. This was attributed to the rapid cooling caused by the introduction of another wire to the melt pool.

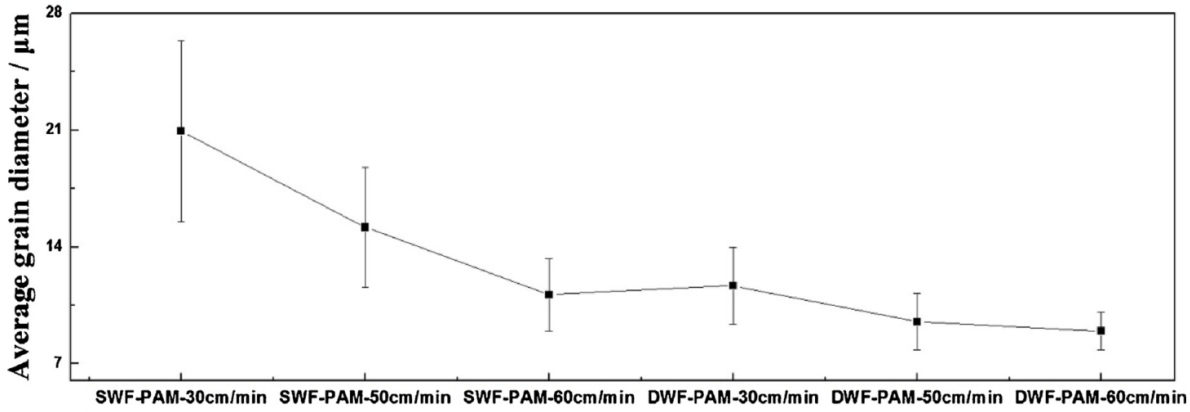

Figure 3.34 Variation in average grain diameter with single wire feed (SWF) and dual wire feed (DWF) plasma-based WAAM of type 309L at various travel speeds (Feng et al., 2018).

3.11 Critique and Research Gaps

In comparison to L-PBF and E-PBF applications, the exploration of the material characteristics has been comparatively limited for WAAM and the current lack of comprehensive understanding of the process-property-microstructure means that the causes of the scatter are not well understood. Aspects of the Type 316L microstructure that have not been investigated for WAAM include nitrogen solid solution strengthening and ODS. Studies investigating the mechanical properties of WAAM austenitic steel have shown that the wrought specification can be exceeded in terms of UTS and σ_{ys} (Chen et al., 2017b, Rodriguez et al., 2018, Wang et al., 2019a, Wu et al., 2019a). However, these characterise Type 316L WAAM material only for authors chosen set-up (welding power supply, fixed parameters). The investigations of the performance of WAAM of Type 316L have yet to study the variable processing conditions such as heat input, deposition rate and interpass temperature control. In addition, the effects of additional processes introduced in Chapter 2 have not yet been investigated which may yield improvements to cost-effectiveness or materials performance.

One of the main challenges in the continued adoption of AM by industries is the uncertainty in the structural properties of their fabricated parts (Yadollahi and Shamsaei, 2017), as predictable and high-quality production is required for certification and qualification purposes. Therefore, for WAAM of Type 316L, the scatter in reported the mechanical properties (Chen et al., 2017b, Rodriguez et al., 2018, Wang et al., 2019a, Wu et al., 2019a) is concerning, especially for elongation. An understanding of how the variable processing conditions such as heat input, deposition rate and interpass temperature control affect the mechanical properties is required to aid the uptake of the process.

Whilst it has been shown that the texture can be changed by different levels of heat input to improve corrosion resistance (Chakkravarthy and Jerome, 2020), the impact of the texture changes on the mechanical properties and anisotropy remains uncertain. Meanwhile, residual stresses remain a significant obstacle to effective production, particularly for parts for which it is difficult to apply heat treatment such as the production of parts of large sizes or feature addition applications. Interpass dwell periods influence the overall heat flux during a build and comprise a non-value adding component of production. However, the research into the effects of interpass temperature is limited (Yadollahi et al., 2015) (Wu et al., 2019a) As oxidation is prevented and phase complete temperatures below 800°C, hotter interpass temperatures may be possible whilst remaining within specification and possibly enabling more homogenous material properties and reduced residual stresses to be developed.

Besides causing a lack of certainty regarding the material properties, an understanding of the process-property-microstructure is also problematic considering the demanding process-planning requirements for WAAM, where low production cost and high deposition rate are expected. However, until a more in-depth understanding of the material property evolution is understood for the range of heat inputs and interpass temperatures possible in WAAM, process parameters development will be highly dependent on trial and error, practice builds or scale-models and destructive testing.

Research Methodology

Chapter 4

4.1 Introduction

This research aims to provide a clear understanding of the effects of heat input, deposition rate, and cooling strategy including interpass temperature control and additional cooling for WAAM of 316L type stainless steel. This research also aims to quantify the effect of additional silicon content with heat input and interpass temperature. To achieve these aims, the overall research methodology presented in Fig 4.1 is applied with the primary activities consisting of Design of Experiments, materials testing and statistical analysis. These activities are described within this chapter, and an overview of the specification and integration of the WAAM platform, the experimental preparatory activities, the experimental design, the experimental procedure, and the experimental data collection activities is provided.

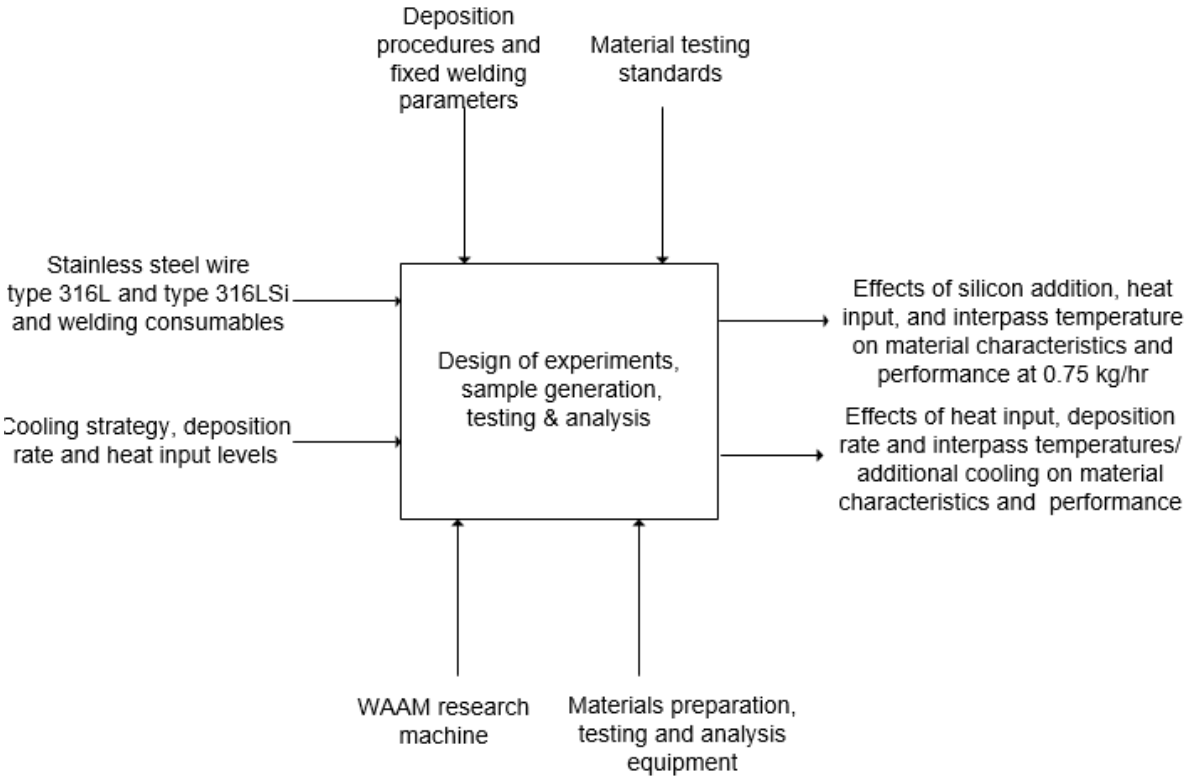

Figure 4.1 Outline of the overall research methodology applied in the investigation of WAAM of Type 316L stainless steel.

4.2 Specification and integration of a WAAM system

4.2.1 Specification of requirements

A specification of requirements for the WAAM system is developed for equipment procurement purposes based on the research aims and objectives detailed in Chapter 1. The requirements specification is categorised according to the functional needs of each sub-system including welding power supply, welding torch, enclosure and local exhaust ventilation (LEV), additional cooling and motion system is presented in Table 4.1.

Table 4.1 Requirements specification for the wire arc additive manufacturing platform sub-systems

	Demand/ Wish	Priority	Ref	Functional Requirements
Welding Power Supply	D	H	1.1	• Negligible EMF interference with motion system electrical drives at arc initiation or shielding to be provided
	D	H	1.2	• 100% duty cycle at the maximum deposition rate
	D	H	1.3	• Pulse current for reduced heat input and spatter
	W	L	1.4	• Deposition rate >=3 kg/hr
	W	L	1.5	• Welding program storage
	D	H	1.6	• Interface integration to motion system hardware: TJ-MC04 28 pin digital I/O connector with 12 inputs, 8 outputs
	D	H	1.7	• Digital I/O's available for the following functions: Input: Arc On/Off Input: Robot Ready/Quick Stop Output: Arc Stable Output: Power source ready
Welding torch	D	H	2.1	• 100% duty cycle at the maximum deposition rate
	D	H	2.2	• MIG based welding technology
	D	H	2.3	• Attachment to the motion system Z-axis directly or by fixture
	D	H	2.4	• Shielding gas routed through the torch
	D	H	2.5	• Protect weld pool from atmospheric gases that cause oxidation
Additional cooling	D	H	3.1	• Laminar flow to not disrupt the electrical arc
	D	H	3.2	• Located behind the inert shielding gas, with an adjustable position relative to the welding torch (X, Y, Z , pitch, yaw)
	D	H	3.3	• Must not disrupt the integrity of protection provided by the shielding gas through the welding torch
	D	H	3.4	• Increase the cooling rate of melt-pool
Enclosure & LEV	D	H	4.1	• Sealed line entrances to the enclosure
	D	H	4.2	• Shield personnel against spatter and optical radiation
	D	H	4.3	• Protect electrical drives and connections from cooling/heating cycles
	D	H	4.3	• Local Exhaust Ventilation System from build chamber or access to outdoors for the exhaust line
	D	H	4.4	• Noise <80dB to avoid PPE requirement
	D	H	4.5	• Shielding gas to be contained in build chamber and workshop oxygen levels monitored
Temperature sensor	D	H	5.1	• Monitoring of interpass temperature range 60°C -150°C
	D	H	5.2	• Interpass temperature spot size 3-4mm
	D	H	5.3	• Peak temperature behind melt-pool spot size 1-2mm
	D	H	5.4	• Distance to target > 50 mm to avoid radiation heating and damage from spatter
	D	H	5.5	• Shroud to shield the lens from spatter
Motion system	D	H	6.1	• Minimum Z-axis stroke length of 100 mm
	D	H	6.2	• Minimum X-axis stroke length of 180 mm to allow for deposition length and interpass temperature monitoring position offset length as per §4.5
	D	H	6.3	• Travel speeds up to 2.32 mm/s to 16.10 mm/s as per §4.3.5
	D	H	6.4	• Minimum 20 µm position repeatability
	D	H	6.5	• Payload 5 kg to accommodate welding torch, additional cooling, and temperature sensor
	D	H	6.6	• Interface to motion system controller TJ-MC04 to carry out deposition cycles following BASIC code

4.2.2 Welding power supply and torch

The welding power supply selected is the Aristo 4004i pulse system (ESAB, Sweden) as shown in Fig 4.2. The equipment is to be used in the MIG set up so that the wire feed is coaxial to the welding torch to increase deposition rates and simplify path planning. The selected is the Aristo 4004i pulse system fulfils the requirements specification by offering the following functions:

- Pulse power supply (16-400A), this reduces heat input and minimises spatter compared to non-pulse power supplies
- Synergic lines for welding stainless steel
- Water-cooler to allow 100% duty cycle
- Stores up to 250 welding programs
- Compatible with standard commercially available wire spools

Figure 4.2 Aristo 4004i pulsed welding power supply and wire feeder

4.2.3 Motion system

A Cartesian, 3-axis servo-drive based motion system is used to coordinate motion between the workpiece and welding torch. The servo-drives are configured as shown in Fig 4.3, which shows the servo-drive configuration before assembly, and once it has been installed within the enclosure. Trajexia software, proprietary to the servo-drives, allows motion instructions to be sent to a controller (Omron, Cambridgeshire UK) using the BASIC coding language. The welding torch is located on the third stage of the motion system, labelled as the Z-axis as shown in Fig 4.3. Moving the welding torch rather than the baseplate enables the servo-drives positioned away from the additional cooling fluid when in use and is more suited to a maximum payload of 5 kg of the servo-drive. Wire entrapment due to the moving torch cable in this motion system configuration is reported to unlikely for welding torch cable lengths <2 m (Dinse, 2017) permitting movement of the welding torch in this configuration.

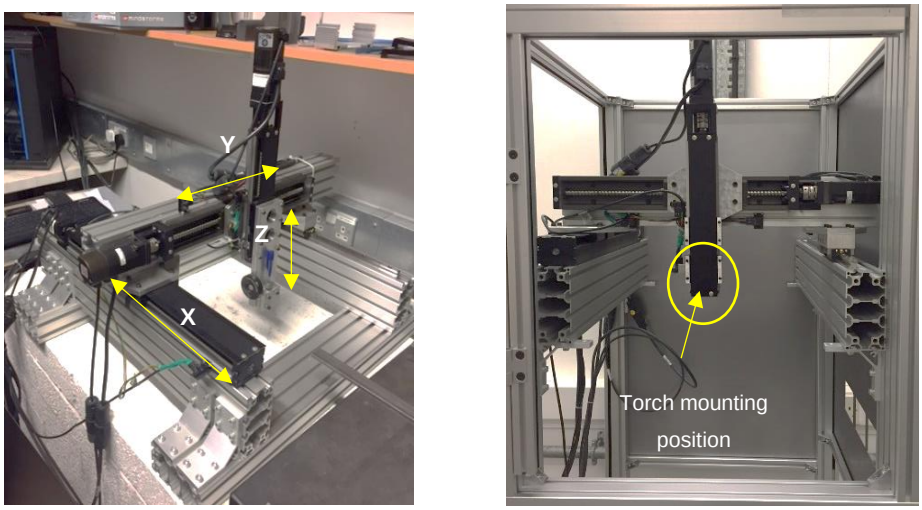

Figure 4.3 a) Three-stage XYZ motion system before integration (b) Assembled motion system within the partially assembled enclosure.

4.2.4 Enclosure and local exhaust extraction

A particularly harmful product of welding fume produced from stainless steel wire is hexavalent chromium and volume must be kept below 5 µg/m^3. As can be seen in Table 4.2, 0.08 g of hexavalent particle is produced every hour for MIG welding. To ensure Cr (VI) is kept to safe levels by air dilution in an open environment, a flow rate of 5350 m^3/hr would need to be provided by the extractor to provide the required number of air changes per hour. To reduce the power and cost of the extractor, an alternative and recommended approach involves the capture of the fume direct at source or enclose the welding activity.

Table 4.2 Fume emission rates and hourly production of Cr(VI) for a 3 kg/hr deposition rate (Kimura et al., 1979)

Overall fume emission rate per mass deposit (mg/g)	**Cr (VI) content of overall fume emission**	**Maximum WAAM deposition rate (3.00 kg/hr)**	**Mass of Cr (VI) particle produced per hour (g)**
6.86	0.39 %	3	**0.08**

The enclosure of the welding activity allows a Kemper SmartMaster extraction filter unit of a flow rate of 950 m^3/hr to be selected as shown in Fig 4.4. This has IFA-Certification and is W3-Approved which means it is suitable for welding high alloy steel including Type 316L stainless steel. The air velocity the extractor can pull at the furthest distance away from the inlet is important. The funnel of the extraction hose is removed, and a flexible hose connected directly to the rear of the enclosure wall at the baseplate fixture level. Below 0.5 m/s suction fume cannot be reliably captured, however, this limit is achieved by the mounting position and positive pressure within the enclosure additionally prevents the escape of fumes. The extraction filter unit is manually turned on and off as part of the experimental procedure.

Figure 4.4 Kemper SmartMaster with Extraction Hose (3m hose length)

4.2.5 Interpass Temperature sensor

To monitor the interpass temperature a non-contact infrared temperature sensor (Pyrocouple PC21HT-X) supplied by Omni Instruments is positioned in front of the welding torch and along the central axis in the direction of travel. The interpass temperature is monitored after a weld bead has been deposited through a rapid travel move that returns the sensor to the start of the deposition position point as discussed in §4.5.

4.2.6 Sub-system integration

The sub-systems were assembled and integrated as shown in Fig 4.5. A key element of the integration was the interface between the motion system controller and the 'manual' welding power supply, which allowed for automatic welding. Several digital inputs (DI) and digital outputs (DO) available for writing and reading on the Trajexia motion system controller were connected via an automatic welding interface unit as shown in Fig 4.6. The automatic welding interface unit is supplied alongside the welding power supply as a customised item (Wellington Welding Ltd, UK).

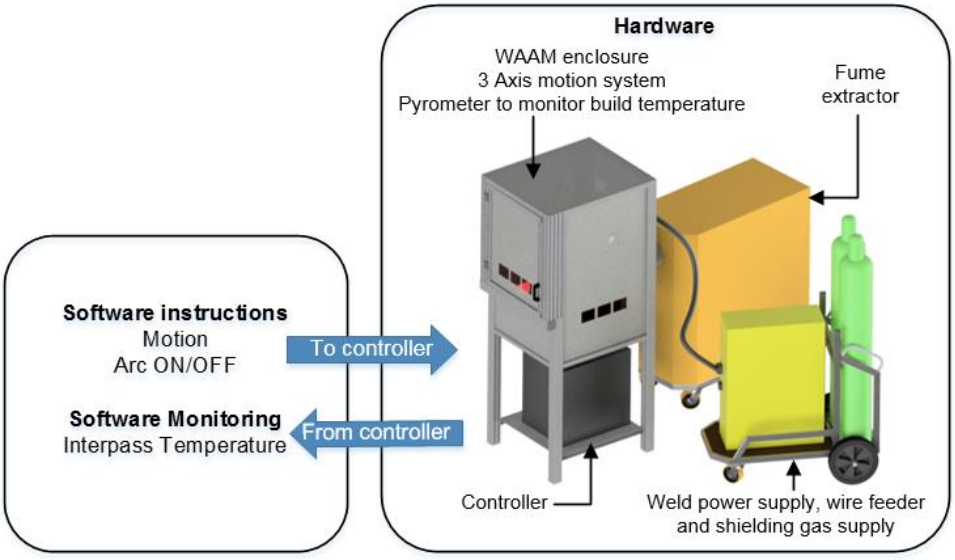

Figure 4.5 Schematic of the integrated WAAM equipment

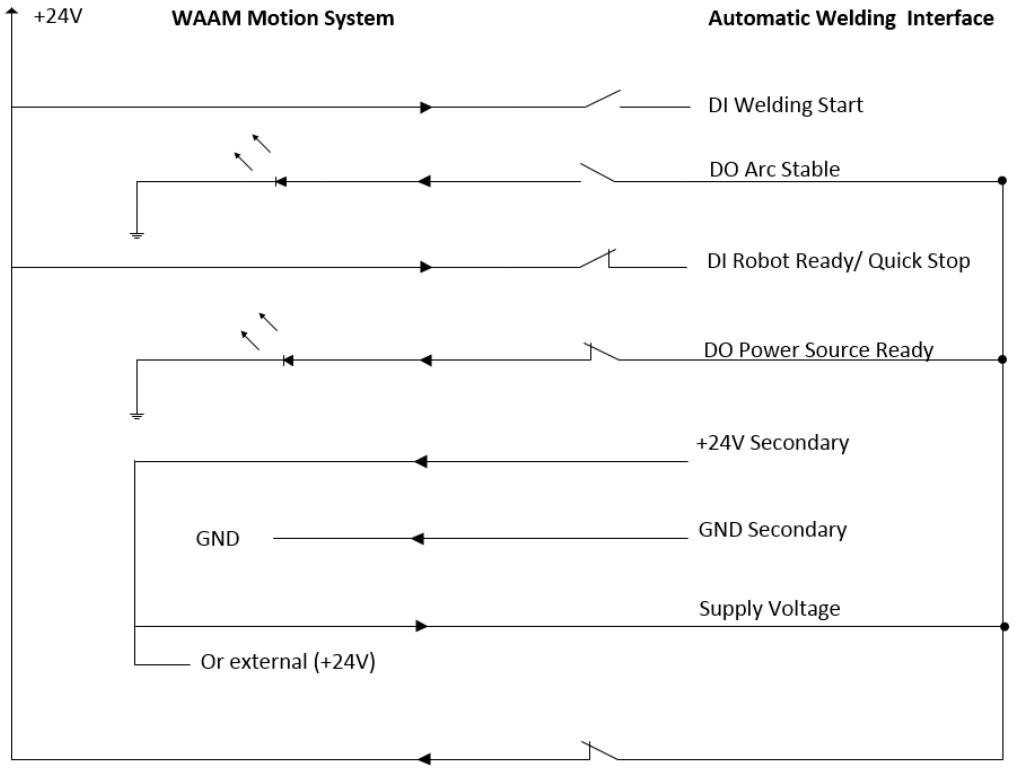

Figure 4.6 Automated welding interface connections of power supply equipment.

The welding torch, motion system stages and interpass temperature sensor were configured within the WAAM enclosure as shown in Fig. 4.7, showing the welding torch during deposition and in the interpass temperature monitoring position, Further details on the experimental procedure relating to the thin-wall deposition can be found in §4.5.

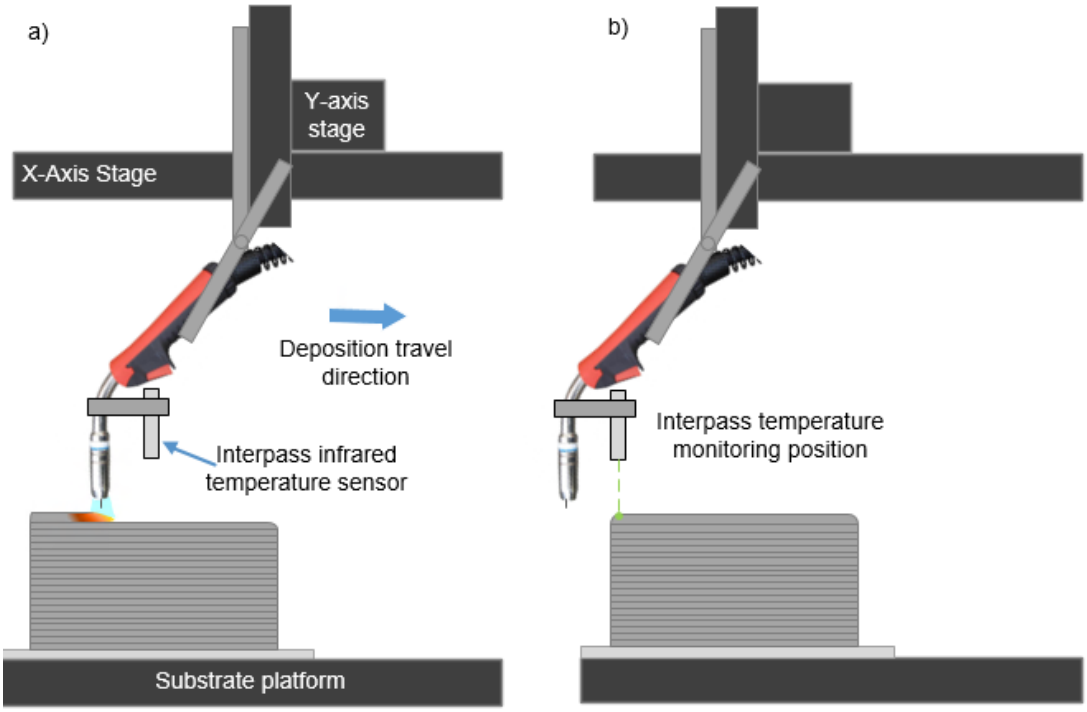

Figure 4.7 Welding torch, motion system stages and interpass temperature sensor configuration showing a) deposition and b) interpass temperature monitoring.

4.3 Experimental preparatory activities

4.3.1 Calibration of an infrared temperature sensor

To calibrate the output of the infrared temperature sensor, the microampere output of the infrared temperature interpass temperature reading is calibrated to the readings of a contact K-Type thermocouple in degrees centigrade (°C). The K-type thermocouple was manually positioned directly adjacent to the infrared temperature sensor focal spot on the top surface of the weld bead using a Pico TC-08 data-logger (Pico technology Cambridgeshire, UK).

To allow a relationship to be developed for the full range of interpass temperature levels (specified in §4.3.6), several test weld beads are superimposed in succession to accelerate the heat accumulation for the calibration procedure. The infrared temperature sensor output data in mA was fitted to the thermocouple data in °C by applying least squares regression to multiple cooling curves to obtain a first-order gain function. An example of the final fit of the pyrometer data to the thermocouple data over the temperature range of 40 °C-170°C is shown in Fig 4.8.

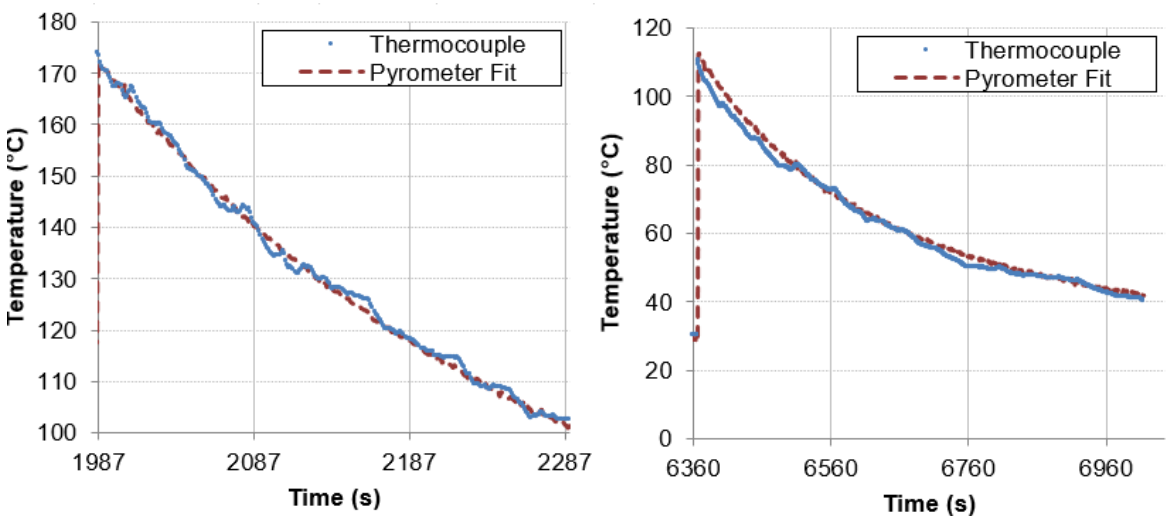

Figure 4.8 Non-contact infrared thermometer data calibrated to a contact K-Type thermocouple measurement.

4.3.2 Wire selection

The chemical composition of the Type 316L and Type 316L wire and Type 316L substrate used in this research is shown in Table 4.3 alongside the BS EN ISO 14343 (2017) standard values. Both types of austenitic stainless steel are of reduced carbon content relative to the parent Type 316 grade to prevent sensitization with the Type 316LSi grade containing additional silicon content to improve weldability by enhancing the filler material wettability.

Table 4.3 Chemical composition wire and substrate relative to standard (BS EN ISO 14343, 2017)

	Cr	Ni	Mo	C	Mn	S	Si	N	Cu	Fe
Wire - 316L	18.437	12.249	2.553	0.015	1.602	0.007	0.408	0.0340	0.069	Bal.
Wire - 316LSi	18.250	12.070	2.530	0.008	1.600	0.0110	0.790	0.0320	0.083	Bal.
Substrate 316L	17.010	10.107	2.152	0.023	1.232	00049	0.460	0.0507	-	Bal.
BS EN ISO 14343	18.0 20.0	11.0 14.0	2.0 3.0	0.03	1 2.5	0.03	0.30 0.65	-	0.75	Bal.

4.3.3 Fixed process parameter selections

To limit the number of variables investigated, the contact tip distance (CTD), argon flow rate, welding angle, wire diameter, and welding pulse type and frequency will be controlled to nominal values shown in Table 4.4.

Table 4.4 Fixed welding parameters

Parameters	Values
Contact tip distance	7.5 mm
Shielding gas flow rate	20 L/min
Shielding gas composition	97.5%Ar/2.5%CO_2
Welding angle	0°
Wire diameter	1 mm
Pulse-type	Primary
Pulse frequency	5 Hz

4.3.4 Selection of deposition rates

The WFS is directly proportional to the deposition rate in WAAM, and in this research, 2 m/min and 8 m/min are selected as the lower and upper levels to be investigated. These values corresponding to a theoretical deposition rate of are selected 0.75 kg/hr to 3 kg/hr respectively. The present range is selected as representative of the current state-of-the-art capability for single-wire feed WAAM systems, and typical commercial WAAM deposition rates.

4.3.5 Identification of heat input levels

The heat input from the electrical arc determines the stability of the WAAM deposition and the ability to meet the required volume of material. The heat input in arc welding is estimated by the following equation:

$$Q = \eta \frac{60VI}{1000(TS)} \tag{4.1}$$

Where η is arc efficiency, V is voltage, I current and TS in m/min.

The ESAB welding power supply controller described in §4.2.2 provides synergic lines that specify the current and voltage according to WFS as shown in Fig 4.9 and Fig 4.10, respectively. As shown in Fig 4.9, I is proportional to the WFS allowing substitution into Eqn. (4.2) to show the heat input in terms of WFS/TS and voltage as follows:

$$Q = \eta \frac{60V(18WFS + 3.6)}{1000(TS)} \tag{4.2}$$

To identify the upper and lower heat input levels, experiments are conducted over a range of heat inputs. As the WFS levels are fixed as outlined in §4.3.4 the heat input is varied by TS parameter. The TS's that result in a stable deposition for minimum and maximum WFS of 2 m/min and 8 m/min respectively are investigated.

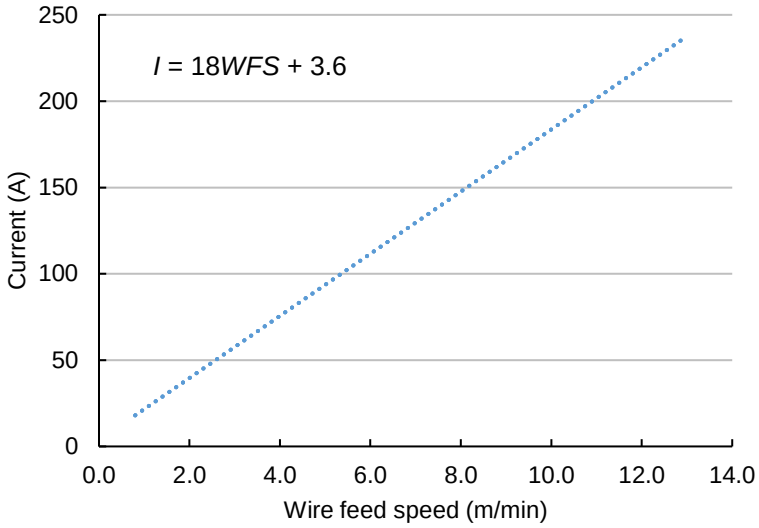

Figure 4.9 Synergic line current provided by ESAB for 1mm wire of composition Type 316L and 97.5% Argon 2.5%CO2 shielding gas.

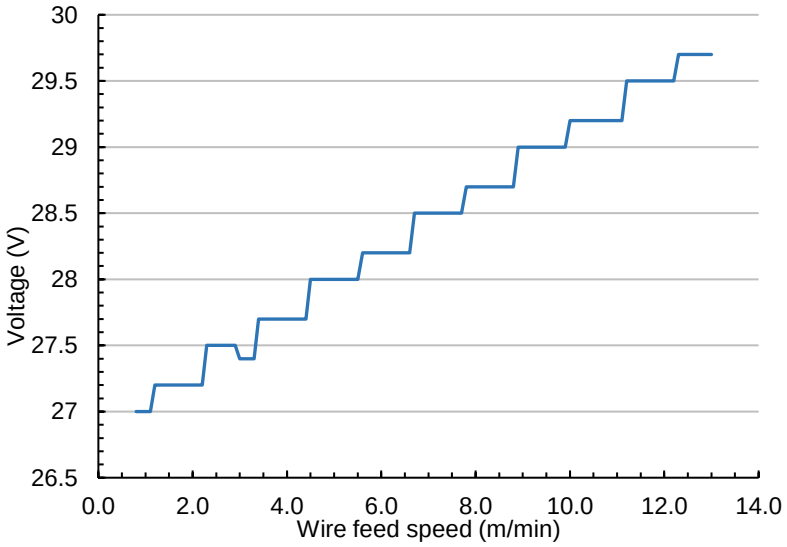

Figure 4.10 Synergic line voltage provided by ESAB for 1 mm wire of composition 316L and 97.5% Argon and 2.5% CO_2 shielding gas.

By manual welding, a stable combination of WFS and TS of 3 m/min and 4 mm/s respectively, equivalent to 0.39 kJ/mm was identified. Fixed ratios of WFS to TS result in stable bead geometry (Williams et al., 2016), allowing this value to be used a starting point for one-factor-at-a-time experimentation to establish the limits of acceptable TS's for the upper and lower WFS levels. The stability of the TS for each WFS is determined experimentally by deposition onto a baseplate at room temperature and the weld bead geometry qualitatively evaluated. Discontinuous beads or humping of the weld bead as shown in Fig 4.11 is indicative of too high of a TS relative to WFS or too low heat input (Adebayo, 2013). Conversely, a built-up weld bead is indicative of an excessively slow TS for the given WFS, or too high heat input.

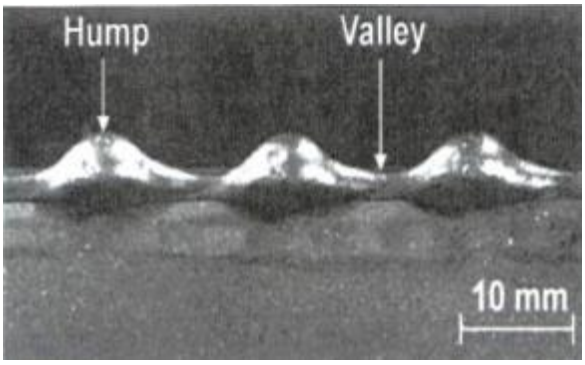

Figure 4.11 Characteristic humping phenomena incurred at high a travel speed in WAAM (Nguyen et al., 2013)

The experimentally determined TS for each high heat input (HHI) and low heat input (LHI) levels for each WFS is shown in Table 4.5.

Table 4.5 Adjusted boundaries of wire feed speed and travel speed combination to avoid welding defects

Heat input boundary	WFS (m/min)	Deposition rate (kg/hr)	TS (mm/s)	Heat Input (kJ/mm)
High heat input **(HHI)**	2	0.75	2.32	0.47
Low heat input **(LHI)**			4.09	0.26
High heat input **(HHI)**	8	3.00	9.11	0.47
Low heat input **(LHI)**			16.10	0.26

The HHI and LHI heat input boundaries are also shown graphically in terms of the WFS and TS as shown in Fig 4.12. It can be seen that the range of acceptable TS is wider a higher WFS's due to the greater heat input available at higher WFS and reduced sensitivity to process disturbances.

The surface quality of the first layer of the deposition is known to be of great importance to the subsequent surface waviness of the wall (Geng et al., 2017). As defect severity accumulates with an increase in layers, uneven first layers can affect the ability thin-wall build to proceed to completion. To ensure stable deposition, the upper and lower limit of TS was moved inward of the stable processing region by 10%. This also limits the heat accumulation, preventing a thermally induced collapse of weld bead geometry with increasing layers as layers due to the pre-heat effect of the previous layers and as the conductive effect from the substrate becomes less effective.

Further, for constant WFS/TS deposition, a reduction in the width of the deposited weld-bead occurs with increasing TS. This is triggered by the reduction in the material as it is being deposited per unit time with a smaller amount of heat input from the arc to the weld pool, and this decreases the weld pool temperature. Moreover, the decreased temperature gives rise to the viscosity of the weld pool, increasing the constricting melt-pool surface energy. This reduces the impact of the arc pressure and aerodynamic forces on the molten metal and results in a narrower weld (Adebayo, 2013).

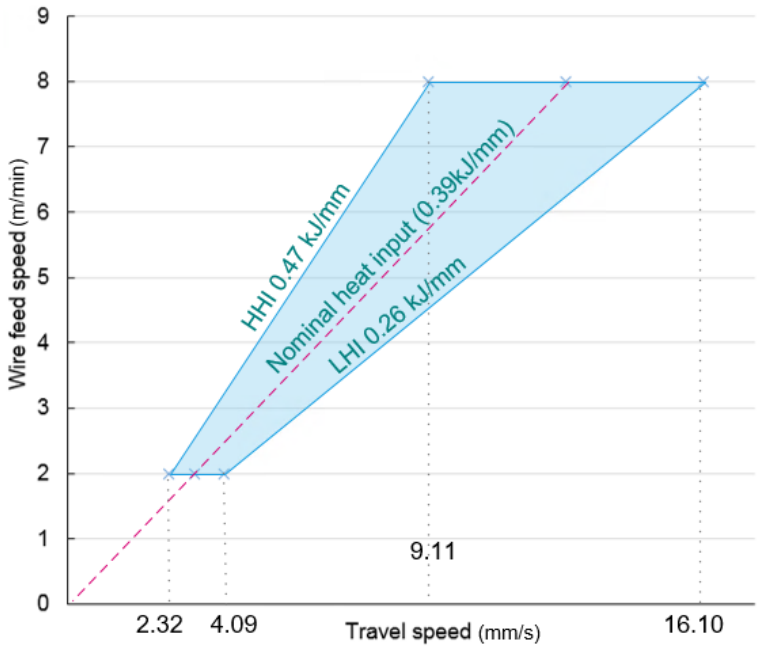

Figure 4.12 Process map showing nominal and boundary limits for the WFS to be investigated

4.3.6 Identification of interpass temperature levels

This section identifies the interpass temperature levels which are investigated in this research. A pre-heat temperature is not often specified for austenitic stainless steel as no phase transformations are expected to occur after solidification (Callister, 2003). It is expected that the higher build temperature will result in different microstructural and residual stress development compared to the low interpass temperature build strategy. The low interpass temperature (LIT) level was specified as 60°C. This is closer to ambient room temperature and represents a process with thermal boundary conditions more closely linked to welding where heat accumulation is limited.

For the high interpass temperature (HIT) level, the interpass temperatures are sustained passively without additional heat input processes. To allow a comparison of effects the upper interpass temperature limit must be possible to maintain for all heat input conditions for the experimental deposition length. As the LHI builds have the highest cooling rates, the upper interpass temperature level was established for this heat input. To do so, interpass temperature monitoring data is collected from a test wall build, with the deposition was restarted by the operator after every layer as soon as reasonably possible. A dwell period, however, was always necessary to allow travel time for the motion system to return the welding torch to the deposition start point and for operator reaction times. The calibration and set up for this pyrometer used to collect this data is described in §4.3.1.

It can be seen in Fig 4.13 that the continued successive deposition resulted in the ability to recommence deposition at 155°C by the 11th layer. There was no further passive increase in interpass temperature by the 12th layer and no thermal breakdown of the weld bead so 150°C was specified as the stable upper level of interpass temperature.

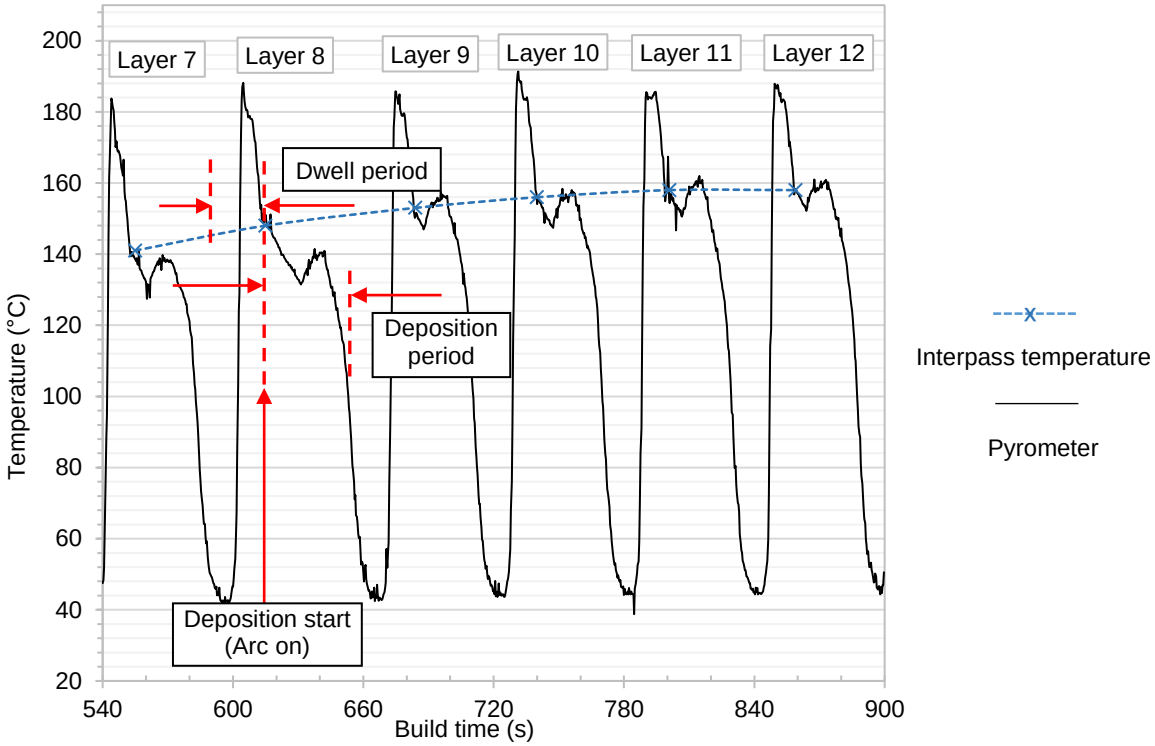

Figure 4.13 Pyrometer measurement showing the increase in interpass temperature for continuous deposition WFS 2m/min and TS 4.09 mm/s between layer 7-12.

4.4 Design of Experiments

This section introduces the experimental design that is employed to establish the performance of WAAM Type 316L stainless steel. To determine the effects of the deposition rate, heat input, and cooling strategy, a $2^2 3^1$ full factorial experiment is developed as shown in Table 4.6. The heat input and interpass temperature levels are defined as discussed in §4.3.5 and §4.3.6, respectively.

Table 4.6 The $2^2 3^1$ full factorial design of experiments, investigating the effects of deposition rate, heat input, and temperature control strategy.

Experimental Group	Experiment	Material	Deposition rate (kg/hr)	Heat input (kJ/mm)	Temperature control strategy
A	1	316L	0.75	HHI	60°C
	2	316L	0.75	HHI	150°C
	3	316L	0.75	LHI	60°C
	4	316L	0.75	LHI	150°C
	5	316L	0.75	HHI	Additional cooling
	6	316L	0.75	LHI	Additional cooling
B	7	316L	3.00	HHI	60°C
	8	316L	3.00	HHI	150°C
	9	316L	3.00	LHI	60°C
	10	316L	3.00	LHI	150°C
	11	316L	3.00	HHI	Additional cooling
	12	316L	3.00	LHI	Additional cooling

For each experiment, a thin-wall is generated with the thin-wall dimensions and the deposition procedure is detailed in §4.5. The effects of silicon content, interpass temperature, and heat input are investigated in a 2^3 full factorial experiment as shown in

Table 4.7. To minimise confounding errors due to procedure, the run-order is randomised for each of the experimental groups.

Table 4.7 The 2^3 full factorial design of experiments investigating the effects of Si content with heat input and interpass temperature.

Experimental Group	Experiment	Material	Deposition rate (kg/hr)	Heat input (kJ/mm)	Interpass temperature
A	1	316L	0.75	HHI	60°C
	2	316L	0.75	HHI	150°C
	3	316L	0.75	LHI	60°C
	4	316L	0.75	LHI	150°C
C	1	316LSi	0.75	HHI	60°C
	2	316LSi	0.75	HHI	150°C
	3	316LSi	0.75	LHI	60°C
	4	316LSi	0.75	LHI	150°C

4.5 Experimental procedure

Substrates of 50 mm × 200 mm × 6 mm are used for the experimental thin-wall builds and are prepared for deposition by grinding and cleaning with acetone. The deposition and interpass temperature monitoring travel paths in Fig 4.14. These paths are repeated for each layer.

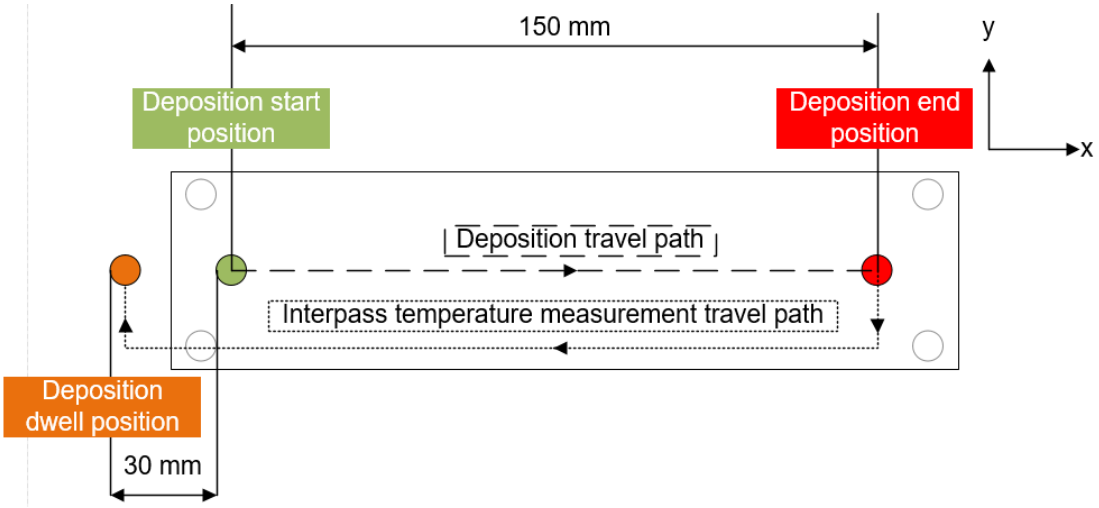

Figure 4.14 Deposition and interpass temperature measurement travel paths.

The temperature is continuously monitored 30 mm ahead of the welding torch by the interpass temperature infrared temperature sensor introduced in §4.2.5. The interpass temperature measurement travel-path returns the welding torch to behind the deposit so that the temperature sensor monitors the temperature at the start of the deposit. Once this has reached the specified temperature, the deposition program is restarted, moving the welding torch moves back to the deposition start position and restarting the deposition. A constant CTD is specified, as presented in §4.3.3. Therefore, to maintain this distance, the

z height of the welding torch the welding program is manually updated every layer with the measurement layer height by a Vernier calliper to offset the addition of material.

4.5.1 In process cryogenic cooling localised to the melt-pool set-up

For the in-process cryogenic cooling (CRYO) localised to the melt-pol was implemented with LN_2 from a 3 bar Dewar as shown in Fig 4.15a. This was connected by a vacuum jacketed pipe to a nozzle mounted to the machine z-axis (see Fig 4.15 b-d).

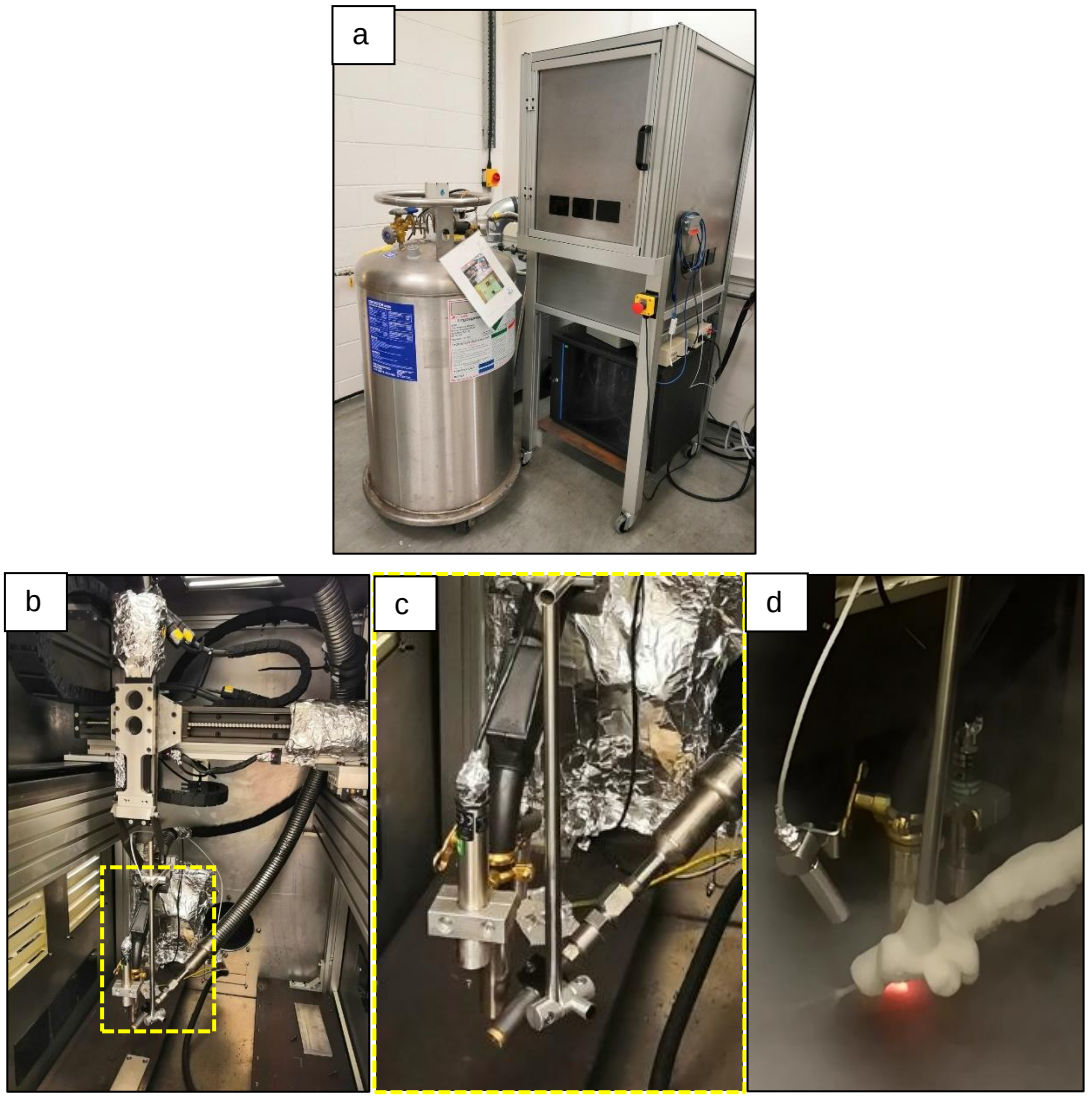

Figure 4.15 a) Overall WAAM platform set up for CRYO experiments b) CRYO nozzle mounted to z-axis c) Magnified view of the location of CRYO nozzle mounted to z-axis d) In-process CRYO showing the LN2 jet striking the WAAM deposit surface.

The nozzle outlet as shown in Fig 4.15d was directed trailing the electric arc and opposite to the travel direction to ensure that the liquid LN_2 and the expanding gaseous N_2 struck the surface of the WAAM deposit without disrupting the arc. The nozzle outlet was placed to be a few millimetres above the building height in the YZ plane allowing the LN_2 to contact the WAAM deposit in the central region of the bead and less than 15 mm from the electric arc.

4.6 Data collection and material testing

This section describes the equipment and procedures that are used in the experimental data collection activities post-deposition. An outline of these activities and the order in which they are conducted is shown in Fig 4.16, alongside a reference to the section in which they are discussed.

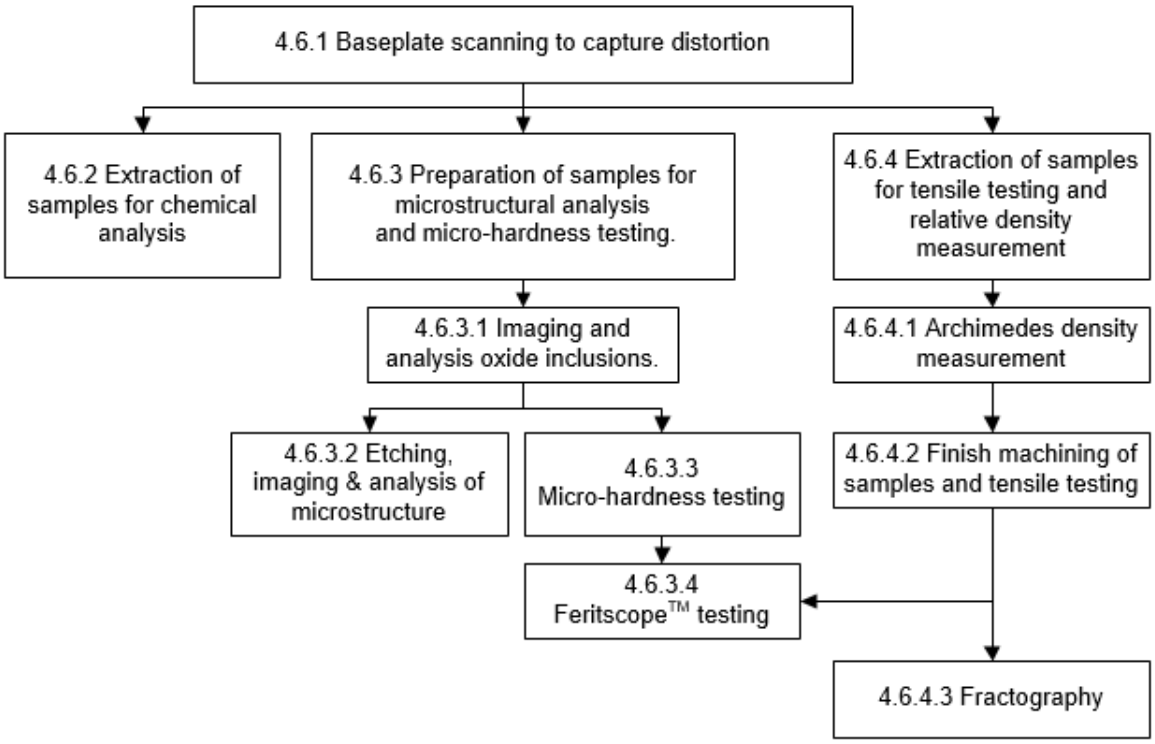

Figure 4.16 Outline of the data collection procedure.

For the analysis of mechanical properties, following finish machining of samples and tensile testing. Statistical analyses were carried out to identify significant effects and interactions via Analysis of Variance (ANOVA) tests using Minitab® 18 software. The factors considered were the cooling strategy (interpass temperatures or in-process cryogenic cooling localised to the melt-pool), heat input (quantitative factors). The data is also checked for violations of normality and equivalence of variance, and outliers as required for performing ANOVA. For a p-value less than 0.05, the null hypothesis that no statistical difference exists between the means is rejected allowing the conclusion that significant main effects and/or interactions exist.

4.6.1 Baseplate scanning to capture distortion

The distortion of the substrates following release from the build fixture is captured using a ROMER Absolute scanning arm (Hexagon Manufacturing Intelligence, UK) and Geomagics Wrap® software (3D Systems Inc). The point cloud is imported to Matlab and processed to obtain the profile of maximum deformation in the XZ and YZ planes as shown in Fig 4.17a.

The imported point cloud is unregistered to the Matlab coordinate axis, so singular value decomposition is used to identify the direction of maximum variance. Subsequently, a rigid transformation is performed to rotate and align the imported point cloud with the x-axis of the Matlab coordinate system (Lorsakul and Suthakorn, 2007, Arun et al., 1987). Once aligned, the section of maximum distortion is identified and point cloud filtered to eliminate points greater or less than 0.5 mm from the section of maximum distortion, as shown in Fig 4.17b which also shows the maximum Z-point is set to zero and inverted to align with the build direction. The smoothing spline function within the Matlab Curve Fitting Toolbox was used to report the maximum plane of distortion.

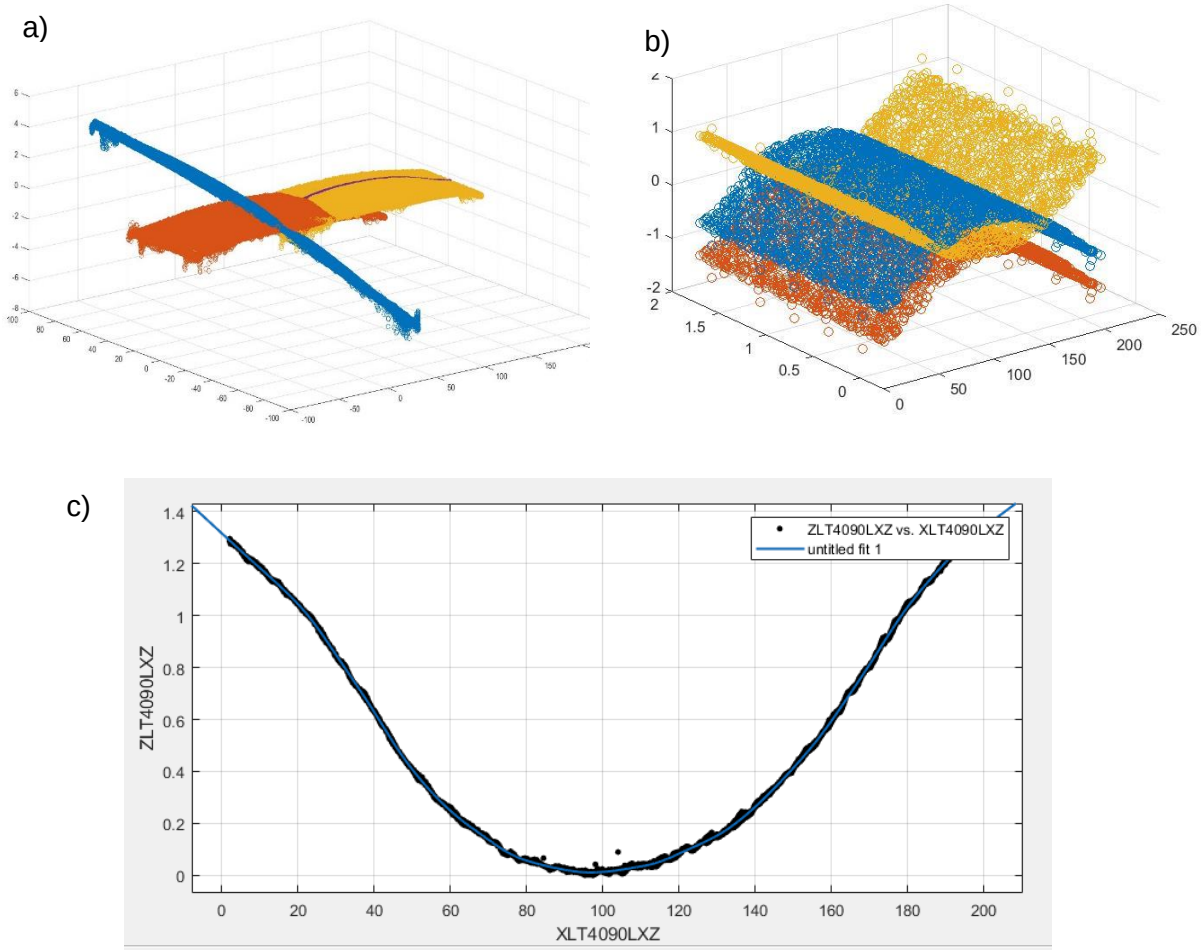

Figure 4.17 a) Graph of the imported and transformed baseplate scan with the maximum distortion centreline highlighted. b) Filtered point cloud showing the section of maximum distortion centre-line set to zero and inverted to align with the build direction.

4.6.2 Extraction of samples for chemical analysis

For chemical analysis, a square sample of dimension 20 x 20 mm was extracted from each experimental wall in the location shown in Fig 4.18. To identify the elemental composition of Ni, Cr, Si, Mn, Mo, C, P, S and N of the samples and wire in wt.% Optical Emission Spectroscopy (OES) was performed.

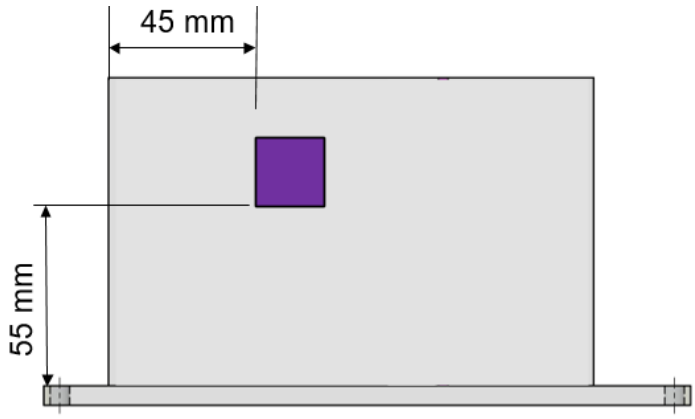

Figure 4.18 Location of the 20 x 20 mm samples extracted from each wall for chemical analysis

The LECO combustion analysis, which employs inert gas fusion technique was used to calculate the wt.% for O. The sample was extracted by water jet cutting at the same height above the transition zone. This allowed a between-sample comparison regarding the chemical composition to be made independent of heat accumulation effects. Samples were ground to remove the surface contaminants and ultrasonically cleaned before testing to remove contaminants.

4.6.3 Preparation of samples for microstructural analysis and micro-hardness testing

To analyse the microstructure throughout the build height of the experimental thin-walls, a 4 mm thick section is extracted from the location shown in Fig 4.19a, using a conventional band-saw. This is subsequently sectioned into upper, middle, and lower section by a Buehler abrasive cutting machine as shown in Fig 4.19b to allow efficient mounting, grinding and polishing for microstructural analysis. The samples were sectioned, mounted and polished according to standard procedures described in ASTM E3 (2011).

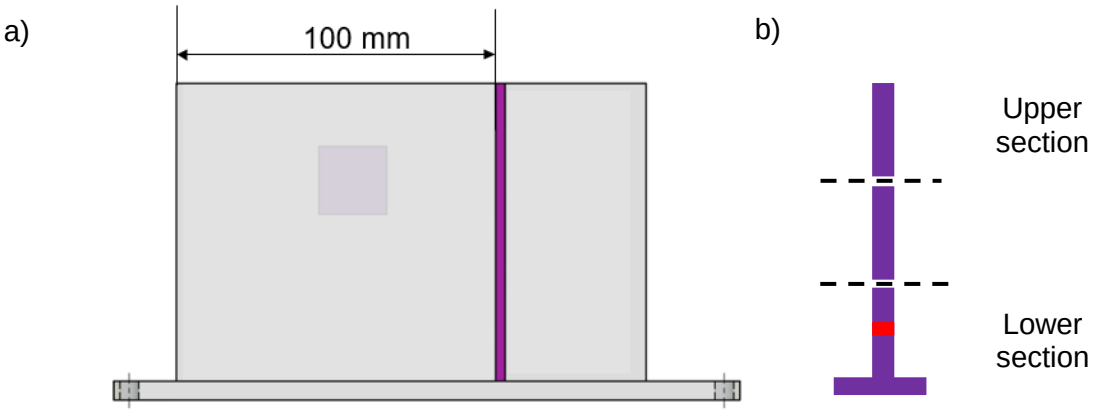

Figure 4.19 a) Location of 4mm thick section extracted from each wall for microstructural analysis and hardness testing b) Subsequent sectioning into three sections for metallurgical preparation.

These sections are ground mechanically with SiC from grit number 400 to 4000 and subsequently polished with 0.5 µm colloidal silica suspension. For Electron Back-Scatter

Diffraction (EBSD) a final stage of 0.2 µm diamond suspension polishing was carried out to obtain a mirror finish. To determine GND for each sample an approximation was made using the TSL OIM Analysis 8 software based on the 50x magnification images, covering 1279x994 pixels. This magnification and step size minimise the sum of the dislocation densities of individual types, the rationale being that this will reflect the stored energy and is less susceptible to local inhomogeneities (Wheeler et al., 2008). For the CRYO samples, the GND values were extrapolated from the 2000x magnification IPF's.

4.6.3.1 Imaging and analysis of oxide inclusions to evaluate ODS

To characterise the fine, spherical oxide inclusions distributed throughout all of the built material, optical micrographs covering a 306 µm by 224 µm area are captured at 4000x magnification and using Keyence VHX-6000. Images were made along the centreline of each of the three polished sections extracted from each wall in the unetched condition. Three repeats were made at the top, middle and bottom region of each section to obtain representative results. An example micrograph displaying oxide inclusions is presented in Fig 4.20a. ImageJ was used to prepare the micrographs and to automatically count the number of particles. ImageJ is a public domain Java image processing program (Rasband, 2012). The 'Inter-modes' Auto Threshold function and binary transformation are applied as shown in Fig 4.20b. The 'Analyze Particles' function is applied to particle size range in pixels of 0-2000 and circularity of 0.55-1.00. The results included each identified particle area and circularity as well as overall particle count and volume fraction. An example of the processed micrograph is shown in Fig 4.20c.

The radius (R_C) extracted from the ImageJ analysis represents that of a random cross-section through each oxide sphere. This can be related to the real mean radius (R_m) of the spheres by the following equation (Ma et al., 2014, Smith et al., 2019):

$$R_c = \sqrt{\frac{2}{3}} R_m \tag{4.3}$$

ODS occurs based either Orowan dislocation bypassing or dislocation shearing depending on which occurs at lower stress and initiates first. The Orowan bypassing mechanism dominates when the coherent particle size exceeds a critical value or when the particles as shown in Fig 4.21 (Wang et al., 2018b), whereas the dislocation-shearing mechanism is generally active when the precipitates are coherent with the matrix, and the particle size is small.

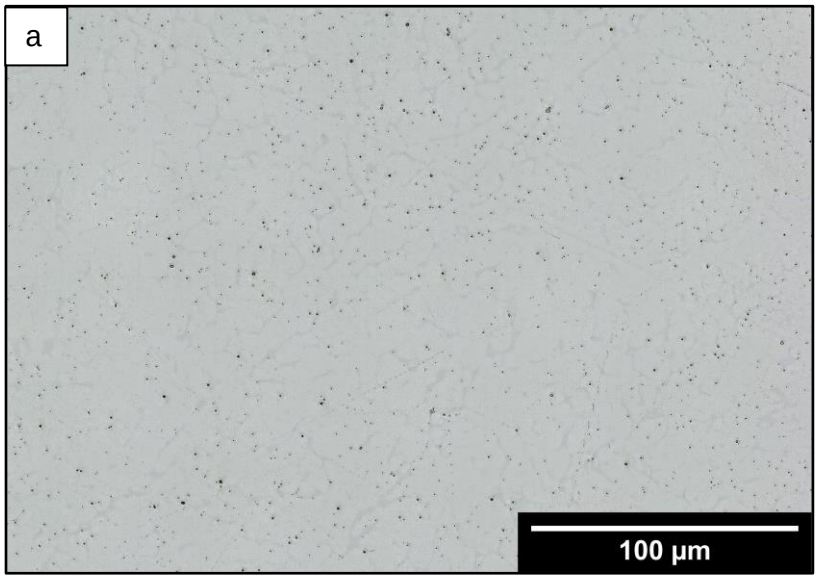

b

```
run("Set Scale...", "distance=196.5 known=10 unit=micron");
run("Specify...", "width=5920 height=4155 x=600 y=630");
makeRectangle(70, 30, 5920, 4155);
run("Crop");
run("Gaussian Blur...", "sigma=2");
run("Enhance Contrast...", "saturated=0.3");
run("8-bit");
run("Auto Threshold", "method=Intermodes white");
setOption("BlackBackground", false);
run("Make Binary");
run("Analyze Particles...", "size=0-2000 pixel circularity=0.00-0.55
show=Outlines display clear summarize add");
```

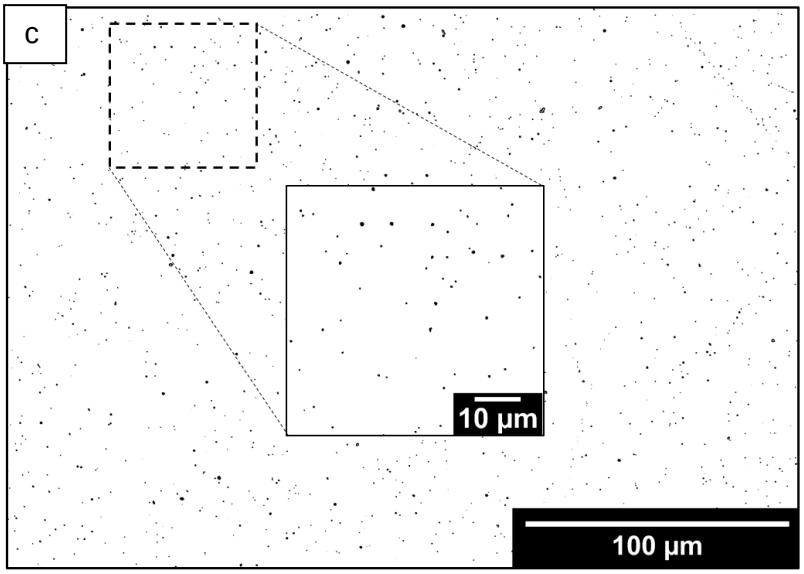

Figure 4.20 a) Example of optical micrograph before processing b) Optical micrograph with Auto Threshold and Binary functions applied within ImageJ.

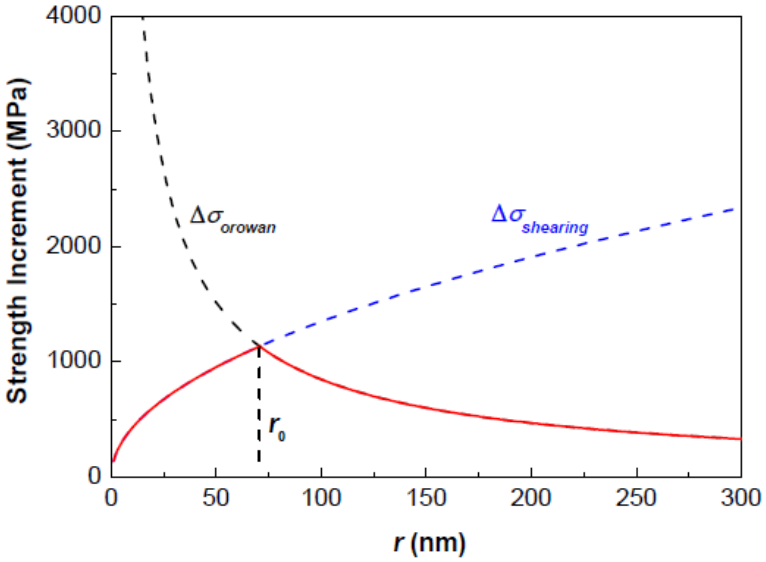

Figure 4.21 Variation of Orowan and shearing yield stress contribution with inclusion size (Wang et al., 2018b).

The contribution of yield strength by dislocation bypassing mechanism caused by ODS to be determined via the oxide inclusion radius (r_c) and spacing of inclusions (λ), the shear modulus (G), the Burgers vector (b), and the mean orientation factor (M), and poisons ratio v, through the application of the following equation (Ma et al., 2014):

$$\Delta\sigma_y = \mathrm{M}\frac{0.4\mathrm{G}b}{\pi\sqrt{1-v}}\frac{\ln\left(\frac{2r_c}{b}\right)}{\lambda} \tag{4.4}$$

Where λ is estimated from the r_m and volume fraction (f):

$$\lambda = 2r_c\left(\sqrt{\frac{\pi}{4f}} - 1\right) \tag{4.5}$$

The parameters used in the contribution to strength calculations are shown in Table 4.8.

Table 4.8 Parameters used in the calculation of oxide contribution to the strength

Parameter	Symbol	Value	Units	Reference
Mean orientation factor	M	2.449	Dimensionless	(Clausen, 1997)
Shear modulus	G	77	GPa	(Hibbeler, 2008)
Burgers vector	b	0.255	nm	Calculated from lattice parameter (Dahm and Dearnley, 2000)
Poisson ratio	v	0.3	Dimensionless	(Youtsos et al., 1989)

4.6.3.2 Metallographic etching, imaging, and analysis of microstructure

A metallographic chemical etch was applied using Marble's reagent solution (4g $CuSO_4$, 20ml HCl, and 20ml H_20) was performed for up to 15 s to provide contrast between the γ-austenite and δ-ferrite phases. The YZ surface of the lower and upper sections was examined at the layer interface using an optical microscope at 5x and 20x magnification.

For imaging of the sample texture, a central region of the middle section was scanned with a Jeol JSM-IT500 InTouchScope™ with Electron Back-Scatter Diffraction (EBSD) capability at 50x and 2000x magnification. The 50x and 2000x magnification images covered an area of 1933 by 2488 µm (step size 4.00 µm) and 62 by 48 µm (step size 90 nm) respectively. The TSL OIM Analysis 8 software was used to analyse the results of the EBSD scans.

4.6.3.3 Micro-hardness testing

The variation in micro-hardness throughout the build height was established using a Leco M400 Vickers micro-hardness tester. The upper sections were tested, starting with an indent 0.25 mm from the top of the final layer, with subsequent indents made in increments of 1 mm in the reverse of the build height direction. Following BS EN ISO 6507-1 (2018) a load of 500 g was applied for 10 s, with the first indentation located 3 mm inwards from the bottom surface of the substrate and at the centreline of the WAAM layers. Following the indentation, the micro-hardness was calculated as follows:

$$HV = 1.8544Fd^2 \tag{4.6}$$

Where F is the load used in kgf, and d is the average of the two measured diagonal lengths in millimetres.

4.6.3.4 Feritscope™ testing

An FMP300 Feritscope™ (Fischer Technology Inc., Windsor, CT, USA) was used to measure the ferromagnetic content within the fractured tensile samples and the upper and lower metallurgical specimens. A non-destructive magnetic method, the Feritscope measures the relative permeability of a material in the alternating magnetic field of its probe. As γ-austenite is not magnetic, it indiscriminately measures the δ-ferrite or α'-martensite content. The surface finish can affect the probe-to-surface contact and influence the Feritscope measurements. However, the difference in surface finish between a CNC machined and the metallurgically prepared sample is not reported to result in any statistical difference in ferrite measurement by Feritscope (Lundin et al., 1999). The Feritscope was calibrated in accordance to the standard specified within AWS A4.2M (2006) and was used at a distance more than 2 mm from the sample edge and for sample thickness greater than 3.3 mm. For the fractured tensile samples, three repeat measurements were obtained along the gauge length, and for the metallurgical samples, five repeat measurements were made along the lower and upper sections.

4.6.4 Extraction of samples for tensile testing and relative density measurement

Tensile specimens were extracted by water jetting cutting or wire Electro-Discharge Machining (EDM) in the locations shown in Fig 4.22. The tensile sample dimensions were based on the sub-size rectangular specimens specified by ASTM E8/E8M (2013).

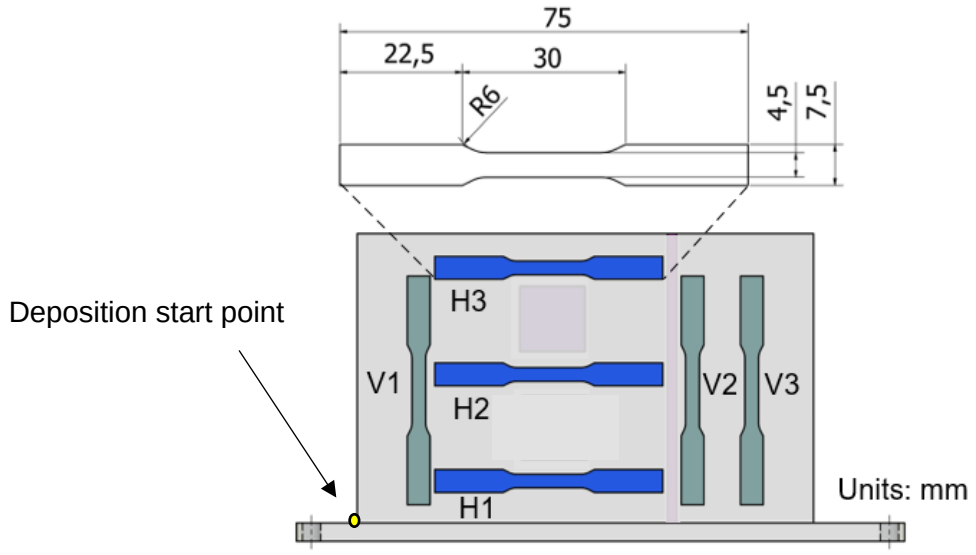

Figure 4.22 Tensile sample dimensions and positioning within WAAM experimental thin walls.

According to this standard, the tensile specimens should have a gauge length of 25 mm, a width of 6 mm, a thickness smaller than 6 mm and a radius fillet of 6 mm. An important requirement is that the gauge length to width should be maintained at a ratio of 4. To fit the WAAM experimental wall height (~85mm), the ASTM E8/E8M dimensions were scaled 0.75:1 to maintain this ratio. The single-pass experimental walls were sized to accommodate the arrangement of three of these tensile samples in the horizontal direction and vertical direction, with repeat samples generated to allow any location effects to be established as well as provide an estimate of the variability of the mechanical properties.

4.6.4.1 Archimedes density measurement

The Archimedes method is used to evaluate the relative density of the WAAM 316L stainless steel. The Archimedes method involves the weighing of samples 'dry' and subsequently submerged in a fluid. In this instance, distilled water was used, and the temperature monitored for each test. The density of the part is then obtained via the following equation:

$$\rho_p = \left(\frac{m_a}{m_a - m_f}\right) \cdot \rho_f \tag{4.7}$$

Where ρ_f is the density of distilled water at the recorded temperature, m_a is the mass of the sample as measured in air, and m_f is the mass of the sample as measured in distilled water.

The samples tested consisted of the six tensile coupons extracted in horizontal and vertical orientations per single pass experimental wall as outlined in §4.6.4. The density of the tensile specimens was tested before the surface CNC machining required for tensile testing as shown in Fig 4.23. The testing of the tensile coupons implemented as the weight was more suited to the weight limit of the analytical balance scale compared to the full wall samples, and also allowed the investigation of location-based density effects.

Figure 4.23 Pre-machined condition of the tensile samples for density measurement.

To aid in the relative density measurement recording a Sartorius™ Balance Density Determination Kit was used with a Sartorius™ A120S Analytical Balance Scale (0.0001g precision, Max. 120g) as shown in Fig 4.24.

Figure 4.24 A120S Analytical Balance Scale with Sartorius™ Balance Density Determination Kit b) Pre-machined test condition of the tensile samples before CNC machining.

Since the density of water varies with temperature, testing was conducted in a temperature-controlled laboratory, and thermometer used to record the temperature. The weight of each tensile sample was measured three times and was recorded after the scale had reached equilibrium. Results could be affected by both microscopic air bubbles in the water as well as the infiltration of the water into any surface-breaking pores. To avoid this, the samples were wetted before submersion and any visible micro-bubbles were removed with a spatula. An advantage of the Archimedes approach compared to image-based density measurements is that the entire volume of each specimen is captured rather than a 2D cross-section. Besides, the high frequency of oxide inclusions introduces difficulty in identifying pores in image-based techniques.

4.6.4.2 Finish machining and tensile testing

For tensile testing, each coupon is CNC machined flat to a uniform thickness of 2.6 – 3.3 mm depending on the effective wall thickness of the as-built WAAM thin-wall as shown in Fig 4.25.

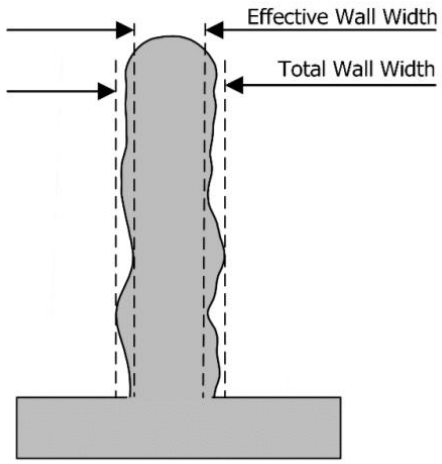

Figure 4.25 Schematic of WAAM wall highlighting the effective wall width and total wall width.

Uniaxial tensile tests were performed at room temperature using an Instron 3369, 50 kN load cell with a clip gauge extensometer as shown in Fig 4.26. The extension rate used was 0.1 mm/s in the elastic deformation region, followed by 0.4 mms^{-1} upon transition to plastic deformation (strain rate of 0.00007 $s^{-}1$ to 0.00024 s^{-1}) (BS EN ISO 6892, 2016), which based on initial experiments, was triggered at 5000N.

Figure 4.26 Experimental Instron 3369 load cell set up with clip-gauge extensometer attached.

The experimental data is processed to determine σ_{ys}, the UTS as shown in Fig 4.27 in accordance with BS EN ISO 6892 (2016). The uniform elongation was also calculated by

measuring the distance between the gauge length markings after fracture following BS EN ISO 6892 (2016).

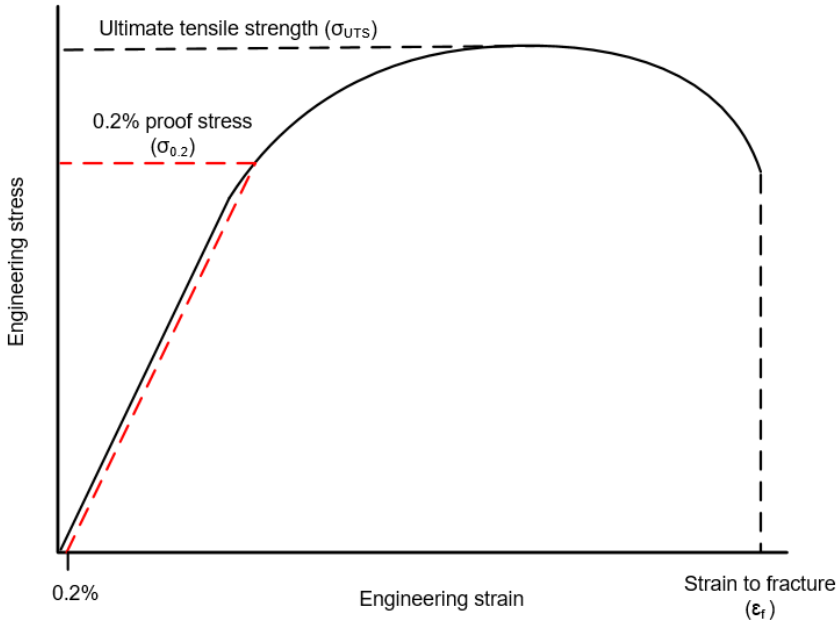

Figure 4.27 Experimental data extracted from the engineering stress vs. engineering strain curves

E was determined considering the linear part of the stress-strain curve and the slope was estimated by a linear calculated as a ratio between the maximum loads reached during the test and the cross-sectional area. To ensure errors were minimised in the data analysis, the first 45 data points were disregarded and at least 100 data points are sampled for each strain increment of 0.1% (NPL, 2006), with any non-linear part of the stress-strain curve due to slip or bending removed from the analysis.

4.6.4.3 Fractography

A JEOL JSM-6480LV scanning electron microscope (SEM) was used to image the fracture surfaces of the tensile specimens. Using customised Matlab code it was possible to map the fracture surface dimples to determine their frequency and size distribution. From a grayscale image, the “imextendedmin” function is used to identify the regional minima that are less than a specified threshold to allow the dimples to be easily identified. The original grayscale image (Fig 4.28a) is then modified by masking the minima regions and converting the masked area to black as shown by an example image in Fig 4.28b.

The masked image is segmented using the watershed transform as shown in Fig 4.28c and processed using the Image Region Analyzer tool within the Matlab Image Processing Toolbox 10.3 as shown in Fig 4.28d, to omit edge dimples and extract data including dimple area, equivalent diameter, and major and minor axis lengths. The micro-graphs presented, show approximately half of the full image presented in the results.

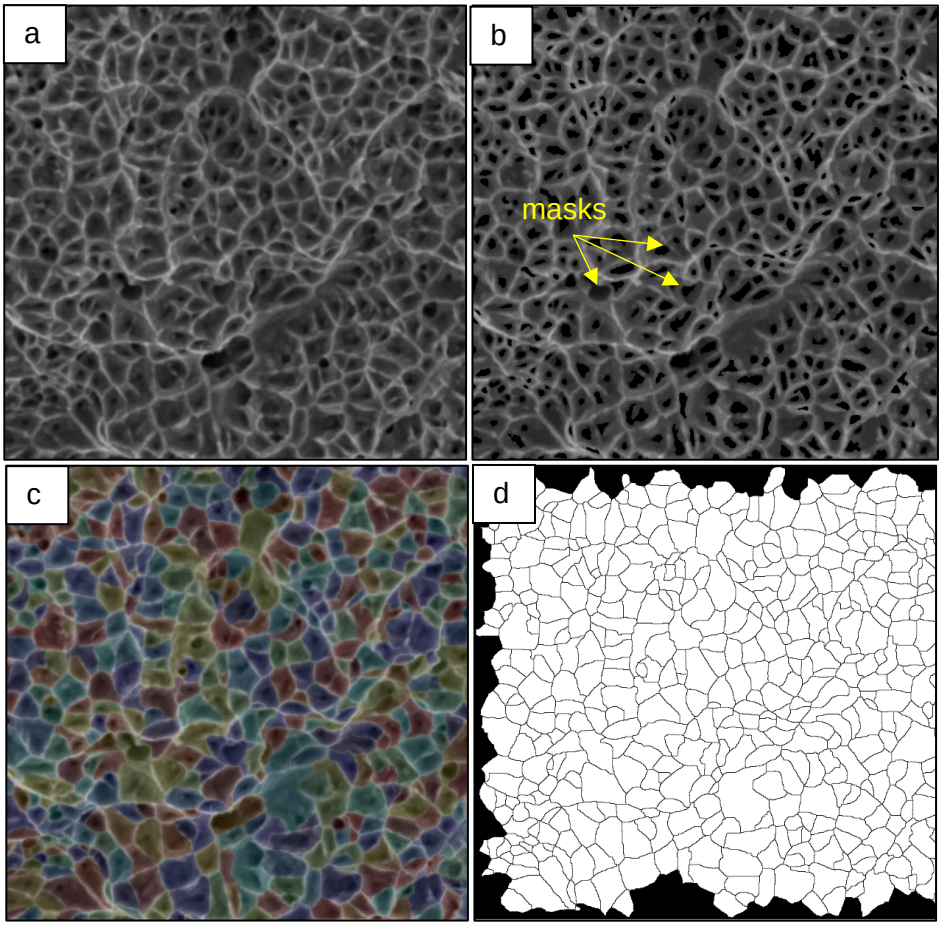

Figure 4.28 a) Original greyscale image from SEM imaging b) with the mask applied on minima regions c) Segmented using the watershed transform showing the individual dimples with coloured labels d) processed image in Image Region Analyzer to omit boundary dimples and extract data.

Results and analysis

Chapter 5

5.1 Introduction

This chapter investigates the effects of interpass temperatures 60°C (LIT) and 150°C (HIT) and in-process cryogenic cooling localised to the melt-pool (CRYO) for deposition rates of 0.75 kg/hr and 3.00 kg/hr in WAAM of Type 316L stainless steel. The effects of heat input are also characterised and reported in this chapter. For the 60°C and 150°C interpass temperatures only, the effects of silicon composition are evaluated through the analysis and characterisation of WAAM samples built using Type 316LSi and 316L stainless steel wires.

As shown in Fig. 5.1, an initial study of the strengthening mechanisms of ODS and solid solution strengthening and an overview of the thermal profiles of each of the experimental builds is also provided. The material characteristics are then outlined for each deposition rate. As outlined within Chapter 4, this includes the following:

- Microstructural characterisation of the layer interface and macrostructure
- Determination of cooling rates based on the microstructural feature scale
- A study of texture, grain size and δ-ferrite morphology
- Measurement of δ-ferrite content
- Identification of oxide size and distribution
- Analysis of chemical composition
- Density analysis and quantification of substrate distortion

The materials characterisations for each deposition rate are subsequently compared and the mechanical properties for each experiment are outlined along with an analysis of the effect of the build parameters. Finally, the strengthening mechanisms present within the Type 316L material produced by WAAM in these experiments are predicted and related to the experimental mechanical results. The flow of information that enables subsequent analysis to be carried out i.e wire chemical composition to solid solution strengthening is shown by the dotted line arrows.

This chapter also includes results published by Cunningham et al. (2019) reporting on the effects of heat input and interpass temperature control on microstructure and mechanical properties of Type 316LSi stainless steel.

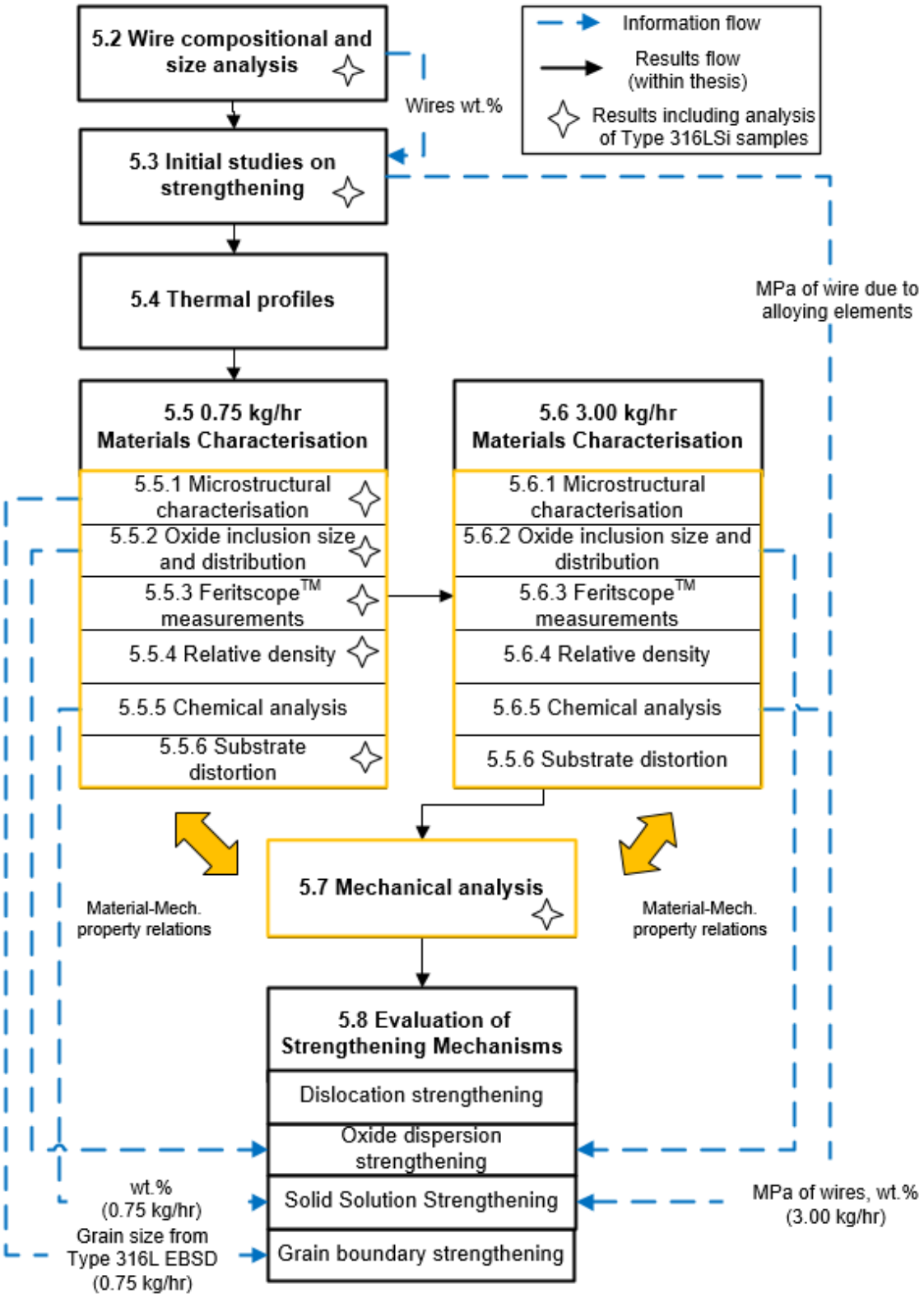

Figure 5.1 Flow chart of the order of results (solid lines) and information flow between sections (dotted line)

5.2 Wire Chemical Composition and Size Analysis

The Type 316L and Type 316LSi wire used in this research were manufactured to the ISO 14343 standard specification. The wire chemical composition for the Type 316L wire and Type 316LSi from manufacturer cast analysis is presented in Table 5.1 with the nominal compositions according to BS EN ISO 14343 (2017).

Table 5.1 Summary of the OES chemical analysis for the Type 316L welding wire, manufacturer cast analysis for Type 316LSi with the ISO 14343 specifications shown for reference.

	Chemical composition (wt.%)									
Wire	**C**	**Si**	**Mn**	**P**	**S**	**Cr**	**Ni**	**Mo**	**N**	**Cu**
316L wire (Manufacturer cast analysis)	0.016	0.408	1.602	0.014	0.007	18.437	12.249	2.553	0.034	0.069
316LSi wire (Manufacturer cast analysis)	0.008	0.790	1.600	0.016	0.011	18.250	12.070	2.530	0.032	0.083
316L ISO 14343	0.03[2]	0.3[i] 0.65[ii]	1[i] 2.5[ii]	0.03[2]	0.03[2]	18[i] 20[ii]	11[i] 14[ii]	2[i] 3[ii]	-	0.75[ii]
316LSi ISO 14343	0.03[2]	0.65[i] 1.2[ii]	1[i] 2.5[ii]	0.03[2]	0.03[2]	18[i] 20[ii]	11[i] 14[ii]	2[i] 3[ii]	-	0.75[ii]

The chemical analysis results presented in Table 5.1 allows the Cr_{eq} and Ni_{eq} of the Type 316L and Type 316LSi wire to be determined. According to WRC-1992 constitution equations, the Type 316L wire has Cr_{eq} of 20.99 and Ni_{eq} of 12.82 (Cr_{eq}/Ni_{eq}=1.64). The Type 316LSi composition leads to a Cr_{eq} of 20.78 and Ni_{eq} of 12.74 (Cr_{eq}/Ni_{eq}=1.63). These values are illustrated in the WRC-1992 diagram in Fig. 5.2, which is also overlaid with the maximum and minimum Cr_{eq} and Ni_{eq} according to the BS EN ISO 14343 (2017) specification. The compositions result in essentially the same FN prediction, with FA solidification mode and a ferrite number (FN) between 8-10 expected. The occurrence of weld solidification cracking is reported to increase for Cr_{eq}/Ni_{eq} ratios slightly less than 1.5 according to WRC-1992 calculations (ASM International, 1980) indicating that such defects are not expected to occur for either welding wire.

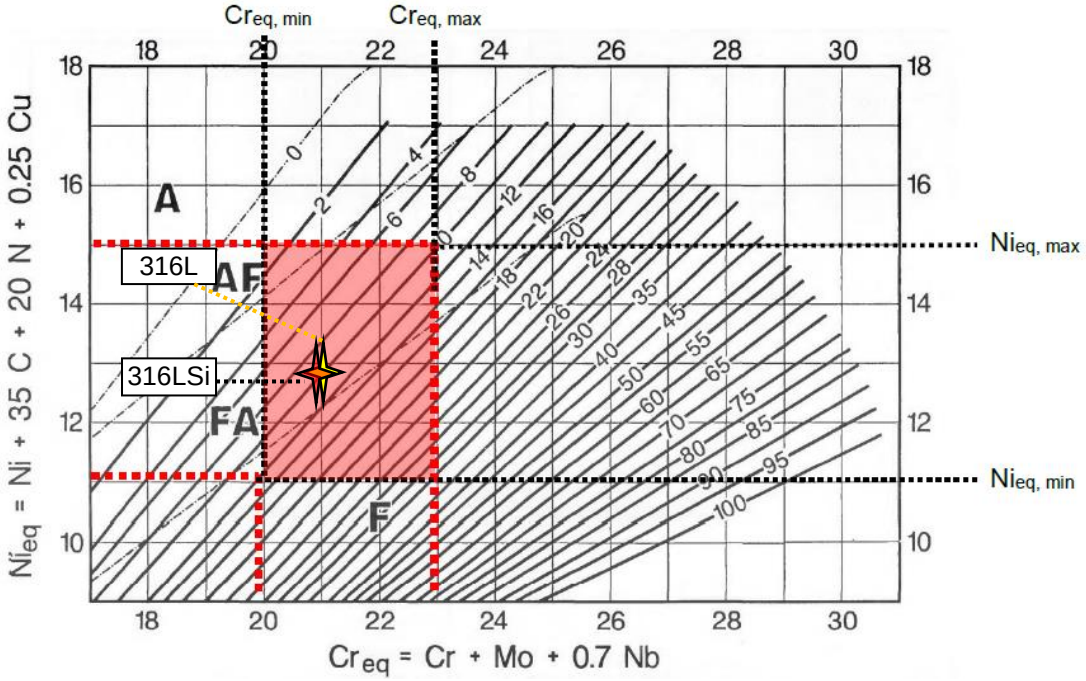

Figure 5.2 WRC-1992 constitution diagram with the acceptable range of 316L according to ISO 14343 and the specific wire compositions used in this research highlighted (Kotecki and Siewer, 1992).

[i] Minimum tolerance limit
[ii] Maximum tolerance limit

Chemical analysis using the LECO inert gas fusion method was carried out to determine the content of O, N and H of the wire used in this research. The results are presented in Table 5.2.

Table 5.2 Summary of the O, N and H chemical composition measurements for the welding wire used in this research. Standard deviation values are based upon three samples per wire.

	O (wt%)		N (wt%)		H(wt%)	
Wire	**Average**	**Std. dev.**	**Average**	**Std. dev.**	**Average**	**Std. dev.**
316L	0.00663	2.0×10^{-4}	0.04380	5.9×10^{-4}	0.00181	7.6×10^{-4}
316LSi	0.00674	1.8×10^{-4}	0.06617	1.9×10^{-4}	0.00150	0.6×10^{-4}

Wire diameter measurements were conducted using a Vernier calliper at several locations over a length of 1 m confirming the wire was of an average diameter of 0.99 mm with a standard deviation of 0.011 mm. This was within the +0.01,-0.04 mm tolerance limits provided by BS EN ISO 544 (2017) for welding wire.

5.3 Initial Studies of the Strengthening Mechanisms

This section provides background to the oxide inclusions within the experimental WAAM samples and estimates of solid solution strengthening due to the interstitial and substitutional solid solution strengthening elemental content of the wire.

5.3.1 Oxide Dispersion Strengthening

As discussed in §3.4.2, ODS can contribute to the strength of additively manufactured stainless steels. Throughout the etched microstructures of the Type 316L and Type 316LSi WAAM samples, circular particles were observed within the WAAM deposit. These were identified as possible sites of oxide inclusions and pits that remain from oxide inclusion pull-out during metallurgical preparation polishing. A representative sample is shown in Fig. 5.3 indicates that these inclusions are a feature of the WAAM deposit only and were not identified within the wrought substrate.

An SEM equipped with energy dispersive spectroscopy (EDS) system was used to investigate the relative elemental composition of these particles compared to the surrounding δ-ferrite dendrite. The EDS maps from the potential oxide inclusion and δ-ferrite are shown in Fig. 5.4a and Fig 5.4b, respectively.

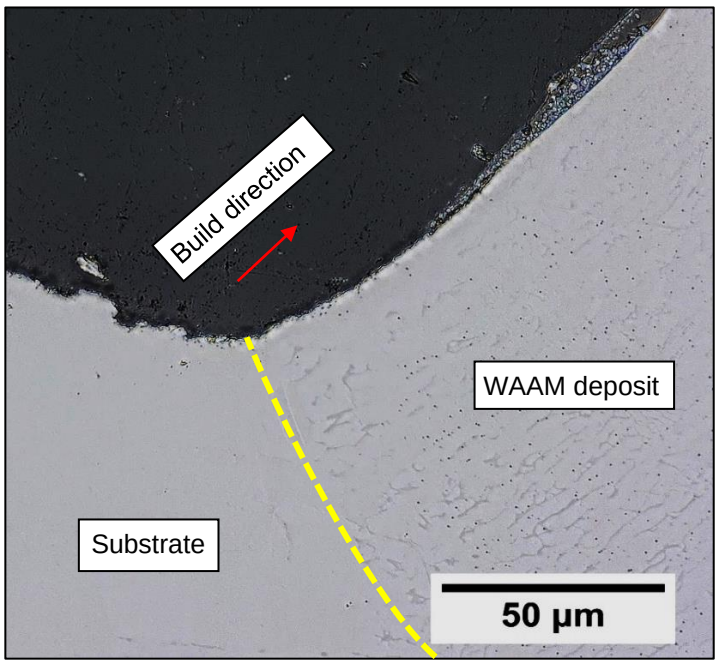

Figure 5.3 Representative micrograph of the oxide inclusions within WAAM Type 316L and Type 316LSi material compared to the substrate.

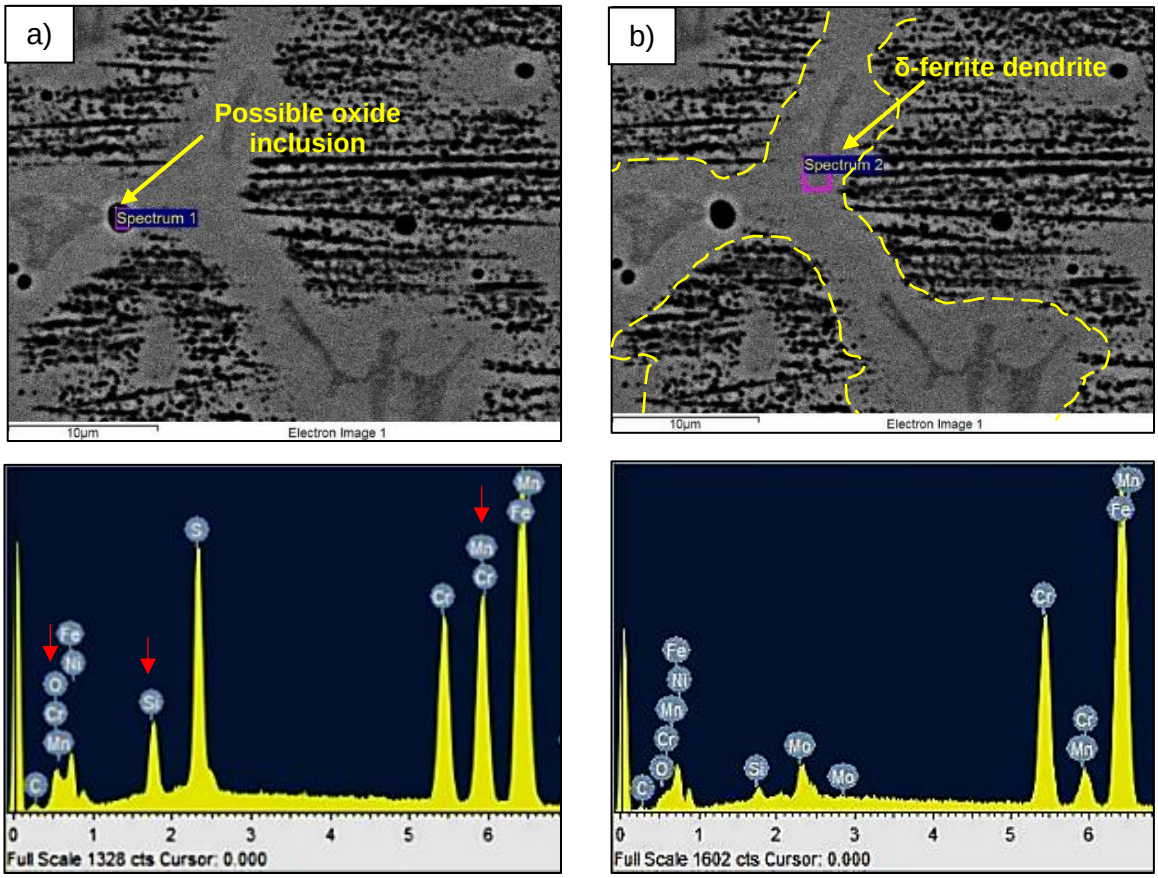

Figure 5.4 Regions investigated for Energy Dispersive Spectroscopy (EDS) for a) potential oxide inclusion b) the surrounding δ-ferrite

An increase in Si, Cr-Mn-O and Mn-Cr can be observed for the region enclosed by the circular particle compared to the δ-ferrite dendrite. This suggests that the particles are oxidizing impurities of the format (Cr_x, Mn, Si) O_2 in agreement with other researchers (Wu et al., 2019a) and contrasts with previous suggestions that they are pits generated from the etching process (Sun et al., 2018b). The size and distribution of the oxide inclusions for deposition rates of 0.75 kg/hr and 3.00 kg/hr are presented in §5.5.2 and §5.6.2, respectively. predicted ODS by the Orowan dislocation bypassing mechanism and the correlation of the predicted ODS with the tested mechanical properties are presented in §5.8.2.

5.3.2 Solid Solution Strengthening

The solid solution strengthening provided by the Type 316L and Type 316LSi wire was calculated using the wire chemical composition and the empirical strengthening equations presented in §4.2 are shown in Table 5.3. A small increase in strength seen for the 316LSi wire because of the additional Si content. Note, however, that adsorption and vaporisation of elements may occur in-process as reported in §5.5.4 and §5.6.5 for the 0.75 kg/hr and 3.00 kg/hr deposition rate experiments, respectively.

Table 5.3 Predicted σ_{ys} solid solution strengthening contribution as a result of wire alloy content.

Wire Type	**Predicted σ_{ys} due to solid-solution strengthening (MPa) (Pickering et al., 1969)**
316LSi	205.4
316L	202.5

The δ-ferrite dendrites identified within the WAAM experimental samples were enriched with Cr and depleted in Ni compared to the γ-austenite matrix as shown in Fig. 5.4. The micro-segregation of elements that accompany the phase transformations results in chemical misfit and solid solution strengthening. High levels of α'-martensite were present in the wire due to the deformation during the wire drawing process, subsequently, the approximations in Table 5.3 do not include the solid solution strengthening due to δ-ferrite.

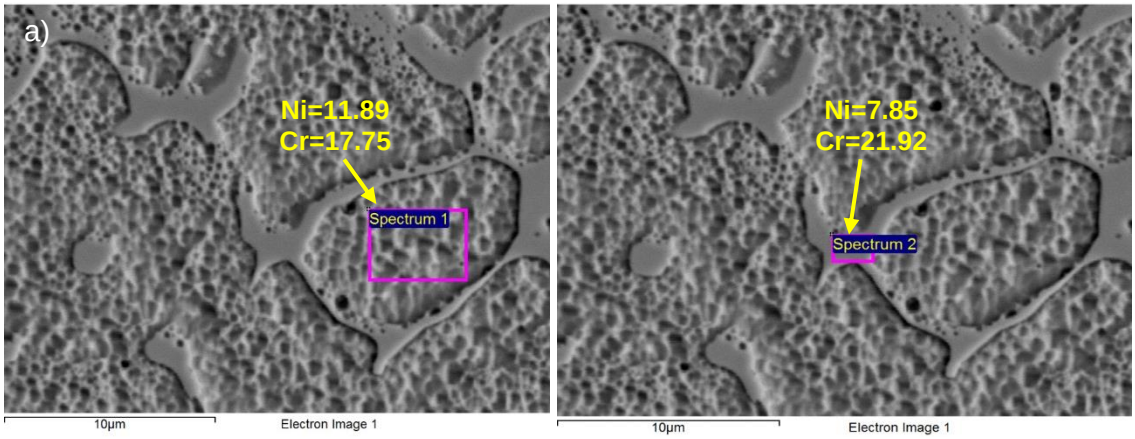

Figure 5.5 EDS analysis of a) γ-austenite and b) δ-ferrite regions displaying the micro-segregation of Chromium and Nickel.

5.4 Experimental Thermal Profiles

5.4.1 Thermal Profiles of the 0.75 kg/hr Experiments

The thermal profiles for the LHI and HHI 0.75 kg/hr experiments are illustrated in Fig. 5.6 and Fig. 5.7, respectively. The stable start temperature at the interpass monitoring position, (T_s) for the LHI's experiment, is approximately 25°C lower for the LIT than HIT. The difference in T_s is greater for the HHI experiments resulting in a difference of 75°C. As the TS and the travel distance are equal, the LIT-LHI samples display the highest cooling rate.

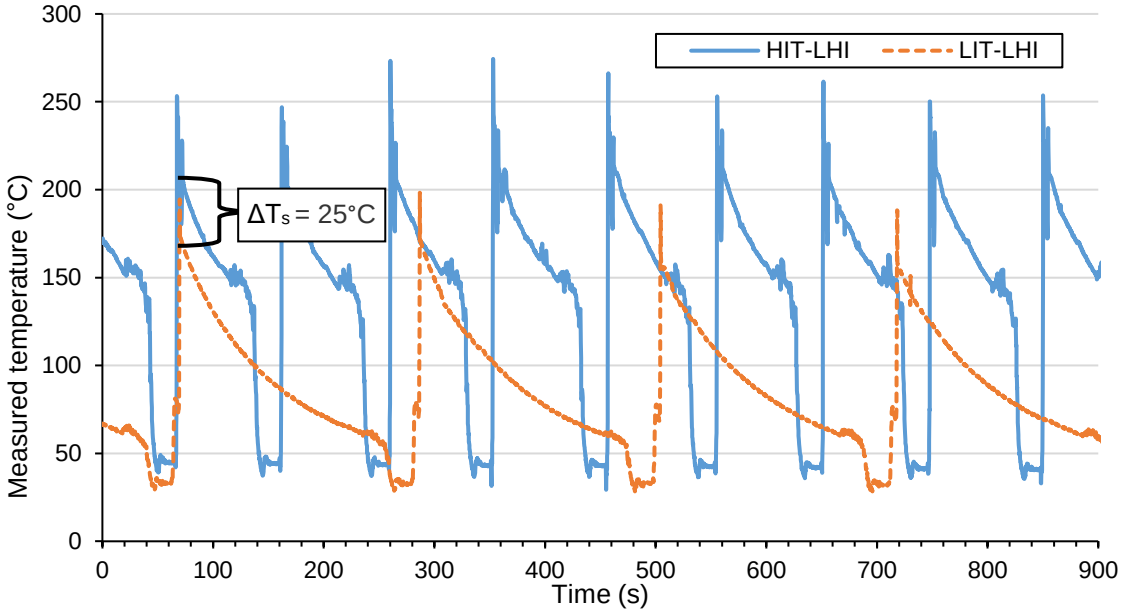

Figure 5.6 Interpass temperature measurements for HIT and LIT, LHI 0.75 kg/hr experiments.

The same trend occurs with the LIT-HHI and HIT-HHI experiments although the effect of cooling strategy on T_s is smaller. Table 5.4 summarises the average interpass dwell time and the total time per layer.

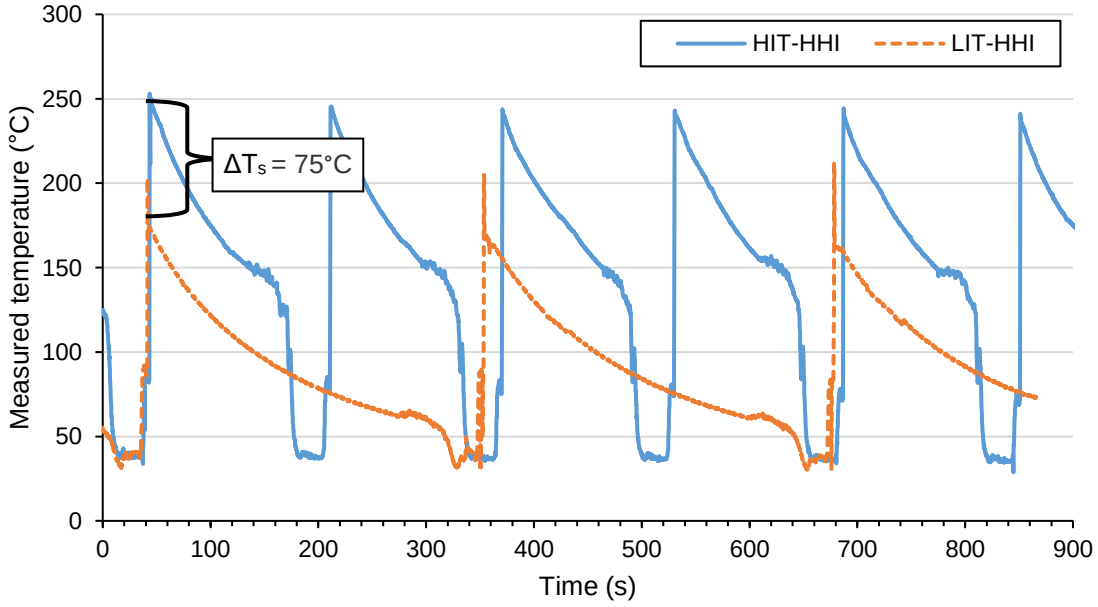

Figure 5.7 Interpass temperature measurements for HIT and LIT, HHI 0.75 kg/hr experiments.

Table 5.4 Comparison of interpass dwell periods for 0.75 kg/hr interpass temperature conditions.

	Heat Input	HIT	LIT
Interpass dwell (s)	LHI	52.8	174.2
Total time per layer (s)		94.0	217.4
Interpass dwell (s)	HHI	105.6	233.6
Total time per layer (s)		168.6	311.8

5.4.2 Thermal Profiles of the 3.00 kg/hr Experiments

The thermal profiles for the 3.00 kg/hr HHI and LHI experiments are illustrated in Fig. 5.8 and Fig. 5.9, respectively. For the CRYO experiments, the interpass temperature was not monitored to avoid thermal shock according to manufacturer recommendations. However, manual thermocouple checks indicated that the build temperature was less than 30°C immediately after deposition layer completion.

The stable start temperature, T_s, at the interpass monitoring position for the LIT-HHI experiment is approximately 65°C lower than for HIT-HHI as illustrated in Fig. 5.9 indicating a higher cooling rate was achieved in this experiment. The LIT-LHI experiment also results in a lower T_s than for the HIT-LHI though the difference is smaller due to the lower overall heat input. Table 5.5 summarises the dwell time and total time per layer for each 3.00 kg/hr with interpass control. Note that any variation in interpass temperature for each layer is a result of the manual restart process and operator reaction time.

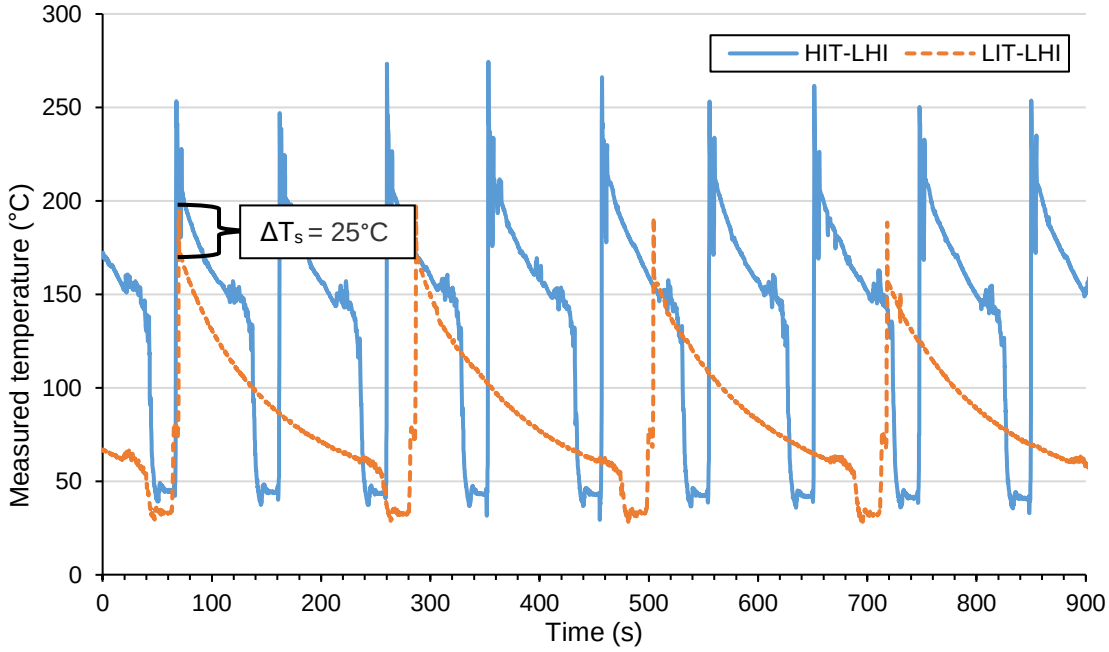

Figure 5.8 Interpass temperature measurements for HIT and LIT, LHI, 3.00 kg/hr.

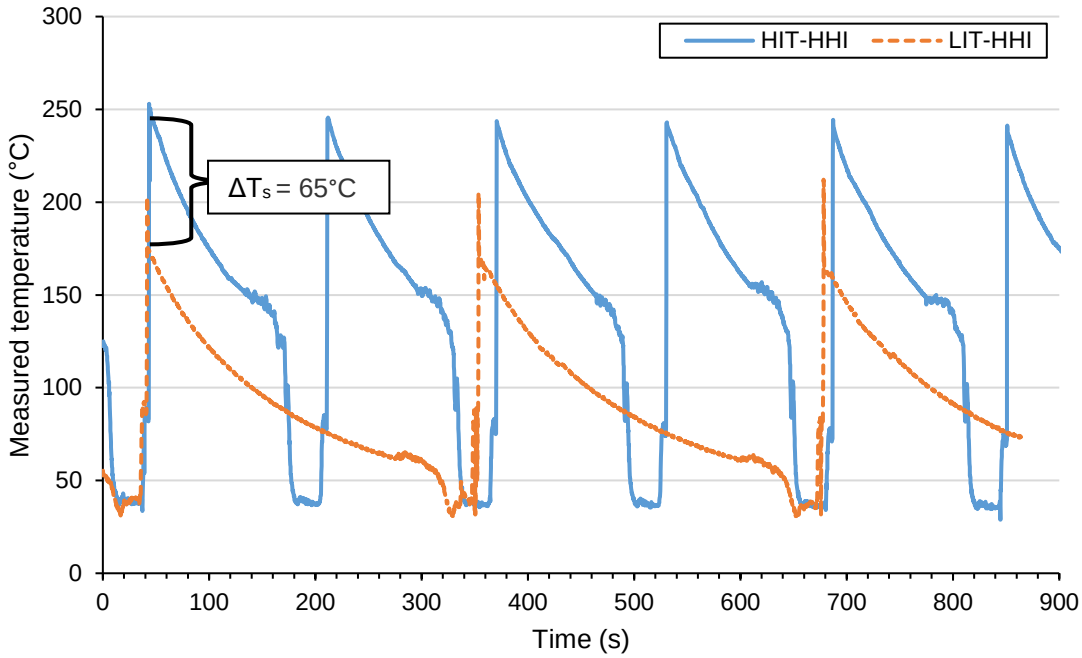

Figure 5.9 Interpass temperature measurements for HIT and LIT, HHI, 3.00 kg/hr.

Table 5.5 Comparison of interpass dwell periods for 3.00 kg/hr interpass temperature conditions.

	Heat input	HIT	LIT
Interpass dwell (s)	HHI	60.0	208.0
Total time per layer (s)		139.2	234.4
Interpass dwell (s)	LHI	55.1	142.0
Total time per layer (s)		70.2	158.2

5.5 Material Characterisation of 0.75 kg/hr Deposition Rate Experiments

5.5.1 Microstructural Characterisation

To characterise the layer interface, optical micrographs covering multiple layers were made. The micrographs showing the macrostructure of the Type 316L, 0.75 kg/hr samples are presented in Fig 5.10. Defined grain boundaries are difficult to identify from these micrographs; however, the dendritic structures appear coarser for the LIT samples for both heat input levels. For the CRYO-LHI samples, it was possible to identify grains with uneven grain boundary edges, indicating greater texture in this sample. Grains can be distinguished by differences in light reflectivity for surfaces of different grain growth directions, which results in lightening and darkening of grains depending on their orientation. These micrographs complements the EBSD grain texture and size results presented in §5.5.1.2, which are limited to a smaller inspection area due to processing time.

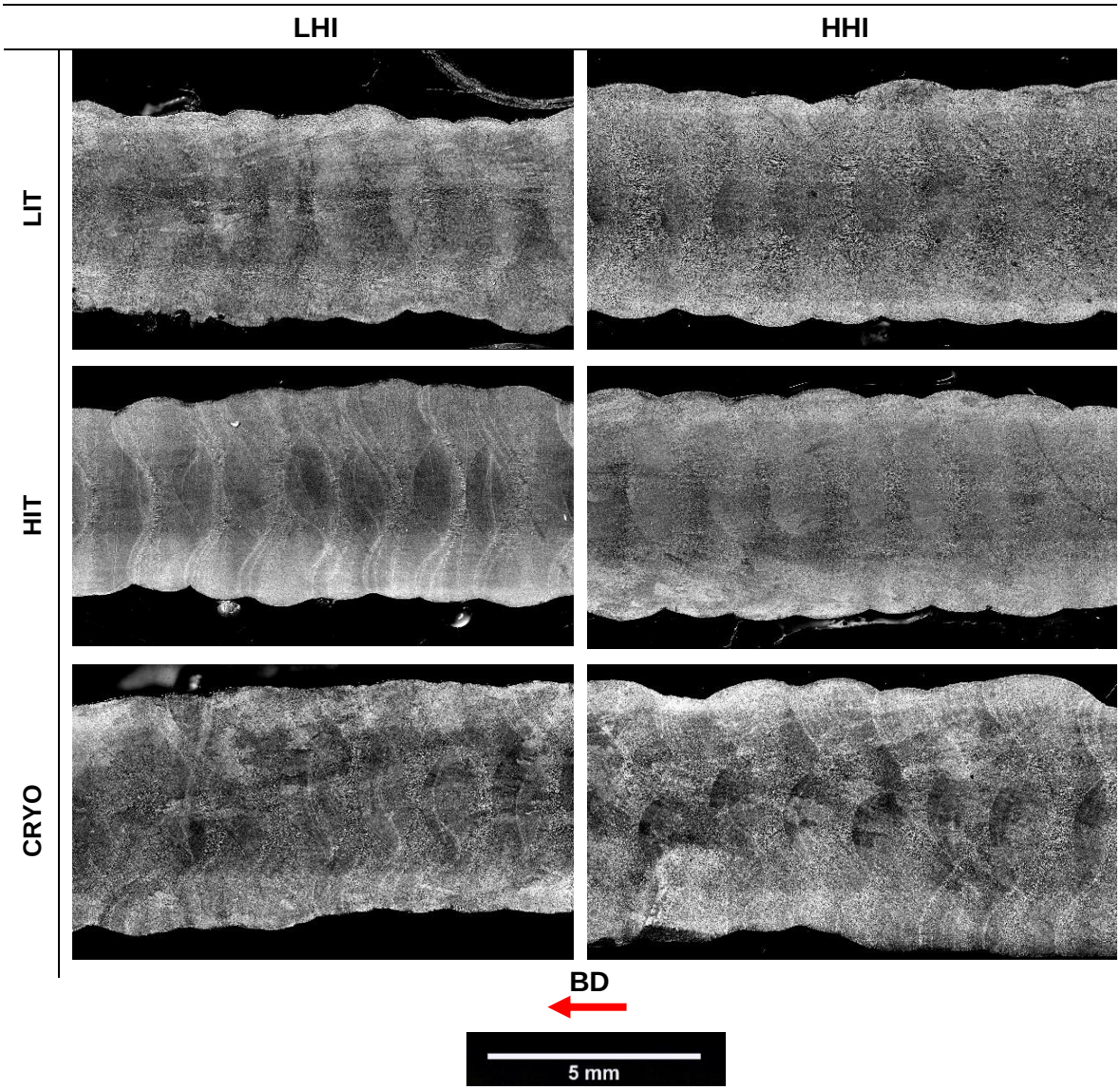

Figure 5.10 Macro-scale optical micrographs of the top sections of 0.75 kg/hr experimental walls (316L)

Higher magnification micrographs of the HHI Type 316L lower and upper sections are shown in Fig 5.11 and Fig 5.12 respectively and for the lower and upper sections of the LHI Type 316L experiments are shown in Fig 5.13 and Fig 5.14, respectively.

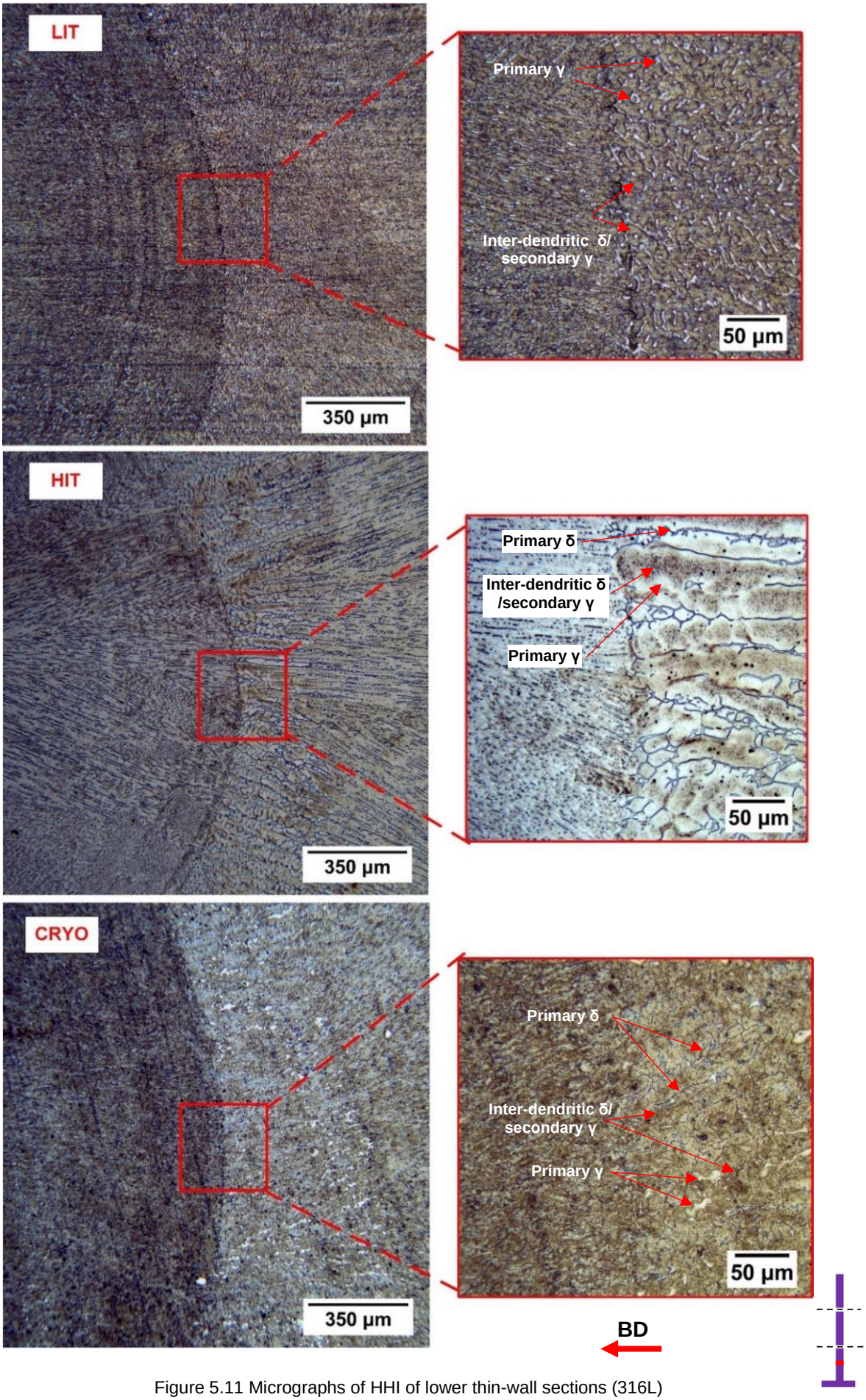

Figure 5.11 Micrographs of HHI of lower thin-wall sections (316L)

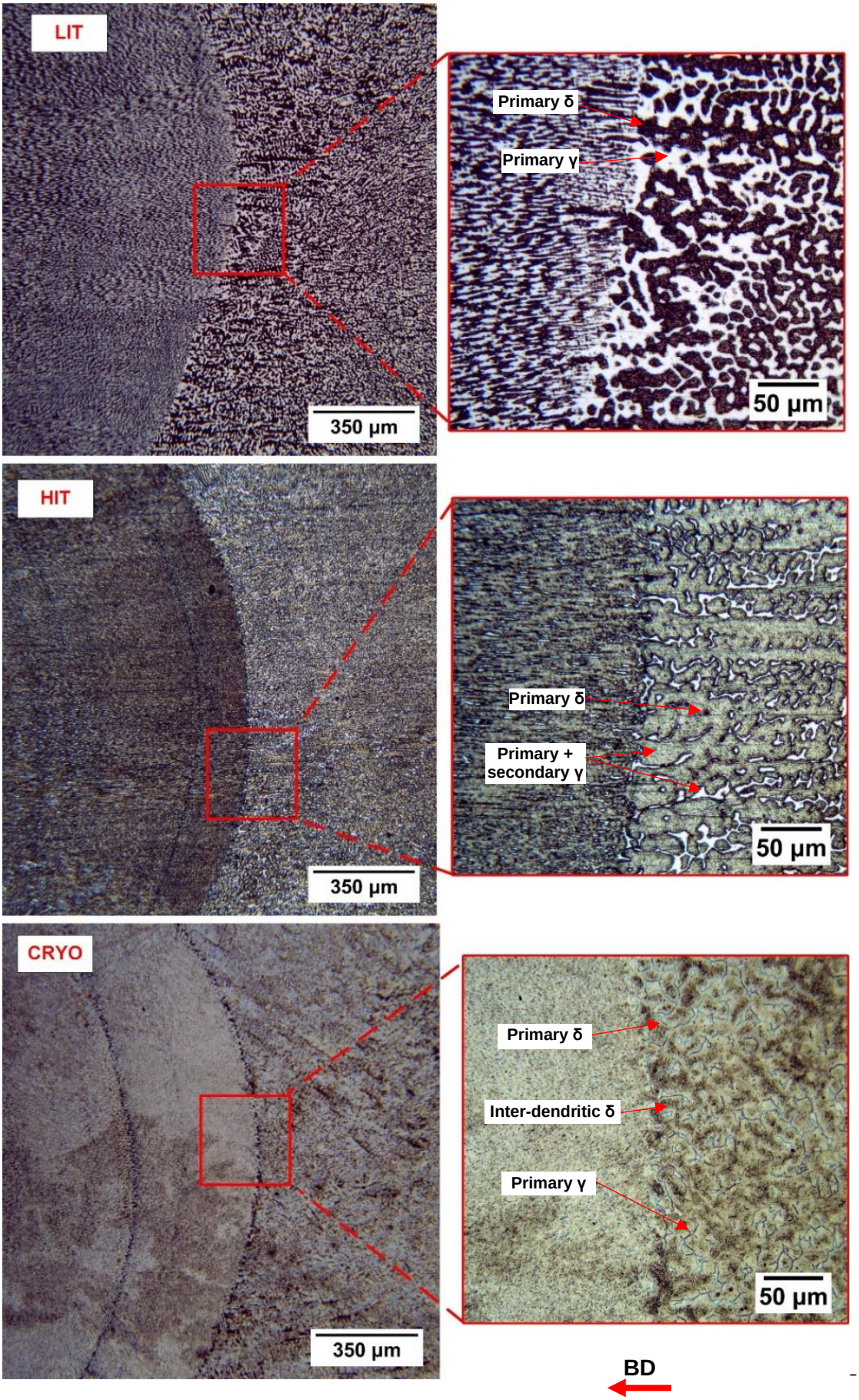

Figure 5.12 Micrographs of HHI of upper thin-wall sections (316L).

.

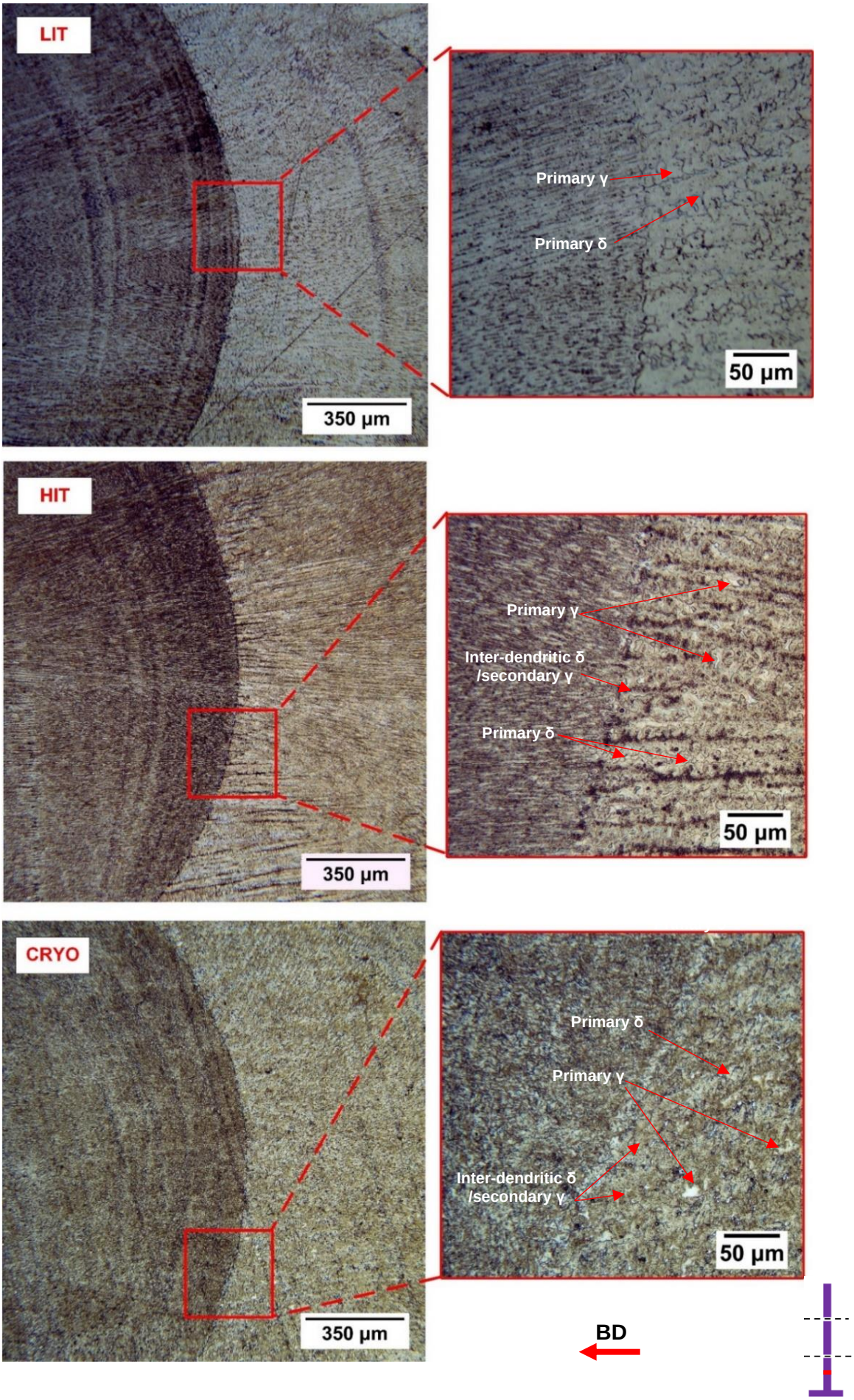

Figure 5.13 Micrographs of the microstructure for the LHI lower section (316L).

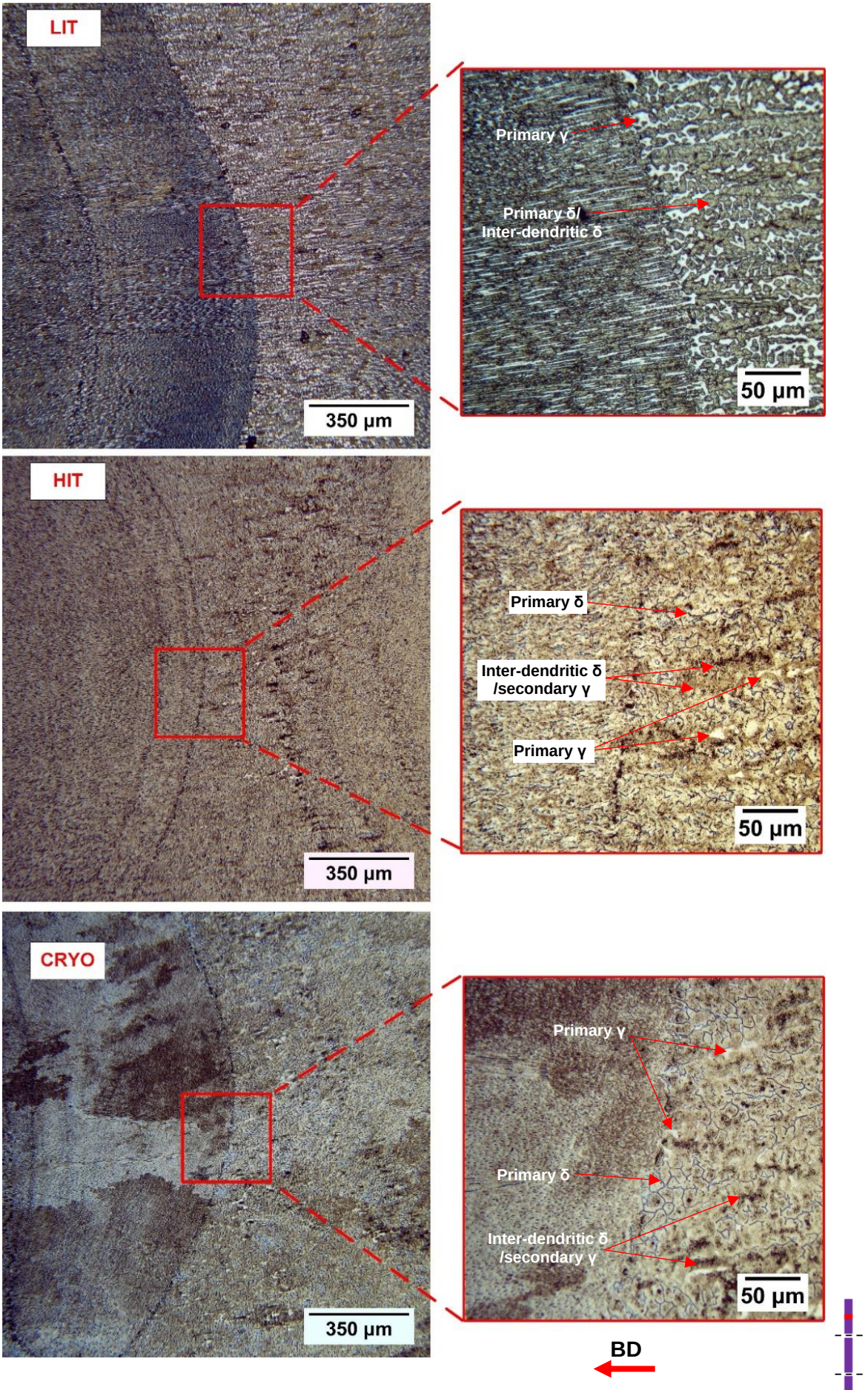

Figure 5.14 Micrographs of the microstructure for the LHI upper section (316L).

A summary of the morphology and details of the δ-ferrite observed in the 3.00 kg/hr samples is shown in Table 5.6. All samples displayed microstructural periodicity in the build direction. Above the re-melt interface, primarily finer, lathy dendritic δ-ferrite morphology existed, whereas below the re-melt interface the microstructure featured coarser vermicular dendrites. The region was exposed to the maximum amount of re-heat from the super-positioned layer without re-melting. As vermicular dendritic morphology coarsens before decomposition into γ-austenite the greater re-heat can result in greater coarsening in this region (Padilha and Rios, 2002). Additionally, minimum solidification rate, R, and thermal gradient, G also occurs in this region which forms the coarsest morphology, as discussed by Kou and Le (1986) and in §1.1.5. With increasing distance below the re-melt line, progressive refinement of the thicker dendritic microstructure occurred, transitioning to the fine lathy morphology once the previous layer re-melt interface is encountered.

Table 5.6 Qualitative evaluation of the morphology present in the 0.75 kg/hr Type 316L samples.

	HHI 0.75 kg/hr (lower section)			**HHI 0.75 kg/hr (upper section)**		
	LIT	**HIT**	**CRYO**	**LIT**	**HIT**	**CRYO**
Morphology type	Vermicular/ Lathy δ	Vermicular/ Lathy δ Secondary γ	Vermicular/ Lathy δ Secondary γ	Vermicular/ Lathy δ	Vermicular/ Lathy δ Secondary γ	Vermicular/ Lathy δ Secondary γ
Thickness	thick	thin	thin δ + very thick sec. γ	thick	thick (γ)	thin δ + thick sec. γ
Directionality	low	high	low	low	high	low
δ SDAS	low	high	low	high	high	high
	LHI 0.75 kg/hr (lower section)			**LHI 0.75 kg/hr (upper section)**		
	LIT	**HIT**	**CRYO**	**LIT**	**HIT**	**CRYO**
Morphology type	Vermicular/ Lathy δ	Vermicular/ Lathy Secondary γ	Vermicular/ Lathy δ Secondary γ	Vermicular/ Lathy δ	Vermicular/ Lathy δ Secondary γ	Vermicular/ Lathy δ Secondary γ
Thickness	thin δ	thin δ + thick sec. γ	thin δ + very thick sec. γ	thick δ	thin δ + thick sec. γ	thin δ
Directionality	Med	High	Low	Med	Low	Low
δ SDAS	High	Low	Low	High	High	High

Despite, the aforementioned periodicity in the build direction, differences in the morphology type, scale, and contrast was observed for each cooling strategy. The dendritic structures within the LHI samples are of smaller length scale and thickness than the HHI samples, which can be attributed to the higher cooling rates present. Similar trends with the cooling strategy were shown for the LHI compared to the HHI samples regarding the cooling strategy. For example, the highest contrast and most extensive dendritic δ-ferrite structures are found in the LIT samples, the upper sections displaying coarsening compared to the lower section. The LIT-HHI sample presented in Fig 5.11 and 5.12 displayed the thickest dendritic network with the highest contrast between phases, indicating the strongest solute segregation and distinctive etching behaviour. The HIT-HHI sample has dendrites of greater length scale, reduced thickness, and stronger alignment to the build direction with greater decomposition resulting in regions of inter-dendritic ferrite or secondary austenite.

In terms of differences in microstructure with build height, the dendrites of LIT-HHI samples are observed to become coarser with increasing build height between Fig 5.11 and Fig 5.12. This can be related to the reduced heat transfer with increasing build height as conduction through the baseplate becomes less effective. The HIT-HHI sample is effectively pre-heated as the interpass temperature maintained throughout the build. As the welding parameters are fixed, the deposition becomes more energetic with build height as the build temperature ramps up and conduction becomes less efficient. The HIT-LHI samples show greater alignment to the build direction in the lower section than upper section micrograph, showing a reduction in directional growth with build height with the higher interpass temperature. High volumes of inter-dendritic δ-ferrite/secondary γ are also observed particularly in the upper sections and the LHI of HIT and CRYO samples, showing areas where the δ-ferrite formed at primary solidification is decomposed to secondary austenite (Baeslack III et al., 1979).

For Type 316LSi wire, macro-scale optical micro-graphs covering multiple layers are presented in Fig 5.15. The LIT-LHI sample shows a strongly textured microstructure with high aspect ratio grains aligned with the build direction. The HIT-HHI sample also displays large grains with less directional feathered grain boundaries.

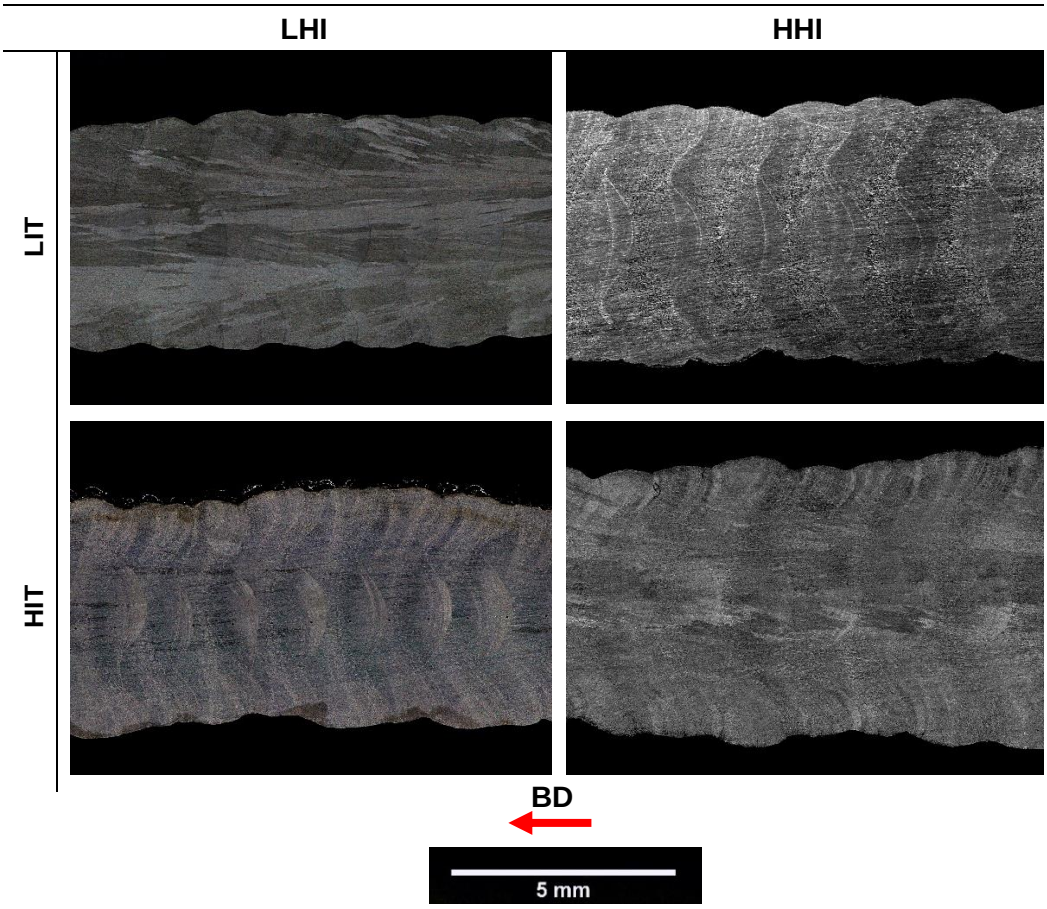

Figure 5.15 Macro-scale optical micrographs of the top sections of 0.75 kg/hr experimental walls (316LSi)

The grain boundaries are difficult to identify in the LIT-HHI and HIT-LHI samples, although the general alignment of the grain texture to build direction remains visible. Micrographs of the re-melt interface for the Type 316LSi HHI and LHI samples are shown in Fig 5.16 and Fig 5.17.

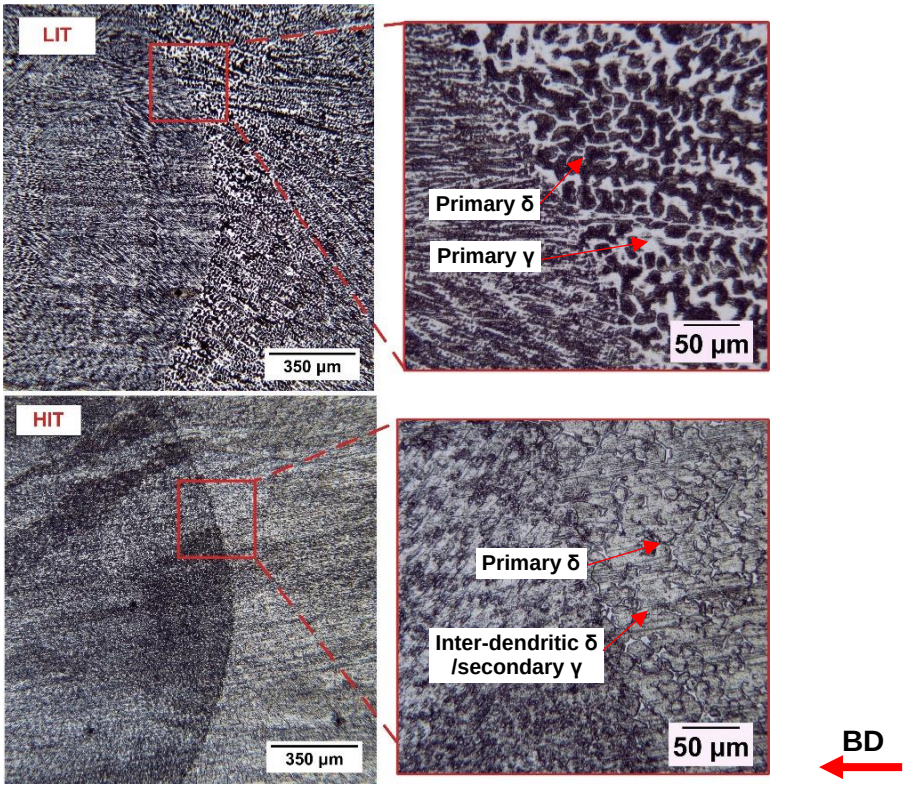

Figure 5.16 Micrographs of the microstructure for the HHI (316LSi)

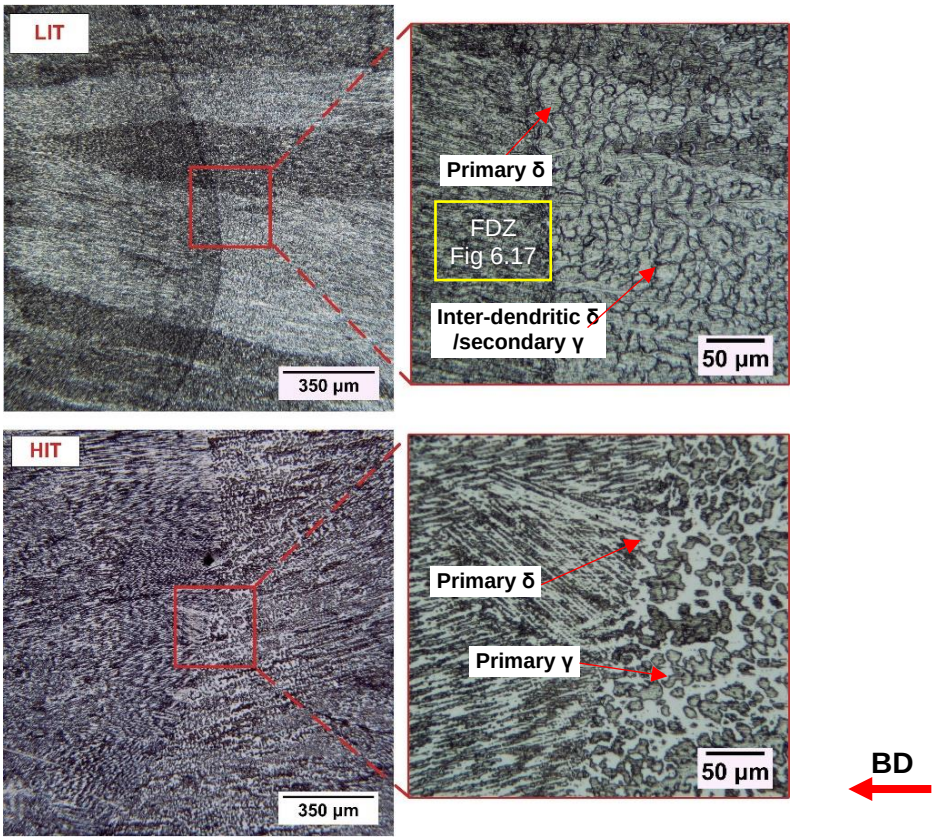

Figure 5.17 Micrographs of the microstructure for the LHI (316LSi)

As observed with the Type 316L samples, the LIT-HHI Type 316LSi sample contains an extensive dendritic network of δ-ferrite and HIT-HHI resulting in finer, more equiaxed dendrites. Further examination of the finer microstructures above the re-melt interface of the LIT-LHI Type 316LSi sample was undertaken with SEM. This identified fine primary dendrites δ-ferrite within the γ-austenite matrix as shown in Fig 5.18.

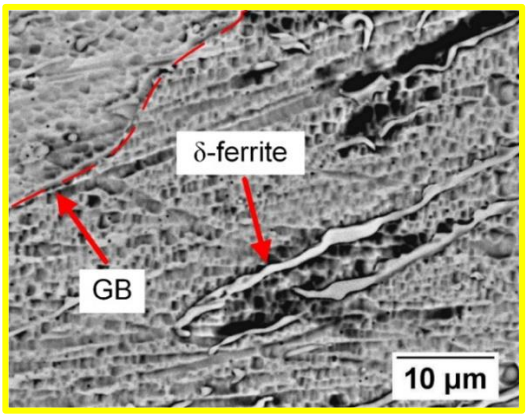

Figure 5.18 SEM (BEI) micrograph of 85mm build height of LIT-LHI showing the lathy δ-ferrite within cellular austenite and a sub-grain boundary.

5.5.1.1 Process Cooling Rates based on the Scale of Microstructural Features

This section relates the microstructural features of primary dendrite arm spacing (PDAS) and primary cell arm spacing (PCAS) to the cooling rate. The PCAS or PDAS is related to the cooling rate, $\dot{T}$, during solidification according to the following equation (Elmer et al., 1989b):

$$(PCAS\ or\ PDAS) = 80\dot{T}^{-0.33} \tag{5.1}$$

Where the PCAS or PDAS depending on the microstructure is calculated as follows:

$$PCAS\ or\ PDAS\ (\mu m) = \frac{d_c}{No\ of\ cells\ or\ dendrites} \tag{5.2}$$

Inspection of the microstructures showed that the 0.75 kg/hr samples primarily consisted of a mixture of lathy, columnar and equiaxed dendrites as outlined in §6.5.1, however, the CRYO-LHI sample also showed isolated regions of cellular primary austenitic solidification structures above the re-melt interface as shown in Fig 5.19. This location above the re-melt interface is considered an “unmixed zone” (Baeslack III et al., 1979).

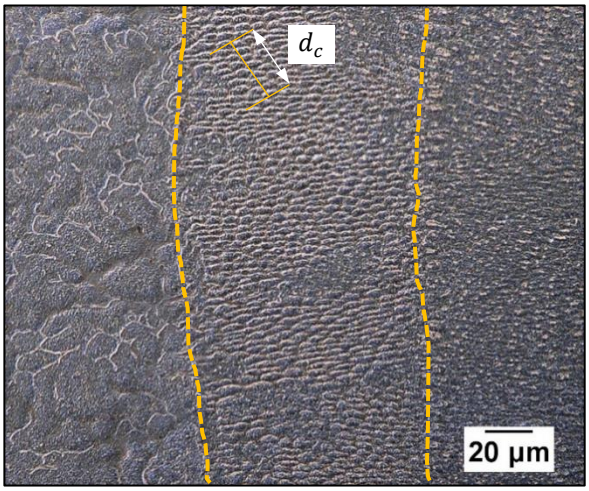

Figure 5.19 Grouping of cellular sub-structures identified at the centreline of the CRYO-LHI re-melt interface

Cellular-dendritic FA structures were also observed at the edges of the HHI experiments (see Fig 5.20b, Fig 5.21b, Fig. 5.22b) and the CRYO-LHI sample (see Fig 5.20a).

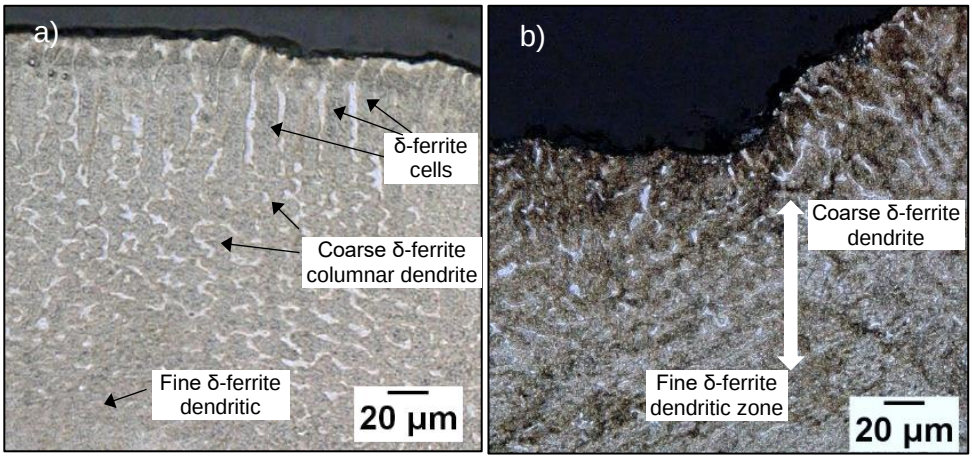

Figure 5.20 Micro-graph of the cellular and dendritic morphology of at the edge of a) CRYO-LHI b) CRYO-HHI Type 316L samples.

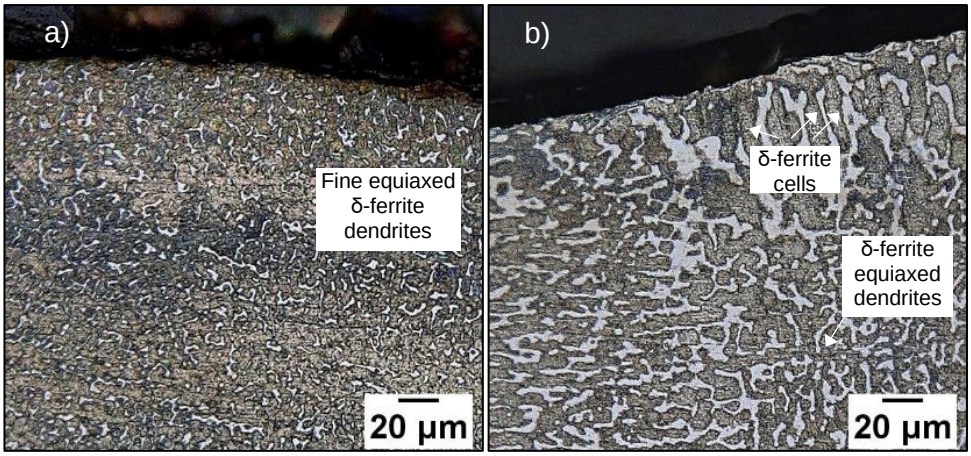

Figure 5.21 Micro-graph of the cellular and dendritic morphology of at the edge of a) LIT-LHI b) LIT-HHI Type 316L samples.

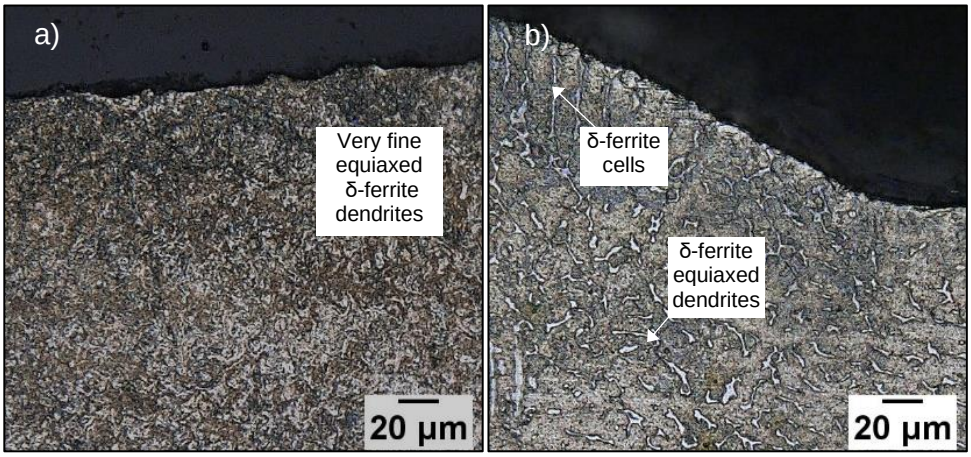

Figure 5.22 Micro-graph of the cellular and dendritic morphology of at the edge of a) HIT-LHI b) HIT-HHI Type 316L samples.

The darkened cell cores (δ-ferrite) and lightened cell boundaries (γ-austenite) represents a FA solidification mode that transitions to columnar dendritic morphology and finer equiaxed dendrites toward the deposition centreline. The LIT-LHI and HIT-LHI samples displayed a fine dendritic morphology that was extended to the edge of the thin-wall samples.

The variation in microstructural feature scale and the cooling rates of the coarsest and finest microstructure at the deposit centreline were determined using equation 5.1 as shown in Fig. 5.23 and Fig. 5.24, respectively. This captures the periodicity in dendrite size that occurs along the build direction observed qualitatively within optical micrographs of §5.5.1.

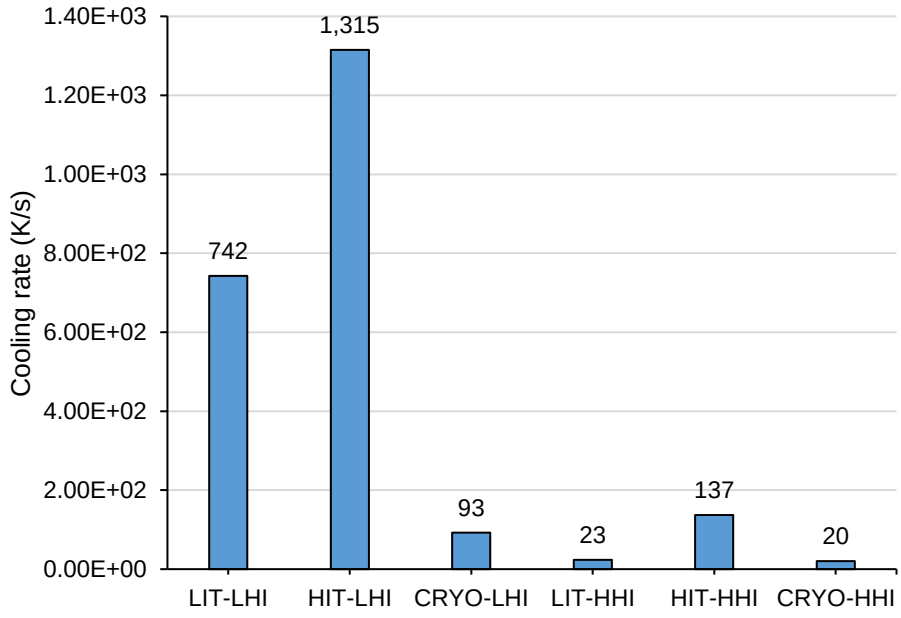

Figure 5.23 Cooling rates calculated for the coarsest dendritic regions along the deposit centreline.

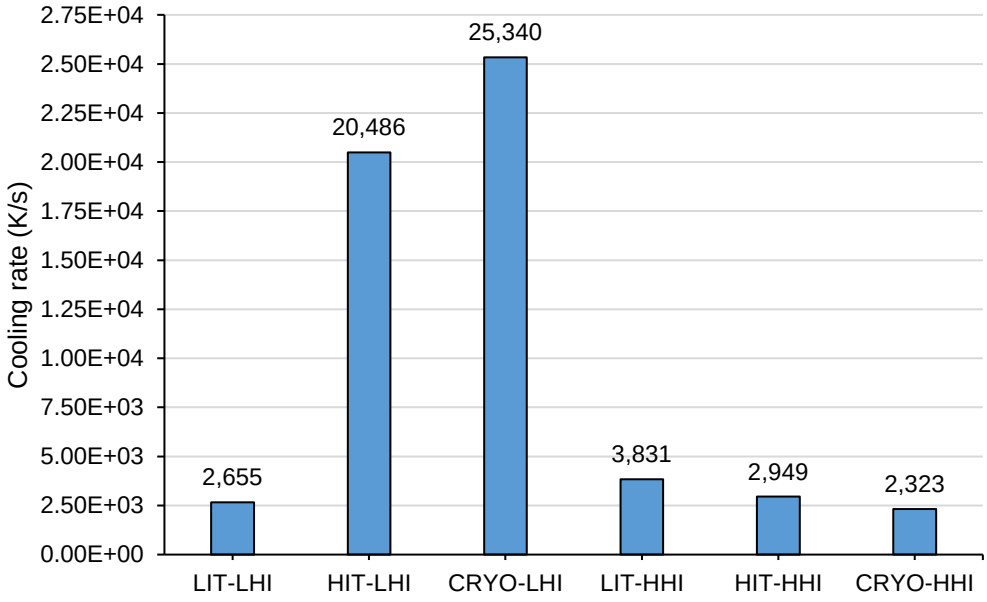

Figure 5.24 Cooling rates derived from the finest dendritic and cellular regions along the deposit centreline.

The microstructures of the HHI samples reflected the lower cooling rates experienced compared to the LHI experiments. This is related to higher arc energy per kilogram deposited and also the greater interaction time with the existing material. The LHI experiments displayed higher cooling rates, however, as shown in Fig. 5.23 and Fig. 5.24, the HIT-LHI sample resulted in a finer microstructure and higher cooling rates than the LIT-LHI samples. In addition, the HIT-LHI coarse structures were finer than the LIT-LHI sample. This was notable as the thermal profiles outlined in §5.4 indicated that the higher interpass temperature would result in a slower cooling rate. The CRYO-LHI samples showed the greatest variation of local cooling rates (57- 25,340 K/s) throughout the sample, with areas of finer and coarser microstructural features than LIT-LHI.

5.5.1.2 Evaluation of Texture and δ-ferrite Morphology by EBSD

EBSD inverted pole figures (IPF's) presented in Fig. 5.25 show the δ-ferrite within the γ-austenite matrix at 2000x magnification. These images cover a small area of the overall sample size (62.3 x 48.3 µm), however, it can be seen that LHI samples generally have coarser δ-ferrite distributions. This is attributed to the reduced solidification time resulting in greater amounts of continuous vermicular retained δ-ferrite. Greater decomposition has occurred with the HHI samples with greater volume of globular and lathy δ-ferrites structures. The CRYO-HHI sample shows regions of fine globular and a continuous vermicular region in the lower-left corner indicative of local variation in cooling rates.

The HIT-LHI the δ-ferrite network is more continuous and of greater length scale compared to LIT-LHI, which can be attributed to the slower cooling rate and greater re-heat aiding in the dissolution of secondary dendrite arms. The CRYO-LHI sample showed the coarsest LHI dendrite morphology indicating that dissolution was hindered by the cryogenic cooling process.

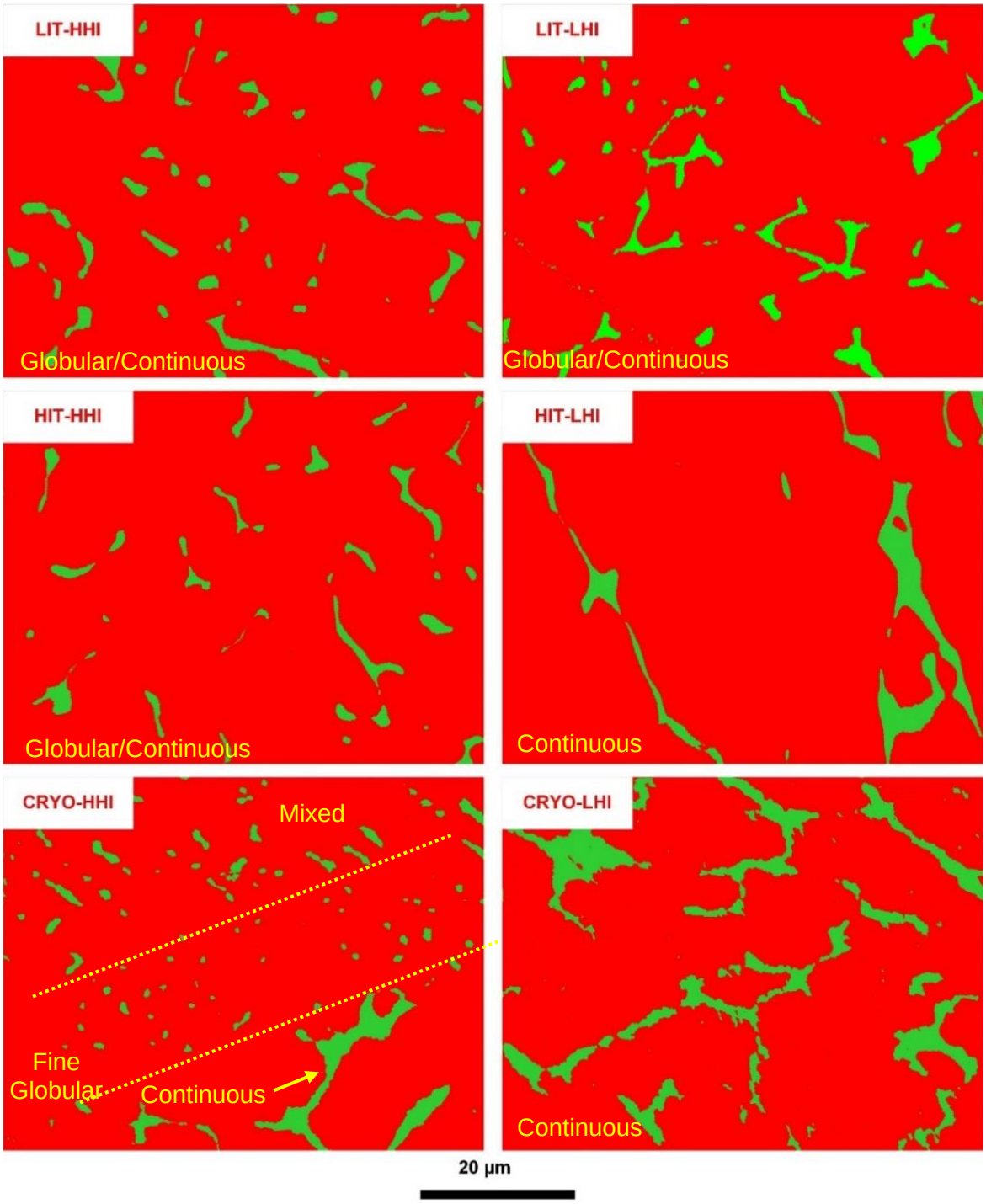

Figure 5.25 EBSD phase maps of the δ-ferrite within the γ-austenite matrix (x2000 mag.)

Lower magnification (x100) IPFs allowed evaluation of the δ-ferrite distribution over a larger and more representative sample area (1.24x0.96 mm). Within the HIT-LHI and HIT-HHI images, it was possible to identify local areas of high δ-ferrite density which occurred periodically in the build direction as shown in Fig. 5.26 and Fig. 5.27, respectively. The δ-ferrite occurs more frequently and is of higher aspect ratio in the LHI compared to the HHI experiment and contains less δ-ferrite of globular morphology as also indicated in Fig. 5.25.

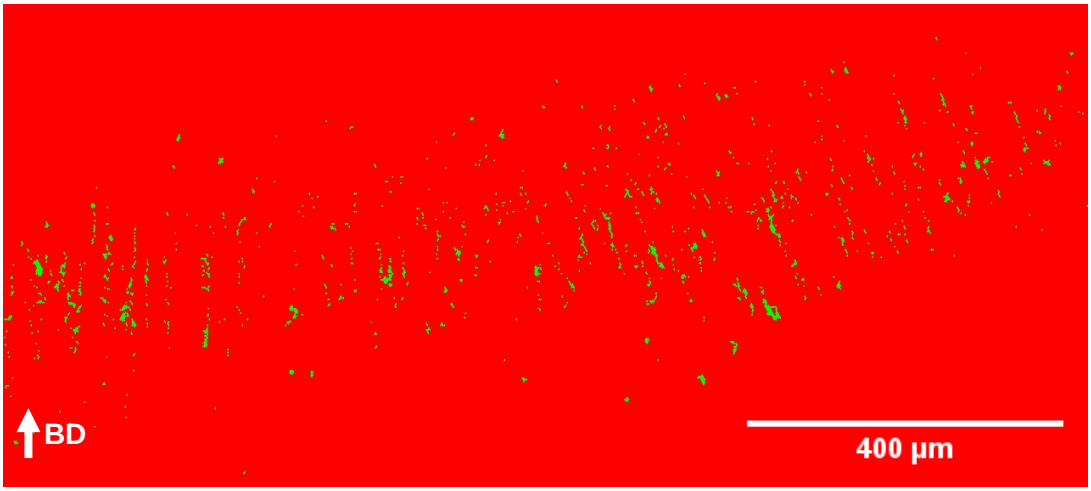

Figure 5.26 IPF map highlighting δ-ferrite content in sample HIT-LHI (x100 mag.)

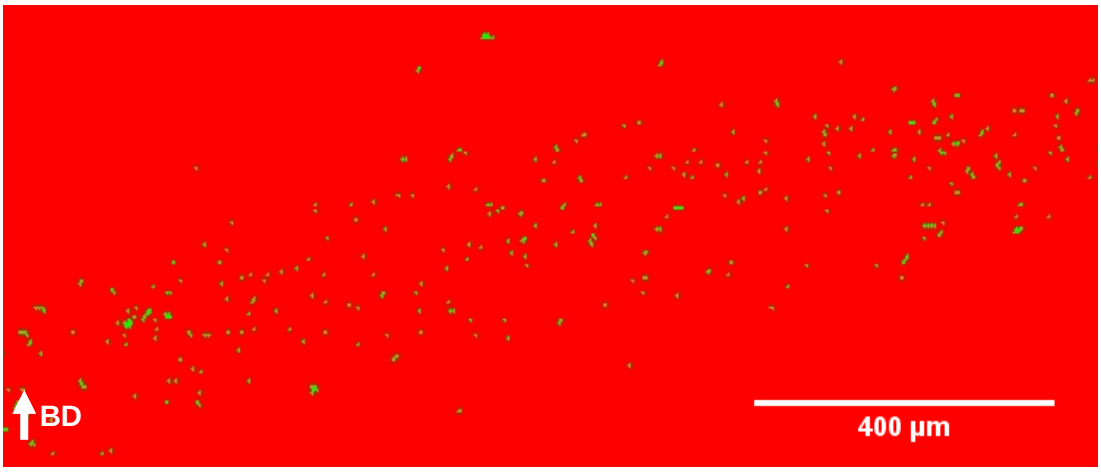

Figure 5.27 IPF map highlighting δ-ferrite content in sample HIT-HHI (x100 mag.)

To highlight the grain orientation and alignment, a texture map (presented in the top right-hand corner of Fig. 5.28, 5.29, 5.30 and 5.31) was used to define the grain directions for the IPFs. The IPF maps show that the columnar grains are predominantly aligned parallel to the build direction <001>. The IPF map and texture scale of the grains of the LIT-HHI shown in Fig 5.29 shows a greater proportion of grains shifted to align to both the <101> and <111> directions. The grains were also of lower aspect ratio than that of the HIT sample, with comparatively uneven grain boundaries.

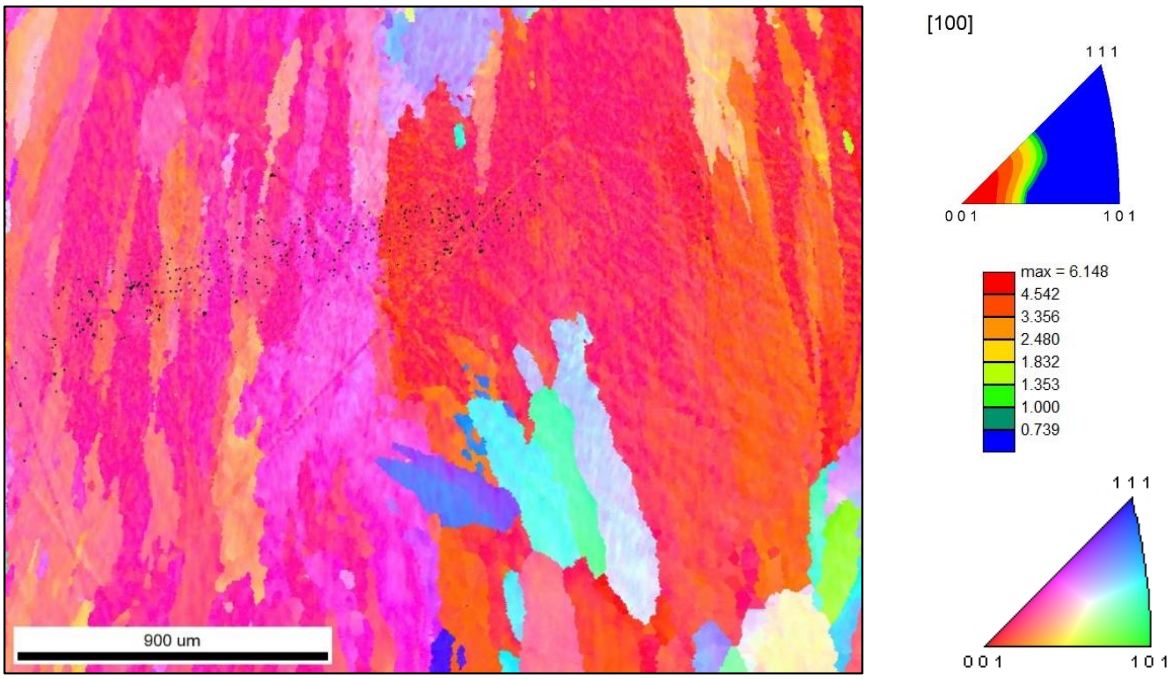

Figure 5.28 IPF map of HIT-HHI, 0.75 kg/hr.

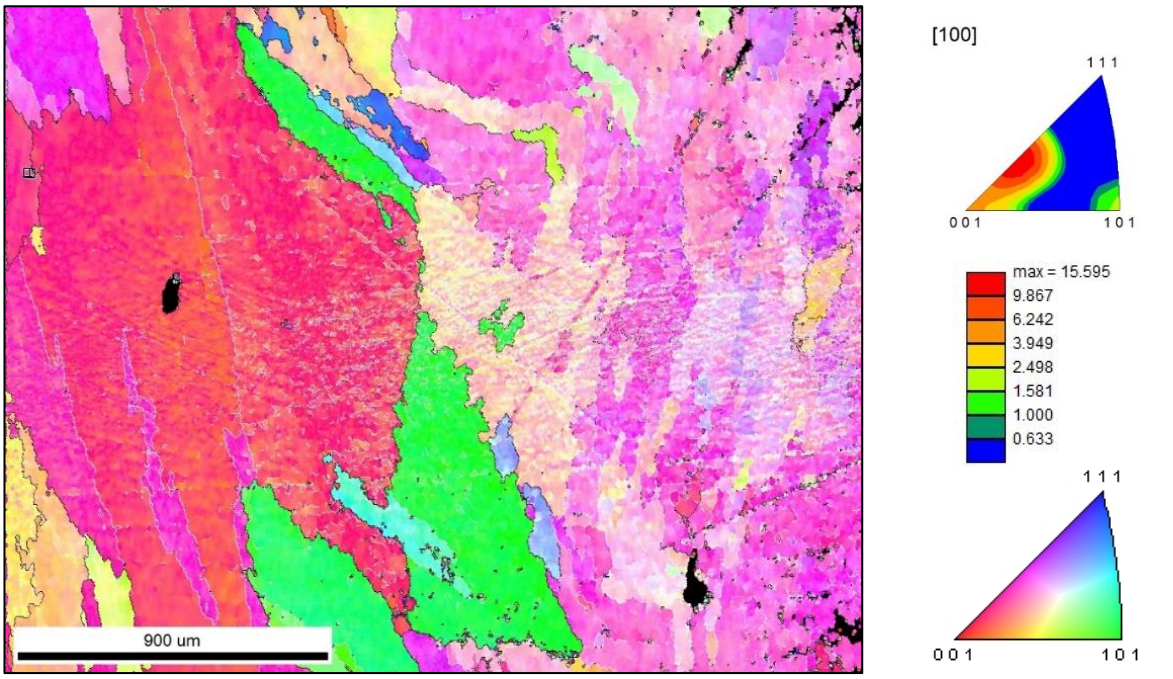

Figure 5.29 IPF map of LIT-HHI, 0.75 kg/hr.

The IPFs for the HIT-LHI and LIT-LHI samples are shown in Fig. 5.30 and 5.31 respectively with both samples showing similar maximum strength of the texture. The LIT-LHI results in a slight increase in the proportion of grains aligned toward the <111> direction, which was also found for the LIT-HHI experiment. The grain size within each IPF is relatively large compared to the IPF area, however, many smaller grains are identified for the LHI experiments.

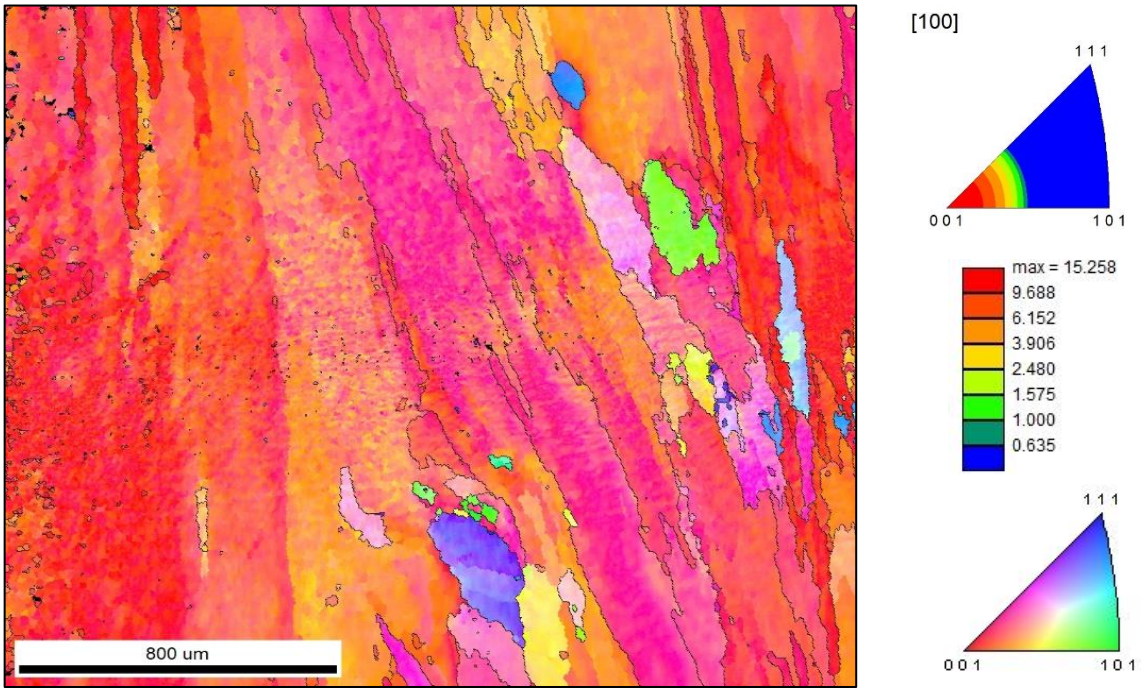

Figure 5.30 EBSD micrograph of HIT-LHI, 0.75 kg/hr.

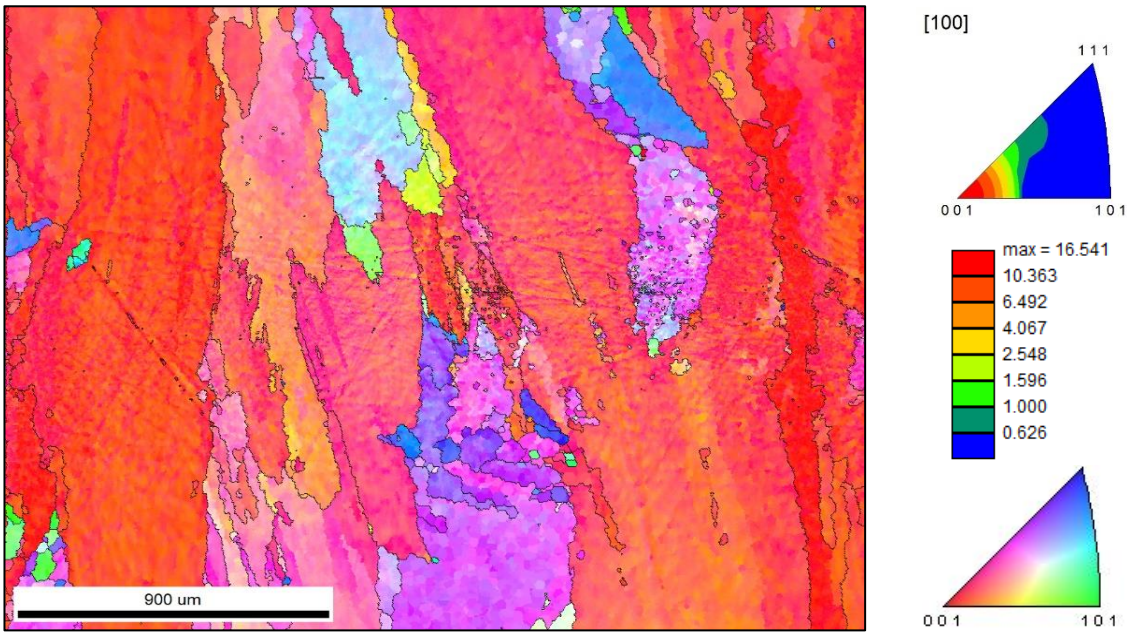

Figure 5.31 EBSD micrograph of LIT-LHI, 0.75 kg/hr.

The grain size measured by the linear intercept method in the horizontal direction for the 50x magnification IPFs revealed large grains of approximately 80 µm for the HIT-HHI, LIT-HHI, HIT-LHI and LIT-LHI samples (see Appendix B). CRYO-LHI and CRYO-HHI samples were unable to be mapped at higher magnification, however, the IPF for 2000x magnification is shown in Fig 5.32.

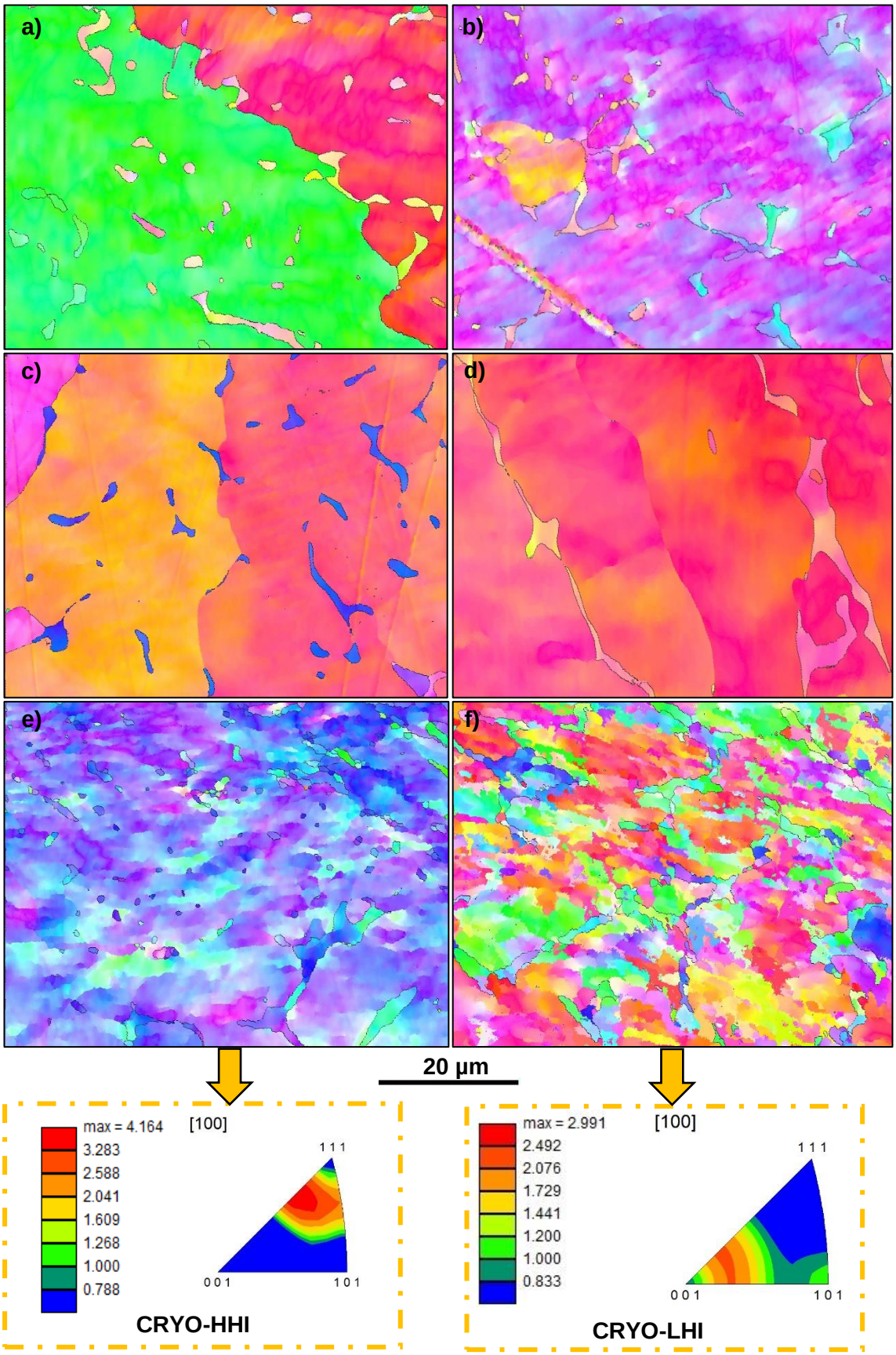

Figure 5.32 IPFs of a) LIT-HHI b) LIT-LHI c) HIT-HHI d) HIT-LHI e) CRYO-HHI f) CRYO-LHI (x2000 mag.)

Most of the CRYO-HHI sample is aligned toward the <111> direction, however, a trend for the greater microstructure cannot be assumed due to the small IPF area. This differs from the LIT and HIT samples which showed strong alignment to the <100>. The CRYO-LHI

showed a wide range of grain texture orientations within a small surface area indicating the development of an isotropic microstructure of finer grain size.

It can be seen for both the LIT-LHI (Fig 5.32b), CRYO-HHI (Fig 5.32e) and CRYO-LHI (Fig 5.32f) that the grains exhibited notable mosaicity (slight fluctuations in the colouration of IPF maps within potential individual grain locations). The mosaicity is indicative of strain within the grains accommodated by dislocations and crystallographic misorientation (Yanushkevich et al., 2017). The colour gradients across the larger regions in the centre portion of the maps indicate that the lattice orientation changes by tens of degrees over a distance of a few tens of microns (Smith et al., 2018). This can be caused in materials subjected to high levels of deformation, where the high levels of dislocation density result in distortion of the EBSD reflection pattern.

5.5.2 Oxide Inclusion Size and Distribution

The results of the image analysis to determine the mean oxide volume fraction and radius for each experiment are presented in Fig. 5.33. The oxide inclusion mean radius for the Type 316LSi and Type 316L samples were very similar at 0.243 µm ± 0.020 and 0.240 µm ± 0.024, respectively. The mean volume fraction for the Type 316L experiments resulted in 0.008 ± 0.0038 volume fraction, slightly higher than the 0.006 ± 0.001 for the Type 316LSi samples, however, this did not result in a significant difference according to a t-test ($p=0.105$, $n=12$). This data allowed a prediction of the contribution to strength due to ODS to be calculated for Type 316L and Type 316LSi in §5.8.2. Further details of oxide size and distribution can be found in Appendix A.

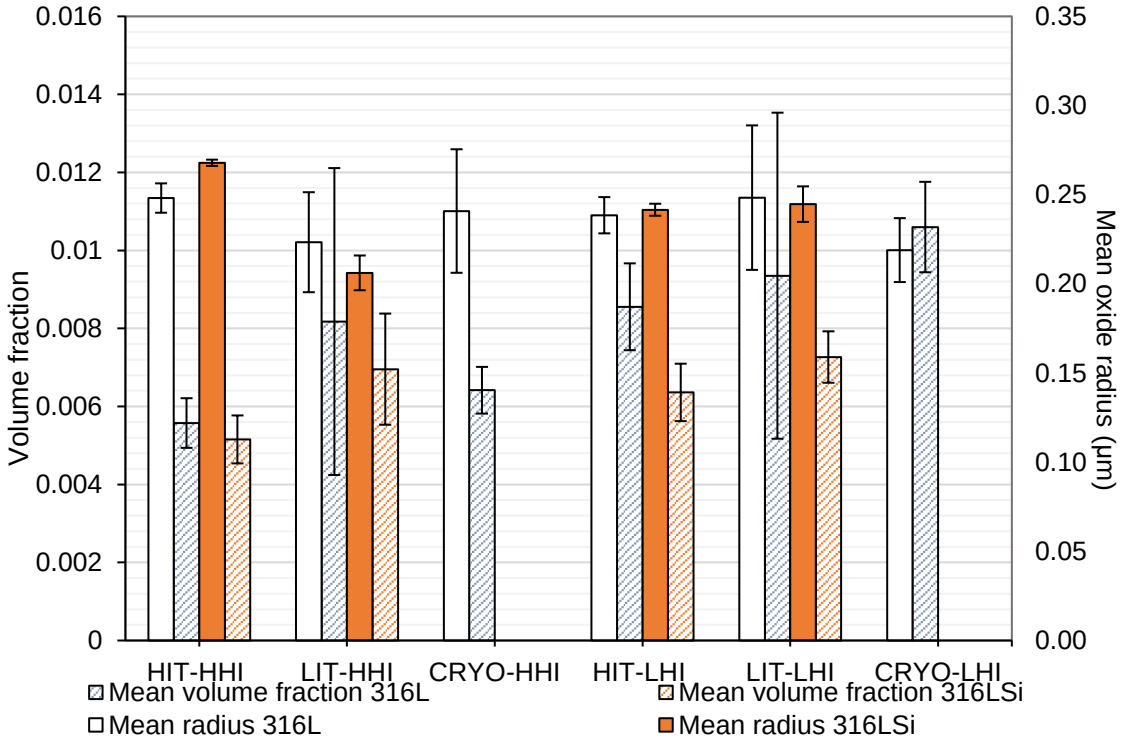

Figure 5.33 Mean oxide volume fraction and radius for the 0.75 kg/hr Type 316L and Type 316LSi experiments.

The inert gas fusion method results for the oxygen wt.% are outlined in Table 5.7 and showed for the WAAM samples tested that there is an increase in oxygen wt.% by a factor of 5 to 6 compared to the wire sample.

Table 5.7 Summary of the O, N and H chemical composition measurements for the welding wire used in this research. Standard deviation values are based upon three samples per wire.

	O (wt.%)	
Sample	**Average**	**Std. dev.**
316L wire	0.00663	2.0×10^{-4}
HIT-HHI	0.037	-
CRYO-HHI	0.034	-

5.5.3 Feritscope™ measurements

The average ferrite content signal (Fe%) for the 0.75 kg/hr samples are shown in Fig 5.34. The data labels represent a 2σ standard deviation. The volume of ferrite Fe (%) is higher for the fractured tensile specimens compared to the metallurgical evaluation specimens, with a smaller difference observed for the CRYO experiments.

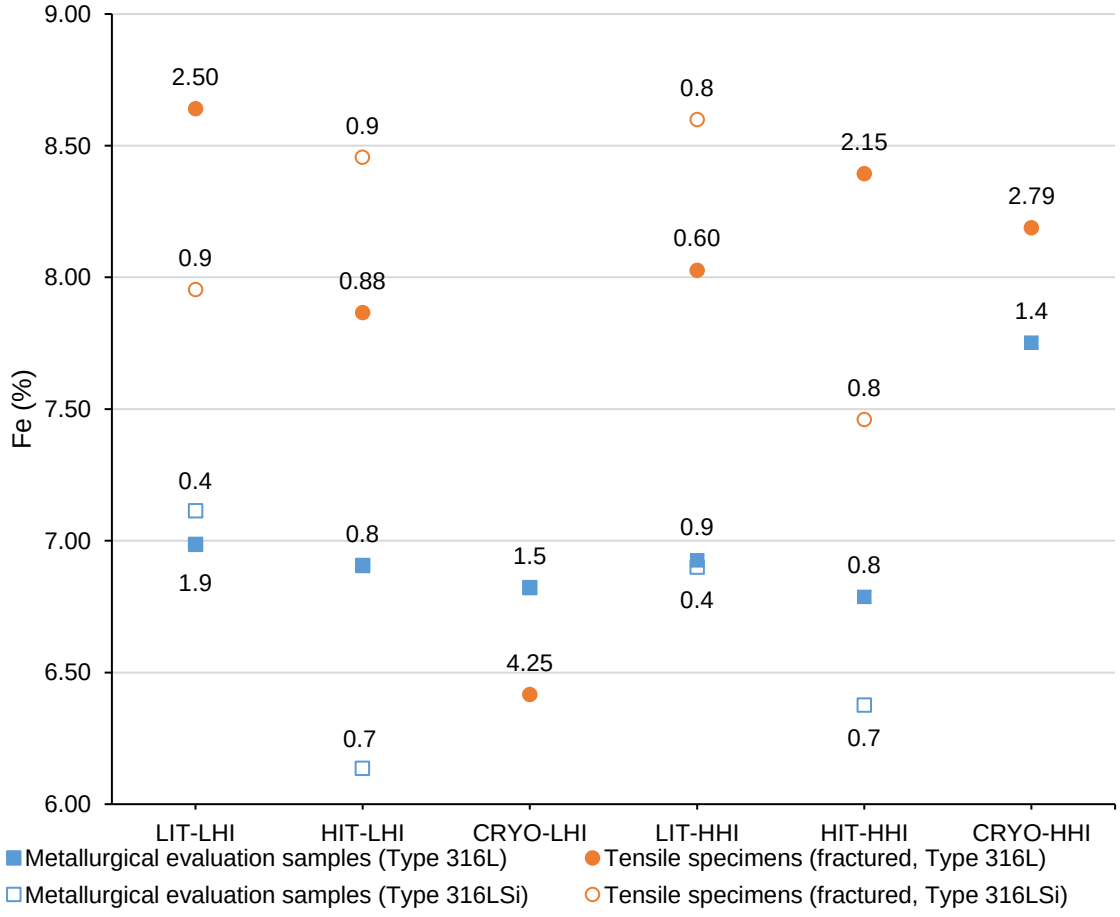

Figure 5.34 Feritscope measurements for the metallurgical evaluation samples and tensile specimens. Data labels show the 2σ standard deviation of the groups.

5.5.4 Relative Density

The average relative density values reported were calculated from an average of the relative density for the six tensile samples before finish machining based on three repeat

measurements with an average measurement standard deviation of 0.023% relative density.

The 0.75 kg/hr deposition rate experiments resulted in high levels of sample density for all Type 316L test conditions, as shown by the average density of the six samples extracted from each wall presented in Table 5.8. Performing ANOVA to investigate the factors of heat input, cooling strategy and sample orientation showed that the heat input had a significant effect on relative density (p=0.001). The difference between deposition rate group means was < 0.05 % as illustrated in Fig 5.35.

Table 5.8 Mean relative density and standard deviation of 0.75 kg/hr experiments

Cooling strategy	Heat input	Average relative density of the experimental wall	The standard deviation of the average relative density of the experimental wall (n=6)
LIT	LHI	99.40%	0.06%
HIT	LHI	99.38%	0.07%
CRYO	LHI	99.41%	0.10%
LIT	HHI	99.41%	0.04%
HIT	HHI	99.42%	0.06%
CRYO	HHI	99.51%	0.05%

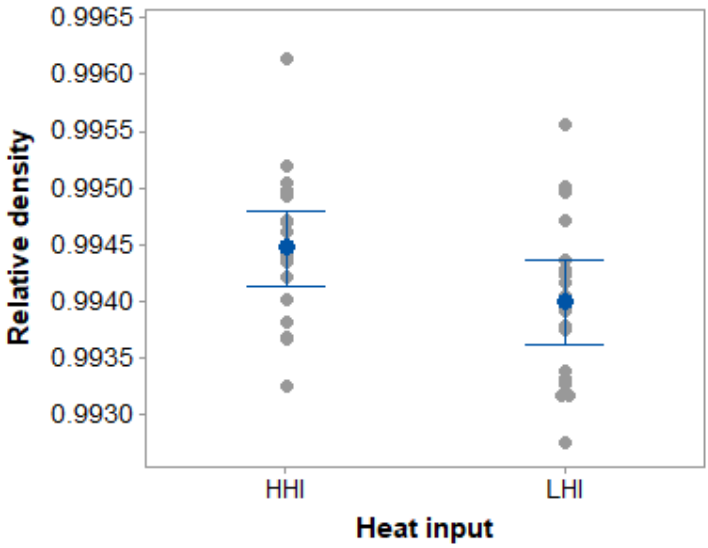

Figure 5.35 Interval plot of the effect of heat input on mean relative density.

5.5.5 Chemical Analysis

OES was used to quantify the percentage weight change in the alloying elements, with the results of this analysis shown relative to the wire analysis in Table 5.9. There was a small increase in nitrogen content in the WAAM samples compared to the wire, with more adsorption of nitrogen apparent for the LHI experiments. The carbon content of the WAAM samples was found to increase relative to the wire sample, however, remains below the maximum specification provided by BS EN ISO 14343 (2017).

Table 5.9 Summary of OES chemical analysis for the deposition samples with the wire and wire manufacturing standard ISO 14343 shown for reference.

	Chemical composition (wt.%)[iii]								
	C	**Si**	**Mn**	**P**	**S**	**Cr**	**Ni**	**Mo**	**N**
Type 316L wire	**0.016**	**0.408**	**1.602**	**0.014**	**0.007**	**18.437**	**12.249**	**2.553**	**0.034**
HIT-HHI	0.026	0.39	1.51	0.016	0.008	18.3	12.1	2.64	0.049
% Change	69%	-4%	-6%	14%	14%	-1%	-1%	3%	44%
CRYO-HHI	0.027	0.41	1.55	0.015	0.007	18.3	12.1	2.63	0.044
% Change	69%	0%	-3%	7%	0%	-1%	-1%	3%	29%
HIT-LHI	0.029	0.58	1.76	0.020	0.014	18.1	11.2	2.67	0.066
% Change	81%	42%	10%	43%	100%	-2%	-9%	5%	94%
CRYO-LHI	0.021	0.39	1.58	0.014	0.007	18.5	12.1	2.68	0.090
% Change	31%	-4%	-1%	0%	0%	0%	-1%	5%	165%

5.5.6 Substrate Distortion

The plane of maximum substrate distortion in XZ and YZ captured using the Hexagon Romer 3D scanner, is presented in Fig 5.36 for the Type 316L samples and Fig 5.37 for the Type 316LSi samples.

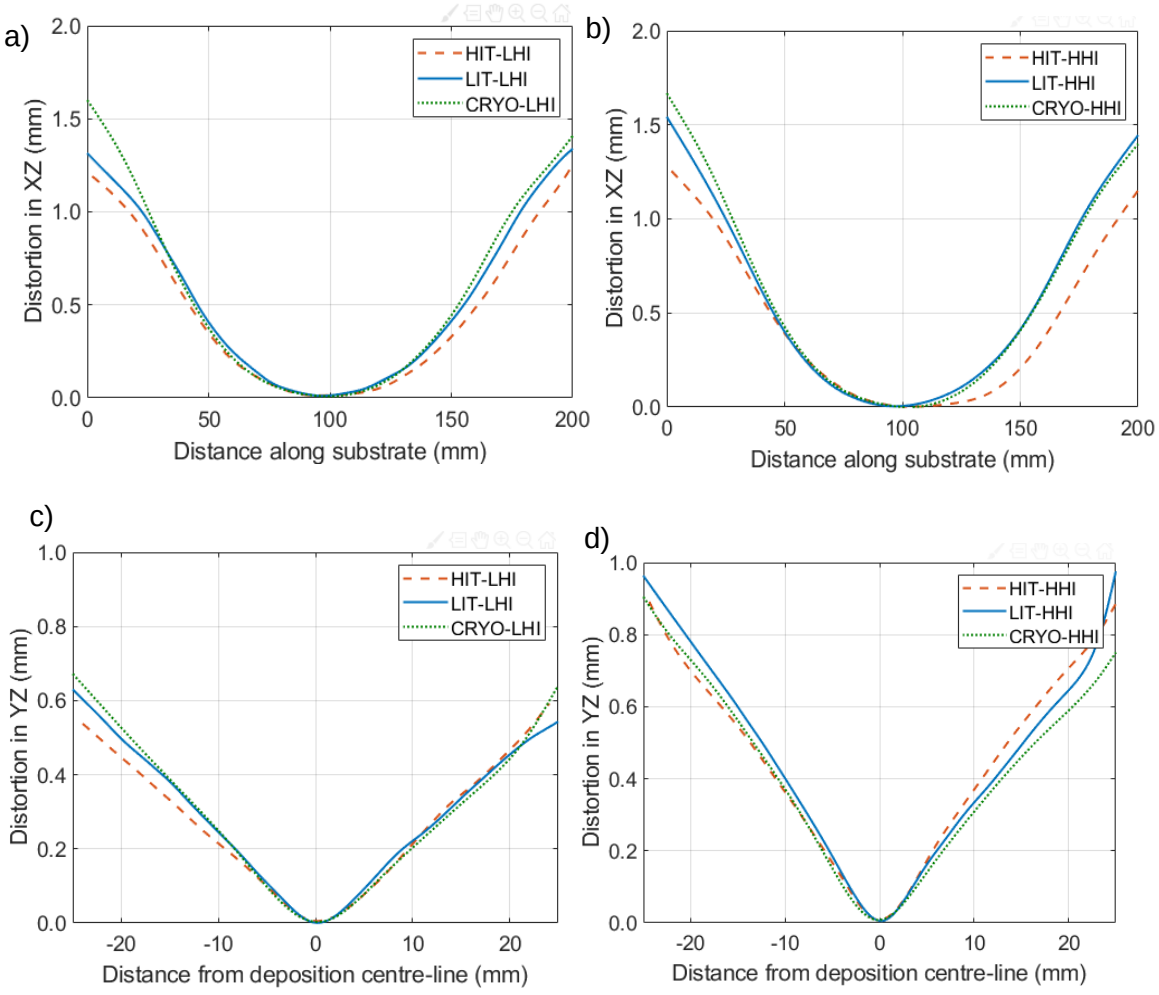

Figure 5.36 Maximum distortion planes for a) LHI XZ b) HHI XZ c) LHI YZ d) HHI YZ for the Type 316L, 0.75 kg/hr deposition rate experiments.

[iii] Tolerances as follows C,S,P < 0.050% (± 0.005%), other elements < 0.050% (±0.015%) Other elements > 0.050% ± 0.040 x √ Conc.

It can be seen in Fig 5.36 and Fig 5.37 that the HIT experiment conditions generally result in a reduction of distortion compared to the LIT and CRYO experiments. CRYO shows a similar level of distortion to the LIT experiments, however, the LHI experiments show a slightly higher level of distortion. Overall, the HHI experiments resulted in higher levels of distortion, which is particularly evident considering the distortion in the YZ plane in Fig 5.37c relative to Fig 5.37d. Higher overall levels of distortion are found for the Type 316LSi experiments which can be attributed to possible variation in deposition start location and/or contact tip distance. These results indicate that the LHI and HIT experimental conditions result in lower levels of residual stress, whilst CRYO could be expected to induce similar or slightly higher levels of residual stress. This correlates well with the results of GND's present (§5.8.1), which provide another indication of residual stress.

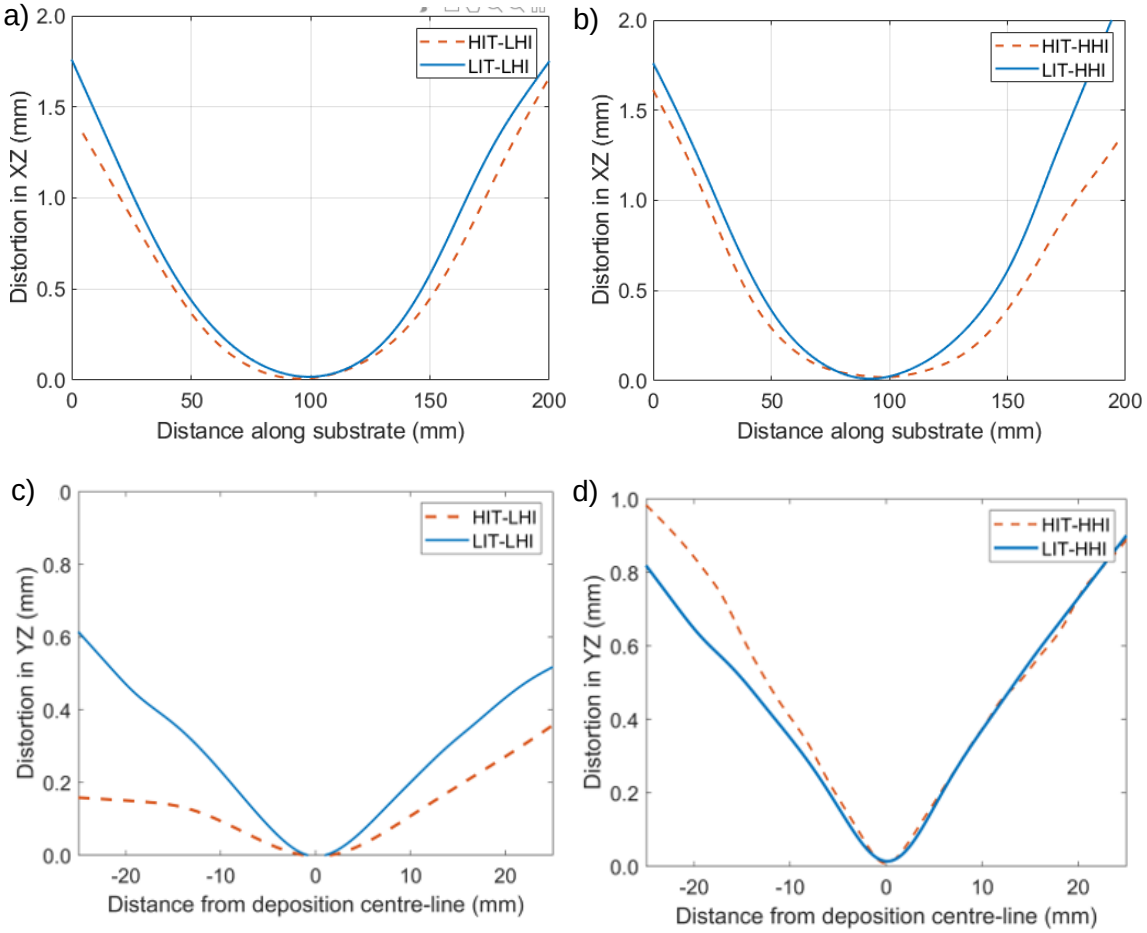

Figure 5.37 Maximum distortion planes for a) LHI XZ b) HHI XZ c) LHI YZ d) HHI YZ for the Type 316LSi, 0.75 kg/hr deposition rate experiments.

5.6 Material Characterisation of the 3.00 kg/hr Deposition Rate experiments

This section includes the material characterisation of the 3.00 kg/hr Type 316L experiments with an investigation of microstructure at the layer interface, process cooling rate, oxide size and distribution, and δ-ferrite content. The results of the physical properties covering the relative sample density and substrate distortion are also presented.

5.6.1 Microstructural Characterisation

The macrostructure of the 3.00 kg/hr Type 316L samples is presented in Fig. 5.38. The LHI samples show high aspect-ratio grains that cover multiple re-melt lines that are aligned toward the build direction are observed. The width of the grains appears to decrease for the LHI samples progressively from HIT→ LIT→ CRYO. The HIT-HHI and CRYO-HHI samples display a coarser dendritic microstructure. The grain structure is less distinct in the HHI samples, although those that can be seen appear smaller and of lower directionality than the LHI samples.

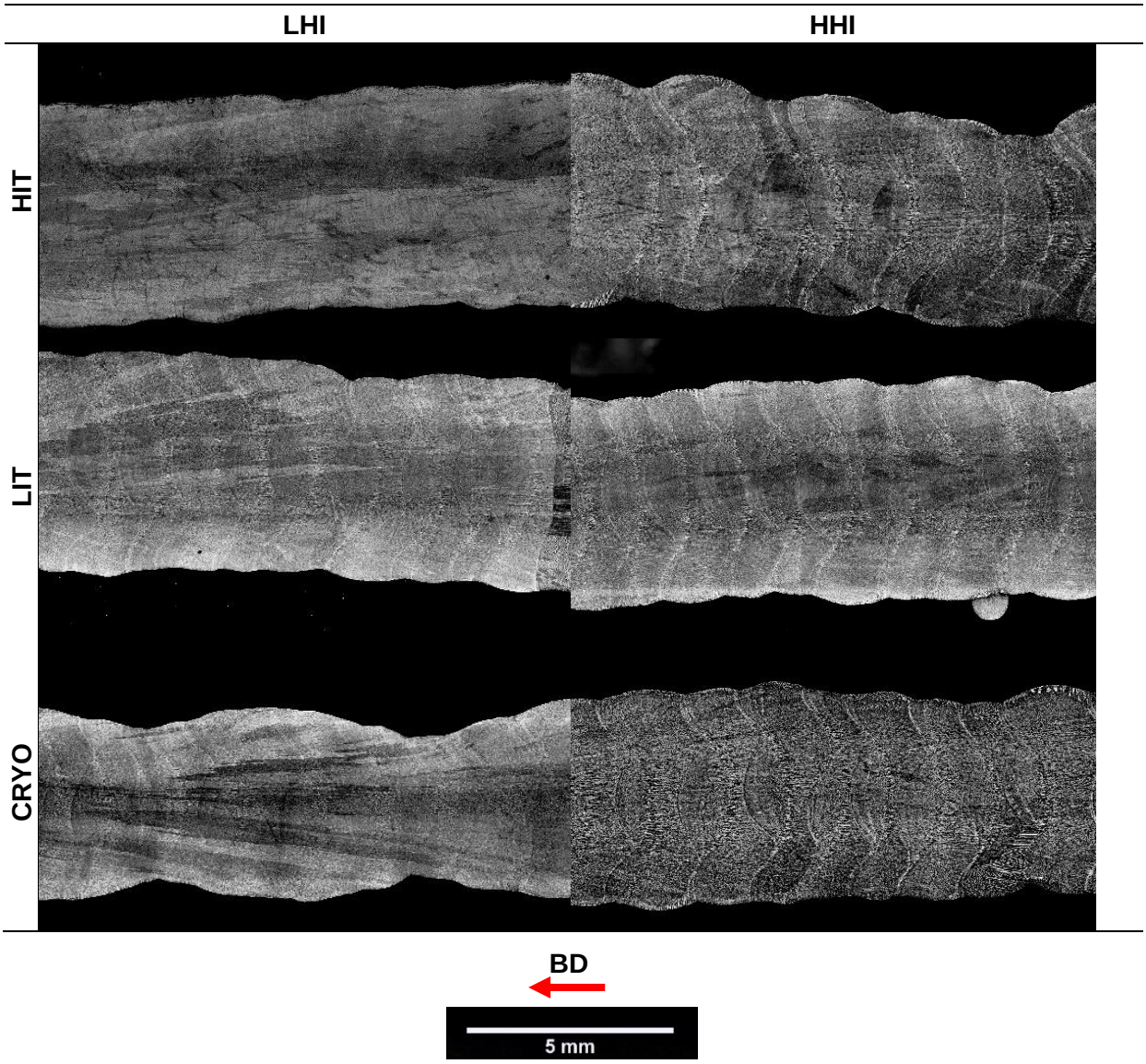

Figure 5.38 Macro-scale optical micrographs of the top sections of the 3.00 kg/hr samples.

Higher magnification micrographs of the re-melt lines of the lower and upper sections of the LHI and HHI experimental samples are shown in Fig. 5.39 and Fig. 5.40, and Fig. 5.41 and Fig. 5.42, respectively. Using the Marble's reagent etchant, the δ-ferrite are darkened, and γ-austenite are lightened upon imaging.

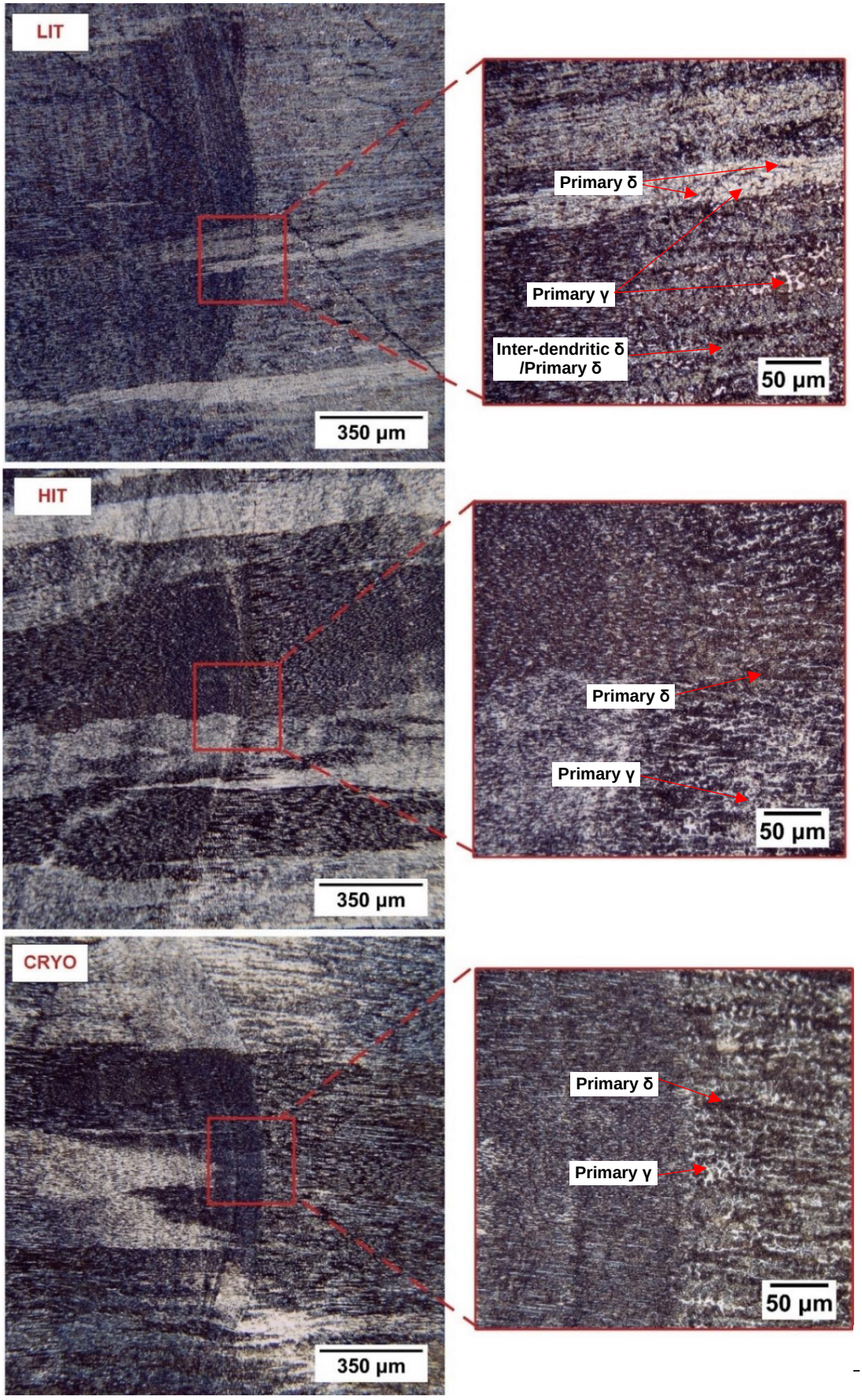

Figure 5.39 Micrographs of 3.00 kg/hr, LHI (lower section).

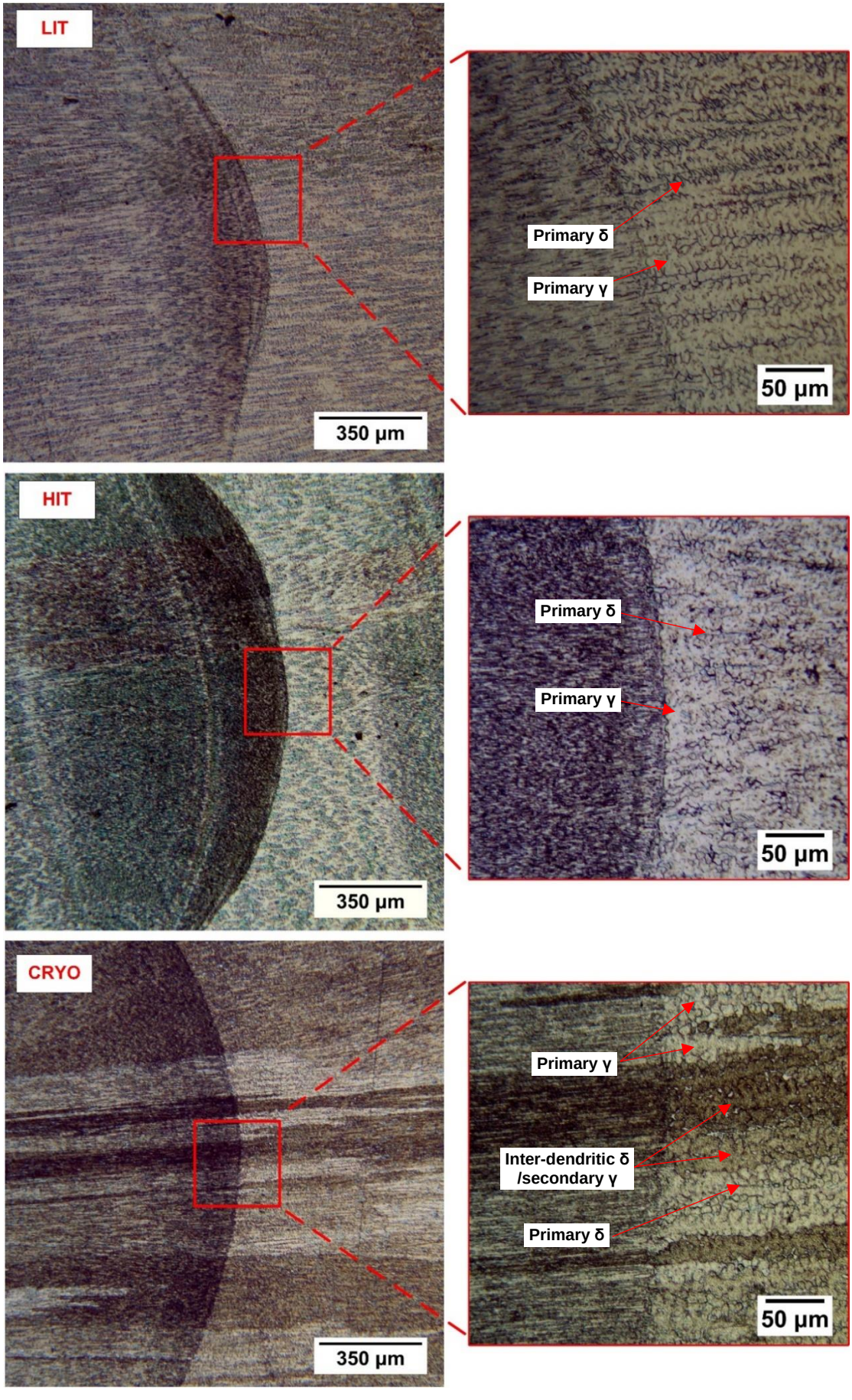

Figure 5.40 Micrographs of 3.00 kg/hr, LHI (upper section).

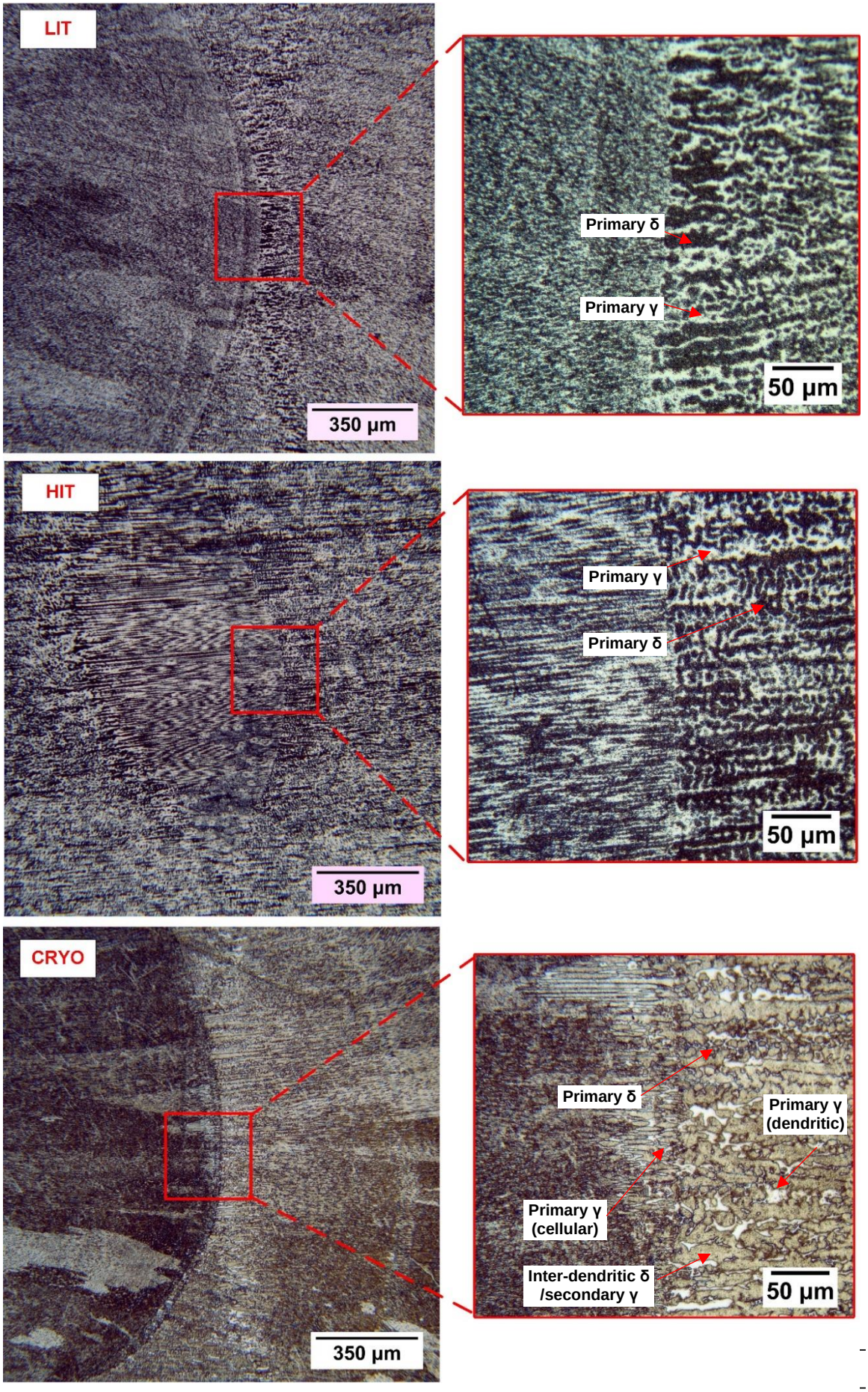

Figure 5.41 Micrograph of 3 kg/hr, HHI (lower section).

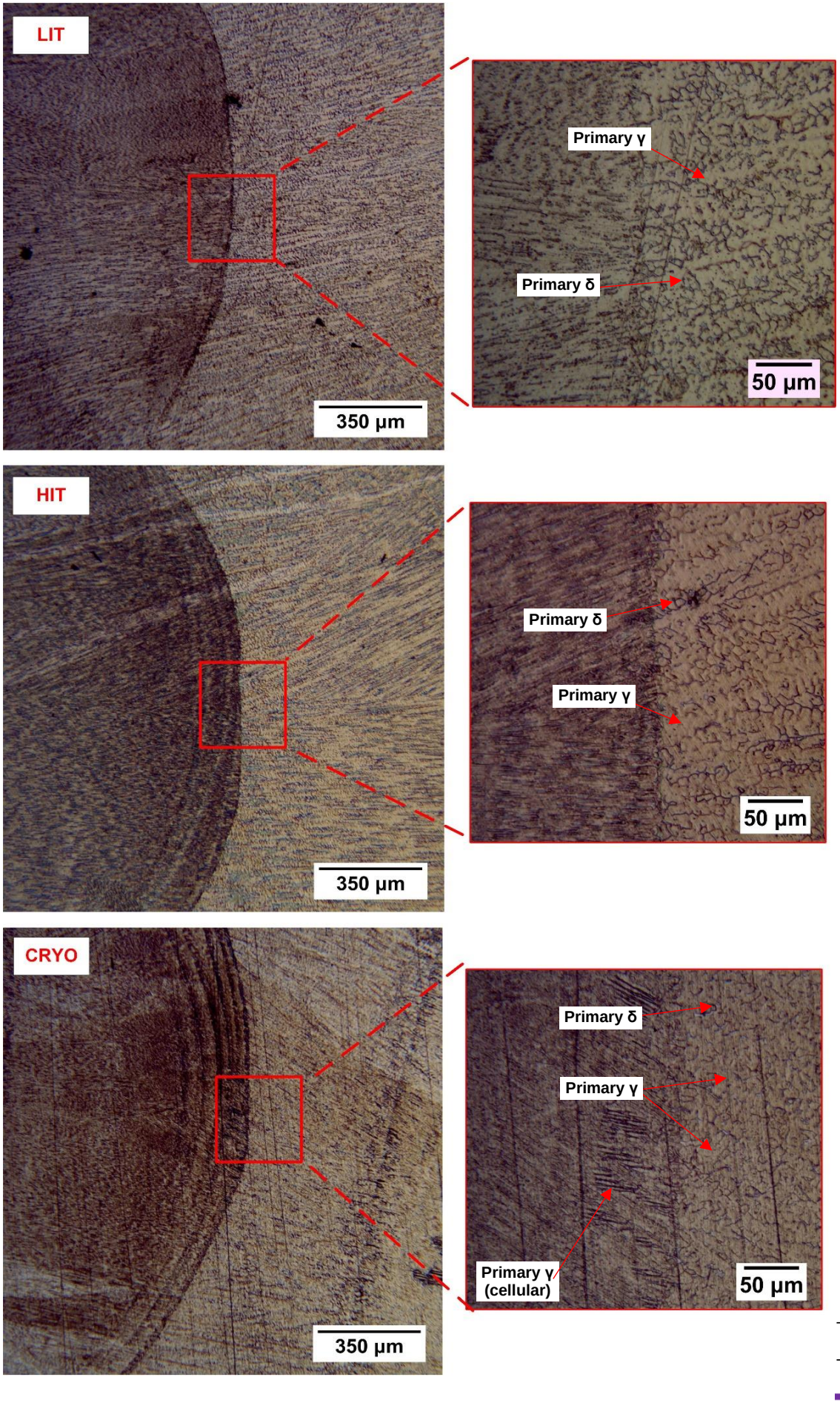

Figure 5.42 Micrograph of 3.00 kg/hr, HHI (upper section).

The lower section LHI microstructures presented in Fig 5.39 show that large amounts of fine dark-etching retained dendritic δ-ferrite, with similar vermicular FA dendritic microstructures occurring independently of the cooling condition. Considering the microstructures of the LHI upper section in Fig 5.40, it can be seen for CRYO-LHI and LIT-LHI that there is a transition from thick vermicular dendrites in the lower sections, to directional skeletal and lathy δ-ferrite dendrites in the upper section. However, the HIT-LHI sample showed finer, more equiaxed dendrites in the upper section. The lower section HHI microstructures presented in Fig 5.41 also shows a thick vermicular δ-ferrite network as in the LHI experiments in Fig 5.39, which also decreases in thickness in the upper section. In contrast to LHI, the dendrites remained strongly directional for both interpass temperatures micro-graph locations. The CRYO-HHI samples show more varied solidification structures including cellular γ-austenite at the lower and upper sections, with greater volumes of inter-dendritic δ-ferrite/ secondary-γ. A summary of the morphology and details of the δ-ferrite observed in the 3.00 kg/hr samples is shown in Table 5.10.

Table 5.10 Qualitative description of the morphology at the layer interface for 3.00 kg/hr Type 316L.

	HHI 3.00kg/hr (lower section)			**HHI 3.00kg/hr (upper section)**		
	LIT	**HIT**	**CRYO**	**LIT**	**HIT**	**CRYO**
Morphology type	Vermicular/ Lathy δ	Vermicular/ Lathy δ	Vermicular/ Lathy δ Cellular-dendritic γ	Vermicular/ Lathy δ	Vermicular/ Lathy δ	Vermicular/ Lathy δ Cellular γ
δ thickness	Thick	Thick	Thin	Thin	Thin	Thin
δ directionality	Med	High	High	High	High	Low
δ scale	Med	Med	High	Med	Med	Low
	LHI 3.00kg/hr (lower section)			**LHI 3.00kg/hr (upper section)**		
	LIT	**HIT**	**CRYO**	**LIT**	**HIT**	**CRYO**
Morphology type	Vermicular/ Lathy	Vermicular/ Lathy	Vermicular/ Lathy	Vermicular/ Lathy	Vermicular/ Lathy	Vermicular/ Lathy
δ thickness	Thick	Thick	Thick	Thin	Thin	Mixed
δ directionality	Med	Med	Med	High	Low	Med
δ scale	Low	Low	Low	Med	Low	High

5.6.1.1 Process Cooling Rates based on the Scale of Microstructural Features

Examination of the exterior edges of the top sections of the thin wall samples showed that the morphology transitioned from a coarser cellular/dendritic at the sample edge to a finer dendritic microstructure toward the centreline. The morphology of the solidification structures for the 3.00 kg/hr experiments at the edge is shown in Fig. 5.43. Cellular-dendritic structures can be observed at the surface edge of the WAAM deposits, which for CRYO-LHI Fig 5.43b extended further inward toward the centreline.

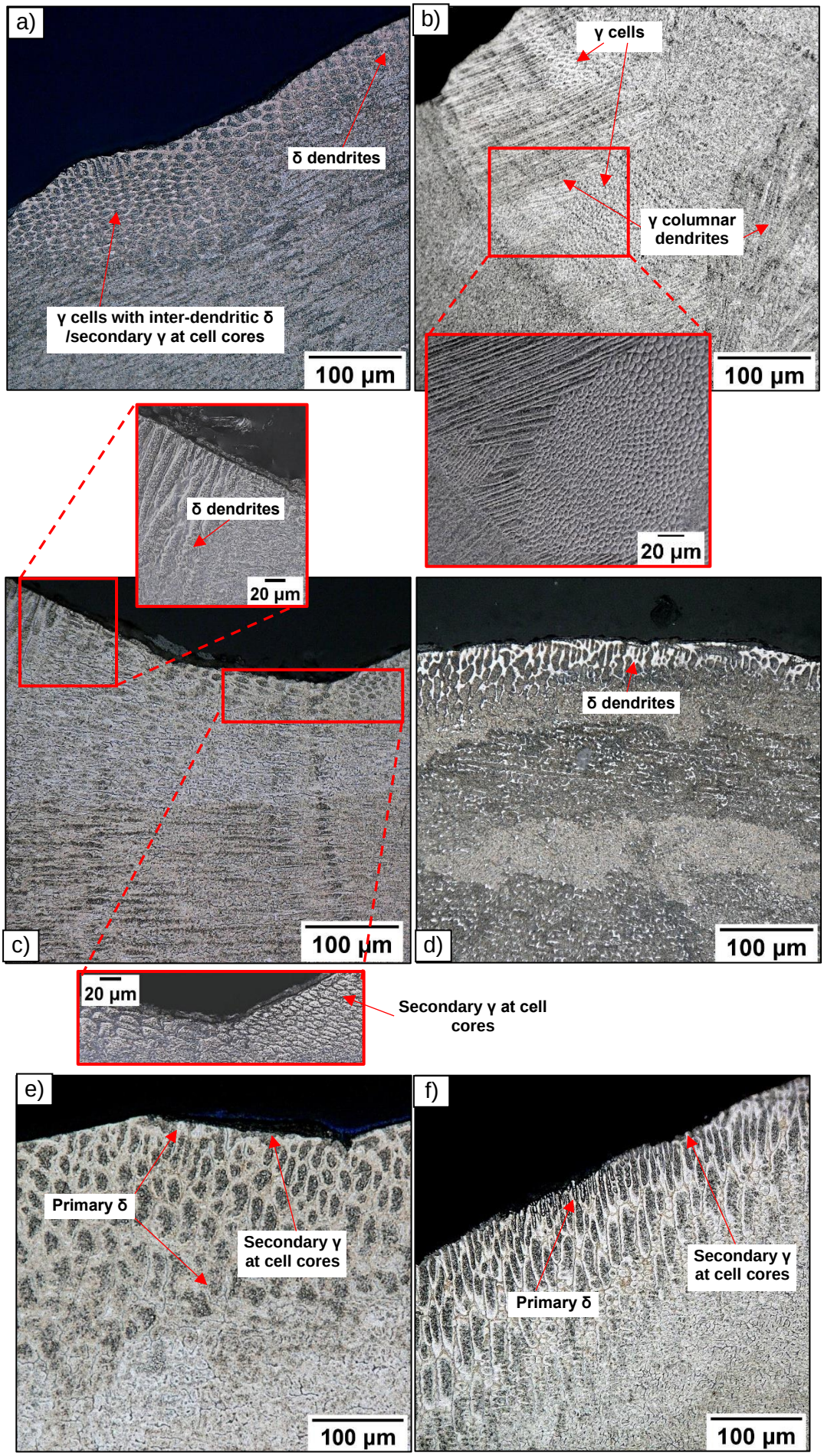

Figure 5.43 Solidification structures for a) CRYO-HHI b) CRYO-LHI c) HIT-HHI and d) HIT-LHI. Cellular and dendritic AF solidification structures for e) LIT-HHI and f) LIT-LHI samples.

Higher magnification micrographs of the cellular structures of the CRYO-HHI and CRYO-LHI are shown in Fig. 5.44. These structures indicate a primary austenitic solidification mode.

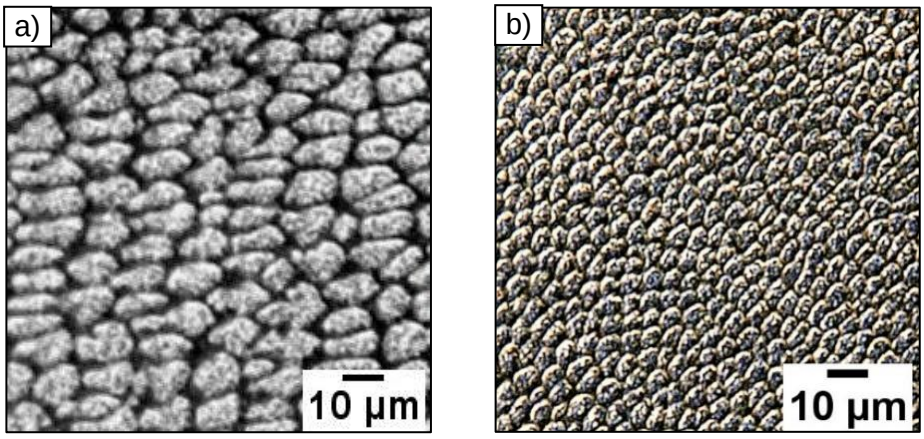

Figure 5.44 Cellular sub-grains present in a) CRYO-HHI b) CRYO-LHI samples.

The variation in microstructural feature scale and the cooling rates of the coarsest and finest microstructure at the deposit centreline were determined using equation 6-3 as shown in Fig. 5.45 and Fig. 5.46, respectively. This captures the quantitatively the minimum and maximum dendrite size that occurs along the build direction, that was observed qualitatively by the periodicity evident within §5.6.1. The microstructures of the HHI samples reflected the lower cooling rates experienced compared to the LHI experiments.

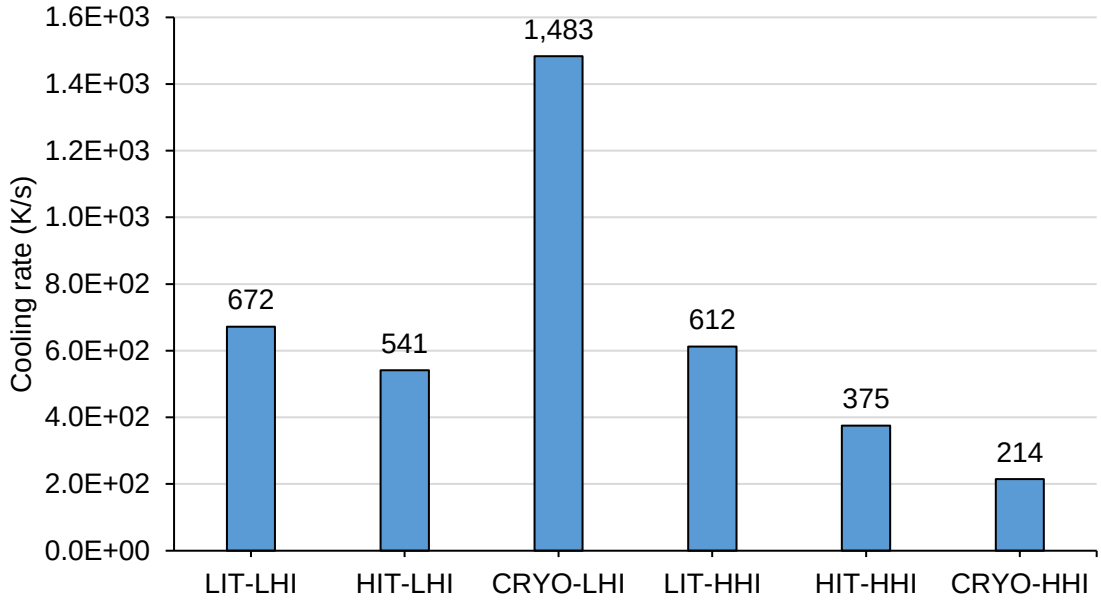

Figure 5.45 Cooling rates calculated for the coarsest dendritic regions along the deposit centreline.

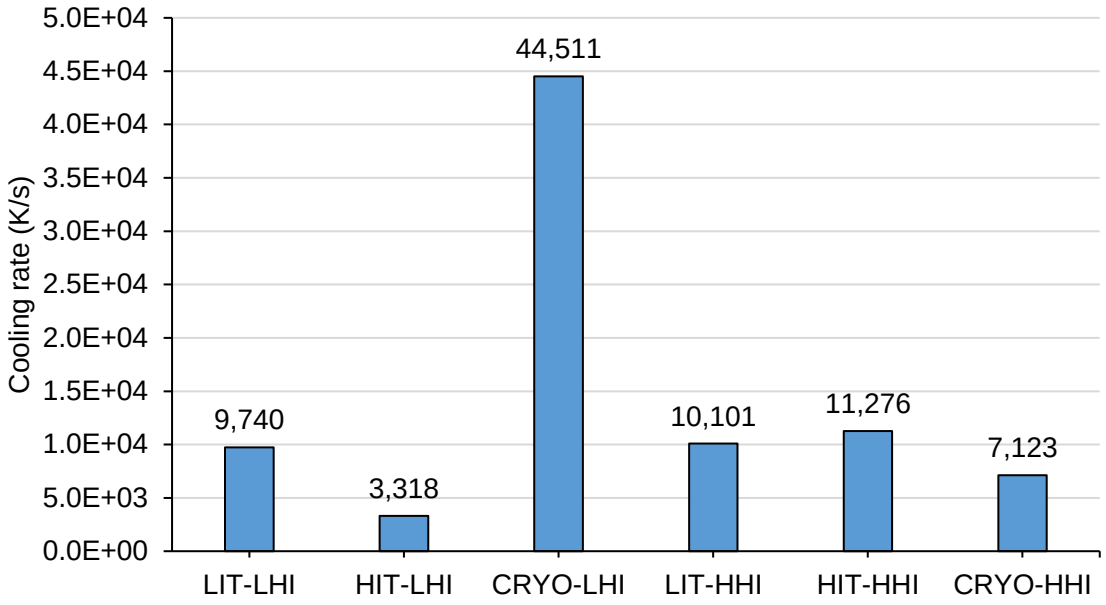

Figure 5.46 Cooling rates calculated for the finest dendritic regions along the deposit centreline.

5.6.2 Oxide inclusion size and distribution

The oxide radius average and volume fraction for all 3.00 kg/hr samples were 0.230 ±0.014 µm and 0.011±0.0023 µm, respectively. The mean oxide inclusion volume fraction and radius for the 3.00 kg/hr samples for each experiment are presented in Fig. 5.47. The error bars show the 2σ standard deviation of the mean oxide radius and volume fraction. Further details of oxide size and distribution can be found in Appendix A.

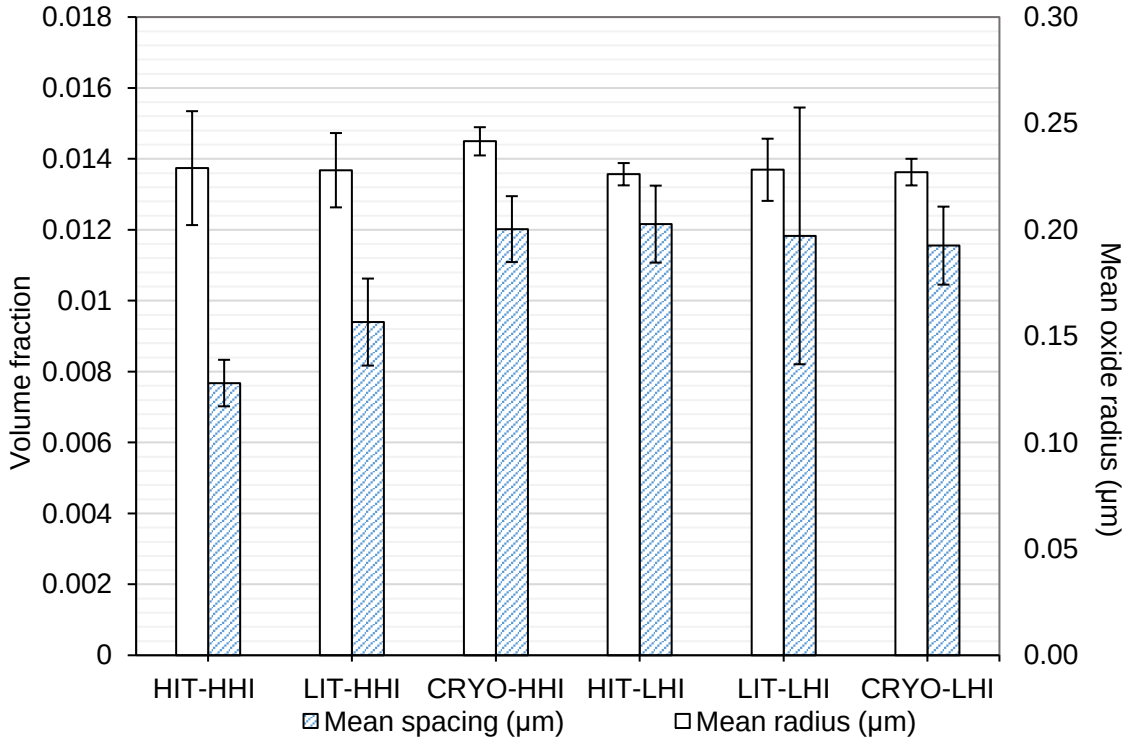

Figure 5.47 Oxide inclusion mean spacing and radius for the 3.00 kg/hr experiments.

For the HHI experiments, there is a progressive increase in the volume fraction for HIT, LIT and CRYO, which subsequently results in a progressive increase in ODS as outlined in §5.8.2. In contrast, the mean radius for both heat input levels and the mean oxide spacing and radius for the LHI experiments is unaffected by cooling strategy.

5.6.3 Feritscope™ measurements

The average ferrite content of the metallurgical samples and fractured tensile specimens are shown in Fig 5.48 based on Feritscope testing with the standard deviation of the results for each group mean presented. The results are based on the average of three readings along the gauge length of the tensile specimens and a minimum of five readings evenly spaced along the metallurgical sample length. The Feritscope signal was measured in the units of ferrite percentage Fe (%).

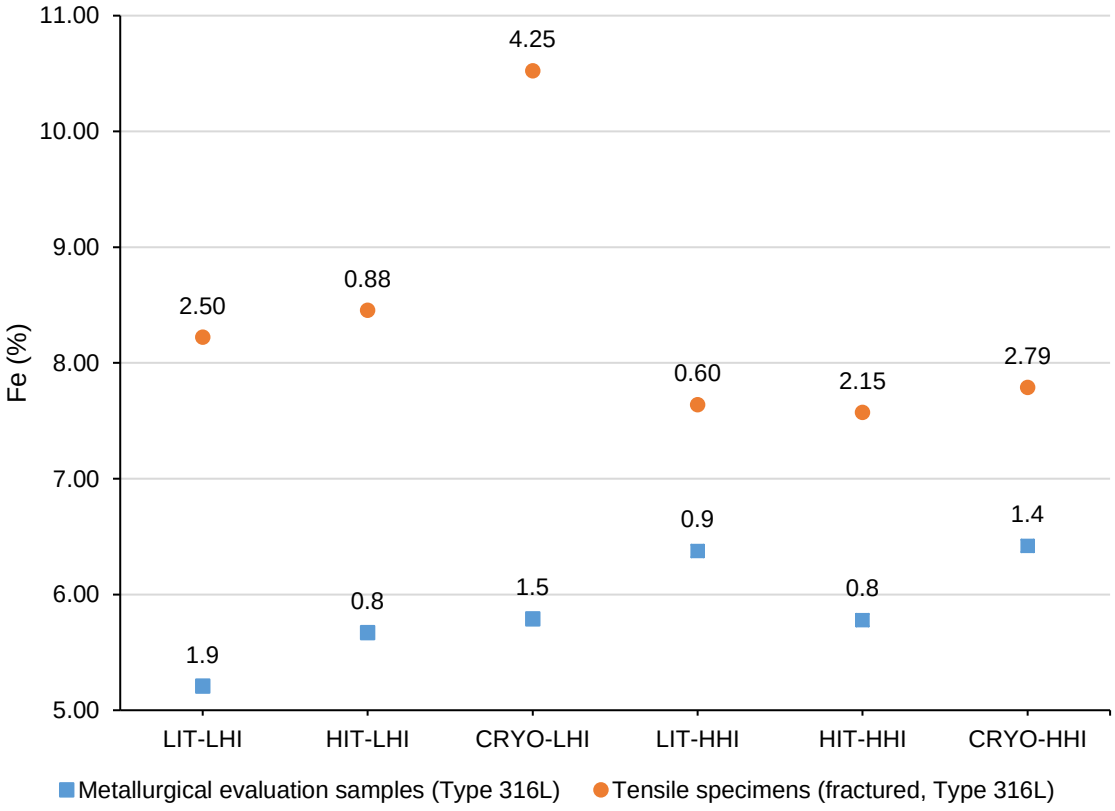

Figure 5.48 Comparison of ferrite content measured in Fe(%) for the 3.00 kg/hr sample. (Data labels show the standard deviation).

The 2σ standard deviation is relatively high for the LIT-LHI, CRYO-LHI and CRYO-HHI tensile specimens. Review of individual Fe (%) values shows for these samples only, the bottom horizontal samples have significantly lower Fe (%) than specimens extracted from other locations as illustrated in Fig 5.49. This contrasts with the general trend within the data set, where the Fe (%) increases with tensile loading.

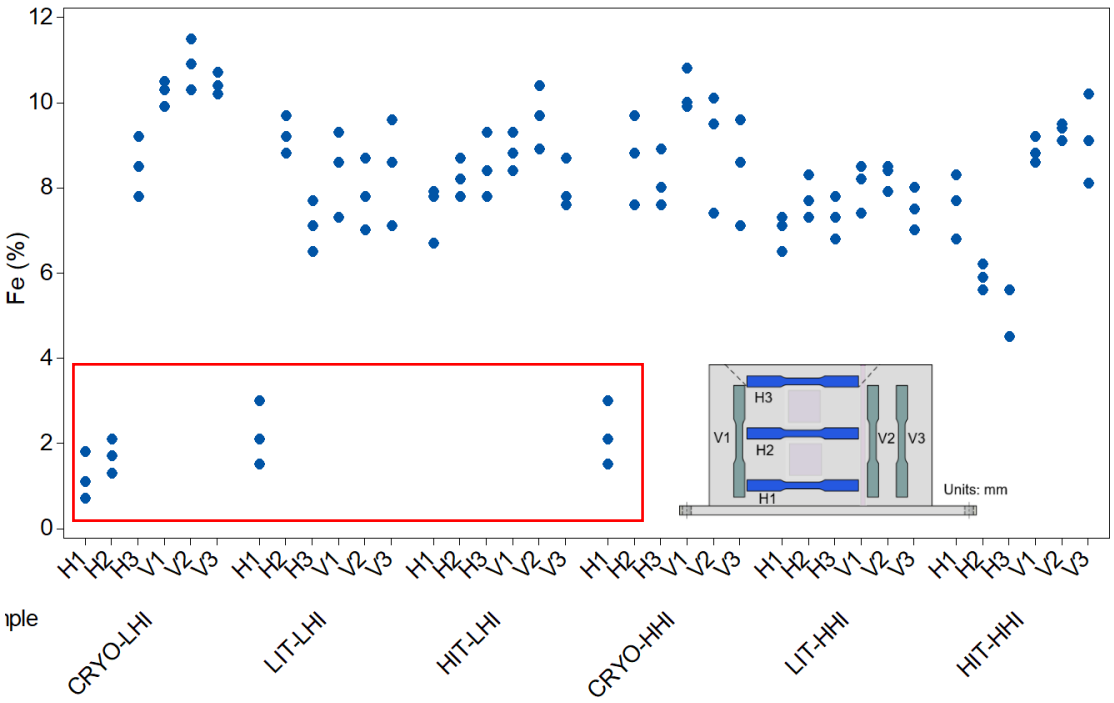

Figure 5.49 Individual value plots of the repeat Feritscope measurements on the tensile specimens with the comparatively low regions in H1 samples highlighted.

5.6.4 Relative Density

The 3.00 kg/hr deposition rate experiments resulted in high levels of relative density for all test conditions, as presented in Table 5.11. ANOVA showed that the cooling strategy had no statistically significant effect on relative density (p=0.158). However, the heat input (p=0.002) and orientation (p=0.002) were shown to significantly affect the relative density as shown in Fig 5.50. The average relative density values reported were calculated from an average of the relative density for the six tensile samples before finish machining based on three repeat measurements with an average standard deviation of 0.019% relative density.

Table 5.11 Average relative sample density of 3.00 kg/hr experiments

Cooling strategy	Heat input	Average relative density of the experimental wall	The standard deviation of the average relative density of the experimental wall (n=6)
LIT	LHI	99.43%	0.04%
HIT	LHI	99.54%	0.06%
CRYO	LHI	99.53%	0.08%
LIT	HHI	99.44%	0.12%
HIT	HHI	99.41%	0.06%
CRYO	HHI	99.43%	0.06%

In addition, a significant interaction effect was found for heat input and cooling strategy (p=0.023) as shown in Fig 5.51. HIT-LHI and CRYO-LHI showed a small improvement in relative density compared to the LIT condition, whereas for the HHI experiments no significant change was observed. This is confirmed by the results of Tukey's Pairwise comparison performed for the interaction effect and shown in Table 5.12.

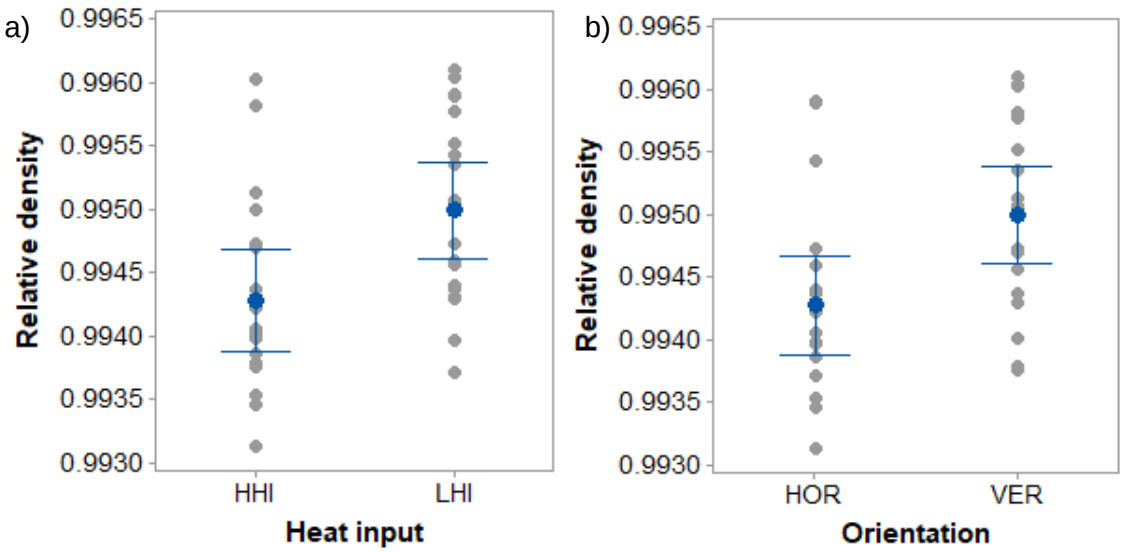

Figure 5.50 Interval plot of significant main effects on relative sample density for 3.00 kg/hr shown for a) heat input and b) specimen build orientation, horizontal and vertical.

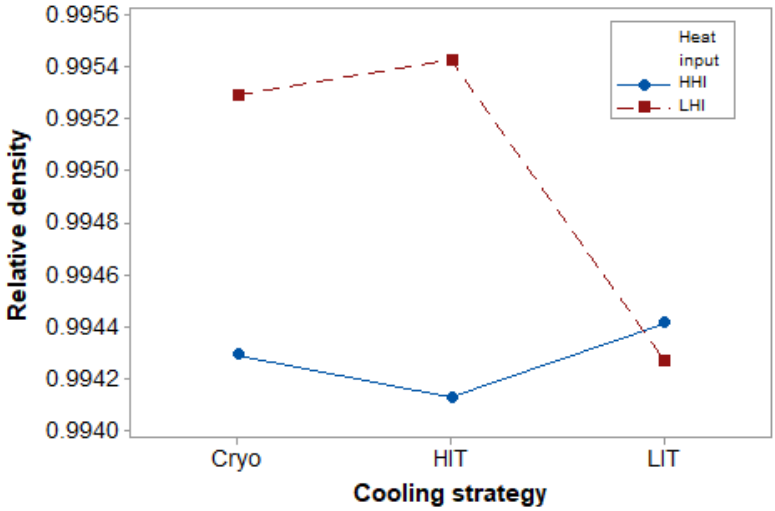

Figure 5.51 Interaction effect plot showing the effect of heat input and cooling strategy on relative density.

Table 5.12 Results of Tukey's Pairwise comparison testing for the effect of heat input and cooling strategy on relative density. Means that do not share a letter are significantly different.

Heat input*Cooling strategy	N	Mean relative density	Grouping		
LHI HIT	6	0.9954	A		
LHI Cryo	6	0.9952	A	B	
HHI LIT	6	0.9944	A	B	C
HHI Cryo	6	0.9943		B	C
LHI LIT	6	0.9942		B	C
HHI HIT	6	0.9941			C

5.6.5 Chemical Analysis

The result of the chemical analysis for the high deposition rate samples is presented in Table 5.13. The nitrogen content increases from that reported for the Type 316L wire, with greater adsorption occurring for the HHI compared to the LHI experiments, with no indication that the cryogenic cooling influences nitrogen adsorption.

Table 5.13 Summary of OES chemical analysis for the deposition samples with the wire shown for reference.

	Chemical composition (wt.%)[iv]								
	C	**Si**	**Mn**	**P**	**S**	**Cr**	**Ni**	**Mo**	**N**
Type 316L wire	0.016	0.408	1.602	0.014	0.007	18.437	12.249	2.553	0.034
HIT-HHI	0.023	0.37	1.48	0.013	0.007	18.4	12.1	2.68	0.100
Change %	44%	-9%	-8%	-7%	0%	0%	-1%	5%	194%
CRYO-HHI	0.024	0.41	1.56	0.014	0.007	18.3	12.0	2.63	0.065
Change %	50%	0%	-3%	0%	0%	-1%	-2%	3%	91%
HIT-LHI	0.022	0.40	1.57	0.013	0.007	18.4	12.1	2.67	0.048
Change %	38%	-2%	-2%	-7%	0%	0%	-1%	5%	41%
CRYO-LHI	0.021	0.40	1.60	0.014	0.008	18.6	12.1	2.67	0.045
Change %	31%	-2%	0%	0%	14%	1%	-1%	5%	32%

5.6.6 Substrate Distortion

The plane of maximum substrate distortion in XZ and YZ captured using the Hexagon Romer 3D scanner is presented in Fig 5.52.

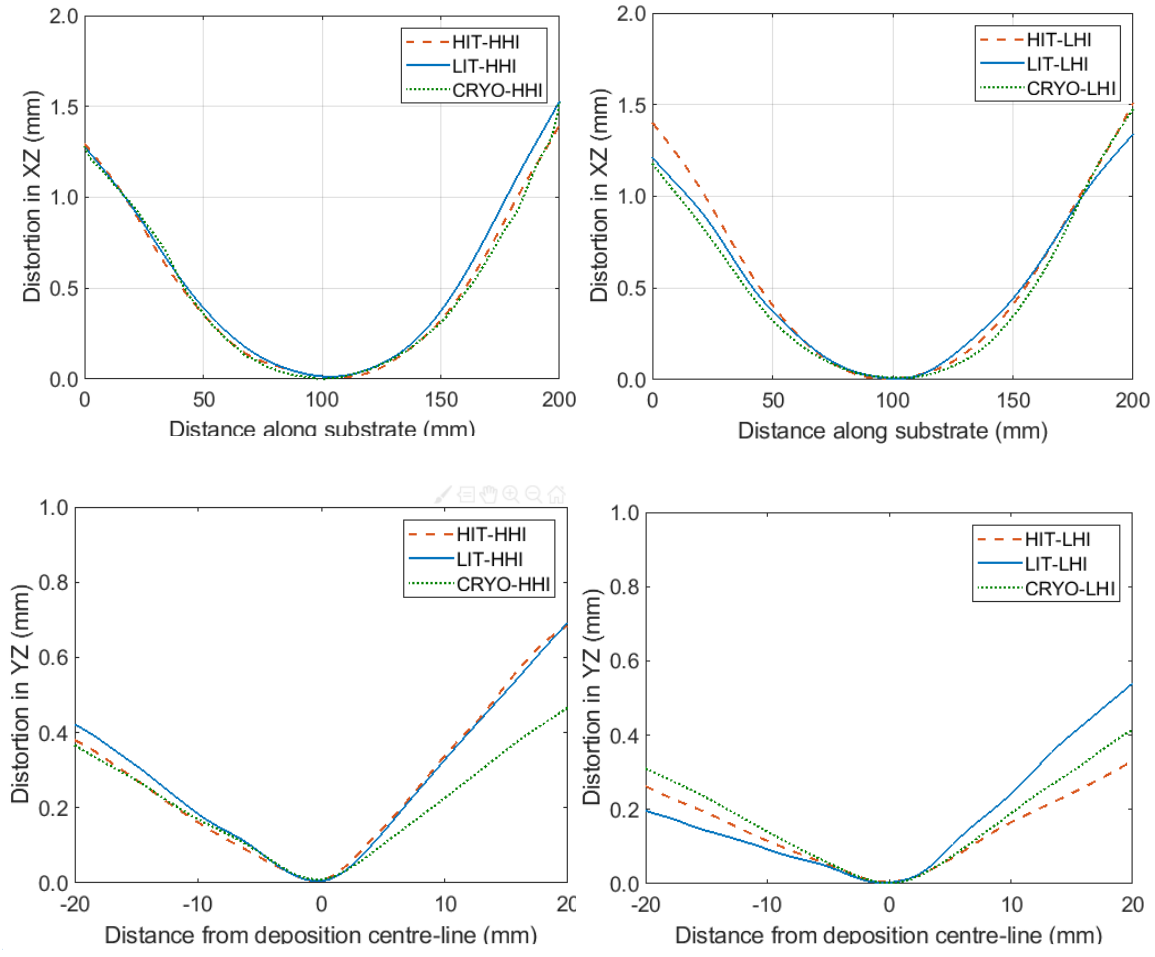

Figure 5.52 Maximum distortion planes for a) LHI XZ b) HHI XZ c) LHI YZ d) HHI YZ for the Type 316L, 3.00 kg/hr deposition rate experiments.

[iv] Tolerances as follows C,S,P < 0.050% (± 0.005%), other elements < 0.050% (±0.015%) Other elements > 0.050% ± 0.040 x √ Conc.

In the XZ plane, the distortion is similar for all experiments and appears unaffected by the cooling strategy and heat input. Asymmetric distortion profiles occurred about the deposition centre-line for the YZ plane. indicates slight variation in YZ substrate positioning errors relative to the welding torch deposition start position and the substrate plate. Despite this uncertainty, the LHI experiments showed overall lower levels of distortion, and the cryogenic cooling did not appear to severely impact the resultant distortion in this plane.

5.7 Mechanical Analysis

The UTS, σ_{ys}, uniform elongation and E for the deposition rates of 0.75 kg/hr and 3.00 kg/hr are shown in Fig. 5.53 – Fig 5.56 respectively, with error bars showing the standard deviation within each experimental group. The minimum requirements according to ASTM A240/A240M (2004) and BS EN 10088-1 (2014) are shown for reference. Detailed results for individual tensile bars are presented in Appendix C.

The mean of the UTS (see Fig. 5.53) and σ_{ys} (see Fig. 5.54) readily exceed the minimum for all experimental groups. In addition, the average E shown in Fig 5.55 fails to achieve specification for all experimental groups and displays a large amount of scatter. However, it can be seen in Fig. 5.56 that the average elongation only exceeds specification for four of the experimental groups.

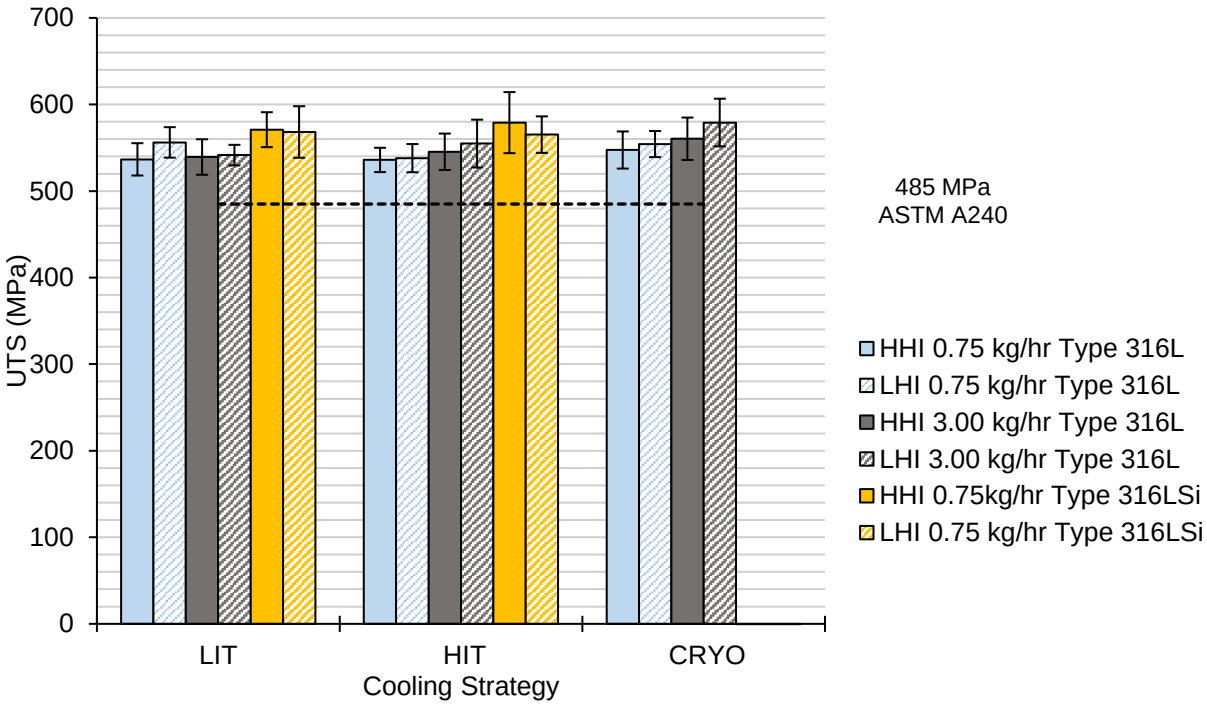

Figure 5.53 Ultimate tensile strength of the high and low heat input and deposition rate levels for low interpass temperature, high interpass temperature and cryogenic cooling strategies.

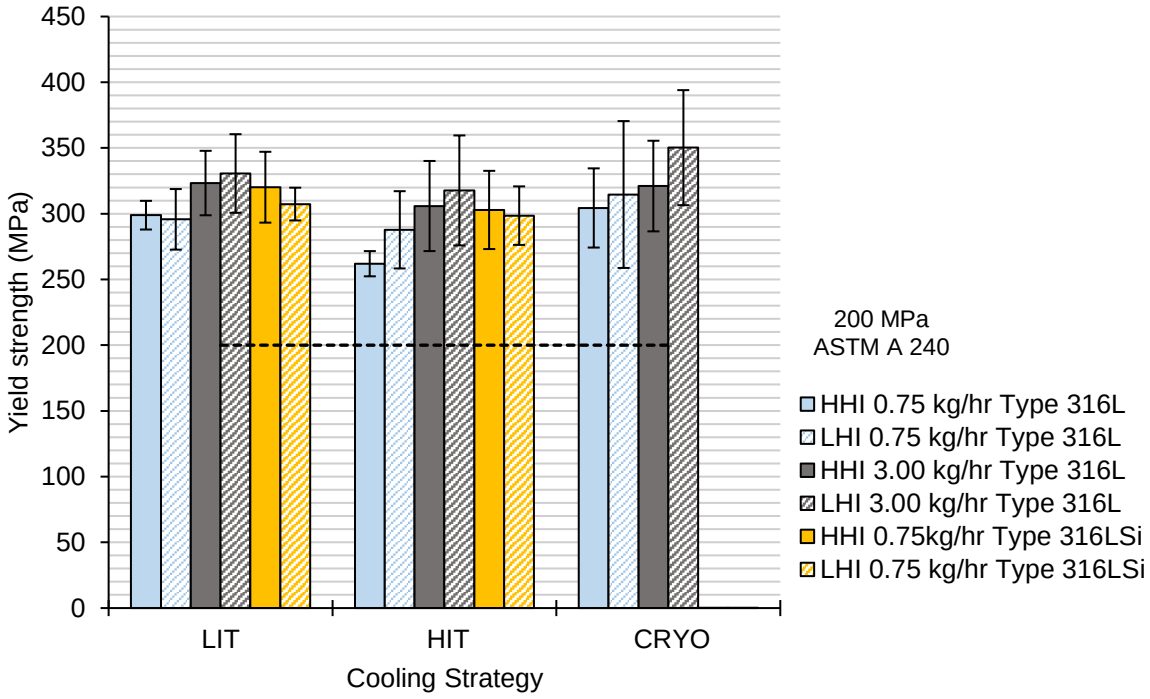

Figure 5.54 Yield strength of the high and low heat input and deposition rate levels for low interpass temperature, high interpass temperature and cryogenic cooling strategies.

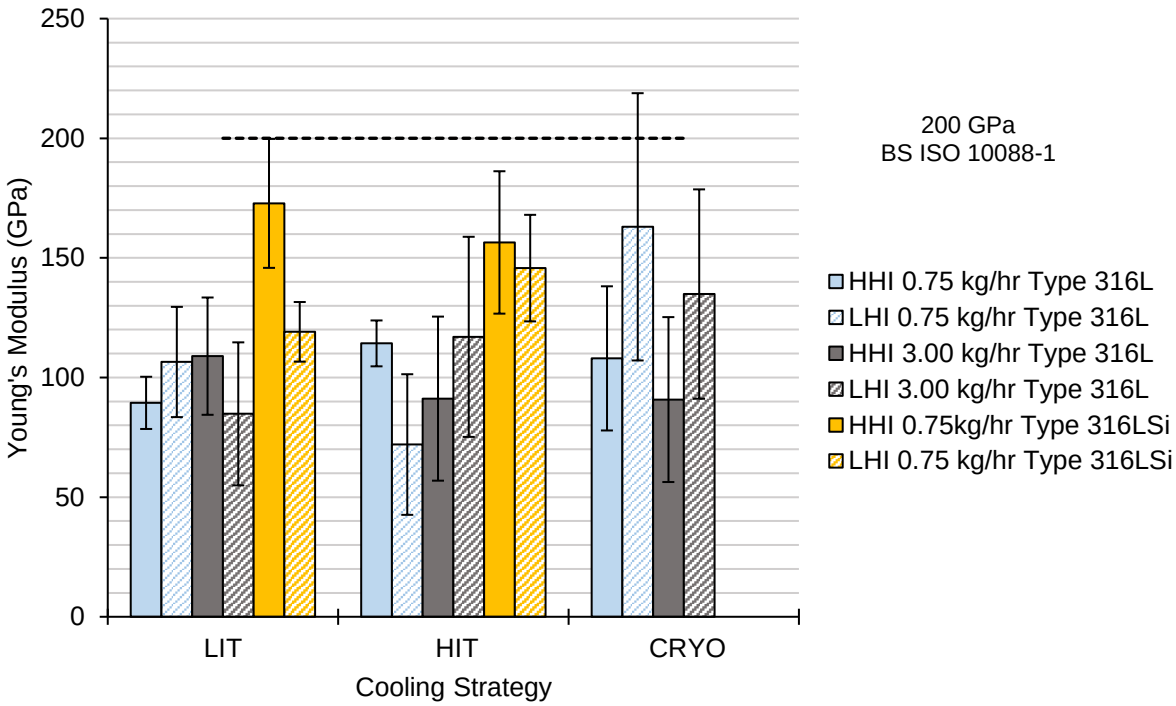

Figure 5.55 Young's modulus of the high and low heat input and deposition rate levels for low interpass temperature, high interpass temperature and cryogenic cooling strategies.

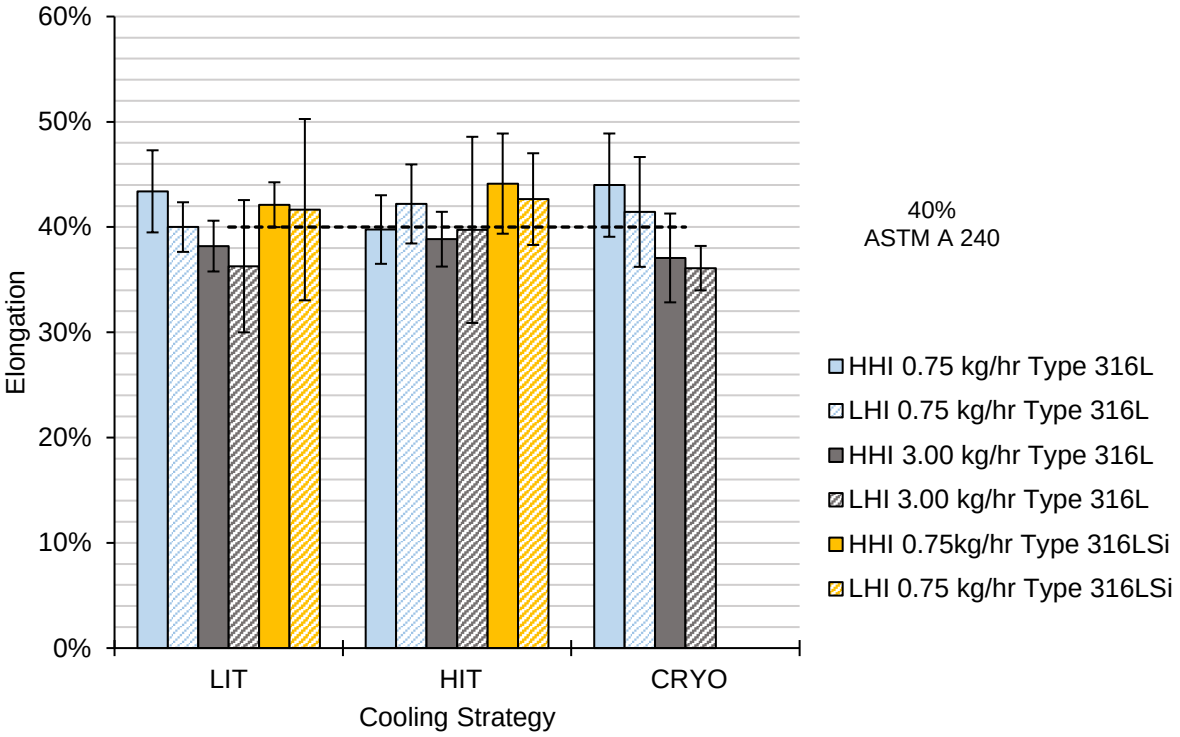

Figure 5.56 Uniform elongation of the high and low heat input and deposition rate levels for low interpass temperature, high interpass temperature and cryogenic cooling strategies.

The anisotropy factor (the difference of the mean horizontal samples and mean of vertical samples as a percentage relative to the vertical mean) is shown in Fig 5.57 and Fig 5.58, respectively.

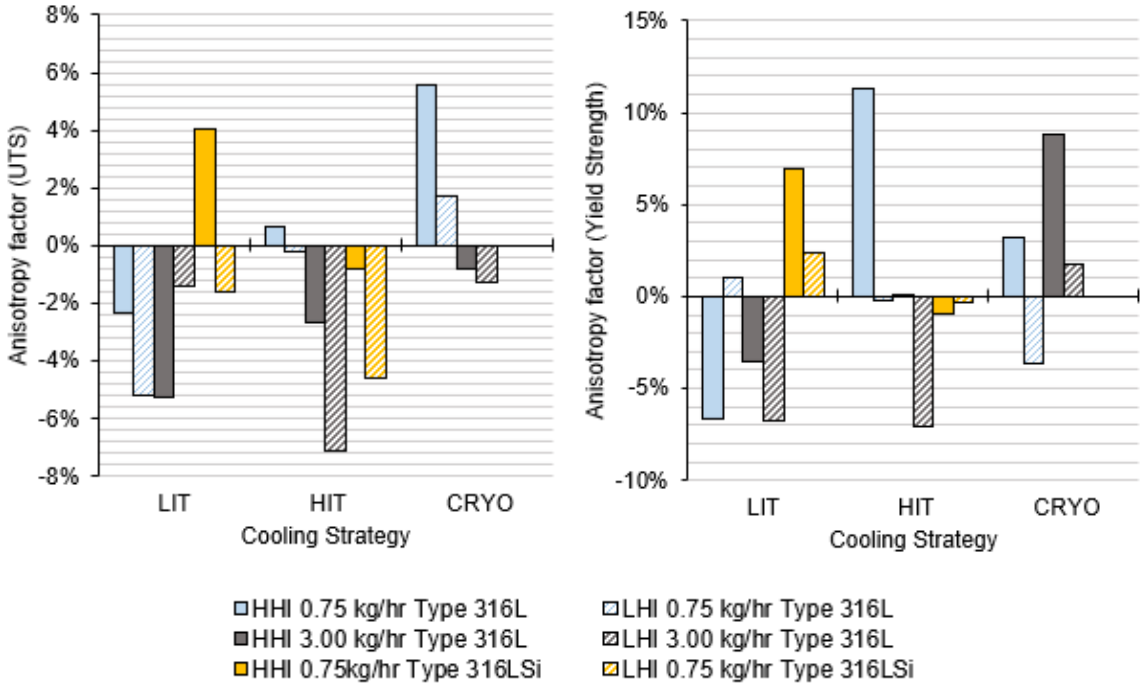

Figure 5.57 The anisotropy factor for a) UTS b) σ_{ys}

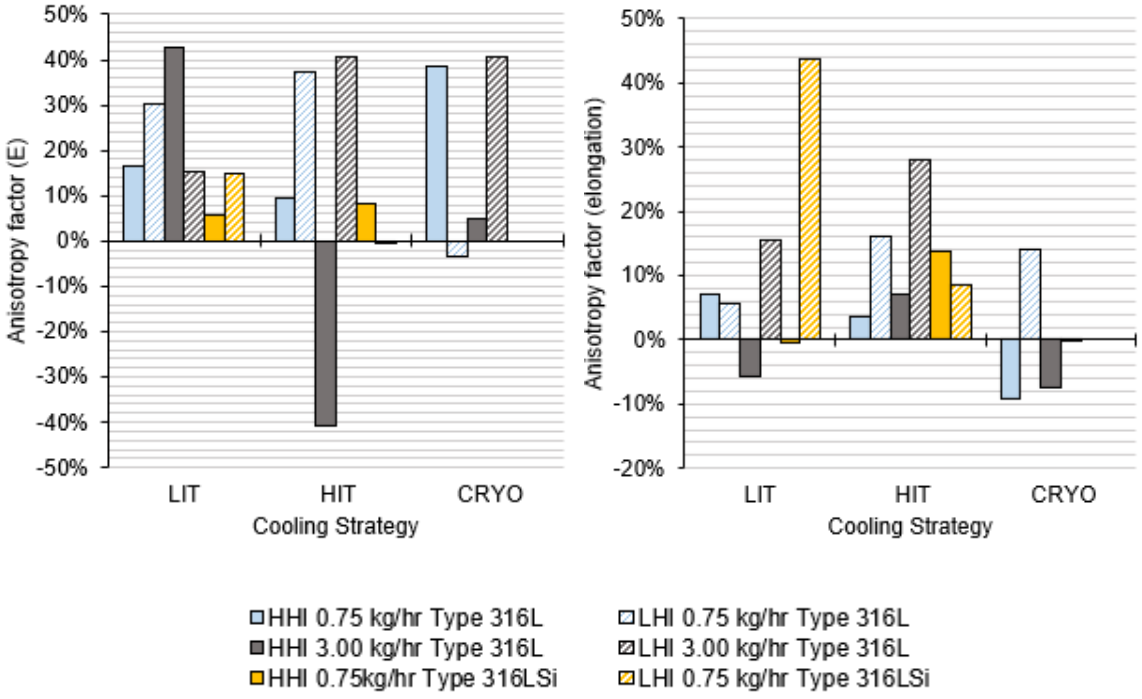

Figure 5.58 The anisotropy factor for a) E b) uniform elongation

To identify the significant effects of the experimental factors investigated the Minitab v.18 software package was used. A general linear statistical model was fitted to the data with the tensile properties under investigation UTS, σ_{ys}, E and uniform elongation specified as responses and the specimen orientation, heat input, deposition rate and cooling strategy as factors in ANOVA.

To ensure the assumptions of ANOVA regarding normality discussed in Chapter 4 were not violated, normality was tested and, where required, a Box-Cox transformation applied. Levene's test and Grubb's test was used to test for equal variances and significant outliers, respectively. The UTS, σ_{ys}, E and elongation investigated here, were shown to be suitable for analysis by ANOVA with the tests for normality, equal variance and residual plots presented in Appendix D, alongside the detailed ANOVA results.

5.7.1 Effects of varying wire composition on tensile properties at 0.75 kg/hr

This section reports on the statistical analyses that test the effects of wire composition on the mechanical properties. The effects of heat input and interpass temperature are investigated for the 0.75 kg/hr Type 316L and Type 316LSi samples.

i. Ultimate tensile stress

Performing the ANOVA to test the effects of heat input, interpass temperature and silicon composition for UTS showed that only the wire composition significantly affected the UTS ($p=0.0003$). The Type 316LSi wire with additional silicon (wt.%) resulted in an increase in mean UTS as shown in the interval plot Fig 5.59 where standard deviations are used to calculate the intervals with the mean, and individual data points shown.

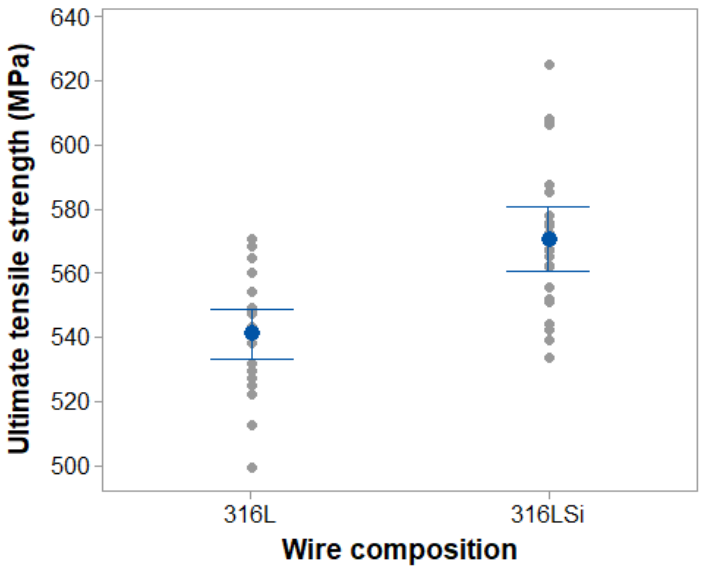

Figure 5.59 Interval plot displaying the effect of the wire composition on the UTS.
(Standard deviations are used to calculate the intervals).

ii. Yield stress

Significant effects on the σ_{ys} were found for the wire composition (p=0.001) and interpass temperature (p=0.003). It can be seen in Fig 5.60, that as found for the UTS, the additional silicon content of the Type 316LSi wire results in higher values of σ_{ys} with an average of 307.2 MPa compared to 286.7 MPa.

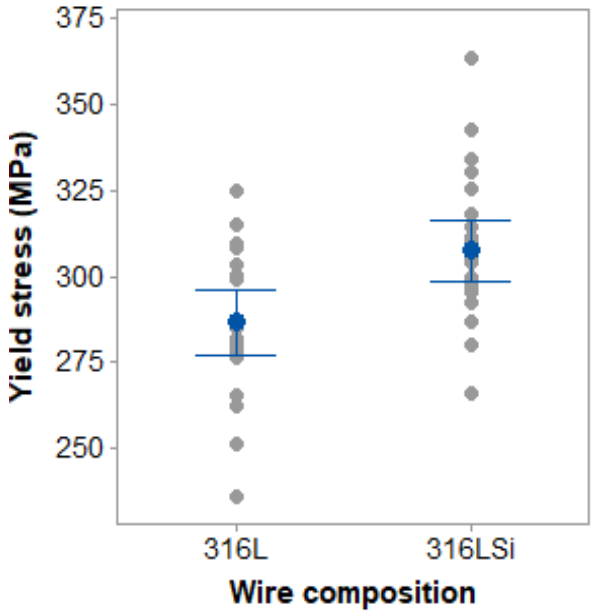

Figure 5.60 Interval plot displaying the effect of wire composition
(Standard deviations are used to calculate the intervals).

iii. Young's Modulus

The heat input (p=0.003) and wire composition (p<0.0001) was found to have statistically significant effects on the E. It can be seen in the interval plot presented in Fig 5.61, that the

wire composition with additional silicon results in an average E of 148.5 GPa compared to 94.2 GPa for Type 316L.

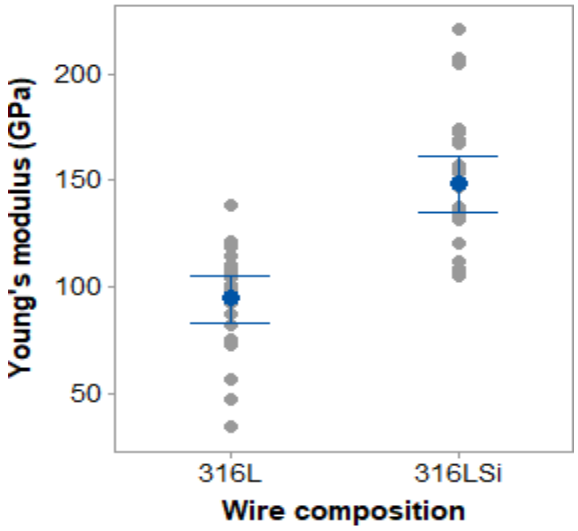

Figure 5.61 Interval plots displaying the effect of wire composition
(Standard deviations are used to calculate the intervals).

It can be seen in Fig. 5.62 that no correlation is observed for the oxide radius relative to Young's modulus values, however, the oxide volume fraction reported for each experiment is slightly lower for the Type 316LSi and the lower Young Modulus values correspond to higher volume fractions for the Type 316L sample.

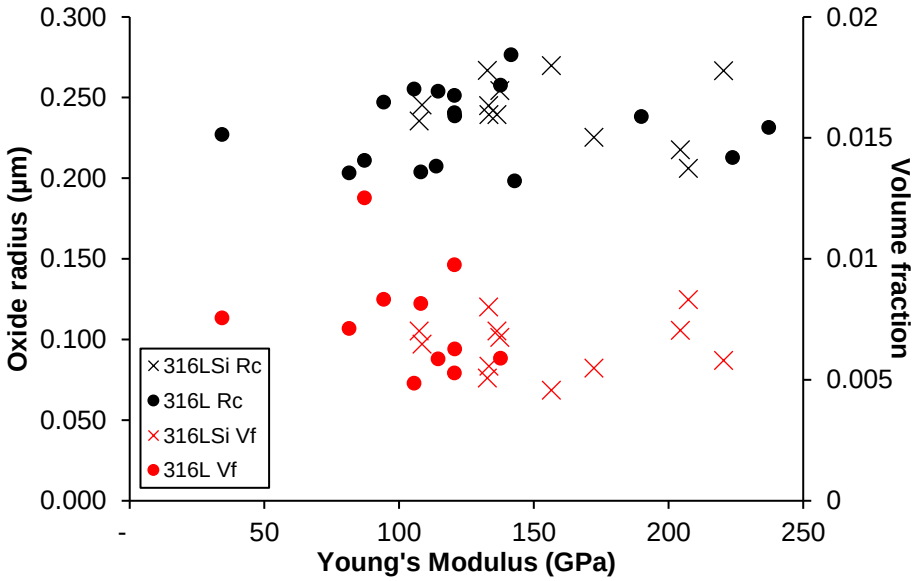

Figure 5.62 Relation of oxide radius and volume fraction to Young's Modulus
(0.75 kg/hr and 3.00 kg/hr Type 316L).

iv. Uniform Elongation

The ANOVA results showed non-significant effects for wire composition (p=0.515) regarding the uniform elongation results.

5.7.2 Effects of heat input (HHI, LHI), cooling strategy (HIT, LIT, CRYO), sample orientation and varying deposition rate on tensile properties of Type 316L

This section reports on the effect of heat input, cooling strategy and deposition rate on the mechanical properties of Type 316L. This considers the effects of LIT and HIT (60°C and 150°C) and CRYO through testing of the cooling strategy factor, and 0.75 kg/hr and 3.00 kg/hr deposition rates. The effect of sample orientation, horizontal (aligned to the travel direction) or vertical (aligned to the build direction) is also considered.

i. Ultimate Tensile Stress

Performing the ANOVA to test the effects of heat input, deposition rate and cooling strategy for UTS showed statically significant effects for the cooling strategy (p=0.004). The interval plot in Fig. 5.63 show the main effects of the cooling strategy. Tukey's pairwise comparisons with a 95% confidence level shown in Table 5.14 confirm that the significant difference exists for CRYO compared to LIT and HIT.

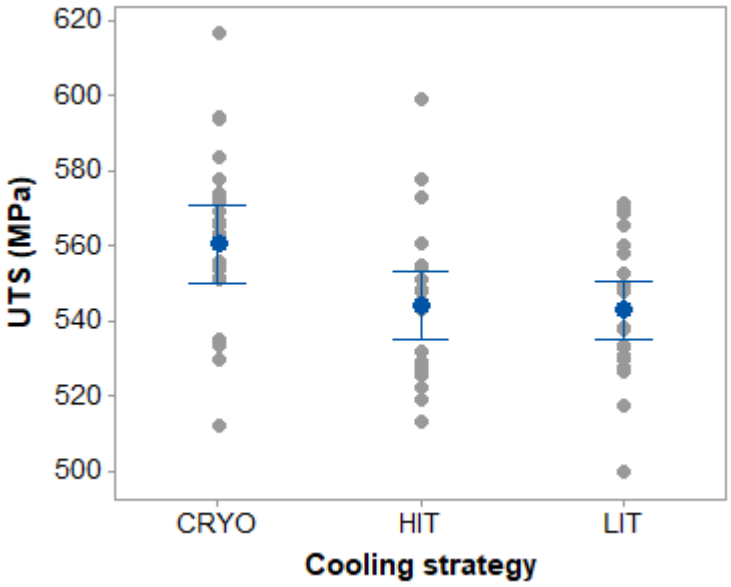

Figure 5.63 Interval plots displaying a) the effect of cooling strategy on the UTS.
(Standard deviations are used to calculate the intervals).

Table 5.14 Results of Tukey's Pairwise comparison testing for the effect of cooling strategy on UTS.
Means that do not share a letter are significantly different.

Cooling strategy	N	UTS (MPa)	Grouping
CRYO	24	560.3	A
HIT	23	543.5	B
LIT	23	543.4	B

ii. Yield Stress

Significant effects on the σ_{ys} were found for the heat input (p=0.021), cooling strategy (p=0.0004) and deposition rate (p<0.0001). The interval plots presented in Fig 5.64a and Fig 5.64b show that that 3.00 kg/hr and LHI results in higher σ_{ys} compared to the 0.75 kg/hr and HHI experiments, respectively.

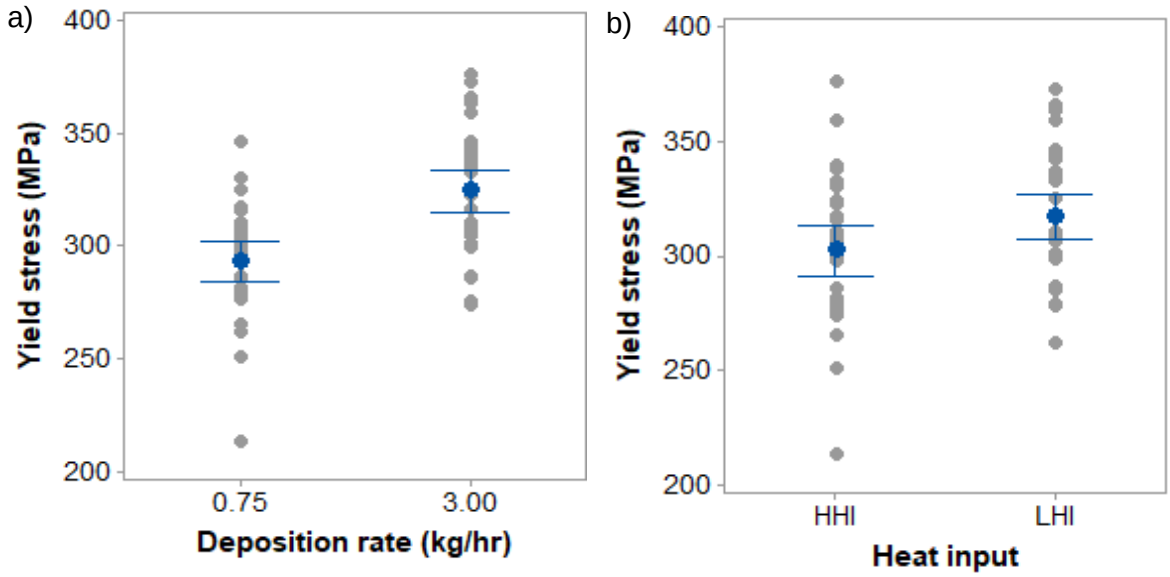

Figure 5.64 Interval plot displaying a) the effective deposition rate and b) the heat input on yield stress. (Standard deviations are used to calculate the intervals).

It can be seen in Fig 5.65 that the CRYO and LIT cooling strategies result in higher mean σ_{ys} compared to HIT. Tukey's pairwise comparisons with a 95% confidence level shown in Table 5.15 confirm that the significant difference exists between these levels.

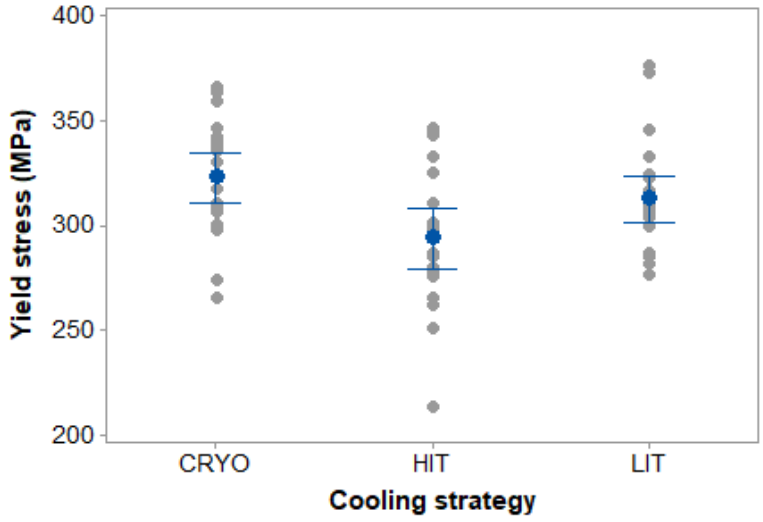

Figure 5.65 Interval plot of the effect of cooling strategy on the yield stress. (Standard deviations are used to calculate the intervals).

Table 5.15 Results of Tukey's Pairwise comparison testing for the effect of cooling strategy on yield stress. Means that do not share a letter are significantly different.

Cooling Strategy	N	Mean Yield Stress (MPa)	Grouping	
CRYO	23	322.6	A	
LIT	23	312.1	A	
HIT	23	292.2		B

A low to moderate positive correlation between σ_{ys} and relative density was found (p=0.001) with a Pearson's coefficient of 0.376 as shown in Fig 5.66. Despite the relatively small maximum variation of the relative density of ~0.3%, this corresponds to a 12 MPa per 0.001 increase in relative density. A similar weaker trend is present for UTS (p=0.013, Pearson coefficient= 0.297). This is expected as the strength of a porous material is proportional to the amount of material available to bear load (Ronneberg et al., 2020). The highlighted data points in Fig. 5.66 refer to samples in which major pores were found on the fractured surface (§6.7.3).

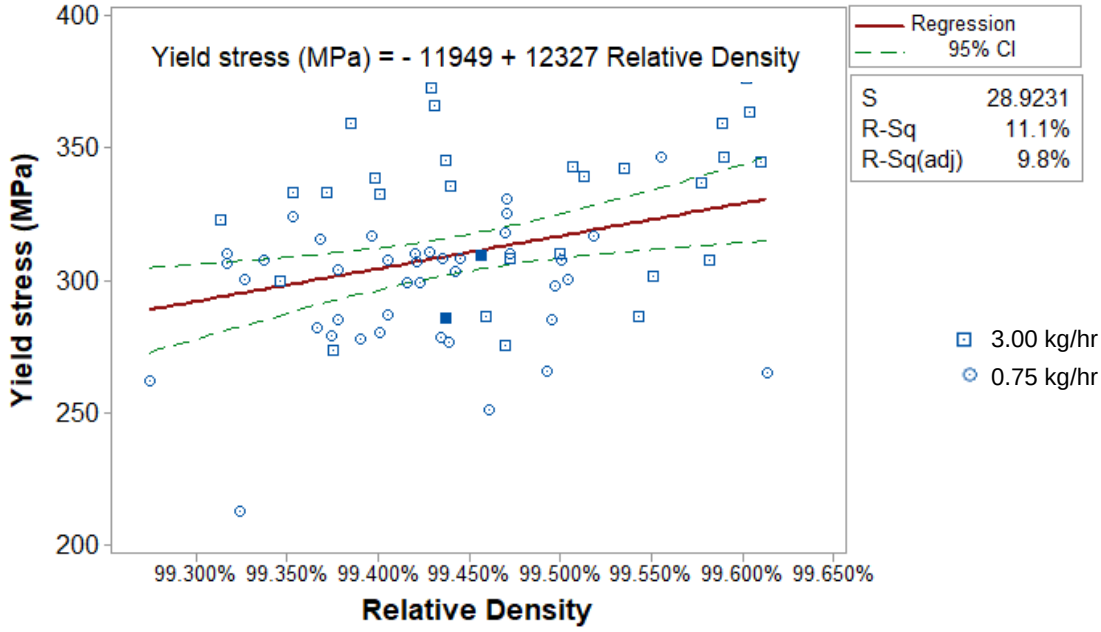

Figure 5.66 Correlation of relative density to yield strength for the Type 316L samples.

iii. Young's Modulus

To perform the ANOVA for E, a Box-Cox transformation (λ=0.5) was performed to obtain normal data. The cooling strategy was found to have a statistically significant effect on the E (p=0.013). The CRYO cooling strategy resulted in a higher mean E of 120 GPa when compared to HIT a 95 GPa or LIT at 96 GPa as shown in Fig 5.67. Statistical difference was confirmed with Tukey's pairwise comparison method with a 95% confidence level shown in Table 5.16.

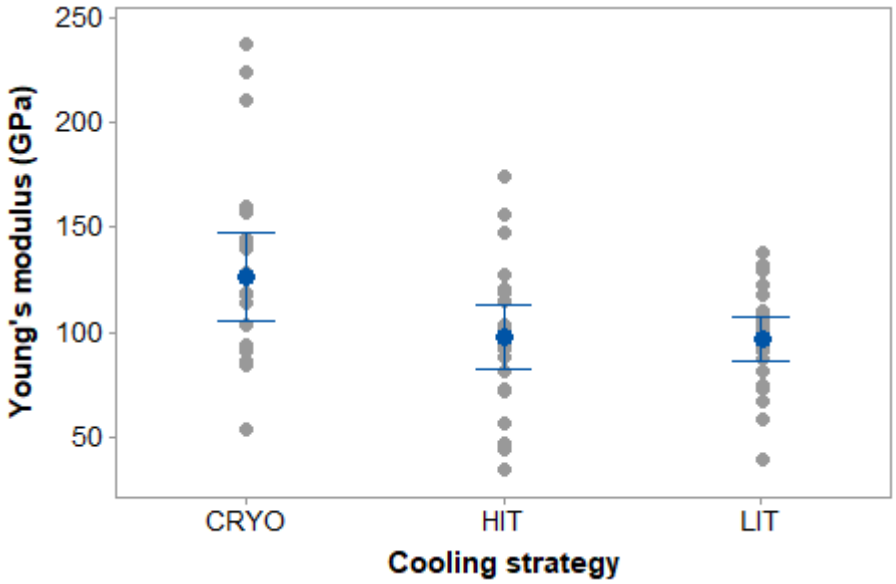

Figure 5.67 Interval plot of the effect of cooling strategy on the Young's Modulus. (Standard deviations are used to calculate the intervals).

Table 5.16 Results of Tukey's Pairwise comparison testing for the effect of cooling strategy on yield stress. Means that do not share a letter are significantly different.

Cooling Strategy	N	Mean	Grouping
CRYO	24	119.9	A
LIT	23	95.8	B
HIT	23	95.4	B

A significant effect was also found for sample orientation (p=0.43), alongside a significant interaction effect between heat input and cooling strategy (p=0.007) as shown in Fig 5.68. The CRYO cooling strategy results in a substantial increase in E for the LHI experiments compared to HHI.

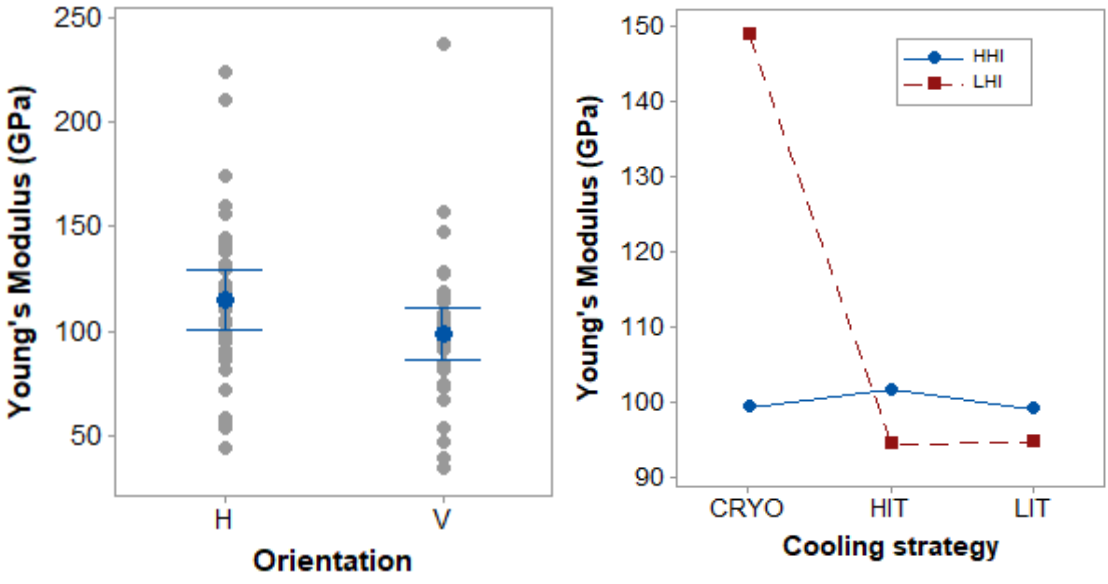

Figure 5.68 Interaction effects plot for heat input and cooling strategy for Young's modulus.

The interaction effects of heat input, cooling strategy and deposition rate were also found to be significant (p=0.018). It can be seen in Fig.5.69 0.75 kg/hr - LHI that there is a significantly larger increase in E for the CRYO cooling strategy compared to 0.75 kg/hr - HHI. However, for 3.00 kg/hr, the CRYO cooling condition has a relatively small positive effect on E for both HHI and LHI. Statistical difference was confirmed with Tukey's pairwise comparison method with a 95% confidence level shown in Table 5.17.

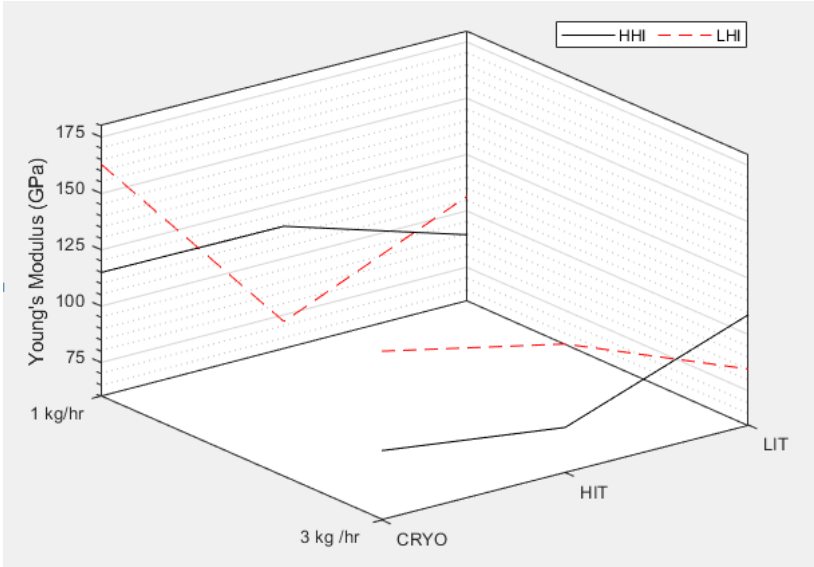

Figure 5.69 Interaction effects of deposition rate, cooling strategy and heat input.

Table 5.17 Results of Tukey's Pairwise comparison testing for the interaction effect of heat input, cooling rate and deposition rate on Young's Modulus. Means that do not share a letter are significantly different.

Heat input*Cooling Strategy*Deposition Rate	N	Mean	Grouping		
LHI CRYO 0.75	6	159.078	A		
LHI CRYO 3.00	6	132.148	A	B	
HHI HIT 0.75	5	114.094	A	B	C
LHI HIT 3.00	6	113.903	A	B	C
HHI CRYO 0.75	6	107.654	A	B	C
HHI LIT 3.00	6	106.251	A	B	C
LHI LIT 0.75	5	105.446	A	B	C
HHI LIT 0.75	6	89.125		B	C
HHI HIT 3.00	6	88.407		B	C
HHI CRYO 3.00	6	87.989		B	C
LHI LIT 3.00	6	82.262		B	C
LHI HIT 0.75	6	69.267			C

It can be seen in Fig. 5.70 that no correlation is observed for the oxide radius or oxide volume fraction relative to Young's modulus values reported for each experiment.

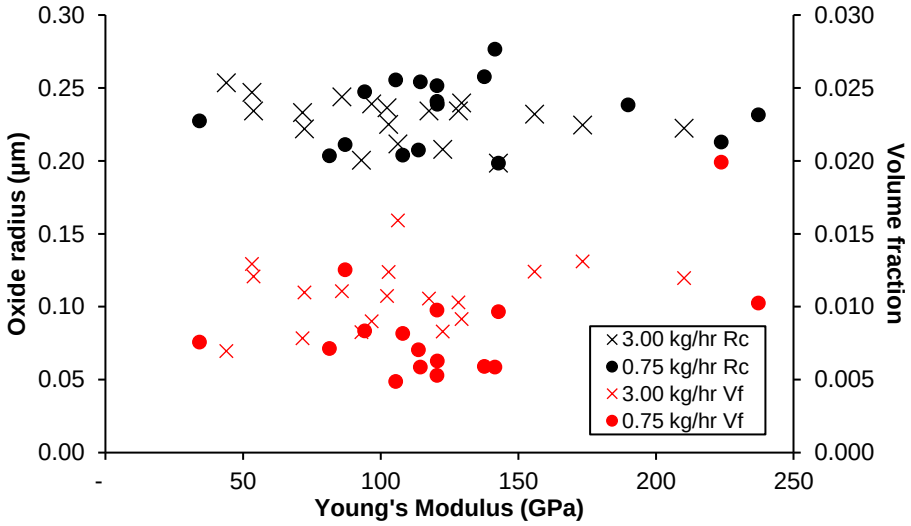

Figure 5.70 Relation of oxide radius and volume fraction to Young's Modulus (0.75 kg/hr and 3.00 kg/hr Type 316L).

Additionally, no correlation of Young's Modulus relative part density was found as shown in Fig 5.71.

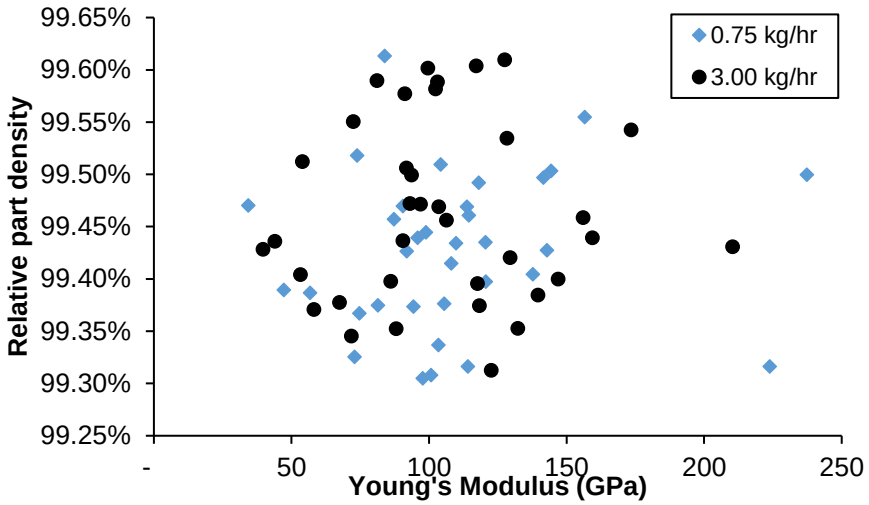

Figure 5.71 Relation of oxide radius and volume fraction to Young's Modulus.

iv. Uniform Elongation

The ANOVA results for uniform elongation identified that deposition rate had a significant effect (p=0.0003). The 0.75 kg/hr deposition rate resulted in a higher mean uniform elongation of 41.9 % compared to 37.7% for 3.00 kg/hr as shown in Fig 5.72.

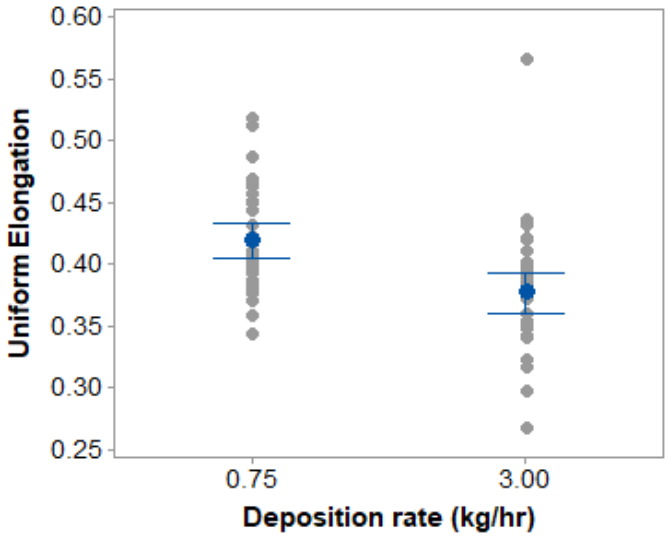

Figure 5.72 Interval plot of the effect of deposition rate on the uniform elongation.
(Standard deviations are used to calculate the intervals).

Sample orientation is found to have a major effect (p=0.043) and the interaction effect between heat input and orientation (p=0.017) as shown in Fig 5.73.

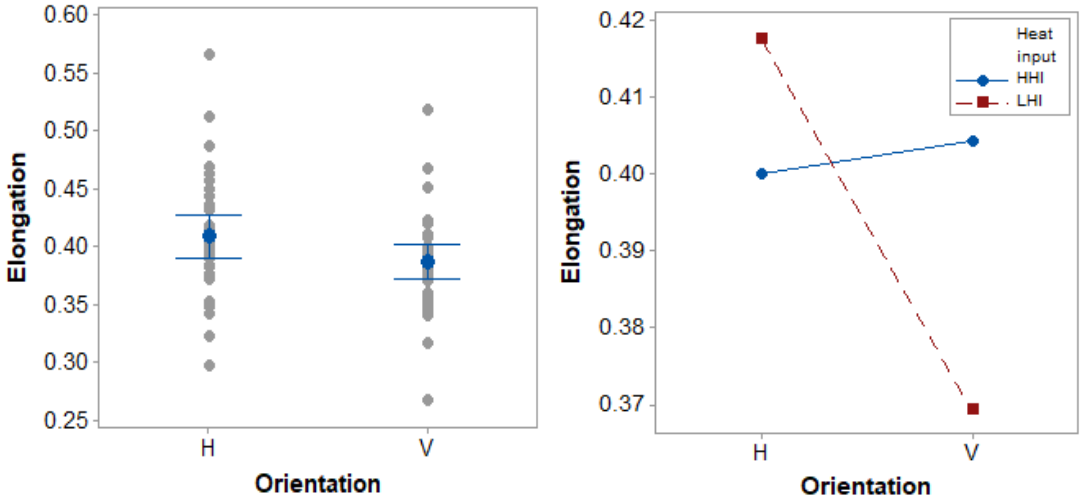

Figure 5.73 Main effects of orientation and interaction effects of heat input and orientation on elongation.

Statistical difference was confirmed with Tukey's pairwise comparison method with a 95% confidence level shown in Table 5.18.

Table 5.18 Tukey pairwise comparisons for the interaction effect between orientation and heat input.
Means that do not share a letter are significantly different.

Orientation*Heat Input	N	Mean	Grouping	
H-LHI	17	0.414	A	
V-LHI	18	0.367	A	B
H-HHI	17	0.399	A	B
V-HHI	18	0.402		B

To further study the impact of orientation, an individual value plot of the elongation categorised by deposition rate, heat input, cooling strategy and orientation was generated as shown in Fig. 5.74.

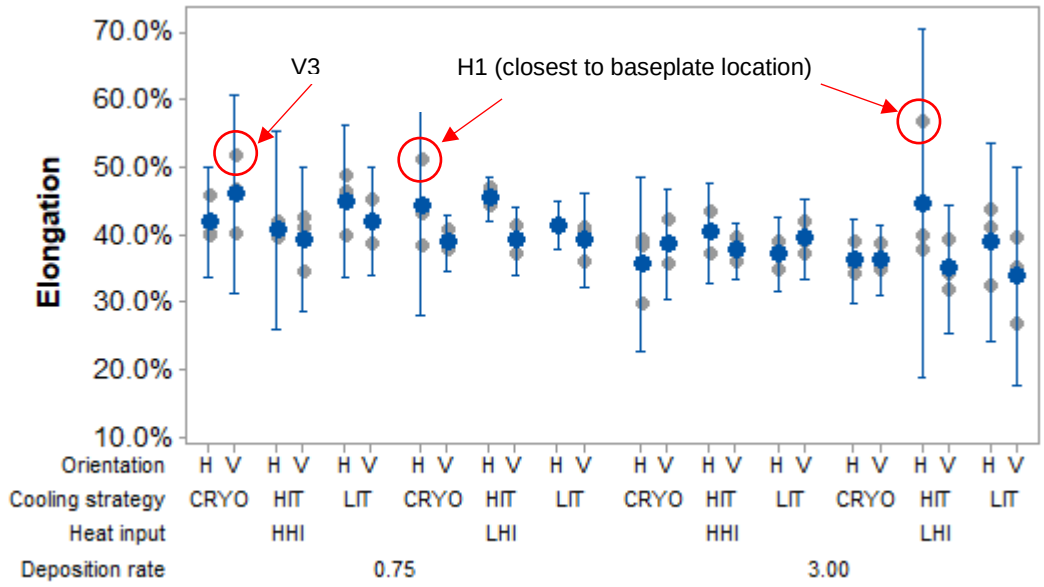

Figure 5.74 Individual value plot of Elongation categorised by deposition rate, heat input, cooling strategy and orientation.

The average uniform elongation can be related to the cooling rates and Fe(%) as shown in Fig. 5.75, with higher cooling rates correlating to lower ductility.

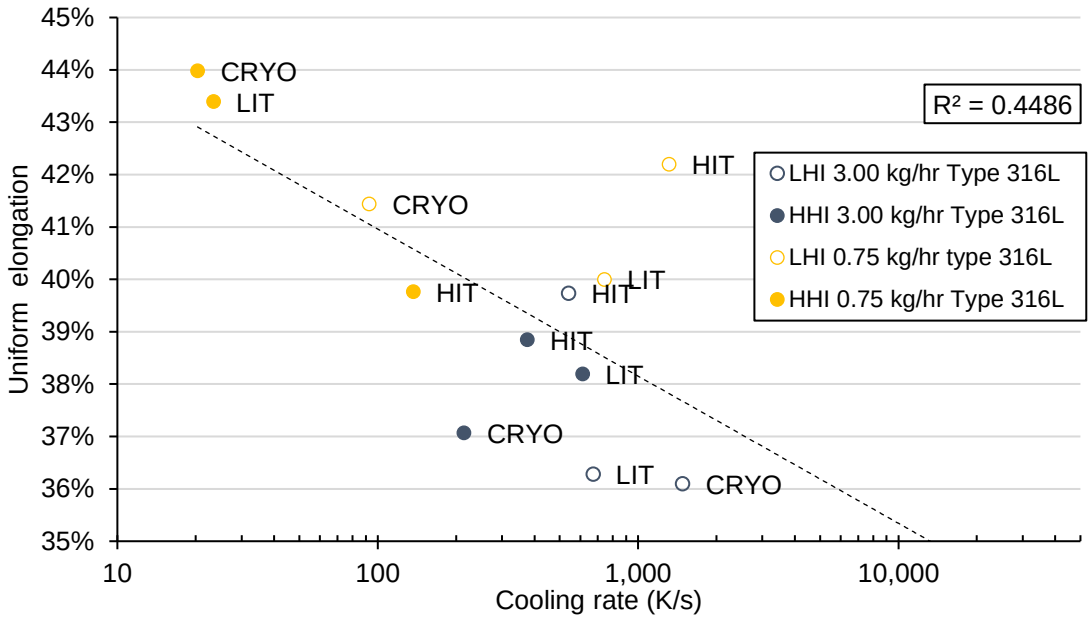

Figure 5.75 Relation between uniform elongation and minimum local cooling rates estimated from the coarse PCAS/PDAS.

The uniform elongation also showed correlation to the Fe(%) content of the metallurgical samples and a lesser extent the fractured tensile specimen Fe(%) shown in Fig. 5.76a and Fig 5.76b, respectively.

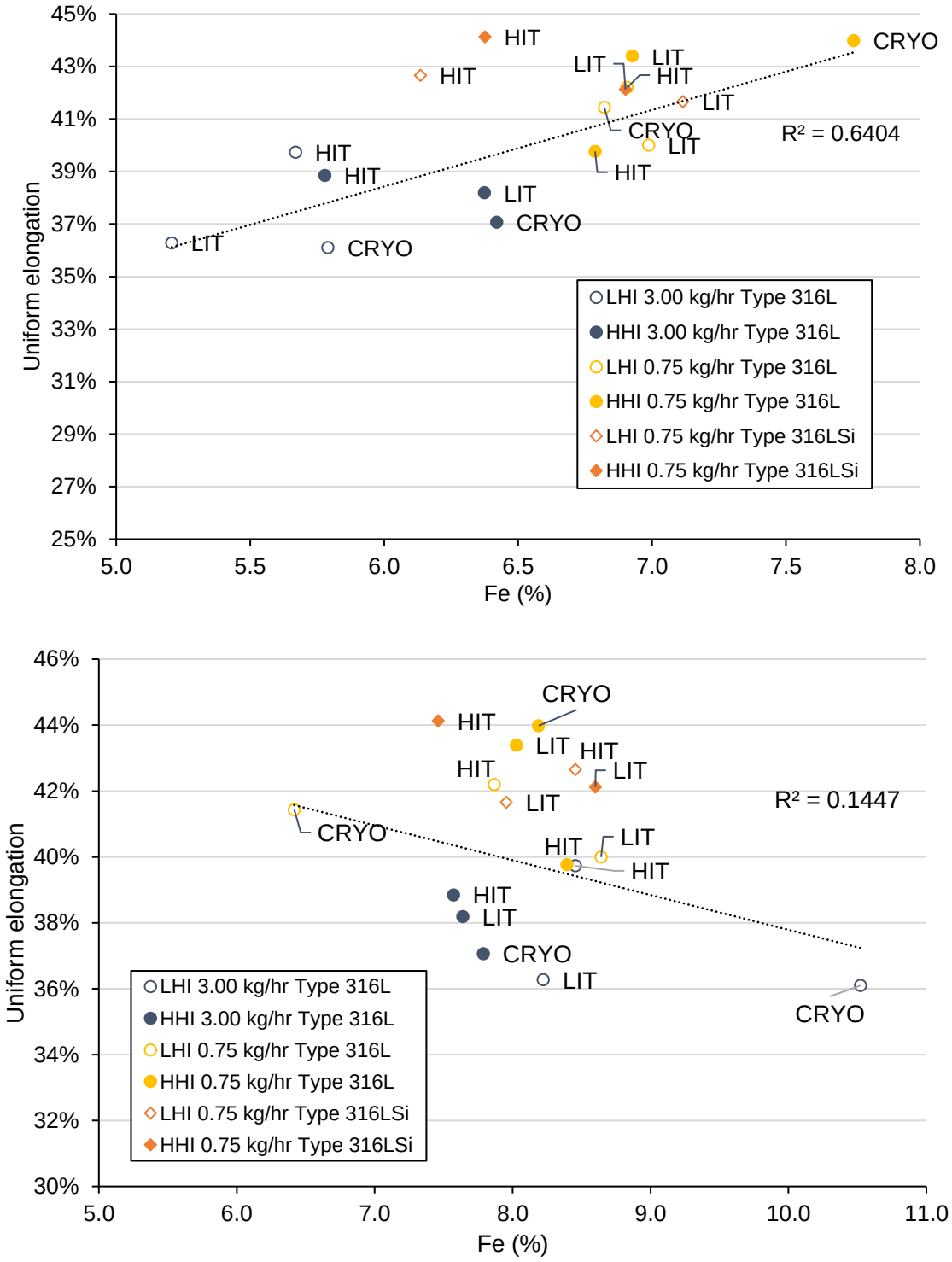

Figure 5.76 Relation between metallurgical sample Fe(%) for a) metallurgical samples b) fractured tensile specimens and uniform elongation.

Also, no significant correlation between relative density and uniform elongation was found (p=0.552, Pearson coefficient= 0.283) as shown in Fig. 5.77.

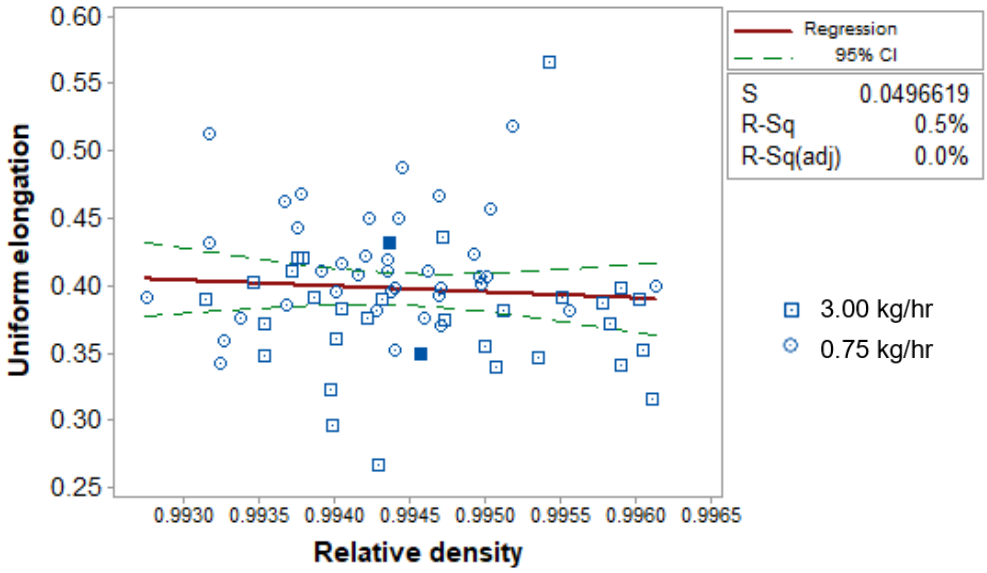

Figure 5.77 Correlation of relative density to uniform elongation for the Type 316L samples

5.7.3 Fractography and effects of dimple distribution

The fracture surfaces of the 316LSi tensile coupons were inspected by SEM and are shown in Fig. 5.78 and Fig. 5.79 for the HHI and LHI samples, respectively. These images were representative of for the 0.75 kg/hr and 3.00 kg/hr Type 316L samples shown in Appendix E showing mixtures of ductile fracture dimples, and cleavage fracture zones. The dimples across the fracture surface, which is consistent with the observed elongation properties described in §5.7.

Mapping of the ductile dimple features was conducted using customised Matlab codes to identify any systematic differences in dimple size or frequency. The dimples measured were of 1.45 μm and 1.62 μm mean diameter for Type 316L samples and Type 316LSi samples, respectively. The dimples were visible throughout the surface with no observed orientation effects between the horizontal and vertical samples.

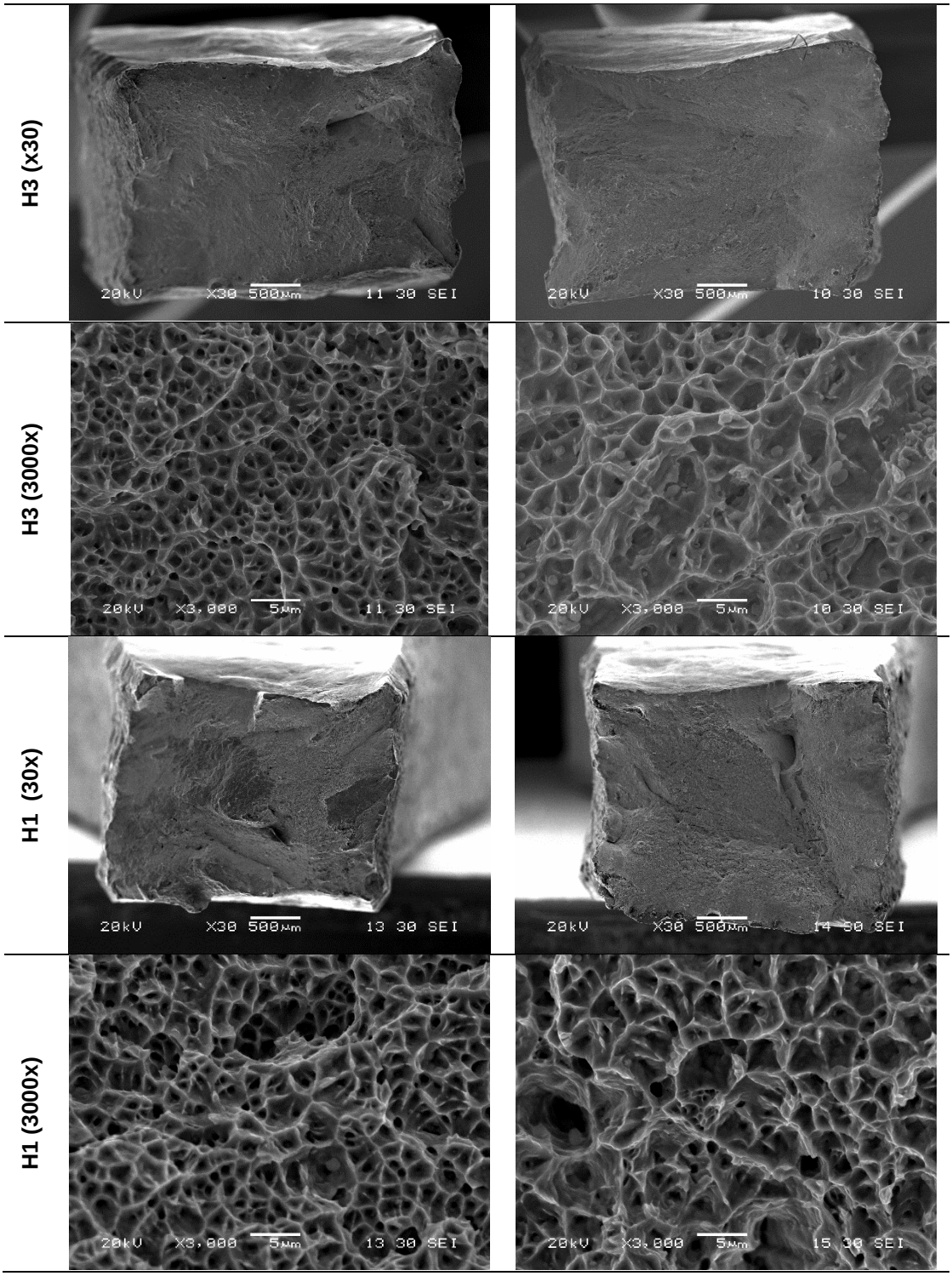

Figure 5.78 Fractography SEM imaging of the tensile specimens produced with HHI process parameters (Type 316LSi)

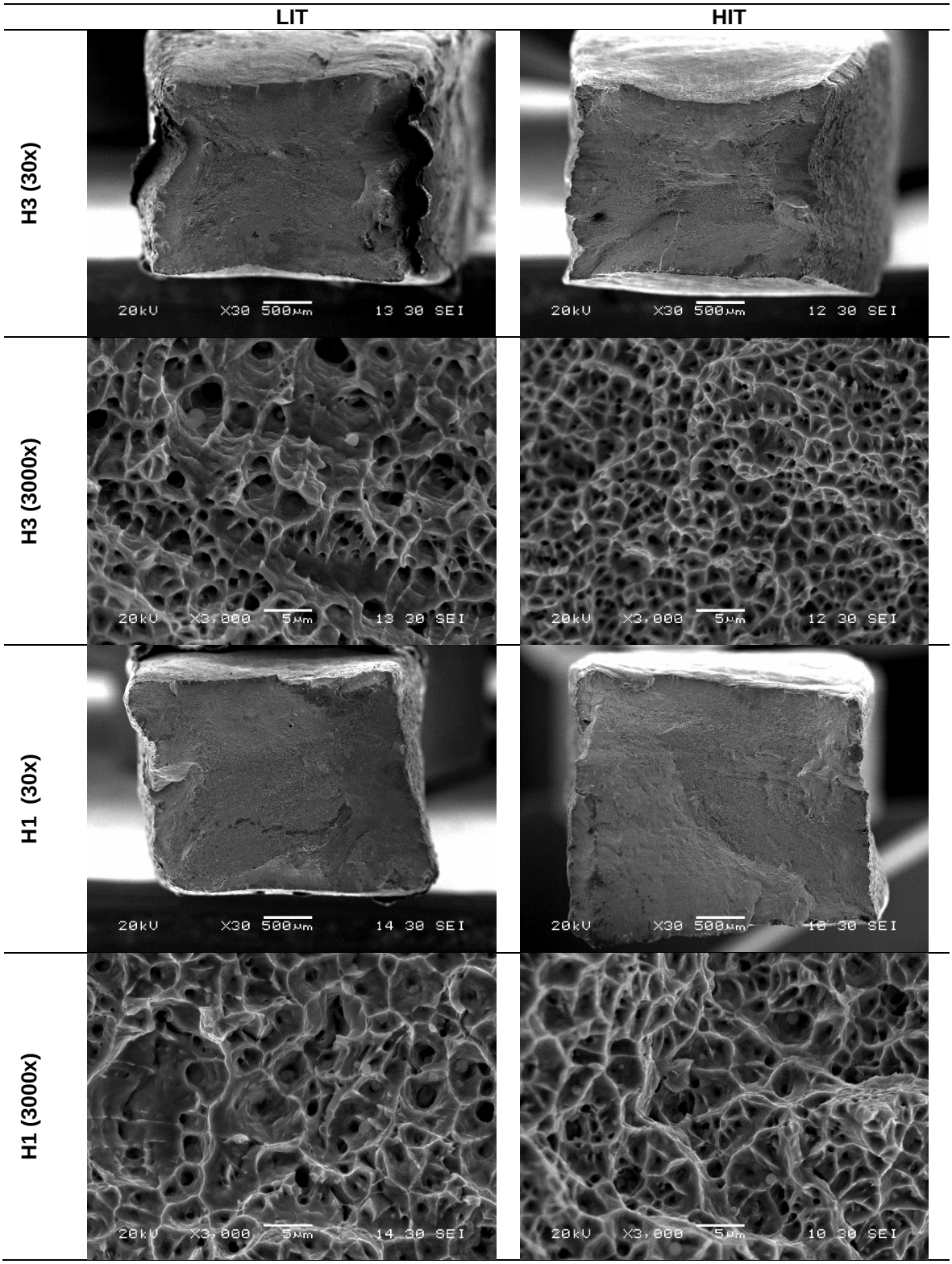

Figure 5.79 Fractography SEM imaging of the tensile specimens produced with LHI process parameters (Type 316LSi)

A relationship between the average of the top 5 dimple diameters and yield strength was found, with samples presenting larger dimples upon fracture shown to have lower σ_{ys} as shown in Fig 5.80. Larger dimple sizes represent larger stress concentration points, which can accelerate the failure of the specimen. The mean of the top 5 dimple diameters resulted in greater correlation compared to average dimple diameter indicating that the yield

behaviour is more strongly governed by the largest dimples present. It can be seen in Fig 5.80 that the Type 316LSi wire provided higher σ_{ys} with average top 5 dimple diameters. However, the E, uniform elongation and UTS correlated poorly to the dimple parameters investigated.

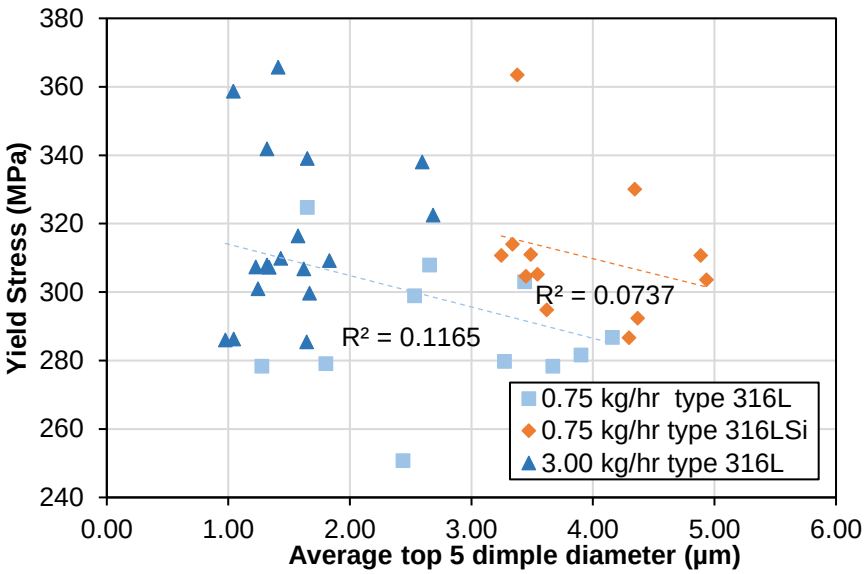

Figure 5.80 Correlation of the average top 5 dimple diameter and the yield stress.

The fracture dimples related to the oxide distribution, with larger dimples correlating to lower oxide number frequency and increased maximum oxide radii as shown in Fig 5.81a and Fig 5.81b. It can be seen that the silicon composition results in reduced oxide frequency and subsequently may cause a change in yielding behaviour by providing fewer stress concentration points.

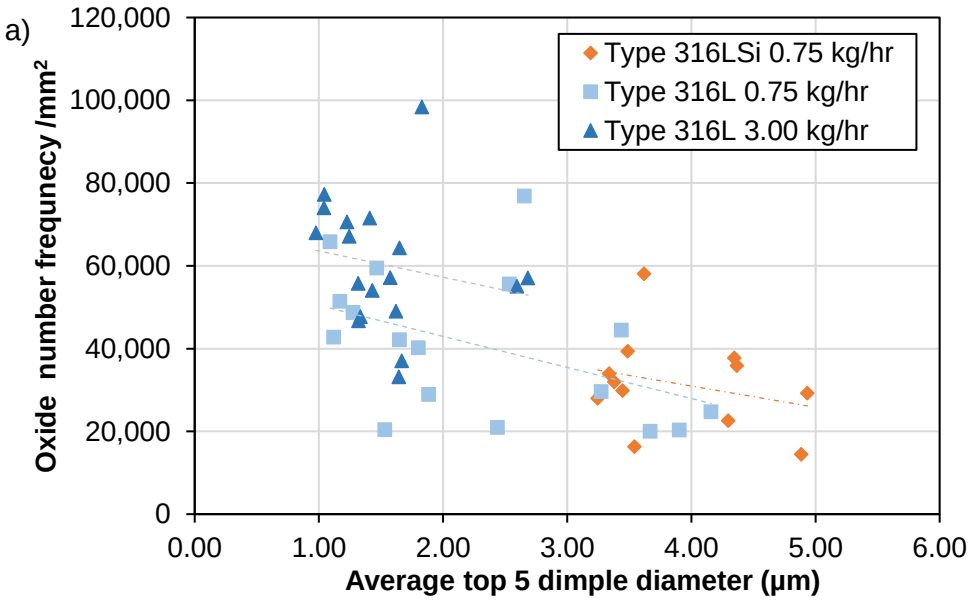

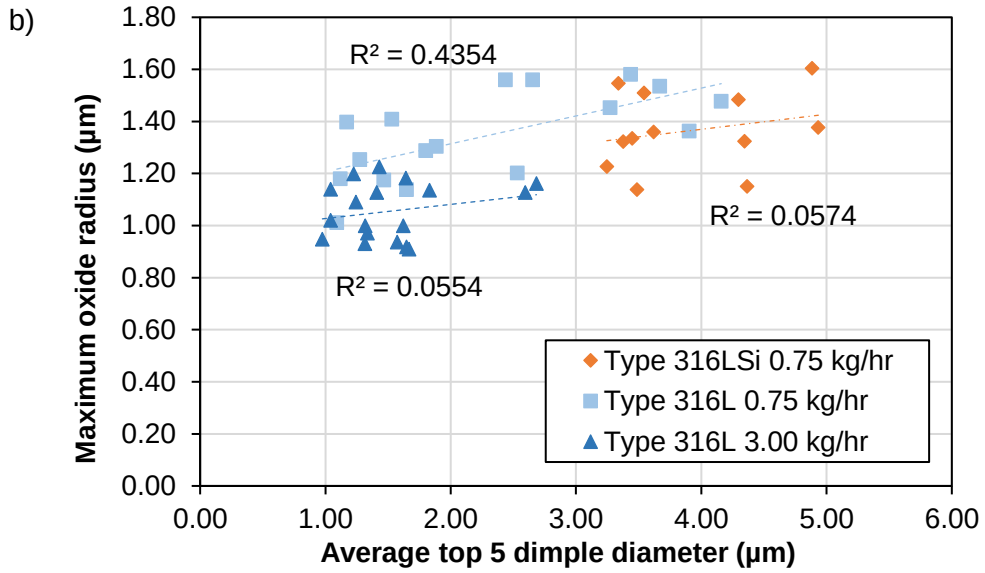

Figure 5.81 Correlation of average top 5 dimple diameter to a) oxide number frequency and b) maximum oxide radius.

Fractography also revealed substantial pores at the fracture surfaces of the Type 316L samples, HIT-HHI H1 (3.00 kg/hr) and LIT-LHI V2 (3.00 kg/hr) respectively. The scale of the pores, compared to the micro-voids previously shown, are representative of trapped gases during the solidification. The large pores were in the region of 0.5 mm diameter shown in Fig 5.82a and Fig. 5.82b.

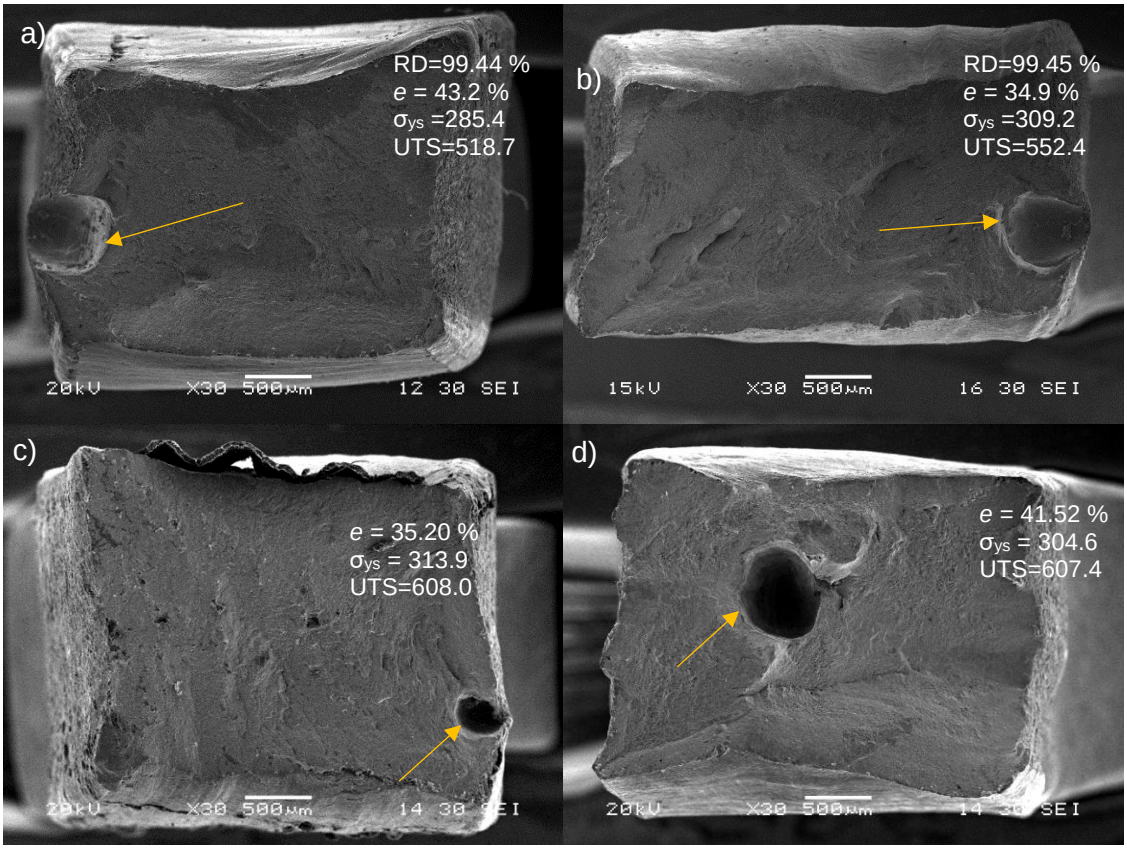

Figure 5.82 Surface pores identified from the fractography for samples a) HIT-HHI H1 (3.00 kg/hr) Type 316L b) LIT-LHI V2 (3.00 kg/hr) Type 316L c) LIT-LHI V2 0.75 kg/hr Type 316LSi d) HIT-LHI V2 0.75 kg/hr Type 316LSi.

The σ_{ys}, UTS and elongation appear to not be drastically affected by the large pores, suggesting a low sensitivity to porosity defects or damage tolerance, which is shown by the overall lack of trend relating uniform elongation to relative density in §5.7.2.

5.7.4 Micro-hardness

The results of the micro-hardness testing for the 0.75 kg/hr Type 316LSi and Type 316L experiments, and 3.00 kg/hr Type 316L experiments are presented in Fig. 5.83 and Fig 5.84, respectively. The results show an average of 25 microhardness indentation measurements spaced 1 mm apart within the top section of the thin wall with the error bars showing the 2σ standard deviation.

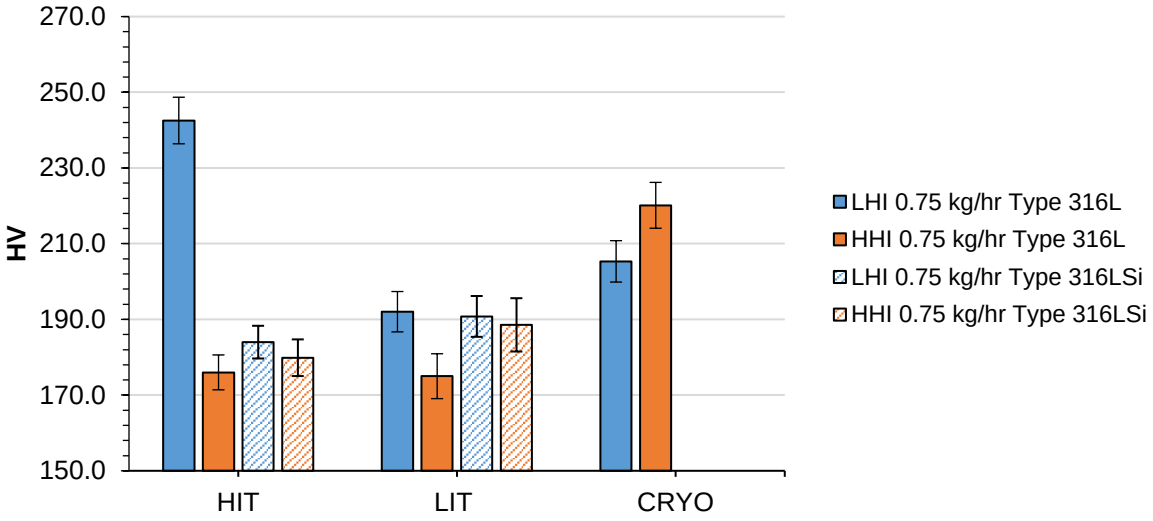

Figure 5.83 Vickers micro-hardness and individual standard deviation for the 0.75 kg/hr experiments.

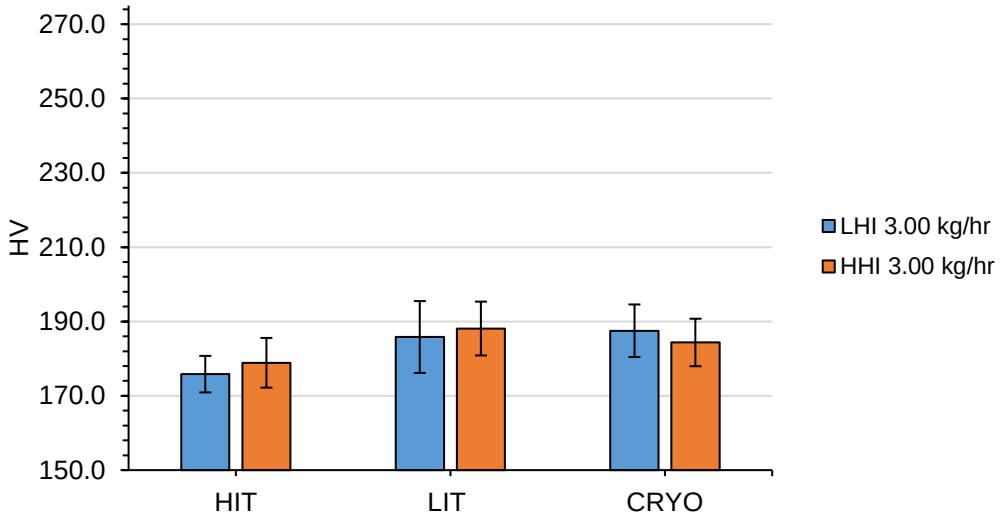

Figure 5.84 Micro-hardness and individual standard deviation for the 3.00 kg/hr experiments.

The micro-hardness shows a major increase with the application of CRYO cooling for the 0.75 kg/hr samples. The CRYO-HHI sample shows greater hardness than the CRYO-LHI. This differs from the application of interpass cooling strategies, where the HHI reduced the micro-hardness. The EBSD analysis in §5.5.1.2 found a strong <111> texture for the CRYO-

HHI sample, which is known to provide additional hardness (Pohl et al., 2020). Additionally, an unusual increase in microhardness for the HIT-LHI 0.75 kg/hr is observed considering the general trend of HIT appears to be a reduction in microhardness. This sample corresponded to a major increase in cooling rates (see §5.5.1.1) and is discussed later in §6.6.1.3. The 3.00 kg/hr showed more homogenous micro-hardness results, with a slight increase in micro-hardness observed for the LIT and CRYO cooling strategies.

5.8 Evaluation of Strengthening Mechanisms

5.8.1 Dislocation Strengthening

Based on EBSD analysis in §5.5.1.2, it was possible to derive an approximation for the density of GNDs, an indication of strain hardening induced by the thermal stresses during the WAAM experiments. The square root of the stored GND's varied linearly with the experimental σ_{ys} as shown in Fig. 5.85, in agreement with the reported literature for conventional metal processing methods and L-DED (Smith et al., 2018, Roa et al., 2019). These dislocation density values are in the range of values estimated for L-DED Type 316L structures (Smith et al., 2019).

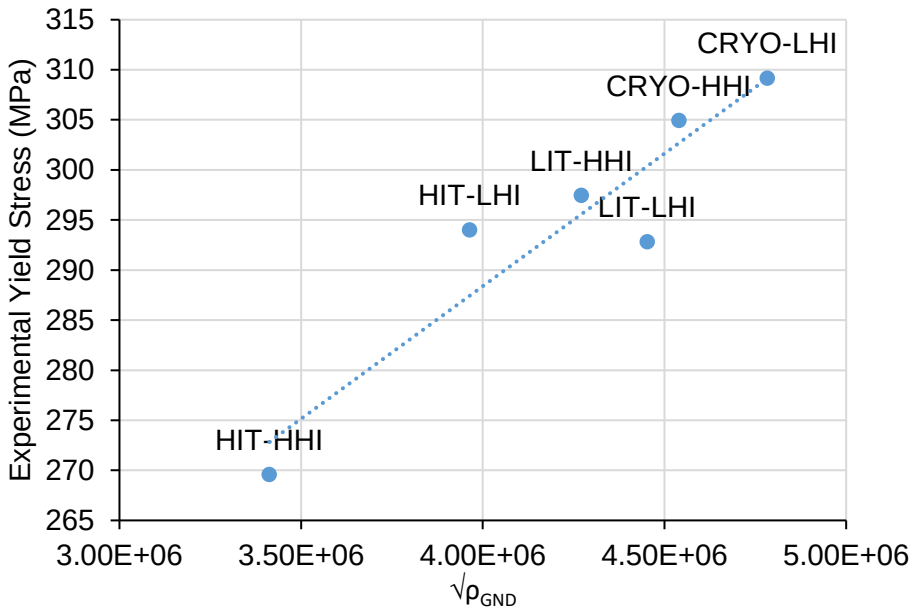

Figure 5.85 Relationship between σ_{ys} and the GND's for each experimental condition (0.75 kg/hr).

The Bailey-Hirsch relation shows that the yield strength varies in proportion to the square root of the dislocation density as follows (Bailey and Hirsch, 1960):

$$\sigma_{dis} = M\alpha bG\sqrt{\rho_{GND}} \tag{6.3}$$

Where M is the Taylors factor (2.449) relating the minimum value of the resolved shear stress needed to initiate slip to the σ_{ys} based on <001> texture (Clausen, 1997), α is a constant (0.3) (Kubin and Mortensoen, 2003), b is the Burgers vector (0.254 nm) (El-Tahawy et al., 2017) and G is the shear modulus (77 GPa).

Based on this relation, an estimate of the contribution to yield strength by dislocation strengthening was determined for each experiment as shown in Fig. 5.86. The difference between experimental yield strength for the experiments correlates closely with the difference in predicted σ_{ys} contribution.

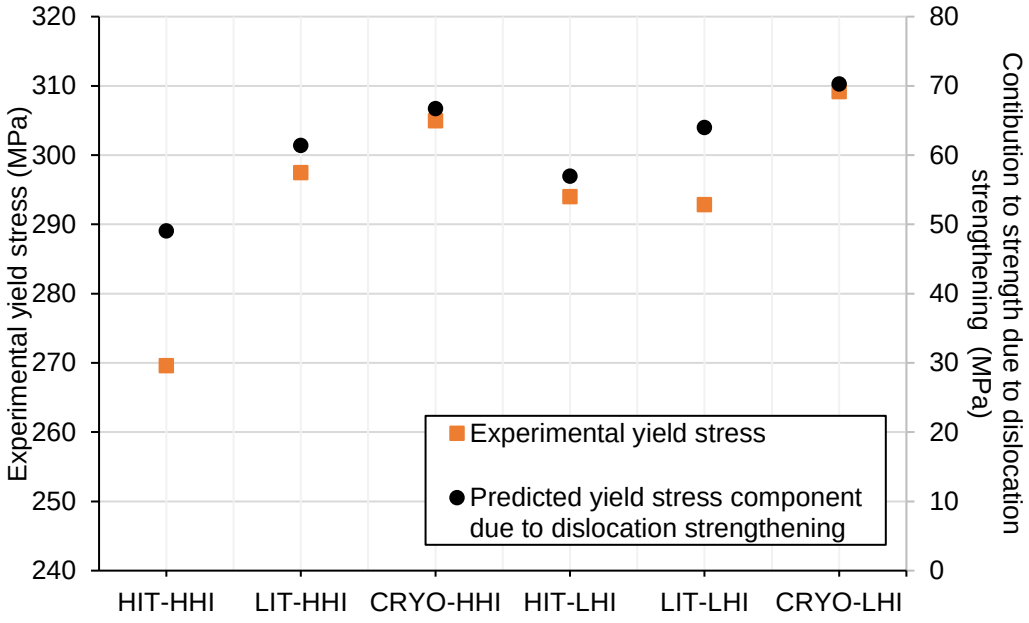

Figure 5.86 The predicted contribution to yield strength from dislocation strengthening with the experimental yield strength.

5.8.2 Oxide Dispersion Strengthening

The mean ODS relative to the experimental mean σ_{ys} is shown in Fig. 5.87 Type 316L and Type 316LSi wire, respectively. The HIT-HHI build parameter resulted in the lowest average ODS for all experiments, with a slight progressive increase in ODS when LIT and CRYO is applied for both heat input levels.

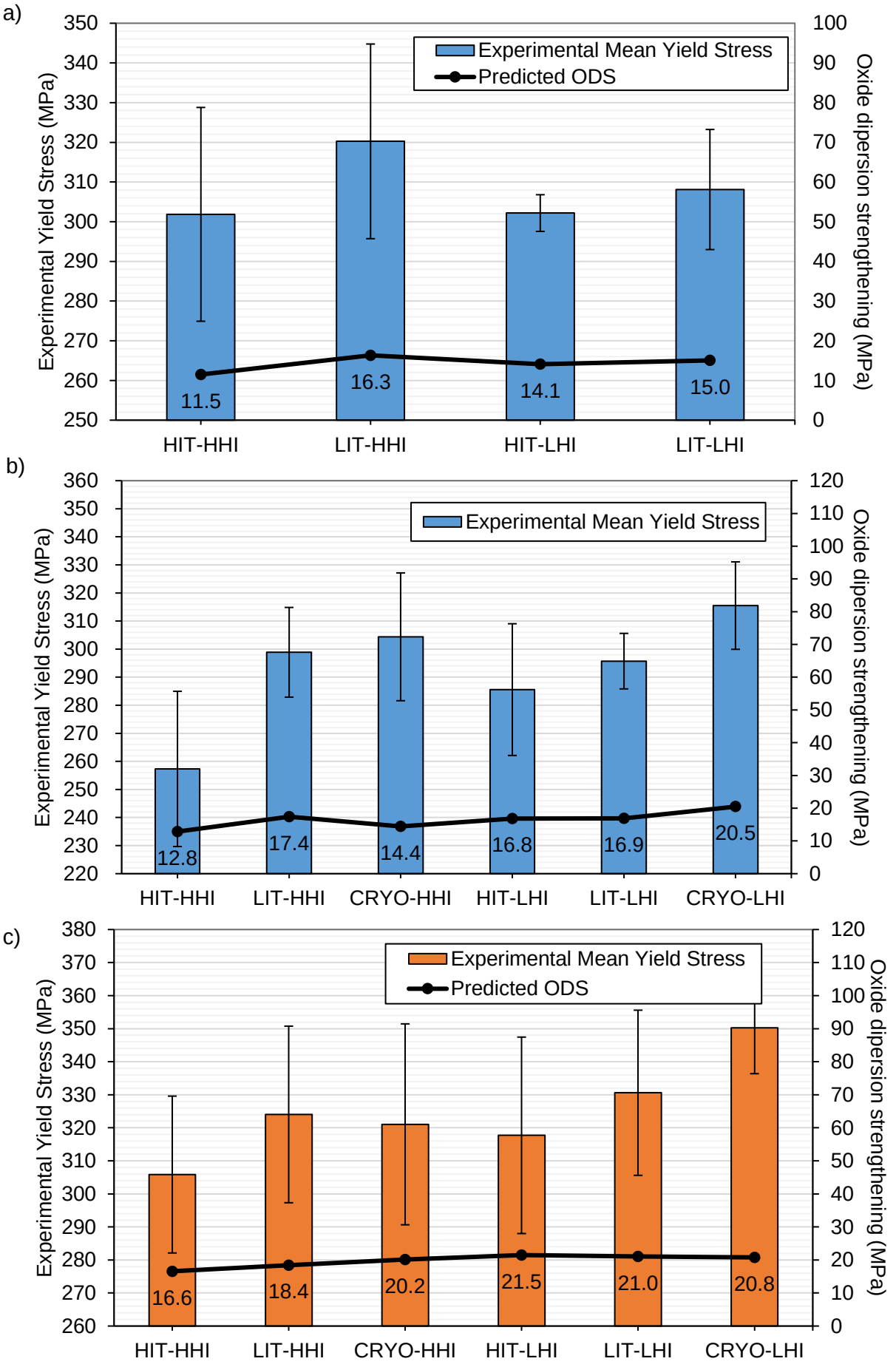

Figure 5.87 Mean experimental yield stress and predicted contribution to strength by oxide dispersion strengthening for a) Type 316LSi (0.75 kg/hr), Type 316L (0.75 kg/hr) and c) Type 316L (3.00 kg/hr). Error bars represent 2σ standard deviation.

5.8.2.1 Effects of heat input and interpass temperature control on ODS with varying wire composition for 0.75 kg/hr

ANOVA was performed to evaluate the effect of wire composition on ODS with interpass temperature control and the heat input. For the Type 316L and Type 316LSi groups, the interpass temperature was demonstrated to have a significant effect on ODS (p=0.029) with the LIT samples showing a higher average ODS as shown in Fig 6.88a. A small difference in ODS between the Type 316L and Type 316LSi alloy materials were identified as shown in Fig 6.89b, however, this was not significant (p=0.127).

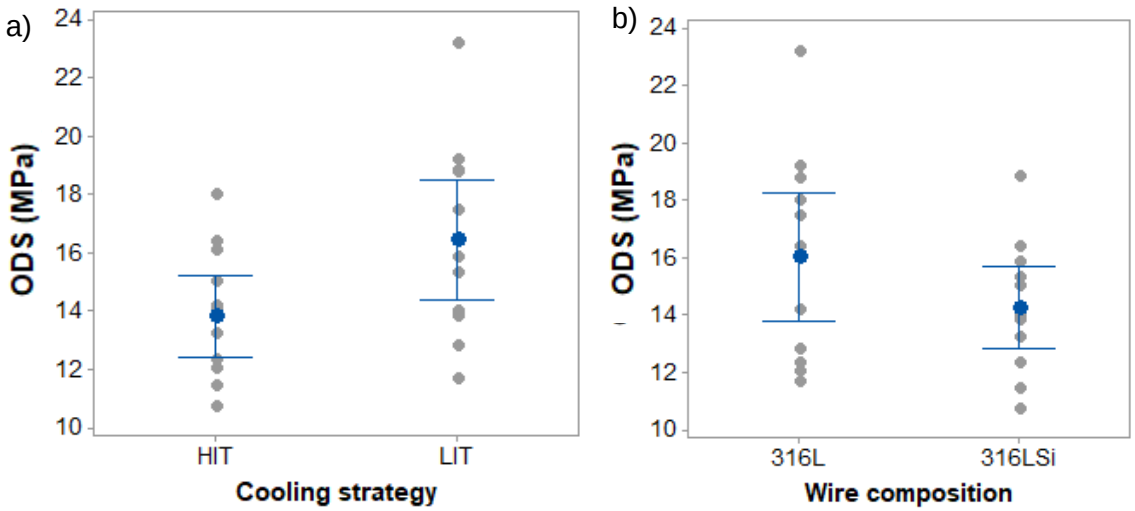

Figure 5.88 Interval plot and mean values for a) cooling strategy b) wire composition

The interaction effect between interpass temperature and heat input was found to be significant (p=0.030). Reducing the build temperatures from HIT to LIT for the HHI test condition results in the largest increase in ODS from 12.17 MPa to 16.88 MPa as shown in Fig 6.89.

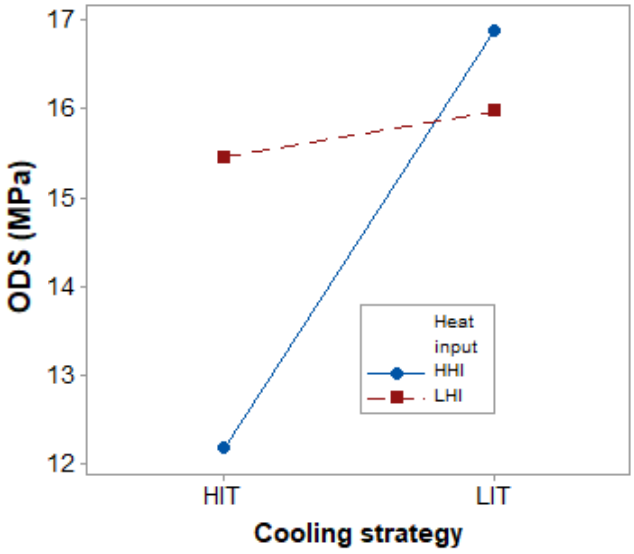

Figure 5.89 Interaction effects plot of the mean contribution to strength based on heat input and interpass temperature.

The increase in strengthening that occurs with the LIT experiments can be attributed to the limitation of the Ostwald Ripening phenomena at lower temperatures, preventing the coarsening and coalescence larger inclusions and diffusion of smaller particles. This is displayed in Fig. 5.90, where it can be observed that the HIT results in a higher degree of negative skew compared to the LIT for the HHI experiments.

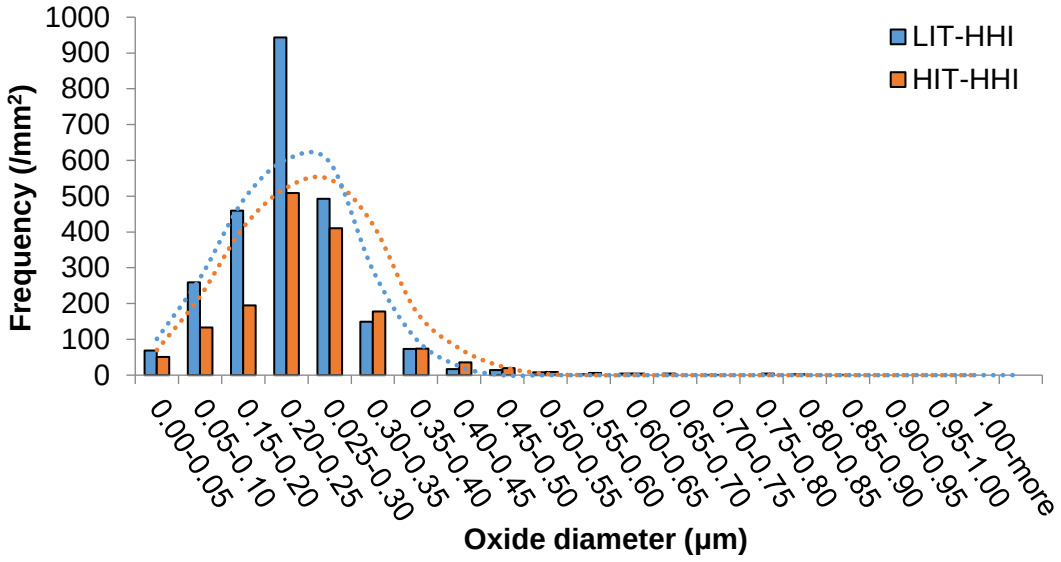

Figure 5.90 Histogram and normal distribution of the oxide diameter for high and low interpass temperatures for HHI 0.75 kg/hr Type 316L.

5.8.2.2 Effects of heat input, cooling strategy (interpass temperature control, cryogenic cooling) with varying deposition rate for Type 316L

An ANOVA of the Type 316L samples found ODS is significantly affected by the heat input (p=0.004) and deposition rate (p=0.002) as shown in Fig 5.91a and Fig. 5.91b, respectively. The LHI heat input level resulted in higher ODS of 19.6 MPa compared to 16.6 MPa for HHI.

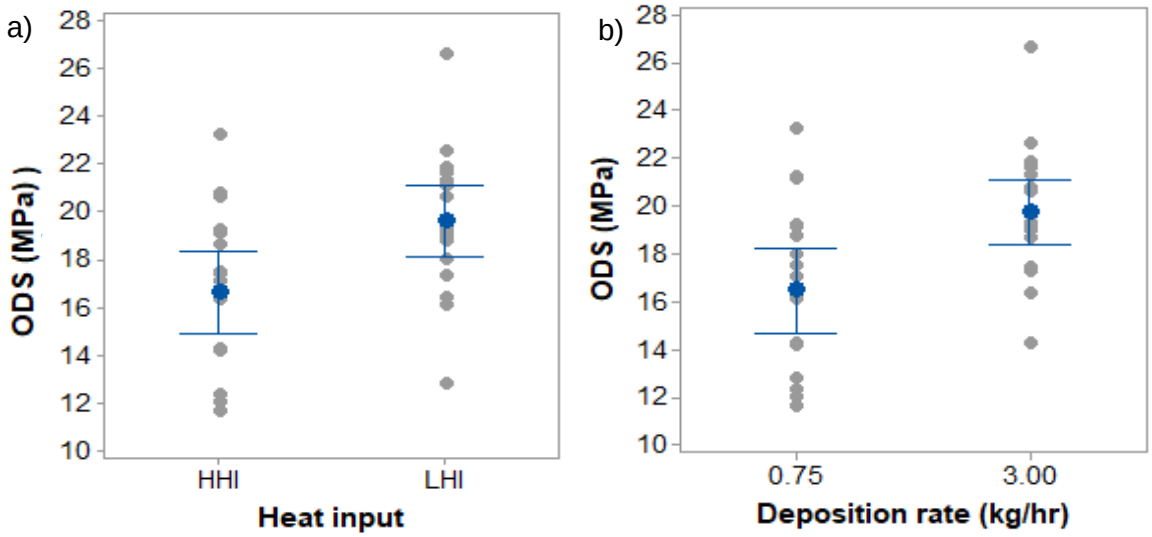

Figure 5.91 Interval plot and mean values of ODS for a) heat input b) deposition rate.

5.8.2.3 Relation to experimental mechanical analysis data

The average σ_{ys} for each test condition was proportional to the average oxide spacing and number frequency for Type 316L as shown in Fig 5.92a and Fig 5.92b, respectively.

a)

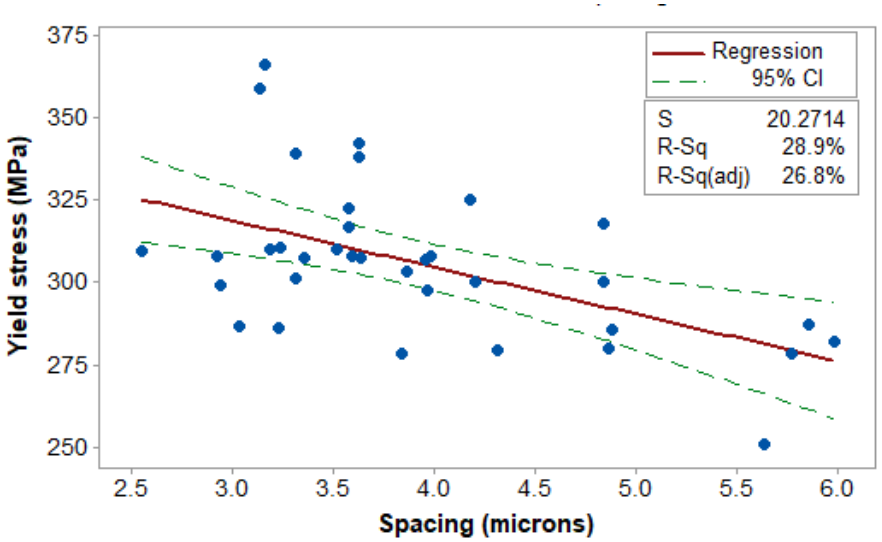

b)

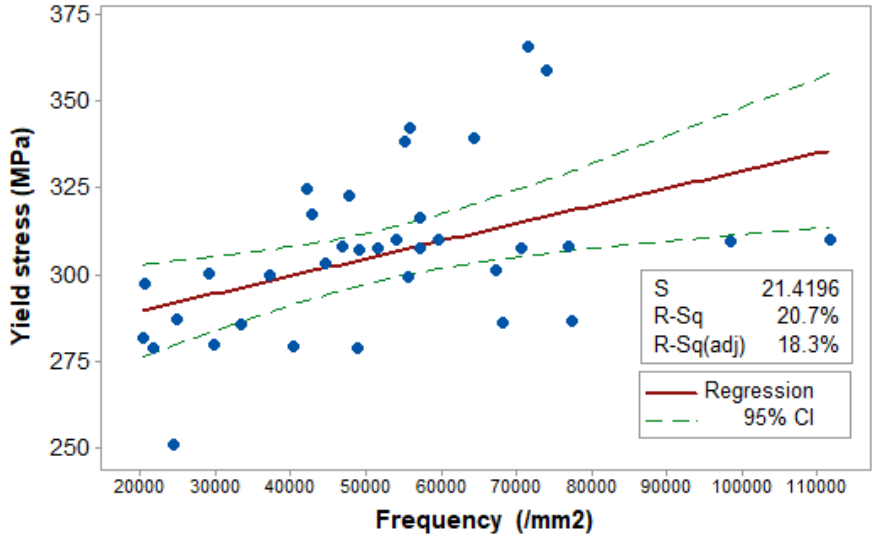

Figure 5.92 Correlation of yield stress with a) oxide spacing b) oxide number frequency.

The yield strength also displays a negative correlation with maximum oxide diameter as shown in Fig 5.93a and elongation as shown in Fig 5.93b with a weaker positive trend, showing that with larger inclusions oxide pull-out can be more readily achieved. In Fig 5.93b the highlighted data-points represent samples extracted from the H1 location closest to the substrate and may be subject to higher levels of dislocation strengthening as discussed in §6.6.1.6. Removal of the two highlighted points results in a stronger fit of R^2=29.2%. As the spacing decreases or number frequency increases, the maximum oxide diameter decreases. This suggests that increasing the ODS by reduction of oxide spacing or inclusion size is likely to occur at the expense of ductility in WAAM of Type 316L.

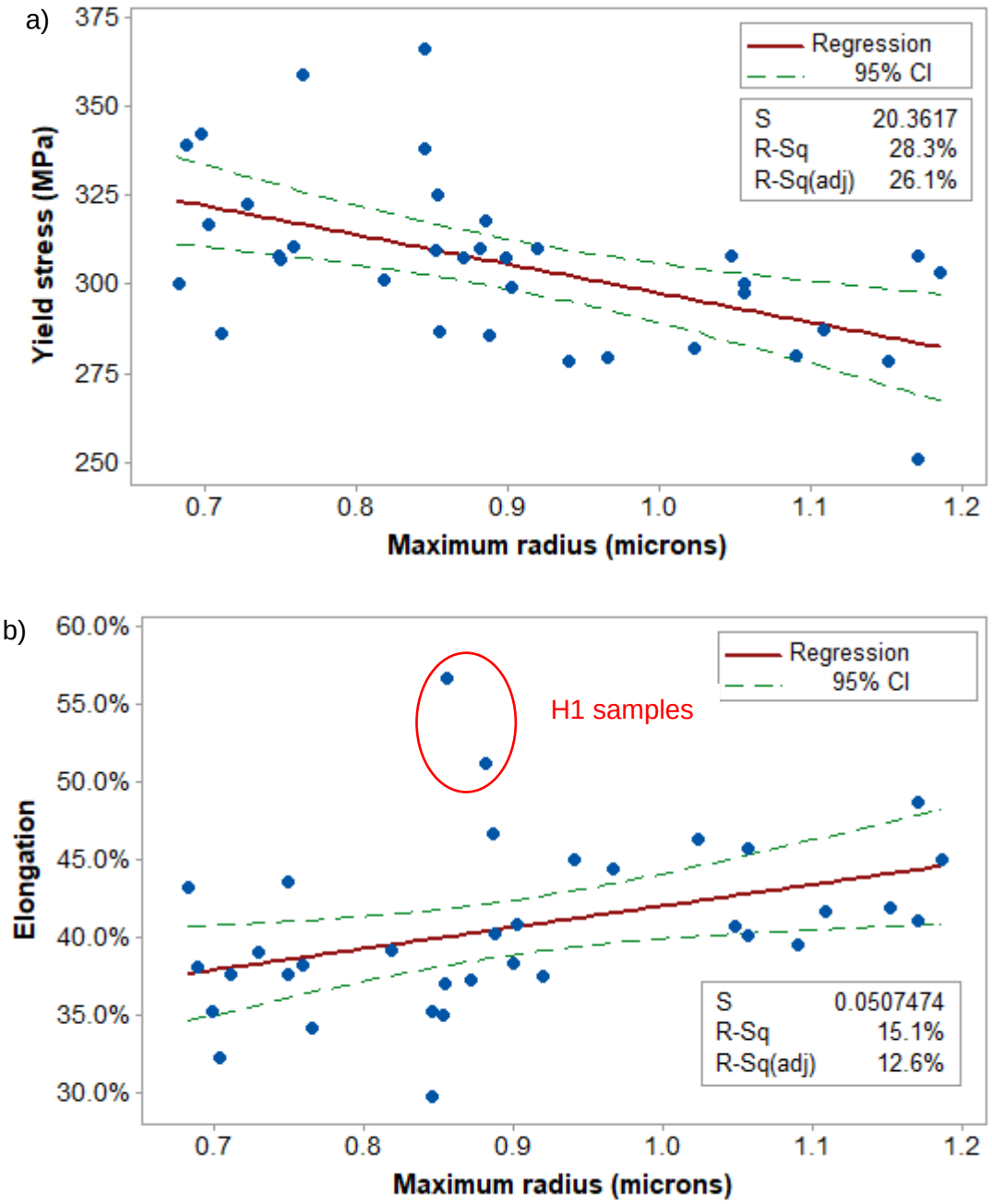

Figure 5.93 Correlation of maximum oxide radius with a) yield stress and b) elongation.

Mapping the oxide frequency and σ_{ys} according to experiment as shown in Fig 5.94 allowed comparison to existing literature (Eo et al., 2018) and visualisation of the effect of the experimental build conditions. A higher oxide inclusion number density for the WAAM samples was found in comparison to L-DED, and the least-squares best-fit line for the 316L WAAM experimental groups showed a decreased rate of σ_{ys} strengthening with oxide frequency. For each group, the HIT-HHI sample resulted in the least oxide number frequency. The cryogenic experiments deviated more strongly from the trendline indicating that the σ_{ys} is not well mapped by oxide frequency for these samples.

Also, the amount of strengthening between samples is greater than predicted by ODS in §5.8.2, other strengthening mechanism account for the increase in yield strength, whilst also increasing the oxide frequency.

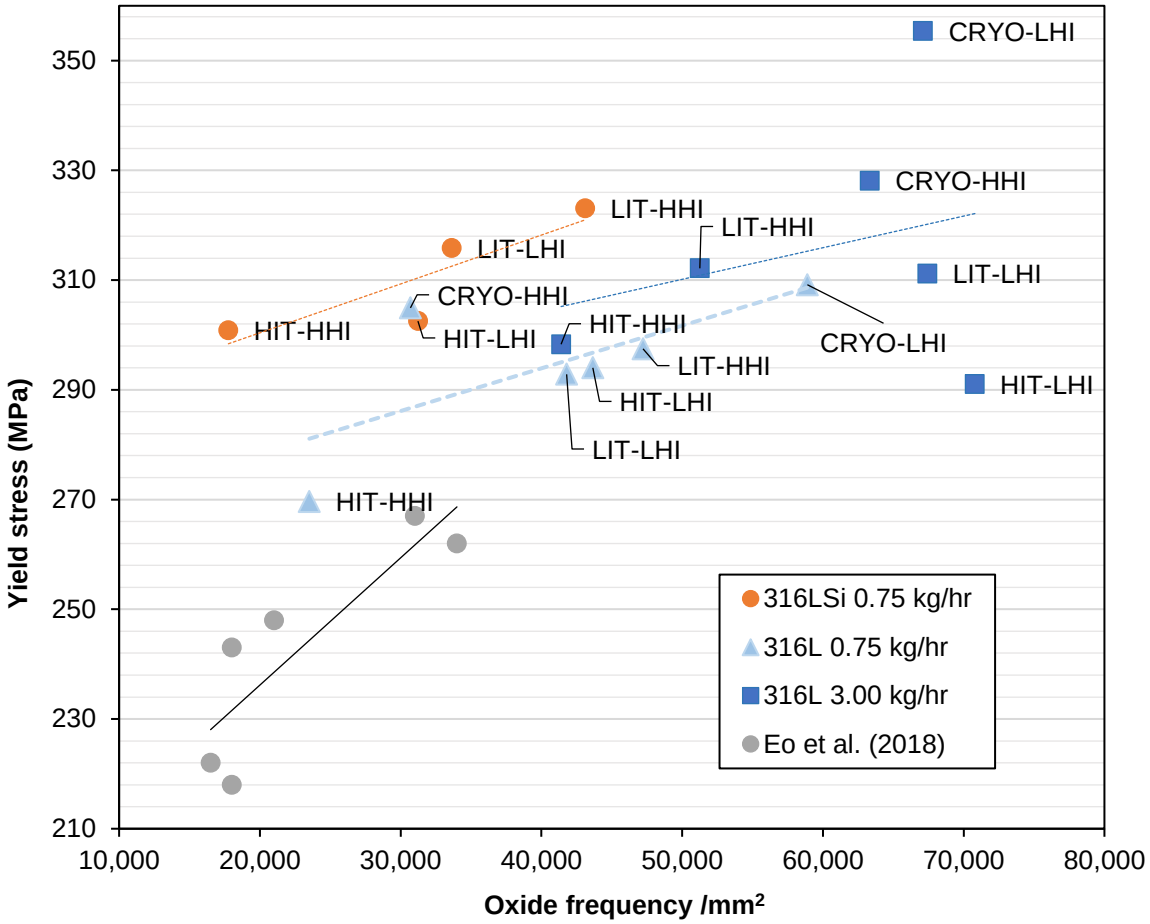

Figure 5.94 Average yield stress (σ_{ys}) versus inclusion number density for each test condition investigated. Trend-line of linear best-fit shows the correlation between inclusion number density and yield stress.

5.8.3 Solid Solution Strengthening

Using the empirical relationships derived by Pickering et al. (1969) the change in composition as a result of WAAM and its effect on the solid solution strengthening can be determined. The analysis of WAAM samples revealed the presence δ-ferrite phase, and the Feritscope measurements were used to estimate wt.%. This research EBSD analysis did not identify σ-phase as shown in §5.5.1.2, therefore, this element was not included in solid solution strengthening calculation. The predicted solid solution strengthening based for the 0.75 kg/hr and 3.00 kg/hr experiments are shown in Fig. 5.95, which allow comparison of these values to the σ_{ys} determined experimentally in §5.7.

The contribution to strength for each of the individual alloying elements are presented in Table 5.19, showing that the solid-solution strengthening between each experiment is mainly driven by the δ-ferrite and nitrogen content.

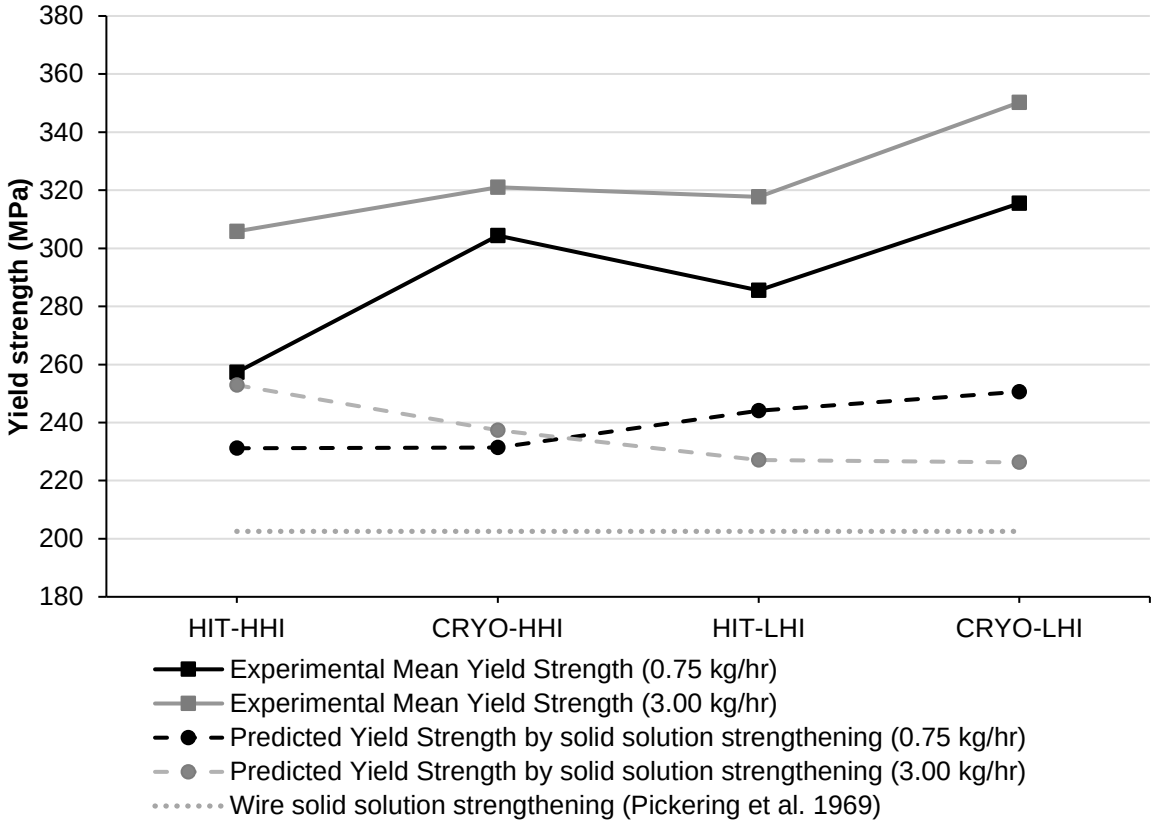

Figure 5.95 Solid solution strengthening predicted by empirical equations compared to the average yield strength determined experimentally (0.75 kg/hr).

Table 5.19 Contribution to strength from individual elements and δ-ferrite phase solid solution strengthening

		Contribution to strength by solid solution strengthening in WAAM samples relative to Type 316L wire (MPa)			
		CRYO-HHI	**HIT-HHI**	**CRYO-LHI**	**HIT-LHI**
0.75 kg/hr	C	3.89	3.89	1.77	4.60
	N	4.93	7.40	27.61	15.78
	Si	0.04	-0.36	-0.36	3.44
	Cr	-0.51	-0.51	0.23	-1.25
	Mo	1.08	1.22	1.78	1.64
	δ-ferrite (obtained from §5.5.3)	19.38	16.97	17.05	17.28
	Total	**28.82**	**28.61**	**48.08**	**41.48**
3.00 kg/hr	C	2.83	2.48	1.77	2.12
	N	15.28	32.54	5.42	6.90
	Si	0.04	-0.76	-0.16	-0.16
	Cr	-0.51	-0.14	0.60	0.14
	Mo	1.078	1.78	1.638	1.64
	δ-ferrite (obtained from §5.6.3)	16.05	14.05	14.48	14.18
	Total	**34.78**	**50.35**	**23.75**	**24.54**

It can be seen in Fig. 5.96 that an increase in nitrogen results in an increase in σ_{ys} as per the prediction empirical equation. The increase in strength varies depending on the deposition rate with 667 MPa/wt.% and 557 MPa/wt.% for 0.75 kg/hr and 3.00 kg/hr, respectively. This is slightly higher than the strengthening predicted by Pickering et al. (1969) of 493 MPa/wt%.

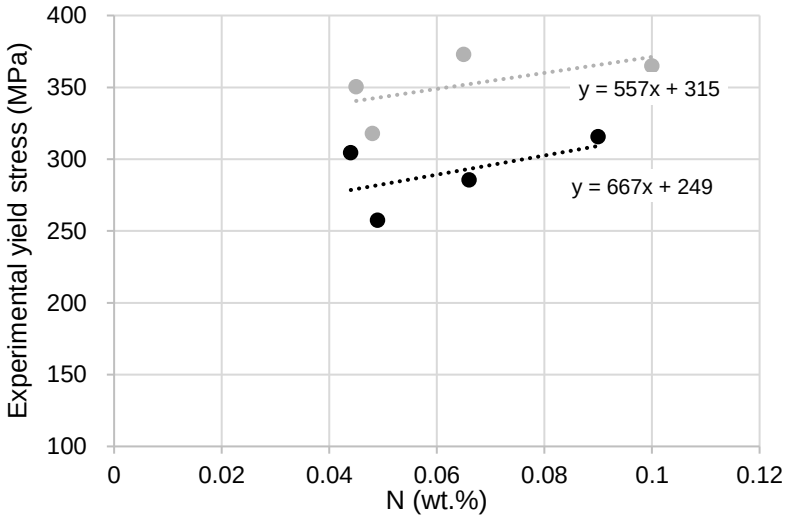

Figure 5.96 Relation between Nitrogen (wt.%) and experimental yield stress showing a trend of 667MPa/wt.% for 0.75 kg/hr and 557MPa/wt.% 3.00 kg/hr.

The chemical composition of the Type 316LSi experiments were not obtained, however, the δ-ferrite content based on Feritscope measurements showed 17.25 MPa and 15.25 MPa strength contribution for HIT-HHI and HIT-LHI, respectively.

5.8.4 Grain Boundary Strengthening

Grain boundary strengthening is a common mechanism by which the strength of single-phase wrought austenitic stainless steels may be enhanced for an otherwise annealed microstructure. The Hall-Petch relation indicates σ_{ys} increases in proportion to the product of a material:

$$\sigma_{gb} = K_{HP} d^{1/2} \tag{6.4}$$

With K_{HP} of 154 MPa (Kashyap and Tangri, 1990) the grain size approximations (Appendix B) from the EBSD analysis in §6.5.1.2 can be used to determine the contribution to strength for grain boundary strengthening. The large average grain size for the samples with interpass temperature control results in a negligible contribution compared to the overall yield strength as shown in Table 5.20. Despite the small area studied by EBSD and the associated uncertainty, the grain boundary strengthening displayed low sensitivity to grain size with a ±50% variation of the interpass temperature control experiment group mean of 94.7 µm, resulting in a contribution to strength fluctuation between 1.9 MPa-5.7MPa.

Table 5.20 Contribution to strength from grain boundary strengthening (0.75 kg/hr Type 316L)

Experiment	Grain Boundary Strengthening (MPa)
HIT-HHI	3.0
LIT-HHI	2.3
CRYO-HHI	76.8
LIT-LHI	3.0
HIT-LHI	3.3
CRYO-LHI	305.3

The grain boundary strengthening for the CRYO samples according to this relationship is much higher than those with interpass temperature control. The predictions of grain boundary strengthening for the CRYO correlate poorly with the experimental yield strength results. This suggests that Hall-Petch relation does not support the physical mechanisms of strengthening in WAAM, which has been suggested previously for L-PBF and L-DED with sub-grain cell boundaries also shown to have much more significant effect on strength and high-temperature properties (Zhong, 2017).

5.8.5 Summary of Strengthening Effects

A summary of the individual strengthening components outlined within the previous sections is presented in Table 5.21. This shows that dislocation strengthening comprises a major portion of the difference in yield strength found between experimental test conditions for 0.75 kg/hr. A graph comparing the sum of predicted components of strength to the experimental yield strengths is presented in Fig 5.97. For solid solution strengthening component for the LIT samples where OES chemical analysis was not performed, an average of the CRYO and HIT samples have been used for each heat input level. Grain boundary strengthening was omitted, as the impact was negligible for the interpass control samples and over-predicted for the CRYO samples as shown in §6.8.4. Accounting for solid solution strengthening, dislocation strengthening and ODS results in an over-prediction of σ_{ys} ranging from 2.5 % to 12.2 %. However, only considering the dislocation and solid solution strengthening, results in a reduction of the error to a maximum of 6.4 %.

Table 5.21 Summary of strengthening components for WAAM (0.75 kg/hr Type 316L samples)

Strengthening component (MPa)	**Predicted Strengthening (MPa)**					
	HIT-HHI	**LIT-HHI**	**CRYO-HHI**	**HIT-LHI**	**LIT-LHI**	**CRYO-LHI**
Dislocation	49.2	61.6	66.9	57.2	64.2	70.5
ODS	12.8	17.4	14.4	16.8	16.9	20.5
Solid solution	231.1	231.2	231.3	244.0	247.3	250.6
Experimental	269.6	297.5	304.9	294.0	292.8	309.2
Total (Dislocation + ODS + Solid Sol.)	293.1	310.2	312.7	318.0	328.4	341.6
Error (Dislocation +ODS + Solid Sol.)	8.7%	4.3%	2.5%	8.2%	12.2%	10.5%
Total (Dislocation + Solid Sol.)	280.3	292.8	298.3	301.2	311.5	321.1
Error (Dislocation + Solid Sol.)	4.0%	-1.6%	-2.2%	2.4%	6.4%	3.9%

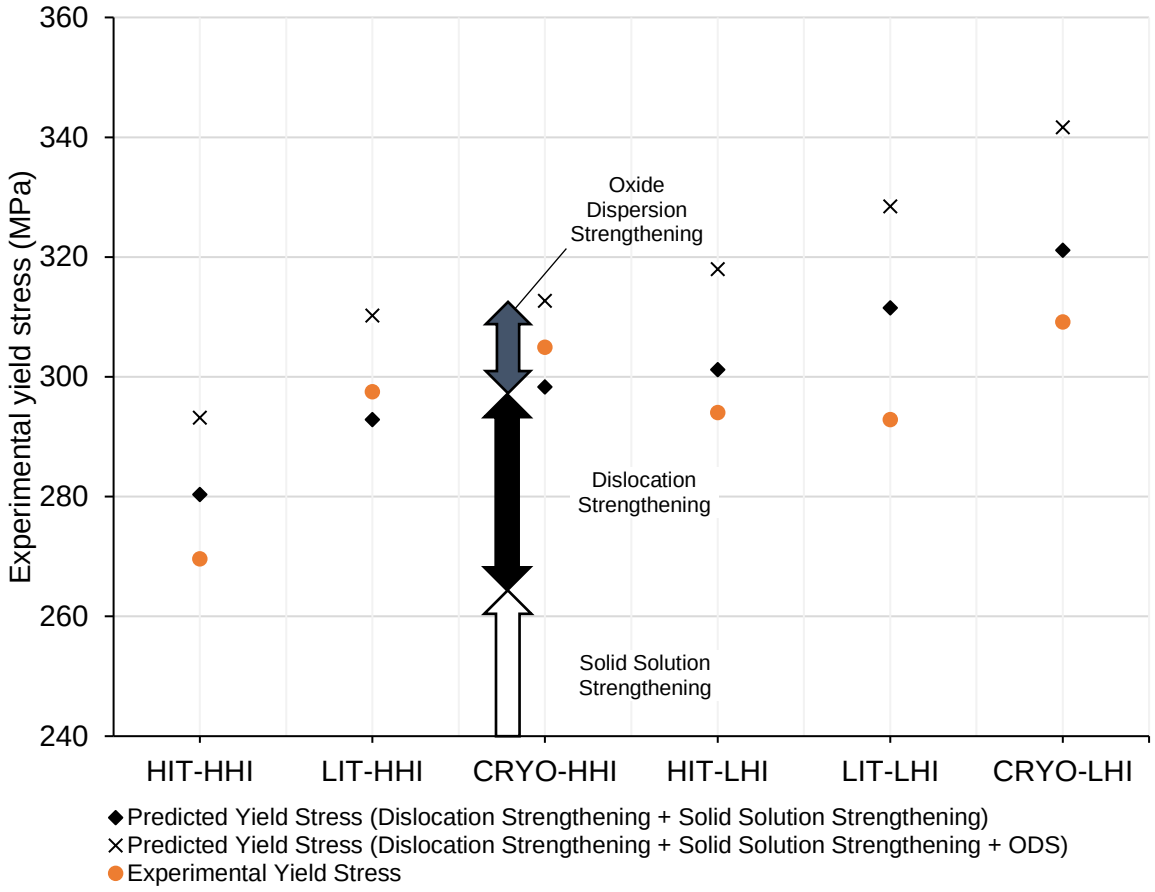

Figure 5.97 Comparison of the sum of predicted components of strengthening to the experimental yield strength.

Discussion

Chapter 6

6.1 Introduction

In this chapter, a discussion of the research presented is provided. This evaluates the research with respect to the research aim and objectives outlined in Chapter 1.

6.2 Review of the process selections, build strategies and additional processes in WAAM

This literature review investigated the range of process selections, the state-of-the-art in build strategies and additional processes that may be employed in WAAM. This allowed the techniques that may be adopted to address the heat-related material processing challenges introduced in Chapter 1, to be identified. The literature review identified the following findings, themes, and research gaps:

i. The primary process selections in WAAM were identified to consist of welding technology, welding process parameters, shielding gas, wire, motion system, fume extraction and the substrate and fixtures. This configuration was used to define the specification for the WAAM research machine used in this research. Whilst the primary process selections can influence the steady-state dynamics of the WAAM process, their influence on the heat-related material processing challenges concerning the mechanical properties, residual stresses and anisotropy are limited. Besides the welding parameters and shielding gas, the primary process selections regarding the substrate or wire, cannot be practically varied in-process resulting in a discrete, rather than a continuous change to the WAAM heat transfer dynamics. Additionally, the adjustment of welding process parameters is constrained by the maintenance of weld bead geometry (Geng et al., 2017), which may be insufficient where more significant adjustments are required to achieve satisfactory material properties.

ii. Review of the build strategies with respect to the management of the heat-related materials processing challenges in WAAM showed that time-based or temperature-based interlayer dwells are employed to manage heat accumulation and control the thermal boundary condition. As passive cooling techniques, they can have limitations regarding productivity, particularly for smaller components where interpass cooling comprises a larger proportion of process time. Also, the temperature decay to room temperature limits the cooling rate that may be applied.

iii. Additional processes were found to have been employed to elevate the material properties above the primary process selections. The range of additional processes that can be employed to improve aspects of WAAM part quality were classified by the timing of their application namely, in-process or inter/intra-layer, and the operative mechanism employed. This led to the categories including oscillation-

based, subtraction-based, deformation based, and heat transfer-based additional processes that can be used to improve WAAM quality as outlined in Fig 2.2.

iv. The capabilities of the additional processes were evaluated with those applied in-process able to affect the melt-pool dynamics directly, offering greater ability to modify grain nucleation rate, solute segregation, and the morphology. In-process cooling localised to the melt-pool can simultaneously affect melt-pool dynamics and the heat accumulation during the build. In-process cooling has been investigated by a limited number of researchers for WAAM, with efforts centred on inter-layer cooling (Henckell et al., 2017, Li et al., 2018a). Additionally, reduction in residual stress levels was reported by van der Aa (2007) for in-process cryogenic cooling in single-pass butt-welding, however, the effects of such a process had not yet been investigated for WAAM.

6.3 Review of welding metallurgy and WAAM of Type 316L stainless steel

This review provided a critical assessment of the current state-of-the-art in WAAM of Type 316L stainless steel. It presented the relevant aspects of welding metallurgy, reported WAAM material properties and the current understanding of the effects of the processing parameters. The findings were identified as follows:

i. Aspects of the welding metallurgy that affect the mechanical properties of WAAM of Type 316L stainless steel were outlined. Adsorption and vaporisation of oxygen and nitrogen affected the ODS and solid-solution strengthening. The δ-ferrite phase transformations δ-ferrite affected the solid solution strengthening. The stability of γ-austenite and processing temperature influence the occurrence of TRIP generating α'-martensite, whereas the stacking fault energy, texture and dislocation density influences the occurrence of the TWIP mechanism both of which act to increase the strength and ductility. Texture also affects the mechanical properties of Type 316L stainless steel, with competitive grain growth leading to anisotropic material properties.

ii. The existing literature for WAAM showed that the σ_{ys} and UTS requirements can be readily surpassed by WAAM (Rodriguez et al., 2018, Chen et al., 2017b). However, the ductility and E were shown to have unsatisfactory performance relative to conventionally produced material. The mechanical properties displayed scatter within the results, and the source of the strength and ductility to date had not been related to the processing parameters or microstructural properties. Previously the higher microstructural refinement has been cited as the cause of the additional strengthening for L-PBF, however, WAAM Type 316L, large epitaxial grain growth was observed. This is problematic for use of WAAM for end-use Type 316L parts, where mechanical properties are required to be repeatable for qualification and

certification purposes. Also, for topological and generative design to be used in WAAM to exploit the design freedom provided by AM, accurate mechanical properties, and an understanding of the directionality relative to the build direction is required.

iii. The primary process selections and additional processes that have been investigated for Type 316L were reviewed. Whilst Wang et al. (2019a) investigated two different heat input levels, and Wu et al. (2019a) varied the interpass dwell period between 0-15 s. For both investigations, the levels only differed by a small amount, not reflecting the true variation that may occur for stable bead deposition in WAAM or the differences in microstructural development that might occur. There has been a drive to increase deposition rates in WAAM to improve production efficiency for large components (Martina et al., 2019), however, there has been no systematic comparison of the difference in material properties as a result for Type 316L. Furthermore, no studies had focused on additional cooling for Type 316L, despite the possibility of interrupting large epitaxial grain growth and the production efficiency benefits. These areas were identified as major research gaps, with the effect of heat input, deposition rate, interpass temperature control and additional cooling comprising the focus of this research.

6.4 The design, specification, and assembly of a WAAM research machine

From a review of the literature in §2.5, a WAAM research machine requirement specification was generated. The priorities that guided the design process was the ability to produce single-pass wall geometries, monitor the interpass temperature and provision of additional cryogenic cooling behind the arc. The welding technology utilised in the WAAM research machine was an ESAB Aristo 4004i MIG machine employing pulse technology typical of state-of-the-art power supplies and the co-axial wire feed provided by the MIG set-up is the most readily manipulated set up for producing complex, freeform structures. The WAAM research machine enabled the experiments to be carried out and is the first research machine reported to employ in-process cryogenic cooling localised to the melt-pool for WAAM.

6.5 Research methodology: Validity and Limitations

6.5.1 Experimental design, factors, and levels

i. The experiments were designed and carried out to establish the range of material characteristics and the mechanical performance of Type 316L stainless steel components produced using WAAM. The primary process parameters of heat input, deposition rate and wire composition were investigated alongside the cooling

strategies of additional in-process cryogenic cooling localised to the melt-pool and interpass temperature control.

ii. This research aimed to determine the effects of the investigated parameters rather than optimisation. The process parameter levels were specified to represent the widest possible range of process parameters. The upper interpass temperature level (150°C) was extracted from the maximum temperature passively achieved by continuous deposition for the LHI 0.75 kg/hr experiments. The lower interpass temperature level (60°C) represented a comparatively cool build strategy, more likely to be adopted for larger parts that have longer tool paths between layers. The deposition rate was selected from the existing literature, whereas the heat input was determined from the upper and lower travels speeds that were possible, whilst maintaining steady deposition bead geometry. It can be seen in Fig 6.1a that the power in watts (related to the heat input in kJ/mm) and TS's investigated covers the average and upper limit relative to previous research. Besides, Fig 7.2b shows that the lower deposition rate 0.75 kg/hr reflects approximately an average of the currently investigated studies in the literature with the 3.00 kg/hr falling slightly higher than the deposition rates currently investigated for Type 316L. Due to the complex interactions, for example, regarding surface homogenisation, TRIP and TWIP, assumptions of linear effects on mechanical properties between the levels cannot be assumed.

a)

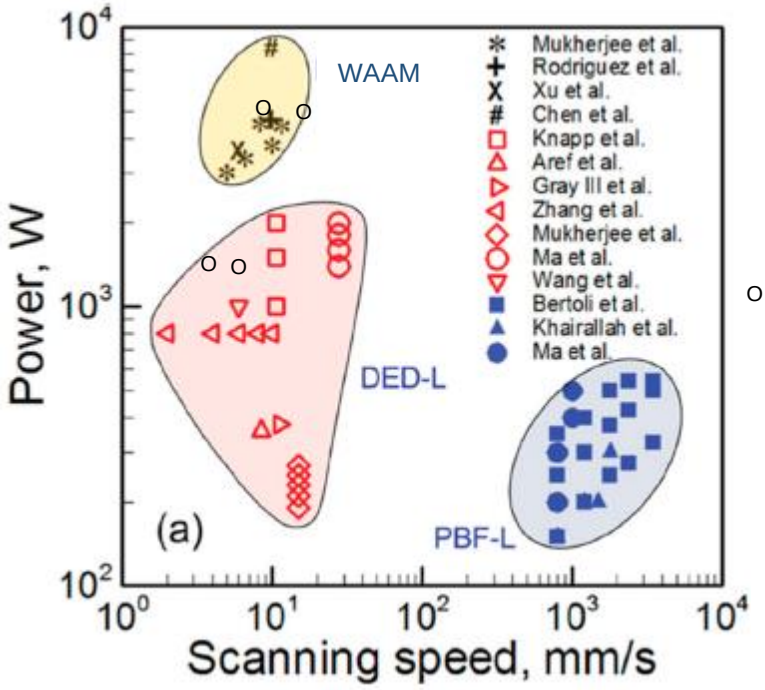

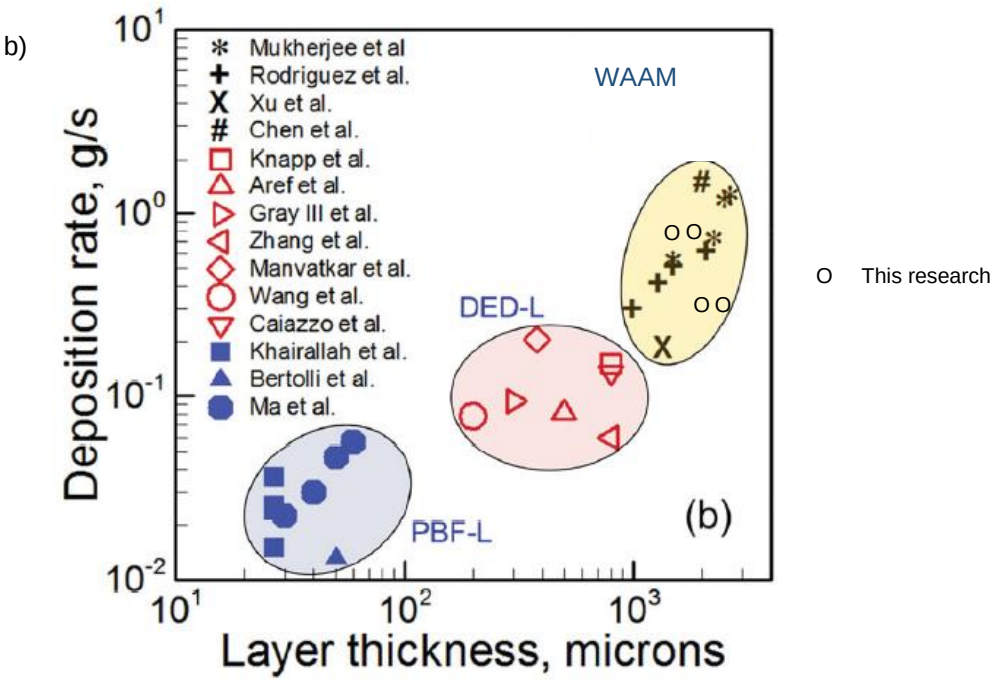

Figure 6.1 Power and scanning speeds of several investigations into AM of Type 316L stainless steel in the literature. Adapted from (Mukherjee et al., 2016).

6.5.2 Materials characterisation

i. Image analysis

The results qualitatively analysed the macrostructure and microstructure of the experimental samples at the layer interface, and quantitative analysis was performed using EBSD and measurement of oxide inclusions and feature size to derive cooling rates. To retrieve the results the stages of sample preparation, image collection and image analysis were followed. The samples were sectioned, mounted and polished according to standard procedures described in ASTM E3 (2011). Micro-etching was carried out according to (ASTM E407, 2007). The specified etching time of <15 seconds and manual etch procedure led to a high relative error in exposure time. Additionally, differences in corrosion resistance can be expected between the samples, affecting the reactivity of the metal to the etchant. Despite these differences the etch allowed the δ-ferrite and γ-austenite was distinguishable in all samples.

For measurement of oxide inclusions, pixel resolution presented a limitation the minimum particle size that can be measured. For the 4000x magnification with the Keyence VHX600 microscope resulted in a distance of 0.01 µm/pixel. The minimum particle size to be identified was specified upon the analysis in ImageJ as 0.058 µm for all micro-graphs, ensuring that that the smallest particles were approximated by more than 5 pixels. As shown in the typical example of oxide distribution in Fig. 6.2 a small number of inclusions (<40) are in the bin 0.06 - 0.12 µm. It can be inferred that an even smaller number of oxides fall below the particle size limit. However, as the overall count of particles was over 1000, the smaller

particles that were not captured have a negligible impact on the mean oxide radius, volume fraction and subsequent ODS calculation.

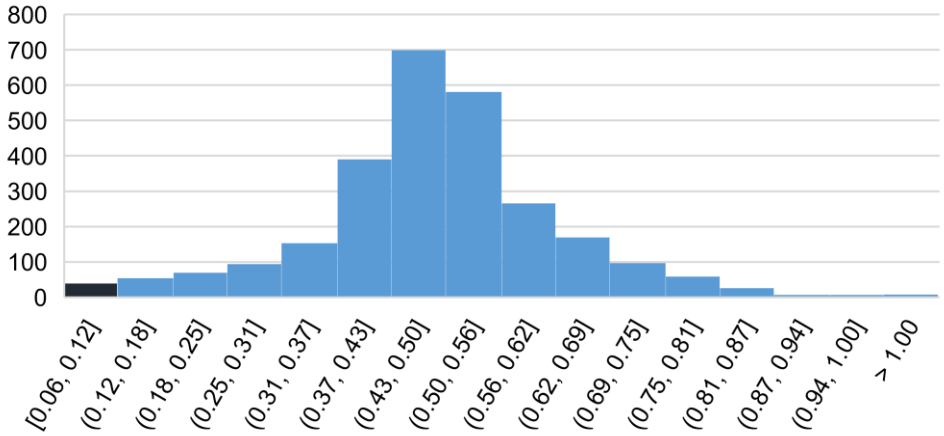

Figure 6.2 Histogram of oxide inclusion diameter distribution highlighting the bin above the minimum size threshold specified in this research.

ii. Tensile specimen location and sizes

For each experiment, a single wall sample of 150 mm length and 100 mm height, with variable width depending on the experiment was built. The sample height was limited by the Z-Axis range on the WAAM research equipment. Based on the ASTM E8 sub-size specimen ratios, and available sample height of 100 mm, miniaturized tensile specimens of 75 mm height and 3.30 mm thickness were produced. Tensile properties and deformation mechanisms may not be representative of larger structures if any dimension is in the order of its microstructural features (Strnadel and Brumek, 2013), so this was considered when specifying tensile coupon thickness. It is known that size effects on tensile properties are negligible for a critical thickness of 6 - 10 times the average grain size (Koyama et al., 1991). Grains of size 150 - 200 µm were also reported by Chakkravarthy and Jerome (2020). Assuming similar grain sizes in this research, with 3.3 mm tensile coupon thickness, grain size effects were expected not to be significant. This was confirmed later in the EBSD analysis in §5.5.1.2.

6.5.3 Mechanical testing

It is known that E has the highest levels of uncertainty when determined by uniaxial testing compared to UTS and σ_{ys} (Lord and Morrell, 2010). However, the Instron 2630-106 clip gauge extensometer used to record strain in this research was classified as class 0.5 according to BS EN ISO 9513 (2012), which is recommended according to the National Physical Laboratory Guidance for E measurement (NPL, 2006). The typical uncertainty for the strain measurement for this class of extensometer is limited to ±0.3%. For the range of E values reported (34.3 GPa-237.3 GPa), this variation in strain equates to an error of approximately ± 0.3 GPa to ± 0.7 GPa. Whilst this error was not accounted for in mechanical analysis error bars it represents a small proportion of error compared to the between-

sample error. Other sources of uncertainty in mechanical testing include force and strain measurement at the load cell, specimen dimension measurement, bending and misalignment of the sample during testing and data analysis.

6.5.4 Prediction of strengthening mechanisms

i. Use of empirical equations for predicting solid solution strengthening

The solid solution strengthening can be calculated analytically according to the equations developed by Fleischer (1961). However, the lack of reported data for the rate of change in unit cell spacing to the fraction of elements in solid solution required for the use of Fleischer (1961) equation within the literature for the alloying elements stainless steel, has led to multiple authors to develop empirical equations for solid solution strengthening. Sieurin et al. (2006) demonstrated high levels of correlation for Pickering's equation (equation 4.1) (p-value $<5\times10^{-16}$ and R^2 of 0.95 for the hundreds of stainless steel compositions studied. This shows that the accuracy of empirical formulas can capture the effects of alloy content on the solid solution strengthening.

i. Orowan bypassing mechanism for calculating ODS

The inclusions were assumed to be amorphous based on results for oxide inclusions for L-PBF (Krakhmalev et al., 2018). Therefore, as explained in §4.6.3.1, the operative mechanism on deformation can be assumed to be based on either Orowan dislocation bypassing mechanism or dislocation shearing. The radius of the particles reported in the results used with Fig 4.21, identified the Orowan bypassing mechanism, rather than the particle shearing mechanism as the operative mechanism (Ma et al., 2014). This allowed the ODS to be determined, following the same methodology as other authors (Smith et al., 2019, Ma, 2011). The Taylor factor, used in the calculation of ODS was assumed to be M=2.45 to account for the strongly textured microstructure, rather than the M=3.06 for a randomly textured material which has been used previously and might over-estimated results for directional additive manufactured material. To determine the ODS the size and volume fraction of the oxide inclusions was required. The micrograph size and the number of repeats used to obtain these parameters represent a significant increase in the number of inclusions mapped compared to the existing literature that has studied oxide inclusions in AM Type 316L material (Eo et al., 2018, Lou et al., 2018, Yan et al., 2018, Saeidi et al., 2015).

6.6 Discussion of the results

This section discusses the major findings regarding the effects of heat input, cooling strategy for each deposition rate on the microstructural characterisation, the mechanical properties and strengthening effects. The effect of wire composition based on the use of Type 316LSi wire with interpass temperature control is also discussed.

6.6.1 Effect of processing parameters on microstructural characterisation

This research qualitatively evaluated the macrostructure and microstructure at the layer interfaces. The microstructural morphology, texture, scale were found to vary with heat input, cooling strategy, and deposition rate.

6.6.1.1 Phase morphology

Through the wide-ranging build parameters explored in this research, several features that have not previously been identified in WAAM of Type 316L were found. Large volumes of speckled black-brown etching features were observed (see Fig 5.11-5.14 and Fig 5.39-5.42), which in this research were identified as regions of inter-dendritic δ-ferrite or secondary γ-austenite with the colour indicative of some δ-ferrite content. Similar features have been visible in the several studies of stainless steel (Wu et al., 2015, Fredriksson, 1972, Saied, 2016, David, 1981, Farshidianfar et al., 2016) several of which are shown in Fig. 6.3, alongside the inter-dendritic structures identified in this research (Fig 6.3d).

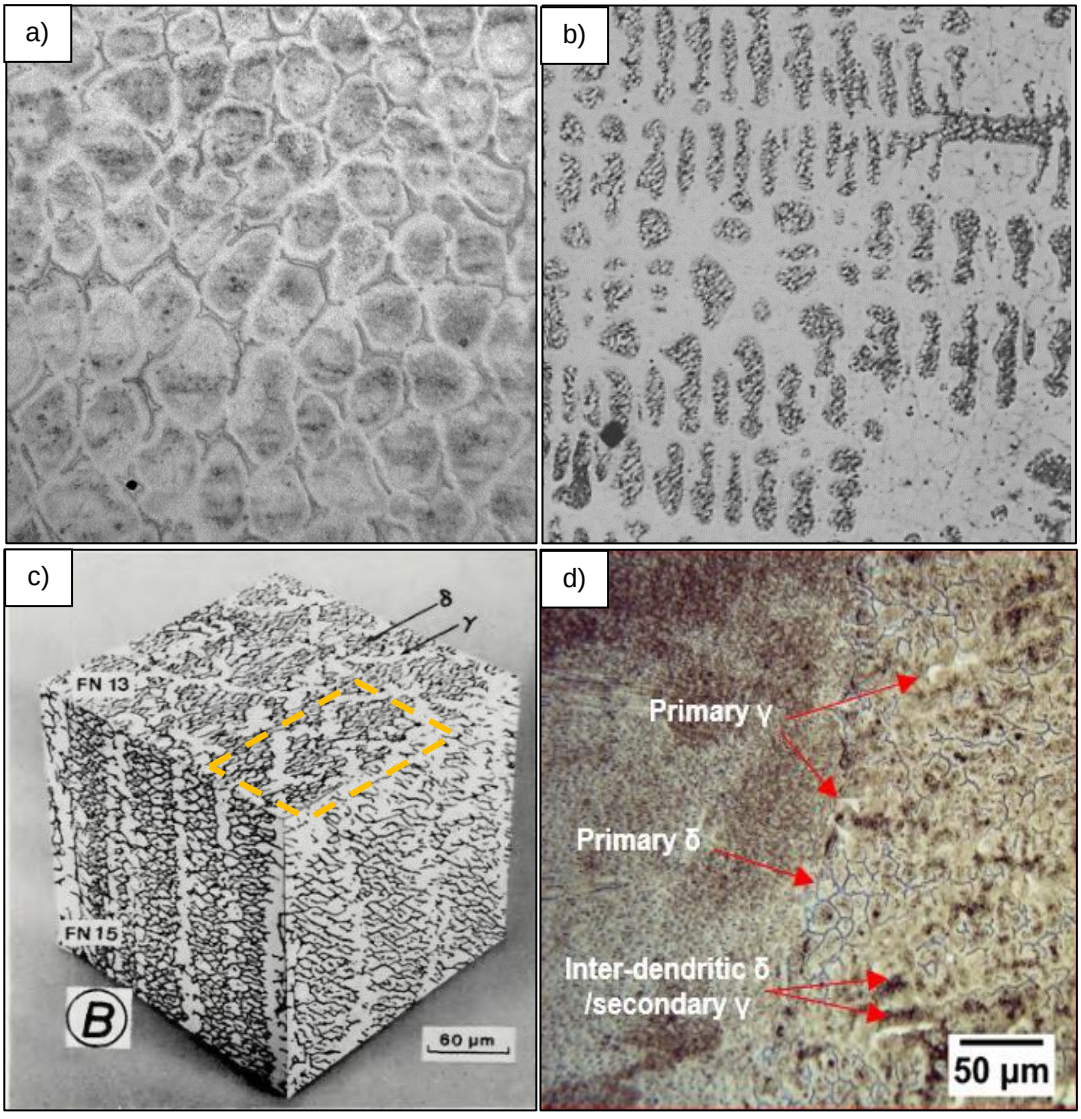

Figure 6.3 Inter-dendritic δ-ferrite identified within the literature a) L-DED (Farshidianfar et al., 2015) b) Quenched directional solidification (Fredriksson, 1972) c) AF lathy solidification (David, 1981) d) Author's research reproduced from Fig. 6.13.

In particular, Fig 6.3b shows similar cellular formations at the edge of the deposit and Fig. 6.3c shows the primary γ formation. Saied (2016) reasoned that this was the result of peritectic solidification, where the remaining δ-ferrite is supplanted by the more thermo-dynamically stable secondary-γ phase, the extent to which determines the speckled effect. Due to increased chemical stability caused by early solute segregation, the enriched primary δ-ferrite dendrites remain stable to room temperature. This effect is supported by several authors, who refer to the phase as a divorced eutectic (Inoue and Koseki, 2007, Lippold and Savage, 1979). The white-etched dendrites were identified as primary γ from the FA lathy ferrite solidification mode as shown in Fig. 6.3c. The consistency of the white colouring contrasts to the inter-dendritic/secondary-γ, which developed later during the solidification process from unstable δ-ferrite. The difference in dendrite thickness compared to the dark etching δ-ferrite in the same local regions supports the identification as different decomposition rates as would be expected for stable γ-austenite dendrites compared to the metastable δ-ferrite.

The peak melt-pool temperatures can be expected to be similar for 0.75 kg/hr CRYO-HHI in comparison the 0.75 kg/hr LIT-HHI. However, the LIT-HHI sample displayed a thick continuous dark etching δ-ferrite whereas thin, the CRYO-HHI samples had thin δ-ferrite dendrites large volumes inter-dendritic features present. Due to the cryogenic processing temperatures, there is even more limited opportunity for solid-state transformation of δ-ferrite dissolution in the CRYO-HHI experiment, confirming that the CRYO cooling was able to stifle the δ-ferrite network development during solidification. The greater volumes of secondary γ can be attributed to the melt reaching the γ-austenite transformation temperature more rapidly.

Austenitic cellular sub-grains and dendrites were also identified within limited areas of the WAAM Type 316L samples as presented in §5.5.1.1 and §5.6.1.1, particularly for the CRYO-LHI sample. Similar sub-grain structures have only previously been shown for L-DED or E- DED at lower deposition rates (Liu et al., 2018, Yang et al., 2016). This is notable, as the cellular sub-grain structures are cited to be responsible for the high levels of strength and ductility in L-PBF of Type 316L stainless steel (Wang et al., 2018c, Shamsujjoha et al., 2018). The presence of cellular sub-grain structures in this research, even in small amounts shows potential for future developments to capture these effects for WAAM.

The micro-graphs also showed a change in the solidification structure size and amount of δ-ferrite dissolution for lower and upper sections of the build height studied in this research. This showed that even with interpass temperature control implemented to maintain a consistent thermal profile, the thermal boundary conditions vary with build height enough and impact the microstructural feature development, with greater δ-ferrite dissolution in the upper regions. The HIT samples also displayed less extensive δ-ferrite networks compared

to the LIT samples. These results indicate that with lower cooling rates, the δ-ferrite dissolution increases with greater time spent within the L + δ + γ phase zone provides more time for the decomposition of δ-ferrite once γ-austenite becomes stable leaving partially decomposed inter-dendritic δ-ferrite. This is supported by several authors state that higher cooling rates result in *more* retained δ-ferrite (Martorano et al., 2012, Sriba et al., 2018, AghaAli et al., 2014). This is a different mechanism to reported results or power beam processes and L-PBF, where δ-ferrite decreases due to a change in solidification mode to primary austenite.

The δ-ferrite shape was also observed in the EBSD analysis of §5.5.1.2, becoming rectangular and long-slender with a greater directionality in the thin lathy microstructures and more roundish for the thick vermicular structures in agreement with (Kokawa et al., 1989). The morphology of the phases developed can be used to make inferences about the corrosion resistance, and impact toughness, however, with solute strengthening occurring but captured in the overall δ-ferrite wt. (%) used to determine the solid solution strengthening. The 0.75 kg/hr CRYO-HHI displayed the widest variety of δ-ferrite shapes which can be attributed to the cryogenic coolant effectively removing heat toward the surface, but with low thermal conductivity of Type, 316L preserves heat further below the surface and resulting in variable dendrite formations.

6.6.1.2 Texture

The texture and grain size for the interpass temperature control experiments are in agreement with Chakkravarthy and Jerome (2020) with strong alignment to the build direction with grains of approximately 150-200 µm length. Substantially different texture strength was observed for the cryogenically cooled experiments. In particular, the 0.75 kg/hr CRYO-LHI showed low texture with much smaller grains approaching random texture. Additionally, the CRYO-HHI sample showed strong alignment to the <111> direction. The same effect was previously shown by increasing the heat input by adjusting the torch angle (Chakkravarthy and Jerome, 2020). This plane offers the greatest passivity to chemical attack and producing WAAM parts with this alignment may be preferred application where the surface is exposed to corrosive media. Besides, the texture can have a major impact on the resultant mechanical properties and is discussed further in § 6.6.2.2.

Whilst the EBSD analysis was performed for the 0.75 kg/hr samples, the increase in power and travel means that increased texture toward the heat source can be expected for the 3.00 kg/hr samples. This can be visualised by the schematic of the melt-pool shape in Fig. 6.4 with grain growth following the contours of the high power/high-speed melt pool. This was confirmed qualitatively with the higher number of elongated macro-grains evident in Fig 5.39 (3.00 kg/hr) compared to Fig 5.10 (0.75 kg/hr samples) and also the greater dendritic

alignment to the build direction in the optical micrographs of the 3.00 kg/hr sample layer interface.

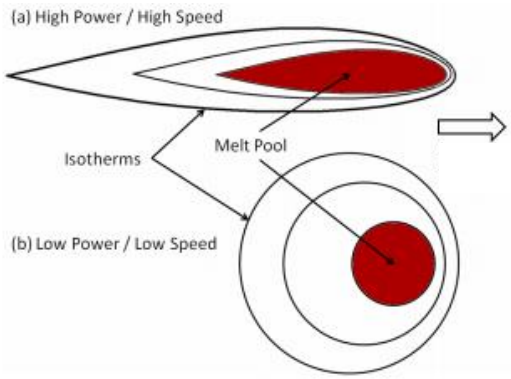

Figure 6.4 Schematic of the melt-pool shape with travel speed and power, adapted from (Carter et al., 2012)

6.6.1.3 Cooling rates

By studying the microstructure length scale for the 3.00 kg/hr experiments, higher cooling rates were found compared to 0.75 kg/hr experiments. This was supported by thermal profile results in §5.4, which showed the greater drop in temperature with time and reduced the dwell period required to achieve interpass temperature for the 3.00 kg/hr experiments for the same heat input levels in kJ/mm. The cooling rates reported were less than the 10^6 K/s in L-PBF but similar to the level of 10^4 K/s - 10^2 K/s found for L-DED as shown in Fig 6.5 with the cooling rate for 3.00 kg/hr CRYO for the fine dendrite zone exceeds the cooling rates found by Ma et al. (2017). Note that the offset of some of the coarse 0.75 kg/hr data points is due to use of SDAS as opposed to PDAS or PCAS which has a slightly different relation of spacing to cooling rate (Yin and Felicelli, 2010).

However, many of the 3.00 kg/hr coarse regions also overlapping with L-DED. The interaction time with existing material is reduced with 3.00 kg/hr experiments due to the much higher TS's used leading to less heat absorption and greater cooling rates despite equivalent linear heat input. Additionally, the wire is introduced into the arc at a much faster rate resulting in a chilling effect (Adebayo et al., 2014). The CRYO-LHI 0.75 kg/hr samples showed the greatest variation of local cooling rates throughout the sample, supporting the EBSD analysis (§5.5.2.1, Fig 5.25), and heterogeneous distribution of δ-ferrite with both globular and large continuous dendrites for the area examined in the CRYO-LHI 0.75 kg/hr sample.

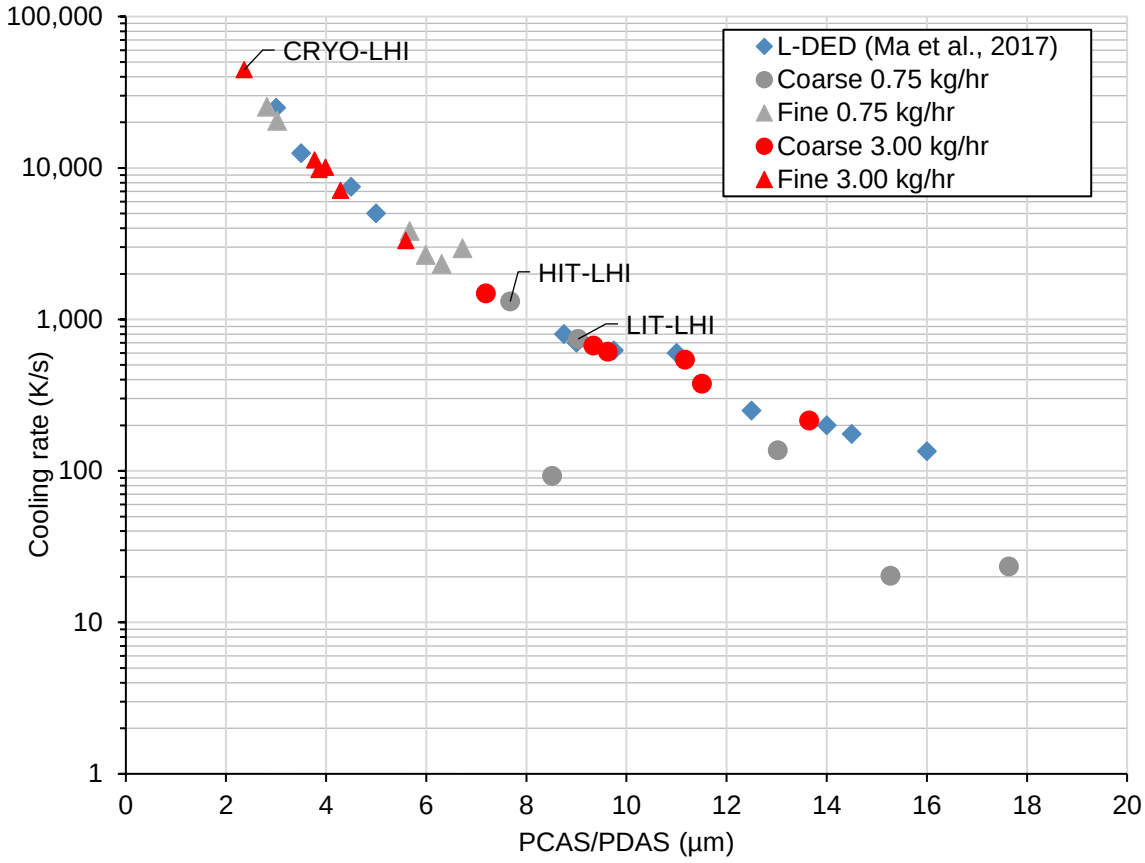

Figure 6.5 Cooling rates and PDAS/PCAS for the experimental samples compared to existing literature.

Unusually, the HIT-LHI 0.75 kg/hr sample displayed much finer δ-ferrite dendrites than the LIT-LHI sample as illustrated in Fig 6.5. As higher interpass temperatures typically result in coarsening of the morphology (Solomon and Solomon, 2010) and lower cooling rates are expected according to the thermal profiles outlined in §5.4. The refined microstructure also corresponded to high levels of micro-hardness of up to 245 HV. To check this result, several repeats of Vickers' Micro-hardness test were performed, and previously measured regions from other samples repeat tested to confirm the result. A possible mechanism of the significant refinement of the microstructure within the HIT-LHI sample is a replication of the conditions of surface homogenisation techniques for this build parameter. This is where refines the microstructure by the melting of the surface with overlapping weld passes, without depositing additional material. This can result in significant refinement as outlined by Elmer et al. (1989b) where a large PDAS and secondary dendrite arm spacing of 35 µm, was refined to a PDAS of 10 µm to a depth of 1.5 mm. The HIT-HHI microstructure also shows some refinement in coarse regions relative to the LIT-HHI indicating that surface homogenisation may also be active within the HHI experiments.

6.6.1.4 Oxide size and distribution

The results in §5.5.2 and §5.6.2 showed that mean volume fraction for the 0.75 kg/hr experiments (0. 006 ±0.001, Type 316LSi and 0.008 ± 0.004, Type 316L) was slightly lower than the 3.00 kg/hr experiments (Type 316L, 0.011). The mean oxide radius was slightly

higher for the 0.75 kg/hr experiments (0.243 µm ± 0.020 Type 316LSi and , 0.240 µm ± 0.024 Type 316L) compared to 3.00 kg/hr (Type 316L, 0.188 µm). The oxygen wt. (%) was slightly lower than that reported by Elmer and Gibbs (2019) also for WAAM (0.032% compared to 0.041%).

The values for oxide radius and volume fraction were similar to that reported by Weisheit et al. (2016) for a sample of 5 layers of 4 weld beads beside each other by arc welding without any shielding gas (0.008, 0.205 µm). For powder L-DED, oxides of radii 0.05-0.075 µm were identified with a volume fraction ~0.002 (Smith et al., 2019). The oxide inclusions identified in this research were larger, however, the inclusions were of higher volume fraction. The radius is magnitude ~10 larger than L-PBF where radii of 0.023 µm have been reported (Lou et al., 2018). Due to the relatively high volume fraction across all experimental samples, the ODS was predicted to be higher than that reported in the literature for L-PBF (Saboori et al., 2020) and L-DED (Smith et al., 2019), contributing up to 10 % of σ_{ys} in this research. This is somewhat expected due to the lower cooling rates in WAAM, as well as reliance on through-torch inert shielding rather than a controlled atmospheric chamber.

This research was the first to investigate oxide inclusion size and distribution with variation in wire composition, heat input, deposition rate and cooling strategy for WAAM. The additional silicon in Type 316LSi resulted in fewer, slightly larger oxides within the WAAM material. This is likely due to its role as an oxidiser, protecting the melt-pool from oxidation, a theory supported by Eo et al. (2018). However, the heat input had more of a significant effect than wire composition. The LHI experiments resulted in higher ODS, which can be attributed to the limitation of the Ostwald Ripening phenomena at lower temperatures (Suzuki et al., 2001), preventing the coarsening and coalescence larger inclusions and diffusion of smaller particles shown in Fig 5.90. As discussed in § 5.8.2.2 the deposition rate had a minor, but significant effect on the ODS for WAAM. This is in agreement with findings by Eo et al. (2018), where higher power energy source resulted in greater ODS for powder L-DED.

6.6.1.5 Chemical analysis

The chemical analysis allowed the effect of the processing parameters on alloy composition to be evaluated. The N content, which strongly affects solid solution strengthening and δ-ferrite to γ-austenite ratio was influenced by the deposition rate. The CRYO strategy with LN_2 showed no direct increase in N content in the deposition material except for the CRYO-LHI 0.75 kg/hr sample which showed up to 0.09 wt%, however, this was less than the 0.1 wt.% identified for HIT-HHI 3.00 kg/hr without LN_2. For all instances, the N wt.% remained below 0.1%, which is a fairly low level of adsorption relative to the wire (0.034 wt%) and translates to a relatively small amount of solid solution strengthening as presented in §5.8.3. This suggests that despite the proximity of the cryogenic cooling gas to the arc in this

research and the additional nitrogen within the atmosphere for the CRYO experiments, the shielding gas column remained an effective barrier to atmospheric gases. Weisheit et al. (2016) found N of up to 0.6 wt.% for multiple welding passes of Type 316L with no shielding gas. That the shielding gas remained relatively undisturbed is notable as several authors (van der Aa, 2007) have previously remarked on arc disruption with cryogenic cooling to be a major obstacle to cooling locally to the welding arc, consequently required a greater distance between the cooling nozzle and the arc.

As the most volatile element in Type 316L (Taparli et al., 2020) a change in Mn wt.% was noted between experiments. Previously, up to 0.0060 wt.% change has been predicted for WAAM (Mukherjee and DebRoy, 2019). The LHI and LIT/CRYO experiments were generally within this expected loss range relative to the wire feedstock, however, losses for the 3.00 kg/hr HIT-HHI and all HHI 0.75 kg/hr samples in this research were greater (up to 0.122 wt.%). This indicated that the higher interpass temperature and greater heat adsorption with the slower TS's for 0.75 kg/hr can lead to additional Mn losses. As an austenite stabliser, it improves the stability of γ-austenite under thermomechanical cycling with respect to strain induced martensitic transformation.

6.6.1.6 Phase composition

The ferrite content of the experimental samples was reported in Fe% was presented in (§5.5.3 and §5.6.3 for 0.75 kg/hr and 3.00 kg/hr respectively). The Fe(%) is an important measure with regards to the as-built phase composition and also the phase composition of deformed samples, as it aids in the understanding of the deformation mechanisms that may occur. The relationship of Fe(%) with the mechanical properties is discussed in §6.6.2.

The reported average Fe(%) for all experiments was 6.5±0.8 Fe(%) for all experiments was above the 3 % recommended by Brooks and Thompson (1991) to avoid hot cracking, and no cracking defects were observed in any of the experimental samples. This research found that the Fe(%) of the fractured tensile specimens was higher than the reported Fe(%) of the metallurgical specimens extracted from the same locations. Strain can shift martensitic γ-austenite → α'-martensite transformation start temperature toward room temperature (Sitko et al., 2010). This transformation occurs for the TRIP class of steels and the transformation induces high levels of strength and ductility as discussed in §3.6.2. As α'-martensite is a magnetic phase and cannot be distinguished from the δ-ferrite by the Feritscope, this can account for the increase the Fe(%) observed post-fracture. This transformation has been demonstrated in L-PBF Type 316L material at low temperatures (Hong et al., 2019) and it is known to also occur in deformed wrought austenitic stainless steels (Xiong et al., 2015, Liu, 2016). As deformation also significantly increases the dissolution rate of the metastable δ-ferrite phase (Liu et al., 2017b, Mataya et al., 2003) the growth in Fe (%) for the fractured

tensile specimens can be attributed to a strain-induced α'-martensite transformation exceeding the amount of δ-ferrite dissolution.

The difference in Fe(%) between metallurgical and tensile specimens, however, was not maintained for the CRYO (0.75 kg/hr) specimens (see Fig 5.34) where the fractured tensile specimens had similar Fe(%) values to the metallurgical samples. The temperature at which 50% of the α'-martensite is produced after 30% true deformation under the tensile condition and is calculated as -27.3°C according to the equation by (Eichelman and Hull, 1953). This temperature could be expected to be readily achieved with the LN_2 with a boiling point of −195.8 °C, although the exact surface temperatures were not recorded. Therefore, a possible cause of this behaviour is the inducement of metastable α'-martensite in-process by the cryogenic processing temperatures. This may be found for the CRYO-0.75 kg/hr samples due to the greater interaction time at the TS's compared to 3.00 kg/hr. However, for TRIP to be effective the onset of α'martensite occurs at the later stages of deformation. The α'-martensite reversion process may occur explaining the reduction in Fe(%) for the CRYO-LHI specimen post-fracture.

The LIT-LHI, CRYO-LHI and CRYO-HHI (3.00 kg/hr) experiments displayed large amounts of scatter with the H1 samples showing much lower Fe(%) values close to the experimental mean (See Fig 5.48). This shows that the δ/α' phase decomposition in the H1 samples occurs during the tensile loading. Residual stresses are maximised at the H1 location (Mukherjee and DebRoy, 2019). The LIT-LHI, CRYO-LHI and CRYO-HHI 3.00 kg/hr samples also appeared to have higher levels of distortion due to the lower processing temperatures (see §6.5.6 and §6.6.6) in agreement with Denlinger and Michaleris (2015). The greater stored energy in these samples, as a result, would promote higher levels of dissolution of δ-ferrite and reversion of any metastable α'-martensite generated in-process. Whilst variation in N content is another possible explanation for the variation in Fe(%) as additional N leads to the reduction in δ-ferrite (Mosa et al., 2017), no relation between Fe(%) and N wt.% was found with the results in §5.5.3 and §5.6.3.

6.6.1.7 Relative density

Investigation of the relative density in §5.5.4 and §5.6.4 showed that the relative density was significantly affected by the heat input for 0.75 kg/hr and 3.00 kg/hr experiments. The LHI experiments reduced relative density for 0.75 kg/hr, however, the opposite occurred in the 3.00 kg/hr samples. The additional density provided by the HHI for the 0.75 kg/hr experiments can be attributed to the lower cooling rate, which provides more time before solidification completion for trapped gases to be released from the melt-pool. However, the LHI experiments, on average improved relative density for the 3.00 kg/hr experiments. Significant improvements were identified for the CRYO and HIT cooling strategy for the LHI experiments showing they can provide more stable heat transfer, whereas the HHI

experiments remained consistent relative density regardless of cooling strategy applied. The presence of major pores (~500 µm) on the fracture surface confirmed that WAAM is relatively insensitive to process-induced porosity, a finding supported by Gordon et al. (2019). However, a weak-moderate relation with σ_{ys} was found corresponding to approximately +12 MPa per 0.001 increase in relative density.

6.6.2 Effect of processing parameters and wire composition on WAAM mechanical properties

This section discusses the effect of wire composition, heat input, cooling strategy, and deposition rate on the WAAM mechanical properties. Table 6.1 summarises the factors and levels that resulted in a statistically significant improvement to UTS, σ_{ys}, E and uniform elongation.

Table 6.1 Summary of the levels that resulted in a statistically significant improvement to the mechanical properties.

Factors	**Responses**			
	UTS	**σ_{ys}**	**E**	**Uniform elongation**
Wire composition	316LSi ↑	316LSi	316LSi ↑	-
Cooling strategy	CRYO ↑	CRYO ↑ LIT ↑	CRYO ↑	-
Heat Input	LHI ↑	LHI ↑	-	-
Deposition rate	-	3.00 kg/hr ↑	-	0.75 kg/hr ↑
Orientation	-	-	H ↑	H ↑
Interaction effects	-	-	CRYO+LIT ↑ CRYO+LIT+0.75 kg/hr ↑	H + LHI ↑

The anisotropy of the mechanical properties was reported in Fig 5.57 and Fig 5.58. The levels of anisotropy were found to be lower for the UTS and σ_{ys} and varied much more widely for E, and uniform elongation.

6.6.2.1 Yield Strength and Ultimate Tensile Strength

The results found that σ_{ys} and UTS exceeded wrought specification of 200 MPa and 485 MPa respectively, in agreement with results for several authors studying WAAM of Type 316L stainless steel shown in Table 3.3 (Chen et al., 2017b, Rodriguez et al., 2018, Queguineur et al., 2017, Wang et al., 2019a, Wu et al., 2019a). The ductility provided was in the same region as previously reported, below the ASTM A240/A240M (2004) requirement, but showed a wider range due to the varied process parameters employed.

Compared to the wrought mechanical properties, this research has shown that the strongest material properties can be obtained with the CRYO/LIT and LHI process parameters. At 0.75 kg/hr CRYO cooling provides a small increase to σ_{ys} with improved ductility, however, this is compromised at higher deposition rates. The LHI and CRYO/LIT parameters typically acted to increase the cooling rate compared to the HIT and HHI conditions, which were

associated with greater δ-ferrite refinement. Several authors also found that improvements to yield and tensile strength could be achieved with reduced laser power or scanning speed by producing finer dendrites (Liu et al., 2020, Yang et al., 2016, Wang et al., 2016b).

The 3.00 kg/hr experiments also resulted in a statistically significant increase in σ_{ys} with an increase in deposition rate increasing the cooling rate. Possible causes of the additional strengthening for the higher cooling rate experiments (CRYO/LIT and 3.00 kg/hr) involve the refinement of microstructure. Strain hardening significantly affects σ_{ys} and elongation, but not UTS (Mehmanparast et al., 2016). Additional strain hardening evidenced by dislocation strengthening and additional distortion in the higher deposition rate samples (CRYO/LIT and 3.00 kg/hr) was shown to contribute to the additional strengthening in §5.8.1. The strong correlation of the dislocation strengthening to experimental yield stress (Fig 5.85) indicates that the dislocation strengthening is a major component of the additional strengthening in these samples. Also, the α′ martensitic transformation occurred in the WAAM experiments, as evidenced in the increase in Fe(%) for the fractured tensile specimens tested in §5.5.3 and §5.6.3.

This research, also allowed systematic evaluation of the effects of wire silicon composition. As shown in Table 6.1, the wire composition with additional silicon content (Type 316LSi) wire had a significant effect on the tensile properties resulting in σ_{ys} of 307.2 MPa compared to 286.7 MPa for the Type 316L wire. The additional silicon composition provided negligible solid solution strengthening in the wire due to additional silicon (§5.3.2) or samples due to δ-ferrite content (§5.8.3). Besides, the wire composition did not have any significant effect on the ODS (§5.8.2.1). However, the Type 316LSi samples had lower values of oxide frequency compared to the Type 316L (see Fig 6.95), which provides fewer sites for the initiation of ductile fracture in the form of voids. This has been cited by several authors as the cause of reduced strength and ductility in Type 316L material as the micro-voids more readily enlarge and coalesce with the increase of the applied tensile stress (Cooper et al., 2018, Lou et al., 2018). The Type 316LSi samples also had higher top five average dimple diameters for a given yield strength (Fig 5.80), which is indicative of greater ductility. Due to lower oxygen volume fraction, larger oxide inclusions were shown to be acceptable allowing greater dimple growth before fracture and, consequently, higher strength and ductility.

Within each experimental group, however, higher oxide inclusion frequencies and smaller oxide radii resulted in higher yield strength as shown in Fig. 5.93 and Fig 5.94, respectively, indicating that for a given volume fraction higher frequencies and smaller oxide radii should be present for enhanced ODS. In addition, the additional silicon content is expected to elevate the nitrogen adsorption, which may indirectly affect the strength increment by solid solution strengthening (Eo et al., 2018). The maximum oxide radii were also linked to the

average of the top five fracture dimple diameters in §5.7.3. Oxide radii were present within the fracture dimples showing micro-void initiation sites.

6.6.2.2 Young's Modulus

This research showed a large variation in E for experimental repeats and between experiments, with the majority of the results falling below the BS EN 10088-1 (2014) specification. This can severely affect the applicability in industrial applications as discussed in §3.9.

Previous research for WAAM Type 316L found slightly higher, but also variable values for E (100-200 GPa), attributing variation in results to extensometer accuracy (Joosten, 2015). However, with the use of a class 0.5 extensometer, this research showed that the results are more likely a representative of the true material characteristics. Within the literature, the presence of oxide inclusions have been cited to cause early tear at the necks during the elastic phase of tensile testing or porosity is also commonly favoured as an explanation (Straffelini et al., 1999, Zheng and Collins, 1998). In this research, the use of wire composition with additional silicon resulted in an average E of 148.5 GPa compared to 94.2 GPa compared to Type 316L, showing content of Si, as an oxidising element can have a significant impact on E. Pham et al. (2017) found higher values for E of 183 GPa±12 GPa for L-PBF, with the shortfall relative to conventionally produced material attributed to the presence of porosity in the AM sample. Pores and cracks were also cited as the cause for L-DED values averaging 3.5 GPa, significantly lower E than previously reported (de Lima and Sankaré, 2014). However, in this research relative density, oxide fraction and size were found to have no significant correlation to E (see Fig 5.70-5.71).

A substantial increase in E was found for the 0.75 kg/hr CRYO-LHI experiment. This coincided with this sample possessing a relatively isotropic texture, showing interruption of epitaxial grain growth in contrast to the other 0.75 kg/hr experiments. This suggested that the E for WAAM of type 316L is driven by the crystallographic texture, which is known to have a major effect on E in conventionally produced material (Turley and Sines, 1971). Young's modulus is a function of direction within a single crystallite. For example, in single-crystal nickel, E_{001} = 130 GPa, E_{011} = 202 GPa, and E_{111} = 219 GPa (Cantwell et al., 2012). The 0.75 kg/hr CRYO-HHI appears to have generated an <111> aligned microstructure, which may have benefits to corrosion resistance, however, further evaluation covering a greater imaging area would be required to confirm this, especially as the E is lower than the CRYO-LHI result indicating content of lower stiffness <001>. Whilst the 3.00 kg/hr CRYO microstructures were not evaluated with EBSD as discussed in §6.6.1.2, greater directionality in <001> is expected. Therefore, reduced average E due to the texture as confirmed by the experimental results in Figure 5.55 are generated, for the high deposition rate experiments.

The scatter in E for samples extracted from the same thin-wall, can be attributed to differences in the local grain texture, which due to the large grain sizes for the non-cryogenically cooled specimens can be highly variable. Inhomogeneous deformation of test specimens may result from the relatively large grains or preferred crystallographic texture associated with columnar grain structure can contribute to the scatter in the results (Mataya et al., 2003). Penn (2017) also found comparatively high levels of E for L-DED of Type 316L >180 MPa in multiple test directions, for an isotropic microstructure achieved with a rotation of the baseplate by 67° after each layer. This supports the claim that the reduced E compared to conventionally produced material is caused by texture. Tensor averages based on texture have been proposed for many physical properties, including dielectric constant, diffusivity, electrical conductivity, magnetic permeability, magneto restriction, piezoelectric constants, and thermal conductivity (Levy et al., 2000). Therefore, a similar variation in these properties can be expected in textured WAAM of type 316L.

6.6.2.3 Elongation

The ANOVA results for elongation did not identify any statistically significant effects for wire composition (p=0.515), heat input (p=0.460) or interpass temperature (p=0.690). The deposition rate, however, had a significant effect on the uniform elongation, with 0.75 kg/hr providing 41.9 % compared to 37.7% for 3.00 kg/hr. The deposition rate increased the cooling rate. The cooling rate based on the calculation of the coarse dendrites shown in Fig. 5.75 had a strong negative correlation to the uniform elongation. This can be attributed to the microstructural refinement. Higher deposition rate also correlated to the lower Fe(%) content in the pre-strained state of the metallurgical samples (Fig 5.76). Stainless steels containing greater volumes of α'-martensite or δ-ferrite as dispersed precipitates usually have greater strengthening performance after yield, but lower deformation capability (Liu et al., 2017a, Yan et al., 2012). However, the opposite occurs in the WAAM samples indicating additional Fe(%) before deformation can be beneficial for enhanced ductility.

The horizontal specimens aligned to the travel direction provided slightly higher levels of ductility than vertical specimens aligned to the build direction, in agreement with several authors (Rodriguez et al., 2018, Akbari and Kovacevic, 2018, Alsalla et al., 2018). This research showed that, excluding the highest values of elongation closest to the build plate, elongation showed a moderately positive trend with oxide maximum radius and Fe(%).

Possible causes of the anisotropy include periodic variation in oxide inclusion radius or Fe(%) with build height. As the gauge length of the vertical specimens covers a larger fraction of the build height, areas of smaller oxide inclusion radius/lower Fe(%) encountered could lower the total uniform elongation in the sample. The H1 specimens of the HIT-LHI (3.00 kg/hr), CRYO-LHI (0.75 kg/hr) tensile specimens provided the highest levels of elongation as shown in Fig.5.74. Yadollahi et al. (2015) and Smith et al. (2019), in

contrast, found increased strength in similar areas close to the baseplate in for L-DED of Type 316LSi and Type 316LSi. This was related to the additional dislocation strengthening, which is usually accompanied by a reduction in ductility for conventionally produced materials. For L-PBF such behaviour has been explained by the sub-grain cellular structure (Sun et al., 2018b), however, this morphology is relatively was found within isolated regions of WAAM microstructures. Due to the increased elongation with similar levels of strength provided, mechanisms that do not follow the typical strength, ductility trade-off may be active. Possible mechanisms include TWIP and TRIP covered in §3.6.1 and §3.6.2 with the possibility of TRIP supported by the typical increase in Fe(%) composition post-fracture as outlined in §6.6.1.6. In addition, a trend was identified with higher Fe(%) prior to fracture resulted in higher levels of uniform elongation (see Fig 5.76). However, it should be noted that high levels of δ-ferrite negatively affects fracture toughness as outlined in §3.3.1. Heat treatment may be required to reduce the δ-ferrite content or fully eliminate the δ-ferrite required for cryogenic applications (Dalder and Juhas, 1985).

A significant relationship between relative density and elongation was not identified in this research (see Fig. 5.77), indicating that pores and residual defects do not affect ductility in WAAM of Type 316L. This was also confirmed by the identification of large pores on the fracture surface with no apparent significant decrease in elongation or tensile strength. This contrasted to results for L-PBF for where the highest level of ductility was achieved through minimization of residual defects and melting pool boundaries (Liu et al., 2020).

Conclusions

Chapter 7

7.1 Introduction

This chapter outlines the conclusions of this research based on the literature review, methodology, and results and analysis. The contribution to knowledge is stated together with future work directions.

7.2 Conclusions

i. A review of the welding metallurgy and WAAM of Type 316L showed that systematic study of the processing parameters of deposition rate, heat input and cooling strategies had not previously been conducted. A review of processes and strategies for WAAM showed that additional processes can be used to improve the quality of WAAM parts. In-process additional cooling was found to be especially useful due to its potential for modifying the microstructural development and residual stresses, whilst preventing heat accumulation that usually requires interpass cooling.

ii. A structured methodology has been designed and implemented to enable the material characterisation and evaluation of the mechanical properties of WAAM of Type 316L stainless steel. This evaluation references the relevant international standards where relevant and is generically applicable for the evaluation of other materials using the WAAM process. A WAAM system has been specified and integrated for generating the experimental thin walls for the evaluation for 316L stainless steel. The WAAM system specification provides the capability for evaluation of different materials via the WAAM process.

iii. The effect of wire composition at 0.75 kg/hr, and the effects of heat input, deposition rate, cooling strategy (low and high interpass temperature and in-process cryogenic cooling localised to the melt-pool) process parameters on the materials characterisation and mechanical properties of Type 316L stainless steel was investigated:

    a. The process parameters affected the solidification mode, morphology, δ-ferrite content, texture, grain size, oxide inclusion size and distribution, relative density, and substrate distortion. The microstructure varied significantly with between lower and upper sections, even with interpass control implemented. Primary austenite and FA cellular-dendritic formations were identified

    The use of cryogenic cooling significantly changed the grain size and texture of the low linear heat input, 0.75 kg/hr 316L samples, which were otherwise large grains of size >80 μm strongly aligned to the <001> direction. Higher Fe(%) was found in the as-built samples at lower deposition rates and an increase in Fe(%) was identified in plastically deformed tensile specimens indicating a strain-induced α'-martensite transformation.

b. A major finding of the research was that the application of higher cooling rates either by higher deposition rates of 3.00 kg/hr, LHI or a LIT or CRYO cooling strategy can improve the yield strength of Type 316L WAAM samples. For the range of process, parameter investigated, however, the yield strength and UTS readily exceeded that of the wrought material based on ASTM A240/A240M (2004). However, the ductility of the WAAM Type 316L material was often below that of the wrought material and dependent on having a lower deposition rate. The source of the loss of ductility at higher deposition rates can be linked to the microstructure refinement, however, TRIP and TWIP mechanisms may also take place as evidenced by the increase in Fe(%) in plastically deformed tensile samples and the greater strength and ductility in the location closest to the build plate.

c. The relative part density was shown to have a small weak-moderate positive effect on the yield strength over the range of relative density produced in the experiments (99.30 %-99.60 %) with ductility unaffected. The presence of pores up to 500 µm at fracture surfaces, with no significant decrease in strength or ductility indicated high levels of damage tolerance.

d. To enhance productivity whilst maintaining ASTM A240/A240M (2004) requirements, CRYO or HIT cooling strategy is recommended at low heat input and lower deposition rates. The CRYO-LHI 0.75 kg/hr sample also had the advantage of a relatively isotropic microstructure of the provided major benefits to the anisotropy factor and mean E, which for the majority of the experiments was significantly lower than the specification for wrought material. These findings are important as higher deposition rates or interpass temperatures can improve productivity and the cost-effectiveness of the WAAM process.

e. The investigation of the effect of wire composition with the use of Type 316LSi wire showed that it can offer higher tensile strength and Young's Modulus than the Type 316L wire composition. This behaviour was attributed to the stronger oxidising effect with higher Si content, which reduced the number of micro-void initiation sites. The use of this grade is particularly beneficial for through-torch shielding gas WAAM set-up where oxygen exposure can be more extensive than for enclosed controlled atmosphere systems.

iv. The source of the strengthening for WAAM of Type 316L compared to wrought equivalent was related to solid solution strengthening, dislocation strengthening and ODS. The δ-ferrite content and the adsorption of nitrogen had the greatest effect on the solid solution strengthening, with more adsorption for the LHI condition at 0.75 kg/hr and greater adsorption for the HHI at 3.00 kg/hr. The use of CRYO, with

additional pressurised N_2 within the WAAM machine, did not increase nitrogen adsorption significantly. For the 0.75 kg/hr samples where the GND density was examined, the more rapidly cooled samples (CRYO, LIT, LHI) had higher dislocation strengthening. The sum of the predicted contributions to strength by these mechanisms was found to fit the experimental results of yield strength with a maximum of 12.2% error.

7.3 Contribution to Knowledge

This research has for the first time investigated the effects of silicon composition, deposition rate, heat input and cooling strategy on the mechanical properties and physical properties of Type 316L stainless steel generated by WAAM. It was found that an increase in deposition rate increases tensile strength, however, at the expense of ductility. It has also demonstrated that in-process cryogenic cooling localised to the melt-pool can be used to improve the overall mechanical properties of the WAAM material, in particular with regards to E, tensile strength and ductility. This provides benefits to industrial applications of WAAM of Type 316L, where a balance between repeatable satisfactory material properties and productivity is required.

7.4 Future Work

As WAAM matures and industrial confidence grows, advancement in the capability will be required. To do so, long-term research efforts are required in the areas of:

- Reliability and resilience for remote operation and defect avoidance
- Accurate prediction of deposition shape, material properties and key production resource requirements (wire, energy, and consumables and total build time)
- Optimisation of set-up and additional process selection based on production priorities i.e (minimisation of total energy requirement/build time/production cost)
- New feedstock production methods and materials for AM based on local resources, AM processability and demand for greater performance.
- Advanced structures with generatively designed and functionally graded properties based on microstructure and multi-material combinations

This will require full integration of computer aided engineering simulation, design and computer aided manufacture, security, and verification tools, as well as development of new hardware for deposition and process monitoring. Applications such as the space industry will evolve specialist solutions based on demanding environmental conditions and local resource restraints.

This research also highlighted topics for which short-term future work may be conducted to further understand WAAM of Type 316L:

- Evaluation of mechanical properties post-heat treatment

Dislocation strengthening was found to be a major component of the yield strength. Several authors have investigated how Type 316L L-PBF responds to heat treatment with the sub-grain structure requiring higher temperatures and longer holding times to anneal the microstructure. However, this has been understood from the sub-grain trapping mechanism, and this hierarchical microstructure is relatively uncommon in WAAM. Subsequently, it is of interest to identify the annealing rate of WAAM samples and at how high temperatures that the strength can be maintained for high-temperature application.

- Exploration of intermittent and post-deformation microstructures

This research showed an average increase in Fe(%) in the fractured tensile samples indicating small amounts of TRIP occurring during plastic deformation which can enhance strength and ductility. However, there are inconsistencies in this result, for example in the samples closest to the baseplate. A study of the deformation behaviour is required to evaluate the dislocation structures and α-martensite formation by TEM. Also, a short period of annealing would allow the CRYO microstructures to be evaluated at lower magnification using EBSD to identify grain refinement by α'-martensite reversion or TWIP. Further understanding of these effects is required to understand the scatter within tensile and elongation results.

The following topics also require short-term further work to advance WAAM processing capability:

- Optimisation of in-process cryogenic cooling

The use of in-process cryogenic cooling localised to the melt-pool in WAAM presents several avenues for further research. The impressive results of van der Aa (2007) in eliminating distortion in butt-welding of thin sheets were not reproduced in this research, although the distortion results did not indicate any increase in residual stress severity. However, residual stresses pose a major problem in WAAM, requiring large fixtures and expensive tooling, and unexpected distortion cannot always be corrected by heat treatment for large parts making this finding worthy of further investigation. Variation of fluid flow rate, pressure, and positioning of the jet relative to the melt-pool may help in addressing this issue. In-situ alloying by designing and implementing new shielding gases may allow more significant nitrogen to be alloyed to the material enhancing the material properties. Also, the cost-effectiveness of the LN_2 at the flow rates used in this research requires further investigation.

- Simulation tools for predicting additive manufacturing material properties

The prediction of the mechanical properties in this research, was accurate to within 9%, however, this required destructive testing of parts to determine solid solution strengthening, dislocation strengthening and oxide dispersion strengthening effects. Thermo-mechanical and metallurgical models are required to be able to predict material properties a-priori. This is especially important for the full exploitation of the design freedom of WAAM, as topological and generative software commonly assume isotropic mechanical properties, (Chiu et al., 2018), which this research showed is not always the case.

- WAAM for repair and hybrid manufacture

Whilst this research has focussed on the material properties for new parts produced by WAAM, future work should also focus on the use of WAAM systems to add features to parts produced by alternative manufacturing routes, repair and remanufacture. This may require new path planning techniques and require the joining of dissimilar materials, or similar materials of different microstructural features.

References

ABD-ELGHANY, K. & BOURELL, D. L. 2012. Property evaluation of 304L stainless steel fabricated by selective laser melting. *Rapid Prototyping Journal,* 18**,** 420-428.

ABIOYE, T. E., FOLKES, J., CLARE, A. T. & MCCARTNEY, D. G. 2013. Concurrent Inconel 625 wire and WC powder laser cladding: process stability and microstructural characterisation. *Surface Engineering,* 29**,** 647-653.

ACHERJEE, B. 2018. Hybrid laser arc welding: State-of-art review. *Optics & Laser Technology,* 99**,** 60-71.

ADEBAYO, A. 2013. *Characterisation Of Integrated WAAM And Machining Processes.* Ph.D., Cranfield University.

ADEBAYO, A., MEHNEN, J. & TONNELLIER, X. 2014. Effects of solid lubricants on wire and arc additive manufactured structures. *Proceedings of the Institution of Mechanical Engineers, Part B: Journal of Engineering Manufacture,* 228**,** 563-571.

AGHAALI, I., FARZAM, M., GOLOZAR, M. A. & DANAEE, I. 2014. The effect of repeated repair welding on mechanical and corrosion properties of stainless steel 316L. *Materials & Design (1980-2015),* 54**,** 331-341.

AKBARI, M. & KOVACEVIC, R. 2018. An investigation on mechanical and microstructural properties of 316LSi parts fabricated by a robotized laser/wire direct metal deposition system. *Additive Manufacturing,* 23**,** 487-497.

ALSALLA, H. H., SMITH, C. & HAO, L. 2018. Effect of build orientation on the surface quality, microstructure and mechanical properties of selective laser melting 316L stainless steel. *Rapid Prototyping Journal,* 24**,** 9-17.

AML3D. 2020. *About Archemy* [Online]. Available: https://aml3d.com/technology/#metals [Accessed 21/04/2020].

AMUDA, M. O. H. & MRIDHA, S. 2013. Grain refinement and hardness distribution in cryogenically cooled ferritic stainless steel welds. *Materials & Design,* 47**,** 365-371.

ANDREAU, O., KOUTIRI, I., PEYRE, P., PENOT, J.-D., SAINTIER, N., PESSARD, E., DE TERRIS, T., DUPUY, C. & BAUDIN, T. 2019. Texture control of 316L parts by modulation of the melt pool morphology in selective laser melting. *Journal of Materials Processing Technology,* 264**,** 21-31.

ANGEL, T. 1954. Formation of Martensite in Austenitic Stainless Steels Effects of Deformation, Temperature, and Composition. *J. Iron and Steel Inst.,* 177**,** 165-174.

ANTONYSAMY, A. 2012. *Microstructure, Texture and Mechanical Property Evolution during Additive Manufacturing of Ti6Al4V Alloy for Aerospace Applications.* PhD, University of Manchester.

ANZALONE, G. C., ZHANG, C. L., WIJNEN, B., SANDERS, P. G. & PEARCE, J. M. 2013. A Low-Cost Open-Source Metal 3-D Printer. *IEEE Access,* 1**,** 803-810.

ARUN, K. S., HUANG, T. S. & BLOSTEIN, S. D. 1987. Least-Squares Fitting of Two 3-D Point Sets. *IEEE Transactions on Pattern Analysis and Machine Intelligence,,* PAMI-9**,** 698-700.

ASALA, G., KHAN, A. K., ANDERSSON, J. & OJO, O. A. 2017. Microstructural Analyses of ATI 718Plus® Produced by Wire-ARC Additive Manufacturing Process. *Metallurgical and Materials Transactions A,* 48**,** 4211-4228.

ASM INTERNATIONAL 1980. *Metals Handbook. 9th Ed. Vol. 3. Properties and Selection Stainless Steels, Tool Materials & Special-purpose Metal*, ASM.

ASM INTERNATIONAL 2008. Austenitic Stainless Steels. *Stainless Steels for Design Engineer.*

ASTM A240/A240M 2004. Standard Specification for Chromium and Chromium-Nickel Stainless Steel Plate, Sheet, and Strip for Pressure Vessels and for General Applications.

ASTM E3 2011. Standard Guide for Preparation of Metallographic Specimens.

ASTM E8/E8M 2013. ASTM E8/E8M, Standard Test Methods for Tension Testing of Metallic Materials.

ASTM E112 2013. Standard Test Methods for Determining Average Grain Size.

ASTM E407 2007. Standard Practice for Microetching Metals and Alloys.
ASTM F3187-16 2016. Standard Guide for Directed Energy Deposition of Metals.
AUFRECHT, J., LEINEWEBER, A., FOCT, J. & MITTEMEIJER, E. J. 2008. The structure of nitrogen-supersaturated ferrite produced by ball milling. *Philosophical Magazine,* 88**,** 1835-1855.
AWS A4.2M 2006. Standard Procedures for Calibrating Magnetic Instruments to Measure the Delta Ferrite Content of Austenitic and Duplex Ferritic-Austenitic Stainless Steel Weld Metal.
BAESLACK III, W. A., LIPPOLD, J. C. & SAVAGE, W. F. 1979. Unmixed zone formation in austenitic stainless steel welds. *Welding Journal,* 168-s.
BAHL, S., MISHRA, S., YAZAR, K. U., KOLA, I. R., CHATTERJEE, K. & SUWAS, S. 2019. Non-equilibrium microstructure, crystallographic texture and morphological texture synergistically result in unusual mechanical properties of 3D printed 316L stainless steel. *Additive Manufacturing,* 28**,** 65-77.
BAI, J. Y., FAN, C. L., LIN, S. B., YANG, C. L. & DONG, B. L. 2017. Mechanical Properties and Fracture Behaviors of GTA-Additive Manufactured 2219-Al After an Especial Heat Treatment. *Journal Of Materials Engineering And Performance,* 26**,** 1808-1816.
BAI, J. Y., YANG, C. L., LIN, S. B., DONG, B. L. & FAN, C. L. 2015a. Mechanical properties of 2219-Al components produced by additive manufacturing with TIG. *The International Journal of Advanced Manufacturing Technology,* 86**,** 479-485.
BAI, X., ZHANG, H. & WANG, G. 2015b. Modeling of the moving induction heating used as secondary heat source in weld-based additive manufacturing. *The International Journal of Advanced Manufacturing Technology,* 77**,** 717-727.
BAI, X. W., ZHANG, H. O. & WANG, G. L. 2013. Electromagnetically Confined Weld-based Additive Manufacturing. *Procedia CIRP,* 6**,** 515-520.
BAILEY, J. E. & HIRSCH, P. B. 1960. The dislocation distribution, flow stress, and stored energy in cold-worked polycrystalline silver. *The Philosophical Magazine: A Journal of Theoretical Experimental and Applied Physics,* 5**,** 485-497.
BAKER, R. 1925. *Method of making decorative articles*.
BALASUBRAMANIAN, V., RAVISANKAR, V. & REDDY, G. M. 2007. Effect of pulsed current and post weld aging treatment on tensile properties of argon arc welded high strength aluminium alloy. *Materials Science and Engineering: A,* 459**,** 19-34.
BALDEV, R., KAMACHI MUDALI, U., VIJAYALAKSHMI, M., MATHEW, M. D., BHADURI, A. K., CHELLAPANDI, P., VENUGOPAL, S., SUNDAR, C. S., RAO, B. P. C. & VENKATRAMAN, B. 2013. Development of Stainless Steels in Nuclear Industry: With Emphasis on Sodium Cooled Fast Spectrum Reactors History, Technology and Foresight. *Advanced Materials Research,* 794**,** 3-25.
BARSOUM, Z. & BARSOUM, I. 2009. Residual stress effects on fatigue life of welded structures using LEFM. *Engineering Failure Analysis,* 16**,** 449-467.
BARTOLOMEU, F., BUCIUMEANU, M., PINTO, E., ALVES, N., CARVALHO, O., SILVA, F. S. & MIRANDA, G. 2017. 316L stainless steel mechanical and tribological behavior—A comparison between selective laser melting, hot pressing and conventional casting. *Additive Manufacturing,* 16**,** 81-89.
BAUFELD, B. 2011. Mechanical Properties of INCONEL 718 Parts Manufactured by Shaped Metal Deposition (SMD). *Journal of Materials Engineering and Performance,* 21**,** 1416-1421.
BAUFELD, B. & VAN DER BIEST, O. 2009. Mechanical properties of Ti-6Al-4V specimens produced by shaped metal deposition. *Sci Technol Adv Mater,* 10**,** 015008.
BAUNE, E., BONNET, C. & LIU, S. 2000. Reconsidering the Basicity of a FCAW Consumable — Part 1: Solidified Slag Composition of a FCAW Consumable as a Basicity Indicator. *Welding Research Supplement,* S**,** 57-65.
BERMINGHAM, M. J., ZHAN, H., STJOHN, D. H., DARGUSCH, M. S. & KENT, D. 2015. Controlling the microstructure and properties of wire arc additive manufactured Ti–6Al–4V with trace boron additions. *Acta Materialia,* 91**,** 289-303.
BHAVAR, V., KATTIRE, P., PATIL, V., KHOT, S. & GUJAR, K. 2014. A review on powder bed fusion technology of metal additive manufacturing. *Additive Manufacturing,* 14**,** 39-48.

BIG METAL ADDITIVE. 2020. *Welcome to Big Metal Additive* [Online]. Available: https://bigmetaladditive.com/ [Accessed 21/04/2020].
BIRADAR, N. S. & RAMAN, R. 2012. Grain Refinement in Al-Mg-Si Alloy TIG Welds Using Transverse Mechanical Arc Oscillation. *Journal of Materials Engineering and Performance,* 21**,** 2495-2502.
BIRNBAUM, A. J., STEUBEN, J. C., BARRICK, E. J., ILIOPOULOS, A. P. & MICHOPOULOS, J. G. 2019. Intrinsic strain aging, Σ3 boundaries, and origins of cellular substructure in additively manufactured 316L. *Additive Manufacturing,* 29**,** 100784.
BOHLKE, T. & BERTRAM, A. 2001. The evolution of Hooke's law due to texture development in FCC polycrystals. *International Journal of Solids and Structures,* 38**,** 9437-9459.
BOUCHE, G., BECHADE, J. L., MATHON, M. H., ALLAIS, L., GOURGUES, A. F. & NAZE, L. 2000. Texture of welded joints of 316L stainless steel, multi-scale orientation analysis of a weld metal deposit. *Journal of Nuclear Materials,* 277**,** 91-98.
BOURELL, D., KRUTH, J. P., LEU, M., LEVY, G., ROSEN, D., BEESE, A. M. & CLARE, A. 2017. Materials for additive manufacturing. *CIRP Annals,* 66**,** 659-681.
BREME, H., BIEHL, V., REGER, N. & GAWALT, E. 2016. Chapter 1a Metallic Biomaterials: Introduction. *In:* MURPHY, W., BLACK, J. & HASTINGS, G. (eds.) *Handbook of Biomaterial Properties.* New York, NY: Springer New York.
BROOKS, J. A. & THOMPSON, A. W. 1991. Microstructural Development and Solidification Cracking Susceptibility of Austenitic Stainless-Steel Welds. *International Materials Reviews,* 36**,** 16-44.
BS EN 3312 2012. Aerospace series - Titanium alloy Ti-6Al-4V - Annealed -Forgings De ≤ 150 mm.
BS EN 10088-1 2014. Stainless steels. Part 1: List of stainless steels.
BS EN 10088-2 2014. Stainless steels. Part 2: Technical delivery conditions for sheet/plate and strip of corrosion resisting steels for general purpose.
BS EN ISO 544 2017. Welding consumables - Technical delivery conditions for filler materials and fluxes - Type of product, dimensions, tolerances and markings.
BS EN ISO 6507-1 2018. Metallic materials – Vickers hardness test Part 1: Test method (ISO 6507-1:2018).
BS EN ISO 6892 2016. Metallic materials — Tensile testing. Part 1: Method of test at room temperature (ISO 6892-1:2016).
BS EN ISO 9513 2012. Metallic materials — Calibration of extensometer systems used in uniaxial testing.
BS EN ISO 14343 2017. Welding consumables — Wire electrodes, strip electrodes, wires and rods for arc welding of stainless and heat resisting steels — Classification.
BS ISO/ASTM 52900 2015. Additive manufacturing. General principles. Terminology.
CALLISTER, W. D. 2003. *Materials science and engineering : an introduction,* New York, Wiley.
CANDEL-RUIZ, A., KAUFMANN, S. & MÜLLERSCHÖN, O. 2015. Strategies for high deposition rate additive manufacturing by Laser Metal Deposition. *Lasers in Manufacturing Conference 2015.* Munich, Germany.
CANTWELL, P. R., KIM, H., SCHNEIDER, M. M., HSU, H.-H., PEROULIS, D., STACH, E. A. & STRACHAN, A. 2012. Estimating the In-Plane Young's Modulus of Polycrystalline Films in MEMS. *Journal of Microelectromechanical Systems,* 21**,** 840-849.
CARTER, L. N., ATTALLAH, M. M. & REED, R. C. 2012. Laser Powder Bed Fabrication of Nickel-Base Superalloys: Influence of Parameters; Characterisation, Quantification and Mitigation of Cracking. *Superalloys 2012: 12th International Symposium on Superalloys***,** 577-586

CASATI, R., LEMKE, J. & VEDANI, M. 2016. Microstructure and Fracture Behavior of 316L Austenitic Stainless Steel Produced by Selective Laser Melting. *Journal of Materials Science & Technology,* 32**,** 738-744.

CATTANT, F., CRUSSET, D. & FÉRON, D. 2008. Corrosion issues in nuclear industry today. *Materials Today,* 11**,** 32-37.
CHAKKRAVARTHY, V. & JEROME, S. 2020. Printability of multiwalled SS 316L by wire arc additive manufacturing route with tunable texture. *Materials Letters,* 260**,** 1-4.
CHEN, Q., LIN, S., YANG, C., FAN, C. & GE, H. 2017a. Grain fragmentation in ultrasonic-assisted TIG weld of pure aluminum. *Ultrason Sonochem,* 39**,** 403-413.
CHEN, X. H., LI, J., CHENG, X., HE, B., WANG, H. M. & HUANG, Z. 2017b. Microstructure and mechanical properties of the austenitic stainless steel 316L fabricated by gas metal arc additive manufacturing. *Materials Science and Engineering a-Structural Materials Properties Microstructure and Processing,* 703**,** 567-577.
CHINAKHOV, D. A. 2017. Dynamic Action of the Shielding Gas Jet Upon the Process of Consumable Electrode Welding. *IOP Conference Series: Materials Science and Engineering,* 221**,** 012002.
CHIU, L. N. S., ROLFE, B., WU, X. & YAN, W. 2018. Effect of stiffness anisotropy on topology optimisation of additively manufactured structures. *Engineering Structures,* 171**,** 842-848.
CLAUSEN, B. 1997. *Characterisation of Polycrystal Deformation by Numerical Modelling and Neutron Diffraction Measurements.* Ph.D., Technical University of Denmark.
COLEGROVE, P. A., DONOGHUE, J., MARTINA, F., GU, J. L., PRANGNELL, P. & HONNIGE, J. 2017. Application of bulk deformation methods for microstructural and material property improvement and residual stress and distortion control in additively manufactured components. *Scripta Materialia,* 135**,** 111-118.
COLLINS, P. C., BRICE, D. A., SAMIMI, P., GHAMARIAN, I. & FRASER, H. L. 2016. Microstructural Control of Additively Manufactured Metallic Materials. *Annual Review of Materials Research,* 46**,** 63-91.
CONG, B., QI, Z., QI, B., SUN, H., ZHAO, G. & DING, J. 2017. A Comparative Study of Additively Manufactured Thin Wall and Block Structure with Al-6.3%Cu Alloy Using Cold Metal Transfer Process. *Applied Sciences,* 7**,** 275-286.
COOPER, A. J., BRAYSHAW, W. J. & SHERRY, A. H. 2018. Tensile Fracture Behavior of 316L Austenitic Stainless Steel Manufactured by Hot Isostatic Pressing. *Metallurgical and Materials Transactions A,* 49**,** 1579-1591.
COOPER, D. E. 2016. *The High Deposition Rate Additive Manufacture of Nickel Superalloys and Metal Matrix Composites.* PhD, Warwick University.
COSTANZA, G., SILI, A., TATA, M. E., COSTANZA, G., TATA, M. E. & SILI, A. 2016. Weldability of austenitic stainless steel by metal arc welding with different shielding gas. *Procedia Structural Integrity, 2***,** 3508-3514.
COULES, H. E. 2013. Contemporary approaches to reducing weld induced residual stress. *Materials Science and Technology,* 29**,** 4-18.
CUI, C., UHLENWINKEL, V., SCHULZ, A. & ZOCH, H.-W. 2019. Austenitic Stainless Steel Powders with Increased Nitrogen Content for Laser Additive Manufacturing. *Metals,* 10**,** 1-11.
CUNNINGHAM, C. R., FLYNN, J. M., SHOKRANI, A., DHOKIA, V. & NEWMAN, S. T. 2018. Invited review article: Strategies and processes for high quality wire arc additive manufacturing. *Additive Manufacturing,* 22**,** 672-686.
CUNNINGHAM, C. R., WANG, J., DHOKIA, V., SHOKRANI, A. & NEWMAN, S. T. 2019. Characterisation of austenitic 316LSi stainless steel produced by wire arc additive manufacturing with interlayer cooling. *Solid Freeform Fabrication 2016: Proceedings of the 30th Annual International Solid Freeform Fabrication Symposium – An Additive Manufacturing Conference,* 2019**,** 426-439.
CUNNINGHAM, C. R., WIKSHÅLAND, S., XU, F., KEMAKOLAM, N., SHOKRANI, A., DHOKIA, V. & NEWMAN, S. T. 2017. Cost modelling and sensitivity analysis of wire and arc additive manufacturing. *Procedia Manufacturing,* 11**,** 650-657.
DAHM, K. L. & DEARNLEY, P. A. 2000. On the Nature, Properties and Wear Response of S-phase (nitrogen-alloyed Stainless Steel) Coatings on Aisi 316l. *Proceedings of the I MECH E Part L Journal of Materials:Design and Applications,* 214**,** 181-199.
DALDER, E. N. C. & JUHAS, M. C. 1985. Austenitic Stainless Steels For Cryogenic Service.: Lawrence Livermore Laboratory.

DAVID, S. A. 1981. Ferrite Morphology and Variations in Ferrite Content in Austenitic Stainless Steel Welds. S**,** 63-71.
DAVID, S. A., BABU, S. S., VITEK, J. M., DAVID, S. A., BABU, S. S. & VITEK, J. M. 2003. Welding: Solidification and microstructure. *JOM,* 55**,** 14-20.
DAVIS, J. R. 1998. *Metals Handbook Desk Edition (2nd Edition)*, ASM International.
DAVIS, J. R. 2001. *Alloying: Understanding the basics* Ohio, ASM International.
DE COOMAN, B. C., ESTRIN, Y. & KIM, S. K. 2018. Twinning-induced plasticity (TWIP) steels. *Acta Materialia,* 142**,** 283-362.
DE LIMA, M. S. F. & SANKARÉ, S. 2014. Microstructure and mechanical behavior of laser additive manufactured AISI 316 stainless steel stringers. *Materials & Design,* 55**,** 526-532.
DEHOFF, R. R., KIRKA, M. M., SAMES, W. J., BILHEUX, H., TREMSIN, A. S., LOWE, L. E. & BABU, S. S. 2014. Site specific control of crystallographic grain orientation through electron beam additive manufacturing. *Materials Science and Technology,* 31**,** 931-938.
DENLINGER, E. R., HEIGEL, J. C., MICHALERIS, P. & PALMER, T. A. 2015. Effect of inter-layer dwell time on distortion and residual stress in additive manufacturing of titanium and nickel alloys. *Journal of Materials Processing Technology,* 215**,** 123-131.
DENLINGER, E. R. & MICHALERIS, P. 2015. Mitigation of distortion in large additive manufacturing parts. *Proceedings of the Institution of Mechanical Engineers, Part B: Journal of Engineering Manufacture,* 231**,** 983-993.
DESKTOP METAL. 2017. *Printer Technical Specifications* [Online]. Available: https://www.desktopmetal.com/products/studio/ [Accessed 15/08/20].
DING, D., PAN, Z., CUIURI, D. & LI, H. 2015a. Wire-feed additive manufacturing of metal components: technologies, developments and future interests. *The International Journal of Advanced Manufacturing Technology,* 81**,** 465-481.
DING, D., PAN, Z., CUIURI, D., LI, H., CUIURI, D., DING, D., PAN, Z. & LI, H. 2015b. A practical path planning methodology for wire and arc additive manufacturing of thin-walled structures. *Robotics and Computer-Integrated Manufacturing,* 34**,** 8-19.
DING, D., PAN, Z., CUIURI, D., LI, H., CUIURI, D., PAN, Z., DING, D. & LI, H. 2015c. Process planning for robotic wire and arc additive manufacturing. *2015 IEEE 10th Conference on Industrial Electronics and Applications (ICIEA)***,** 2000-2003.
DING, D., PAN, Z., CUIURI, D., LI, H., LARKIN, N., LARKIN, N., DING, D., CUIURI, D., LI, H. & PAN, Z. 2016. Adaptive path planning for wire-feed additive manufacturing using medial axis transformation. *Journal of Cleaner Production,* 133**,** 942-952.
DING, J., COLEGROVE, P., MEHNEN, J., GANGULY, S., SEQUEIRA ALMEIDA, P. M., WANG, F. & WILLIAMS, S. 2011. Thermo-mechanical analysis of Wire and Arc Additive Layer Manufacturing process on large multi-layer parts. *Computational Materials Science,* 50**,** 3315–3322.
DONOGHUE, J., ANTONYSAMY, A. A., MARTINA, F., COLEGROVE, P. A., WILLIAMS, S. W. & PRANGNELL, P. B. 2016. The effectiveness of combining rolling deformation with Wire-Arc Additive Manufacture on beta-grain refinement and texture modification in Ti-6Al-4V. *Materials Characterization,* 114**,** 103-114.
DUTTA, B. & FROES, F. H. S. 2014. Additive Manufacturing of Titanium Alloys. *Advanced Materials and Processes,* 172**,** 18-23.
EBRAHIMNIA, M., GOODARZI, M., NOURI, M. & SHEIKHI, M. 2009. Study of the effect of shielding gas composition on the mechanical weld properties of steel ST 37-2 in gas metal arc welding. *Materials & Design,* 30**,** 3891-3895.
EICHELMAN, A. H. & HULL, F. C. 1953. The effect of Composition on the temperature of spontaneous transformation of austenite to martensite in 18-8 Type Stainless Steel. *Trans. ASM,* 45**,** 77-104.
EL-TAHAWY, M., HUANG, Y., UM, T., CHOE, H., LÁBÁR, J. L., LANGDON, T. G. & GUBICZA, J. 2017. Stored energy in ultrafine-grained 316L stainless steel processed by high-pressure torsion. *Journal of Materials Research and Technology,* 6**,** 339-347.
ELIASSON, J. & SANDSTROM, R. 2000. Proof strength values for austenitic stainless steels at elevated temperatures. *Steel Research,* 71**,** 249-254.

ELMER, J. W. 1988. *The Influence of Cooling Rate on the Microstructure of Stainless Steel Alloys.* PhD, Massachusetts Institute Of Technology.
ELMER, J. W., ALLEN, S. M. & EAGAR, T. W. 1989a. The influence of cooling rate on the ferrite content of stainless steel alloys. *Proceedings of the 2nd International Conference on Trends in Welding Research*.
ELMER, J. W., ALLEN, S. M. & EAGAR, T. W. 1989b. Microstructural development during solidification of stainless steel alloys. *Metallurgical Transactions A,* 20**,** 2117-2131.
ELMER, J. W. & GIBBS, G. 2019. The effect of atmosphere on the composition of wire arc additive manufactured metal components. *Science and Technology of Welding and Joining,* 24**,** 367-374.
EO, D.-R., PARK, S.-H. & CHO, J.-W. 2018. Inclusion evolution in additive manufactured 316L stainless steel by laser metal deposition process. *Materials & Design,* 155**,** 212-219.
FAN, C., ZHOU, L., LIU, Z., YANG, C., LIN, S., XIE, W. & TONG, H. 2018. Arc character and droplet transfer of pulsed ultrasonic wave-assisted GMAW. *The International Journal of Advanced Manufacturing Technology,* 95**,** 2219-2226.
FARSHIDIANFAR, M. H., KHAJEPOUR, A. & GERLICH, A. 2015. Real-time control of microstructure in laser additive manufacturing. *The International Journal of Advanced Manufacturing Technology,* 82**,** 1173-1186.
FARSHIDIANFAR, M. H., KHAJEPOUR, A. & GERLICH, A. P. 2016. Effect of real-time cooling rate on microstructure in Laser Additive Manufacturing. *Journal of Materials Processing Technology,* 231**,** 468-478.
FENG, Y., ZHAN, B., HE, J. & WANG, K. 2018. The double-wire feed and plasma arc additive manufacturing process for deposition in Cr-Ni stainless steel. *Journal of Materials Processing Technology,* 259**,** 206-215.
FLEISCHER, R. L. 1961. Solution Hardening. *Acta Metallurgica,* 9**,** 996-1000.
FRAZIER, W. E. 2014. Metal Additive Manufacturing: A Review. *Journal of Materials Engineering and Performance,* 23**,** 1917-1928.
FREDRIKSSON, H. 1972. The Solidification Sequence in an 18-8 Stainless Steel, Investigated by Directional Solidification. *Metallurgical Transactions* 3**,** 2989-2997.
FRONIUS. 2020. *CMT – Cold Metal Transfer: The Cold Welding Process For Premium Quality* [Online]. Available: http://www.fronius.com/en/welding-technology/our-expertise/welding-processes/cmt [Accessed 13/04/2020].
FU, J. W., YANG, Y. S., GUO, J. J. & TONG, W. H. 2013. Effect of cooling rate on solidification microstructures in AISI 304 stainless steel. *Materials Science and Technology,* 24**,** 941-944.
FU, Y., ZHANG, H., WANG, G. & WANG, H. Investigation of the mechanical properties on hybrid deposition and micro-rolling of bainite steel. The 28th Annual International Solid Freeform Fabrication Symposium – An Additive Manufacturing Conference, 2017 Austin. 387-398.
GALLOWAY, A. M., MCPHERSON, N. A. & BAKER, T. N. 2011. An evaluation of weld metal nitrogen retention and properties in 316LN austenitic stainless steel. *Proceedings of the Institution of Mechanical Engineers, Part L: Journal of Materials Design and Applications,* 225**,** 61-69.
GANESAN, V., MATHEW, M. D. & SANKARA RAO, K. B. 2013. Influence of nitrogen on tensile properties of 316LN SS. *Materials Science and Technology,* 25**,** 614-618.
GARNER, A. 2017. Stainless steels and specialty alloys for pulp, paper and biomass conversion. A Practical Guide For Mill Engineers. *Nickel Institute,*.
GEFERTEC. 2020. *3DMP Process* [Online]. Available: http://www.gefertec.de/en/3dmp-process/ [Accessed 13/04/2020].
GENG, H., LI, J., XIONG, J. & LIN, X. 2017. Optimisation of interpass temperature and heat input for wire and arc additive manufacturing 5A06 aluminium alloy. *Science and Technology of Welding and Joining,* 22**,** 472-483.
GENG, H. B., LI, J. L., XIONG, J. T., LIN, X., HUANG, D. & ZHANG, F. S. 2018. Formation and improvement of surface waviness for additive manufacturing 5A06 aluminium alloy component with GTAW system. *Rapid Prototyping Journal,* 24**,** 342-350.
GIBSON, I., ROSEN, D. W. & STUCKER, B. 2010. *Additive manufacturing technologies*, Springer.

GILL, T. P. S., VIJAYALAKSHMI, M., RODRIGUEZ, P. & PADMANABHAN, K. A. 1989. On Microstructure-Property Correlation of Thermally Aged Type-316l Stainless-Steel Weld Metal. *Metallurgical Transactions a-Physical Metallurgy and Materials Science,* 20**,** 1115-1124.

GLENALMOND GROUP. 2020. *Glenalmond Technologies* [Online]. Available: https://www.glenalmondgroup.com/about-glenalmond-technologies/ [Accessed 13/04/2020].

GLOVER, T. J. 1982. Application of stainless steels in chemical plant corrosive environments. *Anti-Corrosion Methods and Materials,* 29**,** 11-12.

GORDON, J., HOCHHALTER, J., HADEN, C. & HARLOW, D. G. 2019. Enhancement in fatigue performance of metastable austenitic stainless steel through directed energy deposition additive manufacturing. *Materials & Design,* 168.

GORDON, J. V., HADEN, C. V., NIED, H. F., VINCI, R. P. & HARLOW, D. G. 2018. Fatigue crack growth anisotropy, texture and residual stress in austenitic steel made by wire and arc additive manufacturing. *Materials Science and Engineering: A,* 724**,** 431-438.

GOWRISANKAR, I., BHADURI, A. K., SEETHARAMAN, V., VERMA, D. N. N. & ACHAR, D. R. G. 1987. Effect of the Number of Passes on the Structure and Properties of Submerged Arc Welds of AISI Type 316L Stainless Steel. *Welding Research Supplement***,** 147-154.

GRAND VIEW RESEARCH INC 2019. Stainless Steel Market Size, Share & Trends Analysis Report By Grade (200 Series, 300 Series, 400 Series, Duplex Series), By Product (Long, Flat), By Application, And Segment Forecasts, 2019 - 2025.

GRASSEL, O., KRUGER, L., FROMMEYER, G. & MEYER, L. W. 2000. High strength Fe-Mn-(Al, Si) TRIP/TWIP steels development - properties - application. *International Journal of Plasticity,* 16**,** 1391-1409.

GRASSO, M. & COLOSIMO, B. M. 2017. Process defects and in-situ monitoring methods in metal powder bed fusion: a review. *Measurement Science and Technology,* 28**,** 044005.

GRIFFITH, M. L., ENSZ, M. T., PUSKAR, J. D., ROBINO, C. V., BROOKS, J. A., PHILLIBER, J. A., SMUGERESKY, J. E. & HOFMEISTER, W. H. 2000. Understanding the microstructure and properties of components fabricated by Laser Engineered Net Shaping (LENS). *Solid Freeform and Additive Fabrication-2000,* 625**,** 9-20.

GU, D. D., MEINERS, W., WISSENBACH, K. & POPRAWE, R. 2012. Laser additive manufacturing of metallic components: materials, processes and mechanisms. *International Materials Reviews,* 57**,** 133-164.

GU, J., CONG, B., DING, J., WILLIAMS, S. W. & ZHAI, Y. 2014. Wire+Arc Additive Manufacturing of Aluminium. *Solid FreeforM fabrication Proceedings, Austin, TX***,** 451-458.

GUAN, S., LIU CAO, AYELLO, F. & TAYLOR, C. 2014. DNV GL strategic research & innovation position paper. Additive Manufacturing: a Materials Perspective.: DNV GL.

GUO, J., ZHOU, Y., LIU, C., WU, Q., CHEN, X. & LU, J. 2016. Wire arc additive manufacturing of AZ31 magnesium alloy: Grain refinement by adjusting pulse frequency. *Materials,* 9**,** 823-836.

GUO, P., ZOU, B., HUANG, C. & GAO, H. 2017. Study on microstructure, mechanical properties and machinability of efficiently additive manufactured AISI 316L stainless steel by high-power direct laser deposition. *Journal of Materials Processing Technology,* 240**,** 12-22.

GUTIERREZ-URRUTIA, I. & RAABE, D. 2012. Grain size effect on strain hardening in twinning-induced plasticity steels. *Scripta Materialia,* 66**,** 992-996.

HADEN, C. V., ZENG, G., CARTER, F. M., RUHL, C., KRICK, B. A. & HARLOW, D. G. 2017. Wire and arc additive manufactured steel: Tensile and wear properties. *Additive Manufacturing,* 16**,** 115-123.

HALL, E. O. 1951. The Deformation and Ageing of Mild Steel: III Discussion of Results. *Proc. Phys. Soc. B,* 64**,** 747-753.

HARISH, K. D., A. SOMIREDDY & GURURAJ, K. 2012. A Review on Critical Aspects of 316LN Austenitic Stainless Steel Weldability. *International Journal of Materials Science and Applications,* 1.

HASELHUHN, A. S. 2016. *Design for Low-Cost Gas Metal Arc Weld-Based Aluminum 3-D Printing.* PhD, Michigan Technological University.

HENCKELL, P., GÜNTHER, K., ALI, Y., BERGMANN, J. P., SCHOLZ, J. & FORÊT, P. 2017. The Influence of Gas Cooling in Context of Wire Arc Additive Manufacturing—A Novel Strategy of Affecting Grain Structure and Size. *TMS 2017 146th Annual Meeting & Exhibition Supplemental Proceedings***,** 147-156.

HIBBELER, R. C. 2008. Mechanics of materials. Upper Saddle River, NJ: Pearson/Prentice Hall.

HONG, Y., ZHOU, C., ZHENG, Y., ZHANG, L., ZHENG, J., CHEN, X. & AN, B. 2019. Formation of strain-induced martensite in selective laser melting austenitic stainless steel. *Materials Science and Engineering: A,* 740-741**,** 420-426.

HÖNNIGE, J. R., WILLIAMS, S. T., ROY, M. J., COLEGROVE, P. & GANGULY, S. 2017. Residual Stress Characterization and Control in the Additive Manufacture of Large Scale Metal Structures. *Materials Research Proceedings* 2**,** 455-460.

HORI, K., WATANABE, H., MYOGA, T. & KUSANO, K. 2003. Development of Hot Wire TIG Welding Methods Using Pulsed Current to Heat Filler Wire-Research on Pulse Heated Hot Wire TIG Welding Processes (Report 1). *Quarterly Journal of the Japan Welding Society,* 21**,** 362-373.

HUA, C., LU, H., YU, C., CHEN, J.-M., WEI, X. & XU, J.-J. 2017. Reduction of ductility-dip cracking susceptibility by ultrasonic-assisted GTAW. *Journal of Materials Processing Technology,* 239**,** 240-250.

HUISMAN. 2020. *Huisman successfully load tests world's first 3d printed offshore crane hook.* [Online]. Available: https://www.huismanequipment.com/en/media_centre/press_releases/news_item/110/Huisman-successfully-load-tests-world-s-first-3d-printed-offshore-crane-hook [Accessed 13/04/2020].

INOUE, H. & KOSEKI, T. 2007. Clarification of Solidification Behaviors in Austenitic Stainless Steels Based on Welding Process. *Nippon Steel Technical Report*.

INOUE, H., KOSEKI, T., OHKITA, S. & FUJI, M. 2013. Formation mechanism of vermicular and lacy ferrite in austenitic stainless steel weld metals. *Science and Technology of Welding and Joining,* 5**,** 385-396.

IRVINE, K. J., LLEWELLYN, D. T. & PICKERING, F. B. 1961. High-strength austenitic stainless steels. *J Iron Steel Inst,* 199**,** 153-175.

JACKSON, M. A., VAN ASTEN, A., MORROW, J. D., MIN, S. & PFEFFERKORN, F. E. 2016. A Comparison of Energy Consumption in Wire-Based and Powder-Based Additive-Subtractive Manufacturing. *44th North American Manufacturing Research Conference, Namrc 44,* 5**,** 989-1005.

JIANG, W., LUO, Y., WANG, B., WOO, W. & TU, S. T. 2015. Neutron Diffraction Measurement and Numerical Simulation to Study the Effect of Repair Depth on Residual Stress in 316L Stainless Steel Repair Weld. *Journal of Pressure Vessel Technology,* 137.

JOOSTEN, S. 2015. *Printing a stainless steel bridge.* MSc, Delft University of Technology.

JOST, E., MIERS, J., ROBINSON, A., MOORE, D. & SALDANA, C. 2019. Effects of spatial energy distribution on defects and fracture of LPBF 316L stainless steel. *Solid Freeform Fabrication 2019: Proceedings of the 30th Annual International Solid Freeform Fabrication Symposium – An Additive Manufacturing Conference***,** 440-454.

KALA, S. R., PRASAD, N. S. & PHANIKUMAR, G. 2014. Studies on multipass welding with trailing heat sink considering phase transformation. *Journal of Materials Processing Technology,* 214**,** 1228-1235.

KASHYAP, B. P. & TANGRI, K. 1990. On the Hall-Petch relationship in type 316l stainless steel at room temeperature. *Scripta Metallurgica et Materiala,* 24**,** 1777-1782.

KESTENS, L. A. I. & PIRGAZI, H. 2016. Texture formation in metal alloys with cubic crystal structures. *Materials Science and Technology,* 32**,** 1303-1315.

KHAIRALLAH, S. A., ANDERSON, A. T., RUBENCHIK, A. & KING, W. E. 2016. Laser powder-bed fusion additive manufacturing: Physics of complex melt flow and formation mechanisms of pores, spatter, and denudation zones. *Acta Materialia,* 108**,** 36-45.
KHEIRI, S., MIRZADEH, H. & NAGHIZADEH, M. 2019. Tailoring the microstructure and mechanical properties of AISI 316L austenitic stainless steel via cold rolling and reversion annealing. *Materials Science and Engineering: A,* 759**,** 90-96.
KIMURA, S., KOBAYASHI, T., GODAI, T. & MINATO, S. 1979. Investigations on Chromium in Stainless Steel Welding Fume. *Welding Research Supplement***,** 195-203.
KISHORE BABU, N. & CROSS, C. E. 2012. Grain Refinement of AZ31 Magnesium Alloy Weldments by AC Pulsing Technique. *Metallurgical and Materials Transactions A,* 43**,** 4145-4154.
KITCHENER, J. A., BOCKRIS, J. O., GLEISER, M. & EVANS, J. W. 1953. The Solubility of Oxygen in Gamma-Iron. *Acta Metallurgica,* 1**,** 93-101.
KLUEH, R. L., SHINGLEDECKER, J. P., SWINDEMAN, R. W. & HOELZER, D. T. 2005. Oxide dispersion-strengthened steels: A comparison of some commercial and experimental alloys. *Journal of Nuclear Materials,* 341**,** 103-114.
KOKAWA, H., KUWANA, T. & YAMAMOTO, A. 1989. Crystallographic Characteristics of Delta Ferrite Transformations in a 304L Weld Metal at Elevated Temperatures. *Welding Journal,* S**,** 92-101.
KOSEKI, T. & FLEMINGS, M. C. 1996. Solidification of Undercooled Fe-Cr-Ni Alloys: Part II. Microstructural Evolution. *Metallurgical and Materials Transactions A,* 27A**,** 3226-3240.
KOTECKI, D. J. & SIEWER, T. A. 1992. WRC-1992 Constitution Diagram for Stainless Steel Weld Metals: A Modification of the WRC-1988 Diagram. *Weldign Journal,* S**,** 171-178.
KOU, S. 2002. *Welding Metallurgy*, John Wiley & Sons.
KOU, S. & LE, Y. 1985. Grain structure and solidification cracking in oscillated arc welds of 5052 aluminum alloy. *Metallurgical Transactions A,* 16**,** 1345-1352.
KOU, S. & LE, Y. 1986. Nucleation mechanism and grain refining of weld metal. *Weld J,* S**,** 305-313.
KOU, S. & WANG, Y. H. 1986. Weld pool convection and its effect. *Welding Research Supplement,* S**,** 63-70.
KOVALEV, A., JAHN, A., WEIß, A., WOLF, S. & SCHELLER, P. R. 2011. Stress-Temperature-Transformation and Deformation-Temperature-Transformation Diagrams for an Austenitic CrMnNi as-cast Steel. *steel research international,* 82**,** 1101-1107.
KOYAMA, A., HAMADA, K. & MATSUI, H. 1991. Specimen size effects on tensile properties of neutron-irradiated steel. *Journal of Nuclear Materials,* 179-181.
KOZUH, S., GOJIC, M. & KOSEC, L. 2009. Mechanical properties and microstructure of austenitic stainless steel after welding and post-weld heat treatment. *Kovove Materialy-Metallic Materials,* 47**,** 253-262.
KRAKHMALEV, P., FREDRIKSSON, G., SVENSSON, K., YADROITSEV, I., YADROITSAVA, I., THUVANDER, M. & PENG, R. 2018. Microstructure, Solidification Texture, and Thermal Stability of 316 L Stainless Steel Manufactured by Laser Powder Bed Fusion. *Metals,* 8.
KUBIN, L. P. & MORTENSOEN, A. 2003. Geometrically necessary dislocations andstrain-gradient plasticity: a few critical issues. *Scripta Materialia* 48**,** 119-125.
KUSSMAUL, K., SCHOCH, F. & LUCKOW, H. 1983. HIGH-QUALITY LARGE COMPONENTS SHAPE WELDED BY A SAW PROCESS. *Welding Journal,* 62**,** 17-24.
LABUSCH, R. 1972. Statistical Theories of Solid-Solution Hardening. *Acta Metallurgica,* 20**,** 917-&.
LAI, J. K. L. 1983. A Review of Precipitation Behavior in Aisi Type-316 Stainless-Steel. *Materials Science and Engineering,* 61**,** 101-109.
LANCASTER, J. F. 1987. *Metallurgy of welding*, Allen & Unwin.

LEUDERS, S., LIENEKE, T., LAMMERS, S., TRÖSTER, T. & NIENDORF, T. 2014. On the fatigue properties of metals manufactured by selective laser melting – The role of ductility. *Journal of Materials Research,* 29**,** 1911-1919.

LEVY, M., BASS, H. & STERN, R. 2000. *Handbook of Elastic Properties of Solids, Liquids, and Gases, Four-Volume Set*, Academic Press.

LEY, F. H., CAMPBELL, S. W., GALLOWAY, A. M. & MCPHERSON, N. A. 2015. Effect of shielding gas parameters on weld metal thermal properties in gas metal arc welding. *The International Journal of Advanced Manufacturing Technology,* 80**,** 1213-1221.

LI, F., CHEN, S. J., SHI, J. B., ZHAO, Y. & TIAN, H. Y. 2018a. Thermoelectric Cooling-Aided Bead Geometry Regulation in Wire and Arc-Based Additive Manufacturing of Thin-Walled Structures. *Applied Sciences-Basel,* 8**,** 1-12.

LI, J., CAO, Y., GAO, B., LI, Y. & ZHU, Y. 2018b. Superior strength and ductility of 316L stainless steel with heterogeneous lamella structure. *Journal of Materials Science,* 53**,** 10442-10456.

LI, J., DENG, D., HOU, X., WANG, X., MA, G., WU, D. & ZHANG, G. 2016. Microstructure and performance optimisation of stainless steel formed by laser additive manufacturing. *Materials Science and Technology,* 32**,** 1223-1230.

LI, Z., LIU, C., XU, T., JI, L., WANG, D., LU, J., MA, S. & FAN, H. 2019. Reducing arc heat input and obtaining equiaxed grains by hot-wire method during arc additive manufacturing titanium alloy. *Materials Science and Engineering: A,* 742**,** 287-294.

LIN, C.-M., LI, J.-C., SU, C.-Y., CHANG, Y.-H., KAI, W.-Y. & CHEN, C.-S. 2017. Effects of water cooling on microstructural evolution, hardness and anti-corrosion properties of Inconel 52 fusion-cladded AISI 316L stainless steel. *Surface and Coatings Technology,* 322**,** 218.

LIPPOLD, J. C. 2005. *Welding Metallurgy and Weldability of Stainless Steels*, Wiley-Interscience.

LIPPOLD, J. C. & SAVAGE, W. F. 1979. Solidification of Austenitic Stainless Steel Weldments: Part I—A Proposed Mechanism. *Welding Journal,* S**,** 362-374.

LIU, J. 2016. *Deformation Induced Martensitic Transformation In 304 Stainless Steels.* Msc., University of South Carolina.

LIU, J., SONG, Y., CHEN, C., WANG, X., LI, H., ZHOU, C. A., WANG, J., GUO, K. & SUN, J. 2020. Effect of scanning speed on the microstructure and mechanical behavior of 316L stainless steel fabricated by selective laser melting. *Materials & Design,* 186**,** 108355.

LIU, L., DING, Q., ZHONG, Y., ZOU, J., WU, J., CHIU, Y.-L., LI, J., ZHANG, Z., YU, Q. & SHEN, Z. 2018. Dislocation network in additive manufactured steel breaks strength–ductility trade-off. *Materials Today,* 21**,** 354-361.

LIU, P., LI, K., PENG, J., PENG, J. & TU, X. 2017a. Mechanical Behavior of 316L Stainless Steel after Strain Hardening. *MATEC Web of Conferences,* 114**,** 02003.

LIU, Y., LV, Y., HE, P., SHU, F., XU, B. & XU, F. 2013. Microstructural Evolution and Mechanical Properties of Inconel 625 Alloy during Pulsed Plasma Arc Deposition Process. *Journal of Materials Science & Technology,* 29**,** 480-488.

LIU, Y., SUN, J., LI, J., JIANG, B. & ZHANG, C. 2017b. Investigation of forging process for eliminating delta ferrites in USC unites last stage blades steel 10Cr12Ni3Mo2VN. *International Conference on the Technology of Plasticity, ICTP 2017, 17-22 September 2017, Cambridge, United Kingdom*.

LIVERANI, E., TOSCHI, S., CESCHINI, L. & FORTUNATO, A. 2017. Effect of selective laser melting (SLM) process parameters on microstructure and mechanical properties of 316L austenitic stainless steel. *Journal of Materials Processing Technology,* 249**,** 255-263.

LOCKETT, H., DING, J., WILLIAMS, S. & MARTINA, F. 2017. Design for Wire + Arc Additive Manufacture: design rules and build orientation selection. *Journal of Engineering Design,* 28**,** 568-598.

LORD, J. D. & MORRELL, R. M. 2010. Elastic modulus measurement—obtaining reliable data from the tensile test. *Metrologia,* 47**,** S41-S49.

LORSAKUL, A. & SUTHAKORN, J. 2007. Dental tool calibration using point-cloud-to-pointcloud technique with the least-square solution: toward developent of a dental navigation system. *WACBE World Congress on Bioengineering 2007***,** 1-4.

LOU, X., ANDRESEN, P. L. & REBAK, R. B. 2018. Oxide inclusions in laser additive manufactured stainless steel and their effects on impact toughness and stress corrosion cracking behavior. *Journal of Nuclear Materials,* 499**,** 182-190.

LU, J., HULTMAN, L., HOLMSTRÖM, E., ANTONSSON, K. H., GREHK, M., LI, W., VITOS, L. & GOLPAYEGANI, A. 2016. Stacking fault energies in austenitic stainless steels. *Acta Materialia,* 111**,** 39-46.

LU, K., LU, L. & SURESH, S. 2009. Strengthening Materials by Engineering Coherent Internal Boundaries at the Nanoscale. *Science,* 324**,** 349-352.

LU, X., ZHOU, Y. F., XING, X. L., SHAO, L. Y., YANG, Q. X. & GAO, S. Y. 2017. Open-source wire and arc additive manufacturing system: formability, microstructures, and mechanical properties. *International Journal of Advanced Manufacturing Technology,* 93**,** 2145-2154.

LUNDIN, C. D., RUPRECHT, W. & ZHOU, G. 1999. Ferrite measurement in austenitic and duplex stainless steel castings-Final Report (No. DOE/ID/13734-1). . *USDOE Idaho Operations Office, Idaho Falls, ID; The University of Tennessee, Knoxville, TN (US).*

MA, D. 2011. *First-principles investigations of solid solution strengthening in Al alloys.* Ph.D., RWTH Aachen UniversitY.

MA, K., WEN, H., HU, T., TOPPING, T. D., ISHEIM, D., SEIDMAN, D. N., LAVERNIA, E. J. & SCHOENUNG, J. M. 2014. Mechanical behavior and strengthening mechanisms in ultrafine grain precipitation-strengthened aluminum alloy. *Acta Materialia,* 62**,** 141-155.

MA, M., WANG, Z. & ZENG, X. 2017. A comparison on metallurgical behaviors of 316L stainless steel by selective laser melting and laser cladding deposition. *Materials Science and Engineering: A,* 685**,** 265-273.

MA, Y. 2015. *Fabrication of gamma titanium aluminide alloys by gas tungsten arc welding-based additive layer manufacturing.* PhD, University of Wollongong.

MACHADO SANTOS CARVALHO NETO, L. 2017. *Studying the Application of Additive Manufacturing to Large Parts.* MSc., Universidade de Lisboa.

MAIER, B., LENLING, M., YEOM, H., JOHNSON, G., MALOY, S. & SRIDHARAN, K. 2019. A novel approach for manufacturing oxide dispersion strengthened (ODS) steel cladding tubes using cold spray technology. *Nuclear Engineering and Technology,* 51**,** 1069-1074.

MARTINA, F., JIALUO DING, S. W., CABALLERO, A., PARDAL, G. & QUINTINO, L. 2019. Tandem Metal Inert Gas process for high productivity Wire Arc Additive Manufacturing in stainless steel. *Additive Manufacturing,* 25**,** 545-550.

MARTINA, F., ROY, M. J., SZOST, B. A., TERZI, S., COLEGROVE, P. A., WILLIAMS, S. W., WITHERS, P. J., MEYER, J. & HOFMANN, M. 2016. Residual stress of as-deposited and rolled wire+arc additive manufacturing Ti–6Al–4V components. *Materials Science and Technology (United Kingdom),* 32**,** 1439-1448.

MARTINA, F. & WILLIAMS, S. 2015. Wire+ arc additive manufacturing vs. traditional machining from solid: a cost comparison. Cranfield University

MARTINA, F., WILLIAMS, S. T. & COLEGROVE, P. Improved microstructure and increased mechanical properties of additive manufacture produced ti-6al-4v by interpass cold rolling. 2013 Annual International Solid Freeform Fabrication Symposium – An Additive Manufacturing Conference, 2013 Austin, Texas, USA. 490-496.

MARTORANO, M. A., TAVARES, C. F. & PADILHA, A. F. 2012. Predicting Delta Ferrite Content in Stainless Steel Castings. *Isij International,* 52**,** 1054-1065.

MATAYA, M. C., NILSSON, E. R., BROWN, E. L. & KRAUSS, G. 2003. Hot working and recrystallization of As-Cast 316L. *Metallurgical and Materials Transactions a-Physical Metallurgy and Materials Science,* 34a**,** 1683-1703.

MATSUDA, F., NAKATA, K. & SANO, N. 1986. Effect of Electromagnetic Stirring on Weld Solidification Structure of Austenitic Stainless Steels (Materials, Metallurgy & Weldability). *Transactions of JWRI,* 15**,** 327-338.

MAZAK. 2020. *HYBRID Multi-Tasking* [Online]. Available: https://www.mazakusa.com/machines/process/hybrid-multi-tasking/ [Accessed 13/04/2020].

MEHMANPARAST, A., DAVIES, C. M., DEAN, D. W. & NIKBIN, K. 2016. Effects of plastic pre-straining level on the creep deformation, crack initiation and growth behaviour

of 316H stainless steel. *International Journal of Pressure Vessels and Piping,* 141**,** 1-10.
MEREDDY, S., BERMINGHAM, M. J., STJOHN, D. H. & DARGUSCH, M. S. 2017. Grain refinement of wire arc additively manufactured titanium by the addition of silicon. *Journal of Alloys and Compounds,* 695**,** 2097-2103.
METAL POWDER REPORT 2017. Norsk Titanium delivers FAA approved AM part to Boeing. *Metal Powder Report,* 72**,** 1.
MIAO, Y., GROSS, D., SANDERS, J. & STUBBINS, J. 2015. Development of Austenitic ODS Strengthened Alloys for Very High Temperature Applications. US Department of Energy.
MICHEL, F., LOCKETT, H., DING, J., MARTINA, F., MARINELLI, G. & WILLIAMS, S. 2019. A modular path planning solution for Wire + Arc Additive Manufacturing. *Robotics and Computer-Integrated Manufacturing,* 60**,** 1-11.
MILEWSKI, J. O. 2017. Lasers, Electron Beams, Plasma Arcs. *Additive Manufacturing of Metals.* Springer International Publishing
MIRSHEKARI, G. R., TAVAKOLI, E., ATAPOUR, M. & SADEGHIAN, B. 2014. Microstructure and corrosion behavior of multipass gas tungsten arc welded 304L stainless steel. *Materials & Design,* 55**,** 905-911.
MISHRA, S., NARASIMHAN, K. & SAMAJDAR, I. 2013. Deformation twinning in AISI 316L austenitic stainless steel: role of strain and strain path. *Materials Science and Technology,* 23**,** 1118-1126.
MISRA, R. D. K., INJETI, V. S. Y. & SOMANI, M. C. 2018. The significance of deformation mechanisms on the fracture behavior of phase reversion-induced nanostructured austenitic stainless steel. *Sci Rep,* 8**,** 7908.
MONTEVECCHI, F., VENTURINI, G., GROSSI, N., SCIPPA, A. & CAMPATELLI, G. 2018. Idle time selection for wire-arc additive manufacturing: A finite element-based technique. *Additive Manufacturing,* 21**,** 479-486.
MOORE, P., ADDISON, A. & NOWAK-COVENTRY, M. 2019. Mechanical properties of wire plus arc additive manufactured steel and stainless steel structures. *Welding in the World,* 63**,** 1521-1530.
MOSA, E. S., MORSY, M. A. & ATLAM, A. 2017. Effect Of Heat Input And Shielding Gas On Microstructure And Mechanical Properties Of Austenitic Stainless Steel 304l. *International Research Journal of Engineering and Technology (IRJET),* 04**,** 370-377.
MOSLEMI, N., REDZUAN, N., AHMAD, N. & HOR, T. N. 2015. Effect of Current on Characteristic for 316 Stainless Steel Welded Joint Including Microstructure and Mechanical Properties. *Procedia CIRP,* 26**,** 560-564.
MOUSAVI, M. G., HERMANS, M. J. M., RICHARDSON, I. M. & DEN OUDEN, G. 2003. Grain refinement due to grain detachment in electromagnetically stirred AA7020 welds. *Science and Technology of Welding and Joining,* 8**,** 309-312.
MUKHERJEE, T. & DEBROY, T. 2019. Printability of 316 stainless steel. *Science and Technology of Welding and Joining,* 24**,** 412-419.
MUKHERJEE, T., ZUBACK, J. S., DE, A. & DEBROY, T. 2016. Printability of alloys for additive manufacturing. *Scientific Reports,* 6**,** 1-8.
MÜNSTERMANN, S., FENG, Y. & BLECK, W. 2014. Influencing parameters on elastic modulus of steels. *Canadian Metallurgical Quarterly,* 53**,** 264-273.
MURPHY, A. B., TANAKA, M., TASHIRO, S., SATO, T. & LOWKE, J. J. 2009. A computational investigation of the effectiveness of different shielding gas mixtures for arc welding. *Journal of Physics D-Applied Physics,* 42**,** 115205.
MURR, L. E. 2015. Examples of Directional Crystal Structures: Gas-Turbine Component Applications in Superalloys. *Handbook of Materials Structures, Properties, Processing and Performance.* Switzerland: Springer International Publishing.
MURRAY, J. W. & CLARE, A. T. 2012. Repair of EDM induced surface cracks by pulsed electron beam irradiation. *Journal of Materials Processing Technology,* 212**,** 2642-2651.
MX3D. 2019. *MX3D Bridge* [Online]. Available: https://mx3d.com/projects/mx3d-bridge/ [Accessed 13/04/2020].

NABARRO, F. R. N. 1977. The theory of solution hardening. *The Philosophical Magazine: A Journal of Theoretical Experimental and Applied Physics,* 35**,** 613-622.
NAKADA, N., ITO, H., MATSUOKA, Y., TSUCHIYAMA, T. & TAKAKI, S. 2010. Deformation-induced martensitic transformation behavior in cold-rolled and cold-drawn type 316 stainless steels. *Acta Materialia,* 58**,** 895-903.
NGUYEN, Q. B., ZHU, Z., NG, F. L., CHUA, B. W., NAI, S. M. L. & WEI, J. 2019. High mechanical strengths and ductility of stainless steel 304L fabricated using selective laser melting. *Journal of Materials Science & Technology,* 35**,** 388-394.
NGUYEN, T. C., WECKMAN, D. C., JOHNSON, D. A. & KERR, H. W. 2013. The humping phenomenon during high speed gas metal arc welding. *Science and Technology of Welding and Joining,* 10**,** 447-459.
NIENDORF, T., LEUDERS, S., RIEMER, A., RICHARD, H. A., TRÖSTER, T. & SCHWARZE, D. 2013. Highly Anisotropic Steel Processed by Selective Laser Melting. *Metallurgical and Materials Transactions B,* 44**,** 794-796.
NITSCHKE-PAGEL, T. & WOHLFAHRT, H. 2002. Residual Stresses in Welded Joints – Sources and Consequences. *Materials Science Forum,* 404-407**,** 215-226.
NORSK TITANIUM AS 2017. Method and arrangement for building metallic objects by solid freeform fabrication. US Patent App. 15/267,027.
NORSTRÖM, L. Å. 1977. The influence of nitrogen and grain size on yield strength in Type AISI 316L austenitic stainless steel. *Metal Science,* 11**,** 208-212.
NPL 2006. A National Measurement Good Practice Guide. No. 98. Elastic Modulus Measurement.
OLA, O. T. & DOERN, F. E. 2014. A study of cold metal transfer clads in nickel-base INCONEL 718 superalloy. *Materials & Design,* 57**,** 51-59.
PACE, M. L., GUARNACCIO, A., DOLCE, P., MOLLICA, D., PARISI, G. P., LETTINO, A., MEDICI, L., SUMMA, V., CIANCIO, R. & SANTAGATA, A. 2017. 3D additive manufactured 316L components microstructural features and changes induced by working life cycles. *Applied Surface Science,* 418**,** 437-445.
PADILHA, A. F. & RIOS, P. R. 2002. Decomposition of Austenite in Austenitic Stainless Steels. *ISIJ International,* 42**,** 325-327.
PAL, K. & PAL, S. K. 2010. Effect of Pulse Parameters on Weld Quality in Pulsed Gas Metal Arc Welding: A Review. *Journal of Materials Engineering and Performance,* 20**,** 918-931.
PALMER, T. A. & DEBROY, T. 2000. Numerical modeling of enhanced nitrogen dissolution during gas tungsten arc welding. *Metallurgical and Materials Transactions B-Process Metallurgy and Materials Processing Science,* 31**,** 1371-1385.
PAN, C. X. & CHEN, B. Q. 1995. Formation of the deformation twinning in austenitic stainless steel weld metal. *Journal of Materials Science Letters,* 14**,** 1798-1800.
PAN, Z., DING, D., WU, B., CUIURI, D., LI, H. & NORRISH, J. 2018. Arc Welding Processes for Additive Manufacturing: A Review. *Transactions on Intelligent Welding Manufacturing,* 1**,** 3-24.
PENN, R. 2017. *3D printing of 316L stainless steel and its effect on microstructure and mechanical properties.* Graduate Theses & Non-Theses, Montana Tech.
PHAM, M. S., DOVGYY, B. & HOOPER, P. A. 2017. Twinning induced plasticity in austenitic stainless steel 316L made by additive manufacturing. *Materials Science and Engineering: A,* 704**,** 102-111.
PICKERING, F. B., IRVINE, K. J. & GLADMAN, T. 1969. The strength of austenitic stainless steels. *J Iron Steel Inst,* 207**,** 1017-1028.
POHL, F., HARDES, C., SCHOLZ, F. & FRENZEL, J. 2020. Orientation-Dependent Deformation Behavior of 316L Steel Manufactured by Laser Metal Deposition and Casting under Local Scratch and Indentation Load. *Materials (Basel),* 13.
PRINT PIONEERS. 2020. *ART 3DMP® – "printed ART" and yet, every piece a unique copy* [Online]. Available: https://www.print-pioneers.com/art-2/ [Accessed 13/04/2020].
PRODWAYS. 2017. *Prodways Group presents its new Rapid Additive Forging technology for the 3D metal printing of large parts* [Online]. Available: https://www.prodways.com/en/wp-content/uploads/sites/2/2017/06/2017-June-Prodways-Group-presents-its-new-Rapid-Additive-Forging-technology-EN1.pdf [Accessed 13/04/2020].

QIAN, Y.-P., HUANG, J.-H., ZHANG, H.-O. & WANG, G.-L. 2008. Direct rapid high-temperature alloy prototyping by hybrid plasma-laser technology. *Journal of Materials Processing Technology,* 208**,** 99-104.
QIN, W., LI, J., LIU, Y., KANG, J., ZHU, L., SHU, D., PENG, P., SHE, D., MENG, D. & LI, Y. 2019. Effects of grain size on tensile property and fracture morphology of 316L stainless steel. *Materials Letters,* 254**,** 116-119.
QUEGUINEUR, A., RÜCKERT, G., CORTIAL, F. & HASCOËT, J. Y. 2017. Evaluation of wire arc additive manufacturing for large-sized components in naval applications. *Welding in the World***,** 1-8.
RAABE, D., SANDLÖBES, S., MILLÁN, J., PONGE, D., ASSADI, H., HERBIG, M. & CHOI, P. P. 2013. Segregation engineering enables nanoscale martensite to austenite phase transformation at grain boundaries: A pathway to ductile martensite. *Acta Materialia,* 61**,** 6132-6152.
RAHMAN, K. M. 2013. *Mechanical Behaviour of Twinning Induced Plasticity (TWIP) Steels.* Ph.D., Imperial College London.
RAMAN, L., GOTHANDAPANI, K. & MURTY, B. S. 2016. Austenitic Oxide Dispersion Strengthened Steels : A Review. *Defence Science Journal,* 66**,** 316-322.
RÄNNAR, L.-E., KOPTYUG, A., OLSÉN, J., SAEIDI, K. & SHEN, Z. 2017. Hierarchical structures of stainless steel 316L manufactured by Electron Beam Melting. *Additive Manufacturing,* 17**,** 106-112.
RASBAND, W. 2012. ImageJ: Image processing and analysis in Java. *Astrophysics Source Code Library*.
RAYAPROLU, D. B. & HENDRY, A. 1988. High nitrogen stainless steel wire. *Materials Science and Technology,* 4**,** 136-145.
READ, D. T., MCHENRY, H. I., STEINMEYER, P. A. & THOMAS, R. D. 1980. Metallurgical Factors Affecting the Toughness of 316l SMA Weldments at Cryogenic Temperatures. *Welding Journal,* 59**,** 104-113.
REED, R. C. 2006. 1.3.2 Historical Development of the Superalloys. *Superalloys - Fundamentals and Applications.* Cambridge University Press.
REED, R. P. 1989. Nitrogen in austenitic stainless steels. *JOM,* 41**,** 16-21.
REED, R. P. & SIMON, N. J. 1988. Nitrogen strengthening of austenitic stainless steels at low temperatures. *HNS-88*.
RELATIVITY SPACE. 2019. *Terran 1, A Rocket Built And Flown In Days Instead Of Years* [Online]. Available: https://www.relativityspace.com/stargate [Accessed 13/04/2020].
RENISHAW. 2016. *The Power of Additive Manufacturing* [Online]. Available: http://resources.renishaw.com/download.aspx?lang=en&data=82843&btn=1 [Accessed 13/04/2020].
RENISHAW. 2017. *Data sheet: laser melting powder titanium alloy Ti6Al4V (grade 23)[a] Processed using AM250 with 200 W laser* [Online]. Available: https://cdn3.starrapid.com/wp-content/uploads/2017/03/StarRapid_RenishawMaterial_TitaniumTi6Al4V.pdf [Accessed 13/04/2020].
RÍOS, S., COLEGROVE, P. A., MARTINA, F. & WILLIAMS, S. W. 2018. Analytical process model for wire + arc additive manufacturing. *Additive Manufacturing,* 21**,** 651-657.
RIZA, S. H., MASOOD, S. H., WEN, C., RUAN, D. & XU, S. 2014. Dynamic behaviour of high strength steel parts developed through laser assisted direct metal deposition. *Materials & Design,* 64**,** 650-659.
ROA, J. J., SUAREZ, S., GUITAR, A., FARGAS, G. & MATEO, A. 2019. Geometrically Necessary Dislocations on Plastic Deformation of Polycrystalline TRIP Steel. *Crystals,* 9**,** 1-7.
RODRIGUEZ, N., VÁZQUEZ, L., HUARTE, I., ARRUTI, E., TABERNERO, I. & ALVAREZ, P. 2018. Wire and arc additive manufacturing: a comparison between CMT and TopTIG processes applied to stainless steel. *Welding in the World,* 62**,** 1083-1096.
RONNEBERG, T., DAVIES, C. M. & HOOPER, P. A. 2020. Revealing relationships between porosity, microstructure and mechanical properties of laser powder bed fusion 316L stainless steel through heat treatment. *Materials & Design,* 189.

RYAN, E. M., SABIN, T. J., WATTS, J. F. & WHITING, M. J. 2018. The influence of build parameters and wire batch on porosity of wire and arc additive manufactured aluminium alloy 2319. *Journal of Materials Processing Technology,* 262**,** 577-584.

SABOORI, A., TOUSHEKHAH, M., AVERSA, A., LAI, M., LOMBARDI, M., BIAMINO, S. & FINO, P. 2020. Critical Features in the Microstructural Analysis of AISI 316L Produced By Metal Additive Manufacturing. *Metallography, Microstructure, and Analysis,* 9**,** 92-96.

SAE INTERNATIONAL 1965. Nickel Alloy, Corrosion and Heat Resistant, Bars, Forgings, and Rings 52.5Ni 19Cr 3.0Mo 5.1Cb 0.90Ti 0.50Al 19Fe, Consumable Electrode or Vacuum Induction Melted 1775°F (968°C) Solution and Precipitation Heat Treated. *AMS 5663.*

SAE INTERNATIONAL 2017. Aluminum Alloy, Sheet and Plate 6.3Cu - 0.30Mn - 0.06Ti - 0.10V - 0.18Zr Solution and Precipitation Heat Treated (2219 -T81/-T851). *AMS4599.*

SAEIDI, K. & AKHTAR, F. 2018. Subgrain-controlled grain growth in the laser-melted 316 L promoting strength at high temperatures. *R Soc Open Sci,* 5**,** 172394.

SAEIDI, K., KVETKOVÁ, L., LOFAJ, F. & SHEN, Z. 2015. Austenitic stainless steel strengthened by the in situ formation of oxide nanoinclusions. *RSC Advances,* 5**,** 20747-20750.

SAEIDI, K., NEIKTER, M., OLSEN, J., SHEN, Z. J. & AKHTAR, F. 2017. 316L stainless steel designed to withstand intermediate temperature. *Materials & Design,* 135**,** 1-8.

SAIED, M. 2016. *Experimental and numerical modeling of the dissolution of delta ferrite in the Fe-Cr-Ni system : application to the austenitic stainless steels.* Ph.D., Université Grenoble Alpes,.

SAKHAWAT, S., FALAHATI, A., DEGISCHER, H. P., SPIRADEK, K. & DOMÁNKOVÁ, M. 2014. Localized ageing in the heat affected zone of welded X5CrNiCuNbl6-4 and X4CrNiSiTi14-7 sheets. *IOP Conference Series: Materials Science and Engineering,* 60**,** 012071.

SAMES, W. J., LIST, F. A., PANNALA, S., DEHOFF, R. R. & BABU, S. S. 2016. The metallurgy and processing science of metal additive manufacturing. *International Materials Reviews,* 61**,** 315-360.

SAMES, W. J., UNOCIC, K. A., HELMREICH, G. W., KIRKA, M. M., MEDINA, F., DEHOFF, R. R. & BABU, S. S. 2017. Feasibility of in situ controlled heat treatment (ISHT) of Inconel 718 during electron beam melting additive manufacturing. *Additive Manufacturing,* 13**,** 156-165.

SANCHEZ-TOVAR, R., MONTANES, M. T., GARCIA-ANTON, J., GARCIA-ANTON, J., SANCHEZ-TOVAR, R. & MONTANES, M. T. 2011. Effect of the micro-plasma arc welding technique on the microstructure and pitting corrosion of AISI 316L stainless steels in heavy LiBr brines. *Corrosion Science,* 53**,** 2598-2610.

SATO, Y., DONG, W., KOKWAWA, H. & KUWANA, T. 2000. Nitrogen absorption by iron and stainless steels during YAG laser welding. *ISIJ International,* 40**,** 20-24.

SEALY, M. P., MADIREDDY, G., WILLIAMS, R. E., RAO, P. & TOURSANGSARAKI, M. 2018. Hybrid Processes in Additive Manufacturing. *Journal of Manufacturing Science and Engineering,* 140**,** 060801-060801-13.

SEIFI, M., GORELIK, M., WALLER, J., HRABE, N., SHAMSAEI, N., DANIEWICZ, S. & LEWANDOWSKI, J. J. 2017. Progress Towards Metal Additive Manufacturing Standardization to Support Qualification and Certification. *Jom,* 69**,** 439-455.

SELVI, S., VISHVAKSENAN, A. & RAJASEKAR, E. 2018. Cold metal transfer (CMT) technology - An overview. *Defence Technology,* 14**,** 28-44.

SEQUEIRA ALMEIDA, P. M. & WILLIAMS, S. W. 2010. Innovative Process Model of Ti-6Al-4V Additive Layer Manufacturing Using Cold Metal Transfer (CMT). *Proccedings of the 21st Annual International Solid Freeform Fabrication Symposium***,** 25-36.

SHAMSUJJOHA, M., AGNEW, S. R., FITZ-GERALD, J. M., MOORE, W. R. & NEWMAN, T. A. 2018. High Strength and Ductility of Additively Manufactured 316L Stainless Steel Explained. *Metallurgical and Materials Transactions a-Physical Metallurgy and Materials Science,* 49a**,** 3011-3027.

SHANKAR, V., GILL, T. P. S., MANNAN, S. L. & SUNDARESAN, S. 2003. Effect of nitrogen addition on microstructure and fusion zone cracking in type 316L stainless steel weld metals. *Materials Science and Engineering a-Structural Materials Properties Microstructure and Processing,* 343**,** 170-181.

SHEN, C., PAN, Z., MA, Y., CUIURI, D. & LI, H. 2015. Fabrication of iron-rich Fe–Al intermetallics using the wire-arc additive manufacturing process. *Additive Manufacturing,* 7**,** 20-26.

SILVA, C. C., DE MIRANDA, H. C., DE SANT'ANA, H. B. & FARIAS, J. P. 2009. Microstructure, hardness and petroleum corrosion evaluation of 316L/AWS E309MoL-16 weld metal. *Materials Characterization,* 60**,** 346-352.

SILWAL, B. & SANTANGELO, M. 2018. Effect of vibration and hot-wire gas tungsten arc (GTA) on the geometric shape. *Journal of Materials Processing Technology,* 251**,** 138-145.

SIMMONS, J. W. 1996. Overview: High-nitrogen alloying of stainless steels. *Materials Science and Engineering a-Structural Materials Properties Microstructure and Processing,* 207**,** 159-169.

SITKO, M., SKOCZEŃ, B. & WRÓBLEWSKI, A. 2010. FCC–BCC phase transformation in rectangular beams subjected to plastic straining at cryogenic temperatures. *International Journal of Mechanical Sciences,* 52**,** 993-1007.

SKIBA, T., BAUFELD, B. & BIEST, O. V. D. 2009. Microstructure and Mechanical Properties of Stainless Steel Component Manufactured by Shaped Metal Deposition. *ISIJ International,* 49**,** 1588-1591.

SMITH, T. R., SUGAR, J. D., MARCHI, C. S. & SCHOENUNG, J. M. 2019. Strengthening mechanisms in directed energy deposited austenitic stainless steel. *Acta Materialia,* 164**,** 728-740.

SMITH, T. R., SUGAR, J. D., SCHOENUNG, J. M. & SAN MARCHI, C. 2018. Anomalous Annealing Response of Directed Energy Deposited Type 304L Austenitic Stainless Steel. *Jom,* 70**,** 358-363.

SOLOMON, N. & SOLOMON, I. 2010. Deformation induced martensite in AISI 316 stainless steel. *Revista de Metalurgia,* 46**,** 121-128.

SPENCER, K., CONLON, K. T., BRÉCHET, Y. & EMBURY, J. D. 2013a. The strain induced martensite transformation in austenitic stainless steels: Part 2 – Effect of internal stresses on mechanical response. *Materials Science and Technology,* 25**,** 18-28.

SPENCER, K., VÉRON, M., YU-ZHANG, K. & EMBURY, J. D. 2013b. The strain induced martensite transformation in austenitic stainless steels: Part 1 – Influence of temperature and strain history. *Materials Science and Technology,* 25**,** 7-17.

SRIBA, A., VOGT, J.-B. & AMARA, S.-E. 2018. Microstructure, Micro-hardness and Impact Toughness of Welded Austenitic Stainless Steel 316L. *Transactions of the Indian Institute of Metals,* 71**,** 2303-2314.

SRIDHARAN, N., NOAKES, M. W., NYCZ, A., LOVE, L. J., DEHOFF, R. R. & BABU, S. S. 2018. On the toughness scatter in low alloy C-Mn steel samples fabricated using wire arc additive manufacturing. *Materials Science and Engineering: A,* 713**,** 18-27.

STEIN, G. & HUCKLENBROICH, I. 2004. Manufacturing and Applications of High Nitrogen Steels. *Materials and Manufacturing Processes,* 19**,** 7-17.

STRAFFELINI, G., FONTANARI, V. & MOLINARI, A. 1999. True and apparent Young's modulus in ferrous porous alloys. *Materials Science and Engineering A,* 260**,** 197-202.

STRNADEL, B. & BRUMEK, J. 2013. The Size Effect In Tensile Test Of Steels. *Proceedings of the ASME 2013 Pressure Vessels and Piping Conference***,** 1-7.

SUN, R., LI, L., ZHU, Y., GUO, W., PENG, P., CONG, B., SUN, J., CHE, Z., LI, B., GUO, C. & LIU, L. 2018a. Microstructure, residual stress and tensile properties control of wire-arc additive manufactured 2319 aluminum alloy with laser shock peening. *Journal of Alloys and Compounds,* 747**,** 255-265.

SUN, Z., TAN, X., TOR, S. B. & CHUA, C. K. 2018b. Simultaneously enhanced strength and ductility for 3D-printed stainless steel 316L by selective laser melting. *NPG Asia Materials,* 10**,** 127-136.

SUZUKI, M., YAMAGUCHI, R., MURAKAMI, K. & NAKADA, M. 2001. Inclusion particle growth during solidification of stainless steel. *Isij International,* 41**,** 247-256.

TAMINGER, K. & HAFLEY, R. A. 2003. Electron Beam Freeform Fabrication: A Rapid Metal Deposition Process. *Proceedings of third annual automotive composites conference*.
TANG, H. P., QIAN, M., LIU, N., ZHANG, X. Z., YANG, G. Y. & WANG, J. 2015. Effect of Powder Reuse Times on Additive Manufacturing of Ti-6Al-4V by Selective Electron Beam Melting. *Jom,* 67**,** 555-563.
TAPARLI, U. A., KANNENGIESSER, T., CIESLIK, K., MORY, D. & GRIESCHE, A. 2020. In situ chemical composition analysis of a tungsten-inert-gas austenitic stainless steel weld measured by laser-induced breakdown spectroscopy. *Spectrochimica Acta Part B: Atomic Spectroscopy,* 167**,** 105826.
THAVAMANI, R., BALUSAMY, V., NAMPOOTHIRI, J., SUBRAMANIAN, R. & RAVI, K. R. 2018. Mitigation of hot cracking in Inconel 718 superalloy by ultrasonic vibration during gas tungsten arc welding. *Journal of Alloys and Compounds,* 740**,** 870-878.
TIAN, Y., SHEN, J., HU, S., LIANG, Y. & BAI, P. 2018. Effects of ultrasonic peening treatment on surface quality of CMT-welds of Al alloys. *Journal of Materials Processing Technology,* 254**,** 193-200.
TORIBIO, J. 1998. Residual stress effects in stress-corrosion cracking. *Journal of Materials Engineering and Performance,* 7**,** 173-182.
TRELEWICZ, J. R., HALADA, G. P., DONALDSON, O. K. & MANOGHARAN, G. 2016. Microstructure and Corrosion Resistance of Laser Additively Manufactured 316L Stainless Steel. *Jom,* 68**,** 850-859.
TURLEY, J. & SINES, G. 1971. The anisotropy of Young's modulus, shear modulus and Poisson's ratio in cubic materials. *J. Phys. D: Appl. Phys.,* 4.
TWI. 2020. *Heat treatment of welded joints* [Online]. Available: http://www.twi-global.com/technical-knowledge/job-knowledge/heat-treatment-of-welded-joints-part-1-114/ [Accessed 13/04/2020].
VAN DER AA, E. M. 2007. *Local Cooling during Welding: Prediction and Control of Residual Stresses and Buckling Distortion.* Ph.D., Delft University of Technology.
WAAM3D. 2020. *WireAM for everyone* [Online]. Available: https://waam3d.com/ [Accessed 21/04/2020].
WADA, H. & PEHLKE, R. D. 1977. Solubility of Nitrogen in Liquid Fe-Cr-Ni Alloys Containing Manganese and Molybdenum. *Metallurgical Transactions B-Process Metallurgy,* 8**,** 675-682.
WANG, C., TAN, X., LIU, E. & TOR, S. B. 2018a. Process parameter optimization and mechanical properties for additively manufactured stainless steel 316L parts by selective electron beam melting. *Materials & Design,* 147**,** 157-166.
WANG, F., WILLIAMS, S., COLEGROVE, P. & ANTONYSAMY, A. A. 2012. Microstructure and Mechanical Properties of Wire and Arc Additive Manufactured Ti-6Al-4V. *Metallurgical and Materials Transactions A,* 44**,** 968-977.
WANG, J. F., SUN, Q. J., WANG, H., LIU, J. P. & FENG, J. C. 2016a. Effect of location on microstructure and mechanical properties of additive layer manufactured Inconel 625 using gas tungsten arc welding. *Materials Science and Engineering: A,* 676**,** 395-405.
WANG, L. & XUE, J. 2017. Perspective on Double Pulsed Gas Metal Arc Welding. *Applied Sciences,* 7**,** 1-18.
WANG, L., XUE, J. & WANG, Q. 2019a. Correlation between arc mode, microstructure, and mechanical properties during wire arc additive manufacturing of 316L stainless steel. *Materials Science and Engineering: A,* 751**,** 183-190.
WANG, M., ZHOU, Z., SUN, H., HU, H. & LI, S. 2013. Microstructural observation and tensile properties of ODS-304 austenitic steel. *Materials Science and Engineering: A,* 559**,** 287-292.
WANG, Q., LI, Z., PANG, S., LI, X., DONG, C. & LIAW, P. 2018b. Coherent Precipitation and Strengthening in Compositionally Complex Alloys: A Review. *Entropy,* 20**,** 1-23.
WANG, X., MUÑIZ-LERMA, J. A., ATTARIAN SHANDIZ, M., SANCHEZ-MATA, O. & BROCHU, M. 2019b. Crystallographic-orientation-dependent tensile behaviours of stainless steel 316L fabricated by laser powder bed fusion. *Materials Science and Engineering: A,* 766.

WANG, X., WANG, A. & LI, Y. 2019c. A sequential path-planning methodology for wire and arc additive manufacturing based on a water-pouring rule. *The International Journal of Advanced Manufacturing Technology,* 103**,** 3813-3830.

WANG, Y., QI, B., CONG, B., YANG, M. & LIU, F. 2017. Arc characteristics in double-pulsed VP-GTAW for aluminum alloy. *Journal of Materials Processing Technology,* 249**,** 89-95.

WANG, Y. M., VOISIN, T., MCKEOWN, J. T., YE, J., CALTA, N. P., LI, Z., ZENG, Z., ZHANG, Y., CHEN, W., ROEHLING, T. T., OTT, R. T., SANTALA, M. K., DEPOND, P. J., MATTHEWS, M. J., HAMZA, A. V. & ZHU, T. 2018c. Additively manufactured hierarchical stainless steels with high strength and ductility. *Nat Mater,* 17**,** 63-71.

WANG, Z., PALMER, T. A. & BEESE, A. M. 2016b. Effect of processing parameters on microstructure and tensile properties of austenitic stainless steel 304L made by directed energy deposition additive manufacturing. *Acta Materialia,* 110**,** 226-235.

WATANABE, T., SHIROKI, M., YANAGISAWA, A. & SASAKI, T. 2010. Improvement of mechanical properties of ferritic stainless steel weld metal by ultrasonic vibration. *Journal of Materials Processing Technology,* 210**,** 1646-1651.

WEISHEIT, A., BARON, C., RAABE, D., JÄGLE, E. A., SPRINGER, H., SZCZEPANIAK, A. & WILMS, M. B. 2016. Efficient additive manufacturing production of oxide- and nitride-dispersion-strengthened materials through atmospheric reactions in liquid metal deposition. *Materials & Design,* 111**,** 60-69.

WEISS, B. & STICKLER, R. 1972. Phase Instabilities during High-Temperature Exposure of 316 Austenitic Stainless-Steel. *Metallurgical Transactions,* 3**,** 851-865.

WELLS, M. E. & LUKENS, W. E. 1986. Effect of Forced Gas Cooling on GTA Weld Pools. *Welding Research Supplement,* S**,** 314-320.

WEN, D., LONG, P., LI, J., HUANG, L. & ZHENG, Z. 2020. Effects of linear heat input on microstructure and corrosion behavior of an austenitic stainless steel processed by wire arc additive manufacturing. *Vacuum,* 173**,** 109131.

WEN, T., LIU, S.-Y., CHEN, S., LIU, L.-T. & YANG, C. 2015. Influence of high frequency vibration on microstructure and mechanical properties of TIG welding joints of AZ31 magnesium alloy. *Transactions of Nonferrous Metals Society of China,* 25**,** 397-404.

WENKAI, X., LI, Z., FUJU, Z., KESUN, D., XIAN, Z., XUE, Y. & BINGJUN, C. 2015. Effect of heat input on cryogenic toughness of 316LN austenitic stainless steel NG-MAG welding joints with large thickness. *Materials and Design,* 86**,** 160-167.

WHEELER, J., MARIANI, E., PIAZOLO, S., PRIOR, D. J., TRIMBY, P. & DRURY, M. R. 2008. The weighted Burgers vector: a new quantity for constraining dislocation densities and types using electron backscatter diffraction on 2D sections through crystalline materials. *Journal of Microscopy,* 233**,** 482–494.

WILLIAMS, S. W., MARTINA, F., ADDISON, A. C., DING, J., PARDAL, G. & COLEGROVE, P. 2016. Wire + Arc Additive Manufacturing. *Materials Science and Technology,* 32**,** 641-647.

WITHERS, P. 2007. Residual stress and its role in failure. *Reports on progress in physics,* 70**,** 2211-2264.

WOOD, S. 2006. *Investigation of The Effect Of Pulsing Shielding Gas in Arc Welding.* MSc., The Ohio State University

WU, A. S., BROWN, D. W., KUMAR, M., GALLEGOS, G. F. & KING, W. E. 2014. An Experimental Investigation into Additive Manufacturing-Induced Residual Stresses in 316L Stainless Steel. *Metallurgical and Materials Transactions A,* 45**,** 6260-6270.

WU, B., DING, D., PAN, Z., CUIURI, D., LI, H., HAN, J. & FEI, Z. 2017a. Effects of heat accumulation on the arc characteristics and metal transfer behavior in Wire Arc Additive Manufacturing of Ti6Al4V. *Journal of Materials Processing Technology,* 250**,** 304-312.

WU, B., MYANT, C. & WEIDER, S. Z. 2017b. *The value of additive manufacturing: future opportunities,* Imperial College London.

WU, B., PAN, Z., DING, D., CUIURI, D., LI, H. & FEI, Z. 2018a. The effects of forced interpass cooling on the material properties of wire arc additively manufactured Ti6Al4V alloy. *Journal of Materials Processing Technology,* 258**,** 97-105.

WU, B., PAN, Z., DING, D., CUIURI, D., LI, H., XU, J. & NORRISH, J. 2018b. A review of the wire arc additive manufacturing of metals: properties, defects and quality improvement. *Journal of Manufacturing Processes,* 35**,** 127-139.

WU, C., LI, S., ZHANG, C. & WANG, X. 2015. Microstructural evolution in 316LN austenitic stainless steel during solidification process under different cooling rates. *Journal of Materials Science,* 51**,** 2529-2539.

WU, Q., LU, J., LIU, C., FAN, H., SHI, X., FU, J. & MA, S. 2017c. Effect of Molten Pool Size on Microstructure and Tensile Properties of Wire Arc Additive Manufacturing of Ti-6Al-4V Alloy. *Materials,* 10**,** 749-750.

WU, W., XUE, J., WANG, L., ZHANG, Z., HU, Y. & DONG, C. 2019a. Forming Process, Microstructure, and Mechanical Properties of Thin-Walled 316L Stainless Steel Using Speed-Cold-Welding Additive Manufacturing. *Metals,* 9**,** 1-21.

WU, W., XUE, J., ZHANG, Z., REN, X. & XIE, B. 2019b. Process Optimization on Multilayer Morphology During 316L Double-wire CMT+P Deposition Process. *Metals,* 9.

WU, Y. & KOVACEVIC, R. 2002. Mechanically assisted droplet transfer process in gas metal arc welding. *Proceedings of the Institution of Mechanical Engineers, Part B: Journal of Engineering Manufacture,* 216**,** 555-564.

XIONG, Y., HE, T., WANG, J., LU, Y., CHEN, L., REN, F., LIU, Y. & VOLINSKY, A. A. 2015. Cryorolling effect on microstructure and mechanical properties of Fe–25Cr–20Ni austenitic stainless steel. *Materials & Design,* 88**,** 398-405.

XU, F., DHOKIA, V., COLEGROVE, P., MCANDREW, A., WILLIAMS, S., HENSTRIDGE, A. & NEWMAN, S. T. 2018a. Realization of A Multi-Sensor Framework for Process Monitoring of the Wire Arc Additive Manufacturing in Producing Ti6Al4V Parts. *International Journal of Computer Integrated Manufacturing,* 31**,** 785-798.

XU, X., GANGULY, S., DING, J., GUO, S., WILLIAMS, S. & MARTINA, F. 2018b. Microstructural evolution and mechanical properties of maraging steel produced by wire + arc additive manufacture process. *Materials Characterization,* 143**,** 152-162.

XU, X., GANGULY, S., DING, J., SEOW, C. E. & WILLIAMS, S. 2018c. Enhancing mechanical properties of wire + arc additively manufactured INCONEL 718 superalloy through in-process thermomechanical processing. *Materials & Design,* 160**,** 1042–1051.

XU, X., MI, G., LUO, Y., JIANG, P., SHAO, X. & WANG, C. 2017. Morphologies, microstructures, and mechanical properties of samples produced using laser metal deposition with 316 L stainless steel wire. *Optics and Lasers in Engineering,* 94**,** 1-11.

XUE, Q., CERRETA, E. & GRAYIII, G. 2007. Microstructural characteristics of post-shear localization in cold-rolled 316L stainless steel. *Acta Materialia,* 55**,** 691-704.

YADOLLAHI, A. & SHAMSAEI, N. 2017. Additive manufacturing of fatigue resistant materials: Challenges and opportunities. *International Journal of Fatigue,* 98**,** 14-31.

YADOLLAHI, A., SHAMSAEI, N., THOMPSON, S. M. & SEELY, D. W. 2015. Effects of process time interval and heat treatment on the mechanical and microstructural properties of direct laser deposited 316L stainless steel. *Materials Science and Engineering: A,* 644**,** 171-183.

YAN, F., XIONG, W., FAIERSON, E. & OLSON, G. B. 2018. Characterization of nano-scale oxides in austenitic stainless steel processed by powder bed fusion. *Scripta Materialia,* 155**,** 104-108.

YAN, F. K., LIU, G. Z., TAO, N. R. & LU, K. 2012. Strength and ductility of 316L austenitic stainless steel strengthened by nano-scale twin bundles. *Acta Materialia,* 60**,** 1059-1071.

YANG, K. & REN, Y. 2010. Nickel-free austenitic stainless steels for medical applications. *Sci Technol Adv Mater,* 11**,** 014105.

YANG, N., YEE, J., ZHENG, B., GAISER, K., REYNOLDS, T., CLEMON, L., LU, W. Y., SCHOENUNG, J. M. & LAVERNIA, E. J. 2016. Process-Structure-Property Relationships for 316L Stainless Steel Fabricated by Additive Manufacturing and Its Implication for Component Engineering. *Journal of Thermal Spray Technology,* 26**,** 610-626.

YANG, Y. P., DONG, P., ZHANG, J. & TIAN, X. 2000. A Hot-Cracking Mitigation Technique for Welding High-Strength Aluminum Alloy. *Welding Research Supplement***,** 9-17.

YANUSHKEVICH, Z., DOBATKIN, S. V., BELYAKOV, A. & KAIBYSHEV, R. 2017. Hall-Petch relationship for austenitic stainless steels processed by large strain warm rolling. *Acta Materialia,* 136**,** 39-48.
YEHOROV, Y., DA SILVA, L. J. & SCOTTI, A. 2019. Balancing WAAM Production Costs and Wall Surface Quality through Parameter Selection: A Case Study of an Al-Mg5 Alloy Multilayer-Non-Oscillated Single Pass Wall. *Journal of Manufacturing and Materials Processing,* 3**,** 1-19.
YILMAZ, O. & UGLA, A. A. 2016. Shaped metal deposition technique in additive manufacturing: A review. *Proceedings of the Institution of Mechanical Engineers, Part B: Journal of Engineering Manufacture,* 230**,** 1781-1798.
YıLMAZ, R. & TÜMER, M. 2012. Microstructural studies and impact toughness of dissimilar weldments between AISI 316 L and AH36 steels by FCAW. *The International Journal of Advanced Manufacturing Technology,* 67**,** 1433-1447.
YIN, H. & FELICELLI, S. D. 2010. Dendrite growth simulation during solidification in the LENS process. *Acta Materialia,* 58**,** 1455-1465.
YOUTSOS, A. G., DONEA, J. & VERZELETTI, G. 1989. ViscoplastiC Behaviour of Stainless Steels AISI 316L and 316H. *Acta Meehanica* 76**,** 161-187.
YU, J., ROMBOUTS, M. & MAES, G. 2013a. Cracking behavior and mechanical properties of austenitic stainless steel parts produced by laser metal deposition. *Materials & Design,* 45**,** 228-235.
YU, J., Y. CHEN, Q. YANG, Y. SHI, Y. YAO, LI, X. & WANG, Y. 1992. Microstructural changes of 316L stainless steel under energetic alpha particle and proton irradiation at 500°C *Journal of Nuclear Materials* 728-732.
YU, X., LIM, Y. C., SMITH, R., BABU, S. S., FARSON, D. F., LIPPOLD, J. C. & MCCRACKEN, S. 2013b. Reducing hot cracking tendency of dissimilar weld overlay by magnetic arc oscillation. *Materials Science and Technology,* 30**,** 930-937.
YUAN, T., KOU, S. & LUO, Z. 2016a. Grain refining by ultrasonic stirring of the weld pool. *Acta Materialia,* 106**,** 144-154.
YUAN, T., LUO, Z. & KOU, S. 2016b. Grain refining of magnesium welds by arc oscillation. *Acta Materialia,* 116**,** 166-176.
ZHANG, C., LI, Y., GAO, M. & ZENG, X. 2018a. Wire arc additive manufacturing of Al-6Mg alloy using variable polarity cold metal transfer arc as power source. *Materials Science and Engineering: A,* 711**,** 415-423.
ZHANG, K., WANG, S., LIU, W. & SHANG, X. 2014. Characterization of stainless steel parts by Laser Metal Deposition Shaping. *Materials & Design,* 55**,** 104-119.
ZHANG, X., MARTINA, F., DING, J., WANG, X. & WILLIAMS, S. W. 2017. Fracture toughness and fatigue crack growth rate properties in wire + arc additive manufactured Ti-6Al-4V. *Fatigue & Fracture of Engineering Materials & Structures,* 40**,** 790-803.
ZHANG, X., MI, G., CHEN, L., JIANG, P., SHAO, X. & WANG, C. 2018b. Microstructure and performance of hybrid laser-arc welded 40 mm thick 316 L steel plates. *Journal of Materials Processing Technology,* 259**,** 312-319.
ZHAO, L., TIAN, Z. L. & PENG, Y. 2013. Control of nitrogen content and porosity in gas tungsten arc welding of high nitrogen steel. *Science and Technology of Welding and Joining,* 14**,** 87-92.
ZHENG, Q. S. & COLLINS, I. F. 1998. The relationship between damage variables and their evolution laws and microstructural and physical properties. *Proceedings of the Royal Society a-Mathematical Physical and Engineering Sciences,* 454**,** 1469-1498.
ZHONG, Y. 2017. *Sub-Grain Structure in additive manufactured SS316L.* PhD, Stockholm University.
ZHONG, Y., LIU, L., WIKMAN, S., CUI, D. & SHEN, Z. 2016. Intragranular cellular segregation network structure strengthening 316L stainless steel prepared by selective laser melting. *Journal of Nuclear Materials,* 470**,** 170-178.
ZHONG, Y., RÄNNAR, L.-E., LIU, L., KOPTYUG, A., WIKMAN, S., OLSEN, J., CUI, D. & SHEN, Z. 2017. Additive manufacturing of 316L stainless steel by electron beam melting for nuclear fusion applications. *Journal of Nuclear Materials,* 486**,** 234-245.
ZIĘTALA, M., DUREJKO, T., POLAŃSKI, M., KUNCE, I., PŁOCIŃSKI, T., ZIELIŃSKI, W., ŁAZIŃSKA, M., STĘPNIOWSKI, W., CZUJKO, T., KURZYDŁOWSKI, K. J. &

BOJAR, Z. 2016. The microstructure, mechanical properties and corrosion resistance of 316L stainless steel fabricated using laser engineered net shaping. *Materials Science and Engineering: A,* 677**,** 1-10.

ZUMELZU, E., SEPULVEDA, J. & IBARRA, M. 1999. Influence of microstructure on the mechanical behaviour of welded 316 L SS joints. *Journal of Materials Processing Technology,* 94**,** 36–40.

Appendix A Oxide Inclusion and Fractography Dimple Sizes and Distribution

This section presents the oxide inclusions and fractography dimple results for individual location, group mean and standard deviation. The results for Type 316L 0.75 kg/hr experiments, 3.00 kg/hr Type 316L experiments and 316LSi 0.75 kg/hr experiments are shown in table A.1-A.3

Table A.1 Oxide inclusions and fractography dimple results for individual location, group mean and standard deviation for 0.75 kg/hr Type 316L

	Spacing (μm)	r_c (μm)	V_f	Frequency (/mm^2)	CTS (MPa)	Dimple average diameter (μm)	Dimple min diameter (μm)	Dimple max diameter (μm)	Dimple number frequency (/mm2)
HIT-HHI bottom	4.9	0.239	0.00629	29,590	14.2	1.43	0.42	3.59	545,603
HIT-HHI middle	5.6	0.254	0.00538	20,951	12.3	1.72	0.40	5.58	323,550
HIT-HHI top	5.8	0.251	0.00506	20,004	12.0	1.27	0.00	4.02	510,000
Average	5.4	0.248	0.00558	23,515	12.8	1.47	0.27	4.40	459,718
Std. Dev	0.5	0.008	0.00064	5,282	1.2	0.22	0.24	1.05	119,261
LIT-HHI bottom	6.0	0.255	0.00487	20,297	11.6	1.69	0.26	4.21	370,384
LIT-HHI middle	3.9	0.203	0.00713	44,479	17.5	1.57	0.43	3.82	436,299
LIT-HHI top	2.9	0.211	0.01253	76,887	23.2	1.20	0.41	2.96	778,582
Average	4.3	0.223	0.00818	47,221	17.4	1.49	0.36	3.66	528,422
Std. Dev	1.6	0.028	0.00393	28,394	5.8	0.26	0.09	0.64	219,138
CRYO-HHI bottom	4.8	0.238	0.00633	28,897	14.3	1.91	0.50	3.93	305,852
CRYO-HHI middle	4.0	0.208	0.00705	42,755	17.1	1.15	0.54	2.29	856,470
CRYO-HHI top	5.9	0.277	0.00586	20,433	12.0	1.44	0.39	3.87	540,495
Average	4.9	0.241	0.00642	30,695	14.4	1.50	0.48	3.36	567,606
Std. Dev	0.9	0.035	0.00060	11,269	2.5	0.38	0.08	0.93	276,308
HIT-LHI bottom	4.3	0.247	0.00833	40,166	16.1	1.63	0.37	4.96	405,328
HIT-LHI middle	4.2	0.227	0.00757	42,096	16.4	1.43	0.37	3.60	534,192
HIT-LHI top	3.8	0.241	0.00976	48,702	18.0	1.28	0.43	2.86	1,531,167
Average	4.1	0.238	0.00856	43,655	16.8	1.45	0.39	3.80	823,563
Std. Dev	0.2	0.010	0.00111	4,476	1.0	0.18	0.03	1.07	616,181
LIT-LHI bottom	5.4	0.258	0.00590	24,763	12.8	1.65	0.33	4.79	380,586
LIT-LHI middle	3.6	0.204	0.00816	55,602	18.8	1.45	0.40	2.80	544,508
LIT-LHI top	3.7	0.283	0.01400	45,016	19.2	*	*	*	*
Average	4.2	0.248	0.00935	41,794	16.9	1.55	0.37	3.80	462,547
Std. Dev	1.0	0.041	0.00418	15,670	3.6	0.14	0.05	1.40	115,910
CRYO-LHI bottom	3.2	0.198	0.00965	59,446	21.1	1.38	0.35	3.60	597,628
CRYO-LHI middle	3.6	0.232	0.01025	51,447	19.1	1.32	0.33	3.59	629,729
CRYO-LHI Top	3.2	0.227	0.01189	65,792	21.2	1.19	0.54	2.21	7,804,108
Average	3.3	0.219	0.01060	58,895	20.5	1.30	0.41	3.13	3,010,488
Std. Dev	0.2	0.018	0.00116	7,188	1.2	0.10	0.12	0.80	4,151,427

Table A.2 Oxide inclusions and fractography dimple results for individual location, group mean and standard deviation for 3.00 kg/hr Type 316L.

	Spacing (μm)	r_c (μm)	V_f	Frequency (/mm^2)	CTS (MPa)	Dimple average diameter (μm)	Dimple min diameter (μm)	Dimple max diameter (μm)	Dimple number frequency (/mm2)
HIT-HHI bottom	4.2	0.233	0.00783	37,052	16.3	1.65	0.41	3.50	407,687
HIT-HHI middle	3.5	0.200	0.00824	54,005	19.2	1.59	0.36	3.30	439,039
HIT-HHI top	4.9	0.253	0.00696	33,143	14.2	1.45	0.41	3.73	522,801
Average	4.2	0.229	0.00768	41,400	16.6	1.56	0.39	3.51	456,509
Std. Dev	0.7	0.027	0.00066	11,090	2.5	0.10	0.03	0.21	59,512
LIT-HHI bottom	4.0	0.240	0.00916	49,019	17.4	1.53	0.38	4.34	471,168
LIT-HHI middle	3.6	0.208	0.00830	47,721	18.6	1.24	0.58	2.23	771,444
LIT-HHI top	3.6	0.236	0.01072	57,025	19.2	1.74	0.41	5.40	335,453
Average	3.7	0.228	0.00940	51,255	18.4	1.50	0.46	3.99	526,022
Std. Dev	0.2	0.017	0.00123	5,039	0.9	0.25	0.11	1.61	223,112
CRYO-HHI bottom	3.4	0.247	0.01292	70,603	20.6	1.29	0.46	3.07	684,031
CRYO-HHI middle	3.3	0.234	0.01207	64,319	20.8	1.43	0.37	3.60	534,192
CRYO-HHI top	3.6	0.244	0.01107	55,052	19.1	1.96	0.38	4.60	273,405
Average	3.4	0.242	0.01202	63,325	20.2	1.56	0.40	3.76	497,209
Std. Dev	0.2	0.007	0.00093	7,823	0.9	0.35	0.05	0.78	207,796
HIT-LHI bottom	3.0	0.225	0.01310	77,269	22.6	1.26	0.54	2.55	715,601
HIT-LHI middle	3.3	0.222	0.01097	67,129	20.6	1.27	0.45	2.54	683,084
HIT-LHI top	3.2	0.232	0.01241	67,987	21.3	1.19	0.47	2.36	803,513
Average	3.2	0.226	0.01216	70,795	21.5	1.24	0.49	2.48	734,066
Std. Dev	0.1	0.005	0.00109	5,623	1.0	0.05	0.05	0.10	62,302
LIT-LHI bottom	4.0	0.239	0.00901	46,690	17.3	1.50	0.45	4.31	479,161
LIT-LHI middle	2.5	0.212	0.01591	98,378	26.6	1.72	0.59	3.55	372,373
LIT-LHI top	3.6	0.234	0.01056	57,166	19.2	1.43	0.32	3.46	549,685
Average	3.4	0.228	0.01183	67,411	21.0	1.55	0.45	3.77	467,073
Std. Dev	0.7	0.015	0.00362	27,324	4.9	0.15	0.14	0.47	89,272
CRYO-LHI bottom	3.2	0.222	0.01197	71,545	21.6	1.55	0.45	3.77	451,937
CRYO-LHI middle	3.6	0.234	0.01031	55,779	19.0	0.15	0.14	0.47	858,072
CRYO-LHI top	3.1	0.225	0.01238	73,978	21.8	1.54	0.51	3.86	7,578,425
Average	3.3	0.227	0.01155	67,101	20.8	1.15	0.46	2.62	2,962,811
Std. Dev	0.3	0.006	0.00110	9,880	1.6	1.11	0.62	2.00	4,002,394

Table A.3 Oxide inclusions and fractography dimple results for individual location, group mean and standard deviation for 0.75 kg/hr Type 316LSi.

Spacing	Spacing (μm)	r_c (μm)	V_f	Frequency (/mm^2)	CTS (MPa)	Dimple average diameter (μm)	Dimple min diameter (μm)	Dimple max diameter (μm)	Dimple number frequency (/mm2)
HIT-HHI bottom	5.7	0.267	0.00580	22,599	12.3	1.81	0.41	4.95	308,925
HIT-HHI middle	6.5	0.270	0.00458	16,263	10.7	1.49	0.14	4.12	463,185
HIT-HHI top	6.1	0.267	0.00508	14,422	11.5	1.68	0.33	5.31	337,187
Average	6.1	0.268	0.00515	17,762	11.5	1.66	0.29	4.79	369,766
Std. Dev	0.4	0.002	0.00061	4,290	0.8	0.16	0.14	0.62	82,128
LIT-HHI bottom	3.6	0.206	0.00833	58,046	18.8	1.95	0.44	4.95	389,685
LIT-HHI middle	4.2	0.218	0.00706	39,370	16.4	1.12	0.06	3.85	710,418
LIT-HHI top	4.9	0.226	0.00548	31,919	13.8	1.38	0.39	3.87	586,508
Average	4.2	0.216	0.00696	43,112	16.3	1.48	0.30	4.22	562,204
Std. Dev	0.7	0.010	0.00142	13,460	2.5	0.43	0.21	0.63	161,742
HIT-LHI bottom	4.6	0.240	0.00702	35,875	15.0	1.76	0.35	4.70	332,605
HIT-LHI middle	4.9	0.245	0.00649	29,836	14.1	1.26	0.06	3.89	582,605
HIT-LHI top	5.2	0.240	0.00557	27,973	13.2	1.55	0.50	3.46	478,513
Average	4.9	0.242	0.00636	31,228	14.1	1.52	0.30	4.02	464,574
Std. Dev	0.3	0.003	0.00074	4,130	0.9	0.25	0.22	0.63	125,582
LIT-LHI bottom	5.0	0.254	0.00676	29,244	14.0	1.89	0.38	5.44	279,420
LIT-LHI middle	4.5	0.235	0.00702	33,912	15.3	1.57	0.42	3.62	461,554
LIT-LHI top	4.4	0.245	0.00801	37,753	15.8	1.94	0.54	4.68	286,893
Average	4.6	0.245	0.00727	33,636	15.0	1.80	0.44	4.58	342,622
Std. Dev	0.3	0.010	0.00066	4,261	1.0	0.20	0.08	0.92	103,066

Appendix B Grain Size extracted from EBSD data

The linear intercept (LI) grain size obtained from EBSD of the 0.75 kg/hr Type 316L experiments is presented in Table B.1. The linear intercept method was used as recommended by ASTM E112 (2013) for non-equiaxed samples. The relatively high standard deviation indicated much larger grain relative to the mean were present. As specimens showed less than 3:1 aspect ratio in grain size from horizontal to vertical, a reasonable estimate of the grain size can be made using the imaged (XZ) plane only (ASTM E112, 2013).

Table B.1 Horizontal and vertical grain size calculated according to the linear intercept method in OIM® software.

Experiment (magnification)	Horizontal LI (μm)	Horizontal Std. Dev. (μm)	Vertical LI (μm)	Vertical Std. Dev (μm)	Grains Included
HIT-HHI (x 50)	89.6	111.2	100.1	197.8	489
LIT-HHI (x 50)	115.8	170.6	108.8	212.8	915
LIT-LHI (x 50)	90.8	122.7	89.5	205.0	753
HIT-LHI (x 50)	82.6	129.5	92.1	196.3	687
CRYO-HHI (x 500)	3.5	6.1	2.8	5.1	722
CRYO-LHI (x 1000)	2.1	2.7	1.4	1.6	2363

Appendix C Mechanical Data

This section details the individual specimen E, σ_{ys}, UTS and uniform elongation (El) and the group averages and standard deviations. The results for the 0.75 kg/hr Type 316LSi and Type 316L are shown in Table C.1 and Table C.2, respectively. The 3.00 kg/hr Type 316L experiments are shown in Table C.3.

Table C.1 Individual specimen E, σ_{ys}, UTS and uniform elongation and group averages and standard deviations for 0.75 kg/hr Type 316LSi

	LIT-HHI				HIT-HHI			
	E (GPa)	**σ_{ys} (MPa)**	**UTS (MPa)**	**El.**	**E (GPa)**	**σ_{ys} (MPa)**	**UTS (MPa)**	**El.**
H3	172.3	363.5	606.1	41.6%	132.8	310.7	567.5	41.0%
H2	153.2	333.8	575.6	45.2%	134.7	307.0	574.9	47.2%
H1	207.4	295.4	565.0	39.4%	220.5	286.7	587.6	52.7%
V1	168.5	292.2	539.1	43.3%	147.9	265.4	533.5	44.7%
V2	204.4	311.0	577.8	43.7%	156.6	305.2	585.4	40.2%
V3	130.8	325.2	561.8	39.7%	146.3	342.3	625.2	39.0%
Group Std. Dev.	30	27	22.1	2.3%	32.6	25.7	29.9	5.2%
Group Av.	173	320	570.9	42.1%	156.5	302.9	579.0	44.1%
Horizontal Av.	177.6	330.9	582.2	42.0%	162.7	301.5	576.7	47.0%
Horizontal Std. Dev.	27.5	34.1	21.4	2.9%	50.1	12.9	10.1	5.9%
Vertical Av.	167.9	309.4	559.6	42.2%	150.2	304.3	581.4	41.3%
Vertical Std. Dev.	36.8	16.6	19.5	2.2%	5.5	38.5	46.0	3.0%
Anisotropy factor	5.8%	6.9%	4.0%	-0.4%	8.3%	-0.9%	-0.8%	13.8%
	LIT-LHI				**HIT-LHI**			
H3	133.2	330.0	571.2	45.2%	133.4	304.1	562.5	49.8%
H2	111.4	299.3	551.9		167.3	297.8	551.0	38.8%
H1	137.4	303.6	567.5	56.7%	136.4	292.3	542.2	44.6%
V1	104.8	279.5	543.9	32.7%	174.2	295.2	555.5	44.7%
V2	107.5	313.9	608.0	35.2%	108.5	304.6	607.4	41.5%
V3	120.2	317.7	566.9	38.5%	154.6	297.1	572.4	36.5%
Group Std. Dev.	13.7	17.4	22.1	9.6%	24.4	4.9	23.1	4.8%
Group Av.	119.1	307.3	568.2	41.7%	145.7	298.5	565.2	42.7%
Horizontal Av.	127.3	311.0	563.5	51.0%	145.7	298.1	551.9	44.4%
Horizontal Std. Dev.	13.9	16.7	10.3	8.1%	18.8	5.9	10.2	5.5%
Vertical Av.	110.8	303.7	572.9	35.5%	145.8	299.0	578.4	40.9%
Vertical Std. Dev.	8.2	21.0	32.5	2.9%	33.7	4.9	26.5	4.1%
Anisotropy factor	14.9%	2.4%	-1.6%	43.7%	0.0%	-0.3%	-4.6%	8.6%

Table C.2 Individual specimen E, σ_{ys}, UTS and uniform elongation and group averages and standard deviations for 3.00 kg/hr Type 316L

	LIT-HHI				HIT-HHI			
	E (GPa)	**σ_{ys} (MPa)**	**UTS (MPa)**	**El.**	**E (GPa)**	**σ_{ys} (MPa)**	**UTS (MPa)**	**El.**
H3	122.6	322.5	517.0	39.0%	71.7	299.7	544.6	40.1%
H2	132.2	323.5	527.0	34.7%	88.0	332.7	550.8	37.2%
H1	129.4	306.7	530.4	37.5%	43.9	285.4	518.7	43.2%
V1	67.4	303.9	532.4	41.9%	146.9	332.2	554.1	36.0%
V2	102.4	307.2	559.6	37.1%	93.0	309.8	577.6	37.4%
V3	99.6	376.1	569.4	38.9%	103.5	275.3	526.4	39.3%
Group Std. Dev.	24.5	27.19	20.5	2.4%	34.3	23.73	21.0	2.6%
Group Av.	108.9	323.3	539.3	38.2%	91.2	305.8	545.4	38.8%
Horizontal Av.	128.1	318	525	37.0%	67.9	306	538	40.2%
Horizontal Std. Dev.	4.9	9	7	2.2%	22.3	24	17	3.0%
Vertical Av.	89.8	329	554	39.3%	114.5	306	553	37.5%
Vertical Std. Dev.	19.5	41	19	2.4%	28.5	29	26	1.7%
Anisotropy factor	43%	-4%	-5%	-5.8%	-41%	0%	-3%	7.0%
	CRYO-HHI				**LIT-LHI**			
H3	86.0	338.0	566.1	29.6%	117.6	316.4	537.4	32.2%
H2	139.6	358.7	534.6	39.0%	58.1	332.7	542.7	41.0%
H1	53.3	307.3	573.4	38.3%	96.8	307.9	532.9	43.5%
V1	118.3	273.3	529.0	42.0%	39.6	372.2	526.2	26.6%
V2	53.9	339.1	594.0	38.1%	106.3	309.2	552.4	34.9%
V3	93.6	309.9	565.2	35.4%	90.4	345.2	557.6	39.5%
Group Std. Dev.	34.5	30.40	24.5	4.2%	29.9	24.99	11.9	6.3%
Group Av.	90.8	321.0	560.4	37.1%	84.8	330.6	541.5	36.3%
Horizontal Av.	92.9	335	558	35.6%	90.8	319	538	38.9%
Horizontal Std. Dev.	43.6	26	21	5.2%	30.2	13	5	6.0%
Vertical Av.	88.6	307	563	38.5%	78.8	342	545	33.7%
Vertical Std. Dev.	32.5	33	33	3.3%	34.8	32	17	6.6%
Anisotropy factor	5%	9%	-1%	-7.4%	15%	-7%	-1%	15.5%
	HIT-LHI				**CRYO-LHI**			
H3	156.0	285.9	548.2	37.5%	103.0	358.6	533.0	34.1%
H2	81.0	346.1	528.8	39.7%	159.4	335.4	577.2	38.9%
H1	173.5	286.2	525.9	56.6%	210.3	365.7	616.3	35.2%
V1	91.7	342.6	554.4	33.9%	117.1	363.4	571.9	34.7%
V2	72.4	301.0	598.9	39.1%	128.3	341.9	583.0	35.1%
V3	127.4	344.3	572.7	31.5%	91.2	336.5	593.6	38.6%
Group Std. Dev.	41.8	29.73	27.6	8.8%	43.8	13.88	27.5	2.1%
Group Av.	117.0	317.7	554.8	39.7%	134.9	350.3	579.2	36.1%
Horizontal Av.	136.8	306	534	44.6%	157.6	353	575	36.1%
Horizontal Std. Dev.	49.1	35	12	10.4%	53.7	16	42	2.5%
Vertical Av.	97.2	329	575	34.8%	112.2	347	583	36.1%
Vertical Std. Dev.	27.9	25	22	3.8%	19.0	14	11	2.2%
Anisotropy factor	41%	-7%	-7%	28.0%	40%	2%	-1%	-0.1%

Table C.3 Individual specimen E, σ_{ys}, UTS and uniform elongation and group averages and standard deviations for 0.75 kg/hr Type 316L

	LIT-HHI				HIT-HHI			
	E (GPa)	**σ_{ys} (MPa)**	**UTS (MPa)**	**El.**	**E (GPa)**	**σ_{ys} (MPa)**	**UTS (MPa)**	**El.**
H3	87.2	307.8	549.2	48.67%	120.5	278.3	521.9	41.81%
H2	95.9	276.4	499.4	39.81%	-	-	-	-
H1	105.5	281.6	542.1	46.21%	120.6	279.7	554.0	39.47%
V1	74.6	315.0	548.1	38.56%	97.7	235.8	547.3	34.25%
V2	81.4	303.0	542.8	44.98%	114.5	250.7	531.5	41.03%
V3	91.8	309.5	538.0	42.13%	118.0	265.2	525.0	42.26%
Group Std. Dev.	10.9	16.0	18.7	3.9%	9.6	18.7	14.0	3.3%
Group Av.	89.4	298.9	536.6	43.4%	114.3	262.0	535.9	39.8%
Horizontal Av.	96.2	288.6	530.2	44.9%	120.6	279.0	537.9	40.6%
Horizontal Std. Dev.	9.2	16.9	26.9	4.6%	0.1	1.0	22.7	1.7%
Vertical Av.	82.6	309.2	543.0	41.9%	110.1	250.6	534.6	39.2%
Vertical Std. Dev.	8.7	6.0	5.0	3.2%	10.9	14.7	11.4	4.3%
Anisotropy factor	16.4%	-6.7%	-2.3%	7.2%	9.5%	11.3%	0.6%	3.7%
	CRYO-HHI				**LIT-LHI**			
H3	141.6	297.4	554.6	40.04%	-	-	-	-
H2	90.5	330.2	562.9	39.82%	109.8	308.2	529	41.06%
H1	144.4	300.0	569.0	45.69%	137.7	286.8	548	41.62%
V1	83.9	265.1	511.5	39.91%	72.8	300.2	571	35.83%
V2	113.8	317.4	532.9	46.65%	108.0	298.9	569	40.81%
V3	73.9	316.2	553.5	51.79%	104.1	284.5	565	40.67%
Group Std. Dev.	30.1	22.8	21.4	4.9%	23.0	9.9	18	2.4%
Group Av.	108.0	304.4	547.4	44.0%	106.5	295.7	556	40.0%
Horizontal Av.	125.5	309.2	562.2	41.9%	123.7	297.5	538	41.3%
Horizontal Std. Dev.	30.3	18.3	7.2	3.3%	19.8	15.2	13	0.4%
Vertical Av.	90.5	299.6	532.6	46.1%	95.0	294.5	568	39.1%
Vertical Std. Dev.	20.8	29.9	21.0	6.0%	19.3	8.7	3	2.8%
Anisotropy factor	38.6%	3.2%	5.5%	-9.2%	30.2%	1.0%	-5.2%	5.7%
	HIT-LHI				**CRYO-LHI**			
H3	98.9	298.6	527	44.88%	142.8	310.1	555.6	38.12%
H2	56.7	284.6	542	46.81%	114.1	306.4	550.5	43.12%
H1	94.3	279.0	543	44.28%	223.8	309.9	570.7	51.17%
V1	100.7	261.8	513	39.14%	103.4	307.5	529.1	37.50%
V2	34.3	324.7	560	36.99%	237.3	307.5	551.1	40.64%
V3	47.2	277.8	543	41.07%	156.6	346.3	568.6	38.07%
Group Std. Dev.	29.4	21.7	16	3.8%	55.9	15.6	15.1	5.2%
Group Av.	72.0	287.7	538	42.2%	163.0	314.6	554.3	41.4%
Horizontal Av.	83.3	287.4	537	45.3%	160.2	308.8	558.9	44.1%
Horizontal Std. Dev.	23.1	10.1	9	1.3%	56.9	2.1	10.5	6.6%
Vertical Av.	60.7	288.1	538	39.1%	165.8	320.4	549.6	38.7%
Vertical Std. Dev.	35.2	32.7	24	2.0%	67.4	22.4	19.8	1.7%
Anisotropy factor	37.2%	-0.2%	-0.2%	16.0%	-3%	-4%	2%	14%

Appendix D ANOVA test statistics and assumption violation checks

The validity of results of the ANOVA's performed in this research depend on the robustness of assumptions regarding outliers, equal variance, and normality of the data. Table D.1 outlines the p-values for the Grubb's, Levenes and Anderson-Darling tests used to determine the validity of each assumption for each ANOVA in this research detailed by its section number within chapter 6. If the p-value is less than 0.05, it was assumed that there is no statistically significant result and the assumptions are not violated. The section number within the appendix where the ANOVA test statistics and the residual plots can be found are highlighted for each ANOVA.

Table D.1 Outline of the p-values for the outlier, equal variance and normality tests and the associated ANOVA test statistics & residual plot section.

Section in Chapter 6	Test p-values			ANOVA test statistics & residual plots
	Outlier (Grubb's)	Equal Variance (Levenes)	Normality (Anderson-Darling)	
6.5.5 Relative Density (0.75 kg/hr)	0.271	0.870	0.563	§D.1
6.6.4 Relative Density (3.00 kg/hr)	1.00	0.956	0.105	§D.2
6.7.1 Effects of heat input, sample orientation, interpass temperature control with varying wire composition on mechanical properties at 0.75 kg/hr				§D.3
i) UTS	0.240	0.949	0.228	
ii) Yield strength	0.149	0.372	0.466	
iii) Young's Modulus	0.473	0.276	0.442	
iv) Uniform elongation	0.038	0.370	0.647	
6.7.2 Effects of heat input, sample orientation and cooling strategy (interpass temperature control, cryogenic cooling) with varying deposition rate on mechanical properties for Type 316L.				§D.4
i) UTS	0.137	0.951	0.341	
ii) Yield strength	0.697	0.327	0.255	
iii) Young's Modulus	0.256	0.179	0.011 Box-Cox Trans. $\lambda=0.5 \rightarrow p=0.150$	
iv) Uniform elongation	0.064	0.301	0.021 Box-Cox Trans. $\lambda=0 \rightarrow p=0.68$	
6.8.2.1 Effects of heat input and interpass temperature control with varying wire composition on ODS at 0.75 kg/hr		0.346	0.461	§D.5
6.8.2.2 Effects of heat input and cooling strategy (interpass temperature control, cryogenic cooling) with varying deposition rate on ODS for Type 316L.	0.455	0.437	0.185	§D.6

D.1 Relative part density 0.75 kg/hr

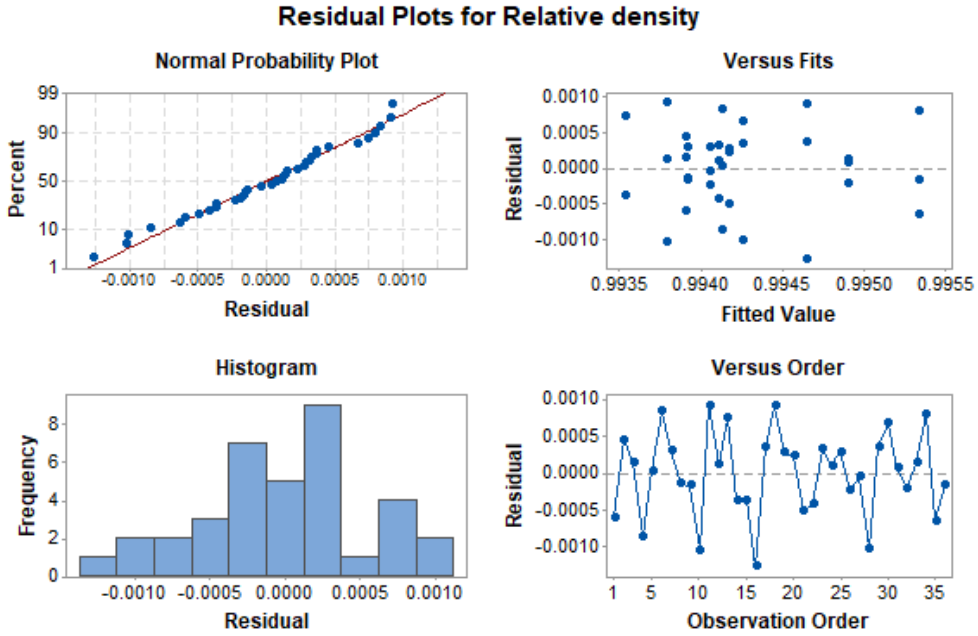

Source	DF	Adj SS	Adj MS	F-Value	P-Value
Cooling Strategy	2	0.000003	0.000001	2.82	0.079
Heat input	**1**	**0.000002**	**0.000002**	**4.62**	**0.042**
Orientation	1	0.000001	0.000001	1.71	0.204
Orientation*Heat input	1	0.000000	0.000000	0.22	0.645
Orientation*Cooling Strategy	2	0.000001	0.000001	1.11	0.346
Heat input*Cooling Strategy	2	0.000001	0.000001	1.51	0.242
Orientation*Heat input*Cooling Strategy	2	0.000000	0.000000	0.42	0.660
Error	24	0.000011	0.000000		
Total	35	0.000019			

D.2 Relative part density 3.00 kg/hr

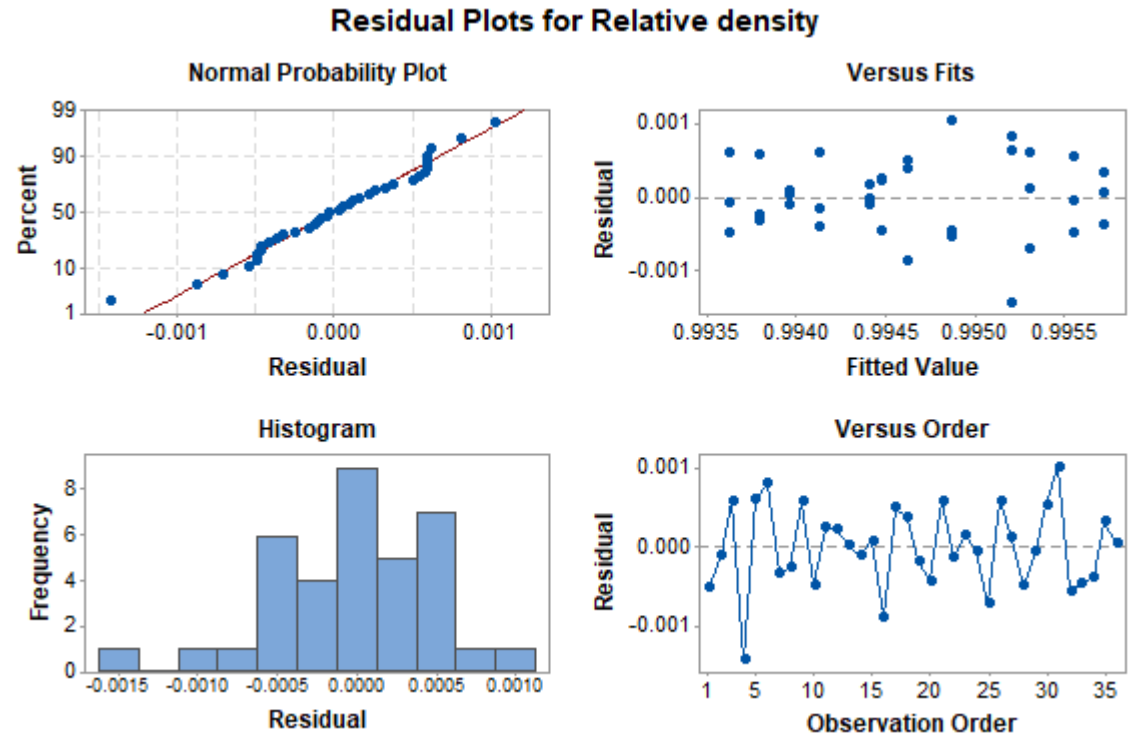

Source	DF	Adj SS	Adj MS	F-Value	P-Value
Cooling strategy	2	0.000002	0.000001	1.99	0.158
Heat input	**1**	**0.000005**	**0.000005**	**11.76**	**0.002**
Heat input*Cooling strategy	**2**	**0.000004**	**0.000002**	**4.43**	**0.023**
Orientation	**1**	**0.000005**	**0.000005**	**11.79**	**0.002**
Heat input*Orientation	1	0.000001	0.000001	1.52	0.229
Cooling strategy*Orientation	2	0.000000	0.000000	0.41	0.670
Heat input*Cooling strategy*Orientation	2	0.000001	0.000000	1.07	0.358
Error	24	0.000010	0.000000		
Total	35	0.000026			

D.3 Effects of wire composition, heat input and interpass temperature on the mechanical properties - (0.75 kg/hr, Type 316L/Type 316LSi)

This section reports the results of the statistical analyses testing the effects of wire composition, heat input, and interpass temperature on the mechanical properties

i. UTS

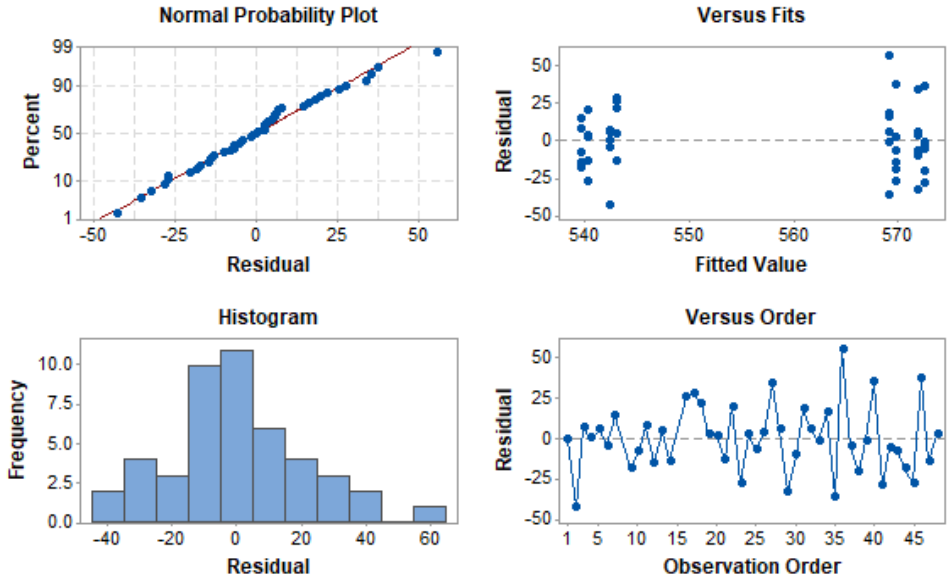

Source	DF	Adj SS	Adj MS	F-Value	P-Value
Heat input	1	3.7	3.7	0.01	0.92901
Cooling strategy	1	86.9	86.9	0.19	0.66445
Material	**1**	**10015.1**	**10015.1**	**22.00**	**0.00003**
Error	42	19120.9	455.3		
Lack-of-Fit	4	1998.2	499.6	1.11	0.36664
Pure Error	38	17122.7	450.6		
Total	45	29225.1			

ii. Yield stress

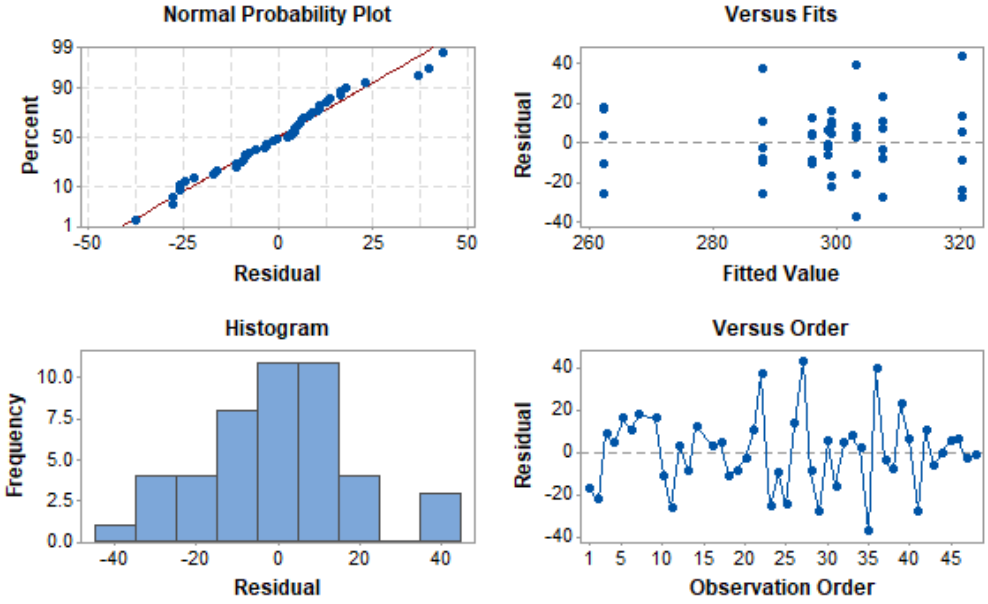

Source	DF	Adj SS	Adj MS	F-Value	P-Value
Heat input	1	21.3	21.27	0.06	0.811
Cooling strategy	**1**	**3599.0**	**3598.96**	**9.82**	**0.003**
Material	**1**	**5111.9**	**5111.87**	**13.95**	**0.001**
Heat input*Cooling strategy	1	1000.4	1000.43	2.73	0.107
Heat input*Material	1	1130.0	1130.00	3.08	0.087
Cooling strategy*Material	1	251.4	251.38	0.69	0.413
Heat input*Cooling strategy*Material	1	298.7	298.67	0.81	0.372
Error	38	13926.6	366.49		
Total	45	24678.7			

iii. Young's Modulus

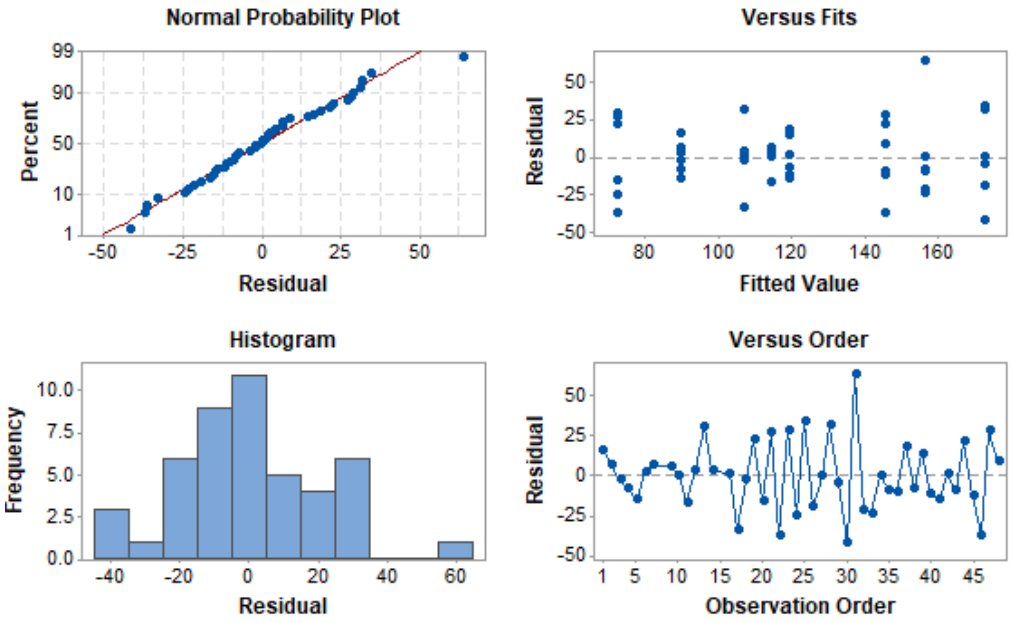

Source	DF	Adj SS	Adj MS	F-Value	P-Value
Heat input	**1**	**5735.2**	**5735.2**	**10.39**	**0.003**
Interpass temperature	1	0.3	0.3	0.00	0.981
Wire composition	**1**	**32076.8**	**32076.8**	**58.10**	**0.000**
Heat input* Interpass temperature	1	192.1	192.1	0.35	0.559
Heat input* Wire composition	1	1099.2	1099.2	1.99	0.166
Interpass temperature *Material	1	284.4	284.4	0.52	0.477
Heat input* Interpass temperature * Wire composition	**1**	**7479.1**	**7479.1**	**13.55**	**0.001**
Error	38	20981.3	552.1		
Total	45	69878.4			

iv. Uniform Elongation

The ANOVA results for elongation did not identify any statistically significant effects for wire composition (p=0.515), heat input (p=0.460) or interpass temperature (p=0.690) on the elongation of the samples.

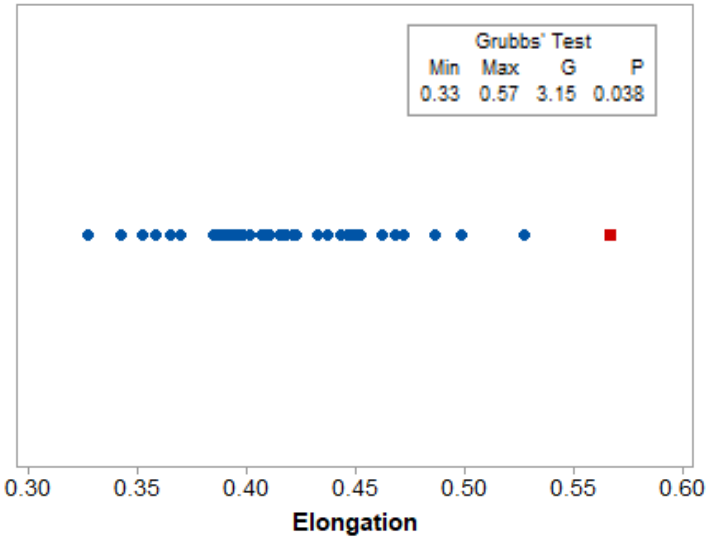

Source	DF	Adj SS	Adj MS	F-Value	P-Value
Heat input	1	0.002994	0.002994	1.87	0.180
Cooling strategy	1	0.001920	0.001920	1.20	0.281
Material	1	0.000141	0.000141	0.09	0.769
Heat input*Cooling strategy	1	0.004971	0.004971	3.11	0.087
Heat input*Material	1	0.001515	0.001515	0.95	0.337
Cooling strategy*Material	1	0.004532	0.004532	2.83	0.101
Heat input*Cooling strategy*Material	1	0.000634	0.000634	0.40	0.533
Error	36	0.057625	0.001601		
Total	43	0.072789			

D.4 Effects of heat input, deposition rate, and cooling strategy for Type 316L wire

i. Ultimate Tensile Stress

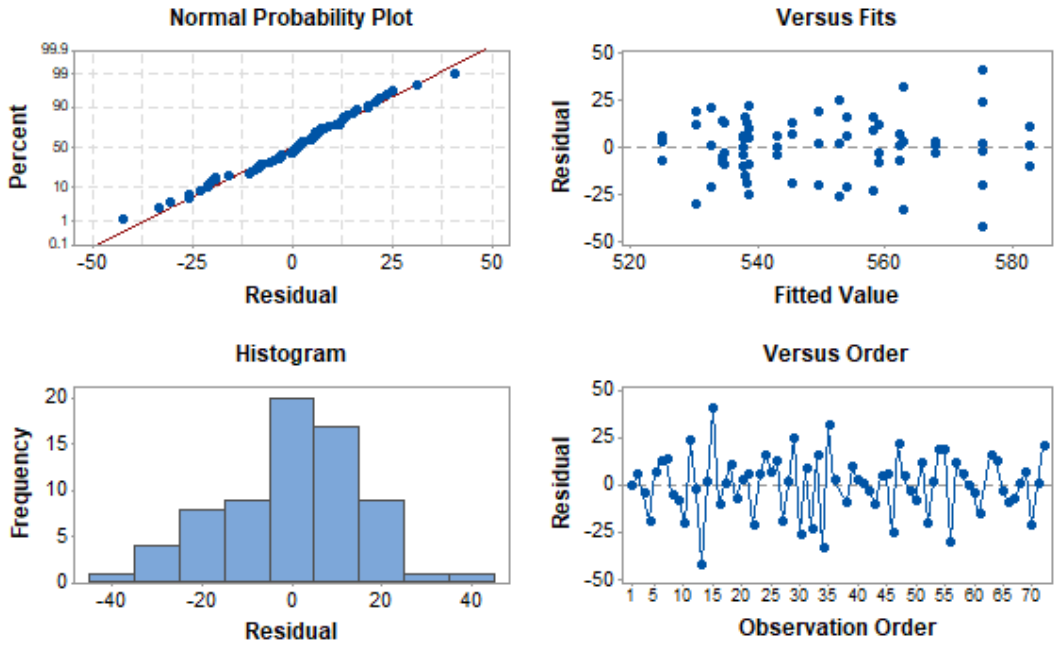

Source	DF	Adj SS	Adj MS	F-Value	P-Value
Cooling strategy	**2**	**4627.5**	**2313.73**	**6.23**	**0.004**
Heat input	1	1484.4	1484.35	4.00	0.052
Deposition rate	1	1441.5	1441.46	3.88	0.055
Orientation	1	1337.5	1337.54	3.60	0.064
Cooling strategy*Heat input	2	152.2	76.12	0.20	0.815
Cooling strategy*Deposition rate	2	1714.2	857.11	2.31	0.111
Cooling strategy*Orientation	2	2237.3	1118.64	3.01	0.059
Heat input*Deposition rate	1	13.0	13.03	0.04	0.852
Heat input*Orientation	1	290.4	290.38	0.78	0.381
Deposition rate*Orientation	1	1283.6	1283.55	3.46	0.069
Cooling strategy*Heat input*Deposition rate	2	573.6	286.82	0.77	0.468
Cooling strategy*Heat input*Orientation	2	241.0	120.48	0.32	0.725
Cooling strategy*Deposition rate*Orientation	2	864.5	432.25	1.16	0.321
Heat input*Deposition rate*Orientation	1	135.5	135.55	0.36	0.549
Cooling strategy*Heat input*Deposition rate*Orientation	2	662.0	330.98	0.89	0.417
Error	46	17089.1	371.50		
Total	69	34516.0			

ii. Yield Stress

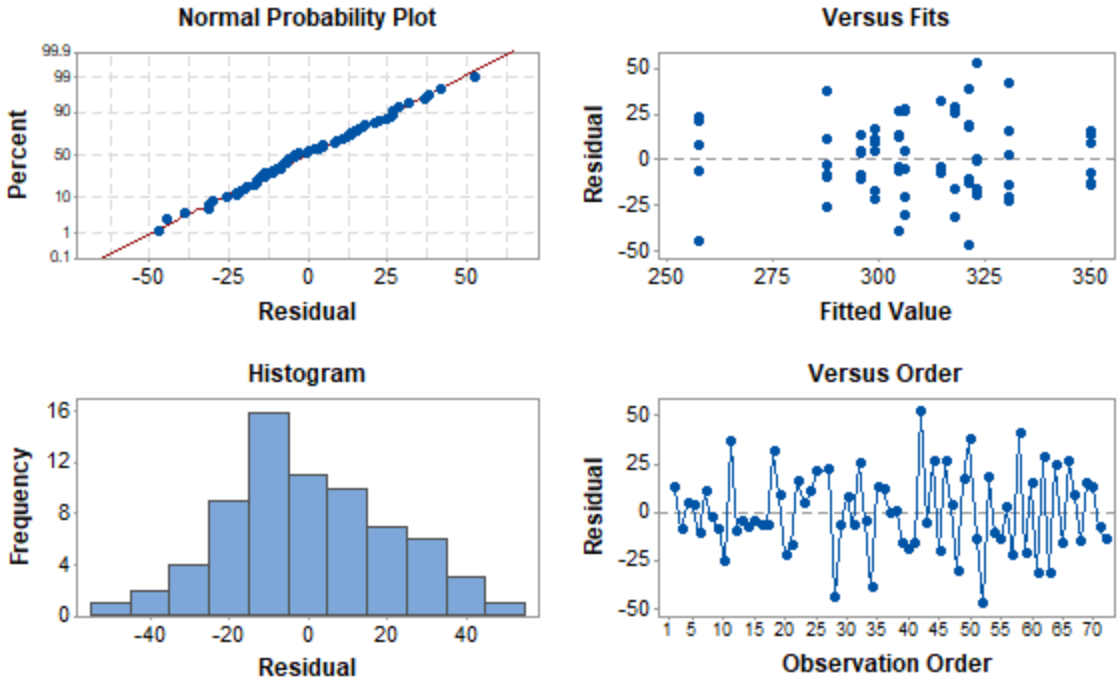

Source	DF	Adj SS	Adj MS	F-Value	P-Value
Cooling strategy	2	9660.5	4830.2	9.29	0.0004092
Heat input	1	2968.6	2968.6	5.71	0.0210439
Deposition rate	1	15962.7	15962.7	30.69	0.0000014
Orientation	1	32.4	32.4	0.06	0.8039016
Cooling strategy*Heat input	2	1036.8	518.4	1.00	0.3769038
Cooling strategy*Deposition rate	2	259.6	129.8	0.25	0.7801969
Cooling strategy*Orientation	2	1317.8	658.9	1.27	0.2913394
Heat input*Deposition rate	1	156.8	156.8	0.30	0.5856028
Heat input*Orientation	1	830.0	830.0	1.60	0.2128390
Deposition rate*Orientation	1	128.5	128.5	0.25	0.6214507
Cooling strategy*Heat input*Deposition rate	2	687.9	344.0	0.66	0.5209833
Cooling strategy*Heat input*Orientation	2	850.5	425.2	0.82	0.4477833
Cooling strategy*Deposition rate*Orientation	2	1372.2	686.1	1.32	0.2772522
Heat input*Deposition rate*Orientation	1	103.7	103.7	0.20	0.6573562
Cooling strategy*Heat input*Deposition rate*Orientation	2	348.8	174.4	0.34	0.7168187
Error	46	23923.2	520.1		
Total	69	59971.7			

iii. Young's Modulus

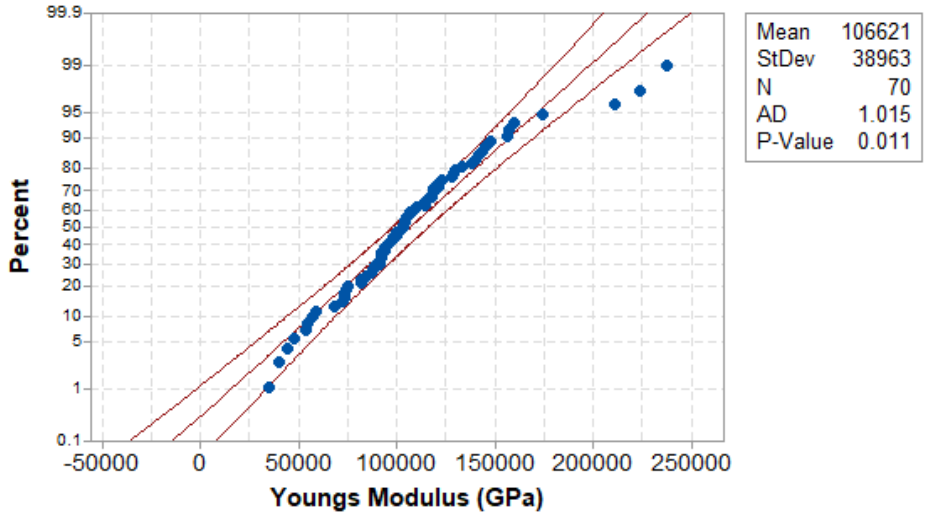

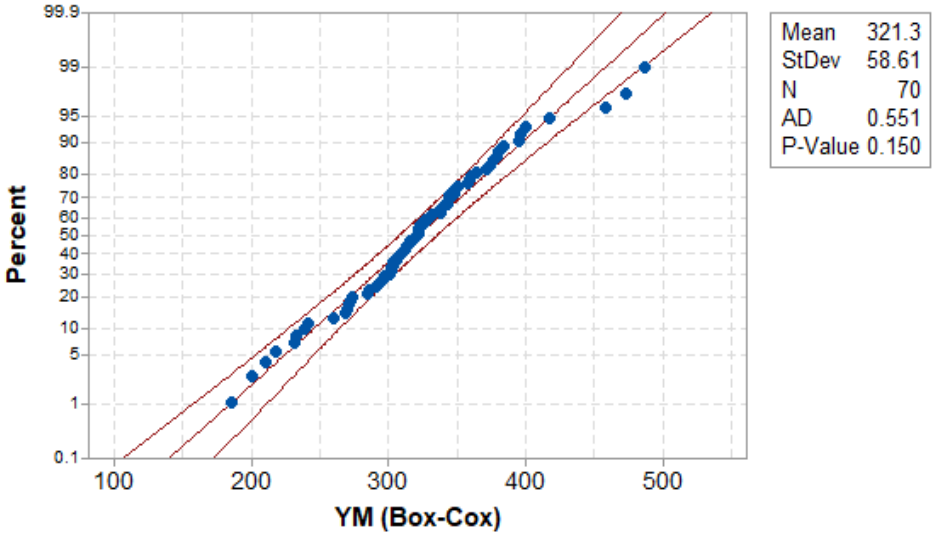

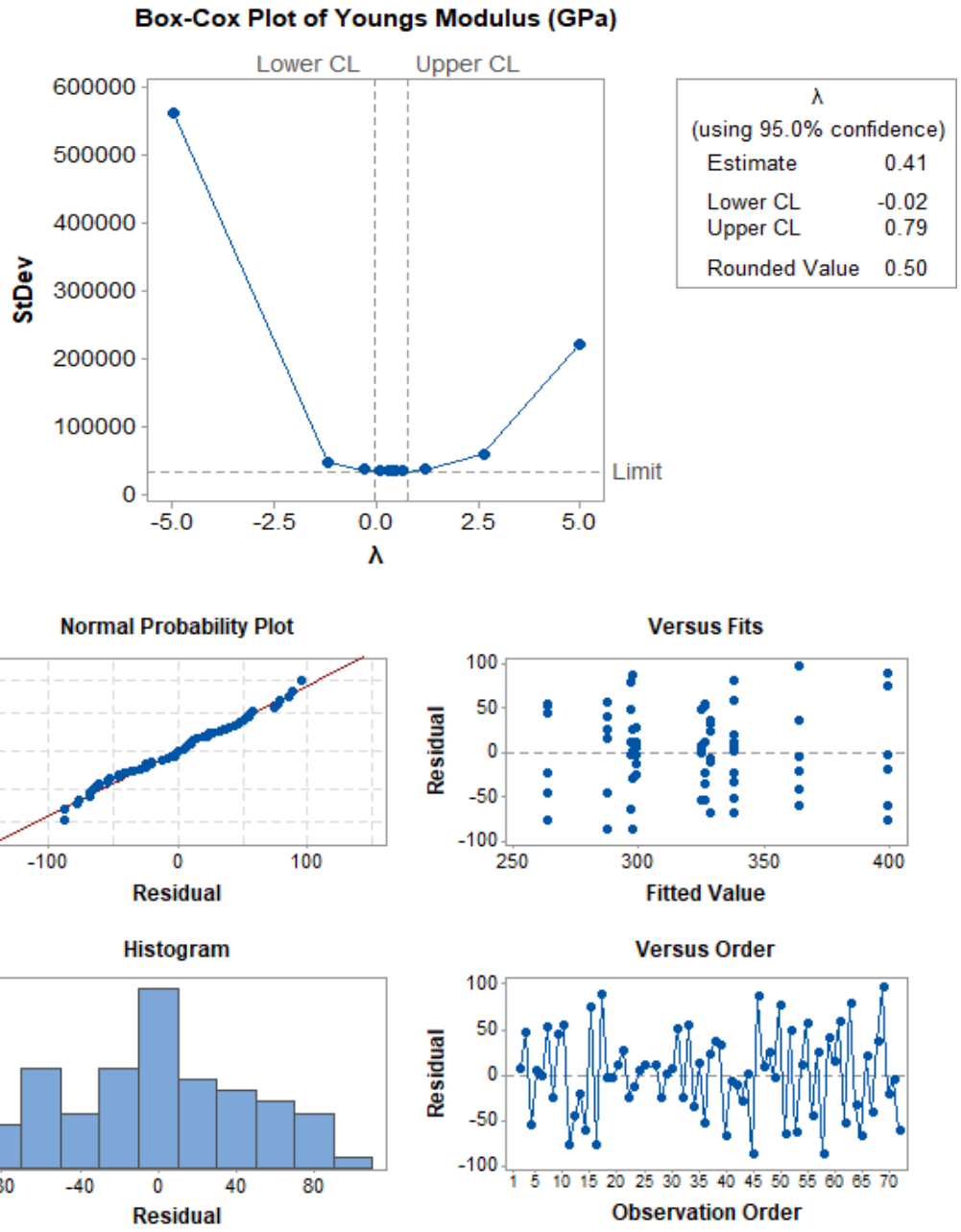
Box-Cox Plot of Youngs Modulus (GPa)
Lower CL
Upper CL
StDev
600000
500000
400000
300000
200000
100000
0
Limit
-5.0
-2.5
0.0
2.5
5.0
λ
λ
(using 95.0% confidence)
Estimate 0.41
Lower CL -0.02
Upper CL 0.79
Rounded Value 0.50
Normal Probability Plot
Percent
99.9
99
90
50
10
1
0.1
-100
0
100
Residual
Versus Fits
Residual
100
50
0
-50
-100
250
300
350
400
Fitted Value
Histogram
Frequency
16
12
8
4
0
-80
-40
0
40
80
Residual
Versus Order
Residual
100
50
0
-50
-100
1 5 10 15 20 25 30 35 40 45 50 55 60 65 70
Observation Order

Source	DF	Adj SS	Adj MS	F-Value	P-Value
Cooling strategy	**2**	**10329**	**5164.44**	**4.76**	**0.013**
Heat input	1	2878	2877.80	2.65	0.110
Deposition rate	1	417	416.67	0.38	0.539
Orientation	**1**	**4699**	**4699.02**	**4.33**	**0.043**
Cooling strategy*Heat input	**2**	**11961**	**5980.35**	**5.51**	**0.007**
Cooling strategy*Deposition rate	2	3251	1625.31	1.50	0.235
Cooling strategy*Orientation	2	876	438.04	0.40	0.670
Heat input*Deposition rate	1	97	96.53	0.09	0.767
Heat input*Orientation	1	925	924.64	0.85	0.361
Deposition rate*Orientation	1	16	16.43	0.02	0.903
Cooling strategy*Heat input*Deposition rate	**2**	**9589**	**4794.48**	**4.41**	**0.018**
Cooling strategy*Heat input*Orientation	2	2568	1283.92	1.18	0.316
Cooling strategy*Deposition rate*Orientation	2	729	364.55	0.34	0.717
Heat input*Deposition rate*Orientation	1	1568	1567.81	1.44	0.236
Cooling strategy*Heat input*Deposition rate*Orientation	2	3395	1697.65	1.56	0.220
Error	46	49960	1086.08		
Total	69	104752			

iv. Uniform Elongation

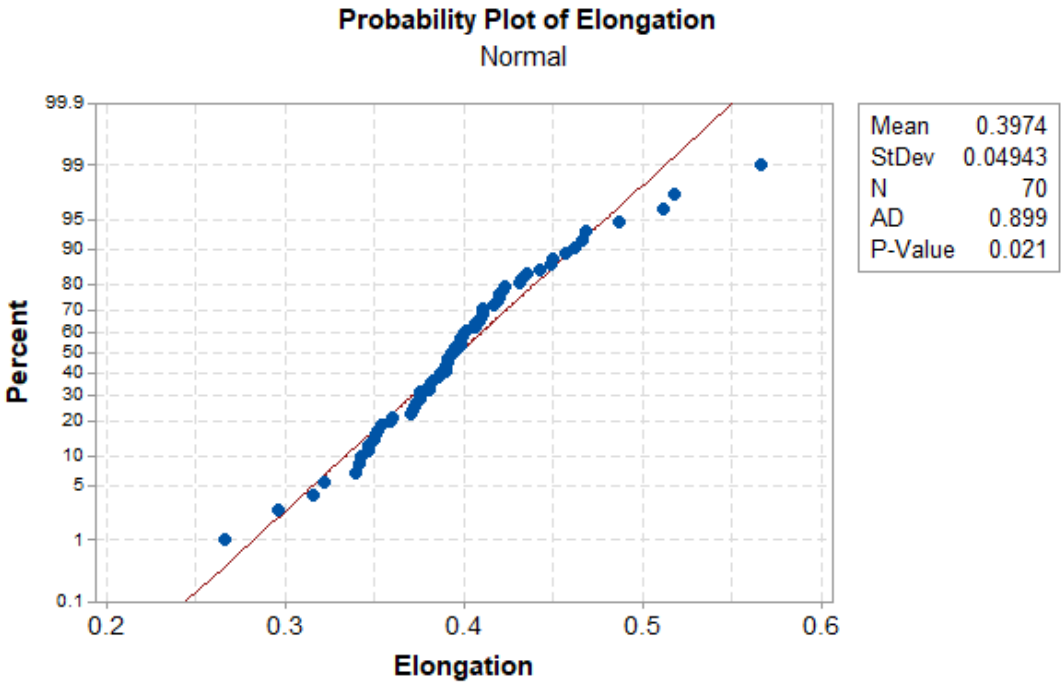

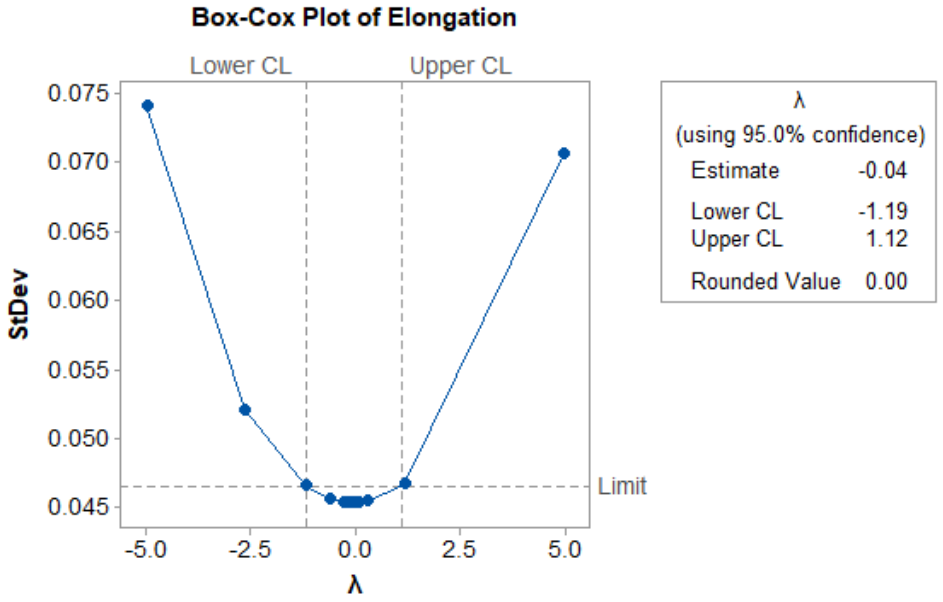
Box-Cox Plot of Elongation
Lower CL
Upper CL
StDev
0.075
0.070
0.065
0.060
0.055
0.050
0.045
Limit
-5.0
-2.5
0.0
2.5
5.0
λ
λ
(using 95.0% confidence)
Estimate -0.04
Lower CL -1.19
Upper CL 1.12
Rounded Value 0.00

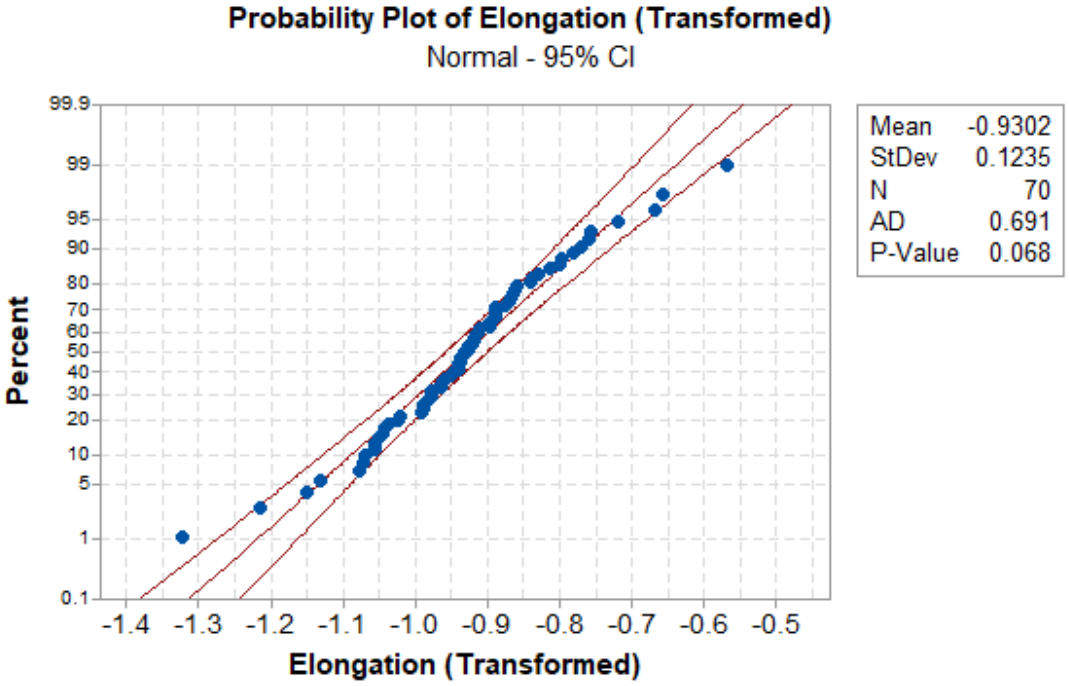
Probability Plot of Elongation (Transformed)
Normal - 95% CI
Percent
99.9
99
95
90
80
70
60
50
40
30
20
10
5
1
0.1
-1.4
-1.3
-1.2
-1.1
-1.0
-0.9
-0.8
-0.7
-0.6
-0.5
Elongation (Transformed)
Mean -0.9302
StDev 0.1235
N 70
AD 0.691
P-Value 0.068

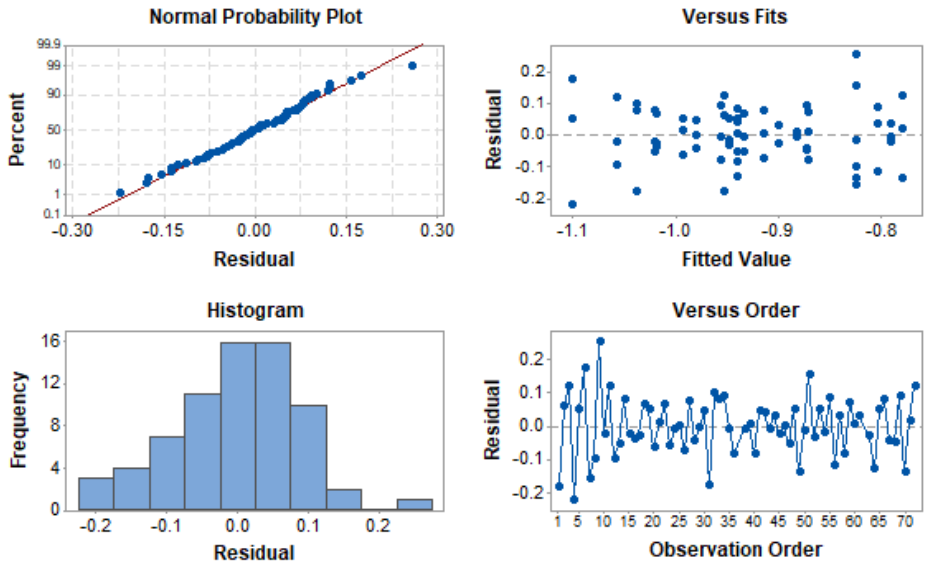
Normal Probability Plot
Percent
Residual
Versus Fits
Residual
Fitted Value
Histogram
Frequency
Residual
Versus Order
Residual
Observation Order

Source	DF	Adj SS	Adj MS	F-Value	P-Value
Cooling strategy	**2**	0.00362	0.001808	0.15	0.857
Heat input	1	0.01207	0.012071	1.03	0.315
Deposition rate	**1**	**0.20139**	**0.201391**	**17.21**	**0.000**
Orientation	**1**	**0.05076**	**0.050762**	**4.34**	**0.043**
Cooling strategy*Heat input	**2**	0.02962	0.014811	1.27	0.292
Cooling strategy*Deposition rate	2	0.03135	0.015676	1.34	0.272
Cooling strategy*Orientation	2	0.05366	0.026828	2.29	0.112
Heat input*Deposition rate	1	0.00000	0.000000	0.00	0.997
Heat input*Orientation	**1**	**0.07150**	**0.071498**	**6.11**	**0.017**
Deposition rate*Orientation	1	0.00019	0.000193	0.02	0.898
Cooling strategy*Heat input*Deposition rate	**2**	0.00573	0.002866	0.24	0.784
Cooling strategy*Heat input*Orientation	2	0.00195	0.000975	0.08	0.920
Cooling strategy*Deposition rate*Orientation	2	0.00943	0.004713	0.40	0.671
Heat input*Deposition rate*Orientation	1	0.00238	0.002384	0.20	0.654
Cooling strategy*Heat input*Deposition rate*Orientation	2	0.02319	0.011594	0.99	0.379
Error	46	0.53835	0.011703		
Total	69	1.05252			

D.5 Oxide dispersion strengthening – (0.75 kg/hr, Type 316L/Type 316LSi)

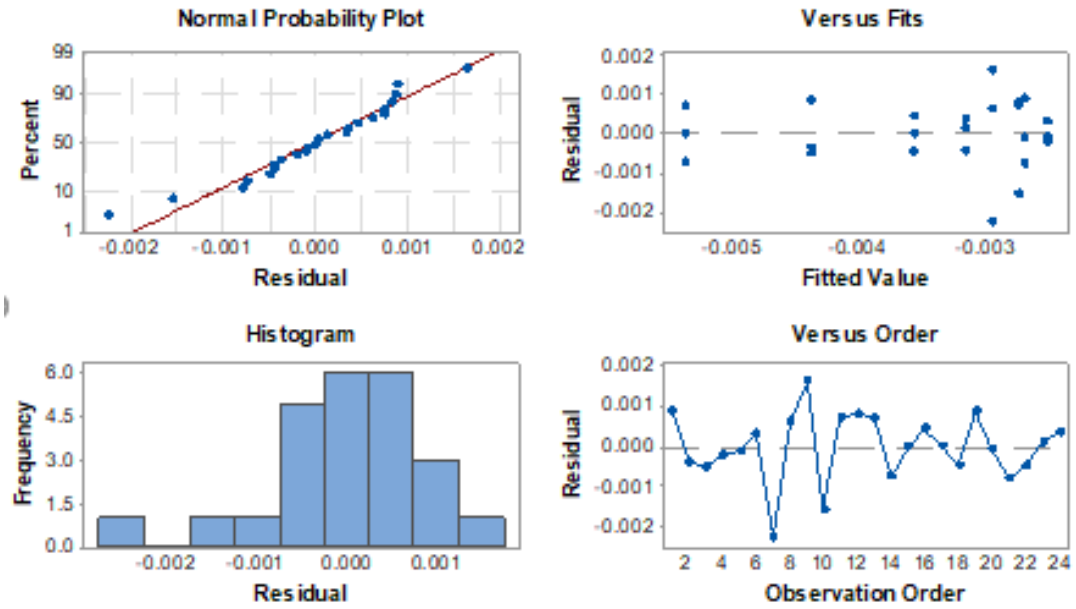

Source	DF	Adj SS	Adj MS	F-Value	P-Value
Heat input	1	8.511	8.5114	1.19	0.291
Cooling strategy	**1**	**40.869**	**40.8689**	**5.73**	**0.029**
Material	1	18.466	18.4661	2.59	0.127
Heat input*Cooling strategy	1	26.335	26.3347	3.69	0.073
Heat input*Material	1	1.700	1.6996	0.24	0.632
Cooling strategy*Material	1	0.437	0.4373	0.06	0.808
Heat input*Cooling strategy*Material	1	0.124	0.1240	0.02	0.897
Error	16	114.082	7.1301		

D.6 Oxide dispersion strengthening – (0.75 kg/hr/3.00 kg/hr, Type 316L)

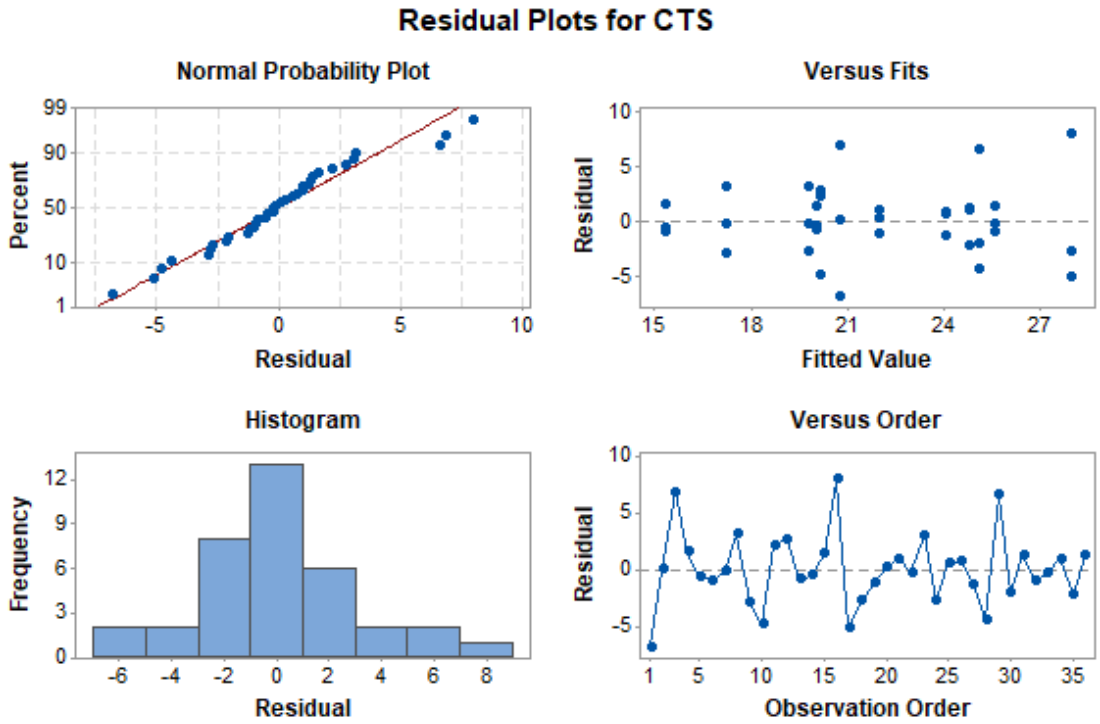

Source	DF	Adj SS	Adj MS	F-Value	P-Value
Heat input	**1**	**77.733**	**77.7334**	**10.19**	**0.004**
Cooling strategy	2	26.958	13.4788	1.77	0.192
Dep rate	**1**	**96.100**	**96.1004**	**12.59**	**0.002**
Heat input*Cooling strategy	2	17.897	8.9484	1.17	0.327
Heat input*Dep rate	1	0.431	0.4307	0.06	0.814
Cooling strategy*Dep rate	2	4.235	2.1175	0.28	0.760
Heat input*Cooling strategy*Dep rate	2	29.245	14.6225	1.92	0.169
Error	24	183.142	7.6309		
Total	35	435.741			

Appendix E Fractography

The fractography SEM images of the tensile bars for Type 316L 0.75 kg/hr and Type 316L 3.00 kg/hr are shown in Fig. E.1-4, and Fig. E.5-8, respectively.

Table E.1 Fractography SEM micrographs for Type 316L 0.75 kg/hr, HHI, H3.

	LIT	HIT	CRYO
H3 (x30)	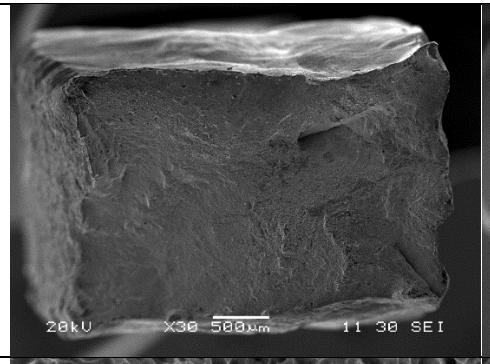	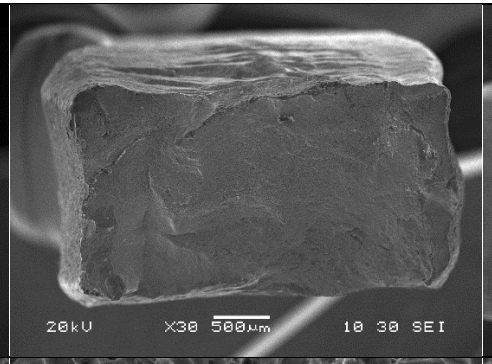	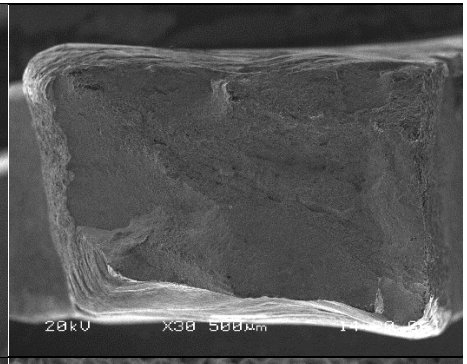
H3 (3000x)	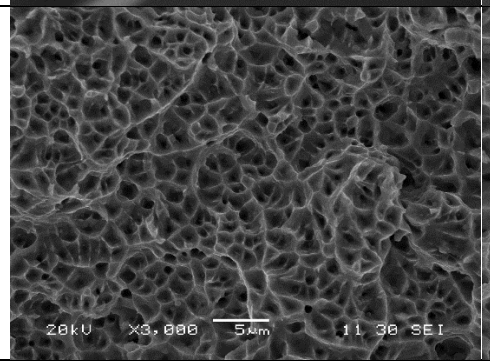	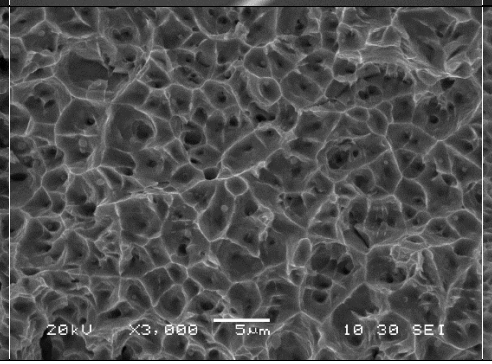	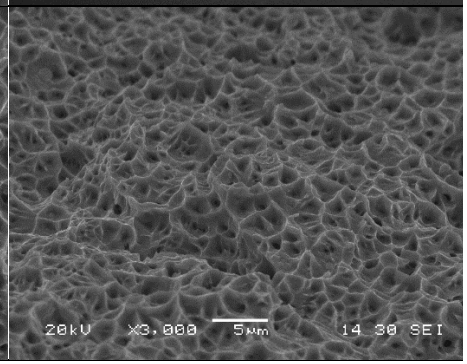

Table E.2 Fractography SEM micrographs for Type 316L 0.75 kg/hr, HHI, H1.

	LIT	HIT	CRYO
H1 (30x)	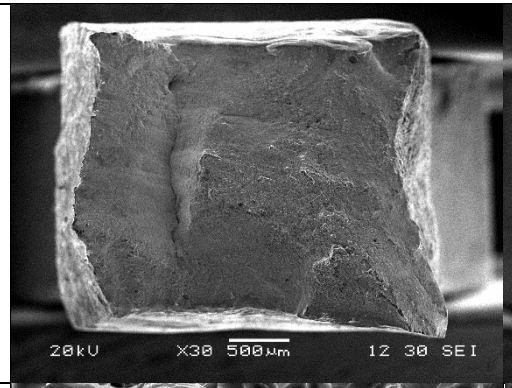	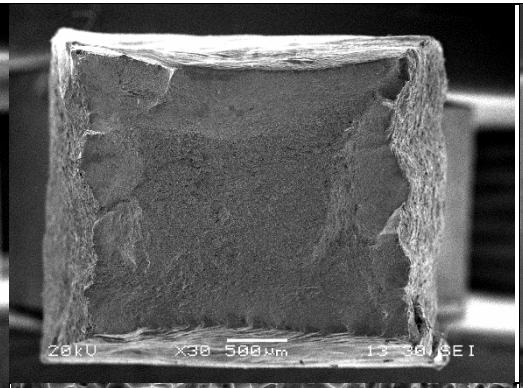	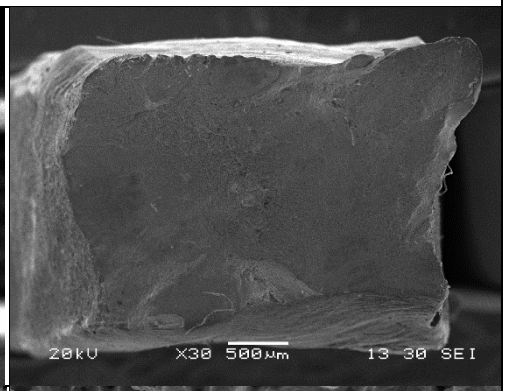
H1 (3000x)	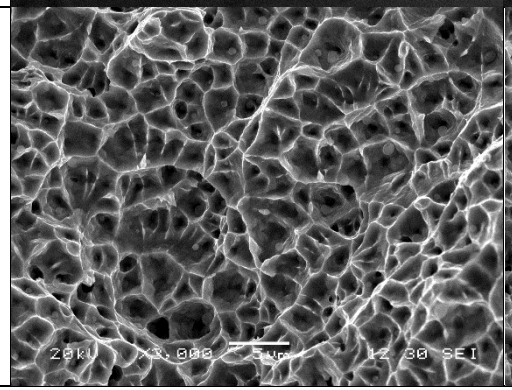	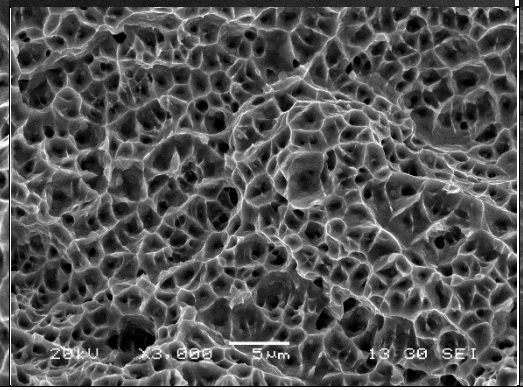	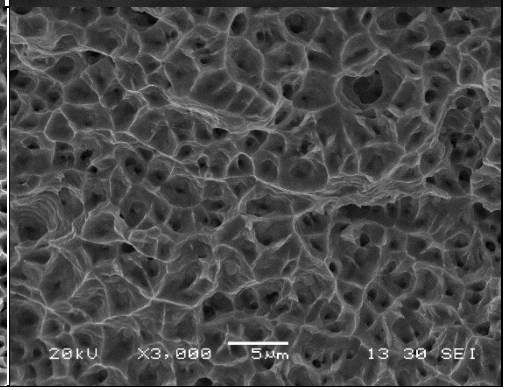

Table E.3 Fractography SEM micrographs for Type 316L 0.75 kg/hr, LHI, H3.

	LIT	HIT	CRYO
H3 (x30)	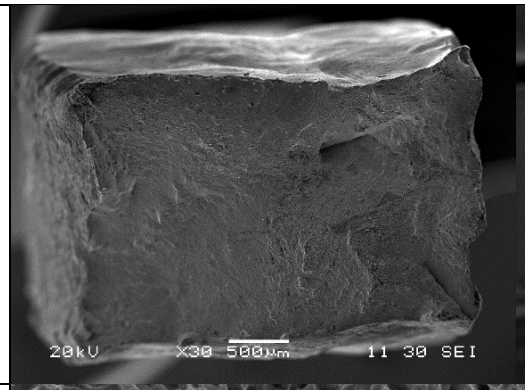	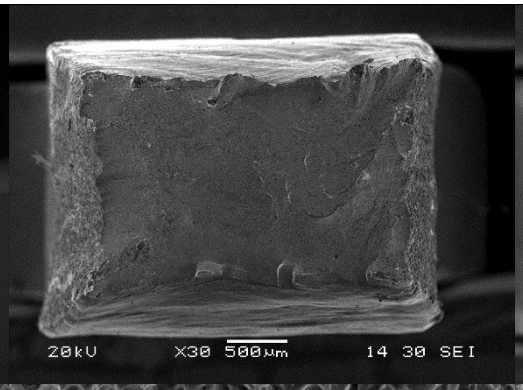	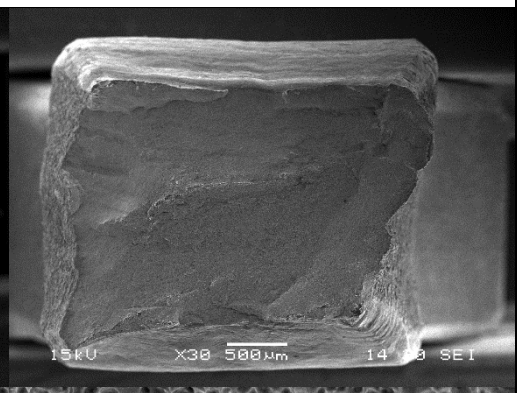
H3 (3000x)	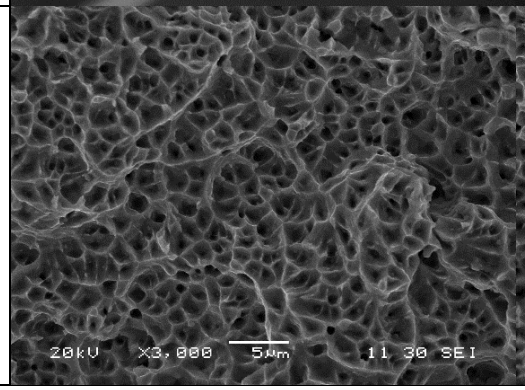	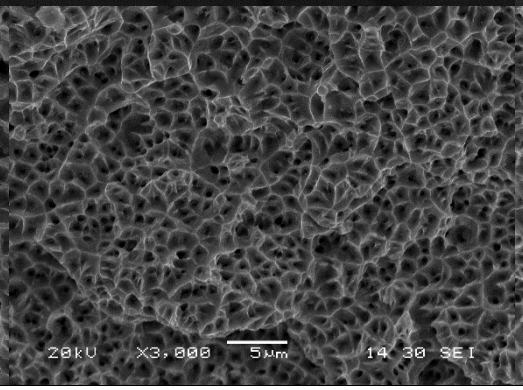	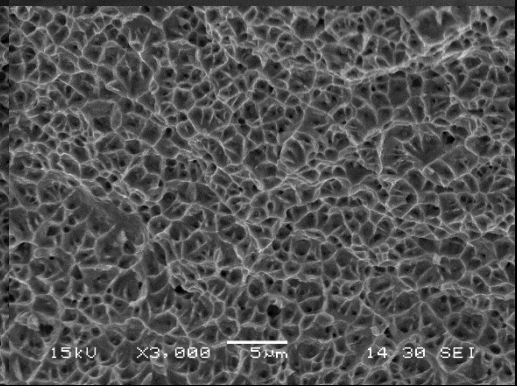

Table E.4 Fractography SEM micrographs for Type 316L, 0.75 kg/hr LHI, H1.

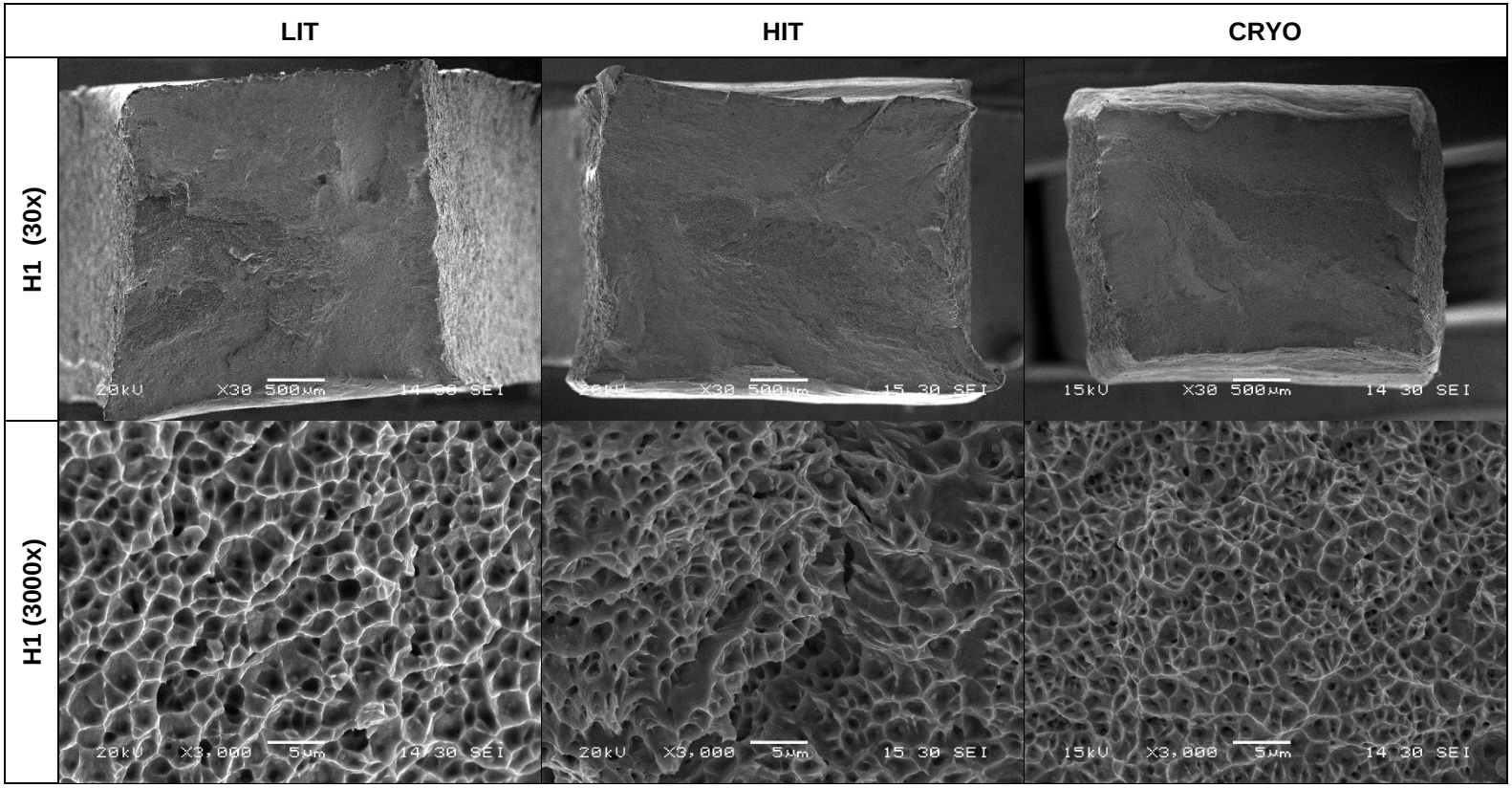

Table E.5 Fractography SEM micrographs for Type 316L 3.00 kg/hr, HHI, H3.

	LIT	HIT	CRYO
H3 (x30)	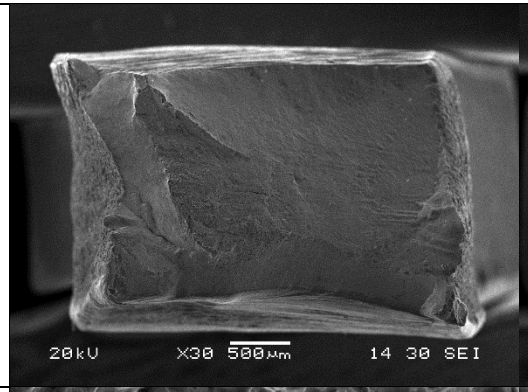	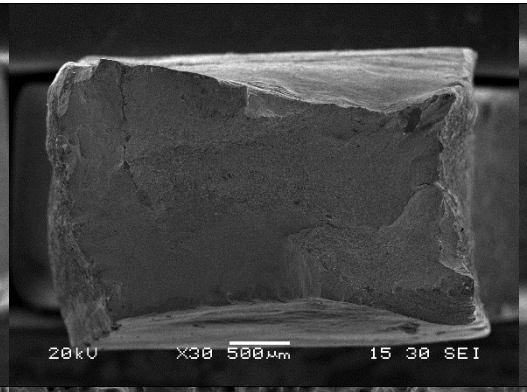	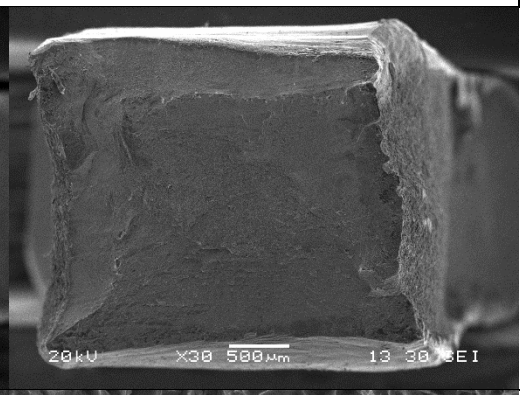
H3 (3000x)	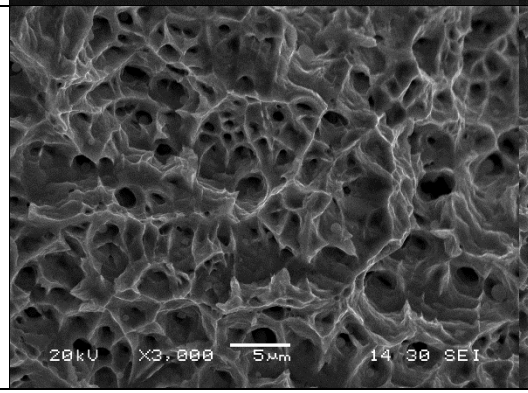	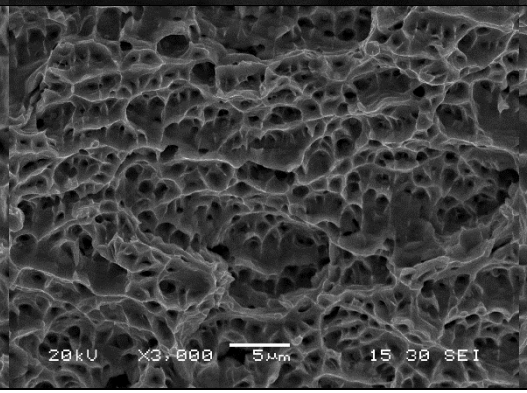	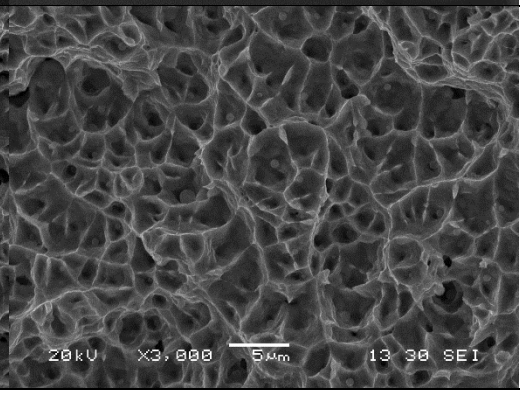

Table E.6 Fractography SEM micrographs for Type 316L 3.00 kg/hr, HHI, H1.

	LIT	HIT	CRYO
H1 (30x)	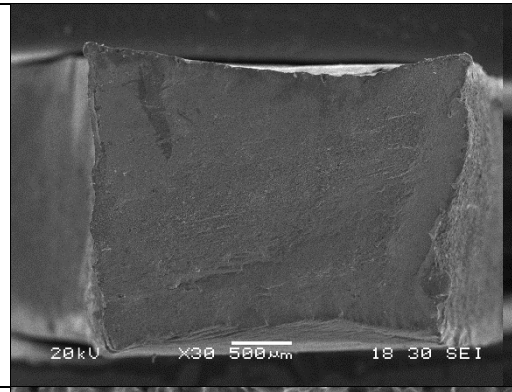	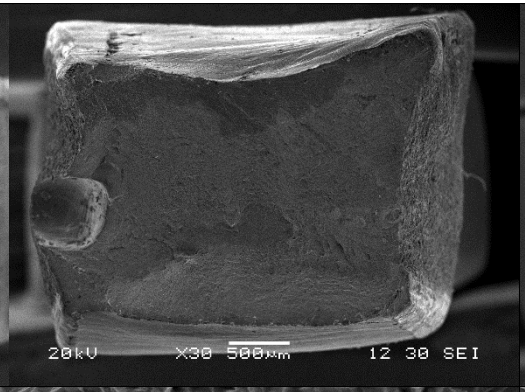	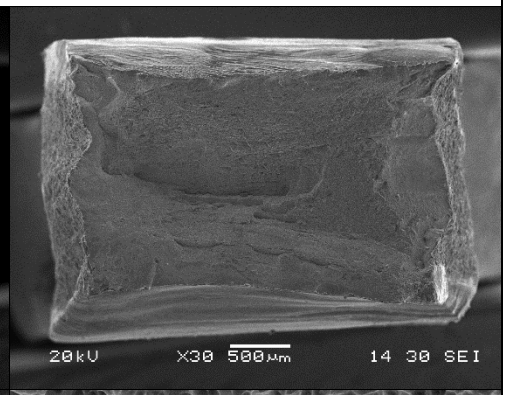
H1 (3000x)	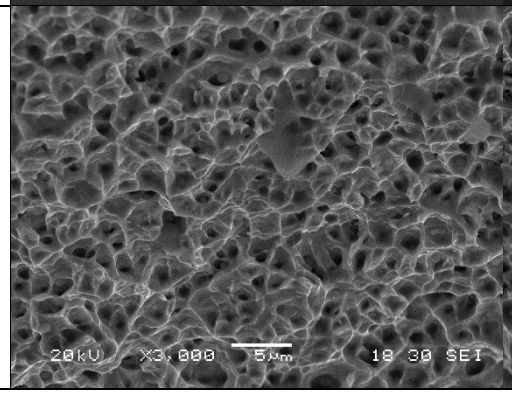	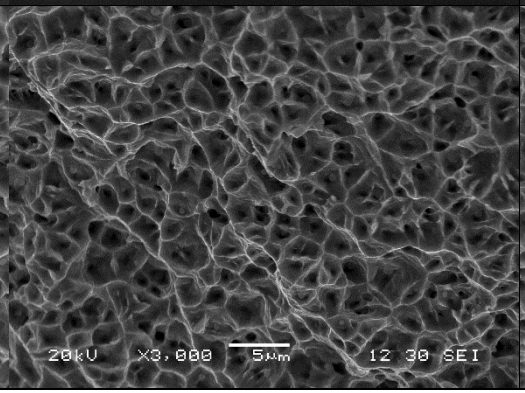	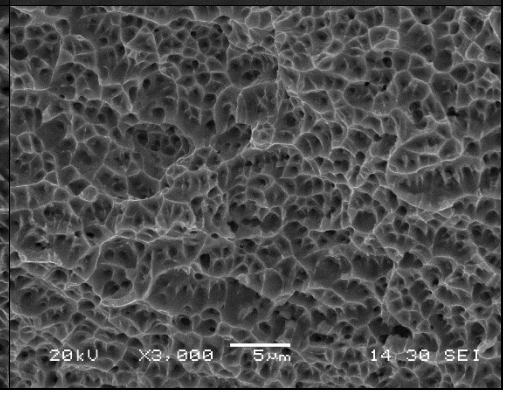

Table E.7 Fractography SEM micrographs for Type 316L 3.00 kg/hr, LHI, H3.

	LIT	HIT	CRYO
H3 (x30)	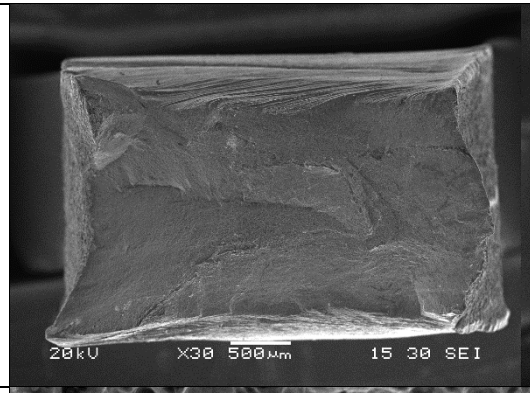	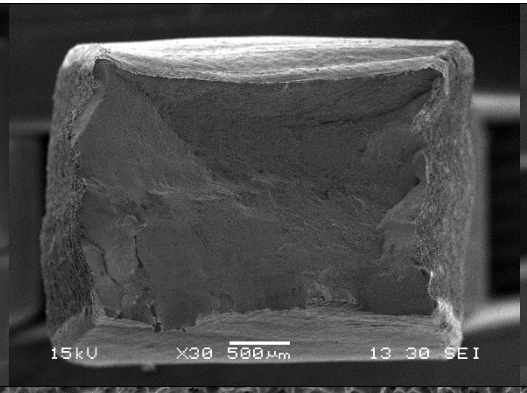	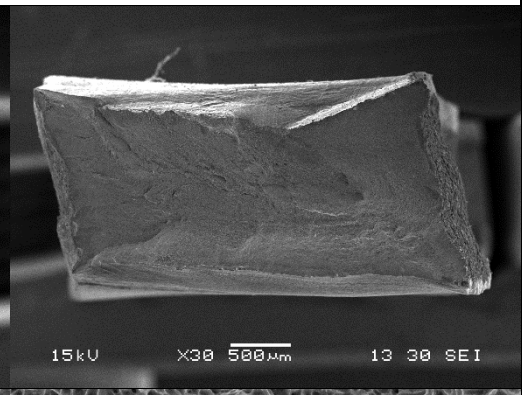
H3 (3000x)	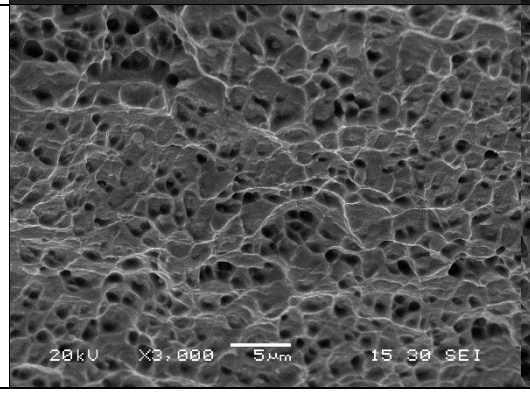	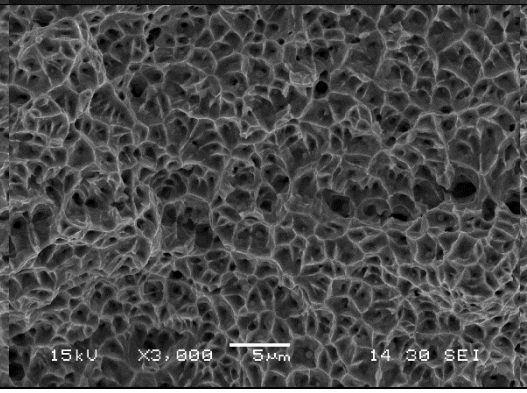	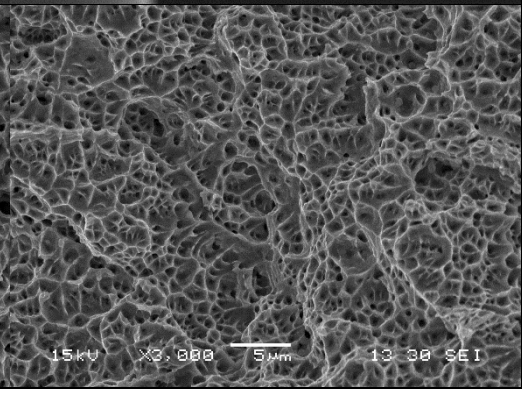

Table E.8 Fractography SEM micrographs for Type 316L, 3.00 kg/hr LHI, H1.

	LIT	HIT	CRYO
H1 (30x)	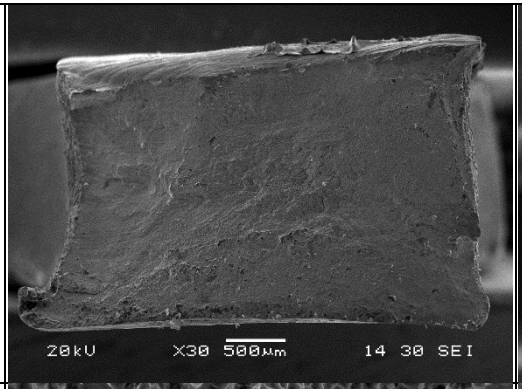	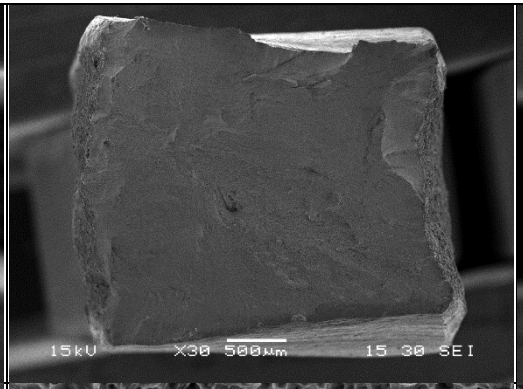	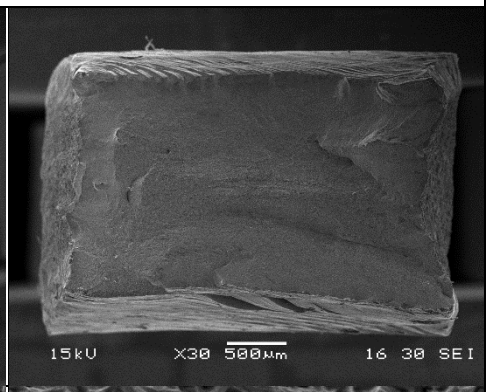
H1 (3000x)